National and Kapodistrian University of Athens

Department of Medicine

Biomedical Foundation of Academy of Athens

Study of Epithelial-to-Mesenchymal Transition via RNA-induced silencing (RISC) complex using thyroid carcinoma substrate

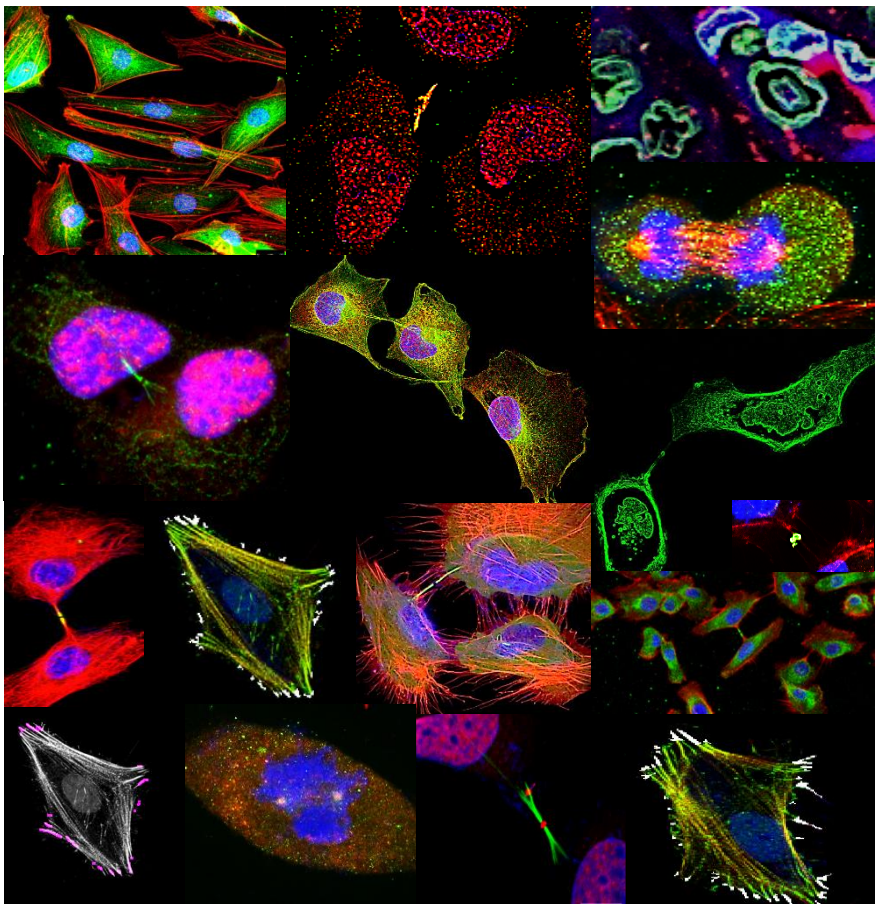

Vasiliki Pantazopoulou

Biologist

PhD thesis

Athens 2021

ΕΘΝΙΚΟ ΚΑΙ ΚΑΠΟΔΙΣΤΡΙΑΚΟ ΠΑΝΕΠΙΣΤΗΜΙΟ ΑΘΗΝΩΝ

ΣΧΟΛΗ ΕΠΙΣΤΗΜΩΝ ΥΓΕΙΑΣ

ΙΑΤΡΙΚΗ ΣΧΟΛΗ

ΤΟΜΕΑΣ ΒΑΣΙΚΩΝ ΙΑΤΡΙΚΩΝ ΕΠΙΣΤΗΜΩΝ

ΕΡΓΑΣΤΗΡΙΟ Α' ΠΑΘΟΛΟΓΙΚΗΣ ΑΝΑΤΟΜΙΚΗΣ

Διευθυντής Καθηγητής Ανδρέας Χ. Λάζαρης

ΔΙΔΑΚΤΟΡΙΚΗ ΔΙΑΤΡΙΒΗ

Μελέτη του υποστρώματος και της Επιθήλιο-Μεσεγχυματικής Μετατροπής στο θυρεοειδικό καρκίνωμα

Study of Epithelial-to-Mesenchymal Transition via RNA-induced silencing (RISC) complex using thyroid carcinoma substrate

Βασιλική Πανταζοπούλου

Βιολόγος

Αθήνα 2021

«Το έργο συγχρηματοδοτείται από την Ελλάδα και την Ευρωπαϊκή Ένωση (Ευρωπαϊκό Κοινωνικό Ταμείο) μέσω του Επιχειρησιακού Προγράμματος «Ανάπτυξη Ανθρώπινου Δυναμικού, Εκπαίδευση και Διά Βίου Μάθηση», στο πλαίσιο της Πράξης «Ενίσχυση του ανθρώπινου ερευνητικού δυναμικού μέσω της υλοποίησης διδακτορικής έρευνας» (MIS-5000432), που υλοποιεί το Ίδρυμα Κρατικών Υποτροφιών (ΙΚΥ)»

Ευρωπαϊκή Ένωση
Ευρωπαϊκό Κοινωνικό Ταμείο

Επιχειρησιακό Πρόγραμμα
Ανάπτυξη Ανθρώπινου Δυναμικού,
Εκπαίδευση και Διά Βίου Μάθηση

Με τη συγχρηματοδότηση της Ελλάδας και της Ευρωπαϊκής Ένωσης

ΕΣΠΑ 2014-2020
ανάπτυξη - εργασία - αλληλεγγύη

ΕΘΝΙΚΟ ΚΑΙ ΚΑΠΟΔΙΣΤΡΙΑΚΟ ΠΑΝΕΠΙΣΤΗΜΙΟ
ΑΘΗΝΩΝ

ΣΧΟΛΗ ΕΠΙΣΤΗΜΩΝ ΥΓΕΙΑΣ

ΙΑΤΡΙΚΗ ΣΧΟΛΗ

ΤΟΜΕΑΣ ΒΑΣΙΚΩΝ ΙΑΤΡΙΚΩΝ ΕΠΙΣΤΗΜΩΝ

ΕΡΓΑΣΤΗΡΙΟ Α' ΠΑΘΟΛΟΓΙΚΗΣ ΑΝΑΤΟΜΙΚΗΣ

Διευθυντής Καθηγητής Ανδρέας Χ. Λάζαρης

ΔΙΔΑΚΤΟΡΙΚΗ ΔΙΑΤΡΙΒΗ

Μελέτη του υποστρώματος και της Επιθήλιο-Μεσεγχυματικής Μετατροπής στο θυρεοειδικό καρκίνωμα

Study of Epithelial-to-Mesenchymal Transition via RNA-induced silencing (RISC) complex using thyroid carcinoma substrate

Βασιλική Πανταζοπούλου

Βιολόγος

Αθήνα 2021

«Το έργο συγχρηματοδοτείται από την Ελλάδα και την Ευρωπαϊκή Ένωση (Ευρωπαϊκό Κοινωνικό Ταμείο) μέσω του Επιχειρησιακού Προγράμματος «Ανάπτυξη Ανθρώπινου Δυναμικού, Εκπαίδευση και Διά Βίου Μάθηση», στο πλαίσιο της Πράξης «Ενίσχυση του ανθρώπινου ερευνητικού δυναμικού μέσω της υλοποίησης διδακτορικής έρευνας» (MIS-5000432), που υλοποιεί το Ίδρυμα Κρατικών Υποτροφιών (ΙΚΥ)»

Ευρωπαϊκή Ένωση
Ευρωπαϊκό Κοινωνικό Ταμείο

Επιχειρησιακό Πρόγραμμα
Ανάπτυξη Ανθρώπινου Δυναμικού,
Εκπαίδευση και Διά Βίου Μάθηση
Με τη συγχρηματοδότηση της Ελλάδας και της Ευρωπαϊκής Ένωσης

ΕΣΠΑ 2014-2020
ανάπτυξη - εργασία - αλληλεγγύη

Η παρούσα διδακτορική διατριβή εκπονήθηκε στο Εργαστήριο Α' Παθολογικής Ανατομικής της Ιατρικής Σχολής του Εθνικού και Καποδιστριακού Πανεπιστημίου Αθηνών υπό την επίβλεψη της Ομότιμης Καθηγήτριας Σοφίας Τσελένη-Μπαλαφούτα. Το πειραματικό μέρος πραγματοποιήθηκε στο Κέντρο Βασικής Έρευνας του Ιδρύματος Ιατροβιολογικών Ερευνών της Ακαδημίας Αθηνών (ΙΙΒΕΑΑ) κατά το χρονικό διάστημα Ιούλιος 2016 – Απρίλιος 2021 στο εργαστήριο της Ερευνήτριας Γ' Ευανθίας Αναστασιάδου.

Ημερομηνία αίτησης υποψηφίου: 03.06.2016

Ημερομηνία ορισμού τριμελούς συμβουλευτικής επιτροπής: 22.07.2016

Ημερομηνία αίτησης αντικατάστασης μέλους της τριμελούς επιτροπής παρακολούθησης της διατριβής (λόγω προαγωγής της εργαστηριακής επιβλέπουσας Ευανθίας Αναστασιάδου σε Ερευνήτρια Γ'): 22.01.2021 (Α.Π. 3704)

Ημερομηνία ορισμού θέματος: 02.09.2016

Ημερομηνία αίτησης συγγραφής και υποστήριξης της διατριβής στην αγγλική γλώσσα: 20.07.2020 (Α.Π. 1920030983)

<u>Τριμελής συμβουλευτική επιτροπή:</u>

1. Δρ. **Σοφία Τσελένη-Μπαλαφούτα** (Επιστημονική Υπεύθυνη), Ομότιμη Καθηγήτρια, Ιατρική Σχολή, ΕΚΠΑ
2. Δρ. **Ευανθία Αναστασιάδου** (Επιστημονική Επιβλέπουσα), Ερευνήτρια Γ', ΙΙΒΕΑΑ
3. Δρ. **Δημήτριος Στραβοπόδης** (Επιστημονικός Συνεπιβλέπων), Αναπληρωτής Καθηγητής, Τμήμα Βιολογίας, ΕΚΠΑ

Στους γονείς μου, *Γιάννη και Βάσω*

Όσο μπορείς

Κι αν δεν μπορείς να κάμεις την ζωή σου όπως την θέλεις,
τούτο προσπάθησε τουλάχιστον
όσο μπορείς: μην την εξευτελίζεις
μες στην πολλή συνάφεια του κόσμου,
μες στες πολλές κινήσεις κι ομιλίες.

Μην την εξευτελίζεις πηαίνοντάς την,
γυρίζοντας συχνά κι εκθέτοντάς την
στων σχέσεων και των συναναστροφών
την καθημερινήν ανοησία,
ως που να γίνει σα μια ξένη φορτική.

Κ.Π. Καβάφης, *Ποιήματα,* τόμ.1, Ίκαρος

One of the hardest lessons in life

is letting go.

Whether it's guilt,

anger, love or loss.

Change is never easy,

You fight to hold on and you fight to let go.

Kahlil Gibran

ΕΥΧΑΡΙΣΤΙΕΣ

Για όσους είναι “δρομείς αντοχής”, η διδακτορική διατριβή σημαίνει πάντα πολύ περισσότερα από έναν τίτλο. Αυτός ο τερματισμός μοιάζει περισσότερο με αφετηρία… γράφοντας -με κάποια συγκίνηση ομολογώ- το ευχαριστήριό μου προς όλους, όσοι στάθηκαν στο πλάι μου όλα αυτά τα χρόνια και στους οποίους οφείλω πολλά. Στην πραγματικότητα, η σελίδα αυτή, έχει γραφτεί πολλές φορές στο μυαλό μου ως το αποτέλεσμα μιας νοερής άσκησης ολοκλήρωσης αυτής της μακράς, επίπονης, συναδελφικής, συντροφικής αλλά ταυτόχρονα απίστευτα μοναχικής προσπάθειας από μέρους μου, να περατώσω μια πειραματική και συγγραφική πορεία που να αφήνει ένα αξιοπρεπές αποτύπωμα. Το ευχαριστήριο αυτό σημείωμα εκφράζει ένα ελάχιστο μέρος της ευγνωμοσύνης που αισθάνομαι για όλους τους ανθρώπους που συνέβαλαν σ ’αυτό το πόνημα.

Το πρώτο θερμό ευχαριστώ δικαιωματικά το οφείλω στην επιστημονική μου υπεύθυνη μου, ομότιμη καθηγήτρια Δρ. Σοφία Τσελένη-Μπαλαφούτα, για την αμέριστη στήριξη και την πολύπλευρη συμπαράστασή της σε κάθε στάδιο αυτού του εγχειρήματος εκφράζοντας πάντα έναν αξιοθαύμαστο ενθουσιασμό για την επιστήμη και με την αντιληπτική ματιά βιολόγου στις πειραματικές διαδικασίες, αποτέλεσε και αποτελεί για μένα αστείρευτη έμπνευση. Την ευχαριστώ θερμά για την ακέραια εμπιστοσύνη που μου έδειξε, την καθοδήγηση της, τις ανεξάντλητες ιδέες της και τον πολύτιμο χρόνο της.

Οφείλω ένα πολύ μεγάλο ευχαριστώ στην επιστημονική επιβλέπουσά μου, Ερευνήτρια, Δρ. Έμα Αναστασιάδου για τη διαρκή επιστημονική καθοδήγηση που μου παρείχε, την στήριξη και την εμπιστοσύνη που μου έδειξε σε κάθε πτυχή της πολυετούς συνεργασίας μας, για τις πολύτιμες ευκαιρίες που μου προσέφερε σε τομείς της έρευνας και της διδασκαλίας, για την ελευθερία και το σεβασμό που επέδειξε στις ερευνητικές επιλογές μου και κυρίως για όλες τις φορές που, υπό τη διακριτική εποπτεία της, με πέταξε μεσοπέλαγα για να μάθω να κολυμπάω. Την ευχαριστώ, επίσης, για τις ατελείωτες συζητήσεις μας -εφαλτήριο βελτίωσής μου- και για την ευκαιρία που μου έδωσε να συνεργαστώ με άλλους έγκριτους επιστήμονες στην Ελλάδα και στην Ευρώπη δίνοντάς μου την ελπίδα πως όπου κι αν βρεθώ θα μπορώ να σταθώ και να αλληλεπιδράσω.

Θα ήθελα, επίσης, να ευχαριστήσω το έτερο μέλος της τριμελούς συμβουλευτικής επιτροπής, Αναπληρωτή καθηγητή Δρ. Δημήτριο Στραβοπόδη, για την κριτική του ματιά και τις επισημάνσεις του, για την επιστημονική στήριξη που αφειδώς μου παρείχε, ήδη από τα πρώτα φοιτητικά χρόνια, για την προτροπή να κάνω διδακτορικό, για την κατανόηση με την οποία διαχειρίστηκε κάθε μου απορία ή σκέψη, για τη σχολαστικότητα και την επιμέλεια με την οποία έσκυψε πάνω από την ερευνητική μου εργασία.

Ευχαριστώ πολύ, επίσης, τον Ερευνητή Δρ. Σταμάτη Παγκάκη, Ερευνητή Δρ. Σαράντη Γκάγκο και τη Δρ. Ελένη Ρηγανά για την πολύ δημιουργική και παραγωγική συνεργασία που είχαμε όλα αυτά χρόνια, η οποία απέδωσε καρπούς.

Θα ήθελα να εκφράσω ένα μεγάλο ευχαριστώ στα μέλη της επταμελούς μου επιτροπής, τον Καθηγητή Νικόλαο Καβαντζά, τον Αναπληρωτή Καθηγητή Γιώργο Αγρογιάννη, τον Ερευνητή Α΄ Δρ. Δημήτριο

Κλέτσα και τον Ερευνητή Δρ. Γιώργο Παυλόπουλο για την καθοδήγησή τους και για τον πολύτιμο χρόνο τους.

Ευχαριστώ θερμά τους φίλους και συνεργάτες μου στο εργαστήριο, αλλά και στα αδελφά εργαστήρια. Ιδιαίτερα τη φίλη και συνεργάτιδα Δρ. Στέλλα Γεωργίου που μαζί κάναμε αυτό το ταξίδι και για την αμέριστη στήριξη, αμιγώς επιστημονική (αποτελέσματα, δημοσιεύσεις) και ψυχολογική, καθ' όλη τη διάρκεια αυτής της διαδρομής. Ευχαριστώ θερμά, επίσης το Δρ. Αναστάσιο Δελή για τη σημαντικότατη συνεισφορά του σε διαφορετικές πτυχές εκπόνησης της εργασίας αυτής και στην βελτίωση της παρουσίασης των αποτελεσμάτων και όχι μόνο.

Ευχαριστώ θερμά, επίσης, τη Βίκυ Φίλιππα, τη Χριστίνα Διαμάντη, Νικόλα Καλαβρό, Πάνο Κακουλίδη και τον Βασίλη Πιέρρο για τις γόνιμες επιστημονικές «μεταφραστικές» συζητήσεις και τη συμβολή τους στα αποτελέσματα, στις αναλύσεις, στις δημοσιεύσεις και στην οπτικοποίηση της διατριβής μέσω βιοπληροφορικών και βιολογικών εργαλείων. Ένα μεγάλο ευχαριστώ στην Ανδριάνα Ακτύπη που περάσαμε πολλά από τα χρόνια μαζί στο εργαστήριο, δημιουργώντας μια πολύ όμορφη σχέση και αλληλεπιδρώντας με πολύ εποικοδομητικό τρόπο. Αυτά τα χρόνια στο εργαστήριο, συνάντησα αξιόλογους επιστήμονες. Οι Βάσω Ταρασλιά, Κωνσταντίνα Βεϊογλάνη, Φαίη Χριστοδούλου, Χριστίνα Λιγνού, Στέλιος Τσαγκρής, Λυδία Κονδυλιού, Μαρία Λαλά, Εριφύλη Λιανοπούλου, Αλέξανδρος Καραγιαννάκος, Δέσποινα Δημάκου, Σταυρούλα Γιαννακοπούλου, Αναστασία Καραντζά, Χαρά Μακρή και Γιούλη Χατζήσαρρου, μαζί με τους φίλους μου από τα διπλανά αδελφά εργαστήρια, αξίζουν ένα εγκάρδιο ευχαριστώ για όλες εκείνες τις φορές που ξενυχτήσαμε παρέα, για αυτά που ανακαλύψαμε μαζί, για τις ατέλειωτες συζητήσεις και αναζητήσεις μας. Πόσα έμαθα από σας και πόσο με χαροποιεί η πορεία σας.

Ένα τεράστιο ευχαριστώ στους φίλους μου, εντός και εκτός κλάδου, που με στήριξαν σε όλη τη διάρκεια της προσπάθειάς μου, χαίρονταν με την πορεία μου, ήταν εκεί όποτε τους χρειαζόμουν και έδειχναν απεριόριστη κατανόηση κάθε φορά που ο όγκος της δουλειάς με ανάγκαζε να επιλέγω τη «σιωπή ασυρμάτου» αλλά και κάθε φορά που τραγουδούσα για την απόσβεση των κραδασμών κι ας τους κούραζα.

Η ολοκλήρωση της διδακτορικής μου διατριβής, βεβαίως, θα ήταν κυριολεκτικά αδύνατη χωρίς την υλική, ηθική και έμπρακτη συμπαράσταση της οικογένειάς μου. Αν και δεν συνηθίζω να το εκφράζω, οφείλω ένα πολύ μεγάλο ευχαριστώ και ευγνωμοσύνη στους γονείς μου, Γιάννη και Βάσω, που με έκαναν πάντα να νιώθω την αδιαπραγμάτευτη αγάπη τους, με έκαναν να αγαπήσω, ανεπιτήδευτα, το διάβασμα και την αναζήτηση/αμφισβήτηση -βασικό συστατικό ενός βιολόγου- και να νιώσω ότι έχω κάπου καλά να ακουμπήσω. Μέσα στο ταξίδι αυτό, η απώλειά σου, μπαμπά, με δίδαξε και το πώς είναι να χάνεις ένα καταφύγιο, αλλά να μπορείς να σταθείς αξιοπρεπώς και χωρίς αυτό. Ευχαριστώ, από την καρδιά μου, τα αδέρφια μου Σοφία και Ανδρέα, για όλα όσα κάνουν για μένα, και κυρίως για την αγάπη και τη βαθιά πίστη τους σε μένα, βασικά συστατικά που, όπως αντιλαμβάνομαι μεγαλώνοντας, έχουν δημιουργήσει μέσα μου πολύ μεγάλα αποθέματα δύναμης και αντοχής. Τους ευχαριστώ για έναν ακόμα λόγο. Παρότι ήταν σχεδόν απίθανο να καταλάβουν εις βάθος το ιδιαίτερο αντικείμενό μας, έμαθαν να κάνουν προσπάθεια να το κατανοήσουν και χαίρονταν με τα αποτελέσματα αυτής της πορείας ακόμα κι όταν ήταν -για μένα- ελάσσονος σημασίας.

Θέλω να γράψω δυο λόγια για τη βαθιά ευγνωμοσύνη στον σύντροφό μου, τον Σώτο, ο οποίος έκανε βουτιά μαζί μου σε αυτήν την περιπέτεια και υπερασπίστηκε σθεναρά και χωρίς δεύτερη σκέψη, την «ασύμφορη» επιλογή της εκπόνησης μιας διδακτορικής διατριβής, με όλες τις θυσίες που αυτή προϋπέθετε. Πάντα είχαν πλάκα τα αστεία σε σχέση με αυτό και ίσως όντως να άξιζε να του χαρίσω μισό τίτλο. Τον ευχαριστώ για τη διαρκή συμπαράσταση και συνοδοιπορία σε κάθε είδους χαρά και δύσκολο γεγονός που συνόδευσε όλα αυτά τα χρόνια αλλά και τα προηγούμενα από αυτά και για τη εκλογικευμένη θεώρησή του που δίνει νόημα στα «καθημερινά» μου, ακόμα κι όταν αυτό τείνει να χαθεί από το συναίσθημα.

Ελπίζω κι εύχομαι να φανώ αντάξια της στήριξης όλων αυτών των ανθρώπων και να καταφέρω, όσο μπορώ, με σοβαρότητα και επιδεξιότητα να κινηθώ μεταξύ διαφορετικών και απαιτητικών ρόλων στη ζωή και να συμβάλλω σε μικρές ανακαλύψεις στην παγκόσμια κοινότητα.

Abbreviations	Explanation
AGO1	Argonaute protein 1
AGO2	Argonaute protein 2
AGO3	Argonaute protein 3
AGO4	Argonaute protein 4
AGOs	Argonaute proteins
AITD	Autoimmune thyroid disease
ALIX	Apoptosis-linked gene 2-interacting protein
AMAS ring	Rho-dependent actomyosin-anillo-septin membrane-anchored ring
AMOs	anti-miRNA Oligonucleotides
anti-TPO	antithyroid peroxidase
APC	Adenomatous polyposis coli
ATC	Anaplastic thyroid carcinoma
AURB	Aurora B
CASTLE	Carcinoma showing thymus-like differentiation/intrathyroidal epithelial thymoma
CCH	C-cell hyperplasia
CEP55	Centrosomal protein of 55 kDa
CITK	Citron kinase
CNS	Central nervous system
C-PTC	Common or classical variant of papillary thyroid carcinoma
DDR	DNA-damage response
DFS	Disease-free survival
DGCR8	DiGeorge Syndrome Critical Region 8 RNA binding protein
diRNAs	Double strand break induced small RNAs
DSBs	Double strand brakes
DSS	Decision support system
DTC	Differentiated thyroid cancer
EIF1AX	Eukaryotic translation initiation factor 1A
EMT	Epithelial–mesenchymal transition
ER-stress	Endoplasmic Reticulum Stress
ESCRT	Endosomal sorting complex required for transport
FAK	Focal adhesion kinase
FNA	Fine Needle Aspiration
FOX	Fork head box
FTC	Follicular thyroid carcinoma
FT-UMP,	Follicular tumor of uncertain malignant potential
FVPTC	Follicular variant of papillary thyroid carcinoma
h	Hours
H&E	Hematoxylin and eosin
HCC	Hepatocellular carcinoma

HIF1α	Hypoxia induced factor 1α
HITS-CLIP	High-throughput sequencing of RNA isolated by crosslinking immunoprecipitation
HR	Homologous recombination
HRMs	Hypoxia-responsive microRNAs
MEN 2	Multiple endocrine neoplasia 2
MET	Mesenchymal-to-epithelial transition
mimic miR	Mimic sequence of a microRNA
min	Minutes
miR	microRNA
mir SNPs	miRNA-binding seed region
MREs	miRNA recognition elements
MTC	Medullary thyroid carcinoma
MVD	micro-vessel density
NIFTP	Non-invasive follicular thyroid neoplasm with papillary nuclear features
OS	Overall survival
PAX8	Paired Box 8
PDTC	Poorly differentiated thyroid tumors
PLK4	Polo-like kinase 4
PNST	Peripheral nerve sheath tumor
PPARγ	PAX8-peroxisome proliferator activated receptor γ
pseudo	Pseudoinclusions
PTBP3	Polypyrimidine Tract Binding Protein 3
PTC	Papillary thyroid carcinoma
RARE	Retinoic acid response element
RISC	RNA-induced silencing complex
RNAi	RNA interference
RNP	Ribonucleoprotein enzyme
sec	Seconds
siRNA	small interference RNA
T3	triiodothyronine
T4	thyroxine
TCV	Tall cell variant
TERT	Telomerase reverse transcriptase
TRBP	TAR RNA-binding protein
TRH	Thyroid releasing hormone
TSAb	Thyroid stimulating antibody
TSG101	Tumor susceptibility gene 101
TSI	Thyroid stimulating immunoglobulin
TTF-1	Thyroid transcription factor 1

WDT-UMP	Well-differentiated tumor of uncertain malignant potential
HT	Hashimoto

Vasiliki Pantazopoulou

Curriculum Vitae

PERSONAL DATA

Date of birth	09.March.1989
Contact	(+30)6970619490, vasopantazo20@hotmail.com
LinkedIn profile	linkedin.com/in/vasiliki-pantazopoulou-9b21b089
Citizen	Athens, Greece

EDUCATION

2016-present

Ph.D. in **Molecular and Cellular Biology of Cancer**

National and Kapodistrian University of Athens, Dept. of Medicine, Greece

2014-2015

M.Sc. in **Biology-Medicine, "Applications of Biology in Medicine**

National and Kapodistrian University of Athens, Dept. of Biology & Medicine, Greece

2007-2012

B.Sc. in **Biology**

National and Kapodistrian University of Athens, Dept. of Biology, Greece

WORK EXPERIENCE

2016-present

Ph.D. candidate in Cancer Genetics

Thesis Title: "Study of Epithelial to Mesenchymal Transition via RNA-induced silencing (RISC) complex using thyroid carcinoma substrate", Biomedical Research Foundation of the Academy of Athens (BRFAA)

- Research on physiological and pathological role of RISC complex and cellular responses during mitosis.
- Molecular analysis of human thyroid cancer cell lines, human surgical specimens (cancerous and healthy adjacent tissue) and mouse model tissues.
- Meta-analysis and statistical analysis of patient medical records.
- Research on potential biomarkers (mRNAs, microRNAs) for diagnostic and therapeutic approaches
- Communicate effectively with the other study team members (bioinformaticians, mathematicians, physicians and biologists) at local and global level
- Build and maintain scientific and medical relations with External Experts – Key Opinion Leaders
- Analyze data to develop insights and communicate to publications

- Problem solving abilities, multitasking, attention to detail and adaptability

01.2016-07.2020

Research assistant in GALAXY molecular profiling of biopsies (Grant No 668031), EU Research and Innovation program Horizon 2020 (top rate 0,5%), "GALAXY: Gut-and-liver axis in alcoholic liver fibrosis", *Biomedical Research Foundation of the Academy of Athens (BRFAA), Greece*

In the current position my responsibilities include:

- Build peer-to-peer relationships and provide scientific information to respond to questions about liver transcriptomics
- Deliver presentations at national and international meetings and conferences to medical doctors, internal and pharmaceutical company stakeholders and external audiences
- Advanced clinical and scientific knowledge in liver, patient-oriented molecular profiling of the tumor and disease management

09.2011-12.2014

Private employee

Diagnostics center "Plusma", Nea Ionia, Greece.

- Molecular diagnostics: prenatal diagnostics (sequencing for cystic fibrosis, CVD test), sexual transmitted diseases diagnosis and analyses of genetic and autoimmune diseases

01.2010-03.2010

B.Sc. Degree

Dissertation Title: "The role of eisosomes in topogenesis and endocytosis of transmembrane transporters in A. *nidulans."*

- Genetic crossings for studying the role of deletions of eisosomes on endocytosis of proline and glutamic/ aspartic acid transmembrane transporters in A. *nidulans*.

OTHER WORK EXPERIENCE

11.2020-present

Invited lecture on 'Introduction to Biology: RNA world' cou
Master's Program "Data Science and Information Technologie
National and Kapodistrian University of Athens (Dept. of Telecommunications) in collaboration with the BRFAA and the ATHEI Innovation Center, Athens, Greece

2009-2018

Biology Tutor in Primary & High school

SKILLS

- Liaising between clinicians and data scientists, encouraging teamwork and colleague interaction as well as working independently
- Grant, Proposals and Technical Writing
- Aptitude to combine, analyze and present data clearly and concisely
- Ability to multitask and work in a fast-paced environment
- Excellent organizational skills including attention to detail and prioritization
- Organization of lab meetings and conferences in BRFAA
- Significant team/people management experience
- Ensure high standard of professionalism to develop and maintain “peer-to-peer” scientific relationships with key opinion leaders in academia

Experimental methodologies and techniques

Nucleic acid isolation and analysis; recombinant DNA techniques; Real-time quantitative PCR; Polymerase Chain Reactions (multiple pcr, nested pcr, RT-PCR, ARMS); Crosslinking immunoprecipitation coupled with high-throughput sequencing (HITS-CLIP); Line-probe assay (LiPA)-Detection technique (quality) of specific sequences in PCR products based on reverse hybridization-; Western blotting; Classical genetics, reverse genetics, growth tests, auxotrophy selection; Mouse handling - Tissue sampling; Histology techniques; Advanced Microscopy techniques; Bright-field and confocal laser microscopy; Immunofluorescence; Passive hemagglutination; Cell cultures; Transfections (stable) of mammalian cell cultures; Sequencing; 3D/4D Visualization, Imaris Image; Analysis Isolation of plasmid DNA on small, medium or large scale (miniprep, midiprep, maxiprep); RNA in situ hybridization; Wound healing assay; Proximity ligation assay; Other software: Image J Fiji, Adobe Illustrator, Cytoscape; knowledge of bioinformatic tools Kegg, Gene Ontologies, Blast, Ensemble, NCBI, INtact, Bioedit, Ilastik, End Note, Imaris; Scientific paper and report writing

SCHOLARSHIPS/ DISTINCTIONS

- State Scholarships Foundation (IKY) (2018-2021)
- Research Fellowship Horizon 2020 (2017-2018)
- Alpha Bank Fellowship (travel grant 2018)
- Chair-Coordination of the oral presentation "IGEM 2018-2019", 7th Forum of Young Scientists

WORKSHOPS / SEMINARS

2017-2021: Has participated in 6 workshops in Greece, France and Denmark
10.2020–02.2021: Postgraduate Training Program - Training Program "Scientific Writing in Health Sciences", Athanasios Tsakris (150 hours), School of Medicine

CONFERENCE PARTICIPATIONS

2011-2021: Has been an invited speaker/ poster in more than 11 international/ national conferences (11 posters and 6 oral presentations)

LANGUAGES

- English: excellent
- Greek: native

MANAGEMENT AND ORGANIZATION

- Organization, supervision, diligence and coordination of BRFAA conferences
- Organizing of meetings and presentations in the lab (lab meetings)
- Accreditation of management procedures (ISO15189)
- Evaluation by the Head of the Molecular Diagnostics lab with the title of “Excellent collaboration” (Plusma)

SOCIAL SKILLS/VOLUNTEERING

Volunteer in the "smile of the child", Corinth Branch
Volunteer at the Museum of Natural History NKUA (storage and conservation of fossils and shellfish)

PARTICIPATION IN ARTS AND SPORTS

- Selection and distinction in singing for 9 consecutive years
- Ranked 2nd in endurance races (high school)
- 1st medal in bicycle races (high school)
- 1st medal in Music song competition
- School volleyball team (participation in local games)
- Swimming & Paint ball
- Collections of books

List of Publications

- Pantazopoulou V.I., Delis A.D., Georgiou S., Pagakis S.N., Filippa V., Kloukina I., Chatzitheodoridis E., Trebicka J., Velentzas A.D., Thiele M., Dragona E., Gagos S., Thanos D., Tseleni-Balafouta S., Stravopodis D.J., and Anastasiadou E., "AGO2 localizes to cytokinetic protrusions in a p38-dependent manner and is needed for accurate cell division.", (2021), *Communications Biology* (accepted), zenodo online source: https://zenodo.org/record/4415734#.YDvjOWgzbIU.
- Aikaterini F. Giannopoulou, Athanassios D. Velentzas, Athanasios K. Anagnostopoulos, Adamantia Agalou, Nikos C. Papandreou, Stamatia A. Katarachia, Dimitra G. Koumoundourou, Eumorphia G. Konstantakou, Vasiliki I. Pantazopoulou, Anastasios Delis, Maria T. Michailidi, Dimitrios Valakos, Dimitris Chatzopoulos, Popi Syntichaki, Vassiliki A. Iconomidou, Ourania E. Tsitsilonis, Issidora S. Papassideri, Gerassimos E. Voutsinas, Polydefkis Hatzopoulos, Dimitris Thanos, Dimitris Beis, Ema Anastasiadou, George Th. Tsangaris and Dimitrios J. Stravopodis, "From Proteomic Mapping to Invasion-Metastasis-Cascade Sys- 2 temic Biomarkering and Targeted Drugging of mutant 3 BRAF-dependent Human Cutaneous Melanomagenesis", (2021), *Cancers (under revision).*
- Maximilian Joseph Brol, Stella Georgiou, Ditlev Nytoft Rasmussen, Sabine Klein, Robert Schierwagen, Frank Erhard Uschner, Sönke Detlefsen, Vasiliki I. Pantazopoulou, Maja Thiele, Cristina Ortiz, Vasiliki Filippa, Sandra Torres, Ema Anastasiadou, Aleksander Krag, Jonel Trebicka*, "A new Western Diet and Ethanol-based Murine Model of Early-stage Metabolic Liver Disease", *Livers*, 2021, *1*(1), 27-39; https://doi.org/10.3390/livers1010003
- Theotoki EI, Pantazopoulou V.I., Georgiou S, Kakoulidis P, Filippa V, Stravopodis DJ, Anastasiadou E. Dicing the Disease with Dicer: The Implications of Dicer Ribonuclease in Human Pathologies. *International Journal of Molecular Sciences (IJMS),* 2020, doi: 10.3390/ijms21197223.
- Pantazopoulou V.I.[1], Stella Georgiou [1], Panos Kakoulidis [1], Stavroula N. Giannakopoulou [1,2], Sofia Tseleni [3], Dimitrios J. Stravopodis [2] and Ema Anastasiadou[1], "From the Argonauts Mythological Sailors to the Argonautes RNA-Silencing Navigators: Their Emerging Roles in Human-Cell Pathologies", *International Journal of Molecular Sciences (IJMS), 2020,* doi:10.3390/ijms21114007.
- S.Georgiou, V. Pantazopoulou, E. Anastasiadou "The human gut-liver axis in health and disease" Edited by Alexander Krag and Torben Hansen, *Springer Nature*, Chapter 12: "The role of microRNA in the gut-liver axis", Special Issue: Advances in Proteomic Research for the Characterization of Bioactive Molecules, *2019*, Springer, Cham & "Biology, Volume III" by Campbell NA & Reecee JB. Ed. by Moschonas NK, Crete University Press
- Vasiliki Taraslia, Stefania Lymperi, Vasiliki Pantazopoulou, Athanasios K. Anagnostopoulos, Issidora S. Papassideri, Efthimia K. Basdra, Marianna Bei, Evangelos G. Kontakiotis, George Th. Tsangaris, Dimitrios J. Stravopodis and Ema Anastasiadou: "A High-Resolution Proteomic Landscaping of Primary Human Dental Stem Cells: Identification of SHED- and PDLSC-specific

Biomarkers", *International Journal of Molecular Sciences (IJMS)*, *2018*, doi: 10.3390/ijms19010158.

Contents

SUMMARY

Malignancies of thyroid gland are the most common malignancies of the endocrine system as they account for 1-5% of all cancer cases worldwide. Papillary carcinomas (PTC) are the most common type of thyroid cancer, accounting for approximately 80% of cases, usually, with good prognosis. However, specific variants such as tall cell variants (TCV) demonstrate aggressive characteristics and poor outcome. Deep understanding of the molecular correlations and gene pathways that dictate the cell programming and therefore, the fate of the disease and the outcome of the patient is crucial for a better stratification and the development of potential treatments.

Towards that direction, we conducted a population study and analyzed the distribution of specific clinicopathological features. We revealed a strong association between TCVs and the presence of nuclear and tissue alterations such as pseudoinclusions and fibrogenesis, respectively. This was associated with deregulation of specific processes such as protein processing in ER, NFKβ, cell-cell adhesion and regulation of cytoskeleton, crucial pathways involved in Epithelial to Mesenchymal Transition (EMT). EMT is a key mechanism in cell differentiation and migration (metastasis) rearranging the location and function of structural proteins (such as molecules of the cytoskeleton) as well as molecules that ensure cell junctions (tight, focal and adherens junction). The nuclear structure and the presence of grooves, invaginations, creases and pseudoinclusions were analyzed through Advanced microscopy techniques. RNA-induced silencing complex (RISC) components such as Drosha, DGCR8, Dicer and Argonaute proteins (AGOs) were intensely present inside these structures in diffused or specific-located punctuate patterns. Strikingly, AGOs, and specifically AGO2, follow these structures demonstrating an intense signal inside and along them. AGOs "load" miRNAs and direct them to the mRNA targets for post-transcriptional gene regulation. The presence of AGO2, the foremost member of the AGO family, most likely reflects the great cellular need for tight gene regulation leading and management of local homeostasis. This fact is not surprising since local protein synthesis in response to specific molecular signals dictates the morphology, function and fate of the cells and therefore, the outcome of the disease. Conclusively, we propose that AGO2 creates a niche, the “AGO2 locasomes”, for proper local homeostasis. Anyhow, AGO2 is known to be compartmentalized into structures such as GW- and P-bodies, stress granules, adherens junctions and midbody, serving the "local" needs for post-transcriptional gene regulation. Using immunofluorescence, image analysis, bioinformatics and cytogenetics, it was demonstrated that AGO2 also resides in membrane protrusions such as open- and close-ended tubes. The open-ended are most likely intercellular channels while close-ended are cytokinetic bridges. In the latter AGO2 colocalizes at the midbody-arms with cytoskeletal components such as α-Tubulin and Aurora B and various kinases. AGO2, phosphorylated on serine 387 colocalizes with Dicer at the midbody ring on a p38 MAPK dependent manner. Further, the stress sensitivity of AGO2 was revealed and its importance for the ensurement and fidelity in chromosome segregation and cytokinetis was demonstrated. We suggested that AGO2 is part of a regulatory mechanism triggered by cytokinetic stress, aiming to generate the appropriate micro-environment for local homeostasis. In conclusion, AGO2 seems to accumulate at specific cellular structures such as pseudoinclusions, and tubular protrusions, together with other RISC components, serving the idea of AGO2 locasomes, for the restoration of the local post-transcriptional homeostasis.

To better understand the mechanisms involved, we attempted to determine the coding and non-coding genes (such as miRNAs), expressed in normal and malignant thyroid substrates. We used

High-Sequencing of RNAs isolated by Cross-Linking Immuno-Precipitation (HITS-CLIP) methodology to record the tripartite complex AGO2::miRNA::mRNA and identify the "active" miRNome, ie the set of miRNAs that bind to the RISC complex and their mRNAs targets. Informatics analysis revealed that a group of 31 deregulated miRNAs with high statistical significance, between normal and cancer cell lines. Comparative analysis based on their differential expression and their mRNA targets revealed implicated molecular pathways such as regulation of actin cytoskeleton pathway, transcriptional dysregulation in cancer, NFK-β signaling pathway and miRNAs in cancer which support the EMT.

Subsequently, we focused on specific miRNAs, such as miR26. miR26 was a promising target as (i) it has the same transcriptional behavior across different cancer cell lines, (ii) it appears to be downregulated in cancer cell lines and patient tissue samples, (iii) all the members of miR26 family have the same transcriptional profile and (iv) our results are in accordance with the literature. In *in vitro* assays, using cell lines, overexpression of miR26 leads to restriction of the oncogenic potential since its expression has a reverse correlation with the ability of cells to proliferate. In mouse xenografts, generated by FTC133 cells transfected with miR26a-5p mimicking sequences, retardation in thyroid tumor development was observed and a promotion of a peripheral and not a central -as expected- tumor necrosis. RNA-seq differential expression analysis between cells carrying mimic miR26 or scrambled sequences revealed 1,201 statistically significant deregulated genes correlated with cell cycle, apoptosis, cell division, cell adhesion and transcriptional deregulation in cancer. 133 were experimentally verified as direct targets of miR26. The 100 top-expressed genes were used for pathway analysis via PathWalks algorithm. The cluster of interest contained fundamental pathways such as cell cycle, miRNAs in cancer and aging processes. Finally, a comparative informatics analysis of HITS-CLIP and RNA-seq data uncovered 50 deregulated molecules including PAWR and STRADB. The latter are correlated with cell proliferation and fate, crucial conditions for EMT. Conclusively, miR26 and its direct targets may constitute crucial molecules for oncogenesis and promising, potential agents for diagnosis and therapy of thyroid malignancies.

ΠΕΡΙΛΗΨΗ

Οι κακοήθειες του θυρεοειδούς αδένα είναι οι πιο συχνές κακοήθειες του ενδοκρινικού συστήματος και αντιπροσωπεύουν το 1-5% όλων των περιπτώσεων καρκίνου παγκοσμίως. Τα θηλώδη καρκινώματα (PTC) είναι ο πιο κοινός τύπος καρκίνου του θυρεοειδούς, αντιπροσωπεύοντας περίπου το 80% των περιπτώσεων με, ως επί των πλείστων, καλή πρόγνωση. Ωστόσο, συγκεκριμένοι υπότυποι όπως οι υπότυποι ψηλών κυττάρων (TCV) διαθέτουν επιθετικά χαρακτηριστικά και κακή πρόγνωση. Η βαθιά κατανόηση των μοριακών συσχετίσεων και των γονιδιακών μονοπατιών που υπαγορεύουν τον προγραμματισμό των κυττάρων και επομένως, η τύχη της νόσου και η επιβίωση του ασθενούς είναι ζωτικής σημασίας. Τα αποτελέσματα από μια τέτοια ανάλυση αναμένεται να συμβάλλουν δραματικά στην καλύτερη ταξινόμηση των περιστατικών αλλά και στην ανάδειξη νέων θεραπευτικών προσεγγίσεων.

Προς αυτήν την κατεύθυνση, πραγματοποιήσαμε μια πληθυσμιακή μελέτη και αναλύσαμε την κατανομή συγκεκριμένων κλινικοπαθολογικών χαρακτηριστικών. Αποκαλύψαμε μια ισχυρή συσχέτιση μεταξύ του TCV φαινοτύπου και της παρουσίας κυτταροπλασματικών ενδοπυρηνικών δομών και ιστικών αλλοιώσεων, όπως των ψευδοεγκλείστων και της ίνωσης, αντίστοιχα. Αυτό συσχετίστηκε με απορρύθμιση συγκεκριμένων διαδικασιών όπως η επεξεργασία πρωτεϊνών στο ενδοπλασματικό δίκτυο (ER), η ενεργοποίηση του NFKβ, η κυτταρική προσκόλληση και η ρύθμιση του κυτταροσκελετού, κρίσιμων μονοπατιών που εμπλέκονται στην επιθηλιακή σε μεσεγχυματική μετάβαση (EMT), βασικό μηχανισμό για την εξαλλαγή και τη μετανάστευση των κυττάρων (μετάσταση). Οι κυτταροπλασματικές και πυρηνικές αλλοιώσεις μελετήθηκαν μέσω των αλλαγών στην τοπολογία και στη λειτουργία δομικών πρωτεϊνών, όπως μορίων του κυτταροσκελετού. Οι πυρηνικές δομές και η παρουσία αυλακώσεων, εκκολπώσεων και ψευδοεγκλείστων αναλύθηκαν μέσω προηγμένων τεχνικών μικροσκοπίας. Οι συνιστώσες του συμπλόκου RNA επαγόμενης αποσιώπησης (RISC) όπως οι Drosha, DGCR8, Dicer και Argonaute (AGO), εντοπίζονταν σε αυτές τις δομές, με διάχυτα ή ειδικά εντοπισμένα μοτίβα. Αξιοσημείωτα, οι AGOs, και ειδικότερα ο AGO2, ακολουθούν τις δομές ψευδοεγκλείστων και παρουσιάζουν έντονο σήμα μέσα και κατά μήκος των δομών αυτών. Οι AGOs «φορτώνουν» miRNAs και τα κατευθύνουν στους mRNA-στόχους για μετα-μεταγραφική γονιδιακή ρύθμιση. Η παρουσία του AGO2, του βασικού μέλους της οικογένειας AGO, πιθανότατα αντικατοπτρίζει τη μεγάλη τοπική κυτταρική ανάγκη για αυστηρή γονιδιακή ρύθμιση και αποκατάσταση της τοπικής ομοιόστασης. Το γεγονός αυτό δεν προκαλεί έκπληξη, καθώς η τοπική σύνθεση πρωτεϊνών σε απόκριση σε συγκεκριμένα μοριακά σήματα υπαγορεύει τη μορφολογία, τη λειτουργία και την κυτταρική μοίρα και ως εκ τούτου, την έκβαση της νόσου. Συμπερασματικά, προτείνουμε ότι ο AGO2 δημιουργεί φωλεές, τα «AGO2 locasomes», για αποκατάσταση της τοπικής ομοιόστασης. Άλλωστε, είναι γνωστό ότι ο AGO2 κατανέμεται σε δομές όπως GW- και P-σωμάτια (bodies), σε κυτταρικούς συνδέσμους καθώς και στο μεσόσωμα (midbody), εξυπηρετώντας τις τοπικές ανάγκες μέσω μετα-μεταγραφικής γονιδιακής ρύθμισης. Χρησιμοποιώντας τεχνικές ανοσοφθορισμού, ανάλυσης εικόνας, βιοπληροφορικής και κυτταρογενετικής, αποδείξαμε ότι ο AGO2 εντοπίζεται, επιπροσθέτως στις αποφυάδες της μεμβράνης, όπως σωλήνες ανοιχτού και κλειστού τύπου. Οι ανοιχτού τύποι είναι πιθανότατα κανάλια διακυτταρικής επικοινωνίας ενώ οι κλειστού τύπου είναι κυτοκινητικές γέφυρες. Στις προαναφερθείσες, ο AGO2 συγκεντρώνεται στους βραχίονες μαζί με κυτταροσκελετικές συνιστώσες όπως α-Τουμπουλίνη, Aurora B και διάφορες κινάσες. Ο AGO2, φωσφορυλιωμένος στη σερίνη 387, συνεντοπίζεται με τον Dicer στον δακτύλιο του μεσοσώματος κατά τρόπο που εξαρτάται από τη δραστηριότητα της p38 MAPK. Επιπρόσθετα, καταδείχθηκε η ευαισθησία του AGO2 στο στρες και η σημαντικότητά του για την εξασφάλιση του σωστού διαχωρισμού χρωμοσωμάτων και της κυτοκινητικής πιστότητας.

Προτείνουμε ότι ο AGO2 είναι μέρος ενός ρυθμιστικού μηχανισμού που ενεργοποιείται από το κυτοκινητικό στρες για τη δημιουργία του κατάλληλου μικροπεριβάλλοντος για τοπική ομοιόσταση. Συμπερασματικά, ο AGO2 φαίνεται να συσσωρεύεται σε συγκεκριμένες κυτταρικές δομές όπως τα ψευδοέγκλειστα και οι κυτταρικές αποφυάδες μαζί με άλλες συνιστώσες του RISC, εξυπηρετώντας πιθανότατα την AGO2-ειδική εντόπιση για την αποκατάσταση της τοπικής μετα-μεταγραφικής ομοιόστασης.

Για την κατανόηση των εμπλεκόμενων μηχανισμών, προσπαθήσαμε να προσδιορίσουμε τα κωδικά και μη-κωδικά γονίδια (όπως τα miRNAs) που εκφράζονται σε φυσιολογικά και κακοήθη υποστρώματα θυρεοειδούς. Χρησιμοποιήσαμε τη μεθοδολογία High-Sequencing of RNAs απομονωμένη με Cross-Linking Immuno-Precipitation (HITS-CLIP) για να καταγράψουμε το τριμερές σύμπλεγμα AGO2::miRNA::mRNA και να αναγνωρίσουμε το "ενεργό" miRNome, δηλαδή το σύνολο των miRNAs που συνδέονται με το RISC και τα mRNA-στόχους. Η βιοπληροφορική ανάλυση αποκάλυψε μια ομάδα 31 απορυθμισμένων miRNAs, με υψηλή στατιστική σημαντικότητα, μεταξύ φυσιολογικής και καρκινικής κυτταρικής σειράς. Συγκριτική ανάλυση με βάση την διαφορική τους έκφραση, αλλά και τα γονίδια-στόχους των miRNAs, ανέδειξε εμπλεκόμενα μοριακά μονοπάτια όπως το μονοπάτι ρύθμισης του κυτταροσκελετού της ακτίνης, μεταγραφικής δυσλειτουργίας στον καρκίνο, σηματοδότησης του NFK-β και το μονοπάτι των miRNAs στον καρκίνο που συνηγορεί στην EMT μετάβαση.

Ακολούθως, επικεντρωθήκαμε σε συγκεκριμένα miRNAs, όπως το miR26. Το miR26 ήταν ένας πολλά υποσχόμενος στόχος, καθώς (i) παρουσιάζει την ίδια μεταγραφική συμπεριφορά σε διαφορετικές καρκινικές κυτταρικές σειρές, (ii) μειορρυθμίζεται τόσο σε καρκινικές κυτταρικές σειρές όσο και σε δείγματα ασθενών, (iii) όλα τα μέλη της οικογένειας παρουσιάζουν αντίστοιχο προφίλ έκφρασης και (iv) τα αποτελέσματά μας είναι σε συμφωνία με την βιβλιογραφία. Σε δοκιμασίες *in vitro,* χρησιμοποιώντας κυτταροκαλλιέργειες*,* υπερέκφραση του miR26 οδηγεί σε περιορισμό του ογκογόνου δυναμικού καθώς η έκφρασή του έχει αντίστροφη συσχέτιση με την ικανότητα πολλαπλασιασμού των κυττάρων. Σε ξενομοσχεύματα ποντικιών, που δημιουργήθηκαν με κύτταρα FTC133 επιμολυσμένα με μιμητικές αλληλουχίες miR26, παρατηρήθηκε επιβράδυνση της ανάπτυξης των όγκων και περιφερική αλλά όχι κεντρική -όπως αναμενόταν- νέκρωση στην καρκινική μάζα. Ανάλυση διαφορικής έκφρασης RNA-seq μεταξύ κυττάρων με mimic miR26 και αλληλουχίες scrambled, αποκάλυψε 1.201 στατιστικά σημαντικά απορυθμισμένα γονίδια που σχετίζονται με τον κυτταρικό κύκλο, την απόπτωση, την κυτταρική διαίρεση, την κυτταρική προσκόλληση και τη εσφαλμένη μεταγραφική ρύθμιση στον καρκίνο. 133 επιβεβαιώνονται πειραματικά ως άμεσοι στόχοι του miR26. Τα 100 γονίδια με κορυφαία έκφραση χρησιμοποιήθηκαν για ανάλυση μονοπατιών με τον αλγόριθμο PathWalks και ανάδειξαν θεμελιώδη μονοπάτια όπως ο κυτταρικός κύκλος, τα miRNAs στον καρκίνο και η κυτταρική γήρανση. Τέλος, συγκριτική πληροφορική ανάλυση δεδομένων HITS-CLIP και RNA-seq αποκάλυψε 50 απορρυθμισμένα μόρια συμπεριλαμβανομένων των PAWR και STRADB. Τα μόρια αυτά συσχετίζονται με τον πολλαπλασιασμό των κυττάρων και την κυτταρική μοίρα, κρίσιμες συνθήκες για την EMT μετάβαση. Συμπερασματικά, το miR26, και οι άμεσοι στόχοι του, αποτελούν σημαντικά μόρια για την ογκογένεση και πολλά υποσχόμενους παράγοντες για διάγνωση και θεραπεία κακοηθειών καταστάσεων του θυρεοειδούς αδένα.

INTRODUCTION

Thyroid gland

The thyroid gland is a midline structure located in the anterior neck (Figure 1). The thyroid functions as an endocrine gland and is responsible for the production of the thyroid hormones and calcitonin, thus participating in the regulation of metabolism, growth, and serum concentrations of electrolytes such as calcium. Thyroid is implicated in a variety of pathological conditions such as hypothyroidism or hyperthyroidism, inflammatory processes, autoimmune processes and cancers. The anatomical location of the thyroid gland and its close relationship to important structures including the parathyroid glands, recurrent laryngeal nerves and certain vasculature is an important feature for its proper function.

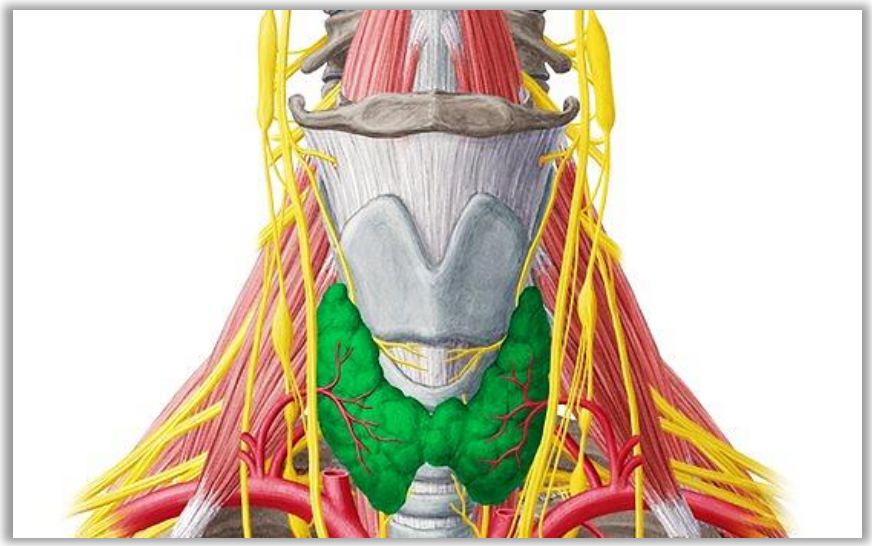

Figure 1 Anterior view of the neck. Clinical anatomy of thyroid gland (Jung, KenHub GmbH).

Anatomy Overview

The thyroid gland lies posterior to the sternothyroid and sternohyoid muscles, wrapping around the cricoid cartilage and tracheal rings. It is resided inferior to the laryngeal thyroid cartilage, typically corresponding to the vertebral levels C5-T1. The thyroid leans on the trachea via a consolidation of connective tissue, referred to as the lateral suspensory ligament or Berry's ligament. The thyroid gland is divided into two lobes that are connected by the isthmus, which crosses the midline of the upper trachea at the second and third tracheal rings. Trachea is connected with the two thyroid lobes through this ligament. The thyroid gland, together with the esophagus, pharynx, and trachea, is resided within the visceral compartment of the neck which is bound by pre-tracheal fascia (Allen & Fingeret, 2021).

The "normal" thyroid gland entails lateral lobes that are symmetrical with a well-marked centrally located isthmus. The thyroid gland typically contains a pyramidal extension on the posterior-most

aspect of each lobe, referred to as the tubercle of Zuckerkandl. Despite these main morphological and functional attributes, the thyroid gland appears to have many morphological variations.

Embryology

The origin of the parenchyma of the thyroid gland is the endoderm gene layer. The thyroid gland originates from the foramen cecum, which is a pit positioned at the posterior one-third of the tongue. Early in gestation, the thyroid gland initiates its descent anterior to the pharynx as a bilobed diverticulum. The thyroid gland then, continues to descend anterior of the hyoid bone and the cartilages of the larynx. By the seventh week, the thyroid gland reaches its destination midline and anterior to the upper trachea. The thyroglossal duct maintains the connection of the thyroid gland to the base of the tongue until involution and disappearance of the duct. The ultimobranchial body, derived from the ventral region of the fourth pharyngeal pouch, then becomes incorporated into the dorsal aspect of the thyroid gland. The ultimobranchial body gives rise to the parafollicular cells or C cells of the thyroid gland (Rosen RD, 2020).

Endoderm development

A deeper view in endoderm and in particular, its anterior part, aids to the understanding of thyroid gland development. During gastrulation of vertebrate embryos, the epiblast will form three germ layers; endoderm, mesoderm and ectoderm (Figure 2a). Key morphogenetic events and molecules implicated in endoderm development will therefore give rise in a variety of tissues (Kaestner, 2005; van den Brink, 2007; Zaret & Grompe, 2008). The endoderm also contributes significantly to the formation of glandular organs like the thyroid, parathyroid, thymus, pancreas and liver (Figure 2b). The mesoderm will form the cardiovascular system, kidneys, muscle, blood and bone. The differentiation of the ectoderm leads to the epithelial lining of the pharynx, lungs, esophagus, stomach and intestines. The ectoderm gives rise to the epithelium of the skin (epidermis) and the central nervous system (Andersson, 2010) (Figure 2c).

C cell development

The neuroectodermal nature of C cells is a well-established event since 1974 (Nilsson & Williams, 2016). They originate from neural crest and fate mapping studies, using Wnt1-Cre/Rosa26R double heterozygous mutant embryos, mapped neural crest-derived cells known to populate the pharyngeal arches (Kameda et al., 2007). However, lack of Wnt1 expressing cells in the ultimobranchial bodies or in thyroid co-localizing with the C-cells was observed. Then, the C-cells were found to express the epithelial marker, E-cadherin, suggesting that C-cells might derive from the endoderm rather than the neuroectoderm. Another important field of research, regarding this, is T-box family which plays crucial roles in the formation of tissues and organs during embryonic development. Tbx1 is a marker for the discrimination between the different thyroid progenitors. Fagman and colleagues investigated the absence of Tbx1 expression in the placode. In experiments with double heterozygous Tbx1-CreRosa26R offsprings for descending progenitors, they were found no β-gal activity detected in the thyroid follicular cells after x-gal staining. The cells that were expressing Tbx1-Cre were basically located centrally in the lobes and a number of them, were co-expressing calcitonin (Fagman et al., 2004). Based on these results, they further investigated whether members of the Foxa family of forkhead transcription factors known to be expressed in all the endoderm, but excluded from neural crest, could be used to label thyroid progenitor cells. The results further strengthened the endoderm origin hypothesis of the C-cells (Fagman et al., 2007).

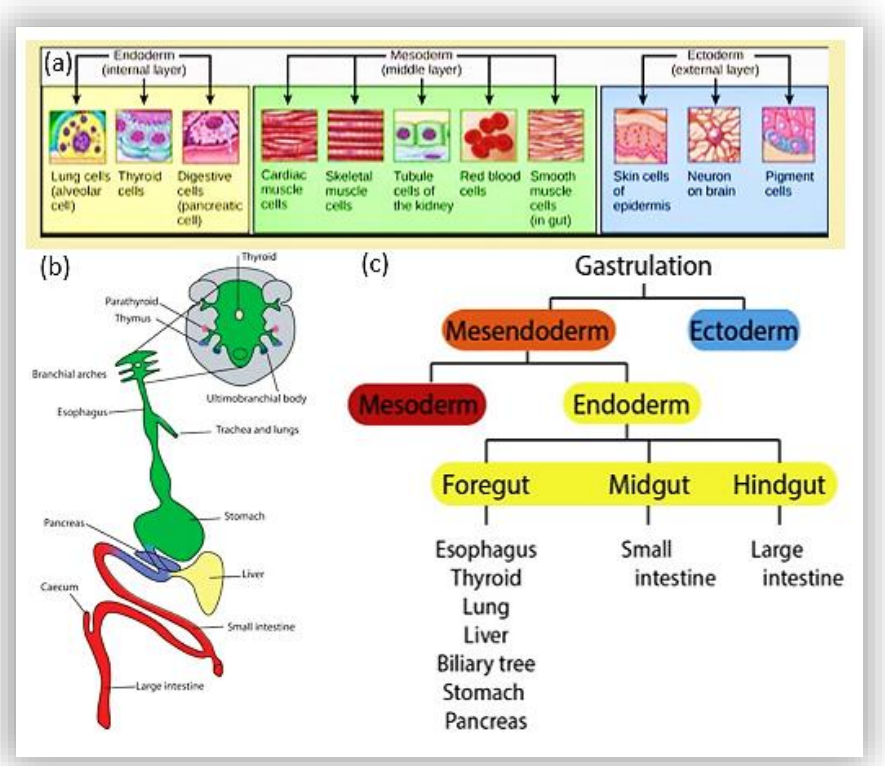

Figure 2 a) The endoderm leads to the production of tissues such as lungs, thyroid and pancreas. The mesoderm supports the production of cardiac, skeletal and smooth muscle, tissues existed within the kidneys and red blood cells. The ectoderm produces tissues within the epidermis and leads to the formation of neurons of the brain and melanocytes. b) The diagrammatic representation depicts the organs and glands that develop from the endoderm. These include the thyroid, the parathyroid and the thymus gland as wells as the digestive and respiratory systems. The thyroid gland is divided into two lobes. The lobes are connected by the isthmus, which crosses the midline of the upper trachea at the second and third tracheal rings. In its anatomic position. c) Germ layers and Vertebrate Endoderm Cell Lineages represented in a diagram of the tissue progressive formation from gastrulation. The formation of distinct germ layers followed by subdivision of endoderm along the anteroposterior axis into foregut, midgut, and hindgut domains eventually leading to the formation of distinct organ domains. Germ layers: ectoderm (blue), mesoderm (red) and endoderm (yellow), as well as mesendoderm (orange) the bipotential pool that will generate both endoderm and mesoderm are indicated (Marcin Wlizla, 2015).

Thyroid histology

A typical arrangement of the cells of an endocrine gland is the cord-like architecture. Their cellular products have to be secreted within the individual cells. The thyroid gland constitutes an exception and it is enclosed by a thin connective tissue as a capsule which enters the substance of the lobes to further subdivide the gland into irregular lobular units. Each lobule contains a cluster of follicles, which constitute the structural and functional units of the thyroid gland (Figure 3). Each individual thyroid follicle is encircled by thin connective tissue, stroma rich in fenestrated capillaries in conjunction with the sympathetic nerves and lymphatics. Follicular epithelium comprises low columnar, cuboidal or squamous cells depending on the level of activity of the follicle. In case that they are active, they appear cuboidal to low columnar, but in case of inactive conditions, the cells are squamous (Khan YS, 2020).

These follicular (principal) cells take up the necessary amino acid precursors and iodine at its basolateral surface. Then, the cells release their final product into the blood stream at its basal end. The responsibility of the follicular is the production of thyroglobulin (an iodine rich, inactive

form of the thyroid hormones), which is then stored as a semi-solid substance (colloid) in the lumen of the follicles (Rousset et al., 2000).

Hematoxylin and eosin (H&E) staining of the colloid is pink, while the follicular cells have a purple appearance. The amount and appearance of colloid contained in a follicle determines the degree of activity. Inactive follicular lumina are larger; colloid is abundant and appears solid. In contrast, active follicular lumina are smaller and there is little colloid or they have a total absence.

Parafollicular cell

Another typical cell type, identified on histological preparations of thyroid tissue, is parafollicular cells, also known as C (clear) cells (Figure 4). C-cells appear with clear appearance due to their light staining from H&E preparation. They can be found within the basal lamina of the thyroid follicles without extending into the follicular lumen or between thyroid follicles in the interfollicular space, either singly or in the form of groups. Parafollicular cells are a subtype of neuroendocrine cells (amine precursor uptake and decarboxylation – AUPD – system) that produce thyrocalcitonin (calcitonin). This hormone aids in the regulation of blood calcium levels by downregulating bone resorption (breakdown of bone and subsequent release of minerals into the blood) and limiting calcium reuptake in the kidneys (Jung, KenHub GmbH).

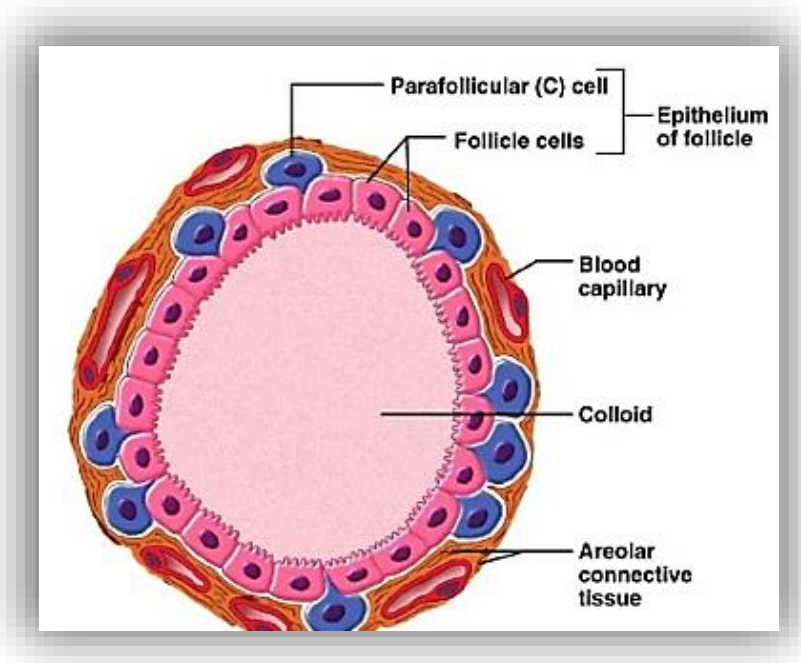

Figure 3 Architecture of the thyroid follicles, the structural & functional units of the gland. Rounded or oval in shape, surrounded by fenestrated blood capillaries. Lined with cubical epithelium, resting on thin basement membrane and surrounding a lumen filled with acidophilic colloid material (iodinated glycoprotein (Abdel-Dayem, 2021).

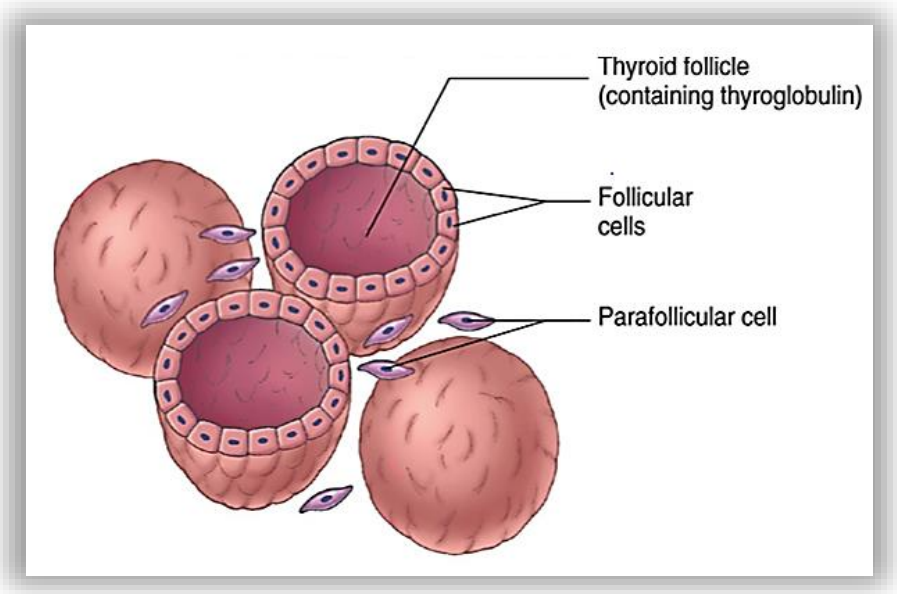

Figure 4 Diagrammatic representation of thyroid follicles. The thyroid follicles are composed of two different endocrine cell populations: (1) the follicular cells, the most abundant endocrine cells in the gland and responsible for secreting T3 and T4, hormones that control the basal metabolism; (2) C cells or parafollicular cells, which are very scarce and mainly known for producing calcitonin, a hypocalcemic and hypophosphatemic hormone.

Thyroid function

The thyroid gland constitutes the primary target of Thyroid-Stimulating Hormone (TSH). More specifically, TSH modulates the release of triiodothyronine (T3) and thyroxine (T4) from thyroid follicular cells. Almost 80% of the thyroid hormone is released as T4. T4 is de-iodinated to T3 and the latter appears to be the more potent thyroid hormone. Only ~20% of T3 derives from the thyroid gland, while 80% originates from peripheral conversion via a deiodinase. More than 99% of thyroid hormones bind to thyroid-binding globulin, prealbumin, and albumin, and only 1% circulates freely in the blood. Once T3 binds to its receptor into the nucleus, DNA transcription activation occurs, followed by mRNA translation, and protein synthesis. These newly synthesized products influence multiple organ systems, promoting growth as well as bone and central nervous system (CNS) maturation.

T3 and T4 act on almost all cells in the body to increase the basal metabolic rate. Specifically, T3 and T4 contribute to NA^+/K^+ synthesis, leading to an increase in oxygen consumption and heat production. They also act on B1 receptors' function in the heart increasing heart rate and contractility through elevating the number of beta-1 receptors on the myocardium such that the myocardium is more sensitive to stimulation by the sympathetic nervous system. Also, of note, thyroid hormones promote the activation of metabolism, with an increase in glucose absorption, glycogenolysis, gluconeogenesis, lipolysis, and protein synthesis and degradation (Delitala et al., 2019).

Mechanism

The hypothalamic-pituitary axis regulates TSH release through hypothalamic neurons that secrete thyroid releasing hormone (TRH), a hormone that stimulates thyrotrophs in the anterior pituitary to secrete TSH (Figure 5). TSH, in turn, stimulates thyroid follicular cells to release thyroxine or T4 (80%), and triiodothyronine or T3 (20%). Another hormone, somatostatin, on the other hand, produced by the hypothalamus promotes the inhibition of the release of TSH from the anterior pituitary. The import of T4 into the circulation leads to a conversion of T4 to T3 through the process of deiodination. T4 and T3 can then exert negative feedback on TSH levels (high levels of T3/T4 decrease TSH release from the anterior pituitary, while low levels of T3/T4 increase TSH release). T3 is the predominant inhibitor of TSH secretion given that this event is very sensitive to minor changes in free-T4 through this negative feedback loop. Abnormal TSH levels are detected earlier than those of free-T4 in hypothyroidism and hyperthyroidism. There is a log-linear relationship between T3/T4 and TSH and minor changes in T3/T4 lead to significant changes in TSH (Rousset et al., 2000).

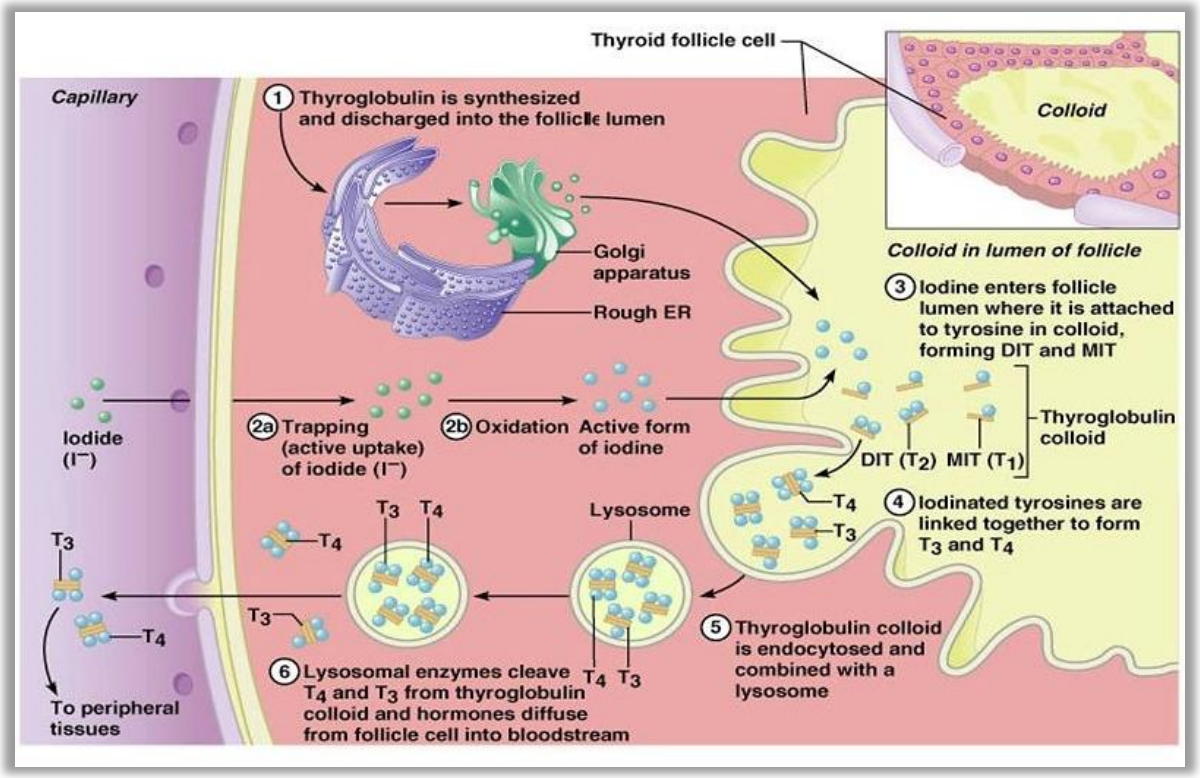

Figure 5 Synthesis of thyroid hormone (Roshani Nuchhen Pradhan, 2018).

Organ Systems Involved

Every organ system in the body could be affected by thyroid hormone including the heart, CNS, autonomic nervous system, bone, GI, and metabolism (Figure 6). Upon binding of the thyroid hormone to its intranuclear receptor, gene activation for the increase of the metabolic rate and thermogenesis occurs. Increasing metabolic rate involves increased oxygen and energy consumption (Shahid MA, 2020).

Heart: thyroid hormones have a permissive effect on catecholamines. The beta-receptors increased expression leads to increase heart rate, stroke volume, cardiac output, and contractility.

Lungs: thyroid hormones stimulate the respiratory centers and guide to increased oxygenation because of elevated perfusion.

Skeletal muscles: thyroid hormones cause increased development of type II muscle fibers. These are fast-twitch muscle fibers capable of fast and powerful contractions.

Metabolism: thyroid hormone elevates the basal metabolic rate. It increases the gene expression of Na+/K+ ATPase in different tissues promoting an increase in oxygen consumption, respiration rate, and body temperature. Depending on the metabolic status, induction of lipolysis or lipid synthesis occurs. Thyroid hormones stimulate the metabolism of carbohydrates and anabolism of proteins. Thyroid hormones can also promote the induction of protein catabolism in high doses. Thyroid hormones do not alter the blood glucose level, but they can cause increased glucose reabsorption, gluconeogenesis, glycogen synthesis, and glucose oxidation.

Growth during childhood: In children, the induction of chondrocytes, osteoblasts, and osteoclasts is due to the synergistic action of the thyroid hormones with growth hormone to stimulate bone growth. Thyroid hormone also aids brain maturation by axonal growth and the formation of the myelin sheath (Mughal et al., 2018).

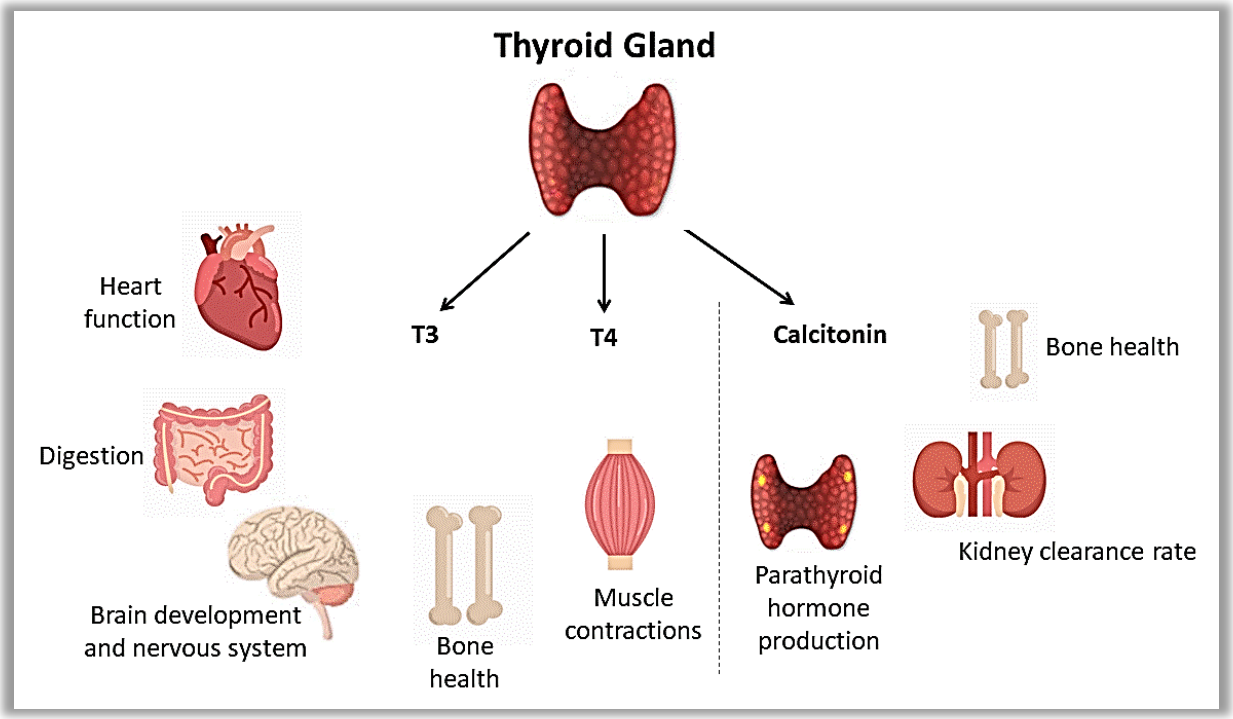

Figure 6 Contribution of thyroid gland in different human functions.

Pathophysiology

The disruption of the proper function of thyroid gland is leading to different pathological conditions such as hypo- and hyperthyroidism, Graves' disease, Hashimoto (Autoimmune Thyroiditis), thyroid cancer.

Hypothyroidism

Hypothyroidism is a hypometabolic state with major clinical symptoms including fatigue, lethargy, cold intolerance, slowed speech and intellectual function, slowed reflexes, hair loss, dry skin, weight gain, and constipation. The prevalence is higher in women than men.

The most typical cause of hypothyroidism is the primary hypothyroidism whose main causality is the chronic autoimmune thyroiditis, called Hashimoto. In this pathological condition, a destruction of the thyroid gland occurs by auto-antibodies or lymphocytes that attack the gland. Other causes experimentally tested are radioactive iodine and surgical therapy for hyperthyroidism or thyroid cancer, thyroid inflammatory disease, iodine deficiency, and several drugs that interfere with the synthesis or availability of thyroid hormone T3 and T4. Hypothyroidism may also occur rarely as a result of deficiency of TRH or impaired TSH secretion

due to hypothalamic or pituitary disease, respectively and it is called secondary or central hypothyroidism.

Treatment with synthetic thyroid hormones is usually simple, safe and effective for these patients (Stone MB, 2003).

Hashimoto (Autoimmune Thyroiditis)

The etiology of Hashimoto disease is still elusive. Most patients develop antibodies to a variety of thyroid antigens, most commonly, the anti-thyroid peroxidase (anti-TPO). Many also form anti-thyroglobulin (anti-Tg) and TSH receptor-blocking antibodies (TBII). The antibodies attack the thyroid tissue, eventually leading to inadequate production of thyroid hormone. There is a small subset of the population, less than 10-15%, with clinically evidence of the disease, that are serum antibody-negative. Positive TPO antibodies presage the clinical syndrome (Leung & Leung, 2019; Yuan et al., 2018).

Epidemiological data demonstrated that after age six, Hashimoto is the most common cause of hypothyroidism in the United States and in those areas of the world where iodine intake is adequate. The incidence is estimated to be 0.8 per 1000 per year in men and 3.5 per 1000 per year in women (Mincer DL, 2020). The physical findings and clinical manifestations include a cold and dry skin, facial edema particularly periorbital, as well as nonpitting edema involving the hands and feet, brittle nails, bradycardia, the delayed relaxation phase of tendon reflexes, elevated blood pressure, slow speech, ataxia, macroglossia (Mincer DL, 2020).

The development of Hashimoto disease is considered to be of autoimmune origin with lymphocyte infiltration and fibrosis as typical features (Figure 7b). The current diagnosis is based on clinical symptoms correlating with laboratory results of elevated TSH with normal to low thyroxine levels. It is interesting to note, however, that there is little evidence indicating the role of antithyroid peroxidase (anti-TPO) antibody in the pathogenesis of autoimmune thyroid disease (AITD). Anti-TPO antibodies can bind and kill thyrocytes. However, to date, there has been no correlation noted in human studies between the severity of disease and the level of anti-TPO antibody concentration in serum (Mincer DL, 2020).

The mainstay of treatment for hypothyroidism is thyroid hormone replacement. The drug of choice is titrated levothyroxine sodium administered orally. It has a half-life of 7 days and can be given daily. It should not be given with iron or calcium supplements, aluminum hydroxide, and proton pump inhibitors to avoid suboptimal absorption (Mincer DL, 2020).

Hyperthyroidism

Hyperthyroidism is a hypermetabolic state that results from T3 and T4 excess production. Its major clinical symptoms are nervousness, anxiety, heart palpitations, rapid pulse, fatigability, tremor, muscle weakness, weight loss with increased appetite, heat intolerance, frequent bowel movements, increased perspiration, and often thyroid gland enlargement (goiter). The prevalent gender is the female.

The most typical cause of hyperthyroidism constitutes Graves' disease, an autoimmune disease characterized by the production of antibodies that activate the TSH receptor leading to T4 stimulation and T3 production and therefore to thyroid enlargement. Other causes of the

hyperthyroidism are a multinodular goiter, solitary thyroid adenoma, thyroiditis, iodide- or drug-induced hyperthyroidism, and, very rarely, a TSH secreting pituitary tumor. Occasionally, people with hyperthyroidism have a normal serum free T4 and high serum free T3 concentrations. This type is called T3-hyperthyroidism (Shahid MA, 2020).

Several treatments are available for hyperthyroidism. Using anti-thyroid medications and radioactive iodine to slow the production of thyroid hormones or the involvement of surgery for the removal of the thyroid gland can be very beneficial for the individuals (Oszukowska et al., 2010).

Graves' disease

Graves' disease is caused by thyroid stimulating immunoglobulin (TSI), also known as thyroid stimulating antibody (TSAb). A variety of environmental factors including pregnancy (mainly postpartum), iodine excess, infections, emotional stress, smoking, and interferon A, trigger immune responses on susceptible genes to eventually cause Graves' disease (Diana et al., 2018).

Pathogenesis of other rare clinical symptoms of Grave's disease like pretibial myxedema and thyroid acropachy are poorly understood and are believed to be due to cytokines mediated stimulation of fibroblasts. Many symptoms of hyperthyroidism like tachycardia, sweating, tremors, lid lag, and stare are thought to be related to increased sensitivity to catecholamine (Pokhrel B, 2020). Treatment for Graves' disease includes the control of the symptoms and the reduction of thyroid hormone secretion. A beta-adrenergic blocker should be initially used for symptomatic patients, specifically for patients with heart rate more than 90 beats/min, patients with a history of cardiovascular disease, and elderly patients (Kahaly et al., 2018).

Crucial point for the treatment is the discrimination between Grave's disease and Hashimoto thyroiditis. Image analysis techniques were used to quantify micro-vessel density (MVD) by measuring major axis length, minor axis length, area, perimeter and shape factor. Significantly higher values were found in Grave's disease in comparison to Hashimoto's thyroiditis. In contrast, major axis length, minor axis length, and area had significantly higher values in Hashimoto's thyroiditis than in Grave's disease making clear their discrimination (Figure 7a).

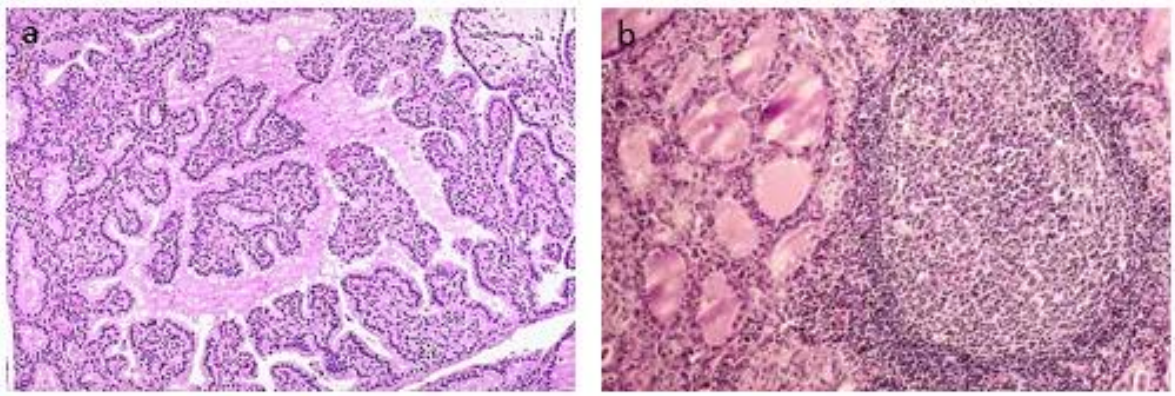

Figure 7 a) A case of Graves' disease on medium power showing cells with round nuclei and even chromatin pattern lining the papillae. b) histological pattern of autoimmune thyroiditis (Hashimoto).

Proofs of principle of Cancer

Origin of the word "cancer"

The origin of the word cancer is credited to the Greek physician Hippocrates (460-370 BC), the "Father of Medicine." Hippocrates used the terms *carcinos* and *carcinoma* to describe non-ulcer forming and ulcer-forming tumor masses. In Greek, these words refer to a crab, probably applied to the disease because the finger-like spreading protrusions from a carcinoma called to mind the shape of a crab. The Roman physician, Celsus (28-50 BC), later translated the Greek term into *cancer*, the Latin word for crab. Galen (130-200 AD), another Greek physician, used the word *oncos* (Greek for swelling) to describe the carcinomas. Although the crab analogy of Hippocrates and Celsus is still a common assertion to describe malignancies, Galen's term is now used as a part of the name for cancer specialists.

Hallmarks of cancer

For many years, scientists have concluded to six fundamental characteristics of the tumor growth and progression (Figure 8,9) which are (Al-Bedeary et al., 2020):

self-sufficiency in growth signals, insensitivity to growth-inhibitory (anti-growth) signals, evasion of programmed cell death (apoptosis), limitless replicative potential, sustained angiogenesis, and tissue invasion and metastasis. Quite recently, more hallmarks were added to the initial ones. These are abnormal metabolic pathways, evading the immune system and two enabling characteristics: genome instability and inflammation.

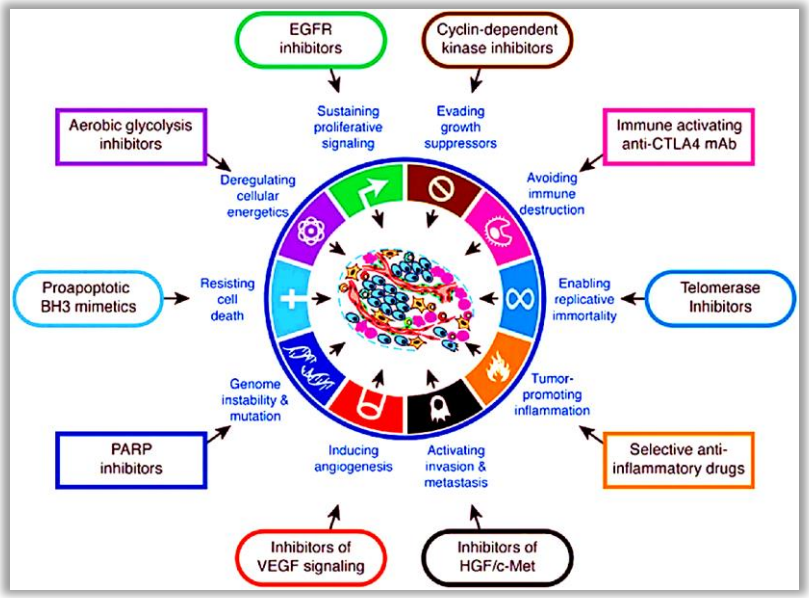

Figure 8 Therapeutic targeting in the hallmarks of cancer (Al-Bedeary et al., 2020).

The Development of Cancer

One of the most crucial pathological features of cancer is the tumor clonality, the development of one mass from single cells that initiate the cancer formation. The clonal origin of tumors does

not imply that the original progenitor cancer cell has initially acquired all of the malignant characteristics. The cancer development is usually a multistep process in which cells gradually transit to malignant through a progressive series of alterations. One indication of the multistep development of cancer is that most cancers develop late in life. The incidences of colon cancer, for example, increase more than tenfold between the ages of 30 and 50, and another tenfold between 50 and 70. This dramatic elevation of cancer incidence across age-decades suggests that most cancers develop as a consequence of multiple abnormalities, which accumulate over periods of many years. During aging cancer has been linked to Epithelial to Mesenchymal Transition (EMT), given that higher levels of EMT proteins have been observed in tissues during normal aging (Santos et al., 2019).

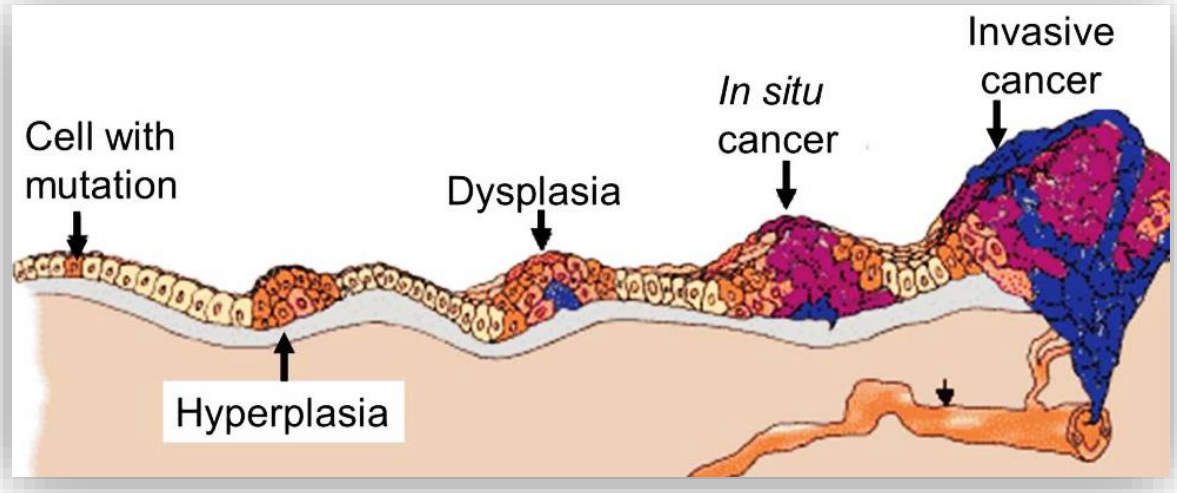

Figure 9 Multistep Progression of Neoplasia. Carcinoma-in-situ vs Invasive carcinoma. Normal tissue to hyperplasia and Low-grade dysplasia to High-grade dysplasia (cancer). (Saren, 2019).

Thyroid cancer

Thyroid cancer incidence is still rising worldwide, mostly as a consequence of the increase of diagnostic imaging and surveillance. In the USA, thyroid cancer constitutes the fifth most common cancer in women and the prevalence of this cancer, in 2017, is estimated to be 859,838 people.

However, mortality from thyroid cancer has changed minimally over the past five decades and the physicians face the challenge of the over treatment of group of patients with lower risk disease, such as benign thyroid nodules or local thyroid neoplasms with a lack of metastatic potential. The 5-year relative survival rate is 98.3% in U.S., however distant cancer with metastatic potential decreases the rate to 54.9% (SEER 18 2010–2016, All Races, Both Sexes by SEER Summary Stage 2000). In 2020 in U.S.A., it is estimated that there will be 52,890 new cases of thyroid cancer and an estimated 2,180 people will die of the disease.

Clinical Presentation and Classification

A histopathological classification of neoplasms reflects the biology and behavior of the tumors and serves as a guide for doctors and clinical management of patients. The World Health Organization (WHO) classification of tumors group publishes the WHO classification of tumors series to provide the international standards for cancer diagnosis including diagnostic criteria, pathological features, and molecular alterations. The classification of thyroid tumors unraveled 15 variants of papillary thyroid carcinoma but only the top 6 listed variants are included in the illustration below: FT-UMP, Follicular tumor of uncertain malignant potential; WDT-UMP, Well-differentiated tumor of uncertain malignant potential; NIFTP, Non-invasive follicular thyroid neoplasm with papillary nuclear features; CASTLE, Carcinoma showing thymus-like differentiation/intrathyroidal epithelial thymoma; PNSTs, Peripheral nerve sheath tumor (Figure 10).

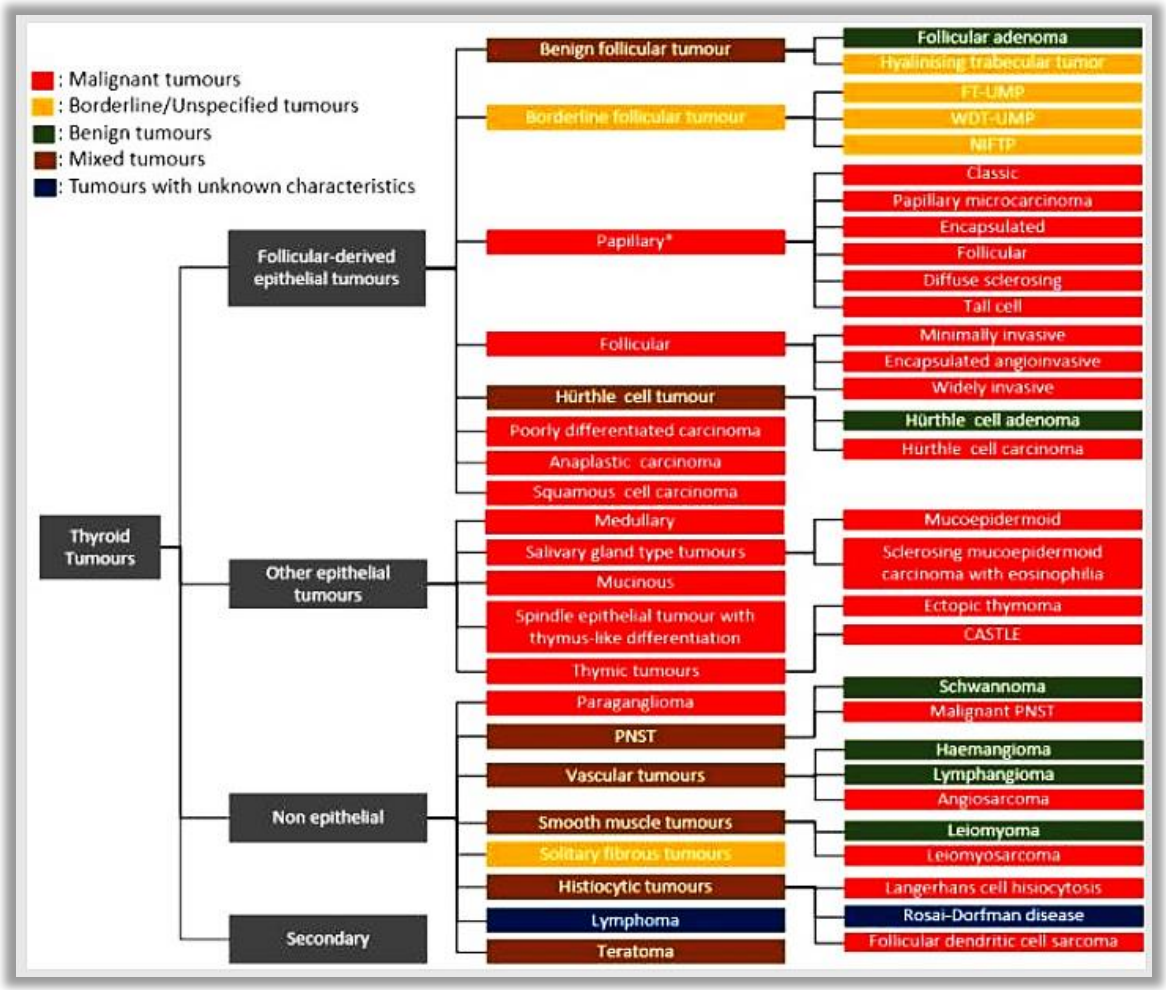

Figure 10 Classification of thyroid tumors. There are 15 variants of papillary thyroid carcinoma but only the top 6 listed variants are included in this illustration; FT-UMP, Follicular tumor of uncertain malignant potential; WDT-UMP, Well-differentiated tumor of uncertain malignant potential; NIFTP, Non-invasive follicular thyroid neoplasm with papillary nuclear features; CASTLE, Carcinoma showing thymus-like differentiation/intrathyroidal epithelial thymoma; PNSTs, Peripheral nerve sheath tumor.

Benign follicular tumors

Currently, three incidents of thyroid nodules increased probably due to the usage of diagnostic tools such as imaging (Figure 11). By using new high-resolution imaging techniques, thyroid nodules were identified that would have not been diagnosed in the past (Jegerlehner et al., 2017;

Smith-Bindman et al., 2013; Sosa et al., 2013). 90% of these nodules are small, non-palpable, benign lesions which would never transit into tumors (Papini et al., 2002). However, a significant percentage of these, become malignant, with or without metastatic potential and in some undiagnosed cases, can cause morbidity.

A thorough record and physical examination, laboratory investigations, neck ultrasonography, and fine-needle aspiration (FNA) are required (Filetti et al., 2006) for accurate distinction between low-risk and high-risk patients. Specific prognostic indexes such as computerized nuclear morphometry of thyroid carcinomas, follow-ups of the patients and platforms such the decision support system (DSS) using fine needle aspiration biopsies (FNAB), allow a reduction of the number of patients undergoing surgical procedures (Figure 11) (Tseleni, Kavantzas, Yova, Alexandratou, loannou-Lambrouli, et al., 1997; Zoulias et al., 2011).

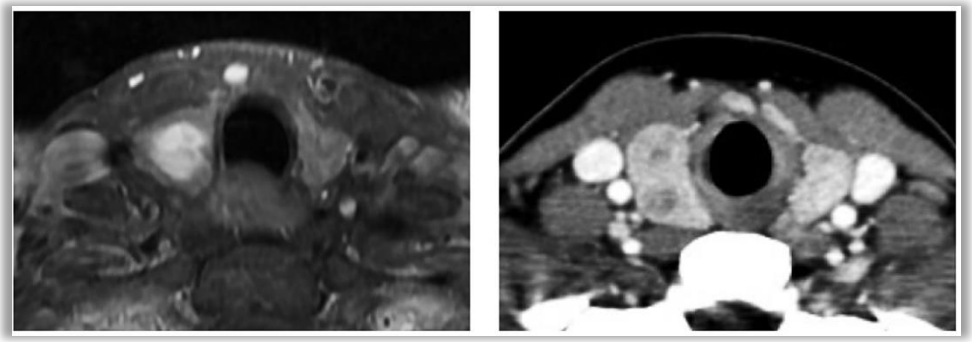

Figure 11 Reporting of incidental thyroid nodules on CT and MRI by Dr Jenny Hoang.

Borderline Follicular tumors

Borderline category is composed of encapsulated tumors with or without nuclear features of PTC and with or without minimal capsular invasion, which includes encapsulated common type PTC, encapsulated follicular variant of PTC, Hyalinizing trabecular tumor, Well differentiated thyroid tumor of uncertain malignant potential (WDTUMP), minimally invasive and capsular invasion only type FTC and FT-UMP in WHO classification 2017 and William's classification (Kakudo et al., 2012) (Figure 10).

However, the diagnosis based on imaging, fine needle aspiration (FNA) or core biopsy preoperatively is insecure. Thus, the diagnosis usually follows lobectomy. Main surgical concerns about borderline tumor are regarding the avoidance of a total thyroidectomy because of relatively indolent nature of these tumors. Unfortunately, some of these tumors can wrongly be diagnosed as malignant tumor preoperatively. The other surgical concern is that a diagnostic lobectomy can, thereafter, lead to a completed thyroidectomy (Chung & Song, 2019).

Differentiated thyroid cancer (DTC)

Differentiated thyroid cancer is the most common thyroid cancer, accounting for more than 95% of cases (Howlader N, 2015). It derives from thyroid follicular epithelial cells. The well-differentiated carcinomas comprise of papillary, follicular and Hürthle-cell thyroid cancer (Figure 10). The latter according to WHO Classification 2017 is considered as a separate entity including Hürthle cell adenoma and Hürthle cell carcinoma. Papillary thyroid cancer is the most common subtype and carries the best overall prognosis. Metastases most commonly involve cervical lymph nodes and, less frequently, the lungs. Follicular thyroid cancer, Hürthle-cell thyroid cancer and

poorly differentiated thyroid cancers are high-risk cancers that have a tendency to metastasize haematogenously to distant sites, in particular, to lung and bones. The staging system for differentiated thyroid cancers depends on age (Cancer, 2002) with older patients (≥45 years according to the current system) having poorer prognosis.

Follicular thyroid carcinoma (FTC)

FTC is an epithelial malignancy arising from follicular cells and demonstrates absence of nuclear features of papillary carcinoma. Its main subtypes are Hürthle cell carcinomas and Insular carcinoma. FTC cannot be adequately covered without dedicating a few words regarding follicular adenoma. The term "follicular" derives from the typical architecture of this type of cancer, which mimics follicles in the normal thyroid. Follicular adenomas appear to be benign epithelial tumors. A frequent problem is that in a multinodular thyroid, it is rather difficult to distinguish between a (polyclonal) hyperplastic nodule and a (monoclonal) follicular adenoma [Diagnostic Surgical Pathology of the Head and Neck (Second Edition, 2009)]. Grossly, a follicular adenoma is presented as a regular round encapsulated solid gray-white to yellow or tan (indicative of the presence of well-developed follicles containing colloid) mass. The follicles are formed of cuboidal epithelial cells surrounding a lumen that may contain colloid. Nuclear features are bland and mitotic potential is decreased. The differential diagnosis of follicular adenoma and carcinoma is difficult to conclude and the only distinction may be the presence of capsular or (preferably) vascular invasion. Vascular invasion of FTC is typically in veins explaining the strong tendency for hematogenous metastasis of FTC. Lymph-vascular invasion is rather uncommon. FTCs express the lineage-specific markers thyroglobulin, TTF-1, and PAX8. At a gross examination, FTCs are usually encapsulated solid gray-whitish lesions. In some cases, macroscopic invasion into surrounding thyroid tissue can be found [Diagnostic Surgical Pathology of the Head and Neck (Second Edition, 2009)].

Papillary thyroid carcinoma

Papillary thyroid cancers constitute the 80% of all thyroid cases (Zhu et al., 2015) and its prevalence is higher in countries having iodine-sufficient or iodine-excess diets (Al-Salamah et al., 2002). The PTC incidence is rising and although the causality is still unclear, it may reflect the environmental implication as well as earlier detection of cancer (Davies & Welch, 2006). PTC can occur at any age and has rarely been diagnosed as a congenital tumor. The age and the gender are risk factors. Women are more frequently affected than men, in ratios ranging from 2:1 to 4:1 (LiVolsi, 2011).

A well-established environmental factor that is related to the progression of PTC is the exposure to radiation (Miura et al., 1987). The dropping of the atomic bomb on Hiroshima and Nagasaki at the end of World War II in 1945 and the explosion of the Chernobyl nuclear power station in 1986 corroborated the tumorigenic effect of radiation that led to PTC. Other suggested risk factors include pre-existing benign thyroid disease or having a family history of PTC (Abdullah et al., 2019).

The diagnostic method of choice in case of a PTC carcinoma is the Fine needle aspiration and cytology (FNAC) (Maia & Zantut-Wittmann, 2012), which involves the use of a narrow gauge needle to obtain a sample of a lesion for microscopic examination. During FNAC, thyroid biopsy specimens are classified by their cytological appearance into benign, suspicious (or

indeterminate), or malignant cells (Vasilis Constantinides, 2013). Aspiration smear from PTC may disclose papillary structure, but preoperative diagnosis is mainly based on the recognition of typical nuclear characteristics, such as 'Orphan Annie' nuclei intranuclear pseudo-inclusions (due to cytoplasmic invaginations) and nuclear grooves(folds in the nuclear membrane)(Tseleni-Balafouta et al., 2007). Additional evidence of PTC could derive from the presence of psammoma bodies (calcium salt deposits) in a cervical lymph node (Hunt & Barnes, 2003). The accuracy rate of diagnosis with FNAC is about 90% when correlated with the postoperative diagnosis of surgical specimens (Neki & Kazal, 2006). However, there are limitations because FNA could fail to recognize the parathyroid origin of the lesions. A safe differential diagnosis between thyroid and parathyroid disease, regarding their morphological ground in cytologic smears, could be difficult due. These diseases, despite their different nature, have shared features in their lesions. Solution for the surgical mismanagement is a detailed pre-operative evaluation (Tseleni-Balafouta et al., 2007).

Main variants of PTC

The most common papillary variants are the classical, follicular and tall cell variants. Among them, tall cell and columnar cell variants are biologically more aggressive. In the present study, common and tall cell variants have been analyzed thoroughly and therefore, their characteristics will be extensively analyzed below.

Classical Variant of PTC

Conventional, or classical, papillary thyroid carcinomas (C-PTC) account for 55-65% of PTC, globally. They demonstrate a characteristic architecture with fibrovascular cores and psammoma bodies (bodies with calcium accumulation) (Figure 12). Tumor cells contain enlarged, overlapping nuclei with nuclear clearing ("Orphan Annie cells"). The existence of nuclear grooves and nuclear membrane irregularities, called pseudo-inclusions are typical in this variant. Classical variant does not present a tendency in metastasis and extra-thyroid extension leading to a good patient prognosis (Lloyd et al., 2011). However, C-PTC indicates higher-risk disease and predicts for significantly poorer long-term outcomes when compared to FV-PTC (Henke et al., 2018). High risk carcinomas have been correlated with male gender, tumor size larger than 5 mm, bilateral or multifocal lesions, location in lower third of the thyroid lobe, lymph node metastasis, capsule invasion/extrathyroidal extension and stromal fibrosis (Baloch & LiVolsi, 2018; Khanafshar & Lloyd, 2011; Lloyd et al., 2011).

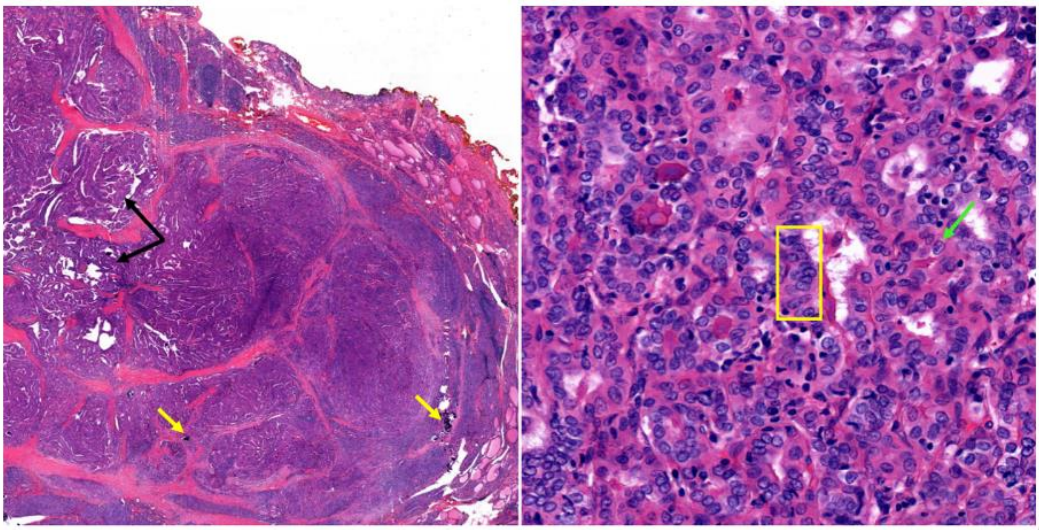

Figure 12 Classical variant of PTC demonstrating papillary architecture with fibrovascular cores (black arrows) and calcified psammoma bodies (yellow arrows) (low magnification, left image). Enlarged overlapping nuclei (yellow box) with nuclear clearing and nuclear grooves (green arrow) (Henry Hoffman, 2019).

Interestingly, nuclear morphometry, in conjunction with the follow-up of thyroid patients, could represent a crucial prognostic index for papillary thyroid carcinoma. More specifically, in an effort to classify these tumors according to the tumor size, it seems that younger people have lower, area perimeter major axis length means of papillary thyroid carcinoma nuclei than older ones. When the classification is based on the presence or absence of the capsule invasion, it was shown that younger people have lower area, perimeter, major axis length means of papillary thyroid carcinoma nuclei than older ones (Tseleni, Kavantzas, Yova, Alexandratou, Karydakis, et al., 1997).

Papillary thyroid microcarcinoma refers to all papillary thyroid carcinomas measuring smaller than 1 cm in size (Figure 13). These tumors are often found incidentally in autopsies or in thyroidectomy specimens, with a recent rise in clinical identification and biopsy probably due to the increased utilization of ultrasound. This type of tumors tends to be located near the thyroid capsule and are frequently non-encapsulated. Due to its small size, they have no distinctive morphology but they can have features of any larger papillary carcinoma subtype. The majority of papillary microcarcinomas exhibit a relatively benign disease course, while 28% demonstrates metastatic nodes and <1% extra nodal metastases.

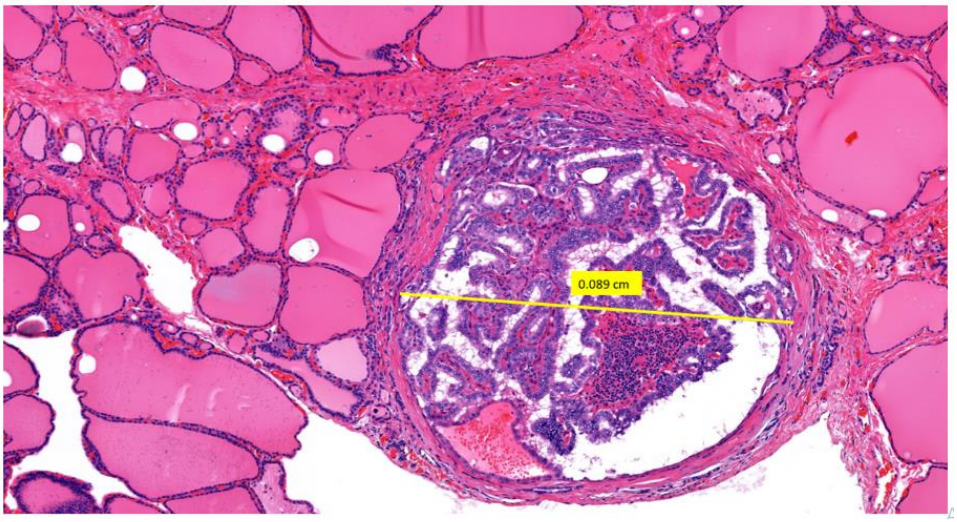

Figure 13 Papillary thyroid microcarcinoma characterized by architectural and cellular characteristics of PTC. The tumor size should be <1cm in diameter (Henry Hoffman, 2019).

Follicular Variant of PTC

These subtypes of tumors grossly resemble follicular carcinoma, with mean tumor size falling between that of C-PTC and follicular thyroid carcinoma (FTC) (Yu et al., 2013). This tumor demonstrates cellular features of a papillary tumor, including enlarged, overlapping irregular/ovular nuclei, nuclear clearings described as "Orphan Annie Eyes," nuclear grooves, and pink cytoplasmic invaginations (Figure 14) (Lloyd et al., 2011). Simultaneously, tumors are composed of follicles that vary in size and are filled with colloid that can be distinguished as darker and more eosinophilic than that of adjacent non-neoplastic follicles. The colloid may also exhibit the scalloped borders characteristic of papillary carcinoma. This is often a well-circumscribed or encapsulated tumor making the distinction between FV-PTC and follicular adenoma difficult and controversial (Yu et al., 2013).

Quite recently, Rivera and colleagues revealed that encapsulated FV-PTCs had a molecular profile similar to that of FTC, with a high rate of RAS and absence of BRAF mutations (Rivera et al., 2010). The prognosis of FV-PTC is similar to that of typical PTC, with the exception of diffuse or multinodular follicular variant, which confers a worse prognosis. Tumors with no metastatic potential and without extra-thyroid extension do not invade. They have a very low risk of adverse outcome, they are classified as "noninvasive follicular thyroid neoplasm with papillary-like nuclear features" (NIFTP) and thereby unnecessary surgical treatment should be avoided (Nikiforov et al., 2016).

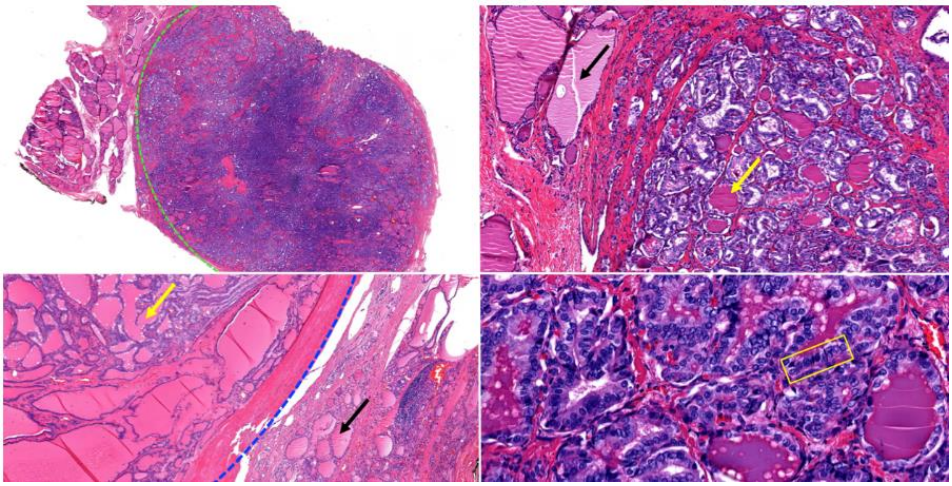

Figure 14 Papillary thyroid carcinoma, follicular variant well-circumscribed (dashed lines) with darker colloid (yellow arrows) than surrounding normal follicles (black arrows), enlarged, overlapping nuclei of PTC (yellow box). Low magnification left, high magnification right (Henry Hoffman, 2019).

Tall Cell Variant (TCV)

Tall cell thyroid tumors tend to emerge in older patients (greater than 50 years of age) and are generally bulkier in size than classical PTCs, often with extension beyond the thyroid capsule. 2017 WHO classification of tumors of endocrine organs requires ≥ 30% of tall tumor cells to define this variant. The majority of cases display lymph node metastases or even distant metastases (LiVolsi, 2011). They have a large size allowing the presence of necrotic areas and high mitotic activity as well as extrathyroidal extension, microcalcifications, and macrocalcifications. The cells, the presence of which define this type of cancer, called tall cells, exhibit height measures at least 2-3 times that of their width and also abundant eosinophilic cytoplasm and nuclear features characteristic of classical PTC (Figure 15). Varied prevalence in $BRAF^{V600E}$ mutations have been reported that demonstrate aggressive behavior and higher overall mortality. Some cases have also been found to be refractory to radioactive iodine treatment, conferring a worse prognosis (LiVolsi, 2011; Roman & Sosa, 2013).

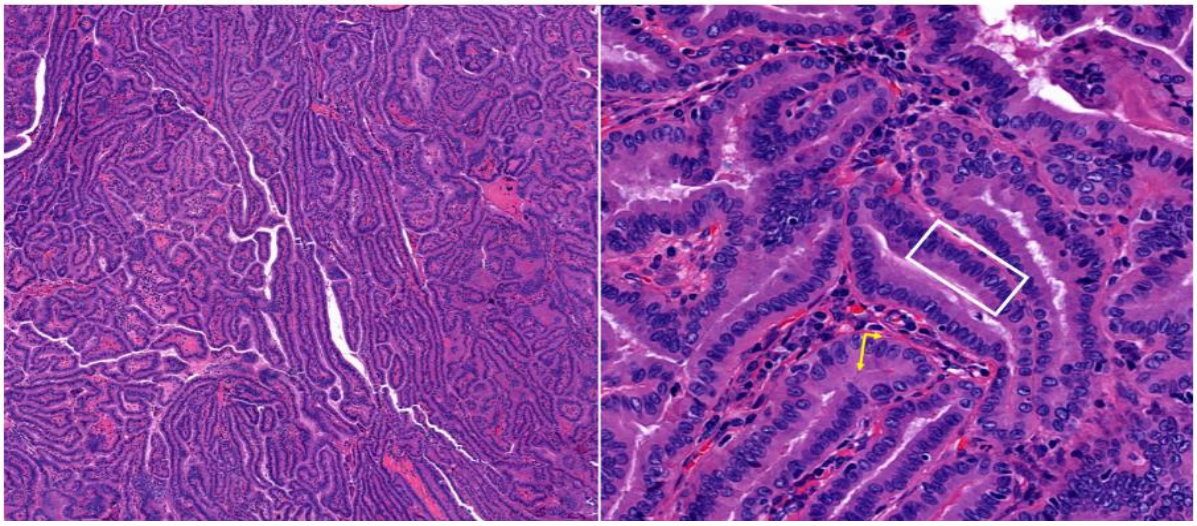

Figure 15 Papillary thyroid carcinoma, tall cell variant, characterized by cell height at least 2-3 times cell width (yellow arrows), eosinophilic cytoplasm and nuclear features characteristic of conventional PTC (white box), low magnification left, high magnification (Henry Hoffman, 2019).

Poorly differentiated thyroid tumors (PDTC)

Poorly differentiated thyroid carcinomas include a heterogeneous group of neoplasms whose behavioral and histologic features are intermediate between well-differentiated and anaplastic thyroid carcinomas. According to WHO classification 2017 constitute a large solitary thyroid mass. Patient may have a history of recent growth in a longstanding uninodular or multinodular thyroid.

Medullary thyroid carcinoma (MTC)

Medullary thyroid carcinomas (MTC) are uncommon thyroid malignancies of C-cell derivation representing approximately 3%-12% of all thyroid cancers (DeLellis, 2006; Roman et al., 2006; Skinner et al., 2005). Medullary thyroid carcinomas can be distinguished from poorly differentiated thyroid carcinomas based on positive reactions for calcitonin and chromogranin. They present a tendency for metastasis to regional lymph nodes, and the average 10-year survival for all types of MTC 61%-75% (Roman et al., 2006). 25%-30% of all cases are heritable, however a majority of MTCs are acquired as sporadic tumors. The inherited tumors have been associated with multiple endocrine neoplasia (MEN) 2A, MEN 2B, or with the familial medullary thyroid carcinoma syndrome (DeLellis, 2006; Kaserer et al., 2001; Kaserer et al., 1998). Also, these forms are due to autosomal dominant mutations of the *RET* proto-oncogene with incomplete penetrance, often presenting as multifocal disease in a background of C-cell hyperplasia (CCH), with largely circumscribed edge, composed of anastomosing sheets of cells with no fibrosis (Figure 16). Patients carrying *RET* proto-oncogene mutations should be tested routinely, as well as their family members, together with screening of serum calcitonin levels (Guyétant et al., 2003). Prophylactic thyroidectomies are increasingly being performed on patients at risk for MTC (Guyétant et al., 2003; Krueger et al., 2000).

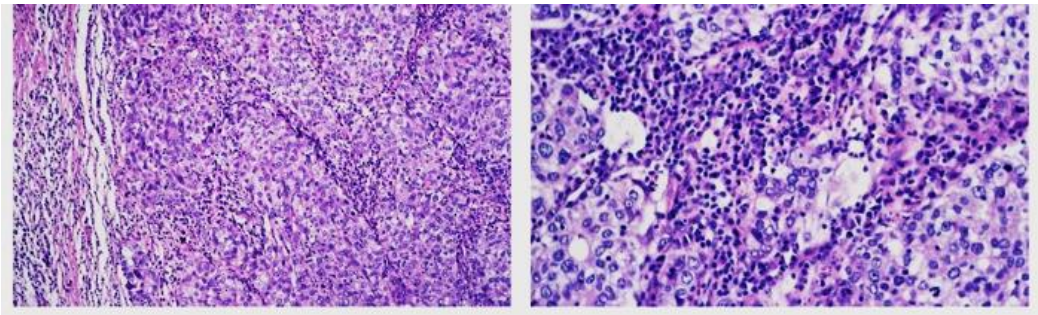

Figure 16 Medullary thyroid carcinoma with largely circumscribed edge, composed of anastomosing sheets of cells with no fibrosis (left, low magnification) and with moderate inflammatory infiltrate (right, high magnification) (Marginean, Rakha, Ho, Ellis, & Lee, 2010).

Anaplastic thyroid carcinoma (ATC)

Anaplastic thyroid cancer constitutes a rare subtype of thyroid cancer characterized by poor prognosis because of rapid tumor growth. The symptoms include hoarseness, dysphagia, and dyspnea. Most patients with anaplastic thyroid cancer have a large, firm palpable mass in the thyroid with or without cervical adenopathy (Cabanillas et al., 2016). A rapid assessment and biopsy of the mass is prompt of this finding which is followed usually by a locoregional disease and distant metastases. They present large pleomorphic, epithelioid, spindle, and multinucleated giant tumor cells, abundant eosinophilic cytoplasm, pleomorphic nuclei, more than two prominent nucleoli, frequent mitosis, and focal tumor necrosis (Figure 17). The most common site of distant metastatic disease is the lungs, followed by bones and brain. Anaplastic thyroid cancer often derives from and can co-occur with differentiated thyroid cancer, but can also exist *de novo*. Clinicians should suspect anaplastic transformation in patients with a history of longstanding differentiated thyroid cancer if they demonstrate the aforementioned features.

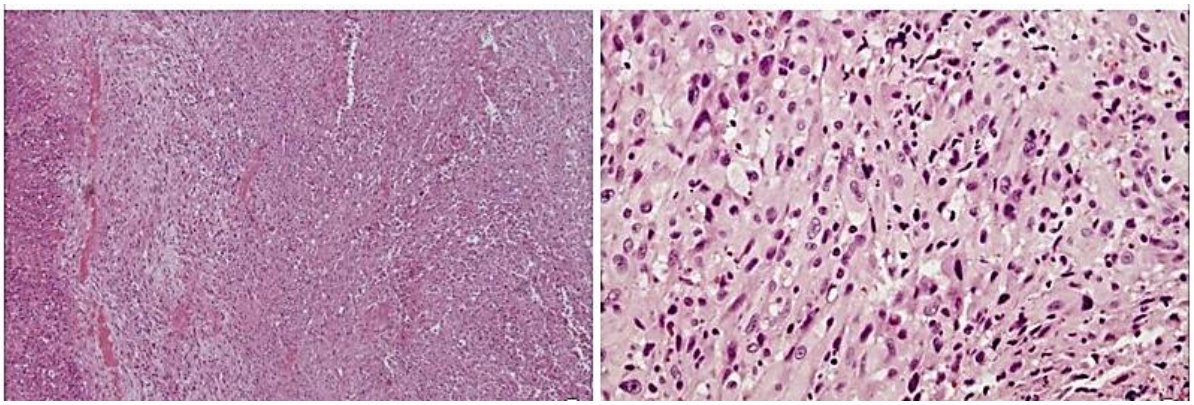

Figure 17 Anaplastic thyroid carcinoma with large pleomorphic, epithelioid, spindle, and multinucleated giant tumor cells, abundant eosinophilic cytoplasm, pleomorphic nuclei, more than two prominent nucleoli, frequent mitosis, and focal tumor necrosis, low magnification left, high magnification right (J. H. Park, Kwon, Park, & Hong, 2014).

Epithelial to Mesenchymal Transition

Epithelial–mesenchymal transition (EMT) is a reversible cellular program that transiently places epithelial cells into quasi-mesenchymal cell states (Nieto, 2009; Nieto et al., 2016; Thiery et al., 2009) and it constitutes a highly dynamic process. During its progression epithelial cells lose their cobblestone epithelial appearance in monolayer cultures and adopt a spindle-shaped, mesenchymal-like phenotype. EMT appears to play crucial roles in specific steps of normal

embryogenic development such as gastrulation, tissue morphogenesis during development and wound healing in the adult, as well as in organ fibrosis (Kalluri & Weinberg, 2009; Nieto, 2009; Thiery et al., 2009). Moreover, its implication in tumor progression with metastatic potential and the generation of tumor cells with stem cell properties leading to resistance in cancer therapeutic approaches are well-established (Lambert et al., 2017; Moustakas & de Herreros, 2017; Nieto et al., 2016).

EMT in cancer

During tumorigenesis and cancer progression, the pleiotropic program confers on individual carcer cells multiple attributes related to high-grade malignancy (Krebs et al., 2017; Mani et al., 2008; Rhim et al., 2012; Singh & Settleman, 2010). Different transitional states and expression of epithelial and mesenchymal genes in cancer cells uncover the fact that EMT can be complete or partial. In the latter, hybrid cells can migrate collectively as clusters and present higher aggressiveness than cells with a complete EMT pattern of gene expression (Jolly et al., 2015). The EMT process entails the disruption of cell–cell adhesion and cellular polarity alterations, cytoskeletal remodeling and changes in cell–matrix adhesion. In cancer, EMT can be induced by hypoxia, cytokines, and growth factors secreted by the tumor microenvironment, stroma crosstalk, metabolic changes, innate and adaptive immune responses, and treatment with antitumor drugs (Jolly et al., 2015). EMT presents reversible properties in the mesenchymal-to-epithelial transition (MET), affect circulating cancer cells when they reach a desirable metastatic niche to develop secondary tumors.

The transformation of epithelial cells (often genetically mutated) is followed by the secretion of autocrine growth factors, such as EGF, HGF, FGF, and TGFβ controlled by specific miRNAs (Figure 18), that sustain their continual proliferation. EMT induction is achieved by the binding to the respective receptor tyrosine kinases and elicit an invasive and migratory state. A potent and a well-established inducer of EMT is TGFβ (Papageorgis, 2015).

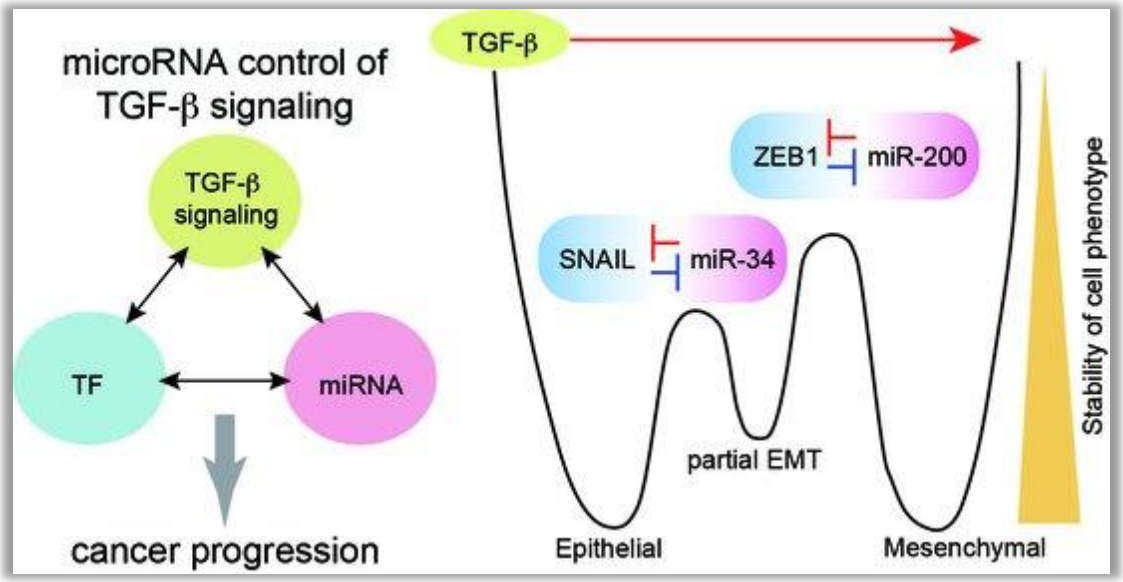

Figure 18 Roles of miRNAs in TGF-β-induced epithelial–mesenchymal transition (EMT) (Suzuki, 2018).

Further, novel transcription modulator families acting as EMT regulators including GATA, SOX, and fork head box (FOX) proteins were emerged in the recent years, besides the typical EMT regulators. EMT decisions taken from cell programming are related to the regulation of the cell fate, differentiation, stemness, cell polarity and cytoskeletal rearrangements (Greening et al., 2015; Lee et al., 2006; Su et al., 2015).

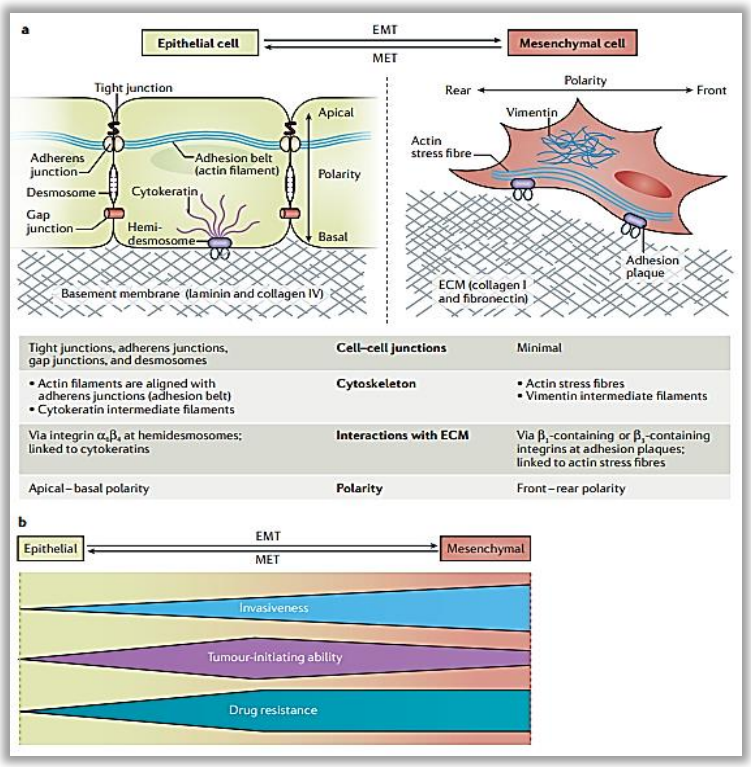

Figure 19 Morphological and physiological alterations related to the epithelial-to-mesenchymal transition (EMT). A) A schematic overview of EMT-associated changes in cell physiology. Activation of the EMT program induces profound changes in various aspects of cell morphology and physiology, most notably in cell–cell junctions, cytoskeletal composition, cellular interactions with the extracellular matrix (ECM), and cell polarity. B) Summary of the physiological outcomes of EMT in carcinoma: the profile of the shapes illustrates how the extent of invasiveness, the tumor-initiating ability, and degree of drug resistance change across the spectrum of EMT-program activation (Shibue & Weinberg, 2017).

In parallel, Matrix metalloproteinases MMPs functioning as EMT regulators can restrict tumor neovascularization (Westermarck & Kähäri, 1999). Epithelial cells seem to be anchorage-dependent and when they lose their adhesion properties and neighboring with other cells to the matrix, typically they enter the blood stream and become apoptosis-prone (Figure 19). This process is known as anoikis, in other words homelessness (Greek term) and it is not observed in fibroblasts and in mesenchymal-like cells, in general. Several signaling mechanisms such as the PI3K/AKT, NF-κB, Wnt/β-catenin, and p53/p63 pathways can protect cells from anoikis (Weidner et al., 1992). A notable member of the cadherin family pertinent to anoikis is E-cadherin (Figure 20).

Markers of EMT

	Phenotype			
	Epithelial		Mesenchymal	
Markers	E-cadherin	ZO-1	N-cadherin	TCFC4
	P-cadherin	EpCAM	Vimentin	SIX1
	Epithelial Membrane Antigen/MUC-1	Occludin	Fibronectin	Twist
		Claudins 3,4,7	FSP1/S100A4	Snail
	Cytokeratins 8,18,19	Laminin 1	Goosecoid	Slug
	Desmoplakin	Entactin	FOXC2	ZEB1
	Desmocollin 2,3	Syndecan 1	MMP2,3,9	Integrins α5β1,αvβ6
	γ-catenin	miR-200	Nuclear β-catenin	α-smooth muscle actin
	Integrin β4		LEF-1	miR-21
			SOX1	

Figure 20 Common expression markers in multiple cell carcinomas with epithelial and mesenchymal nature (Greening et al., 2015; Kalluri & Weinberg, 2009; Zeisberg & Neilson, 2009).

Gene mutations in thyroid cancer

Over the last two decades, researchers have developed a clearer understanding of genetic alterations underlying thyroid carcinogenesis (Figure 21). A number of point mutations and translocations are involved, not only in its tumorigenesis, but also as potential diagnostic and prognostic indicators and therapeutic targets.

The most frequent mutation in non-medullary thyroid cancers is the $BRAF^{T1799A}$ mutation. The gene product, $BRAF^{V600E}$ mutant kinase, a serine-threonine kinase, component of the RAS-RAF-MAPK signaling pathway, is found to be activated in 40–60% of advanced melanoma and originate from the substitution of glutamic acid to valine at amino acid 600 (V600E mutation) in 80-90% of the cases. The tyrosine kinase inhibitor vemurafenib has been used for to address the rapid tumor regressions in patients with V600E mutant (Flaherty et al., 2010; Kantarjian et al., 2002). BRAF mutations are also found in other cancers; about 5-10% of metastatic *colorectal cancer* incidents have been associated with poor prognosis. Additionally, somatic mutations in BRAF are present in 3% of patients with non-small cell lung cancer and 50% of these are V600E mutations. Regarding the context of this study, it is interesting that *BRAF* mutations (mostly V600E mutations) also occur in 30-69% of papillary thyroid cancers, but not in benign or follicular neoplasms, is omen of worse prognosis (Cen et al., 2014). BRAF mutations are identified in 60% of classic PTC, 80% of tall-cell variant PTC, and only 10% of follicular variant PTC. More specifically, point mutation in BRAF were found in approximately 45% of papillary thyroid cancers (PTC) and especially in tall cell variants and less frequently in poorly differentiated and in anaplastic thyroid cancers. In most cases, the p.V600E mutation causes constitutive activation of this serine/threonine kinase. In few cases, other BRAF mutations such as the p.K601E mutation, small in frame insertions or deletions, or BRAF rearrangement can occur (Adeniran et al., 2006; Kim et al., 2005). Findings suggested increased propensity for clinically aggressive papillary thyroid

cancer in tumors bearing a BRAF mutation (Chen et al., 2016; Elisei et al., 2008; Haugen et al., 2016; Xing et al., 2015; Xing et al., 2013). On the other hand, the fact that about 50-70% of PTC harbor a BRAF mutation and most of these tumors remain indolent, guide to the idea of other important determinants of clinical outcome. Therefore, clinical implications of individual mutations are still debatable and further investigation is required to clearly establish the role of these genetic alterations.

Another group of mutations in thyroid cancer is found in the genes of the RAS family. They, more frequently, occur in follicular thyroid cancer and in the follicular variants of papillary thyroid cancer (Nikiforov & Nikiforova, 2011). Chromosomal translocations are also a frequent phenomenon in this type of cancer; the existed genomic rearrangements dictate expression of novel fusion oncogenes that initiate wide range events implicated in thyroid cancer.

PAX8-peroxisome proliferator activated receptor γ (PPARγ) translocation was observed in about 30% of follicular thyroid cancer cases (Raman & Koenig, 2014) and the RET-papillary thyroid cancer family of translocations targeting the RET oncogene was found in about 7% of papillary thyroid cancer cases (Nishant Agrawal et al., 2014). Less common translocation partner genes include BRAF, the NTRK gene family, ALK, and THADA. Although infrequent, these translocation events can directly affect treatment given that ALK rearrangements, for example, was found to be associated with clinically aggressive thyroid cancers (Kelly et al., 2014). Identification of the rearrangements and the involved molecules might have direct therapeutic relevance to patients with thyroid cancer.

Additionally, genetic alterations in TERT have been identified in more aggressive subsets of PTC. $TERT^{C228T}$ is the most common mutation in benign thyroid tumors, PTC, follicular thyroid cancer, poorly differentiated thyroid cancer and anaplastic thyroid cancer, and is often associated with aggressive thyroid tumors. Mutations in the TERT promoter are also linked with aggressive thyroid tumor characteristics, tumor recurrence and patient mortality, similar to the aforementioned $BRAF^{V600E}$ mutation. Co-occurrence of $BRAF^{V600E}$ and TERT promoter mutations has a robust synergistic impact on the aggressiveness of PTC, including a sharply elevated tumor recurrence and patient mortality (Liu & Xing, 2016). Conclusively, TERT, demonstrating genetic alterations both in its gene and its promoter, represents a prominent new oncogene in thyroid cancer and a potential promising diagnostic and prognostic genetic tool.

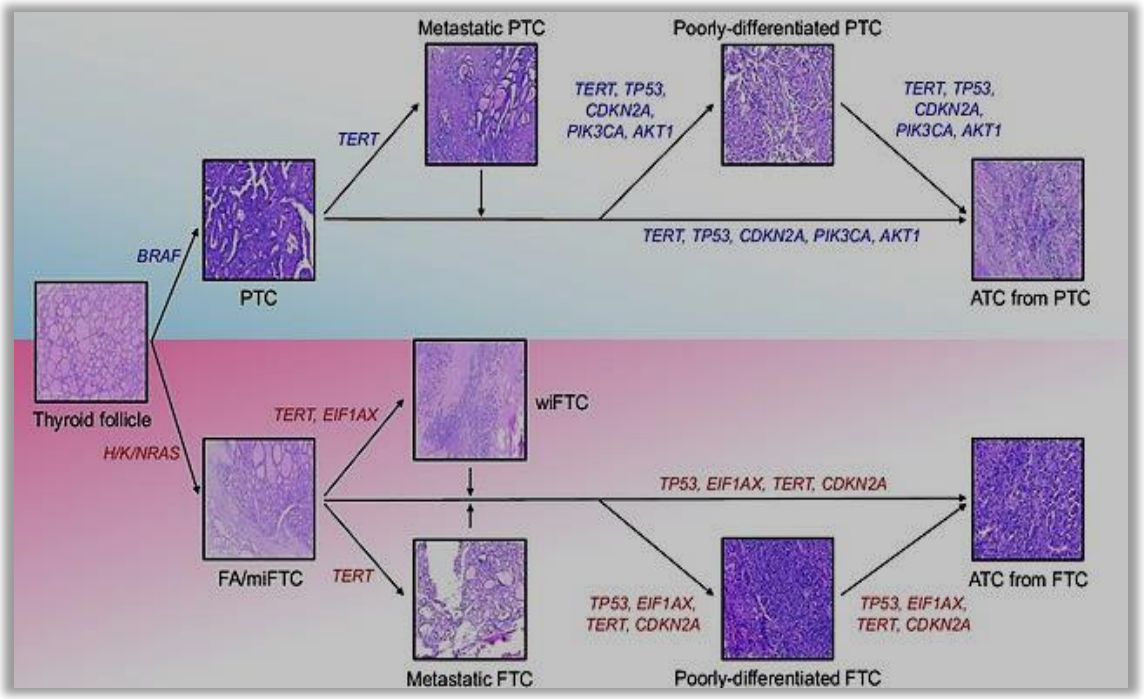

Figure 21 The major genetic contributors to thyroid cancer progression. Illustration of progression mechanisms of BRAF-positive papillary thyroid cancer (PTC) and RAS-positive follicular thyroid cancer (FTC). TERT, telomerase reverse transcriptase; TP53, tumor protein p53; CDKN2A, cyclin dependent kinase inhibitor 2A; PIK3CA, phosphatidylinositol-4,5-bisphosphate 3-kinase catalytic subunit alpha; AKT1, AKT serine/threonine kinase 1; ATC, anaplastic thyroid cancer; EIF1AX, eukaryotic translation initiation factor 1A X-linked; FA, follicular adenoma; FTC, minimally invasive FTC; FTC, widely invasive FTC (Yoo et al., 2020).

DNA sequencing data of poorly differentiated and pure anaplastic carcinomas suggest that the acquisition of additional cooperating mutations contributes to tumor progression. Most commonly, a mutation that affects the phosphatidylinositol-3-kinase or p53 tumor suppressor pathway is present, usually in conjunction with an early initiating mutation such as BRAFT1799A (Nikiforov & Nikiforova, 2011; Nikiforova et al., 2013; Santarpia et al., 2008; Xing, 2010).

Apart from mutations, gene rearrangements/translocations are also involved in thyroid cancer. The molecules that are frequently involved are RET and NTRK1 genes, that both code for transmembrane tyrosine kinases which are usually not expressed in thyroid cells. Due to the rearrangement, a chimeric gene is formed resulting in MAPK-signaling pathway activation. In the case of RET, its chimeric gene is RET/PTC and in the case of NTRK, is TRK. They have been identified in 20–40% of PTC, with a predominance of RET/PTC over TRK (three-fold more frequent) (Bounacer et al., 1997). 15 different *RET/PTC* rearrangements have been identified (Tallini & Asa, 2001), but *RET/PTC1* and *RET/PTC3* are the most frequent [PMID: 12114746], representing ~59% and ~36% of *RET/PTC* cases, respectively. *RET/PTC1* is formed by the fusion of RET with the *H4 (CCDC6)* gene (Grieco et al., 1990) and *RET/PTC3* by fusion of RET with the *ELE1* (also designed *NCOA4*, *RFG* or *ARA70*) gene (Bongarzone et al., 1998; Santoro et al., 1994). The impact of the loss of H4 expression on 14-3-3σ, crucial molecule for the succession of the cell cycle, directly links the deregulation of H4 with pathways in cancer indicating an implication in cancer causality (Thanasopoulou et al., 2012).

A relatively high prevalence of *RET/PTC* rearrangements was reported in tumors associated with radiation exposure (Bounacer et al., 1997) in the contaminated areas near the Chernobyl explosion. The analysis of PTC, which developed after a long latency period following explosion

displayed higher prevalence of *RET/PTC1* rearrangement. *RET/PTC3* is likely to be typical for radiation-induced childhood PTC with a short latency period, while *RET/PTC1* rearrangements may be a marker for later-occurring PTC of radiation-exposed children and adults (Smida et al., 1999). *RET/PTC* rearrangements have not been observed in follicular thyroid carcinomas and anaplastic thyroid carcinomas (Tallini et al., 1998). *RET/PTC* rearrangements have been shown not only in PTC, but also in Hürthle thyroid adenomas and carcinomas and also in Hashimoto's thyroiditis (Cyniak-Magierska et al., 2011).

On the other hand, follicular adenomas and minimally invasive FTCs expressed a similar mutation pattern with H/K/NRAS genetic alterations to be found in almost 40% of tumors, followed by DICER1, EIF1AX, EZH1, SPOP, IDHI, SOS1 and PAX8-PPARγ-1 mutations. All the mutations are exclusive with each other (San Román Gil et al., 2020). Mutations in EIF1AX (eukaryotic translation initiation factor 1A), that plays a role in the recognition of the start codon in the translation process, are found with a higher frequency in follicular patterned carcinomas and adenomas: 5.45% in FTC and FA, 3% in FV-PTC and 0.62% in common PTC (Agrawal et al., 2014).

Another interesting genetic pattern appears in MTC that also includes RET and RAS proto-oncogene aberrations in a striking percentage that reaches 90% (Agrawal et al., 2013). RET activation promote downstream pathways related to cell growth, proliferation, survival and differentiation, including the MAPK and PI3K signaling pathways. The activation of the RET receptor occurs after the glial cell-line derived neurotrophic factor (GDNF) family of ligands (GFLs) bind to GDNF family receptor-α (GFRα), forming the GFL/GFRα complex and allowing the dimerization of the receptor, which leads to the phosphorylation of specific tyrosine residues within the tyrosine kinase domain of the RET receptor (Arighi et al., 2005). Genetic alterations involving the RET proto-oncogene have been typically described in MTCs except from PTCs. The difference is that MTC mainly contains point mutations and few deletions and insertions, whereas in PTCs only chromosomal arrangements are found (Romei et al., 2016).

Not surprisingly, the mutational landscape of ATC appears to be extremely heterogeneous, holding a greater mutation burden than DTC and PDTC. Four genetically distinct clusters of ATC have been proposed. The Cluster 1 includes $BRAF^{V600E}$ cancers, being associated with mutations in the mTOR pathway and resembling PTC, thus probably originating from them. The Cluster 2 comprises ATC with genetic changes in cell cycle regulators like CDKN2A and CDKN2B, but also carrying genetic features of the other three clusters (BRAF, NRAS and PTEN/NF1/RB1 mutations). The Cluster 3 is likely to be derived from NRAS-mutant FTCs since NRAS mutations are frequent in this group. Finally, the Cluster 4 includes ATC with oncogenic mutations in RAS genes, carrying PTEN mutations often coexisting with NF1 and RB1 mutations. Cancers that belong to the latter cluster, have a higher mutational burden with genetic alterations in MSH2 and MLH1 (San Román Gil et al., 2020).

Gene regulation via RISC complex

Besides genetic alterations, gene expression and transcript homeostasis can be perturbed, in thyroid cancer. This can be achieved through miRNA regulation. Their expression profiles and their loader machines, the Argonaute proteins (AGOs) will be extensively analyzed in the next sections. AGOs together with Dicer and TRBP proteins forming the miRNA-induced silencing complex (miRISC) while Drosha and Dgcr8 form the microprocessor complex. Together, they represent core components of the fine-tuning regulation of gene expression.

miRNAs

miRNAs are key regulators of gene expression and therefore, play a crucial role in many essential cellular processes such as proliferation, cell cycle control, signaling pathways and apoptosis. Misguided changes in the expression of miRNAs are involved in the initialization, development and metastasis of several types of human cancer. Recent studies have also uncovered that miRNAs participate in the age-associated processes and pathologies in a wide and diverse spectrum of mammalian tissues, including brain, heart, bone and muscle.

MicroRNAs (miRNAs) constitute short (~23nt) non-coding transcripts that act as regulators of gene expression in the post-transcriptional level. miRNAs identify their target mRNA transcripts through sequence complementarity and guide the RISC for the induction of cleavage, degradation and/or translation suppression of protein-coding genes (Huntzinger & Izaurralde, 2011).

The first miRNA, lin-4, was disclosed in Caenorhabditis *elegans* (C*. elegans*) by Ambros and colleagues (Lee et al., 1993). Initially, it was demonstrated as a small non-protein-coding RNA which affects development through expression regulation of the protein lin-14. Seven years later, Reinhart and colleagues *(Reinhart et al., 2000)* reported another miRNA in *C. elegans*, *let-7*, which negatively regulates the expression of the heterochronic gene lin-41. In 2001, miRNAs were found to exhibit a regulatory function in both invertebrates and vertebrates by three independent groups. Currently, there are 38.589 miRNA entries (http://www.mirbase.org), some of them are highly conserved, with defined as well as still unknown functions. Extensive research regarding miRNA target prediction, miRNA-gene interactions and incorporating miRNA pathways is in progress and multiple supporting tools are developed including DIANA-microT-CDS (Paraskevopoulou et al., 2013; Reczko et al., 2012)(http://www.microrna.gr/microT-CDS), DIANA-micro T-ANN (/DianaTools/index.phpr=microtv4/index) (Maragkakis et al., 2011), TarBase v7.0 (http://www.microrna.gr/tarbase)(Vlachos et al., 2015), DIANA-miRPath (http://www.microrna.gr/miRPathv2) (Vlachos et al., 2012), DIANA-mirExTra (http://diana.cslab.ece.ntua.gr/hexamers/) (Vlachos et al., 2016) among others.

miRNAs are becoming functional through a complex process of maturation called biogenesis, passing through the steps of precursor pri-miRNAs and pre-miRNAs. The mature miRNAs bind to the respective mRNA target, interfering with mRNA translation (Felekkis et al., 2010). miRNAs base-pair with miRNA recognition elements (MREs) typically located at the 3' untranslated region (3'-UTR) of their mRNA-targets, through a critical region, the 'seed region', which includes nucleotides 2-8 from the 5'-end of the miRNA (Figure 22). Base-pairing between the 3′-segment of the miRNA-mRNA target is not always essential for repression. Asymmetry is the general rule for matches between a microRNA and its target. The 5'-end of the microRNA has a tendency for higher bases complementary to the target than that the 3'-end. Cohen and colleagues concluded that the complementarity of seven or more bases at the 5'-end is sufficient for regulation (Cohen et al., 2006).

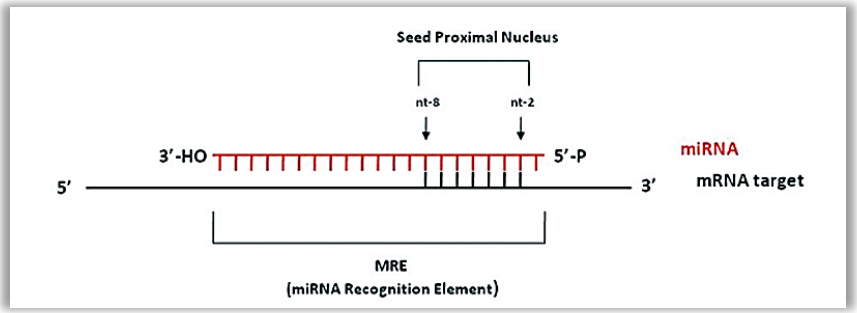

Figure 22 microRNA binding to the target mRNA. The mature miRNA binds to the target mRNA, typically on the 3'-untranslated regions (3'UTR). miRNAs base-pair with miRNA recognition elements (MREs) which are located on their mRNA targets, usually on the 3'UTR, through the seed region (Felekkis et al., 2010).

Due to the stringent recognition requirement between the miRNA seed region and the mRNA target, sequence variations such as SNPs in the miRNA-binding seed region (mir SNPs) can perturb the miRNA-mRNA target site interaction, greatly affecting the expression of the miRNA targets (Felekkis et al., 2010).

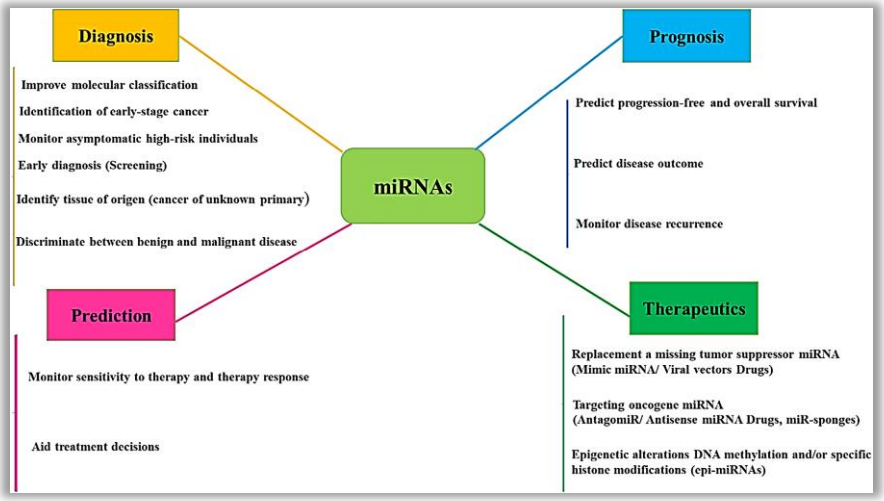

Figure 23 Methods of transferring RNA into cells.

In tumor cells, miRNAs are observed highly dysregulated promoting the capability to sustain the proliferative events, evading growth suppressors, resisting cell death and inducing metastasis and angiogenesis. Although miRNAs can have multiple targets, their function in tumor initiation could be due to their regulation of few specific genes. Consequently, the emerging future challenge will be to identify the critical cancer prone-targets of the miRNAs, establish their contribution to malignant transformation and discover their synergistic action with other coding and non-coding molecules contributing in early diagnosis and new therapeutic approaches (Figure 23). The miRNA deregulation during cancer depends on multiple mechanisms, including amplification or deletion of miRNA genes, abnormal transcriptional control of miRNAs, dysregulated epigenetic changes and defects in the miRNA biogenesis machinery (Peng & Croce, 2016).

miRs in cancer

miRNA expression signatures are different across tumors (Table 1), between stages of malignancy, different histopathological lesions of the same tissue and between the primary tumor and metastasis. Due to this, miRNAs can emerge as a useful tool for the classification of human tumors as well as diagnostic biomarkers and potential targets for therapeutic implementation of patients. The thorough examination of miRNA expression profiles could provide promising molecules for gene therapy aiming the prevention of the tumorigenesis and propagation. As biomarkers, miRNAs are not modified, they provide an increased informative value in comparison to larger set of mRNAs in determining developmental stage and differentiation of tumors (Lu et al., 2005) or cardiovascular diseases (de Gonzalo-Calvo & Thum, 2018) as they highly contribute to the regulation of cell homeostasis. They reflect the pathophysiological changes in the cell types they derive by controlling multiple pathways. Technically, they have the advantage of high stability in biological fluids (saliva, blood, plasma, CSF) and they can participate in less invasive methods as well as time course monitoring. A limitation is that miRNA profile has been demonstrated to be pathognomonic and tissue specific, but not necessarily disease specific (e.g. miR-21). A combination of more than one miRNA might be necessary to understand the fine-tuning regulation. Undeniably, the in-depth characterization of the expression profile of miRNA expression regarding specific pathological conditions such as thyroid cancer would greatly contribute to early diagnosis, accurate stratification, valuable prognosis and novel therapeutic implementations. Individual miRNAs as well as panels of them could be used for this purpose.

Currently, a panel of four miRNAs, miR146b, miR221, miR222 and miR26, have been used together for the distinction of primary lymphomas from ATC with sensitivity greater than 80% and specificity greater than 90% (Fassina et al., 2014). miRNA expression analysis of ATC specimens indicated a decreased expression of miR30, miR26, miR125, miR92, and let7 (Silaghi et al., 2020). A comprehensive analysis regarding the miRNA profiling correlated with overall survival, demonstrates that the high expression of four miRNAs (miR146a, miR146b, miR182, miR203) and the low expression of six miRNAs (miR1271, miR791, miR381, miRlet 7a, miR26a, miR486) was correlated with decreased OS in PTC. Additionally, the high expression of miR-375 correlated with decreased OS in MTC [reviewed by (Silaghi et al., 2020).

Tumor types	Sample	Deregulated miRNAs	Up or down regulation
HCC	Cancer tissues	miR-26a/b	Down
HCC	Cancer tissues and cell lines	miR-26b	Down
HCC	Plasma and cancer tissues	miR-26a	Down
Esophageal carcinoma	Cancer tissues	miR-26	Down
Gastric cancer	Cancer tissues	miR-26a	Down
Breast cancer	Cancer tissues	miR-26a	Down
Osteosarcoma	Cancer tissues	miR-26a	Down
Lung carcinoma	Cancer tissues	miR-26a	Down
Ovarian cancer	Serum	miR-26a	Down
Cutaneous squamous cell carcinoma	Cancer tissues	miR-26a	Down
AML	Primary blasts from PB and bone marrow	miR-26a	Down
Multiple myeloma	multiple myeloma tissues and cell lines	miR-26a	Down
Prostate cancer	Cancer tissues and cell lines	miR-26a	Down
Prostate cancer	Peripheral blood	miR-26a	Up
Pituitary tumor	Cancer tissues	miR-26a/b	Up
GBM	Cancer tissues	miR-26a	Up
Liposarcoma	Cancer tissues	miR-26a-2	Up

.

Table 1 Expression of miR-26 family members in malignant tumors (Li et al., 2021).

miR26 is of great interest as its contribution to the pathogenesis of various pathologic conditions related to cancer was previously reported. Down-regulation of miR-26 was detected across multiple tumor types, including lymphoma, hepatocellular carcinoma, breast cancer, and nasopharyngeal carcinoma (Ji et al., 2009; Lu et al., 2011; Zhang et al., 2011).

Inhibition of proliferation, apoptosis induction, and/or suppression of tumorigenicity are promoted by the ectopic expression of miR-26 in multiple cancer settings. The tumor suppressor activity of miR-26 is mediated through suppression of its direct targets including Cyclin D2 *(*CCND2*),* Cyclin E2 *(*CCNE2), and Enhancer of zeste homolog 2 *(*EZH2*)* (Kota et al., 2009; Lu et al., 2011; Sander et al., 2008; Zhang et al., 2011). On the contrary, in cancers such as glioma, lung cancer, and T-cell lymphoblastic leukemia, miR26 displays amplification on 12q and oncogenic activity through its ability to repress *PTEN* (Huse et al., 2009; Liu et al., 2012). Further investigation regarding the function of miR26 in cancer formation and development is required to clarify its contribution as tumor suppressor or oncomiR. In general, miR-26 regulates tumor cell metabolism, proliferation, differentiation, apoptosis or autophagy, invasion and metastasis through targeting gene expression at the post-transcriptional level in various ways (Figure 24).

Overexpression of miR26a could also lead to the induction of cell cycle G1 arrest in liver cancer cells *in vitro* (Zhu et al., 2011) by directly suppressing the expression of CDK6 and cyclin E1; these results in reduced phosphorylation of pRb. Exogenous elevated expression of miR26a could cause G2 cell cycle arrest, promotes inhibition of proliferation and spheroid formation and promote apoptosis in a CKS2-dependent manner in two PTC cell lines. miR-26a could also suppress tumor growth of papillary cells *in vivo* after injection into the dorsal flank of nude mice (Lv et al., 2013).

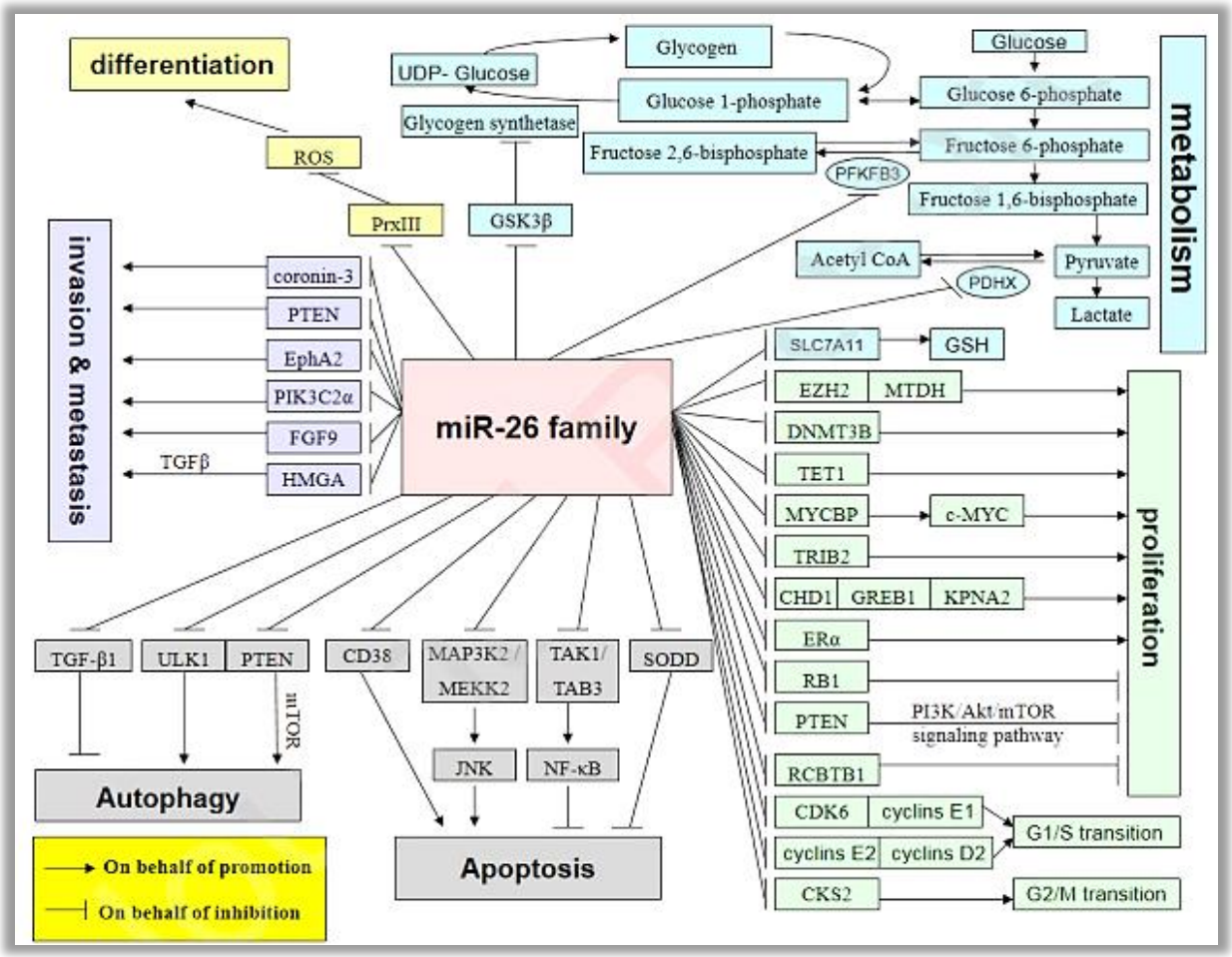

Figure 24 The identified target genes of miR-26s in tumorigenesis and development.

In general, to function as a tumor suppressor or an oncomiR, miR-26 regulates tumor cell metabolism, proliferation, differentiation, apoptosis or autophagy, invasion and metastasis through targeting gene expression at the post-transcriptional level in various ways (Figure 24).

It has been reported that exogenous expression miR26a is capable of decreasing EZH2 and MTDH expression in MCF7 cancer cells, reducing cell vitality and colony formation and increasing cell apoptosis. Overexpression of miR26a promotes inhibition of tumor growth in tumor-bearing mice. Under tumor hypoxia, miR26 expression could be induced in an HIF-dependent manner.

The expression levels of miRNAs could be altered, *in vitro* and in *vivo*, by using mimics to positively modify the expression of miRNAs or inhibitors to down-regulate miRNA expression. More specifically, miRNA mimics are double-stranded RNA molecules that imitate the endogenous miRNA duplexes (Jin et al., 2015). The transfection of cells with miRNA mimics should be used with caution, since it has been reported that the transfection at low concentrations fails to suppress target gene expression and at high concentrations leads to non-specific changes in gene expression (Jin et al., 2015). This event has been attributed to the failure of the guide strand from the transfected miRNA mimics to be incorporated into the RNA induced silencing complex and the accumulation of high-molecular weight RNA species (Jin et al., 2015; Thomson et al., 2013). On the other hand, inhibitors are anti-miRNA Oligonucleotides (also known as AMOs) that have many uses in cell mechanics, since they constitute synthetically designed molecules that

neutralize miRNAs for desired responses. AMOs have been used for fine-tuning regulation as well as for therapeutic approaches for certain cellular disorders through a steric blocking mechanism as well as hybridization to miRNA (Lennox & Behlke, 2011).

Moreover, alternative therapeutic miRNA-based approaches have guided to the identification of miRNAs in secreted exosomes due to their good stability, higher specificity and sensitivity (Lv et al., 2020). The cargos of exosomal material contribute to metastatic niche formation and resistance to therapy (Colombo et al., 2014). Exo-miRNA signature could be proved helpful in identifying cancer staging, metastatic potential although hitherto, exo-miRNA based therapies are in embryonic stage (Ingenito et al., 2019). Such an interventional study aims to recruit malignant glioma patients to perform a phase I human trial (NCT02507583) using an antisense RNA oligonucleotide carried in exosomes. The purpose of this study is to activate the immune system through exosomes released by glioblastoma cells treated with an Insulin-like growth factor receptor-1 Antisense Oligodeoxynucleotide. Another ongoing study in metastatic pancreatic cancer patients uses mesenchymal stromal cell-derived exosomes delivering a small interference RNA (siRNA) against a mutated KRAS (NCT03608631) trying to prove the clinical applicability of exosomes for metastatic pancreatic ductal adenocarcinoma treatment (Ingenito et al., 2019).

miRs in EMT

EMT is controlled by multiple miRNAs either by the influence of EMT-TFs expression or by affecting their related co-factors, such as epigenetic modifiers or chromatin remodeling complexes, including SUZ12 (PRC2 component), DNMTs, and SIRT deacetylase (Tam & Weinberg, 2013). In turn, the aforementioned molecules epigenetically regulate miRNA expression by reduction of suppressive hallmarks, enrichment of permissive hallmarks or DNA methylation processes. Most frequently, the majority of the miRNAs enforce the epithelial phenotype and restrain EMT by the direct reduction of the expression EMT-TFs or other invasion-associated factors (Figure 25). Notwithstanding the above, there are examples of miRNAs, such as miR-544a and miR-21, that act as potent inducers of EMT by targeting epithelial differentiation markers (Liu et al., 2015; Yanaka et al., 2015). In the recent years, a core miRNA signature upon EMT induction has been emerged (Díaz-Martín et al., 2014). miR-200 family members are key regulators of the main components of EMT transition, ZEB1 and ZEB2, safeguarding the maintenance of the epithelial phenotype (Park et al., 2008). Respectively, miR34 acts as a double-negative feedback loop together with SNAI1 (Siemens et al., 2011).

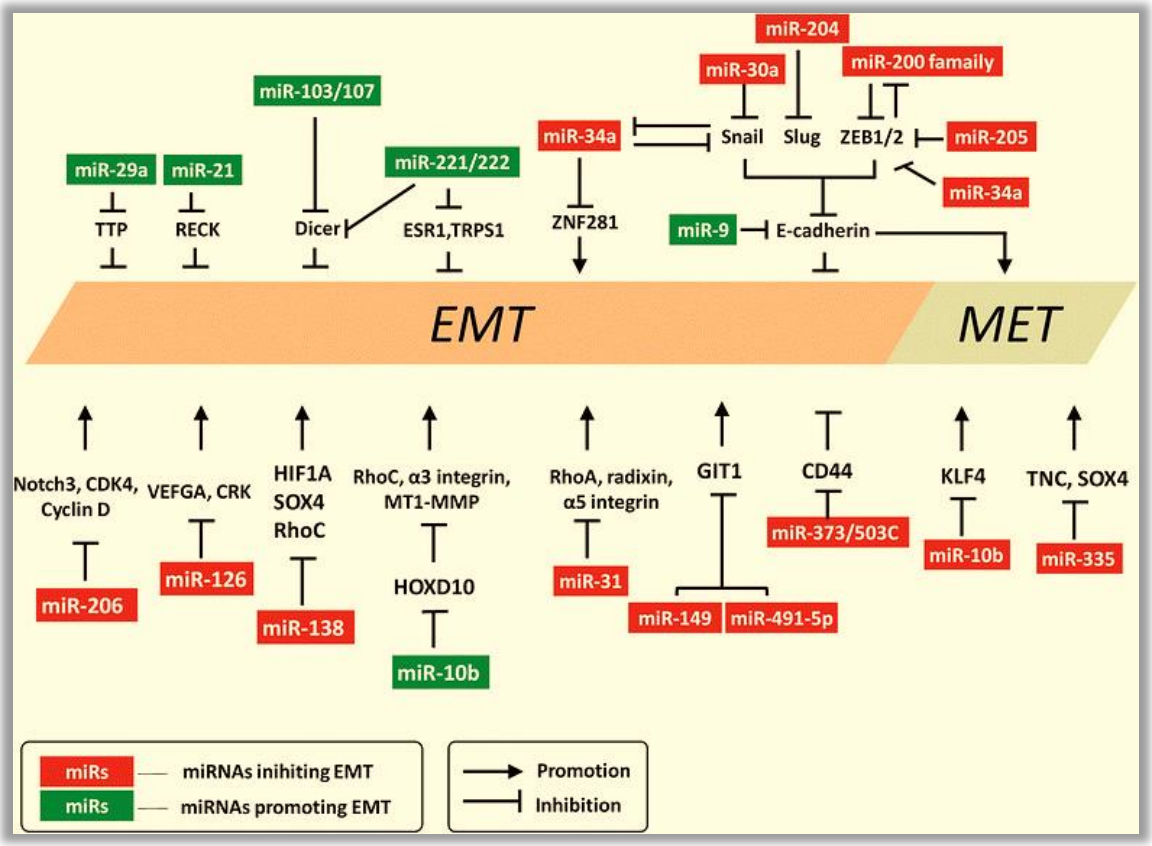

Figure 25 microRNAs that are known to regulate EMT/MET processes and their validated targets (Chan & Wang, 2015).

Argonaute Proteins

Argonaute (AGO) proteins were initially identified due to their implication in plant development (Bohmert et al., 1998; Moussian et al., 1998) and stem cell division in flies (Lin & Spradling, 1997). During the last two decades, extensive research was performed aiming to identify the explicit mechanism of AGO's function. Through this process, its role as essential components of the RNA-induced silencing complex (RISC) was unraveled in mammals and other organisms. AGO dictates post-transcriptional gene silencing by repression of the mRNA targets through small RNA sequence complementarity (Shmushkovich et al., 2018) with or without mRNA degradation (Ambros, 2004). AGO superfamily presents high evolutionary conservation and is ubiquitously expressed. It can be subdivided in AGO, PIWI and SAGO subfamilies (Hutvagner & Simard, 2008). The AGO subfamily includes four different molecules in humans, AGO1, AGO2, AGO3 and AGO4 with extremely high homology among the members, which exceeds 80 percent over the entire length of the protein (Insert Data). They share the same signature domains, N, MID, PAZ, and PIWI; the two latter exist in proteins implicated in RNAi mediated procedures (Höck & Meister, 2008; Joshua-Tor, 2006; Schürmann et al., 2013)(Figure 26). Hence, it becomes obvious that the discrimination between the members of the AGO subfamily constitutes a difficult and ambiguous field. Their functions can be overlapping and/or mutually compensative when needed (Matsui et al., 2015; Meyer et al., 2006; Su et al., 2009).

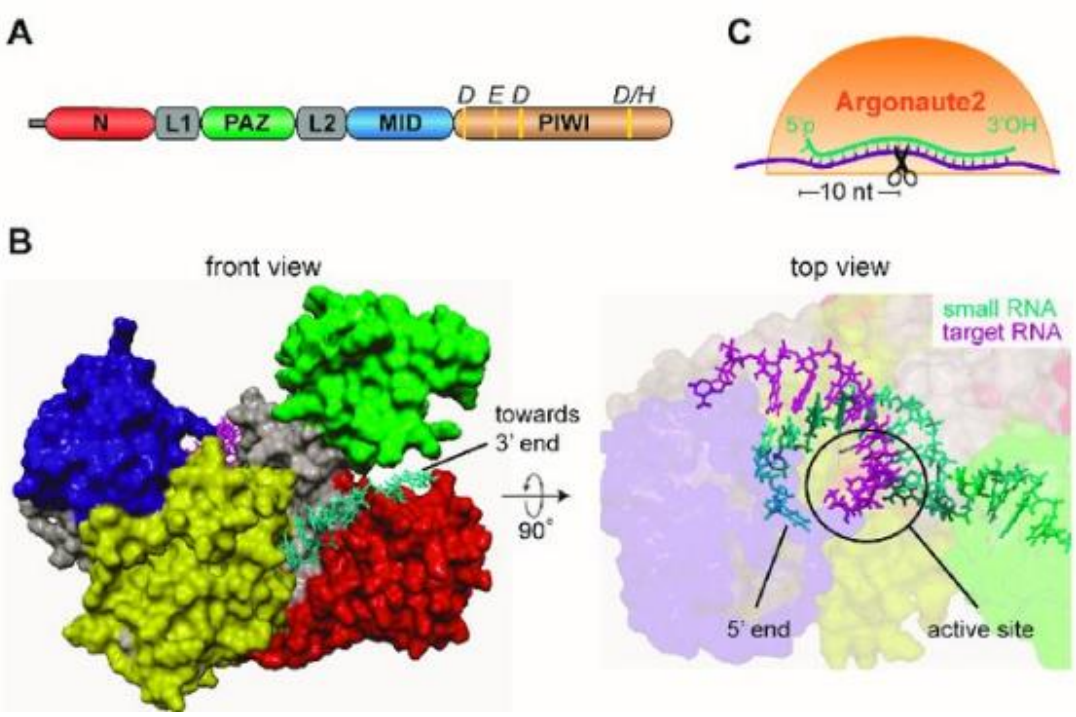

Figure 26 AGO proteins are at the core of small RNA silencing pathways. (a) Schematic representation of AGO2 domains, (b) AGO2 protein structure and the position of miRNA loading (active site) and (c) miRNA loading onto AGO2 complex and cleavage (Schuster et al., 2019).

AGO1 executes a more subsidiary role in gene silencing, whereas AGO4 appears to control the entry into meiosis and sex chromosome silencing, in mouse germ line (Faehnle et al., 2013; Jan et al., 2017; Modzelewski et al., 2012). Although in humans, only AGO2 appeared to have purely slicer-endonuclease and microRNA (miRNA) stabilization activity (Broderick et al., 2011; Hauptmann et al., 2013; Liu et al., 2004; Gunter Meister et al., 2004), a selective cleavage activity of AGO3 was recently discovered (Park et al., 2017). AGO3 has also been implicated in mRNA decay via Alu-elements directed by RNA (QiDong Hu et al., 2012). The same well-conserved motif in the catalytic center, responsible for the cleavage activity, is shared between AGO2 and AGO3. AGO2 is experimentally proved to have catalytic activity towards mRNA targets by an siRNA/miRNA -with perfect complementarity- manner (Liu et al., 2004; G. Meister et al., 2004; Rand et al., 2004). Recently, it was documented that AGO3-RISC complex has the complete catalytic site and the presence of an imperfect nucleic acid-binding channel allowing for AGO3 to have a selective cleavage activity with more intricate substrate requirements (Park et al., 2017). Eventually, AGO2 and AGO3 have different optimum guide lengths for target cleavage (Park et al., 2017). Remarkably, AGO3 besides its catalytic properties, it has been proposed to be involved in stabilization of siRNAs from processed RNA polymerase III-transcribed Alu repeats containing a DR2 retinoic acid response element (RARE) in stem cells (Q. Hu et al., 2012).

With regard to the miRNA pathway, mammalian AGOs may have overlapping functions. Consistently, all four AGO proteins, when overexpressed, were shown to bind endogenous miRNAs indistinguishably (Liu et al., 2004; G. Meister et al., 2004) and when knocked down they appear to function in a compensatory manner (Diederichs & Haber, 2007). The lack of a DNA binding domain in AGOs puzzles regarding the nuclear function of AGO2. However, AGO2 appears to achieve gene regulation through localizing regulatory proteins (i.e., chromatin-modifying enzymes) to specific genomic DNA regions [reviewed by (Li, 2014)]. Subcellular localization studies

demonstrated the differential nuclear distributions of Ago1 and Ago2 contributing to the functionally distinct nature in the nucleus (Ahlenstiel et al., 2012; Huang et al., 2013). While the nuclear localization of AGO1 is generally scattered throughout the nuclear interior, AGO2 predominantly localizes to the inner nuclear periphery. This leads to an explanation for the lack of Ago2-chromatin association at steady-state. It is justifiable to assume that AGO1 and AGO2 have differential nuclear abundance, which may affect their target specificity. Nuclear AGO1 selectively interacts with RNA polymerase II (RNAP II). AGO1, but not AGO2, is pervasively associated with promoters of actively transcribed genes involved in growth, survival, and cell cycle progression (Huang et al., 2013). Moreover, AGO1 and AGO2 facilitate spliceosome recruitment and modulate RNA polymerase II elongation rate, thereby affecting alternative splicing (Ameyar-Zazoua et al., 2012).

The leading canonical pathway of miRNA biogenesis, achieved by AGOs, commences with the transcription of pri-miRNAs which is processed by the microprocessor complex, comprises the DiGeorge Syndrome Critical Region 8 RNA binding protein (DGCR8) and Drosha, a ribonuclease III enzyme(Denli et al., 2004). The produced pre-miRNAs are transferred to the cytoplasmic compartment by Exportin 5 (XPO5)/RanGTP complex. At its new position, the pre-miRNAs will be cleaved by Dicer, an RNase III endonuclease (Okada et al., 2009) removing the terminal loop and leading to miRNA maturation (Ha & Kim, 2014) (Figure 27). Hereafter, the mature miRNAs could be loaded onto AGO complexes in an ATP-dependent manner (Yoda et al., 2010).

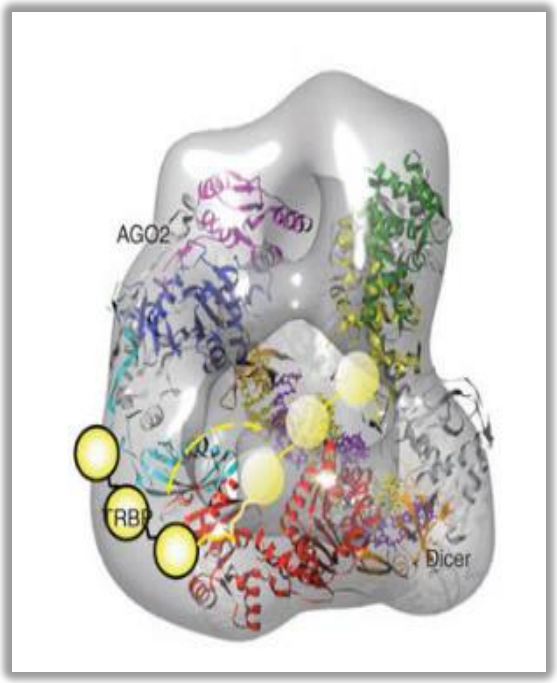

Figure 27 Proposed working model of the human RISC Loading Complex (Wang et al., 2009).

The passenger strand is ultimately released and the preserved strand guides and leads to the advancement of the regulation of gene expression. The retained miRNA guide strand facilitates the transfer of AGO-miRNA complex to the 3’ UTR (untranslated region) of mRNA targets. A crucial aspect is the degree of sequence complementarity between the miRNA seed region (2-8 nts from the 5’ end) and the mRNA target. More specifically, the 5'-end of the microRNA tends to have more bases complementary to the target than the 3'-end does. The complementarity of seven or more bases to the 5'-end miRNA is sufficient for regulation. Base-pairing between the 3'-segment

of the miRNA and the mRNA target is not always essential for repression, but strong base-pairing within this region can partially compensate for weaker seed matches or enhance repression. The miRNA:mRNA matching is ensued by translational repression and destabilization and/or degradation of the bona fide mRNA target sequences (Jonas & Izaurralde, 2015).

In recent years, besides the canonical pathway, a wide spectrum of non-canonical biogenesis pathways has emerged (Hansen et al., 2016; Stagsted et al., 2017). In non-canonical biogenesis, the cleavage of microprocessor complexes is avoided or alternative combinations of Exportin and/or miRISC loading complex proteins are involved (Ruby et al., 2007).

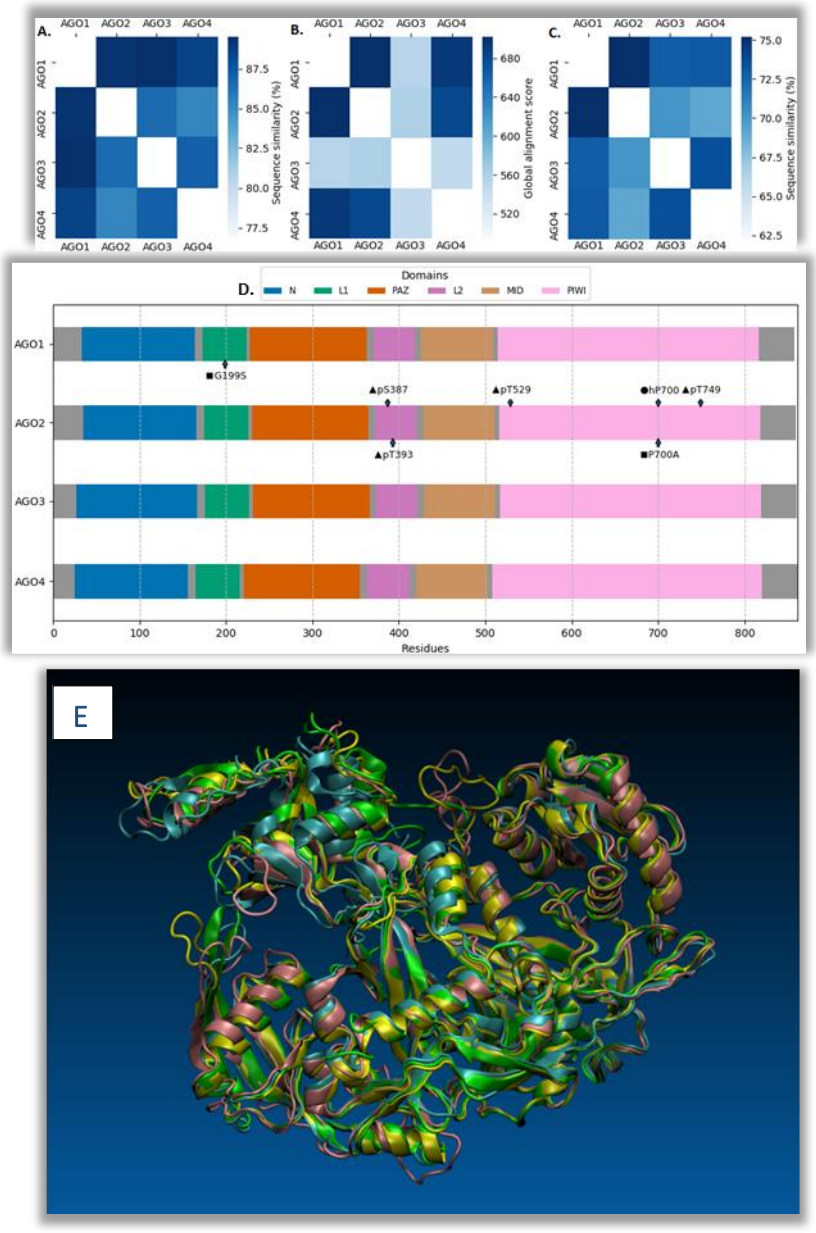

Figure 28 Comparative analysis of the human Argonaute (AGO) (AGO1–AGO4) protein-subfamily members. (A) Protein sequence similarity via global alignment. (B) Protein secondary structure via global alignment. (C) Coding-Sequence (CDS) similarity via global alignment. The alignments in (A) and (C) were yielded by the EMBL EMBOSS Needle with default settings (Madeira et al., 2019). The alignments in (B) were calculated using BioPython package with −2 as open gap penalty score, −1 as a gap extension penalty score, −1 as a mismatch score, and 1 as a matching score. Protein sequences were retrieved from ENSEMBL (Cunningham et al., 2018).Protein-secondary structures (DSSP entries) were retrieved from RCSB PDB (Berman et al., 2000). Plots were generated with

Matplotlib and Seaborn Python packages. (D) Domains of AGO1–4 with annotations for mutations [■ = mutation]: G199S, P700A, and post-transcriptional modifications [● = hydroxylation (h), ▶ = phosphorylation (p)]: hP700, pS387, pT529, pT749, and pT393, respectively. Domain information was retrieved from Pfam database. Plots were generated with Matplotlib and Seaborn Python packages. (E) A superposition of the AGO 1–4 tertiary structures in New Cartoon representation, as displayed by VMD software (Humphrey et al., 1996). These structural models are refined PDB data from the PDB-REDO databank (Klionsky et al., 2016), 4KRE [AGO1, yellow colored], 4Z4D [AGO2, cyan colored] (Schirle et al., 2015), 5VM9 [AGO3, pink colored] (Park et al., 2017), and 6OON [AGO4, green colored] (Park et al., 2019). The structural data were further processed using Schrödinger Maestro Suite (Schrödinger Release 2020-2, (Madhavi Sastry et al., 2013) by removing existing water molecules and ligands and filling missing loops and side chains [Prime], calculating the protonation states on physiological pH 7.4 [PROPKA] (Olsson et al., 2011; Søndergaard et al., 2011), and minimizing the free energy of the resulting structures with the OPLS3 force field (Harder et al., 2016).

The versatile functional role of AGO can be dictated, affected or altered by post-translational modifications. Such modifications include Ago2 SUMOylation (Josa-Prado et al., 2015), acetylation (Zhang et al., 2019) and ubiquitination (Gibbings et al., 2012; Rybak et al., 2009). Moreover, under cell stress, AGOs are modified by poly (ADP-ribose) in order to relieve miRNA-guided repression (Bütepage et al., 2015; Leung et al., 2011). Also of note, phosphorylation state of the serine/threonine cluster is crucial for AGO-mRNA interactions affecting mRNA binding and localization. This modification, especially Ser387, Tyr529 and Tyr393 phosphorylation, is essential for miRNA-guided gene silencing *in vivo* (Figure 28) (Meister, 2013; Quévillon Huberdeau et al., 2017). It has also been reported that mutated proline700 (P700) to alanine drives AGO2 destabilization. In an attempt to measure the efficiency of AGO hydroxylation *in vitro*, Qi and colleagues found that AGO2 and AGO4 appear to be more efficiently hydroxylated than AGO1 and AGO3 (Qi et al., 2008), demonstrating differential properties of the AGO family members.

AGOs in Cancer

The implementation of AGOs in cancer, through microRNA de-regulation, is extensively studied and many reports and review articles presented the populations of the microRNAs that their expression is altered. However, alterations of the AGOs *per se*, their expression, polymorphisms, modifications and interactions also appear to be involved in cancer.

The de-regulated AGO gene expression, including loss, is pinpointed in a variety of malignancies such as breast cancer, melanoma, ovarian, urothelial, prostate, clear cell renal, gastric and colorectal carcinomas as they affect the proliferation rate and/or the migratory potential (Bian et al., 2014; Conger et al., 2016; Di Leva & Croce, 2013; Lee et al., 2019; Völler et al., 2013; Yang et al., 2014). Elevated expression of AGO is often reported in glioma, breast, hepatocellular, gastric, colon, ovarian, bladder and prostate cancer, although there are incidents of lower levels. Expression studies for breast, lung, prostate, gastric and renal cancer as well as glioma, melanoma and reported cases for acute lymphoblastic leukemia support the heterogeneity of the AGO expression levels in cancer. The de-regulation of AGO2, the most abundant molecule of the AGO subgroup, has been associated with tumorigenesis, cancer progression and therefore suggested for therapeutic treatments (De Santa et al., 2013; Iosue et al., 2013; Masciarelli et al., 2014; Xu et al., 2016). Using GeneMANIA (Multiple Association Network Integration Algorithm) for prediction of the gene function, Liu et al. showed that the AGO2 up-regulation was correlated with acceleration in tumor progression and poorer survival in 962 lung cancer patients (Liu et al., 2020). However, in melanoma cells, down-regulation of AGO2 could lead to cell and tumor growth (Zhang et al., 2013). As AGOs demonstrate a cell-type and tissue-dependent subcellular

distribution, differentially regulation of gene expression in normal and in cancerous conditions (Sharma et al., 2016) is anticipated.

The AGO2 chromosomal position, 8q24.3, constitutes a frequently amplified locus in many cancer types, including hepatocellular carcinoma (HCC). The change of DNA copy number of AGO2, through DNA amplification or gain, may lead to up-regulation of AGO2. This subsequently affects the transcription levels of the focal adhesion kinase (FAK) in HCC patient (Cheng et al., 2013). FAK is a non-receptor tyrosine kinase, activated by integrins and growth factors that can influence the cytoskeleton structures, cell adhesion sites and membrane protrusions and therefore regulate cell movement in cell migration and angiogenesis (Zhao & Guan, 2011). The elevation of FAK occurs by microRNA-independent AGO2 function and slicer-independent role in microRNA stabilization (Cheng et al., 2013; Winter & Diederichs, 2011), offering a potential target for promising HCC treatment.

Notably, single-nucleotide polymorphisms of AGO1 and AGO2 were found to be related to the disease-free survival (DFS) and overall survival (OS) in breast cancer and to the risk impact of gastric and renal cell carcinoma, (Györffy et al., 2010; Horikawa et al., 2008; Mihály et al., 2013; Sung et al., 2012). More specifically, AGO2 rs3864659 seems to have a protective effect on breast cancer patients, whereas AGO2 rs11786030 and rs2292779 have been linked with poor prognosis, in Korean cohorts (Guo et al., 2016). Additionally, the AGO1 rs595055 polymorphism has been related to low breast cancer risk (Bermisheva et al., 2018). In the Chinese Han population, a genetic variant (AA and A allele of rs636832) of AGO1 influence gastric cancer by demonstrating a lower level of lymphatic metastasis (Song et al., 2017). In a Caucasian male cohort, the AG+GG genotypes of *AGO1* rs595961 had a significant protective effect (Fang et al., 2016). Further, the impact of the genetic variants rs636832 and rs595961 located within AGO1 may have susceptibility for specific types of cancer such as pediatric acute lymphoblastic leukemia, hematological malignancy, lung cancer (Dobrijević et al., 2020).

Besides the de-regulation of AGO expression levels and single-nucleotide polymorphisms, post-translational modifications of AGO can lead to an increase of the invasive potential of tumors. Under normoxia, c-Src appears to have a stronger binding affinity to AGO2 and therefore it constitutes the major kinase for AGO2. However, phosphorylation at tyr393, tyr529 or/and tyr749 sites in AGO2, shows an apparent tumor-promoting effect (Liu et al., 2020). Clinical data of breast cancer patients reveal a link between AGO2 phosphorylation in Tyr393 and poorer overall survival (Liu et al., 2020). This phosphorylation, dictated by EGFR and not c-Src, inhibits Dicer binding to AGO2 and subsequently the maturation of a particular microRNA subset. Moreover, hypoxia-mediated prolyl 4-hydroxylation at Pro700, another crucial modification, leads to the accumulation of AGO2 protein in stress granules through association with Hsp90. This dictates the elevation of the microRNA levels influencing the protein stability and affecting the tumorigenesis and tumor growth (Wu et al., 2011). Besides AGO2, AGO1 is also a target of hypoxia, as *in silico* bioinformatics and *in vitro* validation showed that Hypoxia induced factor 1α (HIF1α) induces hypoxia-responsive microRNAs (HRMs) that target AGO1 (Chen et al., 2013). Subsequently, the latter promotes translational de-suppression of *VEGF* mRNA, associated with tumour angiogenesis and poor prognosis and providing a suitable potential target for anti- or pro-angiogenesis strategies.

DNA damage is an important contributor to tumor formation as double strand brakes (DSBs) are hot spots of genome instability with demanding need of proper repair. DNA-damage response (DDR) foci formation studies and checkpoint assays in human, mouse and zebrafish,

demonstrated that elements of the RNAi pathway such as DICER and DROSHA but not AGO, are necessary to activate DDR upon exogenous DNA damage and oncogene-induced genotoxic stress (Francia et al., 2012). Wei et al. reported that double strand break induced small RNAs (diRNAs) are produced in vicinity of the DSBs, which then serve as guiding molecules to facilitate DNA repair. AGO2/diRNAs can either directly recruit DSB repair proteins or assist in modifying local chromatin and indirectly facilitate the repairing process (Wei et al., 2012). How exactly AGO proteins are involved in DSB repair is a fascinating question that remains to be addressed. However, Gao et al., showed that AGO2 forms a complex with Rad51, a protein that forms nucleoprotein filaments that facilitate strand invasion and initiate the homologous recombination (HR) process (San Filippo et al., 2008). Rad51 accumulation at DSB sites and HR repair depends on the catalytic activity and the small RNA-binding capability of AGO2. These findings support a model in which Rad51 is guided to DSB sites by diRNAs through interacting with AGO2 (Gao et al., 2014).

Finally, AGO appears to play a role in the telomere-regulation, essential for maintaining genome stability and controlling cell proliferation. The length of human telomeric DNA is maintained by telomerase, a ribonucleoprotein (RNP) enzyme that its activity is highly elevated in 85–90% of human cancers (Kim et al., 1994; Shay & Bacchetti, 1997). Telomerase contains two catalytic components, the telomerase reverse transcriptase (TERT) and the H/ACA box telomerase RNA component (TERC), which is the template used for the synthesis of telomeres. AGO2 promotes telomerase activity and stimulates the association between TERT and TERC, by interacting with TERC and with a newly identified sRNA (*terc*-sRNA). AGO2 depletion results in shorter telomeres as well as in lower proliferation rates *in vitro* and *in vivo* (Wei et al., 2012). Collectively, these data uncover a new layer of complexity in the regulation of telomerase activity by AGO2 and might lay the foundation for new therapeutic targets in tumours and telomere diseases.

AGOs in EMT

Recently, a couple of studies demonstrate the indirect role of AGOs in EMT transition. Specifically, Wang and colleagues showed that AGO2 appears to be a direct target of miR-100. Downregulation of AGO2 repressed migration, invasion, EMT and stemness of prostate cancer cells, and reversed the effects seen with miR-100 downregulation. Downregulation of AGO2 enhanced expression of miR-34a and miR-125b which can suppress migration, invasion, EMT and stemness of cancer cells. All things considered, miR-100 seems to negatively regulate the metastatic potential partially via AGO2 targeting (M. Wang et al., 2014). Hou and colleagues indicated the involvement of AGO2 in EMT through a Polypyrimidine Tract Binding Protein 3 (PTBP3) interaction. PTBP3 contains four RNA recognition motifs found to be implicated in miRNA-mediated gene decay and RNA splicing. PTBP3 binding to AGO2 and simultaneously to the 3' UTR of *ZEB1* stabilizes the *ZEB1* mRNA for EMT induction (Hou et al., 2018). Although indicative, the information regarding the involvement of AGOs in EMT is still restricted. We strongly believe that further investigation will highlight the role of AGOs in EMT.

Cell cycle and cytokinesis in cancer

Cytokinesis is the final step of cell cycle that the daughter cells eventually separate. The process is spatiotemporally regulated with great accuracy ensuring that each daughter cell receives an equal share of DNA, organelles and other cellular materials (Atilla-Gokcumen et al., 2010). A well-functional cytoskeleton, cell cycle molecules and membrane machineries of cells as well as their

coordination are fundamental prerequisite for the successful completion of cytokinesis as they safeguard the bisection of the axis of chromosome segregation with the cleavage furrow occurrence (Eggert et al., 2006).

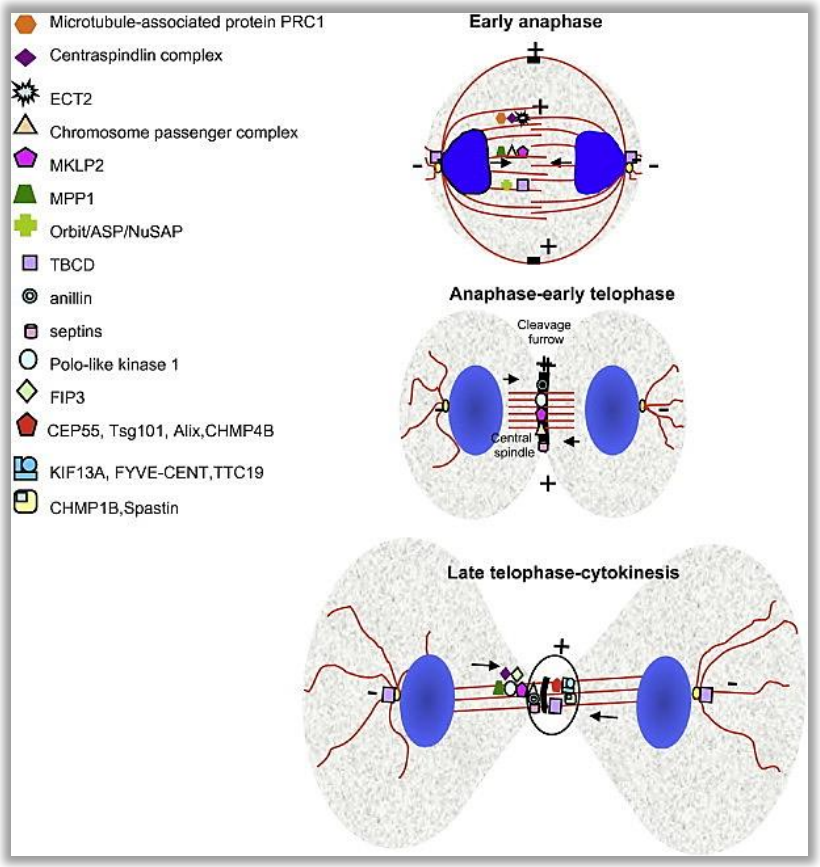

Figure 29 Schematic representation illustrating the roles of spindle proteins that function during the various stages of cell division. DNA is indicated in blue, centrosomes in yellow and microtubules in red (Sagona & Stenmark, 2010).

Cytokinesis is separated into six discrete subprocesses (Eggert et al., 2006):

Timing: Proteolysis is involved in regulating C phase (the period during the cell cycle in which cytokinesis can occur in animals), the time during which the cortex can contract.

Cleavage plane specification: Multiple mechanisms operate in parallel; the Rho pathway and a number of kinases are involved. The recruitment of RhoA GTPase at the cleavage plane is the most important one. The accepted scenario of the Rho-dependent actomyosin equatorial contractile ring includes the Rho-dependent actomyosin-anillo-septin membrane-anchored ring (the AMAS ring), and is controlled by Rho and organized by Anillin (Carim et al., 2020). The AMAS ring can buffer its own tension. The function of furrow asymmetry considered as a mechanical benefit that makes cytokinesis robust, suggesting that the contractile ring possesses an intrinsic symmetry-breaking mechanism to promote asymmetric furrowing. Anillin and septins are required for the Geometry of Furrow Ingression (Figure 29). Anillin depletion in embryos seems to lead in failure of furrow asymmetry and defects (Maddox et al., 2005), whereas septin-depleted embryos exhibit furrow asymmetry failure (Nguyen et al., 2000).

Rearrangement of microtubule structures: Microtubules rearrange into different arrays that have varied functions (Figure 30).

Ring assembly: Cortical flow and local nucleation contribute to assembly of actomyosin filaments. Requirement of continuous signals from microtubules leads to the maintenance of the position of the cleavage furrow, and to the formation of the midbody ring (or alternatively Fleming body). These signals control the localization of myosin II independently of other furrow components (Straight et al., 2003).

Ring ingression: Force generation mechanisms for different orientations relative to the furrow are discussed. The traditional purse-string model is most likely an over-simplification. Narrowing of the intercellular bridge to ~100nm, a step that is known as the secondary ingression aiding to organelle segregation (Figure 31), is regulated by FIP3-endosomes (Schiel & Prekeris, 2013).

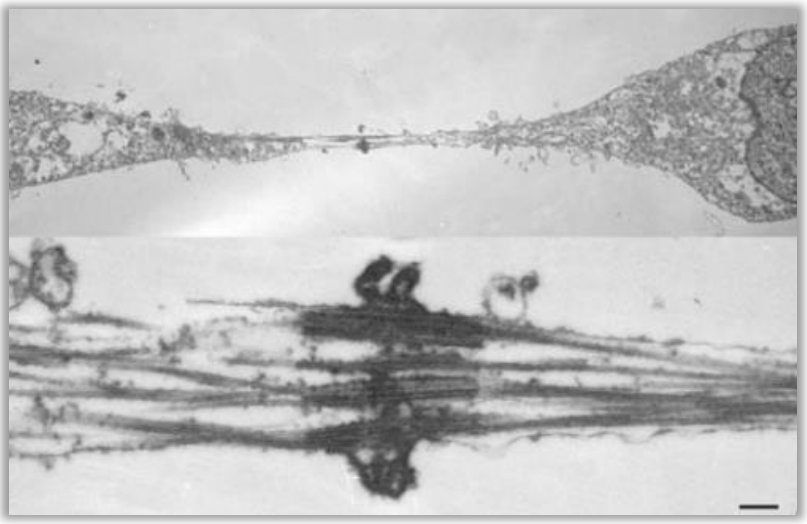

Figure 30 An electron micrograph of a dividing HeLa cell. The upper panel shows an intercellular bridge between two daughter cells. The nucleus of the right-hand cell is visible. The lower panel is a higher resolution image of the same bridge. Note the bundled microtubules in the midbody and the electron-dense material (stembody) concentrated in a discrete zone at the center of the bridge (lower panel). Stembodies typically bulge outward at their center. The bar shown in the lower panel corresponds to 2 μm (upper panel) and 250 nm (lower panel). Image's courtesy of Margaret Coughlin.

Completion: In this final step, cleavage of the membrane bridge, is mediated by the endosomal sorting complex required for transport (ESCRT) proteins responsible for membrane remodeling activities (Hurley & Hanson, 2010). When the midbody diameter is 25 times greater than the estimated threshold for membrane remodeling by ESCRT proteins, the midbody appears at its thickest point, a condition called secondary abscission. Thereby, a membrane scission is followed (Elia et al., 2011; Guizetti & Gerlich, 2010) (Figure 32). Revolutionary findings placed this process in the center of cancer research, since plagiochiline A, an anticancer-antiproliferative agent that in a variety of solid tumor cell lines derived from prostate, colon, breast, lung, and cervical cancers, as well as several leukemia cell lines (Aponte et al., 2010) inhibits cell division by preventing completion of cytokinesis at the final abscission stage (Stivers et al., 2018).

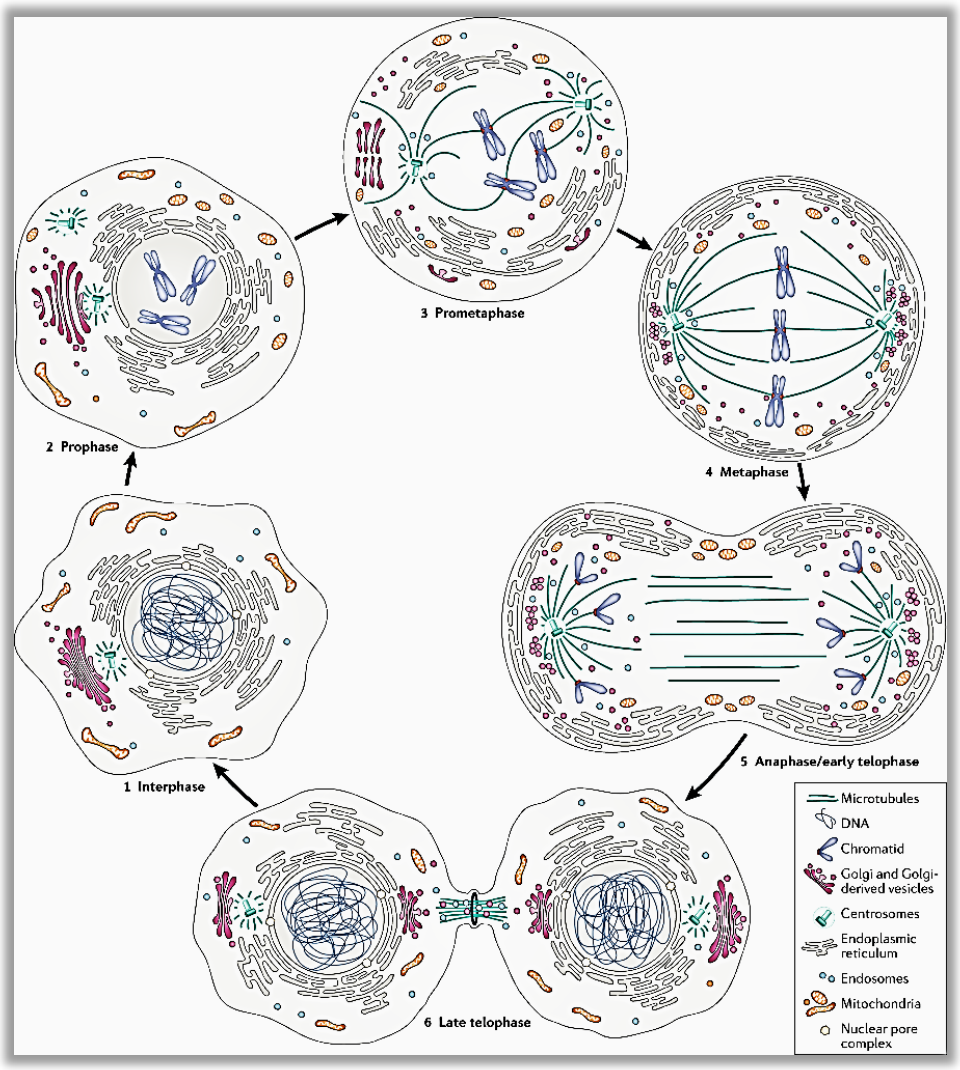

Figure 31 Schematic representation illustrating the organelles segregation (Carlton et al., 2020).

Tumor susceptibility gene 101 (TSG101), an ESCRT-I component, and apoptosis-linked gene 2-interacting protein (ALIX) were detected to reside to the midbody during cytokinesis via interaction with CEP55 (Stivers et al., 2018) functioning with downstream ESCRT pathways members in membrane fission. Cep55-depleted cultured human cells remain connected through a cytokinetic intercellular bridge for a protracted period, however, finally, become binucleated (Carlton & Martin-Serrano, 2007; Fabbro et al., 2005; Morita et al., 2007; Zhao et al., 2006). Accordingly, Cep55 appears to be a regulator of cancer cell progression and in fact, this happens through its association with PI3K/AKT pathway (Tandon & Banerjee, 2020). ALIX and ESCRT-III interaction are vital for cytokinesis, as disruption of this module, or RNAi-mediated depletion of either TSG101 or ALIX, promotes abscission inhibition (Carlton & Martin-Serrano, 2007; Morita et al., 2007).

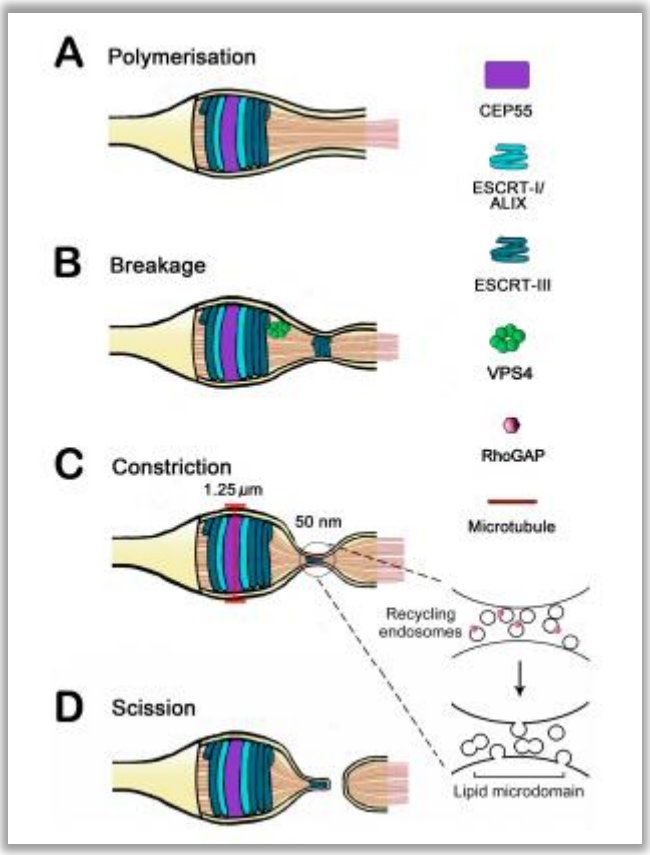

Figure 32 Schematic model for abscission in mammalian cells. In panel (A), CEP55 (Centrosomal protein of 55 kDa) has first recruited ESCRT-I components (Tumor susceptibility gene 101 (TSG101), apoptosis-linked gene 2-interacting protein (ALIX) to the Flemming body, followed by the recruitment of ESCRT-III. (B) The Recruitment of the ATPase VPS4 to this assembly is proposed to mediate breakage or remodeling of the ESCRT-III, facilitating the appearance of ESCRT-III at the abscission zone. (C) Constriction at the secondary ingression site may be driven either by fusion of endosomal vesicles with the plasma membrane (inset) or by ESCRT-III interactions with the plasma membrane and (D) Scission is thought to be driven by the ESCRT-III/VPS4 complex (Bhutta et al., 2014).

Interestingly, pluripotent mouse ES cells follow a slow dividing tempo as the cells remained connected by cytoplasmic bridges for a long time after cell division, but abscission accelerates during naive pluripotency exit (Chaigne et al., 2020). Abscission that can occur in G1 phase or later during division constitutes a permissive cue for naive pluripotency exit (Gershony et al., 2014).

During abscission, midzone microtubules, vesicle transport, and centrosomes are important for the completion of the process. In general, cell divisions must also follow a predetermined orientation to preserve correct tissue architecture (Mascanzoni et al., 2019). During mitosis, DNA segregation, proper reorganization and segregation of cellular organelles, called organelle inheritance, is indispensable to ensure the correct cell division. Hitherto, the only evidence of the importance of correct organelle inheritance for organism development has been provided by the effects of peroxisome misplacement, which drives in structural alterations of the epidermis (Asare et al., 2017). Moreover, lack of DEPDC1B expression, a cell-cycle gene involved in the transition from G2 phase to mitosis which guides to severe defects of zebrafish morphogenesis (Marchesi et al., 2014).

Finally, the concluding step of this process is the intracellular accumulation of postmitotic midbodies, also known as midbody remnants. These remnants were shown to correlate with an

increase in cell division rate and stemness (Kuo et al., 2011), proposing postmitotic midbodies (midbody inheritance) interplay in regulating cell proliferation, stem cell differentiation, and fate determination (Peterman & Prekeris, 2019). Any interference in the progression of this procedure can induce cytokinesis failure and the genesis of binuclear tetraploid cells or binuclei formation (Pandit et al., 2013). Remarkably, in normal tissues, cytokinesis failure is a physiological part of some processes, such as the respond of ventricular cardiomyocytes to an amplification of blood flow by an adaptive increase in volume of the heart (hypertrophy), right after birth. During this event, a drastic decrease of RhoA and its effector ROCK account for defects in the process of cytokinesis. Indeed, in some diploid cardiomyocytes, a not-functional cytokinetic ring is formed, cytokinesis is never achieved, and tetraploid binucleated cell is consequently generated (Donné et al., 2018). Another paradigm of polyploidization implicating cytokinesis failure occurs in hepatocytes. During the weaning period, in liver parenchyma, diploid hepatocytes can provide two daughter diploid cells through normal cell division or follow the program of cytokinesis failure. With the lack of a contractile ring, cleavage-plane specification of diploid hepatocytes is never established due to the deficiencies of actin cytoskeleton reorganization (Celton-Morizur et al., 2009; Margall-Ducos et al., 2007).

The crucial kinases for an intact contractile ring are Aurora B and PLK which cooperate and regulate through phosphorylation (Zhou et al., 2014) a common downstream factor, the centralspindlin complex consisting of MKLP1 and MgcRacGAP, a Rho GTPase activating protein (Mishima et al., 2002). Specifically, among PLKs, PLK4 (polo-like kinase 4) plays a critical role in centrosome duplication during cell division. Inhibition of its activity prevents translocation to the spindle midzone/cleavage furrow and thereby, alters abscission. This leads to the generation of polyploidy, increased numbers of duplicated centrosomes, and vulnerability to anaphase or mitotic catastrophe (Press et al., 2019).

Unstable aneuploid cells undergoing malignant transformation is the other side of the coin of cytokinesis failure. During Fanconi anemia's pathology, characterized by bone marrow failure and cancer predisposition, FANCA protein-hematopoietic deficient cells have ultra-fine bridges leading to cytokinesis failure (Vinciguerra et al., 2010). The cells that failed cytokinesis, could trigger an apoptotic program or a tumorigenic program. Recent studies demonstrate that APC (adenomatous polyposis coli) mutations detected in human colorectal cancer may prevent mitotic spindle anchoring at the anaphase cortex, inhibiting the initiation of cytokinesis. This supports the idea that tetraploidy may represent the first step in genomic instability and, eventually, cancer (Vinciguerra et al., 2010).

The harmful effects of mitotic errors on genomic stability give rise in the question: "how frequently these events occur in vivo?". Direct observation of the mitotic errors is difficult to be achieved. Consequently, several studies have measured the degree of aneuploidy in normal cells using fluorescence *in situ* hybridization (FISH), chromosome spreads or spectral karyotyping. In specific, the detection of aneuploidy leads to genomic plasticity facilitation that allows rapid evolution of aggressive genotypes. Classic solid tumors are polyploidy-prone but also harbor chromosome abnormalities, presumably resulting from failures in both mitosis and cytokinesis. These two events are closely associated with centrosome abnormalities and chromosome mis-segregation, triggering failure of completion (Shi & King, 2005). Centrosome abnormalities could cause spindle assembly and cytokinesis defects such as centrosomal amplification and spindle multipolarity [reviewed by (Saunders, 2005)]. Transient cytokinesis blockage leads to the formation of genetically unstable tetraploid cells, promotes tumorigenesis in p53 -/- mouse mammary epithelial cells (Fujiwara et al., 2005).

Towards the same direction, McKenzie and colleagues reported that cytokinesis failure caused by depletion of Citron kinase (CITK) dramatically decreased cell proliferation in breast, cervical and colorectal cancer cells. Also, CITK depletion promotes the activation of the Hippo tumor suppressor pathway in normal, but not in cancer cells. This depletion promotes cancer cells to die via apoptosis in a caspase-7 dependent manner. Consistently, p53-deficient HCT116 colon carcinoma cells failed to induce apoptosis after cytokinesis failure. Additionally, cancer cells were more susceptible to CITK depletion, providing that the induction of cytokinesis failure could be a potential anti-cancer therapeutic approach for a wide range of cancers, especially those characterized by fast cell proliferation and polyploidy (McKenzie & D'Avino, 2016).

A promising field for therapeutic strategies involves Aurora kinase inhibitors (Table 2) that are currently in clinical trials (Jayanthan et al., 2014; Lin et al., 2020; Lu et al., 2008).

Aurora kinase inhibitors in clinical trials.

Name	Clinical trial	Disease condition	Starting date	Sponsors	Current status
Alisertib (MLN8237)	Phase 3 NCT01482962	Relapsed or refractory peripheral T-Cell lymphoma	June 2012	Millennium pharmaceuticals, inc. Takeda	Ongoing
	Phase 2 NCT02560025	Induction Chemotherapy in patients with High-risk acute myeloid Leukaemia	December 2015	Millennium pharmaceuticals, inc. Takeda	Ongoing
	Phase 2 NCT01316692	Patients with unresectable stage iii-iv melanoma	October 2011	Vanderbilt-ingram cancer centre	Terminated (April 2016)
	Phase 2 NCT02038647	Small-cell-lung Cancer (SCLC) treatment in combination with paclitaxel	February 2014	Millennium pharmaceuticals, inc. Takeda	Ongoing
	Phase 1 NCT02551055	Neoplasms, Advanced or Metastatic	October 2015	Millennium pharmaceuticals, inc.|takeda	Ongoing
	Phase 1 NCT02214147	Advanced solid tumors or Relapsed/Refractory lymphoma	September 2014	Millennium pharmaceuticals, inc	Completed
Tozasertib (VX-680, MK0547)	Phase 2 NCT00290550	Non-small-cell lung carcinoma	June 2006	Merck sharp & dohme corp.	Terminated
	Phase 2 NCT00405054	Leukaemia	December 2006	Merck sharp & dohme corp.	Terminated
	Phase 1 NCT00500006	Chronic myelogenous leukaemia, lymphoblastic, acute, philadelphia-positive	October 2007	Merck sharp & dohme corp.	Terminated
	Phase 1 NCT00111683	Chronic Myelogenous leukaemia in blast crisis, lymphocytic leukaemia, B Cell acute and chronic myelogenous leukaemia	June 2005	Merck sharp & dohme corp.	Completed August 2015
	Phase 1 NCT02532868	Advanced solid tumors	May 2005	Merck sharp & dohme corp.	Terminated
	Phase 1 NCT00099346	Colorectal cancer	January 2005	Merck sharp & dohme corp.	Terminated
MLN8054	Phase 1 NCT00249301	Advanced solid tumors	October 2005	Millennium pharmaceuticals, inc takeda	Terminated
	Phase 1 NCT00652158	Advanced malignancies	April 2006	Millennium pharmaceuticals, inc Takeda	Terminated
Danusertib (PHA739358)	Phase 2 NCT00872300	Multiple myeloma	October 2008	Nerviano medical sciences	Completed May 2014
	Phase 2 NCT00766324	Hormone refractory prostate cancer	September 2007	Nerviano medical sciences	Completed May 2014
AT9283	Phase 2 NCT01145989	Patients with relapsed or refractory multiple myeloma	June 2010	Ncic clinical trials group	Completed November 2015
	Phase 2 NCT00522990	Leukaemia	September 2006	Astex pharmaceuticals	Terminated
	Phase 1 NCT00985868	Relapsed and Refractory Solid Tumors	September 2009	Cancer research uk	Completed April 2013
	Phase 1 NCT01431664	Patients With Relapsed or Refractory Acute Leukaemia	September 2011	Cancer research uk	Completed December 2014
	Phase 1 NCT00443976	Advanced or metastatic solid tumors or non-hodgkin's lymphoma	January 2007	Ncic clinical trials group	Completed January 2012
AMG-900	Phase 1 NCT00858377	Advanced solid tumors	August 2009	Amgen	Ongoing
	Phase 1 NCT01380756	Acute myeloid leukaemia	July 2011	Amgen	Completed February 2015
VX-689 (MK-5108)	Phase 1 NCT00543387	Advanced and/or Refractory solid tumors	March 2008	Merck sharp & dohme corp.	Completed April 2011
SNS-314 Mesylate	Phase 1 NCT00519662	Advanced solid tumors	August 2007	Sunesis pharmaceuticals	Completed March 2009

Name	Clinical trial	Disease condition	Starting date	Sponsors	Current status
TAK-901	Phase 1 NCT00807677	Advanced hematologic malignancies	March 2009	Millennium pharmaceuticals, inc. Takeda	Completed March 2013
	Phase 1 NCT00935844	Advanced solid tumors or lymphoma	October 2009	Millennium pharmaceuticals, inc. Takeda	Completed November 2011
CYC116	Phase 1 NCT00560716	Advanced solid tumors	June 2007	Cyclacel pharmaceuticals, inc	Terminated
GSK1070916	Phase 1 NCT01118611	Advanced solid tumors	March 2010	Cancer research uk	Completed March 2013
PF03814735	Phase 1 NCT00424632	Advanced solid tumors	November 2006	Pfizer	Completed June 2009
ENMD-2076	Phase 2 NCT01914510	Ovarian clear cell cancers	September 2013	University health network, toronto	Ongoing
	Phase 2 NCT01639248	Previously treated locally advanced + metastatic tnbc	July 2012	Casi pharmaceuticals, inc	Ongoing
	Phase 2 NCT02234986	Advanced fibrolamellar carcinoma	October 2015	Casi pharmaceuticals, inc.	Ongoing
	Phase 2 NCT01104675	Patients with ovarian cancer	April 2010	Casi pharmaceuticals, inc.	Completed December 2012
	Phase 1 NCT00658671	Advanced cancer	April 2008	Casi pharmaceuticals, inc.	Completed June 2012
	Phase 1 NCT00806065	Multiple myeloma	December 2008	Casi pharmaceuticals, inc.	Completed January 2012

Table 2 Aurora kinase inhibitors in clinical trial (PMID: 28918096).

Cells treated with these drugs gain polyploidy before eventually dying, a mechanism of cell killing different from mitotic spindle poisons such as taxol. However, given that blocking cytokinesis in p53-/- cells can cause cancer in mice, there is a risk that these drugs will cause cancer as well as treat it, a concept familiar regarding DNA-damaging agents. Moreover, cancer drugs targeting generic cell division mechanisms could kill normal stem cells and thus lead to bone marrow and gut toxicity. An ideal group of drugs would selectively block only cytokinesis of tumor cells through mechanisms for the selective inhibition of cancer components.

Research Aim & Objectives

Thyroid tumors are the most common malignancies of the endocrine system, usually with good prognosis. However, specific subtypes such as tall cell variants (TCV) exhibit aggressive characteristics and poor outcome. Severe cytoskeletal remodeling, often through Epithelial to Mesenchymal Transition (EMT) molecular pathways is a key event in cancer. *The goal of this study is the characterization of this phenomenon and the deep understanding of the molecular associations and gene pathways that dictates the cell programming and therefore, the fate of the disease and the outcome of the patient. Through this knowledge, we aim to achieve better stratification and new targets for potential diagnosis and treatment.*

Towards that direction, a retrospective cohort study of thyroid cancer patients was performed to investigate the substrate of thyroid carcinoma. We focused on the characterization of the aggressive subtype tall cell variant (TCV) through micro-staging of tumors. Morphological changes and cytoskeletal remodeling were addressed, gene deregulation was recorded and the molecular pathways involved were identified. Compounds of RNA-induced silencing complex (RISC), such as Argonautes (AGOs), were investigated to contribute to the molecular characterization of the cells. We focused on AGO2, the foremost member of the AGO family, responsible for the "loading" of microRNAs (miRNAs) and directing them to the mRNA targets, for post-transcriptional gene regulation. The role of the active miRNome, the miRNAs that are part of the miRNA::AGO2::mRNA complexes, in thyroid cancer was further examined. A specific miRNA, miR26, was selected for investigation as a therapeutic target for thyroid cancer.

MATERIALS & METHODS

Lab Equipment

- Vortex Genie, K-550-GE Scientific Industries Inc., USA
- Centrifuge, Z-323-K HERMLE Germany
- Compact high speed refrigerated centrifuge, 7780, Kubota, Japan
- Automatic CO2 incubator, 5425-1 NAPCO, USA
- Microflow advanced biosafety cabinet, Bioquell, class II, USA
- Laminar Cabinet, Flow Laboratories, USA
- Digital Scale, P-1200, Mettler, USA
- Digital MicroScale TE64 Sartorius, Sartorius Mechatronics AG, Germany
- Heatblock Accublock, Labnet International Inc., D1200, USA

Cell cultures

Cell cultures carried out under strictly controlled conditions in an incubator in which a constant temperature of 37^{o}C was maintained. The levels of CO_2 were 5 % and the relative humidity was almost 95 %. The medium used for cell culture was Dulbecco's Modified Eagle's Medium (DMEM, Gibco, Germany). 10 % fetal bovine serum solution (FBS), inactivated at 56^{o}C for 30 min, 1 % penicillin/streptomycin solution (10,000 U/mL, Lonza), and 1 % L-Glutamine solution (Lonza) were added. The preparation of the medium and the cell manipulations are achieved in conditions of complete sterilization in a thread flow chamber, in special culture flasks (Cellstar, Greiner Bio-one, USA).

Materials

- Dulbecco's Modified Eagle's Medium 10x culture medium (DMEM 10x, F-0455, Biochrom AG, Germany)
- P HEPES Buffer (L-1613, Biochrom AG, Germany)
- L-Glutamine Solution (L-Glutamine, K-0282, Biochrom AG, Germany)
- Bovine fetal serum (FBS, S-0115, Biochrom AG, Germany)
- Penicillin / streptomycin solution (Penicillin/Streptomycin, A-2122, Biochrom AG, Germany)
- Sodium bicarbonate salt solution (Sodium bicarbonate, L1713, Biochrom AG, Germany)
- Sodium pyruvate (Sodium pyruvate, L-0473) solution, Biochrom AG, Germany)
- Trypsin / EDTA Solution (L-2143, Biochrom AG, Germany)
- DMSO (D8418, Sigma-Aldrich, Germany)
- Sterile flasks with an area of 25 and 75 square centimeters (CellStar, Greiner Bio-one, USA).
- 60 Sterile plates 60 or 100 mm in diameter (CellStar, Greiner Bio-one, USA).
- Sterile pipettes 1, 5, 10 and 25 mL (CellStar, Greiner Bio-one, USA.).
- Sterile Pasteur type pipettes (CellStar, Greiner-Bio-one, USA).
- Falcon 15- and 50-mL polypropylene test tubes.
- Eppendorf Tubes (0.5 and 1.5 mL).

Procedure

Observation of the cells under the microscope till 80-90% confluency of the surface of the flask (or plate).
Aspiration of cell medium in vacuo and washing of the cells twice with PBS 1x, to remove traces of serum containing trypsin inhibitors.
Addition of 1mL trypsin (Trypsin/EDTA, Lonza, USA) per 25 cm^2, and incubation for a few minutes in the incubator followed. The detachment of the cells was monitored under a microscope.
Inhibition of trypsin, after detachment of cells, was achieved by adding 3 mL of complete medium and light pipetting to break down any aggregates.

Cell Storage & Freezing

The cells were stored by freezing in plastic vials (Nalgene Labware, ThermoFischer Scientific, Denmark) and were transferred into freezers at -80°C. After 24 hours, the plastic vials were placed in a liquid nitrogen.

Procedure

- Aspiration of the cell medium in vacuo followed, once it has reached the required cell density (~ 80 %).
- Addition of 1mL of trypsin solution (Trypsin / EDTA, Lonza, USA) per 25 cm^2 and incubation for a few minutes in the 37^oC incubator.
- Addition of complete DMEM medium and transfer to a sterile falcon tube of 15mL capacity.
- Centrifugation of the cells at 1200 rpm (rpm), at 4^oC for 5 min.
- Resuspension of the cells in 1 mL of freezing solution (10% DMSO, 90% fetal bovine serum).
- Transfer the cell suspension to the freezing vials.

Thawing

Procedure

- The vials are then inserted into the freezer in an appropriate cryoprotectant. The rate of temperature decreases 1^oC per minute, until they reach a temperature of -80^oC. This cooling rate was achieved with a polyethylene container, which contains isopropanol solution (100 %, # 33539, Sigma-Aldrich, Germany). This procedure allows the cell line to be preserved indefinitely.
- For thawing cells, the vial was placed in the 37^oC water bath for a few minutes and then quickly transferred to an equal or double amount of prewarmed, complete DMEM medium.
- A placement in a sterile falcon tube of 15 mL capacity and centrifugation for 5 min at 1,200 rpm at 4^oC followed.

- The cell pellet was resuspended in a capable quantity of cell medium, transferred in flasks or plates and incubated at 5 % CO_2 and 37^{o}C.

Growth Curves

To count the cell number in order to create growth curves or to complete any experiment that needed to know the cell number, the technique of Trypan blue staining was used. Trypan blue dye is used to selectively stain dead cells, as their membrane is permeable. On the contrary, living cells do not absorb Trypan blue, and thus remaining colorless.

The count is performed on a Neubauer hemocytometer, which is a modified slide with two treated, smooth surfaces. Each surface contains a square grid, consisting of 9 main squares with a side length of 1 mm (area 1 mm^2). Each square is defined by parallel lines with a distance of 2.5 μm from each other, which serve to determine the position of the cells, whether they are inside or outside the grid, while in the original squares there are additional gradations. The level of the grid is 0.1 mm lower than the two protrusions, existed to support the coverslip. The cell suspension spreads on the square surface through the capillary effect. The volume of the suspension covering one out of nine squares is 0.1 mm^3 or 1 * 10^{-4}mL. Thus, the total number of cells per mL is obtained by multiplying the average of the resulting cells.

Procedure

- Centrifugation of the cells and resuspend the pellet in a small volume (eg 1mL)
- Addition of 10 μl Trypan Blue and 10 μl of the cell suspension inside an eppendorf tube.
- Stirring lightly and letting them stand for 1-2 min at RT.
- Addition of 10 μl of the cell solution in a Neubauer hemocytometer and counting of the number of living (colorless) and dead cells (blue).

Wound Healing Assay

The wound healing experiments check the ability of the cells to multiply and migrate at the same time. Specifically, an artificial wound (notch) is created with a 20-200 μl nozzle on the surface of the cell culture monolayer and leave the cells in standard culture conditions to determine the ability of the cells to heal wounds. At regular intervals, time courses of cells are taken.

Procedure

- Cells were plated in a 60 mm diameter plate and incubated until the bottom becomes completely covered (approximately 16 hours).
- Using a nozzle, a straight line was drawn being extended from one pole of the plate to the other.
- The detached cells were washed away with PBS.
- The addition of full medium followed.

- Observation and imaging followed, every 5 hours, to assess the progress of the cell migration in the engraved surface.

Cloning Protocols

Digestion with restriction enzymes

Restriction enzymes were used (New England Biolabs and Roche) according to manufacturer instructions.

Agarose gel electrophoresis

0.8-1 % agarose gels (SIGMA) in 1x TAE were used (with Ethidium bromide). TAE 1x was prepared by diluting 50x TAE to dH_2O (for 200 mL: 242 gr Trizma base (SIGMA), 57.1 mL Glacial Acetic Acid (Schanlau), 100 mL 0.5 M EDTA pH 8). 1 kb DNA Ladder was used (Invitrogen).

Bacterial Transformation

DH5a bacteria were used for the transformation which are prepared in the laboratory with transformation efficiency reaching 10^6 when tested with plasmid pUC19 (50 pg).

Preparation of DH5a bacteria

All steps were performed in a cold-room (4^{o}C).

- A cell colony was isolated by inoculation into a solid nutrient substrate by the method of parallel lines in sterile conditions (streaking). Incubation at 37^{o}C overnight until colonies appear.
- Start a culture of 5 mL that will result with inoculation of a single colony from the plate. Incubation overnight at 37^{o}C with shaking.
- Vaccination of 4 mL cell culture in 400 mL LB.
- Incubation at 37^{o}C with shaking at 300 rpm until optical culture density to be OD_{600} 0.4.
- Division of the culture into 8 (50 mL) pre-chilled conical flasks and incubation on ice for 10-15 min.
- Centrifugation for 5 min at 4,000 rpm.
- The supernatant was removed and the precipitate was resuspended at 200 mL of the initial volume with sterile and filtered $CaCl_2$ (50 mM).
- Incubation on ice for 20 min.
- Discard the supernatant and resuspension of the precipitant in half (200 mL) of the original volume with sterile and filtered $CaCl_2$ (50mM) (each residue will be resuspended in 25 mL).
- Centrifugation for 5 min at 4000 rpm.

- Supernatant removal and resuspension of the precipitate at a half (200 mL) of the initial volume with sterile and filtered $CaCl_2$ (50 mM).
- Supernatant removal and resuspension of the precipitate at 1/100 (4 mL) of the initial volume with $CaCl_2$.
- Transfer of the contents of all tubes in one.
- Incubation on ice, 1hour at least or overnight in room 4^oC. Storage at 80^oC, adding 1/3 (1.3 mL) of the final volume of sterile $CaCl_2$ 50% glycerol (final concentration, 15% glycerol).
- Division of the samples in sterile Eppendorf tubes (100 µl).
- Quick-freeze of the cells with dry ice and EtOH and transfer to -80^oC.

Small scale DNA isolation

QIAprep Spin Miniprep Kit Protocol (QIAGEN)

- Pick a colony from a bacterial solid culture nutrient substrate (LB agar with Amp/Kan) incubating for 16 hours.
- Inoculation in 5 mL LB (Amp/Kan) and incubation for 16 hours at 37^oC under shaking (225 rpm) conditions.
- Centrifugation of 3 mL bacterial culture at 13,000 rpm for 60 sec.
- Resuspension of the bacterial pellet in 250 µl Buffer P1.
- Addition of 250 µl Buffer P2 and gentle inversion of the tubes 4-6 times to stir the mixture.
- Addition of 350 µl Buffer N3 and inversion of the tubes (4-6 times) to gently mix the mixture.
- Centrifugation for 10 min at 13,000 rpm.
- Transfer the supernatant from the previous step to a QIAprep column Spin Column.
- Centrifugation for 10 min at 13,000 rpm.
- Rejection of the filtrate.
- Washing the column by adding 0.75 mL Buffer PE.
- Centrifugation for 60 sec.
- Filtrate removal.
- Centrifugation for 60 sec.
- Installation of the column in a clean centrifuge tube (1.5 mL)
- Addition of 30-50 µl elution buffer or water for injection.
- Incubation for 5 minutes.
- Centrifugation for 60 sec.

Medium scale DNA isolation

QIAGEN Plasmid Midi Kits

- Pick a colony from a bacterial culture of LB agar (Amp/Kan) and inoculation of 205 mL of nutrient LB broth (Amp/Kan).

- Incubation for 5-8 hours at 37^{o}C with shaking (225 rpm)
- Centrifugation at 6,000 rpm (GS3 Sorval head).
- Resuspension of the bacterial pellet in 4 mL Buffer P1.
- Addition of 4 mL Buffer P2 and inversion of the tubes (4-6 times) to mixture gently.
- Incubation for 5 min at RT.
- Addition of 350 µl Buffer P3 and mix by inverting the tube 4-6 times.
- Incubation on ice for 15 min.
- Centrifugation for 30 min at 13,000 rpm (SS-34 Sorval rotor) at 4^{o}C and collect the supernatant.
- Centrifugation of the supernatant for 15 min at 13,000 rpm (SS-34 Sorval motor) at 4^{o}C.
- Collect the supernatant that contains plasmid DNA.
- Equilibrate the QIAGEN-tip 100 column with 4 mL of QBT solution.
- Place the supernatant from the previous step in the column and allow to pass through the column via gravity.
- Rinse the column with 2x10 mL QC solution.
- Elution of the DNA with 5 mL of QF solution.
- Precipitation of DNA with 3.5 mL isopropanol at RT.
- Immediate centrifugation at 1,100 rpm for 30 min at 4^{o}C (Sorvall SS-34 rotor).
- Discard the supernatant.
- Rinse the DNA with 2x2 mL 70 % EtOH.
- The DNA is air-dried and resuspended in an appropriate volume of dH2O.

Transfection assays

Transfection assays with DNA plasmids

Gene overexpression with plasmid vectors

Gene overexpression was performed by transient transfection of primary cultures and cell lines with plasmid expression vectors using Lipofectamine 2000 reagent.

Plasmid vectors

- EGFP-hAgo2 from Phil Sharp (Addgene plasmid #21981; http://n2t.net/addgene:21981; RRID: Addgene_21981)

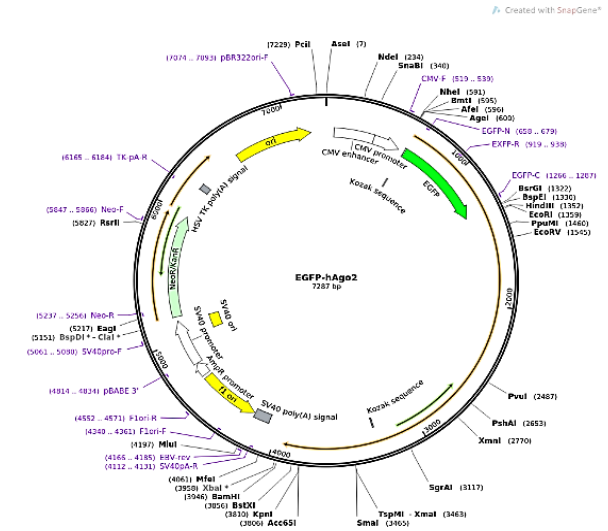

· Ago4-GFP was a gift from Edward Chan (Addgene plasmid #21536; http://n2t.net/addgene:21536; RRID: Addgene_21536).

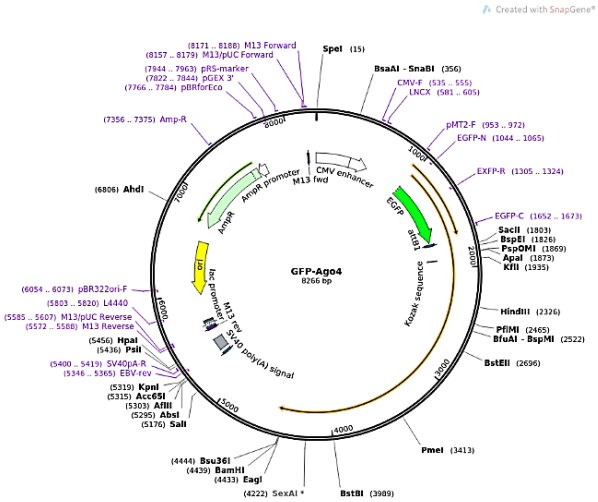

· pmCherry-C1_SEPT9 i1 from Elias Spiliotis (Addgene plasmid #71622; http://n2t.net/addgene:71622 ; RRID:Addgene_71622)

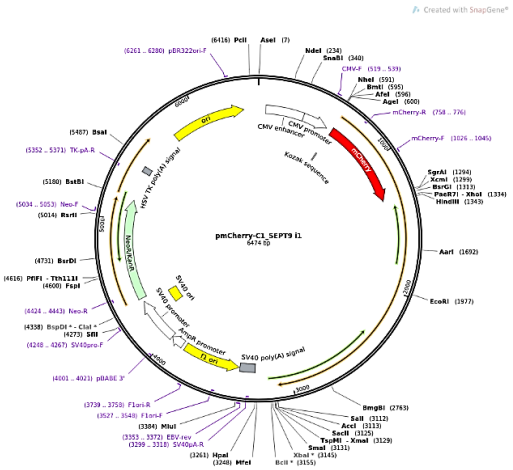

- pEGFP-N1 (Addgene, #6085-1)
  encodes a red-shifted variant of wild-type GFP (1-3) which has been optimized for brighter fluorescence and higher expression in mammalian cells. (Excitation maximum = 488 nm; emission maximum = 507 nm)

- pEGFP-N1 H4 wt

- The same pEGFP-N1 (Addgene, #6085-1) vector.
  H4 wt cDNA is cloned Bgl II-BamH I; the Bgl II site has been lost after the ligation. To recover the insert, you need to use Nhe I – BamH I.

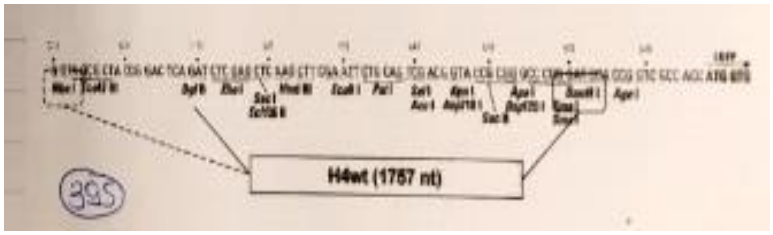

- The same pEGFP-N1 (Addgene, #6085-1) vector.
  H4 truncated cDNA is cloned Bgl II-Hind III; the Bgl II site has been lost after the Ligation. To recover the insert, you need to use Nhe I – Hind III.

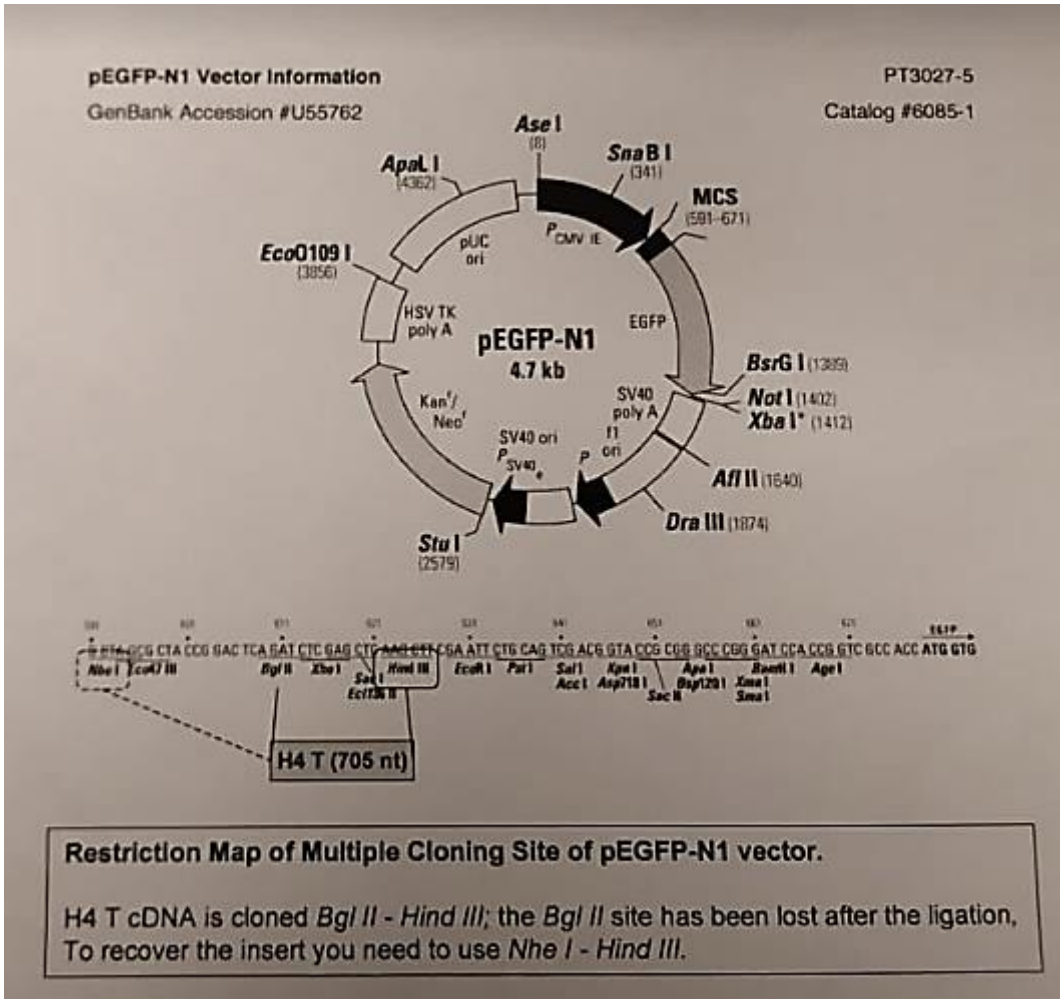

Procedure

Cells were plated (3 or 5 x 10^4) in 1600 µl of RPMI serum- and antibiotic-full medium. The wells were washed with 1xPBS and 1600 mL of free-RPMI* was added. The cells were cultured at 37^{o}C for at least 20 min.

For each transfection, the preparation of the following was required:

- Dilution of 2 µg (= µl/well) DNA in 100 µl RPMI serum- and antibiotic-free medium by gently mixing.
- Gentle mix of Lipo2000 was required before each use; addition of 4 µl Lipo2000 in 96 µl of RPMI serum- and antibiotic-free medium. Incubation for 5 min at RT.
- Mix the solutions and incubate for 30 min at RT.
- Addition of 200 µl free-RPMI and transfer (dropwise) to each well.

-
- Gentle mixing by rocking the plate, back and forth and incubation of cells at 37°C in a 5 % CO_2 incubator for 6 hours.
- Removal of the medium and replacement with full medium. The transgene expression was tested after 24 & 48 hours.

**free-RPMI: serum- and antibiotic-free RPMI medium*

Transfection assays with miRNA mimics

Procedure

One day before transfection, 3 or 5 x 10^4 cells suspended in 400 mL of RPMI serum- and antibiotic-full medium were plated in a 24 well plate, so that the cells will be >90% confluent at the time of transfection.

For each transfection, the preparation of the following was required:

- Washing the wells once with 1x PBS and adding 400 mL of free-RPMI. The samples were incubated for at least 20 min at 37°C.
- Dilution of 3.1 µl DNA in 21.9 µl (20 µM in stock to 19 nM) of free-RPMI per well and gentle mixing.
- Gentle mixing of Lipo2000 before use and addition of 1.5 µl Lipo2000 in 23.5 µl of RPMI serum- and antibiotic-free medium. The cells were incubated for 5 min at RT.
- Combine the DNA and the Lipo2000 solutions by pipetting gently (total volume 50 µl) and incubate for 30 min at RT.
- Add 50 µl free-RPMI and transfer the 100 µl of complexes (dropwise) to each well.
- Gentle mixing by rocking the plate, back and forth, and incubation of cells at 37°C for 6 hours.
- Replacement the culture medium with fresh full medium and check for the transgene expression after 24 and 48 hours.

Transfection assays with Small interfering RNA (siRNAs)

IDT DsiRNAs are chemically synthesized 27mer RNA duplexes that are optimized for Dicer processing and show increased potency when compared with 21mer siRNAs. Dicer-substrate RNAi methods take advantage of the link between Dicer and RISC loading that occurs when RNAs are processed by Dicer.

TriFECTa RNAi Kit

The TriFECTa Kit includes all of the reagents you need for a successful knockdown. This kit includes:

- 3 Predesigned DsiRNAs that are specific for a single target gene.
- 3 control DsiRNAs for optimizing your RNAi experimental setup:
- TYE 563 Transfection Control DsiRNA, 1 nmol (a Transfection Control DsiRNA to visually monitor transfection efficiency)
- HPRT-S1 Positive Control DsiRNA, 1 nmol
- Negative Control DsiRNA, 1 nmol
- Nuclease-Free Duplex Buffer (2 mL) for resuspending your DsiRNAs, which are delivered dry.

Transfection assays with mimic miR and antagomir sequences

The ready-to-use miRNA mimics are small, double-stranded RNA molecules designed to mimic endogenous mature miRNA molecules when introduced into cells. miRNA is known to regulate gene expression in a variety of manners, including translational repression, mRNA cleavage and deadenylation. miRNA Mimics, a member of RNAi product family, provides miRNA researchers with a range of options from individual mimics to a full library of human miRNA mimics based on latest version of miRBase (currently hosted by the University of Manchester, previously hosted by the *Sanger Institute*).

Ambion® Anti-miR™ miRNA Inhibitors are chemically modified, single-stranded nucleic acids designed to specifically bind to and inhibit endogenous microRNA (miRNA) molecules. These ready-to-use inhibitors can be introduced into cells using transfection or electroporation parameters similar to those used for siRNAs. Anti-miR™ Negative Control #1 is a random sequence Anti-miR molecule that has been extensively tested in human cell lines and tissues and validated to produce no identifiable effects on known miRNA function.

Anti-miR™ miRNA Inhibitor Negative Control #1, AM17010

Ambion™ Pre-miR26 miRNA Precursor and scramble, AM17100

Procedure

One day before transfection, 3 x 10^4 cells suspended in 400 mL of RPMI serum- and antibiotic-full medium were plated in a 24 well plate, so that the cells will be >90% confluent at the time of transfection.

For each transfection, the procedure was as following:

- Wash the cells once with 1x PBS.
- Add 400 mL of free-RPMI per well and incubate for at least 20 min at 37^{o}C.

- Dilute 0.3 µL (20 µM in stock to 20 nM mimic miR26 or scramble respectively) in 50 µl of free-RPMI/well.
- Mix gently Lipo2000 before use and resuspend 1.5 µl Lipo2000 in 48.5 µl of RPMI serum-and antibiotic-free medium. The samples were incubated for 5 min at RT.
- Combine the mimic and the Lipo2000 solutions by pipetting gently (total volume 100 µl) and incubate for 30 min at RT.
- Add 100 µl free-RPMI and transfer the 200 µl of the total volume (dropwise) to each well. Gentle mixing by rocking the plate, back and forth, and incubation of cells at 37^{o}C for 6 hours.
- Replacement the culture medium with fresh full medium and check for the knockdown expression after 24 hours.

Trials were performed to identify the ideal concentration and combinatorial function of siRNAs of the mimics. SiRNA1, SiRNA2, SiRNA3, SiRNA1+2, SiRNA2+3, SiRNA1+3, SiRNA1+2+3 was tested. SiRNA1 was chosen due to its efficiency. 18, 20 and 40 nM concentrations of siRNA1 were tested. 24, 40 and 48 hours post transfection was analyzed. 18nM and 40 hours post transfection were selected as the most suitable condition for a successful knock-down.

Experimental Intervention in Cell Cultures

Heat Shock

Cells in culture were incubated at 41^{o}C for 16 hours and then left for 2 hours to recover.

Drug Treatments

Demecolcine Treatment

Demecolcine (D1925, 10 µg/mL in HBSS, ACF Qualified, BioXtra, Sigma/Aldrich, St. Louis, MO, USA) was used at 10 µg/mL concentration and the cells were exposed for 5 and 7 hours.

Cytochalasin D Treatment

Cytochalasin D (C8273, *Zygosporium mansonii* - CAS 22144-77-0, Calbiochem) was used at 10 µM concentration and the cells were exposed for 30 minutes.

SB205380 Treatment

SB205380 (p38 MAP Kinase Inhibitor-CAS 219138-24-6-Calbiochem, 506126, Sigma/Aldrich, St. Louis, MO, USA) was used at 20 µM concentration and the cells were exposed for 2.5 hours.

Mitotracker Treatment

Mitochondrial labeling was performed by MitoTracker® (Red CMXRos #9082) at a concentration of 50-200 nM and incubation for 15 min at 37^{o}C. Then the cells were fixed in ice-cold methanol for 15 min at -20^{o}C and rinsed 3 times with PBS for 5 min.

Etoposide Treatment

Etoposide (10 μM, 50 μM for 24 hours), UO126 (30-50 μM for 2-48 hours), 17AAG (1-20 μM for 24 hours), UV (0,09 J/cm^2, 25 seconds) and cycloexamide (1-4 μM for 6 hours) treatments were performed with no significant effect.

All the appropriate controls were included.

Duolink PLA assay

The following protocol is for a 1 cm2 sample on a slide, requiring 40 μl of solution for adequate coverage. The volume was adjusted according to the reaction area and number of samples. All incubations performed in a 24 well-plate, used as a humidity chamber.

Reagent Preparation

- Wash buffers A and B were prepared by dissolving the contents of one pouch in high purity water to a final volume of 1,000 mL. Solutions stored for short term storage (less than two weeks) or at 4^{o}C for long term storage.
- 0.01x Wash Buffer B was prepared by diluting 1x Wash Buffer B 1:100 in high purity water.
- Many Duolink PLA reagents were supplied as concentrated stocks and were diluted immediately prior to use. Do not store diluted Duolink® PLA reagents.

Duolink PLA Protocol

Before starting, the samples were deposited on glass slides and pre-treated with respect to fixation, retrieval, and/or permeabilization.

- Blocking
  Vortexing of the Duolink® Blocking Solution. 1 drop (~40 μl) of Duolink® Blocking Solution was added to each 1cm2 sample, protected from light. The slides were Incubated for 60 min at 37oC, in a heated humidity chamber.

- Primary Antibody Incubation
  Vortexing the Duolink® Antibody Diluent.
  Dilution of the primary antibody or antibodies of interest to suitable concentration in the Duolink® Antibody Diluent.
  Tapping off the Duolink® Blocking Solution from the slides.
  Addition of the primary antibody solution to each sample.
  Incubation of the slides in a humidity chamber. Usage of the optimal incubation temperature and time for the primary antibodies used.

Duolink® PLA Probe Incubation

- Vortexing of PLUS and MINUS PLA probes
- Dilution of the PLUS and MINUS PLA probes 1:5 in the Duolink® Antibody Diluent.
- Tapping off the primary antibody solution from the slides.
- Washing of the slides twice for 5 min in 1x Wash Buffer A at RT.
- Tapping off excess wash buffer and application of the PLA probe solution.
- Incubation of the slides in a pre-heated humidity chamber for 1 hour at 37°C.

Ligation

- Dilution of the 5x Duolink® Ligation buffer 1:5 in high purity water and mix.
- Tapping off the PLA probe solution from the slides.
- Washing the slides twice for 5 min in 1x Wash Buffer A at RT.
- During the wash, retrieval of the Ligase from the freezer using a freezer block (-20°C).
- Resuspend the Ligase in the 1x Ligation buffer from the previous step at a 1:40 dilution and mixing.
- *Addition of 1 µl of Ligase to 39 µl of the 1x ligation buffer.*
- Tapping off excess wash buffer and application of the ligation solution.
- Incubation of the slides in a pre-heated humidity chamber for 30 min at 37°C.

Amplification

- The Amplification buffer is light-sensitive and thereby protection of all solutions containing buffer from light was required.
  Dilution of the 5x Amplification buffer (1:5) in high purity water.
- For 40 µl reaction, addition of 8 µl of the 5x Amplification buffer to 32 µl of high purity water.
  Tapping off of the ligation solution from the slides.
  Washing of the slides twice for 5 min in 1x Wash Buffer A at RT.
  During the wash, retrieval of the Polymerase from the freezer using a freezer block (-20°C).
  Addition of the Polymerase to the 1x Amplification buffer at a 1:80 dilution and mixing.
  For 40 µl amplification solution, addition of 0.5 µl of Polymerase to 39.5 µl of the 1x amplification buffer.
  Tapping off excess wash buffer and application of the amplification solution.
  Incubation of the slides in a pre-heated humidity chamber for 100 min at 37°C.

Final Washes

Tapping off the amplification solution from the slides. Washing the slides twice for 10 min in 1x Wash Buffer B at RT. Washing the slides in 0.01x Wash Buffer B for 1 minute.

Preparation for Imaging

- Duo link mounting media with DAPI is aqueous and does not solidify. Clear nail polish can be used to seal the edges of the coverslip to the slide. Avoid getting air bubbles caught under the coverslip.
- Clearing the nail polish used to seal the edges of the coverslip to the slide. Avoid air bubbles caught under the coverslip.
- Tapping off excess wash buffer from the slides.
- Mounting of the slides with a coverslip using a minimal volume of Duolink® In Situ Mounting Medium with DAPI.
- The samples were observed after 15 min before analyzing in a fluorescence or confocal microscope, using at least a 20x objective.
- The slides can be stored in the dark at 4°C for up to 4 days or at -20°C for up to 6 months.

Image Acquisition

The result from a Duolink® PLA experiment is typically viewed using a fluorescence microscope with the appropriate filters for the detection fluorophore used. The Duolink® PLA signal is recognized as discrete fluorescent spots in various locations of the studied cells (see Figure 33). Individual signals are of sub-micrometer size and may be in multiple focal planes. Negative controls were performed with IgG antibody.

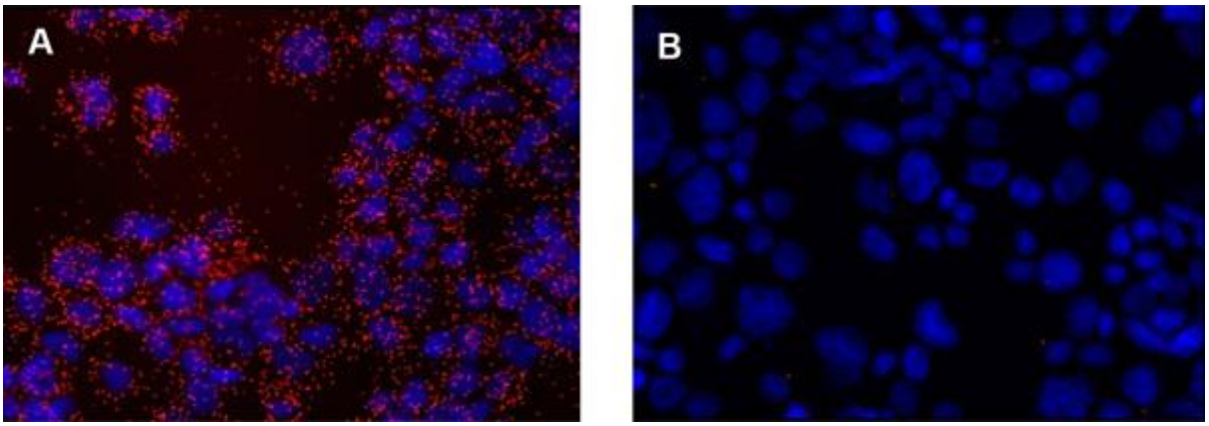

Figure 33 Detection of interaction foci. PLA signals are shown in red and the nuclei in blue. The nucleus image was acquired in one z-plane. a) Positive reaction. b) Negative control without primary antibodies.

Immunoblotting

Protein isolation - Cell lysates - Sonication

This method allows the selective detection of a protein (immunogen) with the usage of specific antibodies against the immunogen.

- Whole cell extracts (~30 μg) were isolated from petri-dishes (confluency ~90 %, on ice for proteolysis prevention). The cell medium was removed and followed by washing the cells with PBS 1x (twice). In each petri dish, Lysis buffer (1 mM Tris at pH 7.5, NaCl 5 M, EDTA 0.5 mM, 10 % Triton X-100) with protease/phosphatase inhibitors (100 mM PMSF -phenyl-methane-sulfonyl fluoride in isopropanol) was added.
- Cells were scraped (with cell scraper) and collected into an Eppendorf tube. Sonication process follows for 15 sec with output level 2.5 (Q125 Sonicator).
- The samples were centrifuged at 13,000rpm for 20 min at 4^{o}C.
- Supernatant collection and replacement of the cell lysate in a new Eppendorf tube.
- Storage in 4^{o}C.
- Quantitative evaluation of protein concentration with the BCA colorimetric protein assay (Thermo Scientific™ Pierce™). The BCA reaction (Bicinchromic acid) is based on the reaction of the proteins with Cu^{+2} ions in alkaline environment.
- The result of this reaction is the reduction of divalent Cu^{+2} ions to monovalent Cu^{+1} ion, which upon reaction with two BCA molecules gives rice to a purple product. The product presents optical absorption at a wavelength of 562 nm, which shows linearity with increasing protein concentrations (20 μg/ml - 2,000 μg/ml).

Materials

Bovine albumin solutions (BSA) at concentrations of 0, 0.125, 0.25, 0.5, 1, 1.5 and 2 μg/mL BCA working solution 1:50 (consisting of 1part BCA reagent A and 49 parts reagent B).

96-well polypropylene microplate (400 μl) were used.

Procedure

- Preparation of BCA reagent (1A:49B) and mix gently to homogenize and observe the characteristic green color.
- Preparation of BSA solutions in known concentrations.
- Addition to the wells of the microplate 25 μL of each standard BSA solution and protein sample.
- Addition of 200 μl BCA reagent and incubation at 37^{o}C for 30 min.
- The microplate left at RT to quench the reaction. A measurement at a wavelength of 562 nm was performed.

The concentration of proteins in each sample is calculated by the curve formed by the absorptions of BSA solutions in known concentrations as a function of their concentrations and is expressed in μg/ml.

Detection and analysis of detected proteins

Electrophoretic protein profile analysis

SDS-PAGE electrophoresis (Sodium Dodecyl Sulfate Poly Acrylamide Gel Electrophoresis) is a technique used to separate proteins based on their electrophoretic mobility, which is determined by factors such as the molecular weight of the proteins, their secondary structure and post-translational modifications.

Each protein has a different primary structure, different molecular weight and isoelectric point. Thus, proteins with similar molecular weights exhibit different electrophoretic mobility due to different mass to charge ratios. To separate proteins based on their molecular size alone, sodium dodecyl sulfate (SDS, Sodium Dodecyl Sulfate) is used, a well-known anionic detergent with a constant weight ratio (1.4 g SDS per gram of protein) that helps to denature the protein chains and gives each protein a negative electric charge, proportional to its molecular weight. At the same time, in this technique, reducing agents such as DTT (dithiothreitol) and β-mercapto-ethanol are used to cleave the disulfide bonds of the proteins. In order to completely denature the proteins after the addition of the above, the samples are heated for 5 min at 100^{o}C.

Polyacrylamide gels forms three-dimensional polymer networks. by polymerization of acrylamide monomers and NN-methylene-bis-acrylamide molecules formatting polyacrylamide chains. The pore size of the gel is based on the ratio of acrylamide:bis-acrylamide. The polymerization of the gel is carried out by the addition of NNN'N'-tetra-methyl-ethylenediamine (TEMED) and supported by free radicals which are chemically generated with persulphate ions ($S_2O_{32}^-$), in the presence of the catalyst Ammonium Persulphate (APS).

Polyacrylamide gels consist of two parts, the stacking gel and the resolving gel. The stacking gel ensures the simultaneous entry of the polypeptides into the separation gel, where the proteins are separated based on their molecular weight.

Each separation gel was prepared as follows:

Components	5 ml	10 ml	15 ml	20 ml	25 ml	30 ml	50 ml
6% Gel							
Water	2.60	5.30	7.90	10.6	13.2	15.9	26.5
30% Acrylamide	1.00	2.0	3.00	4.0	5.0	6.0	10.0
1.5 M Tris (pH 8.8)	1.30	2.50	3.80	5.0	6.30	7.50	12.50
10% SDS	0.05	0.10	0.15	0.20	0.25	0.30	0.50
10% APS	0.05	0.10	0.15	0.20	0.25	0.30	0.50
TEMED	0.004	0.008	0.012	0.016	0.02	0.024	0.04
8% Gel							
Water	2.30	4.6	6.90	9.3	11.5	13.9	23.2
30% Acrylamide	1.30	2.7	4.0	5.3	6.70	8.0	13.3
1.5 M Tris (pH 8.8)	1.30	2.5	3.80	5.0	6.30	7.50	12.5
10% SDS	0.05	0.1	0.15	0.2	0.25	0.30	0.50
10% APS	0.05	0.1	0.15	0.2	0.25	0.30	0.50
TEMED	0.003	0.006	0.009	0.012	0.015	0.018	0.03
10% Gel							
Water	1.90	4.0	5.90	7.90	9.90	11.9	19.80
30% Acrylamide	1.70	3.30	5.00	6.70	8.30	10.0	16.70
1.5 M Tris (pH 8.8)	1.30	2.50	3.80	5.0	6.30	7.50	12.50
10% SDS	0.05	0.10	0.15	0.20	0.25	0.30	0.50
10% APS	0.05	0.10	0.15	0.20	0.25	0.30	0.50
TEMED	0.002	0.004	0.006	0.008	0.01	0.012	0.02
12% Gel							
Water	1.60	3.30	4.90	6.6	8.20	9.90	16.5
30% Acrylamide	2.00	4.0	6.00	8.0	10.0	12.0	20.0
1.5 M Tris (pH 8.8)	1.30	2.50	3.80	5.0	6.30	7.50	12.5
10% SDS	0.05	0.10	0.15	0.20	0.25	0.30	0.50
10% APS	0.05	0.10	0.15	0.20	0.25	0.30	0.50
TEMED	0.002	0.004	0.006	0.008	0.01	0.012	0.02
15% Gel							
Water	1.10	2.3	3.40	4.6	5.70	6.90	11.5
30% Acrylamide	2.50	5.0	7.50	10.0	12.5	15.0	25.0
1.5 M Tris (pH 8.8)	1.30	2.50	3.80	5.0	6.30	7.50	12.5
10% SDS	0.05	0.10	0.15	0.20	0.25	0.30	0.50
10% APS	0.05	0.10	0.15	0.20	0.25	0.30	0.50
TEMED	0.002	0.004	0.006	0.008	0.01	0.012	0.02

5 % stack gel contains 30 % 29 acrylamide solution:1 bis-acrylamide, 1 M Tris pH 6.8, 10 % SDS, 10 % APS, TEMED and ddH_2O. The solutions and their concentrations are presented below:

1M DTT	
dithiothreitol (DTT)	1.54 g
dH_20	up to 10 ml

Filtration and store at -20°C.

5x Laemmli Sample buffer	15mL

SDS	1.5 g
1M Tris pH 6.8	3.75 mL
Bromophenol blue	0.015 g
DTT	1.16 g
Glycerol	7.5 mL
dH_20	up to 15 mL

Vortexing, storage in -20^{o}C.

1M Tris pH 6.8	0.25 L
Tris-Base	30.29 g

pH s*tandardization* at 6.8 (~20 ml of concentrated HCl).

1M Tris pH 8.8	0.25 L
Tris-Base	30.3 g

pH s*tandardization* at 8.8 (~ 5 ml of concentrated HCl).

10% SDS	100 mL
SDS	10 g
dH_20	80 mL

10x Running buffer (SDS-PAGE)	1 L
Tris-Base	30.31 g
Glycine	150 g
SDS	10 g

Electrophoresis device: Mini Protean II (Bio-Rad Laboratories, USA)

Experimental process

- Preparation of the separating gel and carefully insertion into the electrophoresis apparatus. The addition of isopropanol keeps the upper phase hydrated. 30 min for its polymerization.

- Preparation of the stacking gel (5 %) and insertion into the device above the separation gel. Immediate addition of the plastic combs to form the wells where the protein samples will then be added.
- Addition of Laemmli solution in each sample at a final dilution of 1X, and placing them at a temperature of 100^{o}C, where they boiled for 5 min.
- After the polymerization of the stacking gel, the plastic combs were removed from the device.
- Loading of the samples and addition of 1x electrode buffer until the electrode was covered. Application of an electric voltage field of 80-100 V. When the dye front has passed from the stacking gel to the separating gel, the voltage can be adjusted to 120 V (depending on the content of the separation gel).
- When the protein front reaches near to the bottom of the separation gel, the electrophoresis process must be stopped because the proteins must not be diffused into the solution. At the same time, preparation for the subsequent transfer of proteins to nitrocellulose membrane has begun.

Western Immunoblotting

Protein Transfer to Nitrocellulose Membrane-Protein & Detection.

This method allows the selective detection of a protein (antigen) using specific antibodies against it. The method involves the electrophoretic analysis of a protein solution on a polyacrylamide gel, the electro-transport of proteins to membranes and the binding of specific antibodies to the antigen. After blocking the membrane gaps, the membrane is incubated with a specific antibody to the antigen of interest. The membrane is then incubated with an antibody that recognizes the Fc region of the first antibody. The second antibody is labeled either enzymatically or radioactively, so it is possible to detect the antibody antigen complex after the addition of a suitable substrate. In the experiments performed in the present work, all the second antibodies used, were enzyme-labeled with peroxidase (horse-raddish peroxidase, HRP).

Buffers

Transfer Buffer (10X)	500 mL
Tris-Base	15 g
Glycine	72 g

For 1x working solution, addition of 1 Volume of 10x transfer buffer, 7 Volumes dH_2O and 2 Volumes of ethanol. Storage at 4^{o}C.

Tween 10X	500 mL
1M Tris pH 7.5	0.25 L
5M NaCl	0.15 L (ή 43.83 g NaCl)

Tween-20	2.5 mL

dH_20 up to 500 mL.

Ponceau S staining

0.5 % Ponceau S in 5 % TCA (trichloro-acetic acid).

Electro-transport of proteins

- Dipping of two Whatman papers into the protein-transfer buffer and placing them on one of the two sponges in the protein transfer grid, which was constantly in the protein transfer buffer.
- The separating gel is placed on Whatman paper and any discontinuities (bubbles) were removed so that they come into direct contact at their whole surface.
- The nitrocellulose membrane (#BA-85 Protran, Whatman, UK) was soaked in water for 1 min (activation), then, in the buffer and consequently were placed on the separating gel.
- Two Whatman papers, already dipped into the protein transfer buffer and placed on the nitrocellulose membrane, were followed by the second sponge in the protein transfer grid.
- Closure of the device to avoid bubbles and transfer to the Mini Protean II conveyor (Bio-Rad Laboratories, USA), replenishing the amount of transport buffer to cover the entire protein transport grid.
- Placing of the lid of the device properly, applied to the electrodes of the tank (negative pole on the side of the gel) and application of an electric current of 320 mA for 1.5 to 2 hours at room temperature 4^{o}C.

Immuno-enzymatic detection of proteins

- The nitrocellulose membrane was incubated with a 5% (w/v) solution of lyophilized milk in 1x TBS-T buffer at RT for 1 hour. This process covers the free sites on the membrane to which no proteins have been transferred, thus preventing the non-specific binding of antibodies.
- Wash of the membrane for 10 min with 1x TBS-T buffer. Repeat this step three times.
- Incubation of the membrane with the primary antibody, diluted in TBS-T solution containing 5% (w/v) milk powder for 16 hours at 4^{o}C.
- Wash the membrane for 10 min with 1X TBS-T buffer. Repeat three times.
- Incubation with a secondary antibody that recognizes specific antigenic epitopes of the first antibody depending on the host animal used for the production. It is conjugated to the peroxidase enzyme (HRP) and used in a 1:2000 dilution (v/v) in TBS-T solution containing 5 % (w/v) milk powder. Incubation for two hours at RT and mixing constantly.
- Wash the membrane for 10 min with 1x TBS-T buffer. Repeat three times.

The presence of the protein is detected indirectly by the method of enhanced chemiluminescence (ECL, GE Healthcare Life Sciences, USA) by the addition of a solution of luminol on the nitrocellulose membrane. The peroxidase enzyme, which is bound to the secondary antibody, reacts with the substrate, hydrogen peroxide-H_2O_2 and luminol, a component that has the ability to emit light. The membranes to which luminol has been added are transferred to a special device

impermeable to light and come into contact with photographic films. The light emission darkens the film and thus indicates the existence of the protein of interest.

Removal of immune complexes from nitrocellulose membrane (stripping)

To detect more than one protein in the same nitrocellulose membrane, the immune complexes were removed from the membrane surface without alterations in the quantity and quality of the proteins that have been electrocuted. Once the primary-secondary antibody complexes have been removed, the antigenic epitopes of the membrane are free for antibody binding to a new epitope. BIORAD Stripping Solution (Bio-Rad Laboratories, USA) was used to release the immunoblocks according to the manufacturer's protocol.

MTT assay

The most commonly used viability assay is the MTT, initially described by Tim Mosmann in 1983. This colorimetric assay uses reduction of a yellow tetrazolium salt (3-(4,5-dimethylthiazol-2-yl)-2,5-diphenyltetrazolium bromide, or MTT) to measure cellular metabolic activity as a proxy for cell viability. Viable cells contain NAD(P)H-dependent oxidoreductase enzymes which reduce the MTT reagent to formazan, an insoluble crystalline product with a deep purple color. Formazan crystals are then dissolved using a solubilizing solution and absorbance is measured at 500-600 nanometers using a plate-reader. The darker the solution, the greater the number of viable, metabolically active cells.

Procedure

- ~37,000 cells were plated per well in a 24-well plate and incubated for 18 hours at 37^{o}C and in the presence of the appropriate stimulus.
- Cell medium removal and wash of the cells with PBS 1x followed.
- 3-4 hours incubation for adaptation in 96-well plate and MTT buffer 1x (made up in medium to a final concentration of 0.5 mg/mL, Applichem, A2231.005).
- Incubation for 3 hours at 37^{o}C, until intracellular purple formazan crystals are visible under microscope.
- Removal of MTT and addition of DMSO (472301, Merck).
- Incubation at RT or at 37^{o}C for 30 min until cells have lysed and purple crystals have dissolved.
- Measurement of the absorbance at 570 nanometers.

Cryostat handling

Placement of a tissue block covered with cryoprotective medium O.C.T. (Tissue-Tek) with the required orientation each time on an iron piece (dimensions approximately 1 x 1 cm). Then, the section (~5-12 μM) was placed with the carrier in a special slot of the cryotome, to which a cryoprotectant had been previously added, overlapping again and in total with the same cryoprotectant. Polymerized L-lysine or Super frost plus coverslips were used. Samples were stored at -20^{o}C.

Microtome Handling

Paraffin embedded tissue (FFPE) were cut 1-20 µm thick (usually 3-8 µm), stretched in a water bath, further processed and applied on a slide Samples were stored at RT and eventually observed under an optical microscope.

Immunocytochemistry

Immunocytochemistry (ICC) is a common laboratory technique that is used to anatomically visualize the localization of a specific protein or antigen in cells by using of a specific primary antibody that binds to it. The primary antibody allows visualization of the protein under a fluorescence microscope when it is bound by a secondary antibody that has a conjugated fluorophore. ICC allows researchers to evaluate whether or not cells in a particular sample express the antigen. In cases where an immuno-positive signal is found, ICC also allows researchers to determine which sub-cellular compartments are expressing the antigen and its distribution pattern.

The subcellular localization of selected cell proteins was tested and cells were observed under a Laser Scanning Focus Microscope. Known number of cells were plated on positively charged lysine-coated coverslips and placed in a 24-well culture dish and cultured under normal conditions. In 24 hours, the medium was removed and cells were rinsed twice with PBS 1x.

Procedure

- The cells were fixed with 4 % paraformaldehyde solution, incubated for 10 minutes at room temperature and then rinsed three times with PBS 1X solution.
- The cells were incubated in buffer B (0.1 % Triton X-100 in PBS), followed by buffer A (0.5 % Triton X-100 in PBS) for 10 min. This step was repeated three times.
- Cell incubation in a solution of non-specific binding sites of the antibody [BSA 0.5 % (w / v), in PBS 1x solution] for 90 min at RT, followed.
- Incubation with primary antibody in buffer C (0.1 % Triton X-100 in PBS and 1 % BSA (Bovine Serum Albumin) for approximately 16 hours at 40^{o}C and washing with buffer A (0.5 % Triton X-100 in PBS) for 10 min were performed. This step was repeated three times.
- Incubation with secondary antibody in buffer A with 1.5 % BSA (Bovine Serum Albumin) for 2 hours. The secondary antibodies used were from the Alexa Fluor Molecular Probes series (Invitrogen Carlsbad, CA, USA) and specifically Alexa Fluor 488 goat anti-rabbit (A-11070) and Alexa Fluor 555 goat anti-mouse (A-21425) in dilution 1: 300.
- Washing in buffer A (0.5 % Triton X-100 in PBS) for 10 min (three times) and staining with Phalloidin-Rhodamine (Molecular Probes) for 30 min were conducted.
- Washing with PBS 1x three times.
- A drop of Vectashield solution (VECTOR Laboratories, Peterborough, UK) was placed on a slide containing DAPI.
- Application of a coverslip on top of the drop and solidification with nail polish application.

Immunohistochemistry

Immunohistochemistry (IHC) is the most common application of immunostaining. It implicates the process of selectively identifying proteins-immunogens in cells of a tissue section by exploiting the principle of antibodies binding specifically to antigens of biological tissues. Albert Coons conceptualized and first implemented the procedure in 1941.

Visualizing an antibody-antigen interaction can be accomplished in a number of ways, mainly either of the following:

- *Chromogenic immunohistochemistry* (CIH), wherein an antibody is conjugated to an enzyme, such as peroxidase (the combination being termed immuno-peroxidase), that can catalyze a color-producing reaction.
- *Immunofluorescence*, where the antibody is tagged to a fluorophore, such as fluorescein or rhodamine.

Immunohistochemical staining is widely used for cancerous cell diagnosis. Specific molecular markers are characteristic of particular cellular events such as proliferation or cell death (apoptosis). Immunohistochemistry is also widely used in basic research to understand the distribution and localization of biomarkers and differentially expressed proteins in different parts of a biological tissue.

Procedure

Preparation of Solutions and Reagents

The following solutions and reagents should be available to be able to perform the IHC protocol:

- Xylene
- Ethanol, anhydrous denatured, histological grade (100 % and 95 %).
- Hematoxylin (optional).
- Wash buffer 10X Tris Buffered Saline with Tween-20 (TBST, #9997). To prepare 1 L of 1x TBST: add 100 ml 10x TBST to 900 mL dH_2O; mix.
- Antibody diluent.
- Antigen unmasking
  - Citrate: 10 mM Sodium Citrate Buffer (for 1 L, add 2.94 g sodium citrate trisodium salt dihydrate ($C_6H_5Na_3O_7 \bullet 2H_2O$) to 1 L dH_2O and adjust to pH 6.0).
- Blocking Solution: TBST/5% Normal Sheep Serum.
- Detection System: SignalStain® Boost IHC Detection Reagents (Alexa, Mouse; Alexa Rabbit)
- Glycine Solution 20x and working solution 1x.
- Proteinase K solution [25 µl proteinase k (20 mg stock), 1 mL Tris-HCl pH 7.5 (stock 1 M), 100 µl EDTA pH 7,5 (stock 0,1 M) in PBS 1x up to 50 mL]. Incubation at 37°C.

Sample Preparation

A paraffin infiltrated tissue was placed in a mold with a small volume of liquid paraffin. Cool briefly to immobilize the tissue. Place the base of a cassette on top of the mold. Fill with liquid paraffin, and then cool.

Cut thin slices (4-6 µm) on a microtome, and float sections in a water bath.

Mounting of the sections on to charged slides and dry overnight. Using charged slides helps the section to adhere to the slide.

Deparaffinization/Rehydration

- To perform antibody staining, paraffin wax must be removed from the sample (5 min in 60°C in thermo-wealtec) and the sample must be rehydrated. *NOTE: Do not allow slides to dry at any time during this procedure as this can lead to inconsistent staining.*
- To remove paraffin wax, sections were placed in three containers of xylene for 5 min each. Fresh xylene should be used as incomplete deparaffinization can also lead to inconsistent staining.
- To start rehydration, the sections were placed in two containers of 100 % ethanol for 5 min each and then, in two containers of 95 % ethanol for 10 minutes each, followed by two containers of 75 % ethanol for 10 min each.
- To complete the rehydration process, washing of the sections twice in PBS 1x for 5 min each was required.
- The sections were placed in proteinase K solution for 6 min at 37°C and then, in glycine 1x solution for 5 min in RT.
- Washing the samples with PBS 1x (twice) for 5 min.
- Addition of 4 % PFA for 15 min in RT.
- Washing of the samples with PBS 1x (twice) for 5 min.
- Antigen Unmasking with Citrate Buffer and placement into the steamer followed.

For Citrate**:** Bring slides to a boil in 10 mM sodium citrate buffer, pH 6.0; maintain at just below boiling temperature for 50 min inside a steamer. Cool slides on bench top for 30 min in RT and 10 min at 4°C.

It was important not to over or under heat samples as this can cause inconsistent staining results.

Staining

First Day

- The sections were washed in dH_2O three times for 5 min each and then, with PBS 1x for 10 min.
- To prevent non-specific binding of the antibody to the tissue, blocking each section with 100 µL blocking solution [10 % sheep serum (from 100 % stock solution), Triton-X 0.1 % (from 10 % stock solution)] and covered with parafilm.
- Each section was incubated in 100 µl primary antibody solution [2 % sheep serum (from 100 % stock solution), primary antibodies, up to 1mL PBS 1x] and covered with parafilm.
- Incubation overnight at 4°C.

Second Day

- Wash the samples with PBS 1x (twice) for 15 min.
- Cells were incubated in 100 µl of secondary antibody solution [2 % sheep serum (from 100 % stock solution), secondary antibodies, Triton-X 0,1 % (from 10 % stock solution) up to 1 mL PBS 1x] and the samples were covered with parafilm.
- The samples were washed with PBS 1x (three times) for 15 min.

- Fluoroshield for DAPI staining [Mounting Medium with DAPI-Aqueous, Fluoroshield (ab104139)] was added and the samples were stored at 4^{o}C, until observed under a microscope.

Antibodies, Chemicals, Drugs	Company	Code	Host	Concentrations
16% paraformaldehyde	Thermo Scientific	28906		
Triton-X 100	Sigma/Aldrich, St. Louis, MO, USA	11332481001		
Bovine Serum Albumin	Sigma/Aldrich, St. Louis, MO, USA	B2064		
anti-α actinin 4	Abcam, Cambridge, MA, USA	ab198608	rabbit	(1/50)
anti-argonaute-2	Abcam, Cambridge, MA, USA	ab57113	mouse	(1/80)
anti-α-tubulin	Abcam, Cambridge, MA, USA	ab18251	rabbit	(1/1000)
anti-α-tubulin	Cell Signaling	DM1A#3873s	mouse	(1/100)
anti-Citron kinase	Novus	NBP2-38592	rabbit	(1/100)
anti-Argonaute-2	Abcam, Cambridge, MA, USA	ab186733	rabbit	(1/50)
anti-Drosha	Abcam, Cambridge, MA, USA	ab12286	rabbit	(1/100)
anti-DGCR8	Novus	NBP1-30115	rabbit	(1/100)
anti-Dicer	Novus	NBP1-06520	rabbit	(1/120)
anti-ATF4	GenScript	Ab-245	rabbit	(1/100)
anti-Aurora B	BD Biosciences	611082	mouse	(1/200)
anti-Staufen/STAU1	Abcam, Cambridge, MA, USA	ab50914	rabbit	(1/100)
anti-Phospho-p38 MAPK (Thr180/Tyr182)	Cell Signaling	9211	rabbit	(1/100)
anti-phospho-AMPK1 (Ser485)/AMPK 2 (Ser491)	Cell Signaling	4185	rabbit	(1/100)
anti-Phospho-MEK1/2 (Ser217/221) (41G9)	Cell Signaling	9154	rabbit	(1/100)

anti-Phospho-p38 MAPK (Thr180/Tyr182)	Cell Signaling	9211	rabbit	(1/100)
anti-Phospho-Akt (Thr308)	Cell Signaling	9275	rabbit	(1/100)
anti-Phospho-sAPK/JNK (Thr183/Tyr185)	Cell Signaling	9251	rabbit	(1/100)
Donkey Anti-Rabbit IgG (H + L) Secondary Antibody Fluor®488 conjugate	Invitrogen, Waltham, MA, USA			(1/250)
Goat anti-Rabbit IgG (H + L) Secondary Antibody Alexa Fluor 594	Invitrogen, Waltham, MA, USA			(1/250)
Goat anti-Mouse IgG (H + L) Cross-Adsorbed Secondary Antibody Alexa Fluor 488	Invitrogen, Waltham, MA, USA			(1/250)
Goat Anti-mouse IgG Dylight 594 Conjugated	Invitrogen, Waltham, MA, USA			(1/250)
Rhodamine - Phalloidin	Biotium			(5/200)
VECTASHIELD® Mounting Medium with DAPI	Vector Laboratories, Inc., 30 Ingold Road, Burlingame, CA 94010 USA			
phospho-ago kit [Argonaute 2 (a.a. 389-398), Argonaute 2 (Tyr-393) Argonaute 2 (Ser-387)]	ECM BIOSCIENCES	AK6970	rabbit	(1/50)
Upf1 antibody (D15G6)	Cell Signaling	12040	rabbit	(1/100)
TIAR antibody	Cell Signaling	8509	rabbit	(1/100)
Dynactin antibody	Cell Signaling	69399	rabbit	(1/100)
lipofectamine 2000	Invitrogen	11668-027		
CF 488 anti-streptavidin	Biotium	#29034		(1/250)
biotinylated oligo(dT) probe	Biotrans	Z5261		(1/50)

DsiRNAs and TriFECTa Kits in tubes	IDT			according to the manufacturer's protocol
Phospho-eIF2α (Ser51) (D9G8)	Cell Signaling	3398	rabbit	(1/100)
Duo link kit	Merck	92101		according to the manufacturer's protocol
anti-phospho-p44/42 MAPK (Erk1/2) (Thr202/Tyr204)	Cell Signaling	9101	rabbit	(1/100)
demecolcine	Sigma/Aldrich, St. Louis, MO, USA	D7385		0,4μg/ml
cytochalasin D	Sigma/Aldrich, St. Louis, MO, USA	C8273		10μM
anti-chk2 (1C12)	Cell Signaling	3440	mouse	(1/100)
anti-chk1	Cell Signaling	2345	rabbit	(1/100)
anti-phospho-Chk1 (Ser345)	Cell Signaling	2341	rabbit	(1/100)
anti-phospho-Chk2 (Thr68)	Cell Signaling	2661	rabbit	(1/100)
anti-lamina/c	Abcam, Cambridge, MA, USA	ab108595	rabbit	(1/400)
anti-Wee1	Cell Signaling	4936	rabbit	(1/100)
anti phospho Wee1 (Ser642) (D47G5)	Cell Signaling	4910	rabbit	(1/100)
anti-phosphop53	Cell Signaling	9286	mouse	(1/100)
p53	Cell Signaling	2433	rabbit	(1/100)
TRI Reagent	Sigma/Aldrich	T9424		

Table 3 Reagents, chemical/drug compounds and antibodies (primary and secondary). Details of the materials used in the methodology of the manuscript.

RNA extraction

500 μl TriFast (30-2010, PeqLab) were added to the sample. The tissue was homogenized with a pestle in a 1.5 mL tube with two intervals for cooling on ice. Samples were left for 5 min at RT. 200 μl chloroform was added and the tubes were shacked vigorously for 15 sec minimum. Samples were left for 10 min at RT and then, centrifuged at max speed, at 4^{o}C for 5 min. The aqueous phase was transferred (80 % of the aqueous phase volume, without mixing with the interphase) to a fresh tube.

500 µl isopropanol (100 %, #33539, Sigma-Aldrich, Germany) was added and the tubes were inverted a few times. Samples were left on ice for 15 min. Samples were centrifuged at 12,000 g max at 4°C for 10 min. The supernatant was discarded and the RNA pellet was washed once with ice-cold 75 % ethanol. Centrifugation for 12,000 g at 4°C for 10 min followed the wash. Excess ethanol (75 %, #32221, Sigma-Aldrich, Germany) was removed and the RNA pellet was air-dried.

31 µl of RNase-free water (DEPC treated H_2O, RNAse free) was added to resuspend the RNA pellet and stored at -80°C.

The quantity and quality of RNA samples were measured with Nanodrop, indicatively, as following:

	RNA		
Code given	ng/µl	260/280	260/230

cDNA synthesis

Almost 1 µg RNA is required for cDNA synthesis. The calculations were indicatively done according to the following table.

Code given	ng/µl	µg/µl	1µg in X µl

Samples were generated at a final volume of 12µl each.

	ul sample	µl NF H_2O

In each sample, 2 µl of gDNA wipe-out (Quantitect RT kit, Qiagen, 205311Q) was added.

Samples were heated for 2 min at 42°C in a PCR machine and then snap freezed.

6µL of the following mix were added in each sample:

- 5x RT buffer: 4µl (x9 = 36µl)
- RT primer: 1µl (x9= 9µl)
- RT transcriptase: 1µl (x9= 9µl)

Quantitect RT kit (Qiagen, 205311) was used for cDNA synthesis

Samples were heated for 40 min at 42°C, followed by 3 min at 95°C in a PCR machine and then were stored at -20°C.

Relative quantification of gene expression by real-time PCR analysis

Real-time PCR (QPCR) was conducted in a Roche LightCycler® 96 System in duplicates or triplicates using the KAPA SYBR FAST qPCR (2x) (KAPA Biosystems). All reactions were set up using 300-500 nmol/L of each primer and 0.5 μg/μl cDNA (1:5 diluted) in the reaction volume (Table 6). The PCR conditions were as followed: an initial denaturation step at 95°C for 3 min, 40 cycles of amplification (each cycle is 30 seconds at 95°C, 1 min at 61°C, 1 min at 72°C), followed by the dissociation curve step (1 min at 95°C, 30 sec at 55°C, 30 sec at 95°C) to verify the amplification of a single product (Table 7). Efficiency curves were obtained for each cDNA template by plotting CT values against the $\log_{10}$ of six serial dilutions of a cDNA pool generated for all samples analyzed. Q-PCR efficiency (E) was calculated with the formula $E=10^{[-1/slope]}$ according to the relative quantification of Michael W. Pfaffl and varied between 95 % - 100 %. Primers used are presented in Table 4,5. Housekeeping genes (b actin, lamin a, gapdh) were validated for use. The normalization factor was calculated as the geometric mean of the three most stably expressed housekeeping gene of lamin a.

Relative gene expression was calculated using the 2−ΔΔCt method. Expression of genes of interest (goi) was normalized by the reference gene lamin a or gapdh. Fold change in gene expression was calculated as $2^{-\Delta\Delta CT}$ where ΔΔCT = ΔCT (goi) − ΔCT (lamin/gapdh). The relative change of Ago2 following the treatment with siAgo2 or mimic miR26 was calculated using the gene expression of the respective scrambled control cells.

Gene name	Sequence of primer sets	Working concentration
hsa_GAPDH5b_F	AGTCAGCCGCATCTTCTTTTG	10uM
hsa_GAPDH5b_R	CGCCCAATACGACCAAATCC	10uM
lmna_R	TTGTCAATCTCCACCAGTCG	10uM
lmna_R_gsp	GTCTTCTCCAGCTCCTTCTTA	10uM
AGO1F2	GAAGGCAGAACGCTGTTACC	10uM
AGO1R2	CCCT GTTCCCCACTCTTACA	10uM
AGO2_Fd	CACTCTGCGCACCATGTACT	10uM
AGO2_Rd	TTTGAAATCTGGGACGGAAG	10uM
AGO3FW	GCACCAGCGTATTATGCTCA	10uM
AGO3RV	GGCAAGAGCTTGTGGATCTC	10uM
AGO4_FW	TGGGAAGAAACCTTCCAT	10uM
AGO4_RV	GGTCCTGGATGACCTCTTGA	10uM
ago2_F	AGAAGTGCCCGAGGAGAGTT	10uM
Ago2_R	GCTTCCGATCCCCAAAGAT	10uM
ago2gfpFW	CGACCACTACCAGCAGAACA	10uM
ago2gfpRV	GAACTCCAGCAGGACCATGT	10uM

ago3cherFW	GCACCAGCGTATTATGCTC	10uM
ago3cherRV	AAGCGCATGAACTCCTTGAT	10uM
ago4gfpFW	AGTCTGAGGACATCAACAAGTTT	10uM
ago4gfpRV	GCTTGATCTCCGGAATATTGG	10uM
SEPT9FW	CAGGGCTTCGAGTTCAACAT	10uM
SEPT9RV	ACCGACTTCCGGCTGATT	10uM
dicer1FW	TTGGCTTCCTCCTGGTTATG	10uM
dicer1RV	CACATCAGGCTCTCCTCCTC	10uM
DGCR8FW	AGGAGAAGCGGTGATGGAG	10uM
DGCR8RV	TTACCTCTGCACCACTGGAC	10uM
DGCR8bFW	CTGGAGTCCCGGTGTACC	10uM
DGCR8bRV	TCAGAGGAGGGTCGTGTTTC	10uM
droshaFW	TGAGTTTGAAGAAGCAATTGGA	10uM
droshaRV	GGCTACCAGTTGCATTATGG	10uM
hsa-RNU48	AGTGTGTCGCTGATGCG	10uM
hsa-miR-let7f_R	AACTATACAATCTACTACCTCA	20uM
hsa-miR-26_F	TCAAGTAATCCAGGATAGGCTG	10uM
hsa-miR-30d_R	CTTCCAGTCGGGGATGTTTACA	20uM

Table 4 Primers for humans & mice

Primers	Concentration for qpcr reaction	Concentration for pcr reaction	Amplicon	Tm
Ago1 F2/R2	200nM	500nM	164bp	60°C
Ago2 FD/RD	400nM	500nM	195bp	60°C
Ago3 F/R	200nM	500nM	130bp	60°C
Ago4 F/R	450nM	500nM	155bp	59°C

Table 5 Argonaute Primers for humans & mice

Components	Volumes	Final Concentration
Sybr Green	5 uL	1x
Primer Forward 10μM	See table 1	
Primer Reverse 10 μM	See table 1	
cDNA	1 uL	<20ng
H20	up to 10 uL	

Table 6 qPCR reaction - Components

Cycle step	Temperature	Time	Cycles
Enzyme activation	95°C	10min	

Denaturation	95 °C	15sec	40cycles
Annealing/Extension/ Data acquisition	60 °C	1min	
Dissociation curve	95 °C	10sec	
	65 °C	1min	
	95 °C	15sec	

Table 7 qPCR reaction – Cycling Conditions

miRNA reverse transcription RT protocol

RNA isolation was performed according to the abovementioned protocol.

miQPCR and microRNA validation were conducted according to the EMBO Course 2014, Galway. The original protocol has been designed by Mirco Castoldi.

Complete miQ PCR RT program

Temperature	Time
25°C	Hold (skip)
25 °C	30 min
10 °C	Hold(skip)
85 °C	2min
46 °C	Hold(skip)
46 °C	30min
85 °C	3min
10 °C	Hold

1. Step 1: Elongation Step

Tailing Mix	Volume	x Samples(+negRT)	Check
Neb 10x Buffer (NEB)	0,85		
MgCl2 (200 mM)	0,35		
PEG (50%)	2,6		
miQ Linker (5 µM)	0,3		

(14,5+3,2 µl)			
RNAse Inhibitor (40 U/µl)	0,10		
T4 RNA ligase2 NEB (200 U/µl) (truncated almost 12 µl)	0,20		

- Program the thermal cycle with miQPCR RT program
- Dilution of the RNA to 2.5 ng/µl of ddH_2O (RNAse free)
- (Dilution RNA to 10 ng/µl in some cases)
- Writing down samples in the cDNA Tracking Table.
- Pipetting 4 µl diluted RNA (e.g 10 ng) into 200 µl PCR tubes (or PCR plate)
- (Scaling down) 1 µl RNA + 3 µl H_20.
- Preparation of the tailing mix T1 and add 4 µl of T1 to 4 µl of RNA.
- Centrifugation and loading the plate in the cycler and incubation for 30 min at 25^oC.
- T2 mix was prepared.
- At the end of this step the samples will be incubated at 10^oC.

2. Step 2: cDNA synthesis step

cDNA mix1- T2	Volume (µl)	X Samples(+negRT)	Check
dNTPs (10mM)	0,5		
ddH2O (RNAse free)	7,0		
miQ RT primer (10 µM) (250µl)	0,25		

cDNA mix2- T3	Volume (µl)	X Samples	Check	x1 negRT
5x RT Buffer (Takara)	4.10			4,10
PrimeScript (Takara)	0,25			-

ddH2O (RNAse free)	1,15			1,40

- From this step tubes are staying in PCR cycler (also while pipetting).
- Preparation of cDNA mix T2 a little before the end of first incubation step.
- Addition of 7.0 µl of cDNA mix1-T2 to the tubes (F.V. 15 µl).
- Incubation at 85°C for 2 min and holding at 46°C (preparation of T3 quickly, but the temperature should have been dropped at 46).
- Preparation cDNA mix2-T3 and add 5 µl of T3 to the tubes (F.V. 20 µl)
- Incubation at 46°C for 30 min, denaturation at 85°C for 30 min and hold at 10°C.

3. Step 3: Dilution of cDNA

After the run cDNA stock was almost 0,5 ng/µl.

Performing of cDNA stock; dilution to 200 µl (add 180 µl ddH_2O) to 0.05 ng/µl.

In the qPCR usage of 2 µl of diluted cDNA (or 100 pgr) with the amount of master mix recommended for your qPCR cycler.

(Usage of 5 µl cDNA and 15 µl master mix in mi_QPCR)

Storage of the stock and dilution of cDNAs at -20°C.

DNA extraction from FFPE

- Addition of 4-5 paraffin slices of 5 µm thickness.
- Add 800 µl xylene and gently shake for 5-15 min at RT or 3-5 min at 55°C for disintegration of the paraffin.
- Centrifuge at 14,000 rpm for 3 min and remove the xylene carefully without agitating the pellet.
- Repetition of the previous two steps.
- Addition of 800 µl 100 % EtOH (v/v), vortexing and incubation for 5 min, followed by 3 min centrifugation at 14,000 rpm. Discard the supernatant.
- Addition of 800 µl 70 % EtOH (v/v), vortexing and incubation for 5 min, followed by 3 min centrifugation at 14,000 rpm. Discard the supernatant.
- Addition of 800 µl 50 % EtOH (v/v), vortexing and incubation for 5 min, followed by 3 min centrifugation at 14,000 rpm. Discard the supernatant.
- Air-dry the pellet for 5 min.
- Addition of 200-500 µl (300 µl) lysis buffer and resuspension. Homogenization is a critical step (for better yield of DNA).
- Incubation at 56°C at the heat block. If tissue cores still exist, add 20 µl of proteinase K 20 µl proteinase K (20 mg/mL stock) for few hours (3hours) or overnight.

- Addition of phenol: chloroform: isoamyl alcohol (25:24:1), equal volume with the lysis buffer (300 µl).
- Mixing for 5 min and centrifugation for 5 min at 14,000 rpm.
- Transfer the aqueous phase and addition of RNAase A (100 µg/mL) for 1 hour at 37^{o}C.
- Addition of 1 volume phenol:chloroform:isoamyl alcohol (25:24:1) (300 µl)
- Mix for 5 min and centrifuge for 5 min at 14,000 rpm.
- Estimation of the volume of the sample and addition of the 1/10 3 M sodium acetate pH 5.2. Addition of 1 volume 100 % isopropanol (v/v).
- Well mixing and incubation on ice or at-20^{o}C for 30 min or overnight.
- Centrifugation at 14,000 rpm at 4^{o}C for 10 min.
- Discard the supernatant.
- Wash the pellet with equal volume of ice-cold 70 % EtOH.
- Resuspension of the pellet in H_2O.

Lysis Buffer

- 10 mM Tris-HCL pH 8
- 100 mM EDTA pH 8
- 50 mM NaCl
- 0.5 % SDS
- 200 µg proteinase K (freshly made)

Up to 100 mL with dH2O.

RNA extraction with Trizol

- 500 µl TriFast (TriFast, 30-2010, PeqLab) were added. The tissue was homogenized with a pestle in a 1.5 mL tube with two intervals for cooling in ice.
- Samples were left for 5 min at RT.
- 200 µl chloroform were added. Tubes containing the samples were shacked vigorously for 15 sec minimum.
- Samples were left for 10 min at RT.
- Samples were centrifuged at max speed, 4^{o}C for 5 min.
- The aqueous phase was transferred (80 % of the aqueous phase volume, without mixing with the interphase) to a fresh tube.
- 500 µl isopropanol was added. Tubes containing the samples were inverted a few times.
- Samples were left on ice for 15 min.
- Samples were centrifuged at 12,000 g max at 4^{o}C for 10 min.
- The supernatant was discarded and the RNA pellet was washed once with ice-cold 75 % ethanol.

- Centrifugation for 12,000 g max at 4°C for 10 min followed.
- Excess ethanol was removed and the RNA pellet was air-dried.
- 31 µl of RNase-free water was added to resuspend the RNA pellet.

The quantity and quality of RNA samples were measured with Nanodrop, indicatively, as following:

		RNA		
	Code given	ng/µl	260/280	260/230

cDNA synthesis

Code given	ng/µl	µg/µl	1µg in X µl

New samples were created with a final volume of 12µL each.

	ul sample	µl NFH_2O

In each sample 2 µl of gDNA wipe-out (Quantitect RT kit, Qiagen, 205311Q) was added.
Samples were heated for 2 min at 42°C in a PCR machine and then snap freezed.
6 µl of the following mix were added in each sample:

- 5x RT buffer: 4 µl (x9 = 36 µl)
- RT primer: 1 µl (x9 = 9 µl)
- RT transcriptase: 1 µl (x9 = 9 µl)

Quantitect RT kit (Qiagen, 205311) was used for cDNA synthesis
Samples were heated for 40 min at 42°C, followed by 3 min at 95°C in a PCR machine and stored at -20°C.

RNA extraction from cultured cells with columns (Nucleospin XS, Qiagen, 740902)

Reagents

- 96-100 % ethanol (to prepare Wash Buffer RA3 and for the clean-up procedure)
- 70 % ethanol

Consumables

- 1.5 mL microcentrifuge tubes
- Sterile RNase-free tips

Procedure

NucleoSpin® RNA methods aid to avoid RNA degradation, because of cell lysis by incubation in a solution containing large amounts of chaotropic ions. This lysis buffer immediately inactivates RNases – which are present in virtually all biological materials – and creates appropriate binding conditions which favor adsorption of RNA to the silica membrane. Contaminating DNA, which is also bound to the silica membrane, is removed by an rDNase solution, directly applied onto the silica membrane during the preparation (RNase-free rDNase is supplied with the kit). Simple washing steps with two different buffers remove salts, metabolites and macromolecular cellular components. Pure RNA is finally eluted under low ionic strength conditions with RNase free H2O. The RNA preparation using NucleoSpin® RNA kits can be performed at RT.

RNA purification from cultured cells

Cell pelleting of 10^5 cultured cells was provided.

Cell Lysis and homogenization

Addition of 100 µl Buffer RA1 and 2 µl TCEP to the cell sample and vortexing vigorously (2 x 5 s) were performed. If multiple samples were processed, the preparation of a master-premix was recommended (e.g. 1.1 mL Buffer RA1 and 22 µl TCEP for 10 preparations). Usage of 102 µl of the premix followed by the addition of 5 µl Carrier RNA (working solution 20 ng) to the lysate. Mix by vortexing (2 x 5 sec). Spin down briefly (approx. 1 sec, 1000 x g) to clear the lid. For preparation of Carrier RNA working solution see section 3 + 5 µl Carrier RNA Mix.

Filtration of the lysates

NucleoSpin® Filter (violet ring) was placed in a Collection Tube (2 mL; supplied), the mixture was applied, and then centrifugation was performed for 30 s at 11,000 g. This step may be skipped when working with small amounts of sample, for example less than 10^5 cells.

Adjustment of the RNA binding condition Discard the NucleoSpin® Filter (violet ring). Addition of 100 µl ethanol (70 %) to the homogenized lysate and mixing by pipetting up and down (5 times) were followed. Alternatively, addition of 100 µl ethanol (70 %) to the sample in a 1.5 mL microcentrifuge tube (not provided) and mixing by vortexing (2 x 5 sec) were performed, before spinning down briefly to clear the lid. Pipetting of the lysate up and down two times was needed before loading the lysate.

RNA Binding

For each preparation, a NucleoSpin® RNA XS Column (light blue ring) was placed in a Collection Tube. The lysate is loaded to the column. Centrifugation for 30 sec at 11,000 g and placement of the column in a new Collection Tube (2 mL) followed. The maximum loading capacity of NucleoSpin® RNA XS Columns is 600 µl. Repetition of the procedure was required, if larger volumes were to be processed.

Desalination of silica membrane

Addition of 100 µl MDB (Membrane Desalting Buffer) and centrifugation at 11,000 g for 30 sec to dry the membrane were performed. It is not necessary to use a fresh Collection Tube after this centrifugation step. Salt removal will make the following rDNase digestion much more effective. If the column outlet has come into contact with the flow-through for any reason, the flow-through must be discarded and centrifugation again for 30 sec at 11,000 g is needed.

Digestion of DNA Prepare rDNase reaction mixture in a sterile microcentrifuge tube (not provided): for each isolation, add 3 µl reconstituted rDNase (also see section 3) to 27 µl Reaction Buffer for rDNase. Mixing by flicking the tube and application of 25 µl rDNase reaction mixture directly onto the center of the silica membrane of the column followed.

Incubation at RT for 15 min. It is not necessary to use a new Collection Tube after the incubation step.

Washing and drying of the silica membrane

1st wash

Addition of 100 µl Buffer RA2 to the NucleoSpin® RNA XS Column. Incubation for 2 min at RT. Centrifugation for 30 sec at 11,000 g and placement of the column into a new Collection Tube (2 mL). Buffer RA2 will inactivate the rDNase.

2nd wash

Addition of 400 µl Buffer RA3 to the NucleoSpin® RNA XS Column. Centrifugation for 30 sec at 11,000 g, flowthrough removal and placement of the column back into the Collection Tube.

Note: Make sure that residual buffer from the previous steps is washed away with Buffer RA3, especially if the lysate has been in contact with the inner rim of the column during loading of the lysate onto the column. For efficient washing of the inner rim flush, it with Buffer RA3.

3rd wash

Addition of 200 µl Buffer RA3 to the NucleoSpin® RNA XS Column and centrifugation for 2 min at 11,000 g to dry the membrane. Placement of the column into a nuclease-free Collection Tube.

If for any reason the liquid level in the Collection Tube has reached the NucleoSpin® RNA XS Column after centrifugation, discard flow-through and centrifuge again.

Elution

Highly pure RNA was eluted in 10 µl H_2O (RNase-free; supplied) and centrifuged at 11,000 g for 30 sec. If higher RNA concentrations or higher elution volumes were desired, elution volume may be varied in the range of 5-30 µl.

Argonaute HITS-CLIP Method

High-throughput sequencing of RNA isolated by crosslinking immunoprecipitation (HITS-CLIP, also known as CLIP-Seq) is a genome-wide means of mapping protein-RNA binding sites or RNA modification sites, in vivo. HITS-CLIP was originally used to generate genome-wide protein-RNA interaction maps for the neuron-specific RNA-binding protein and splicing factor NOVA1 and NOVA2;

since then a number of other splicing factor maps have been generated, including PTB, RbFox2, SFRS1, hnRNP C and N6-Methyladenosine (m6A) mRNA modifications.

HITS-CLIP of the RNA-binding protein, AGO2 has been performed for the identification of microRNA targets by decoding microRNA-mRNA and protein-RNA interaction maps in mouse brain, and subsequently in *Caenorhabditis elegans*, embryonic stem cells and tissue culture cells.

Materials

Preparation of solutions:

• 1M Na - Phosphate buffer pH 8 (final volume 50 mL)

Na_2HPO_4 (Sodium phosphate dibasic dihydrate) - MW: 177.99 g/mol

For 50 mL: Weight 8.9 g,

add 30 mL Nuclease Free H_2O

heat to 60^oC to clear the solution

NFH_2O up to 50 mL

NaH_2PO_4 (Monosodium phosphate) - MW: 137.99 g / mol

For 50 mL: weight 6.89 g

add 30 mL NFH_2O

NFH_2O up to 50 mL

Mix 1 volume of solution (ii) causes increase in acidity (decrease in pH) - with 13.7 volumes from solution causes increase in alkalinity (increase in pH) till pH = 8.

Filter the solution with a syringe having pores 0.22 μm in diameter.

Save to RT on falcon tube.

• Antibody Binding buffer (final volume 250 mL)

9 washes are reported in the protocol (1mL per wash and 6 additional washes are calculated = 15 washes/sample), ie 15 mL / sample. For 15 samples: 15 mL/sample * 15 samples = 225 mL (~ 250 mL).

	Stock	Calculations
0.1M Na - Phosphate pH 8	1M	1M * X = 0.1M * 250 mL, X=25 mL

0.1 % NP- 40	10%	10% * X = 0.1% * 250 mL, X=2.5 mL
5% Glycerol	87%	87% * X = 5% * 250 mL X=14.36 mL

Add NFH_2O up to 200 mL followed by stirring, RT.

Adjust the final volume up to 250 mL on a volumetric cylinder by adding NFH_2O.

Filter the solution, cover with foil and store at 4°C.

• 1x PMPG (final volume 200mL)

8 washes are reported in the protocol, 1 mL per wash and 6 additional washes are calculated = 14 washes / sample, ie 14 mL /samples

For 15 samples: 14 mL/sample * 15 samples = 210 mL (~200 mL).

	Stock	Calculations
1x PBS (Mg^{2+}/Ca^{2+})	10x	10x * X = 1x * 200 mL, X=20 mL
2 % Empigen	35 %	35% * X = 2% * 200 mL, X=11.43 mL

Filter the solution, cover with foil and store at 4°C.

• 5x PMPG (final volume 100 mL)

4 washes are mentioned in the protocol, 1ml per wash and 3 additional washes are calculated = 7 washes/sample, ie 7 mL/ samples

For 15 samples: 7 mL/sample * 15 samples= 105 mL (~100 mL)

	Stock	Calculations

5x PBS (Mg^{2+}/Ca^{2+})	10x	10x * X = 5x * 100 mL X=50 mL
2 % Empigen	35 %	35% * X = 2% * 100 mL X=5.7 mL

Filter the solution, cover with foil and store at 4^{o}C.

• 1x PNK buffer (final volume 250 mL)

11 washes are mentioned in the protocol, 1mL per wash and I calculate 4 extra washes=15 washes/sample, ie 15 mL/sample. For 15 samples: 15 mL/sample * 15 samples=225 mL (~250 mL).

	Stock	Calculations
50 mM Tris-HCl pH 7.4	1M	1M * X = 0.05M * 250mL X=12.5 mL
10 mM MgCl2	1M	1M * X = 0.01M * 250mL X=2.5 mL
0.5 % NP-40	10%	10% * X = 0.5% * 250mL X=12.5 mL

Filter solution, cover with foil and store at 4^{o}C.

• 1xPNK & EGTA buffer (final volume 50mL)

1 wash was mentioned in the protocol/1mL per wash, additional 2 washes = 3 washes/sample were calculated, ie 3mL / sample

For 15 samples: 3mL/sample * 15 samples = 45mL (~50mL).

	Stock	Calculations
50mM Tris-HCl pH 7.4	1M	1M * X = 0.05M * 50mL X=2.5mL
20mM EGTA	0.5M	0.5M * X = 0.02M * 50mL X=2mL
0.5% NP-40	10%	10% * X = 0.5% * 50mL X=2.5mL

Filter solution, cover with foil and store at 4°C.

• 5x PK buffer (final volume 50 mL)

	Stock	Calculations
500 mM Tris-HCl pH 7.5	1 M	1M * X = 0.5 M * 50 mL X=25 mL
250 mM NaCl	5 M	5M * X = 0.25 M * 50 mL X=2.5 mL
50 mM EDTA	0.5 M	0.5M * X = 0.05 M * 50 mL X=5 mL

Add NF H2O up to 50 mL.

The following solutions should be prepared shortly before use:

• 4mg / mL Proteinase K in 1x PK buffer (for every 1mL buffer)

	Stock	Calculations
1x PK	5x PK	5x= 1x * 1000 µl, X=200 µl
Prot K 4mg/mL	Prot K 20mg/mL	20 mg/mL * X = 4 mg/mL * 1000 µl X=200µl

Mix 200 µL 5x PK buffer with 200 µL Prot K (20 mg/mL) and add 600 µl NFH_2O (final volume 1mL).

• 1x PK / 7M Urea solution (for 5mL):

	Stock	Calculations
1x PK	5x PK	5x * X = 1x * 5000 µl X=1000 µl
7M Urea	MW: 60.06 g/mol	2.10 g

NF H2O up to a final volume of 5 mL.

• Chloroform: isoamyl alcohol (24:1) Remove 1 mL from the 25 mL (Sigma) and add 1 mL isoamyl alcohol.

• 10x TBE buffer (RT storage)

- 890 mM Tris-HCl
- 890 mM Boric Acid
- 20 mM EDTA

Cell line Preparation

- Required 50 plates/cell line: 3 * 10 plates (replicates), 10 plates (No UV control) and 10 plates (IgG control - antibody specificity test/immunoprecipitation)
- When the cells are at 90 % confluency the irradiation process can begin. The process requires ice-cold 1x DPBS and 1x DPBS, RT.
- Cell suspension was achieved and collected in 10*50 mL-falcon tubes (approximately for every 10 plates, 100 mL of cell suspension are collected)
- Centrifuges (large and small) must have already been cooled to 4^{o}C.

- Discard the nutrient medium of 2 cell plates (incubator).
  10 mL 1x DPBS was added at RT being careful of cell detachment.
- Ice was placed on the lid of the plate (create a flat surface with the surface of another plate with no slope)
- 1x DPBS was removed and placed the plate in the irradiator (Stratagene UV Stratalinker 1800) on ice. For each irradiation, two plates were placed inside the device under the irradiation lamps.
- The cells were irradiated with an intensity of 400 mJ/cm^2 (the indication on the device is 4000 µJ*100).
- The irradiation lasts about 3 min (the device has a sensor for measuring the energy emitted in the irradiation chamber).
- When the plates were irradiated, 2-3 mL ice-cold 1x DPBS was added and the scraping process begins. Initially, linear movements were made by rotating the plate gradually to make the process over the entire surface. Then, the cell suspension was drained on one side of the plate at an angle and the suspension was pipetted into a 50 mL falcon.
- 3 mL ice-cold 1xDPBS was added again and the above procedure was repeated.
- When the process was completed on all 50 plates, 10*50 mL-falcon tubes were collected.
- Centrifugation (in the large centrifuge) for 5 min at 200 g at 4^{o}C.
- Supernatant removal with aspiration.
- 0.5 mL ice-cold 1x DPBS was added to each falcon.
- In a 2 mL DNA LoBind tube the cell suspensions were collected from two 50 mL falcons.
- Centrifugation (in the small centrifuge) for 5 min at 3,000 rpm (1,000 g) at 4^{o}C.
- Aspiration of the supernatant and tubes were placed in liquid nitrogen to cool the cells abruptly.
- After 10 min, the tubes were stored at -80^{o}C until used.

Procedure

Day 1st

Sample preparation and UV cross-linking

- For adherent culture cells, seed cells onto a 145 mm cell culture dish. When cells reach ~90% confluence, discard the culture medium and briefly wash cells with 10 mL room temperature 1x DPBS. For fresh tissue, transfer the tissue to a clean 100 mm cell culture dish and keep it covered with 8 mL of ice-cold 1x PBS. Dice it using a surgical blade to create small pieces of several mm^3 (UV can penetrate small chunks of tissue). An input of 10 cell culture dishes or 100 mg of tissue is sufficient for one CLIP sample.
- For adherent culture cells, place two cell culture dishes without lids on ice in the UV cross-linker (254 nm; Stratalinker model 1800 from Stratagene) and irradiate the cells once with power settings 400 mJ/cm^2. For fresh tissue, irradiate the tissue suspension on ice three times at 400 mJ/cm^2 in the UV cross-linker with 30 sec intervals for cooling. Mix suspension between

each irradiation to maximize exposed surfaces for cross-linking. A negative control is cells or tissue that has not been irradiated with UV.

- For adherent culture cells, add 3 mL of ice-cold 1x DPBS on the culture dish and scrape the cells. Collect cell suspension into a 50 mL conical tube. Add another 3 mL of ice-cold 1x DPBS on the culture dish in order to collect the remaining cells. Pellet cell suspension by centrifugation at 200 g for 5 min at 4°C. Discard the supernatant, resuspend the cell pellet in 1 mL of ice-cold 1x DPBS and transfer it to a 2 mL microcentrifuge tube (DNA Lo Bind Tube). Re-pellet cells at 1000 g for 5 min at 4°C. Remove the supernatant, freeze the cell pellet in liquid nitrogen and store at -80°C until use. For fresh tissue, collect the tissue suspension into a 15 mL conical tube and pellet by centrifugation at 200 g for 5 min at 4°C. Discard almost all of the supernatant (leave ~1.5 - 2 mL) and transfer the tissue to a 1.5 mL microcentrifuge tube (DNA LoBind Tube). Re-pellet tissue suspension at 1,000 g for 30 sec at 4°C. Remove the supernatant, freeze the packed tissue pellet in liquid nitrogen and store at -80°C until use.

Day 2nd

Bead preparation

- Pipette 150 µl of protein G Dynabeads into a 1.5-mL microcentrifuge tube (DNA LoBind Tube).
- Wash the beads three times with 1 mL of ice-cold Ab binding buffer each time. For bead washing steps in the subsequent steps always use 1 mL of ice-cold buffer.
- Resuspend the beads in 350 µl of Ab binding buffer and add 500 µl of anti-Ago2 mouse hybridoma or 100 µl of pre-immune mouse IgG serum (negative control for immunoprecipitation).
- Rotate the tubes end over end at 4°C for 6 hours.
- Wash the beads with bound Ab one time with Ab binding buffer and three times with 1x PMPG.

Cell lysis, RNase digestion and Immunoprecipitation

- Thaw frozen cell or tissue pellets on ice and resuspend each pellet using 500 µl of Lysis buffer (make fresh each time). With a 1 mL pipette, mix until flow is unforced, with care not to foam. For hard tissue, lysis can be done using further mechanical means, such as an Eppendorf-pestle.
- Add 7 µl of RNasin to each tube and let sit on ice for 10 min.
- Add 10 µl of RQ1 DNase and incubate at 37°C for 10 min at 1000 rpm in a Thermomixer.
- For RNase treatment, add 1 µl of diluted RNace-IT (1:50 dilution) and incubate the mixture for 7 min exactly at RT. During the digestion, flick tubes regularly to prevent beads from settling.
- Centrifuge the lysates in a pre-chilled tabletop centrifuge at max-speed (13,000 rpm/16,060 g) for 50 min at 4°C.

- Save 15 µl of the supernatant as pre-IP sample for immunoblot analysis and store at -20°C.
- Transfer the supernatant to the tube containing the Ab-bound beads from step 8 (after removing the final wash buffer).
- Rotate the beads/lysate mix end over end at 4°C overnight.

Day 3rd

- Place the tubes in the magnetic rack and, once the beads are pulled on the side of the tube, save 15 µl of the supernatant as post-IP sample for immunoblot analysis and store at -20°C.
- Remove the supernatant and wash the beads two times with 1x PMPG, two times with 5x PMPG (High-salt Wash Buffer) and two times with 1x PNK buffer.

Dephosphorylation of Ago-bound RNA tags

- Remove the final wash buffer and add 80 µl of the following dephosphorylation mixture prepared in bulk for all the samples together. Incubate the samples in a Thermomixer at 20°C for 45 min agitating at 1,000 rpm.

Reagent	Volume (µl) per reaction	Final concentration
Water	54 µl	
Multi-core buffer, 10x	16 µl	
RNAsin	2 µl	1 U μL^{-1}
TSAP	8 µl	0.1 U μL^{-1}
Mix total volume	80 µl	

- Wash the beads one time with 1x PNK buffer, one time with 1x PNK+EGTA buffer and two times with 1x PNK buffer.

3'-end adapter ligations on beads

- Remove the final wash buffer and add 80 µl of the following ligation mixture prepared in bulk for all the samples together. Incubate the samples in a Thermomixer at 16°C overnight agitating at 1,000 rpm.

Reagent	Volume (µl) per reaction	Final concentration
Water	32.4 µl	
T4 RNA ligase buffer, 10x	8 µl	
PEG 8000, 25% (wt/vol)	32 µl	10 %
miRCat-33 3'-linker, 50µM	1.6 µl	1 µM
RNAsin	2 µl	1 U μl^{-1}
T4 RNA ligase 2, truncated, K227Q	4 µl	10 U μl^{-1}

Mix total volume	80 µl	

Day 4th

- Wash the beads one time with 1x PMPG, one time with 5x PMPG and two times with 1x PNK buffer.

Radioactive labeling of the 5'-end of RNA tags

- Remove the final wash buffer and add 80 µl of the following phosphorylation mixture prepared in bulk for all the samples together. Incubate the samples at 37°C for 30 min and flicker tubes regularly to ensure mixing.

Reagent	Volume (µl) per reaction	Final concentration
Water	66 µl	
PNK buffer, 10x	8 µl	
^{32}P-γ-ATP (3,000 Ci/mmol)	2 µl	
T4 PNK	4 µl	0.5 U µL^{-1}
Mix total volume	80 µl	

- Add 1 µl of cold 10 mM ATP to each tube and incubate the mixture for an additional 5 minutes at 37°C to ensure complete phosphorylation of RNA tags and therefore efficient 5' linker ligation, as the total concentration of ATP in ^{32}P-γ-ATP preparations is very low.
- Wash the beads one time with 1x PMPG, one time with 5x PMPG and three times with 1x PNK.

SDS-PAGE and nitrocellulose transfer

- After removing the final wash buffer, resuspend the beads in 20 µl of this mix: 15 µl of 1x PNK buffer + 15 µl of 4x LDS reducing sample buffer. Heat the samples for 10 min at 65°C.
- Flash-spin the beads and place the tubes in a magnetic rack in order to separate the protein eluate from beads. Load 20 µl of sample per well of a 10-well Novex NuPAGE 4-12 % Bis-Tris gel. If anything of each eluate is left, keep for immunoblot analysis and store at -20°C. Include in the run a pre-stained protein standard and load all the "empty" lanes with the loading buffer used for the samples.
- Run the gel using 1x NuPAGE MOPS SDS running buffer at 80 V in the cold room until the dye reaches the bottom of the gel.
- After the gel run, open the gel cassette and transfer the gel into a container with 2x NuPAGE transfer buffer supplemented with 10 % (vol/vol) methanol. Equilibrate gel for 10 min. Dip the nitrocellulose membrane in another container with 2xNuPAGE transfer buffer supplemented with 10 % (vol/vol) methanol.

- Transfer the gel to nitrocellulose membrane in a semi-dry apparatus at constant 90mA (should reach 5-10 V) for 1 hour and 40 min.
- After transfer, rinse the nitrocellulose membrane with RNase-free water and gently blot the edge on a Kimwipe.
- Heat-seal the nitrocellulose membrane in a clean plastic bag. Attach a phosphorescent ruler and at least two tiny phosphorescent sticker pieces, so that the membrane can be aligned with the respective signal on the film for accurate excision of the desired bands after exposure.
- Expose the nitrocellulose membrane to the autoradiography film at -80°C for 2 hours in an autoradiography cassette. Bands that give clear signal after 1-2 hours are ideal for subsequent RNA extraction step.

Day 5th

Extraction/Purification of RNA tags

- On a light table, carefully align the nitrocellulose membrane on top of the developed autoradiography film by using the signal from the phosphorescent ruler and sticker pieces. It is important to tape the film and the nitrocellulose membrane so that they cannot shift during excision.
- With a clean disposable scalpel each time, cut out the membrane area which corresponds to the desired band. For Ago2, excise the bands from two regions using the ladder: the region at ~110 kDa containing Ago2 loaded with miRNAs and the smear above the previous band at ~138 kDa containing Ago2-loaded with mRNAs and miRNAs.
- Transfer the nitrocellulose membrane piece to a clean surface (e.g. the inside of an RNase-free pipette tip box lid) with the tip of the scalpel. Carefully dice each excised band into 1- to 2- mm squares and then transfer these to a 1.5 mL microcentrifuge tube (DNA Lo Bind Tube).
- For each sample, prepare 200 µl of 4 mg/mL Proteinase K by diluting stock in 1x PK buffer. Pre-incubate this solution at 37°C for 20 min to degrade any present nucleases.
- Add 200 µl of Proteinase K solution to each tube containing nitrocellulose membrane pieces from step 36. Incubate at 37°C for 20 min agitating at 1,200 rpm in a Thermomixer.
- Add 200 µl of 1x PK/7 M Urea solution to each tube. Incubate at 37°C for 20 min agitating at 1,000 rpm in a Thermomixer.
- Add 200 µl of TRIzol (acid phenol) and 130 µl of chloroform:isoamyl alcohol (24:1) to the samples. Shake well for 15 sec to mix and agitate samples at 1,000 rpm for 20 min at 37°C in a Thermomixer.
- Centrifuge tubes at max-speed in a tabletop centrifuge (13.000 rpm/~16,000 g) for 10 min at RT to separate the phases. Immediately collect the aqueous (upper) phase and transfer it to a 1.5 mL microcentrifuge tube (DNA Lo Bind Tube).
- Add 40 µl of 3M sodium acetate pH 5.2 and 0.75 µl of GlycoBlue and vortex briefly to mix.
- Add 700 µl of ethanol:isopropanol (1:1) and precipitate RNA overnight at -20°C.

Day 6th

5' RNA adapter ligation

- Centrifuge extracted and precipitated RNA at max-speed in a tabletop centrifuge (13,000 rpm/~16,000 g) for 30 min at 4°C. Carefully discard the supernatant and wash the pellet by adding 750 µl of ice-cold 70 % (vol/vol) ethanol. Vortex briefly to mix and spin at max-speed for 5 min at RT.
- Remove the supernatant completely and air dry the pellets (no longer than 5 min) to evaporate the remaining ethanol.
- Resuspend each pellet in 15 µl of phosphorylation mixture prepared in bulk for all the samples together. Incubate the samples at 37°C for 30 min.

Reagent	Volume (µl) per reaction	Final concentration
Water	11 µl	
T4 RNA ligase buffer, 10x	1.5 µl	
ATP, 10 mM	1.5 µl	1mM
T4 PNK	1 µl	0.67 U μl^{-1}
Mix total volume	15 µl	

- Add 5 µl of 5' adapter (linker) ligation mixture, prepared for each sample separately as follows. Incubate the samples at 16°C overnight.

Reagent	Volume (µl) per reaction	Final concentration (volume = 20 µl)
Water	2 µl	
T4 RNA ligase buffer, 10x	0.5 µl	
ATP, 10 mM	0.5 µl	1 mM
Barcoded 5' adapter, 100 µM	1 µl	5 µM
T4 RNA ligase 1	1 µl	0.5 U μl^{-1}
Mix total volume	5 µl	

Day 7th

- Dilute samples with 380 µl of water and then add 300 µl of TRIzol (acid phenol) and 130 µL of chloroform:isoamyl alcohol (24:1).
- Shake well the samples for 15 sec and vortex them very briefly. Centrifuge the tubes at max-speed in a tabletop microcentrifuge (13,000 rpm/~16,000 g) for 5 min at RT to separate the phases.

- Immediately collect the aqueous (upper) phase and transfer it to a 1.5 mL microcentrifuge tube (DNA Lo Bind Tube).
- Add 40 µl of 3M sodium acetate pH 5.2 and 0.75 µl of GlycoBlue and vortex briefly to mix.
- Add 1 mL of ethanol:isopropanol (1:1) and precipitate RNA overnight at -20°C.

Day 8th

Reverse transcription

- Centrifuge extracted and precipitated RNA at max-speed in a tabletop centrifuge (13,000 rpm/~16,000 g) for 30 min at 4°C. Carefully discard the supernatant and wash the pellet by adding 750 µl of ice-cold 70 % (vol/vol) ethanol. Vortex briefly to mix and spin at max-speed for 5 min at RT.
- Resuspend each pellet in 13 µl of RT mix I prepared in bulk for all the samples together. Incubate the samples for 3 min at 80°C and then immediately place the samples on ice for 5 min.

Reagent	Volume (µl) per reaction	Final concentration (volume = 20 µl)
Water	11 µl	
dNTPs, 10 mM	1 µl	0.5 mM
miRCat-33 primer, 10µM	1 µl	0.5 µM
Mix total volume	13 µl	

- To each sample, add 6 µl of RT mix II prepared in bulk for all the samples together. Incubate the samples for 3 min at 50°C.

Reagent	Volume (µl) per reaction	Final concentration (volume = 20 µl)
First strand buffer, 5x	4 µl	
0.1 M DTT	1 µl	5 mM
RNAsin	1 µl	2 U μl^{-1}
Mix total volume	6 µl	

- Add 1 µl of Superscript III reverse transcriptase and incubate the samples for 60 min at 50°C.
- Incubate the samples for 15 min at 65°C to inactivate reverse transcriptase.
- Add 2 µL of RNase H to degrade template RNA and incubate samples for 30 min at 37°C. Prepared cDNA can be stored indefinitely at -20°C.

Hematoxylin and Eosin (H&E) Staining – Manual Protocol

From Baylor College of Medicine

Reagents for H&E staining:

- Acid Ethanol: 1 mL concentrated HCl + 400 mL 70 % ethanol
- Hematoxylin: Poly Scientific (Bayshore, NY) #s212A, Harris hematoxylin with glacial acetic acid
  Eosin: Poly Scientific (Bayshore, NY) #s176
- DPX Mountant for histology, 44581, Histological mounting medium, Sigma-Aldrich

Procedure

- Place slides containing paraffin sections in a slide holder (glass or metal)
- Deparaffinize and rehydrate sections:
- 3 x 3 min in Xylene (blot excess xylene before going into ethanol)
- 3 x 3 min in 100% ethanol
- 1 x 3 min in 95% ethanol
- 1 x 3 min in 80% ethanol
- 1 x 3 min in 50% ethanol
- 1 x 5 min in deionized H_2O
- While sections are in water, skim surface of hematoxylin with a Kimwipe to remove oxidized particles. Blot excess water from slide holder before going into hematoxylin.
- 30 seconds Hematoxylin
- Rinse with deionized water 1 x 5 minutes in tap water (to allow stain to develop)
- Dip 8-12x (fast) in Acid ethanol (to destain)
- Rinse 2 x 1 min with tap water
- Rinse 1 x 2 min with Deionized water (can leave overnight at this stage)
- Eosin staining and dehydration:
  - 30 sec Eosin (up to 45 sec for an older batch of eosin)
  - 3 x 5 min in 80% ethanol
  - 3 x 5 min in 95% ethanol
  - 3 x 5 min in 100% ethanol (blot excess ethanol before going into xylene)
  - 3 x 15 min in Xylene
- Coverslip slides using DPX (xylene based)
- Place a drop of DPX onto the coverslips.
- Angle the coverslip and let fall gently onto the slide.
- Allow the Permount to spread beneath the coverslip, covering all the tissue.
- Dry overnight in the hood.

Chromosome measurements

Chromosome preparations were obtained from logarithmically growing HCT116 cell cultures after been exposed to Colcemid (0,1μg/ml) (Gibco, Grand Island, USA) for 1 to 3 hours, at 37^{o}C in 5% CO2. Cells were harvested by trypsinization (Gibco, Grand Island, USA), exposed in hypotonic solution (5 ml of 0.075 M KCl, Sigma) (20 minutes incubation) and fixed [3x methanol (Applichem GmbH, Darmstadt, Germany)/1x CH3COOH (Merck, Darmstadt, Germany)] with sequential centrifugations and supernatant removals.

For karyotypic analysis (Raftopoulou et al., 2020), we applied inverted DAPI banding: slides were stained and mounted with 0.6 μg/ml DAPI in Vectashield antifade medium (Vector Laboratories, USA). Cytogenetic analyses were performed using a 63x magnification lens on a fluorescent Axio-Imager Z1, Zeiss microscope, equipped with a MetaSystems charge-coupled device (CCD) camera, and the MetaSystems Isis software (MetaSystems GmbH, Germany). Karyotypes were recorded according to International System for Human Cytogenetic Nomenclature (ISCN) 2016. Micronuclei analysis was performed in cytologic preparations treated as above and stained by DAPI.

Microscopy

Images were acquired with a Leica TCS SP5 inverted confocal laser scanning microscope (CLSM), using Leica HC PLAPO 63x1.4NA CS immersion objectives. Acquisition was performed sequentially to avoid cross-talk. Time-lapse videos were started 18h post-transfection at 30 sec or 1 min time-lapse intervals for 45 min.

For Transmission Electron Microscopy (TEM) the cells were cultured in 35mm CellStar cell-culture dishes (Greiner Bio-One, GmbH, Germany), on a clarfilm, for 24-48 hours, under standard conditions, fixed in 2,5 % glutaraldehyde (in 0.1 M phosphate buffer) and post-fixed with 1 % osmium tetroxide. Next, samples were dehydrated via a graded series of ethanol concentrations, 30, 50, 70, 90 and 100 %, followed by propylene-oxide (PO) treatment. They were further processed in a mixture of Epon/Araldite resins diluted in PO, flat-embedded in fresh epoxy-resin mixture and allowed to polymerize at 60^{o}C for 24 hours. Small epoxy pieces were peeled away from petri-dishes, glued on epoxy blocks and allowed to polymerize for 24 hours. Ultra-thin sections of 65-70 nm (Leica EM UC7 Ultra-microtome, Leica Microsystems, Austria) were mounted onto 200 mesh nickel grids, stained with uranyl acetate and lead citrate, examined with a Philips 420 transmission electron microscope at an acceleration voltage of 60 kV and photographed with a MegaView G2CCD camera (Olympus SIS, Germany). Immunogold experiment has been also done according to the manufacturer's protocol.

Scanning Electron Microscopy (SEM) was performed with a Jeol 6380LV electron microscope (JEOL Ltd., USA) which was operated at 15 kV and was equipped with an Oxford EDS system for chemical analysis. The XRD patterns were recorded by means of a Siemens D5005 (Bruker AXS, USA) using Cu K radiation. For the evaluation of the surface structural configuration, NTHY ori 3-1 cells were prepared and cleansed with ethanol. For the electron microscopy imaging and analysis, cells were attached on aluminum stubs and were analyzed in a low-vacuum mode (around 30 Pa) to minimize cell stress due to the progressive lack of humidity of the samples during the process in instrument's vacuum chamber, as well as to eliminate charging effects after the cells have dried.

Details for the Materials, reagents, drug compounds and antibodies (primary and secondary) used in the described Methodology are presented in Table 3.

Protrusion measurements

The number and length of filopodial protrusions were measured in 102 cells from CLSM fluorescence images (3 independent biological experiments) using the FiloDetect algorithm. The algorithm is implemented in Matlab and was suitably modified so that filopodia shape could also be modeled. A filopodium's midpoint width was defined as the number of pixels occupied on the minor axis of the ellipse created by Matlab's "regionprops" function. The corresponding numbers for parallel translations of the minor axis for a distance equal to 2/3 of half the major axis towards both ends of the major axis were also evaluated. Between these two points the one at greater distance from the cell's centroid (also identified using "regionprops") was defined to be the filopodium tip width. The shape model was obtained by evaluating the average tip-to-midpoint width ratio among all filopodia detected in the cells measured. The same procedure was followed for the calculation of the corresponding quantities for AGO2 protrusions in 66 cells. Since this type of protrusion is unique per cell no averages were required. The AGO2 protrusion of each cell along with other protrusion-like structures were automatically identified using Matlab's "fibermetric" function. To isolate the real AGO2 protrusion among them, a region of interest was manually cropped around it and superimposed with the "fibermetric" image.

Image analysis

3D surface reconstruction was implemented using Imaris 9.1.2 (Bitplane, South Windsor, CT, USA). Images used for colocalization analysis were acquired with Nyquist sampling; the Richardson-Lucy Total Variation (RLTV) algorithm was selected from DeconvolutionLab2 plugin for image deconvolution. Theoretical PSFs according to the Born & Wolf 3D Optical Model were constructed from the PSF Generator plugin (Kirshner et al., 2013). Different channels were processed independently. Further preprocessing consisted of background subtraction (3D rolling ball algorithm (Sternberg, 1983)) and thresholding (triangle method (Zack et al., 1977)) all run in Fiji (Schindelin et al., 2012). The Pearson Correlation Coefficient (R), and Manders' coefficients (M1, M2) were used to quantify colocalization. R measures the correlation between probes while M1 and M2 are measures of co-occurrence; M1 captures the proportion of above-threshold pixels in the red channel occupying above-threshold pixels of the green channel, and vice versa for M2. Controls for specificity of primary and secondary antibodies, autofluorescence, specificity of PLA interaction foci, colocalization analysis, biological colocalization negative control and negative control (scramble) of siAGO2 are provided.

Statistics of AGO2 and Actin-filopodial protrusions

One-tailed Student's t-test (McDonald & Dunn, 2013) was used to evaluate the significance of Pearson (R) and Manders' values. The sample size for each test was n=6 fluorescence images and the α-level were set to 0.01. Mann-Whitney U-tests (two-sided) were used to compare the differences obtained in the lengths and ratios between Actin-filopodial and AGO2 protrusions. Although filopodial protrusions are log-normally distributed, a non-parametric test was chosen since q-q plot and Shapiro test did not reveal a similar distribution for AGO2 protrusions. Actin filopodial protrusions were measured on 102 cells (at least n=3 biologically independent experiments, statistical sample size

n=3849 Actin filopodial protrusions) while AGO2 protrusions on 66 cells (n=5 biologically independent experiments, statistical sample size n=66 AGO2 protrusions). The α-level was set at 0.01 for both tests. z-test was employed to test the proportion of non-lagging chromosomes (n1=176 GFP cells, n2=169 AGO2-GFP cells), micronuclei formation (n1=174 GFP cells, n2=168 AGO2-GFP cells) and chromosomal deregulation (n1=188 GFP cells, n2=182 AGO2-GFP cells) in GFP/AGO2-GFP assays.

The same procedure was employed to test the proportion of micronuclei formation (n1=117 SCR cells, n2=117 siAGO2 cells), and chromosomal deregulation (n1=103 SCR cells, n2=114 siAGO2 cells) in SCR/siAGO2 knocked down cells. For the analyses 3 biologically independent experiments were conducted. The use of z-test was justified based on the expected frequencies that occurred in all our measurements (Cochran, 1952, 1954). The α-level was set at 0.01.

Statistics for gene expression, growth and migration data

Differences among time points (e.g. wound healing) were analyzed using one-way analysis of variance (ANOVA). Gene expression data were square-root transformed to meet the assumptions of normality and/or homogeneity. Morphometric and Q-PCR results are expressed as means ± standard error of the mean (SEM). Morphometric data failed to fit Kolmogorov–Smirnov test for normality and were analyzed using a non-parametric Kruskal–Wallis ANOVA median test. When a significant difference was observed, further statistical analysis was performed by post-hoc non-parametric Dunn's test in order to determine the influence of age on larvae development. The frequency distribution of <5 μm diameter of white muscle fibers was evaluated with Pearson's chi-squared test, pearman's rank correlation was run in order to assess the statistical dependence between two variables. For all statistical tests, differences were considered to be significant from a value of $P<0.05$. Data were analysed using the SigmaStat software (version 3.5; STATCON) and R studio (version 3.6.1; R studio, Boston).

RNA-seq

RNAseq experiments were carried out in the Greek Genome Center (GGC) of the Biomedical Research Foundation of the Academy of Athens (BRFAA). RNAseq libraries were prepared with the illumina TruSeq RNA v2 kit using 1 μg of total RNA. Libraries were checked with the Agilent bioanalyzer DNA1000 chip, quantitated with the qubit HS spectrophotometric method and pooled in equimolar amounts for Sequencing. 100 bp Single-End reads were generated with the illumina NovaSeq sequencer.

RNA-Seq analysis workflow

Quality Control (QC)

For the quality control of RNA-Seq raw reads, FASTQC software was used in order for bases with low quality to be removed to improve Mapp ability. QCl of raw reads also included the analysis of read alignment (read uniformity and GC content), quantification (3' bias, biotypes, and low-counts), and reproducibility (correlation, principal component analysis, and batch effects).

Preprocessing

Trimming of the adapters achieved by using Cutadapt 3.2.

Alignment

Mapping to the mouse genome (GRCm38 - mm10) performed by using STAR 2.7.0a aligner.

The percentage of sequencing reads that were uniquely mapped to the reference genome on average was 89.5 %.

Quantification

In order to count the reads that were aligned to genes, HTSeq 0.13.5. software was used.

Differential Expression

DESeq2 package in R, was used to compare *gene expression* differences in samples between miR26-mimic and scramble samples and conclude to the most statistically significant up-regulated and down-regulated genes.

In vivo studies – Generation of xenografts

NOD.CB17-*Prkdc* ^{scid}/J (SCID) immunodeficient mice (The Jackson Laboratory, Maine, USA) were used for thyroid cancer xenografts establishment. Mice were subcutaneously inoculated with ~$2*10^5$ and $5*10^5$ cells per injection, NTHY ori 3-1, TPC1 or FTC133, and closely followed till the development of tumors. The size of each tumor was carefully monitored and its size was determined by caliper measurement. For disease progression studies, mice experiments were performed as described above, injecting FTC133 cells, FTC133 with mimic-miR26 or FTC133 with scramble sequences. For the welfare of the animals, they were euthanized when the tumors were large and were further analyzed by imaging assays. Animals were treated according to Greek laws (2015/92), guidelines of European Union and European Council (86/609 and ETS123, respectively), and in compliance with standards for human care and use of laboratory animals (NIH, USA, assurance no. A5736-01).

RESULTS

CHAPTER 1

The incidence of thyroid cancer has increased dramatically during the three past decades and it is now the fastest growing cancer in women and one of the most prevalent endocrine malignancy. The reason for this rise is unclear, although there is an increase in imaging studies of the neck where small, thyroid nodules are discovered before they become apparent on physical exam. To better understand the thyroid cancer and to unravel the molecular mechanisms underlying this pathophysiology, we characterized a Greek cohort and a TCGA large PTC cohort and examined the most aggressive thyroid cancer subtypes with poor outcome and their clinicopathological features. Finally, we aimed to link these features with gene expression and molecular pathways.

Generation of Database

A database was generated based on surgically removed specimen-records of Dr Sofia Tseleni-Balafouta, Professor of Pathological Anatomy at the Medical School of National and Kapodistrian University. We selected 704 cases distributes almost equally among twelve consecutive years (2001-2012). 470 histological specimen records were randomly selected while an additional 234 were selected based on a specific reference criterion for tumor micro-staging. The latter was necessary as some phenotypic features, such as the presence of tall cell variants (TCV) or pseudoinclusions, are presented in small numbers in the general population and therefore, it is impossible to carefully and conclusively study them. The records included histological reports and were accompanied by paraffin embedded surgically removed tissue and the consent of the individuals involved. The histological reports included information regarding the pathophysiology, the year of surgery, the patient's age at the year of surgical removal, the gender, the existence of benign nodules or malignancies. In case of malignancy, the subtypes of cancer, the focality, thyroid weight, tumor size, the presence of extra-thyroid extension, the presence of metastasis/infiltration, additional unique information of each sample, such as staining and other important histological characteristics (Grave’s or Hashimoto), the presence of tall cells, the occurrence of grooves or pseudo-inclusions and psammoma bodies were reported. All the above-mentioned information was used to generate a database, called "Lab_App" (Fig. 34). The existence of the database facilitated the meta-analysis of the collected features as it allows to perform multifactorial studies, easily calculate the number of samples having aone, two or more specific characteristics, highlight interrelated properties and identify new trends that can be linked to clinical behavior such as tumor aggressiveness.

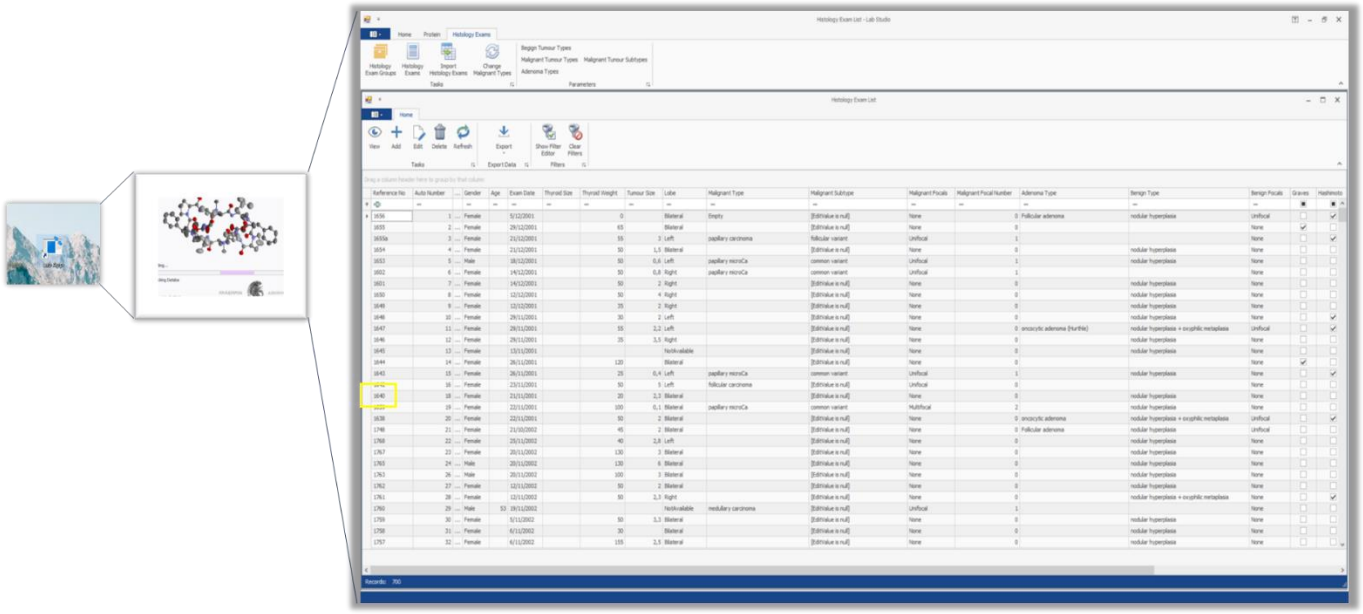

Figure 34 Preview of the Lab_app interface.

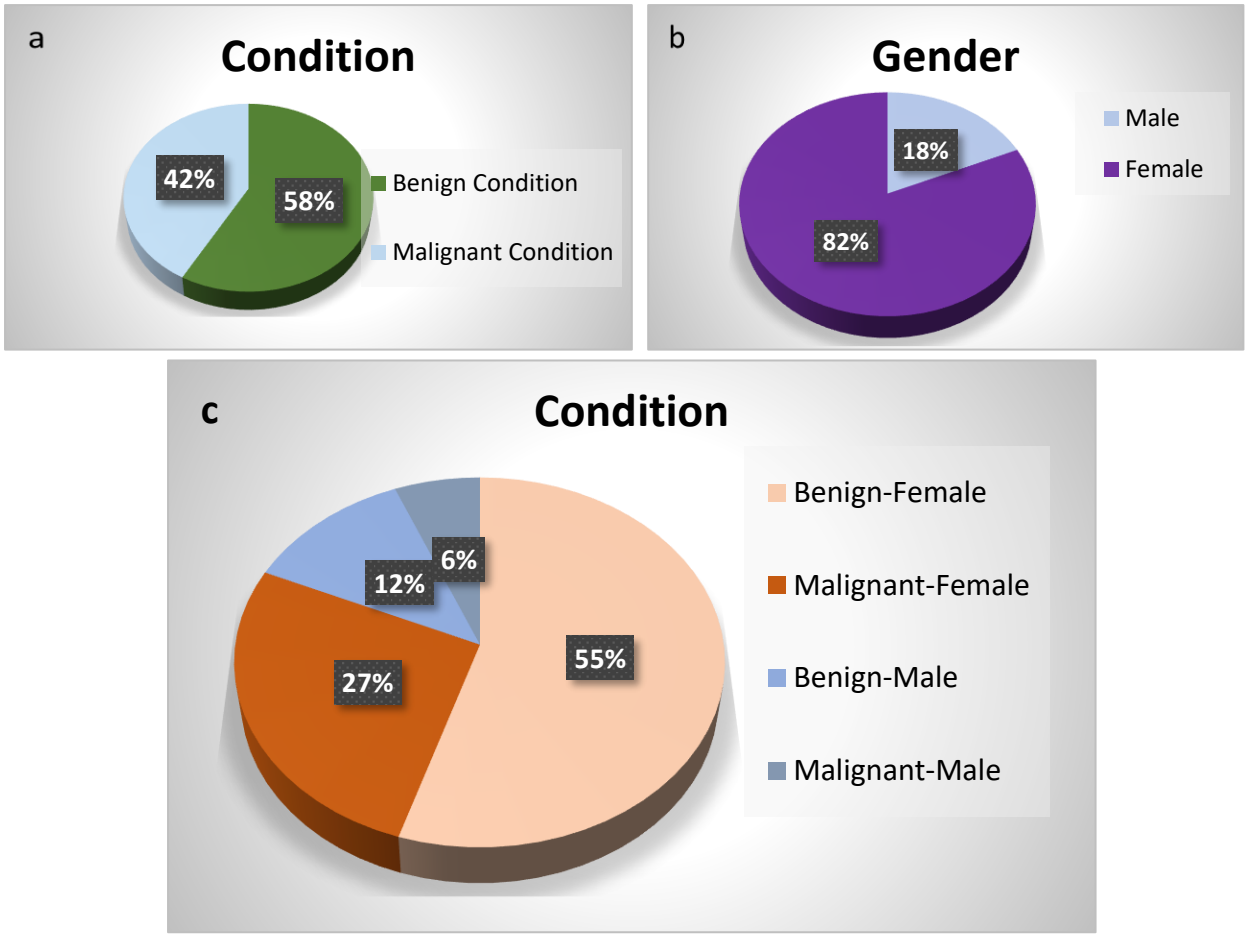

Figure 35 Population data regarding the presence of absence of Malignancy, gender and Gender in conjunction with the presence of Malignancy. Percentages of a) benign and malignant condition, b) genders (male-female) and c) genders (male-female) in conjunction with benign and malignant condition.

Focusing on the 470 histological specimen records that were randomly selected, ~42% of the surgically removed samples were malignant while the rest 58% were benign (Figure 35a). The vast majority of the patients (~4/5) were females (Figure 35b), a fact that is not surprising as it is according to the existing literature. The gender ratio is unchanged in the malignant or benign population (Figure 35c) indicating that there is no gender-predisposition related to malignancy. In accordance, the gender distribution upon the presence of Hashimoto autoimmune thyroiditis followed the above ratios regardless the presence or absence of malignancy (Figure 36).

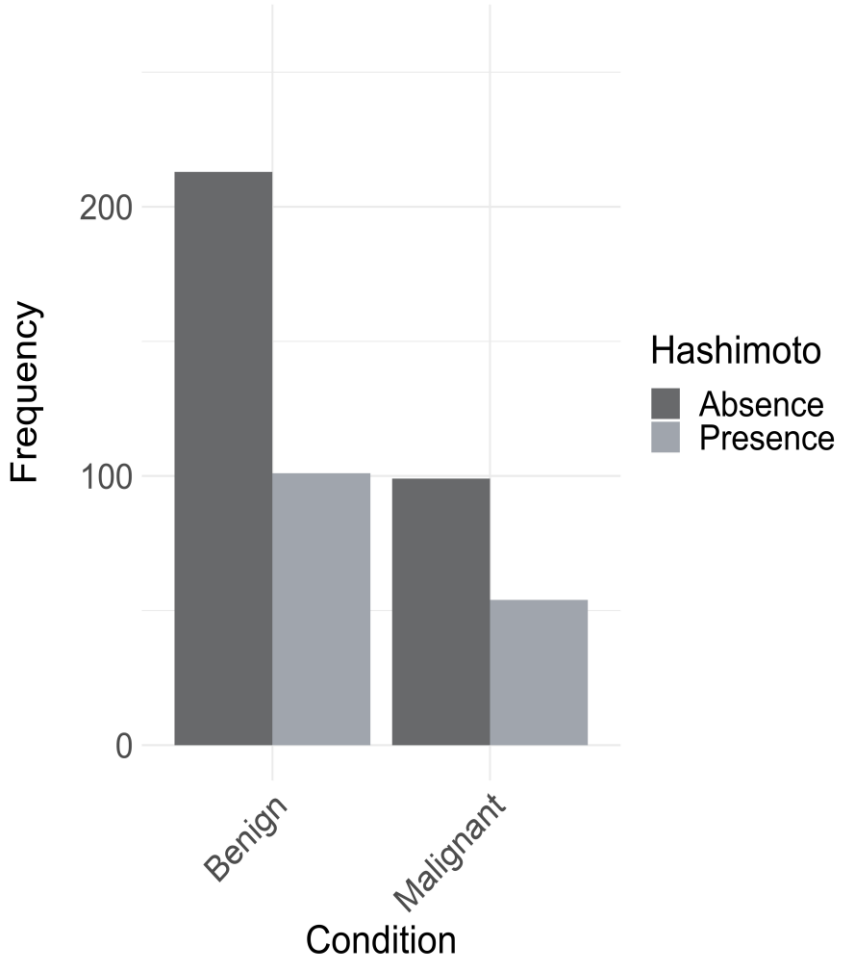

Figure 36 Distribution of Hashimoto thyroiditis background in benign conditions and malignancies in the Greek cohort.

Surprisingly, Hashimoto was present in the same percentage (1/3) in almost half of malignant and non-malignant cases, in our cohort (Figure 36). This does not necessarily indicate that Hashimoto has no implication in cancer formation as our cohort is biased containing surgically removed specimens. Further investigation needs to be conducted, based on long-term follow-ups of Hashimoto patients, to conclusively determine the role of autoimmune thyroiditis in cancer causality.

Interestingly, the presence of malignancy in our cohort appeared to be earlier that of the SEER stat of U.S.A. The Greek cohort study demonstrates that the age decades of onset are 20-44 and less prevailing age decades 65-74, 75-84 while SEER stat of U.S.A recorded as the main age decades of onset the periods between 45-64 (Figure 37). Our cohort distribution uncovered a much earlier onset probably demonstrating the early intervention regarding thyroid pathologies in our country. This is in

accordance with the finding that the surgically removed tumors have usually small sizes, as 76% is <1,9 cm (Figure 38), reflecting the early intervention as well as the public awareness for thyroid cancer, in recent years.

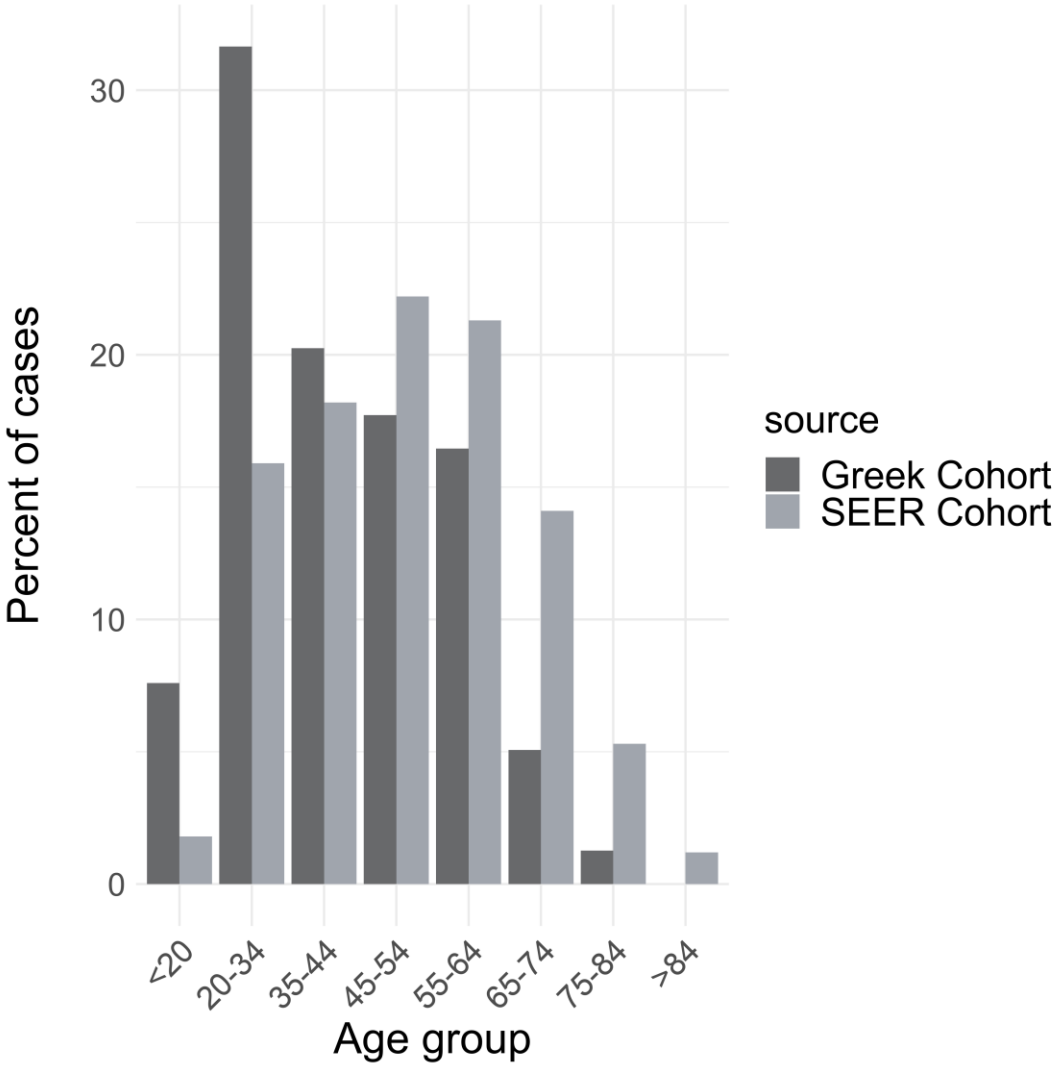

Figure 37 Compared distribution of thyroid cancer in patients of Greek and U.S.A. cohort by age decade groups.

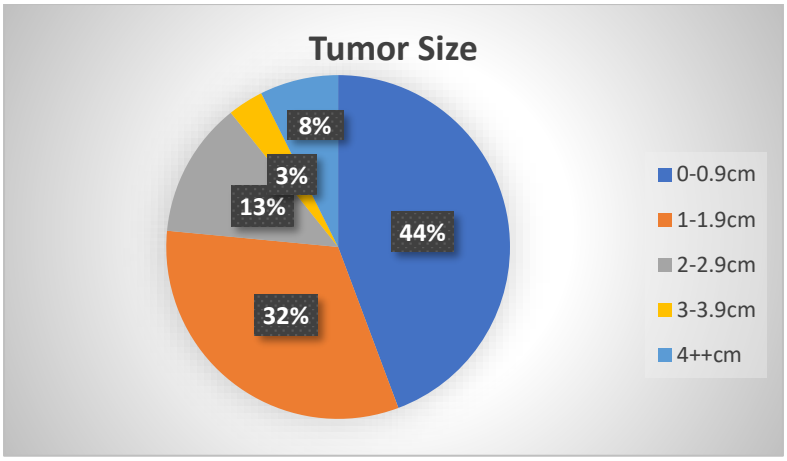

Figure 38 Distribution of thyroid cancer patients in the Greek cohort by tumor size groups.

155 individuals of the 470 participants in our cohort were diagnosed with thyroid cancer. The distribution of subtypes of thyroid cancer in this subgroup is similar to the one in other European countries as presented in the bibliography. As expected, the predominant type is PTC (46,65%) (Figure 39).

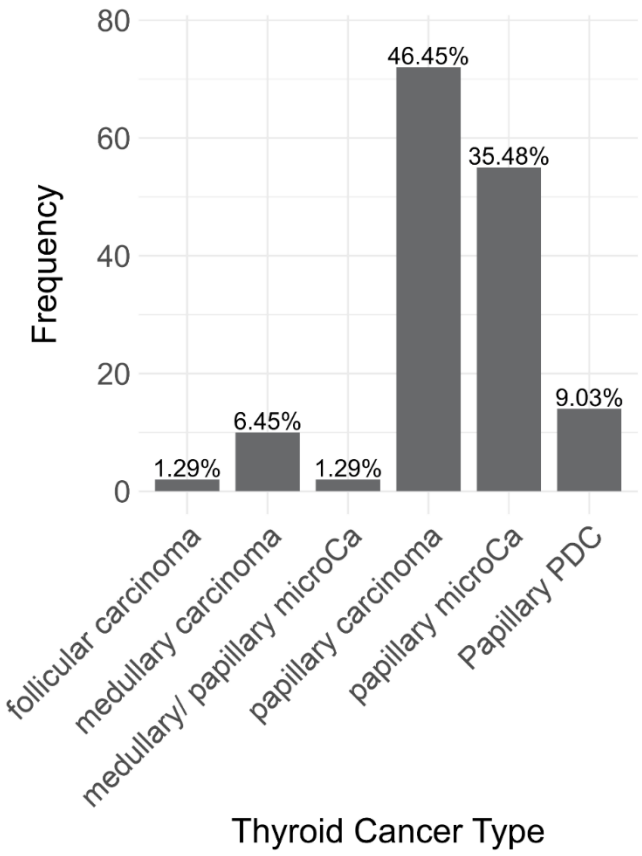

Figure 39 Distribution of thyroid cancer patients in the Greek cohort.

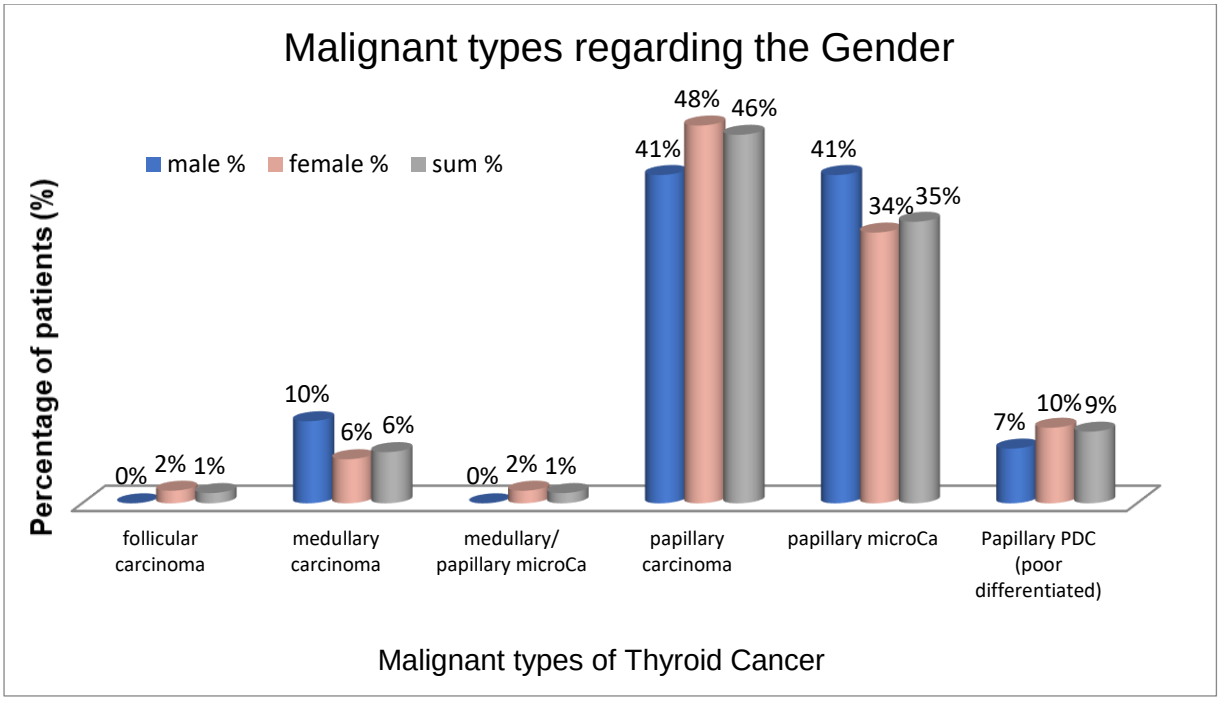

Figure 40 Distribution of patients with malignant subtypes between gender in the Greek cohort.

Microcarcinomas (microPTC) were considered as a separate category, even in the case of a papillary origin, as they seem to have different clinical and pathological characteristics. Although microPTC are not recognized as a specific entity in the tumor mass, they are considered as a subset of PTC, exhibiting a more benign behavior. microPTC usually follow an indolent course and carry an excellent prognosis. Distant metastases and mortality rates of these tumors are reported to be <0.5% for microPTC(Roti et al., 2008). Their percentage is increasing in recent years, probably due to fairly early diagnosis along with other environmental aggravating factors, such as Chernobyl emissions. PDC, the most aggressive type of thyroid cancer in our cohort is present in a smaller percentage, 9,03% (Figure 39). Notably, in microPTC and in MTC, an interesting slight increase in male percentages was observed (Figure 40). The latter needs further validation and investigation.

Investigating the correlation between malignancy and thyroid gland weight, we found a high rate of carcinomas in the lighter thyroid glands, while the presence of thyroid cancer in heavy thyroid glands were extremely rare (Figure 41a). In conclusion, ~75% of the cancer participants in our cohort exhibit thyroid gland weight under ~30 grammars which is closed to normal-weight of the thyroid gland. This is in agreement with the fact that thyroid cancer is a 'few hit' cancer. The benign nodules are present in more heavy thyroid glands and this is not surprising due to thyroid inflammation, swelling, hyperplastic masses and goiter (data not shown). An interesting observation is that PDC were present in heavier glands when compared to PTC and the latter have a more intense tendency to be developed in heavier glands than microPTC. Also, MTC are slightly shifted and they present an increase in ~60 grammar-thyroid glands (Figure 41b). However, focality seems not to affect the patient's distribution across the different ranges of thyroid weight besides an increase in the presence of multifocal tumors in ~100 grammar-thyroid glands (Figure 41c).

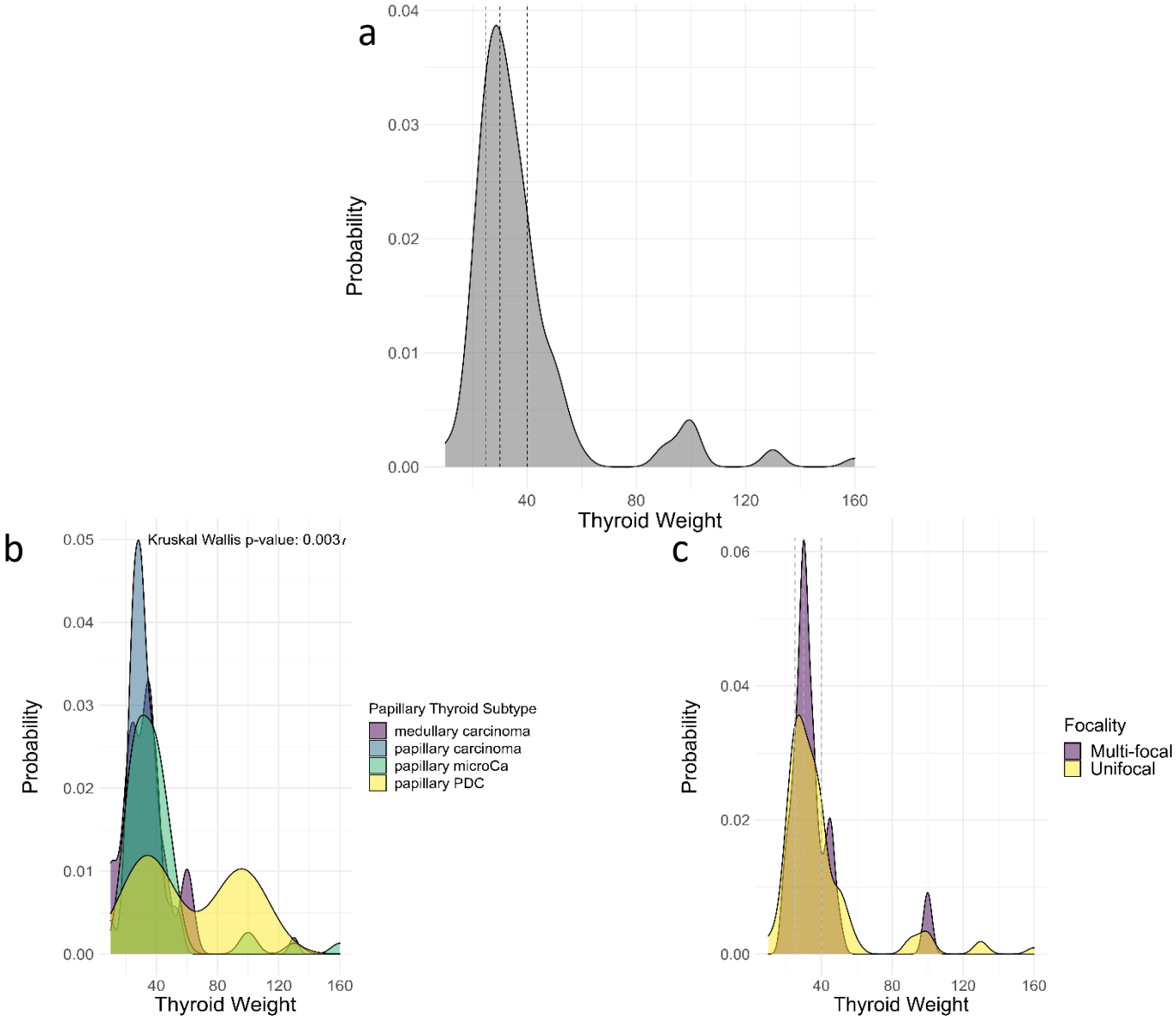

Figure 41 (a) Distribution of thyroid weight of all malignancies. (b) Distribution of thyroid weight in the different types of thyroid cancer, p-value=0,0037, (c) Distribution of thyroid weight between malignant focals (unifocal or multifocal carcinoma). Dust lines are at 25, 50, 75% quantized regions.

Then, a possible correlation between thyroid carcinoma and the lobe preference was studied and the right lobe was found to have a higher frequency in malignancies (45.58% the right lobe when compared to 34.69% of the left accordingly, Figure 42a). The frequency of the right lobe preference in TCVs (Figure 42d) continues to be responded. When we tested the TCV-enriched group the difference has been strikingly increased (Figure 42e). Statistically significant difference was observed between two lobes in the cohort of malignancies. The differences, present in the groups of microPTC and TCVs reached the statistical significance (Figure 42c,e). The cancer preference of the one organ side is not a new finding in general, since Right-sided colorectal cancer (RCRC) patients were found to respond in different therapies compared to those with left-sided carcinoma (Baran et al., 2018). Therefore, this evidence may have a prognostic value.

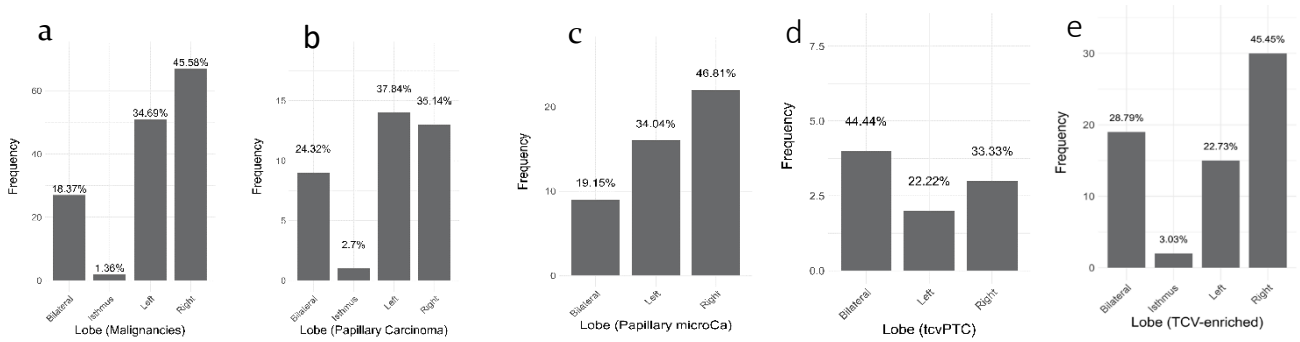

Figure 42 Lobe preference between left and right lobe in (a) malignancies p-value=0.00026 (b) in cPTC (p-value=0.558), (c) in PTC microCa p-value=0.06, (d) in TCVs in the randomly selected Greek cohort p-value=0.71 and (e) in TCVs from the TCV-enriched group of a Greek cohort (p-value= 0.059).

After the population study of the location of the tumorigenesis, we further pursue the investigation of the representation of each thyroid cancer subtype in the Greek cohort. Focusing on the PTC subtypes, the most predominant ones are the common variant (52.78%), followed by follicular variants (26.39%) and TCVs (11.11%) (Figure 43). Then, we focused on TCVs, probably the most aggressive subtype of PTC and we investigated the micro-staging of the tumors analyzing specific histological features.

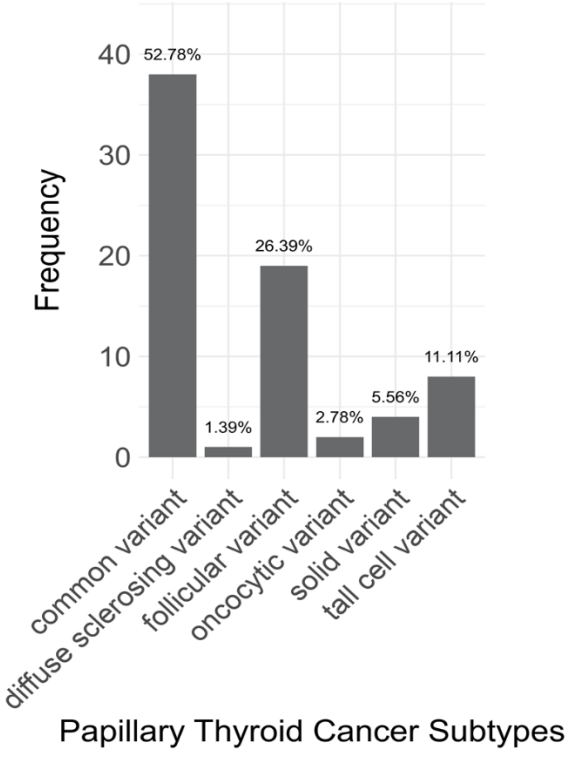

Figure 43 Distribution of different variants of PTC in the Greek cohort.

More specifically, we examined the thyroid capsule invasion and extra-thyroidal extension which reflects the aggressiveness of the tumor mass. We found that there are statistically significant differences between thyroid capsule invasion in the General Greek cohort (Figure 44a) when compared with the TCV-enriched cohort (Figure 44b) (p-value=$2{,}92*10^{-9}$) enhancing the idea of a highly metastatic potential of TCV cancers.

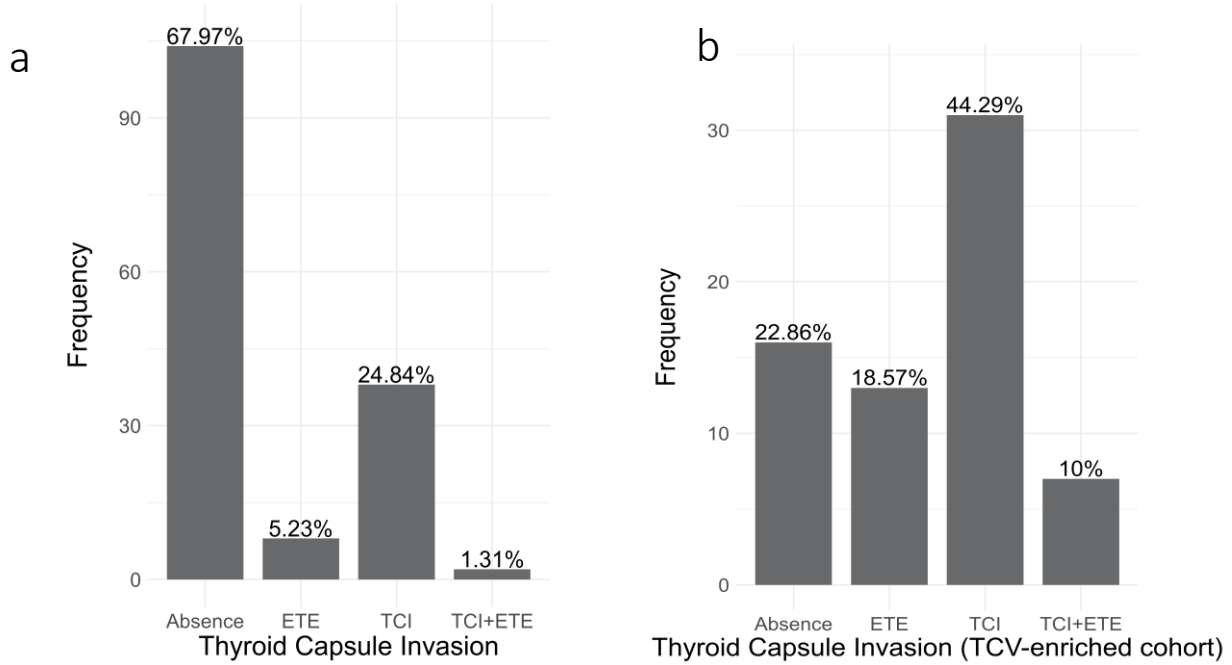

Figure 44 Thyroid capsule invasion (a) in thyroid malignancies in randomly selected samples of the Greek cohort and (b) in TCVs of TCV-enriched Greek group. Absence of Invasion, Extrathyroidal Extension (ETE), Thyroid Capsule Invasion (TCI), simultaneous Thyroid Capsule Invasion with Extrathyroidal Extension (TCI+ETE) (Bars from left to right).

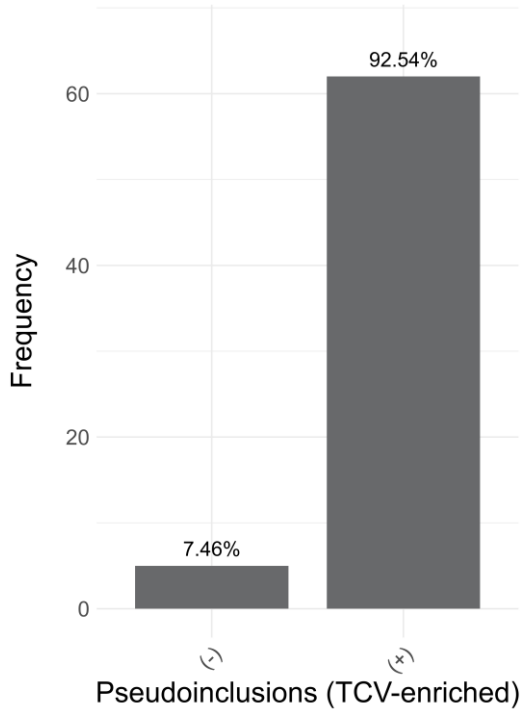

Figure 45 Presence of pseudoinclusions in PTC variants (left) and in TCV-enriched group (right) in the Greek cohort.

Interestingly, TCV specimens exhibit high number of cells with nuclear alterations called pseudoinclusions. These structures appear in more than 90% of the TCV cases, which is a striking percentage when compared to that observed in other PTC subtypes such as common, follicular and

solid variant (Figure 45). This fact probably indicates the link of the pseudoinclusions with the aggressive subtypes of cancer.

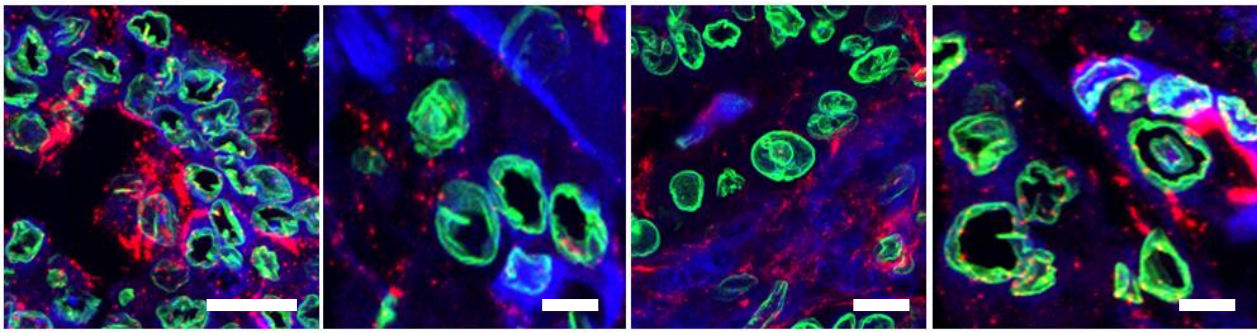

Figure 46 Representative immunofluorescence images depicting invaginations and pseudoinclusions, lamina A/C in green, nuclei in blue and actin in red.

These structures appear to involve cytoskeletal rearrangement and remodeling. Therefore, to further characterize them, we investigated the distribution of cytoskeletal molecules such as actin in histological specimens with pseudoinclusions. We initially performed colocalization experiments (CLSM) of actin, using aslo Lamin A/C to indicate nuclear membrane boundaries (Figure 46). 3D reconstruction models were created by Imaris in order to unravel the subnuclear location of the cavity of pseudoinclusions and the diaphragm's formation (Figure 47).

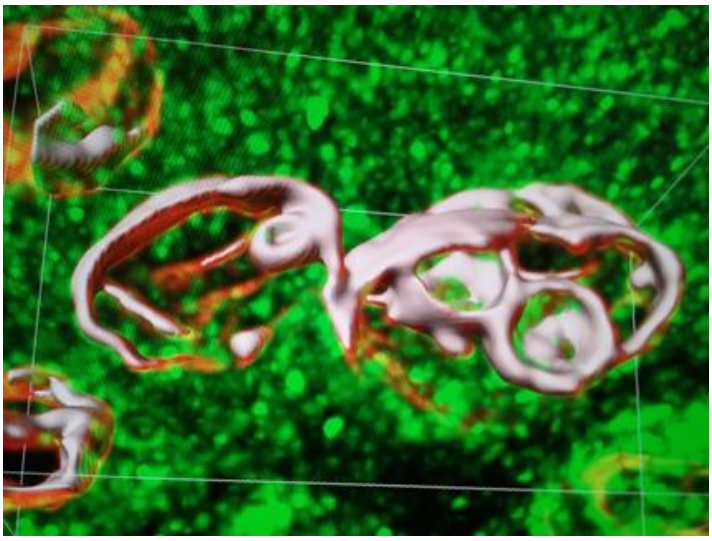

Figure 47 3D reconstruction models of pseudoinclusions.

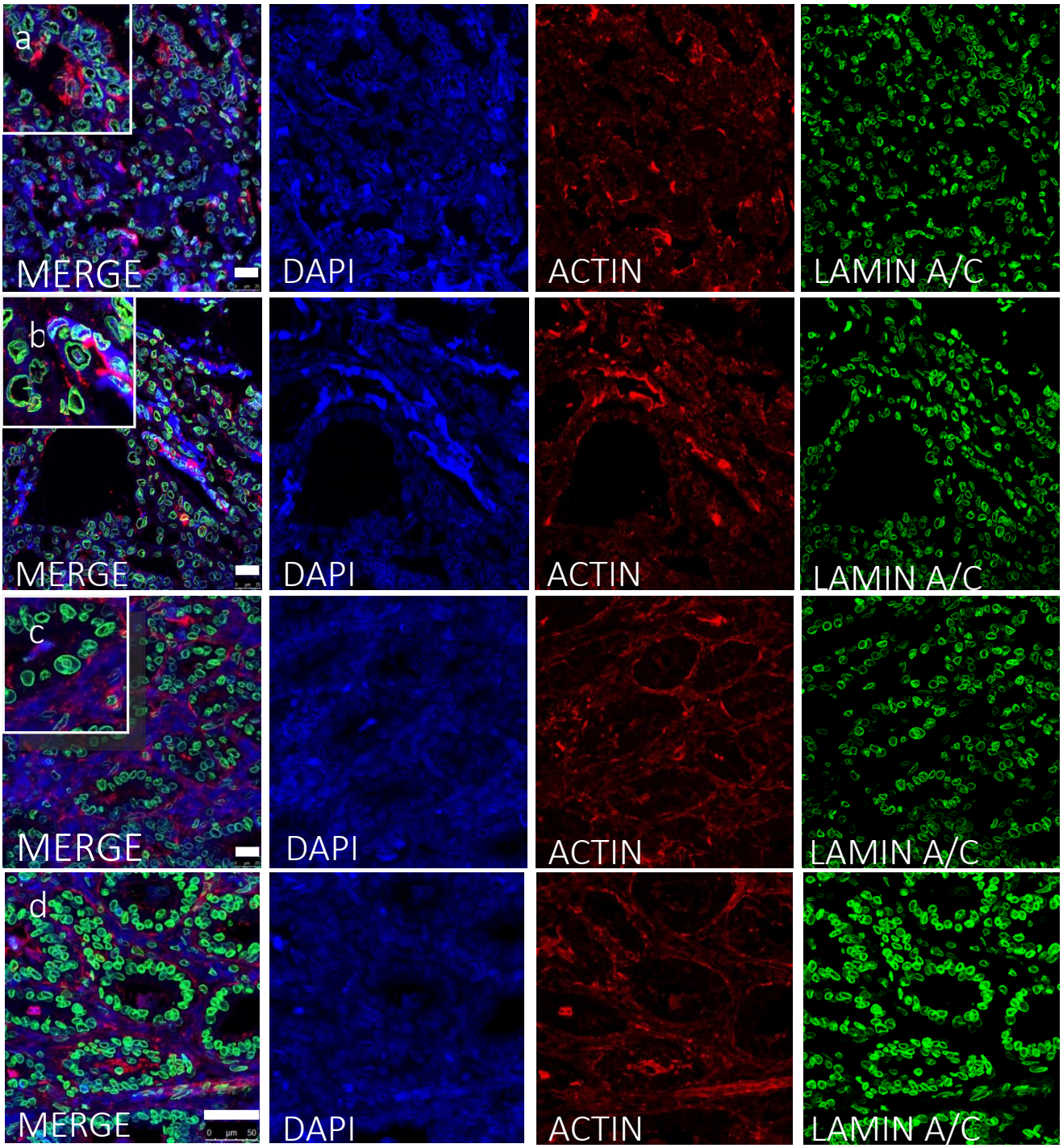

Figure 48 Representative image of cancer (a,b,c) and adjacent normal (d) tissue sections from individuals having TCV papillary variant. Nuclei stained by DAPI (blue), actin in red and lamin a/c in green. Magnification, 63x. In focused images are illustrated a nucleus with intense invaginations and grooves (a) and nuclei with pseudoinclusions (b,c) Scale bar:50μm.

The number of pseudoinclusions that co-exist within the nucleus varies usually from one to three or more in rare cases (Figure 48 b,c). The size of these structures can fluctuate from extremely small to significantly large (Figure 48 b,c). Additionally, to pseudoinclusions, other nuclear irregularities were observed such as grooves, creases and invaginations (Figure 48a). Actin was inside these structures in most cases and had intense signal in the well-organized follicles as well as the cancer areas (Figure

48b,c). Also, the pseudoinclusions were usually found in fibrotic areas (Figure 48c) and their functional role remains to be elucidated.

RNAi components in pseudoinclusions of thyroid cancer tissue

Interestingly, given that the pseudoinclusions are formed through cytoskeletal remodeling processes and the latter are under the tight regulation of gene expression, pseudoinclusions were tested regarding the subcellular and subnuclear distribution of RISC complex and microRNA biogenesis components. Drosha, DGCR8, microprocessor complex components, Dicer and AGO2, miRISC complex components act as key regulators of post-transcriptional events. We examined tissue specimens from 7 patients that their histological reports indicated the presence of a plethora of pseudoinclusions. The images of three representative ones are exhibited below (Figure 49-52).

Drosha was observed inside the nucleus, concentrated in specific areas inside the pseudoinclusions or in the nuclear matrix, into the cytoplasm (Figure 49) and in some cases, in the apical zone of the follicular cells (Figure 49c). DGCR8 had a dispersed punctuate pattern into the nucleus, around the nucleus and into the cytoplasm. We observed intense signal across intercellular bridges between cells (Figure 50). It seems that AGO2 and Dicer present an accumulated signal inside the pseudoinclusions compared to the rest nuclear area (very low signal) (Figure 51,52). Also, AGO2 and Dicer distributed across the invaginations of the nucleus and across the grooves (Figure 51,52). Into the cytoplasm, AGO2 and Dicer had similar distribution and visual signal intensity with those into the pseudoinclusions (Figure 51,52,53).

AGO2 seems to follow the nuclear membrane irregularities. In some cases, AGO2 accumulates in specific subregion of the nucleus probably constituting an initial cue for cytoskeletal remodeling leading to pseudoinclusion formation (Figure 53).

.

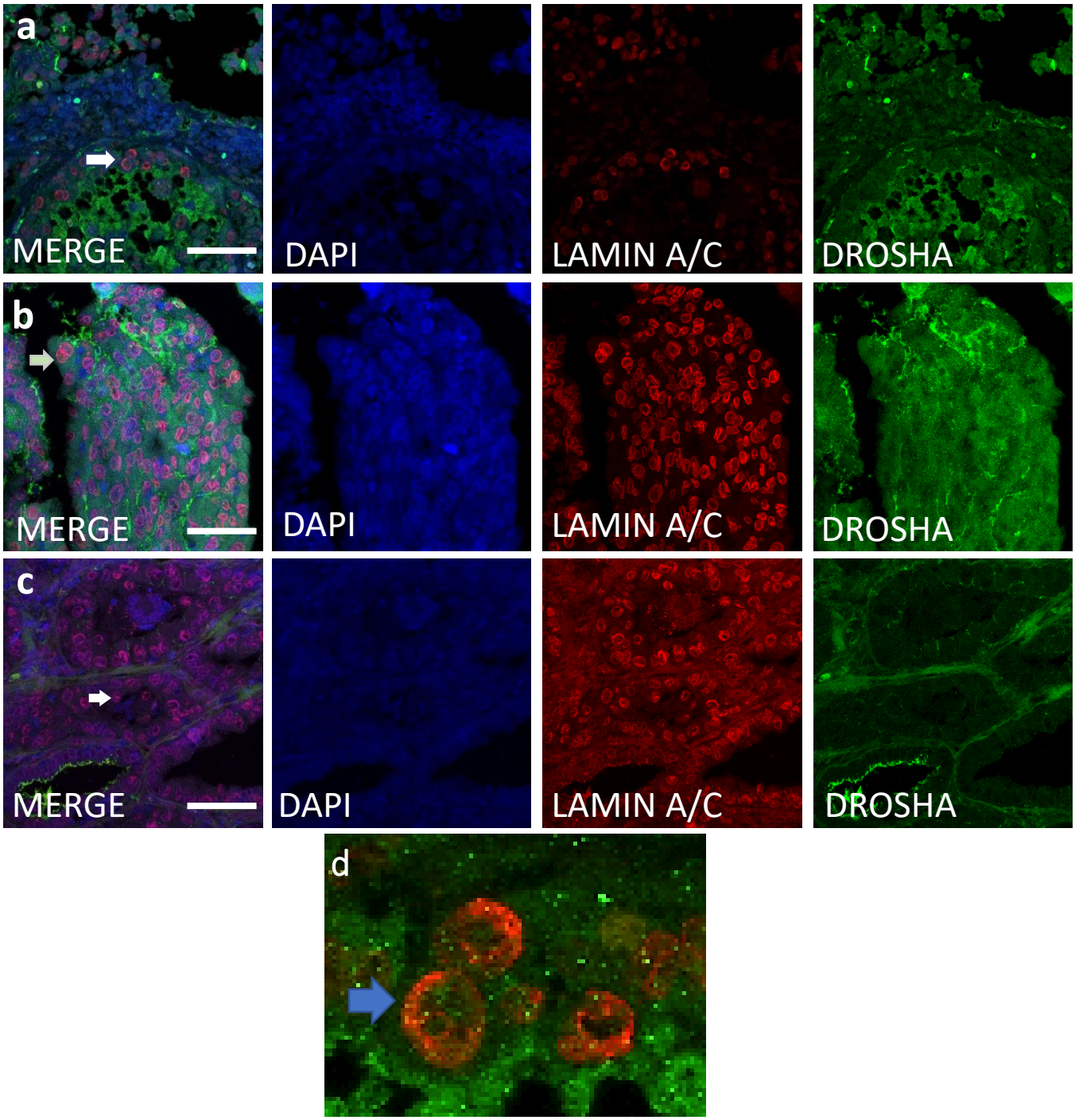

Figure 49 Representative images of tissue sections from TCV samples. Nuclei stained by DAPI (blue), Lamin A/C in red, DROSHA in green. Magnification, 63x. d) Zoomed image of pseudoinclusions (blue arrow) with Lamin A/C in red and DROSHA in green.

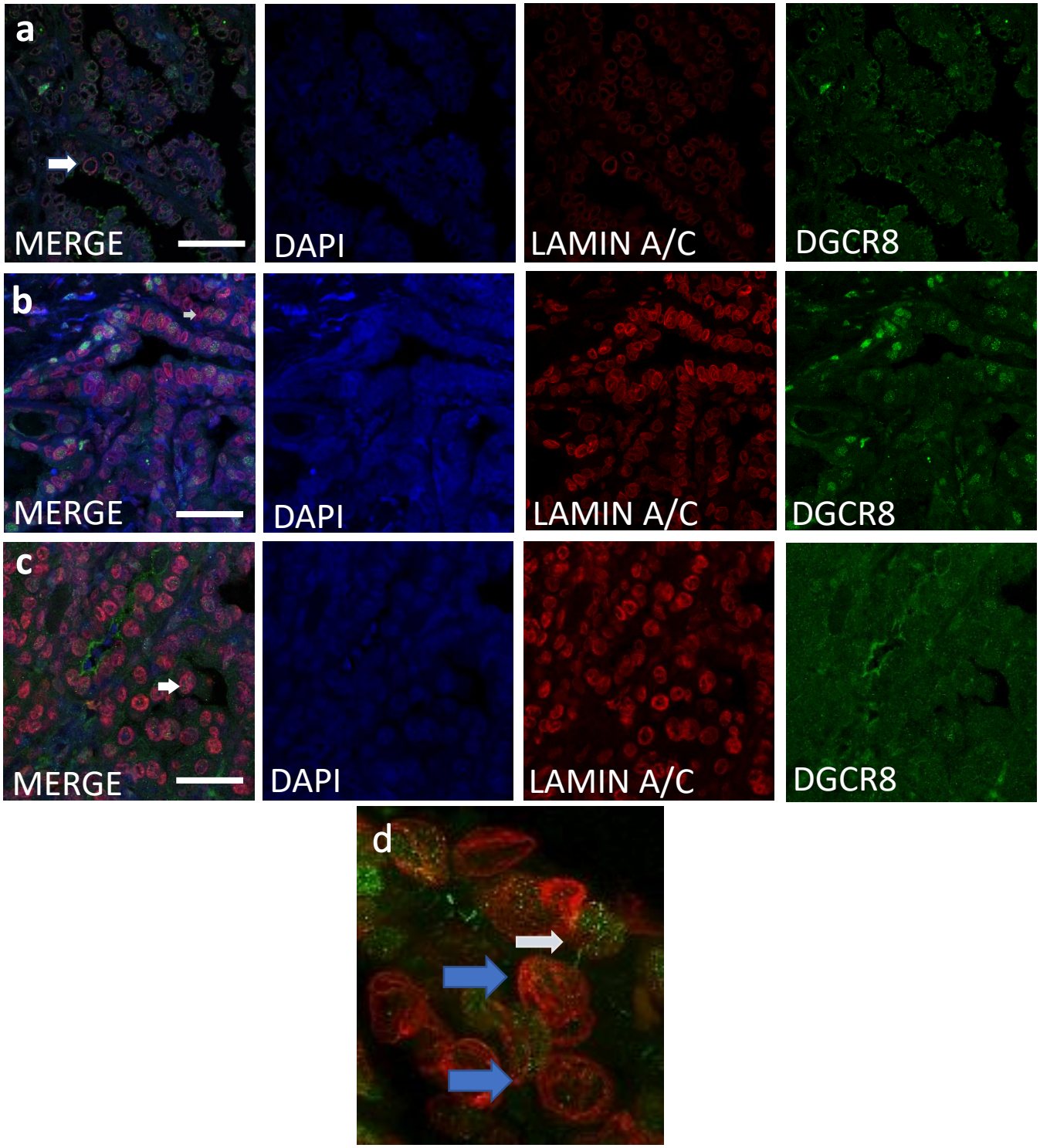

Figure 50 Representative images of tissue sections from TCV samples (a,b,c). Nuclei stained by DAPI (blue), Lamin A/C in red, DGCR8 in green. Magnification, 63x, d) Zoomed image of pseudoinclusions (blue arrows) and intercellular bridges with DGCR8 (white arrows), Lamin A/C in red and DROSHA in green.

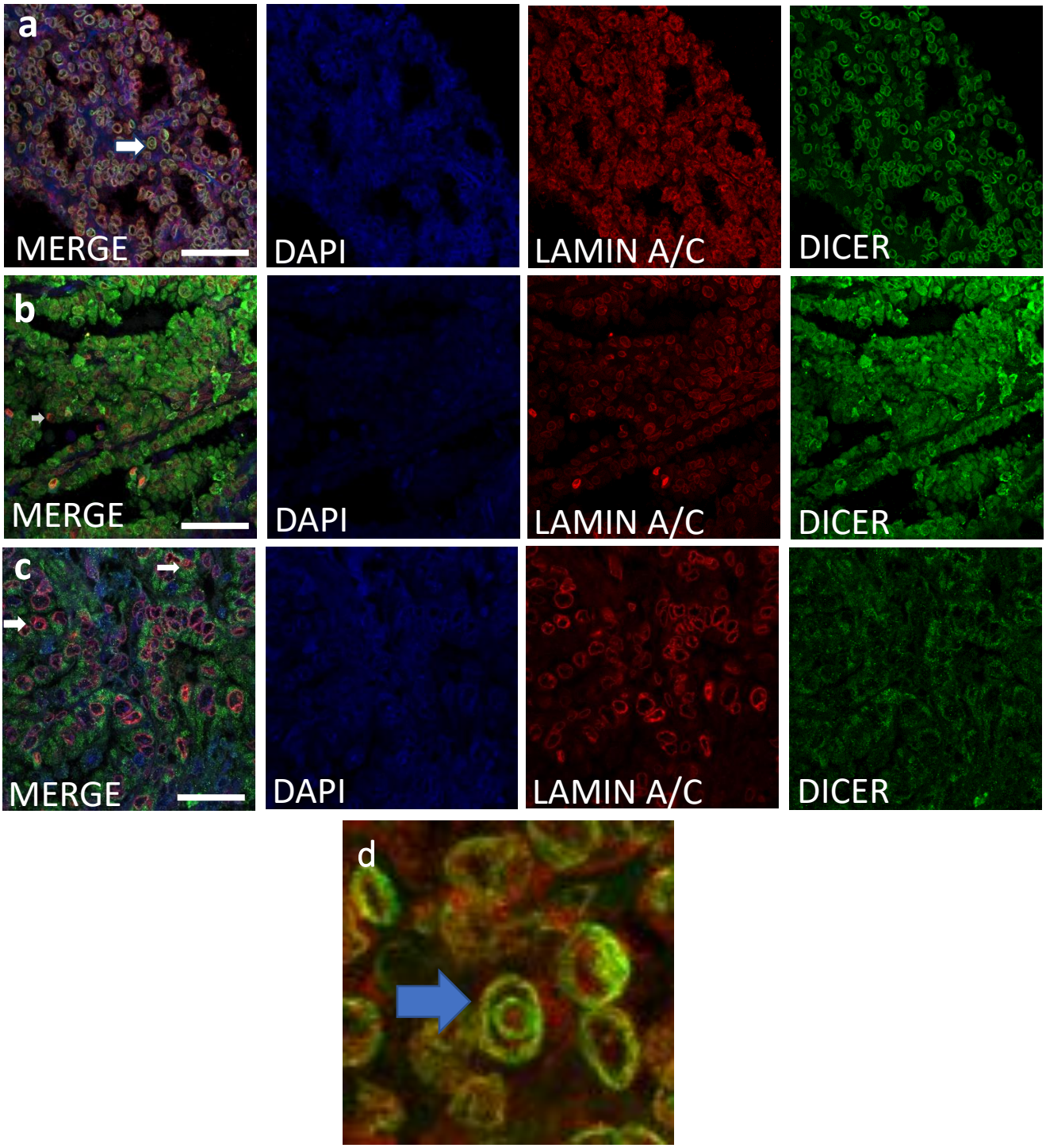

Figure 51 Representative images of tissue sections from TCV samples. Nuclei stained by DAPI (blue), Lamin A/C in red, DICER in green. Magnification, 63x. d) Zoomed image of pseudoinclusions (blue arrow) with Lamin A/C in red and DICER in green.

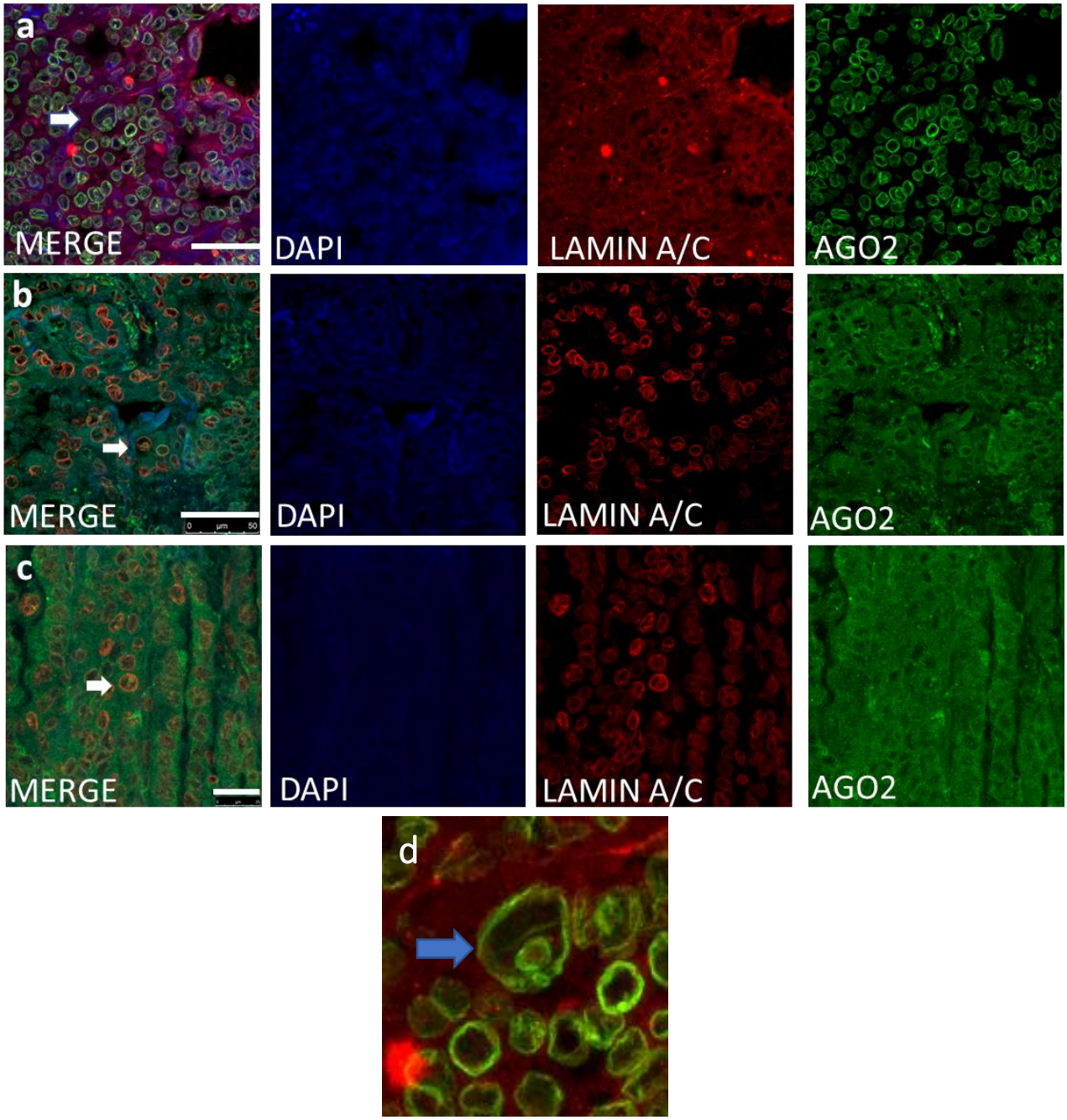

Figure 52 Representative images of tissue sections from TCV samples. a,b,c) Nuclei stained by DAPI (blue), Lamin A/C in red, AGO2 in green. Magnification, 63x, d) Zoomed image of pseudoinclusions (blue arrow) with Lamin A/C in red and AGO2 in green.

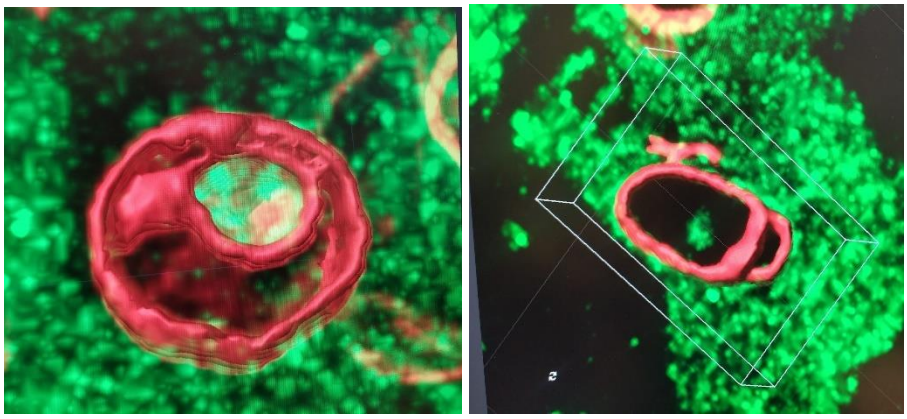

Figure 53 AGO2 distribution inside a pseudoinclusion in a nucleus of a TCV (left) and inside a specific loci in a deranged nucleus with a budding membrane (right) . AGO2 stained in green and Lamin A/C stained in red.

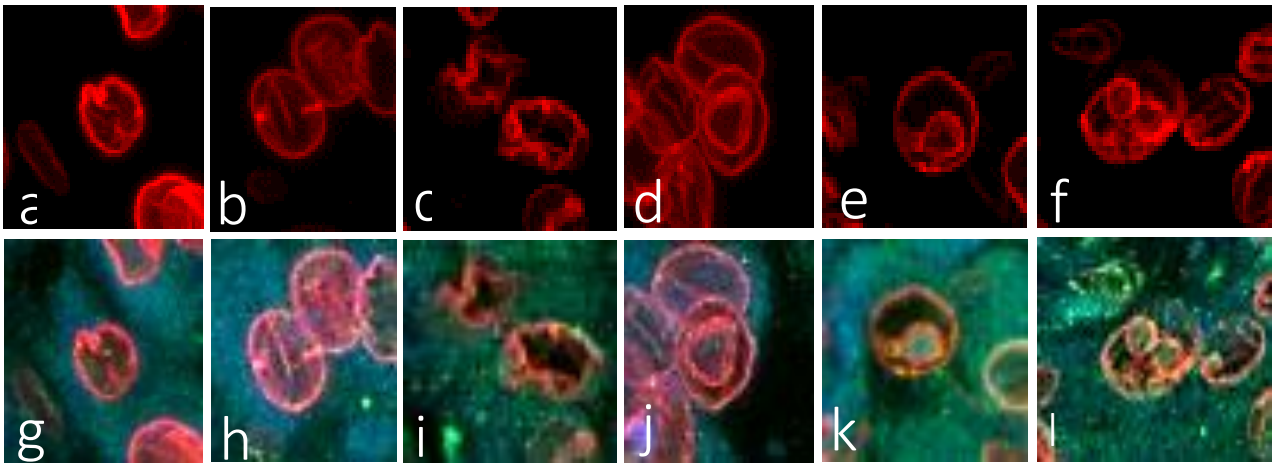

Figure 54 Representative images of (a,g) crease, (b,h) invaginations, (c,i) general nuclear envelope irregularities, (d,j) pseudoinclusion in a nucleus, (e,k) pseudoinclusion in a nucleus with connection with the membrane and (f,l) three pseudoinclusions in a nucleus. Lamin A/C stained in red, AGO2 in green.

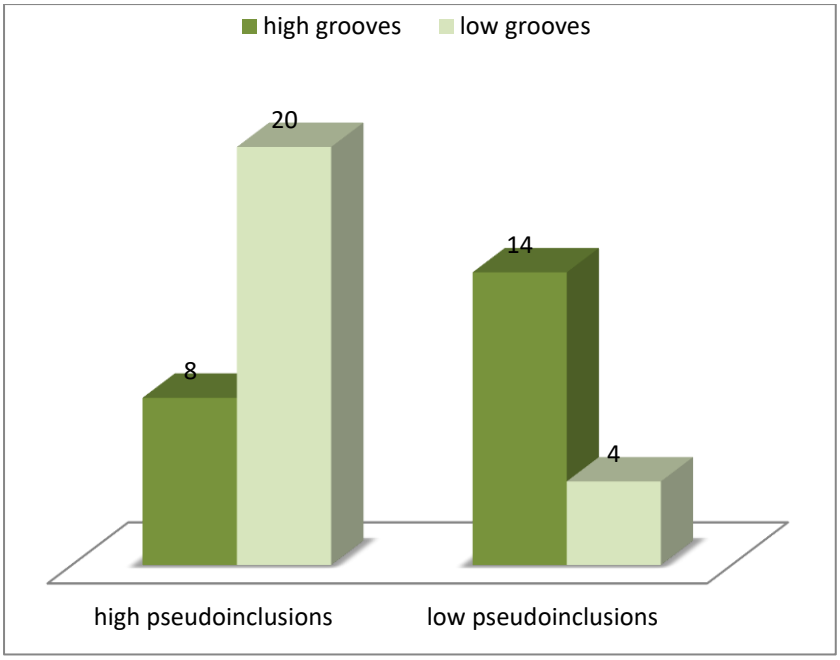

Figure 55 Diagram of the Co-presence of pseudoinclusions and grooves in cBioportal cohort.

Creases, grooves and other intranuclear invaginations may be precursors of pseudoinclusions that probably occurred in a coordinated manner (Figure 54a-l). This is supported by the fact that co-presence of pseudoinclusions with invaginations is a rare phenomenon; samples that have grooves, have a lack of pseudoinclusions and vice versa, leading to the assumption that the cells are synchronized in each step (Figure 55).

BRAFV600E is correlated with pseudoinclusions and fibrosis

Aiming to better characterize TCVs, we investigated for genetic events that occurred, such as mutations. Therefore, we analyzed papillary thyroid cancer cases with normal adjacent tissue from a reference group of Cancer Genome Atlas (TCGA) project (cBioportal, Institutional Review Boards). The predominant mutations were in BRAF, RAS and RET genes, as expected.

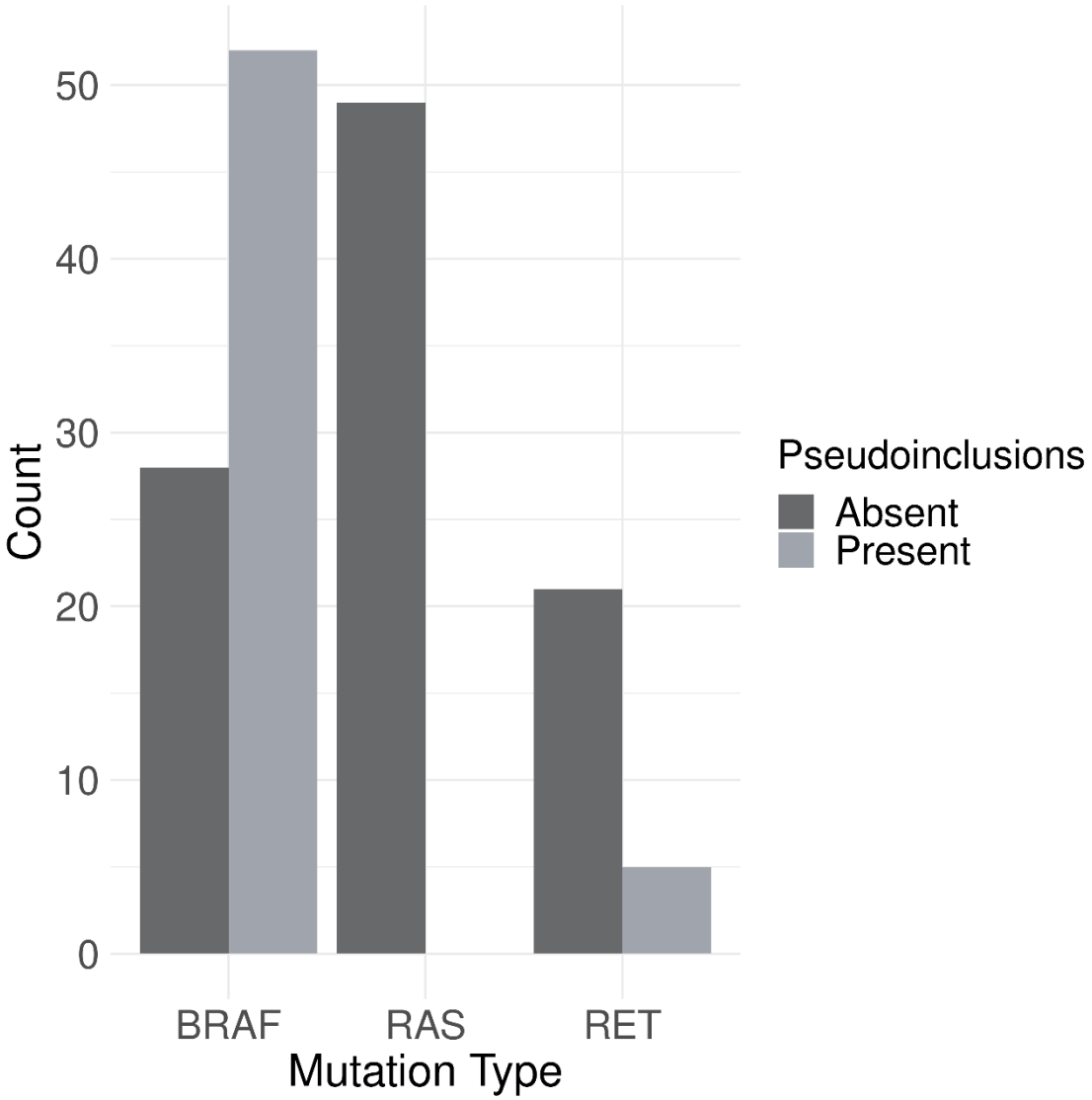

Figure 56 Presence of pseudoinclusions in cBioportal samples. Pseudoinclusions are highly correlated with $BRAF^{V600E}$, but not with the presence of RAS or RET mutations.

As $BRAF^{V600E}$ mutation is frequently related to tumor aggressiveness, cell motility and migration, we investigated its presence in TCV variant. We believe that $BRAF^{V600E}$ could contribute to the increase of cytoskeletal reprogramming and thus enhancing cytoplasmic motility into the nucleus leading to the formation of grooves and subsequently, inclusions. This is supported by the finding that pseudoinclusions are present in specimens with $BRAF^{V600E}$ but not RAS or RET mutations (Figure 56).

The causal effect of $BRAF^{V600E}$ to the formation of pseudoinclusions was enhanced by image analysis of thyroid cell lines. For that purpose, we performed confocal microscopy of NTHY ori 3-1 and ARO anaplastic thyroid cells. The latter carries the BRAF mutation. AROs seem to have multiple nuclear irregularities and intense invaginations probably due to the existence of BRAF mutation in their genetic pool, while that was not the case regarding NTHY ori 3-1 (Figure 57).

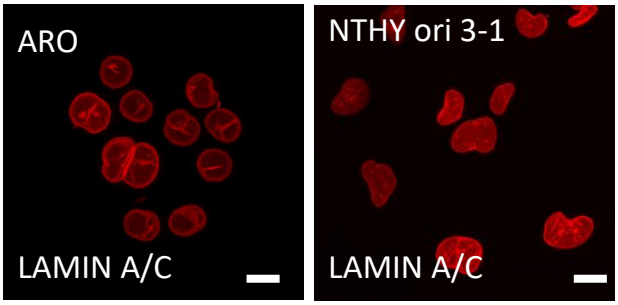

Figure 57 Representative image of ARO thyroid anaplastic cell line and NTHY ori 3-1 cell line. Nuclei stained by DAPI (blue), Lamin A/C in red and AGO2 in green. Magnification, 63x. Scale bar:10μm.

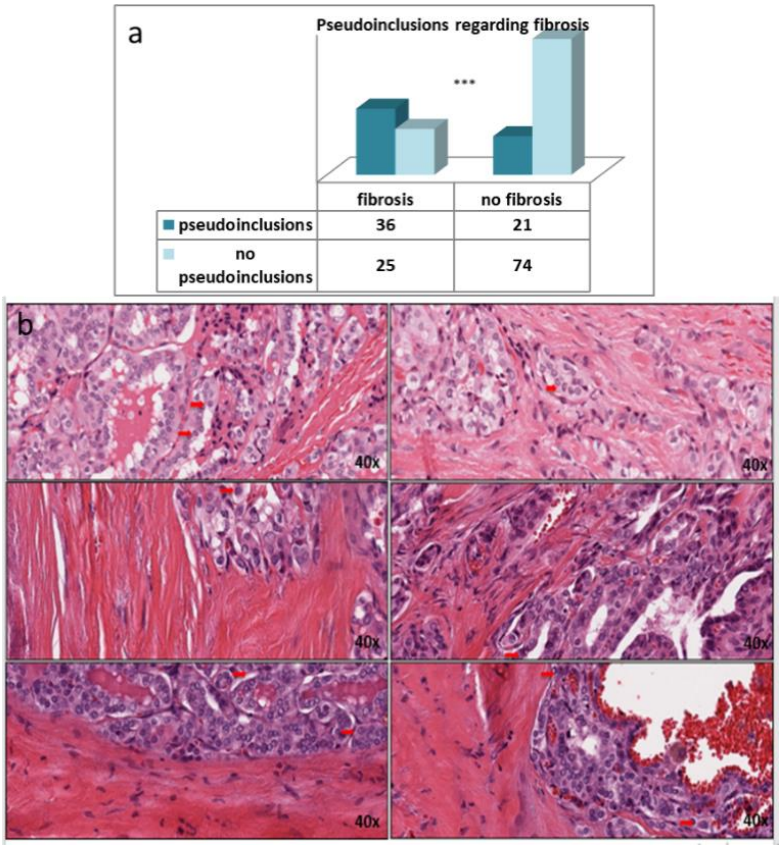

Figure 58 (a) Presence of pseudoinclusions regarding co-occurrence of fibrotic areas in cBioportal patients and (b) Fibrotic profile in sections of TCVs. Red arrows indicate the pseudoinclusions existing closely to fibrotic areas.

Conclusively, $BRAF^{V600E}$ mutation and TCV phenotype are most likely linked and frequently accompanied by the existence of pseudoinclusions and fibrotic phenomena. Therefore, we hypothesized that $BRAF^{V600E}$ mutation may constitute the first hit for fibrogenesis and the formation of pseudoinclusions.

An interesting observation was that cells with structural alterations such as pseudoinclusions, nucleic creases and invaginations were usually found proximal to fibrotic tissue (Figure 58a,b). Most likely, the fibrotic inflammatory background promotes the formation of these intranuclear structures containing

apoptosis-related components as a result of the effort of the cell to reverse the fibrotic phenotype (Collison, 2018).

Survival Rates

Based on the above findings, it appears that the appearance of pseudoinclusions in the cells is correlated to an aggressive phenotype of the malignancy. To evaluate this observation, we examined the survival rates of the individuals in the cohort. Patients that present these structures in their cancer tissues demonstrated poorer survival (Figure 59a). In the presence of $BRAF^{V600E}$ mutation, this observation was enhanced (Figure 59b). The most important and statistically significant difference was found in samples that have a concurrent existence of pseudoinclusions and a fibrotic profile (Figure 59c) enhancing the idea of the pseudoinclusion-genesis and formation of the invagination in a fibrotic and inflammatory background.

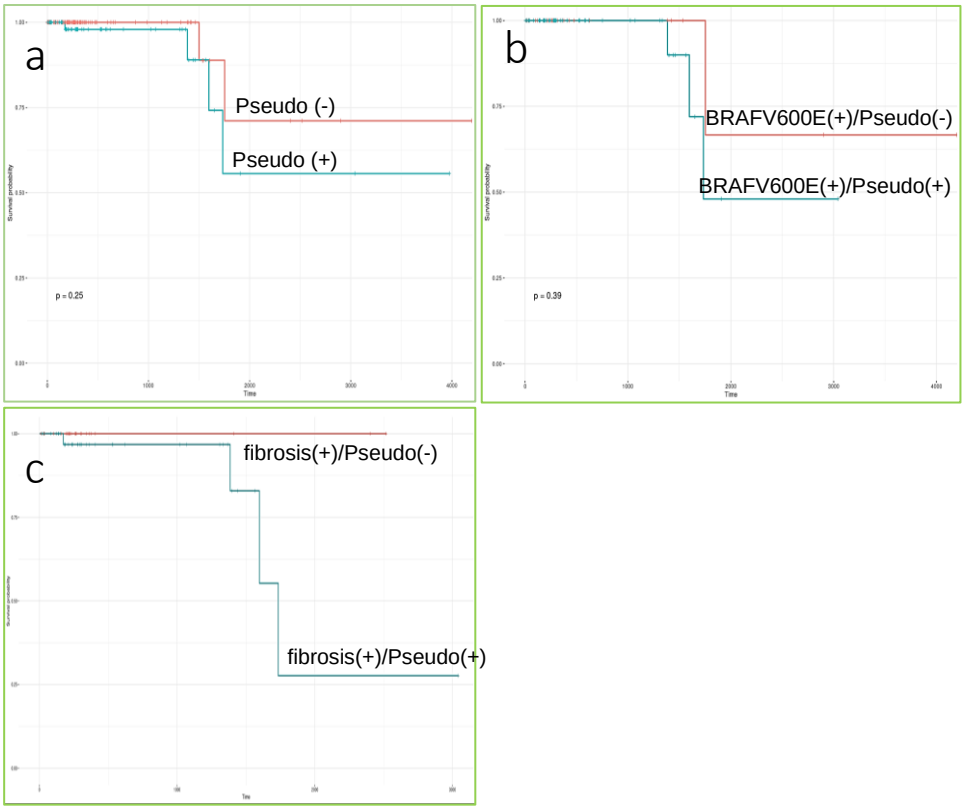

Figure 59 Kaplan-Meier survival analysis for (a) the presence of pseudoinclusions, (b) the presence of pseudoinclusions in correlation with $BRAF^{V600E}$mutation and (c) the presence of pseudoinclusions in correlation with the fibrotic profile of a cohort.

Pathways from differential analysis of pseudoinclusions

To unravel the genes and the molecular mechanisms responsible for the poor prognosis of the disease, we performed informatics analysis of gene expression profiles. The individuals, and therefore their gene expression profiles, were subgrouped according to the presence or absence of pseudoinclusions, fibrosis and/or $BRAF^{V600E}$ mutation. Specifically, three comparative studies were performed. The first one compared the expression profiles of patients that present pseudoinclusions in their tissues versus

individuals without these structures. Protein processing ER, NFKβ signaling, adherens junction and regulation of actin cytoskeleton (ie integrins) pathways emerged from the study, suggesting that the enclosing mass into the inclusion supposed to be components of the cytoplasm such as endoplasmic reticulum (Figure 60). RISC complex molecules are directly related with the aforementioned pathways. Towards that direction, Kim YJ and colleagues found that loaded and active hsAgo2 was found to be mostly membrane-associated, while the slicing product was solely associated with rER fractions. These findings led to the conclusion that both hsAgo2 RISC formation and target RNA slicing occur on the rER and that the outer rER membrane thus acts as a central nucleation site for siRNA-mediated RNA silencing (Kim et al., 2014).

The second grouping, $BRAF^{V600E}$ (+)/ pseudo(-) and $BRAF^{V600E}$(+)/ pseudo(+), samples disclosed pathways related to spliceosome, ECM interaction receptors, lupus and Parkinson (especially mitochondrial components) (Figure 60). Finally, the last grouping, pseudo(+)/$BRAF^{V600E}$ (+)/fibrosis (+) and pseudo(-)/$BRAF^{V600E}$ (+)/fibrosis(-) samples include pathways related to cell-to-cell adhesion, Parkinson, PI3K-Akt and focal adhesion (Figure 60).

Molecular pathways

pseudoinclusions vs non pseudoinclusions

ID	Pathway	Fold_Enrichment	occurrence	lowest_p	highest_p	Up_regulated	Down_regulated
hsa04141	Protein processing in endoplasmic reticulum	22.868750	10	1.1e-26	1.0e-22	SEC23A, EDEM1, HSPA1B, HSPA6, DNAJB1, HSP90AA1, HSPH1, BAG2, RAD23B, UBQLN4, MAP3K5, BAX, CAPN1, CAPN2, FBXO2, FBXO6	SEC61A2, SEC61B, SEC62, SEC63, RPN1, RPN2, DDOST, STT3A, STT3B, RRBP1, HYOU1, HSPA5, DNAJB11, DNAJC1, DNAJC3, DNAJC10, HSP90B1, GANAB, CANX, PDIA3, CALR, MAN1A2, PREB, SAR1A, SAR1B, SEC23B, UGGT1, EDEM3, PHB, PDIA4, PDIA6, OS9, ERLEC1, SSR1, BCAP31, DERL2, HSPA1L, DNAJA2, DNAJC5, YOD1, EIF2AK3, EIF2AK4, DDIT3, BCL2, WFS1, ERN1, MAPK8, MAPK10, CASP12, MARCH6, UBE2G2, SYVN1, SEL1L, HERPUD1, UBE2D2, UBE2D3
hsa04064	NF-kappa B signaling pathway	26.855046	10	2.2e-18	9.3e-17	LCK, ZAP70, SYK, LYN, BTK, CARD11, BCL10, IL1B, IL1R1, MYD88, TNFRSF1A, BIRC3, DDX58, LY96, TICAM1, CD40LG, CD40, LTB, TNFSF14, MAP3K14, TNFSF13B, UBE2I, RELA, CFLAR, BCL2L1, BCL2A1, NFKB2, CXCL8, PTGS2, CCL4, VCAM1, PLAU, RELB, CCL13, CCL19, ICAM1, CXCL2	PLCG1, PRKCQ, IRAK1, TRAF6, TRAF3, IKBKB, BCL2, CSNK2A1, GADD45B
hsa04520	Adherens junction	31.123870	10	1.7e-17	1.0e-16	PARD3, RAC2, WAS, IQGAP1, BAIAP2, WASF1, LMO7, ACTN4, CTNNA1, ACTB, ACTG1, PTPRF, TCF7, MET, FYN, TGFBR1	RAC3, WASF3, PTPRB, PTPRJ, CSNK2A1, TCF7L1, INSR, FGFR1, TGFBR2, SMAD4, NLK, ACP1
hsa04810	Regulation of actin cytoskeleton	20.390712	10	2.3e-17	1.0e-14	FGF2, FGF9, FGF18, PDGFRA, FN1, ITGA2, ITGA3, ITGA11, ITGAV, ITGAL, ITGAM, ITGAX, ITGB2, ITGB4, ITGB6,	EGF, FGF17, PDGFB, PDGFD, FGFR1, FGFR2, ITGA1, ITGA2B, ITGA5, ITGA6, ITGA8, ITGA10, BDKRB2, CHRM3,

BrafV600E mutation/pseudoinclusions

vs BrafV600E mutation/non pseudoinclusions

ID	Pathway	Fold_Enrichment	occurrence	lowest_p	highest_p	Up_regulated	Down_regulated
hsa03040	Spliceosome	64.82480	10	1.2e-12	1.2e-12		SNRPD3, SNRPA, SF3A3, PUF60, LSM3, PRPF38A, PRPF6, CTNNBL1, PPIE, CCDC12, RBM22, RBM8A, MAGOH, SRSF8, TRA2B
hsa04512	ECM-receptor interaction	119.40793	3	7.2e-11	7.2e-11	FN1, TNC, ITGA2, ITGA3	COL9A1, THBS4, ITGA1, ITGA2B, CD36, CD47
hsa05322	Systemic lupus erythematosus	32.09649	10	9.5e-10	2.2e-08	CD80	HIST1H2AE, H2AFV, HIST1H2AC, HIST1H2BD, HIST2H2BE, H3F3B, HIST1H3D, HIST1H3H, HIST1H4I, HIST1H4H, SNRPD3
hsa05012	Parkinson disease	59.17520	10	1.4e-08	6.8e-07	ND1, ND2, ND4, ND4L, CYTB, COX3, COX1, ATP6	GNAL, SNCAIP, NDUFA4L2, NDUFA5, COX4I2, PARK7
hsa04510	Focal adhesion	44.27485	10	4.0e-08	2.2e-03	FN1, TNC, ITGA2, ITGA3, EGF, CAPN2, FLNA	COL9A1, THBS4, ITGA1, ITGA2B, PDGFB, PDGFD, VEGFA, VEGFC, KDR, FLT1, FLT4, MAPK10
hsa05034	Alcoholism	18.88029	10	5.2e-07	7.8e-06		HDAC1, HDAC7, HIST1H2AE, H2AFV, HIST1H2AC, HIST1H2BD, HIST2H2BE, H3F3B, HIST1H3D, HIST1H3H, HIST1H4I, HIST1H4H, GNG11. PKIA

BrafV600E mutation/pseudoinclusions/fibrosis

vs BrafV600E mutation/non pseudoinclusions /non fibrosis

ID	Pathway	Fold_Enrichment	occurrence	lowest_p	highest_p	Up_regulated	Down_regulated
hsa04512	ECM-receptor interaction	129.358586	10	3.3e-11	3.3e-11	FN1, TNC, ITGA2, ITGA3, SDC1	COL9A1, THBS4, ITGA1, ITGA2B, ITGA7, CD36, GP6
hsa05012	Parkinson disease	61.366876	10	8.3e-10	8.3e-10	ND1, ND2, ND4, ND4L, ND5, SDHA, SDHC, CYTB, COX3, COX1, COX2, ATP6, SLC25A5	GNAL, SEPT5, SNCAIP, UCHL1, NDUFA4L2, COX4I2, COX6B2, CASP9
hsa04151	PI3K-Akt signaling pathway	30.975661	10	1.6e-08	1.6e-08	EGF, EREG, FGF2, MAP2K1, MAPK1, SYK, OSMR, IL2RA, IL4R, FN1, TNC, ITGA2, ITGA3, CDKN1A, BCL2L1	FGF9, FGF20, PDGFB, PDGFD, VEGFA, VEGFC, ANGPT2, FGFR3, NGFR, FLT1, FLT4, IL3RA, COL9A1, THBS4, ITGA1, ITGA2B, ITGA7, GNG11, HSP90B1, CASP9
hsa04510	Focal adhesion	47.964419	10	1.9e-08	1.9e-08	FN1, TNC, ITGA2, ITGA3, EGF, DIAPH1, CAPN2, PARVA, MAP2K1, MAPK1, BIRC3	COL9A1, THBS4, ITGA1, ITGA2B, ITGA7, PDGFB, PDGFD, VEGFA, VEGFC, FLT1, FLT4, PAK1, MAPK10

PSEUDOINCLUSIONS-NON PSEUDOINCLUSIONS
• Protein processing in endoplasmic reticulum
• NF-kappa B signaling pathway
• Adherens junction
• Regulation of actin cytoskeleton
• Ubiquitin mediated proteolysis

$BRAF^{V600E}$ PSEUDOINCLUSIONS- $BRAF^{V600E}$ NON-PSEUDOINCLUSIONS
• Spliceosome
• ECM-receptor interaction
• Systematic lupus erythematosus
• Parkinson disease
• Focal adhesion
• Alcoholism
• Transcriptional misregulation in cancer

$BRAF^{V600E}$ PSEUDOINCLUSIONS FIBROSIS - $BRAF^{V600E}$ NON-PSEUDOINCLUSIONS NON-FIBROSIS
• ECM-receptor interaction
• Parkinson disease
• PI3K-Akt signaling pathway
• Focal adhesion

Figure 60 Molecular pathways related to the subgroupings of pseudoinclusion-clusters.

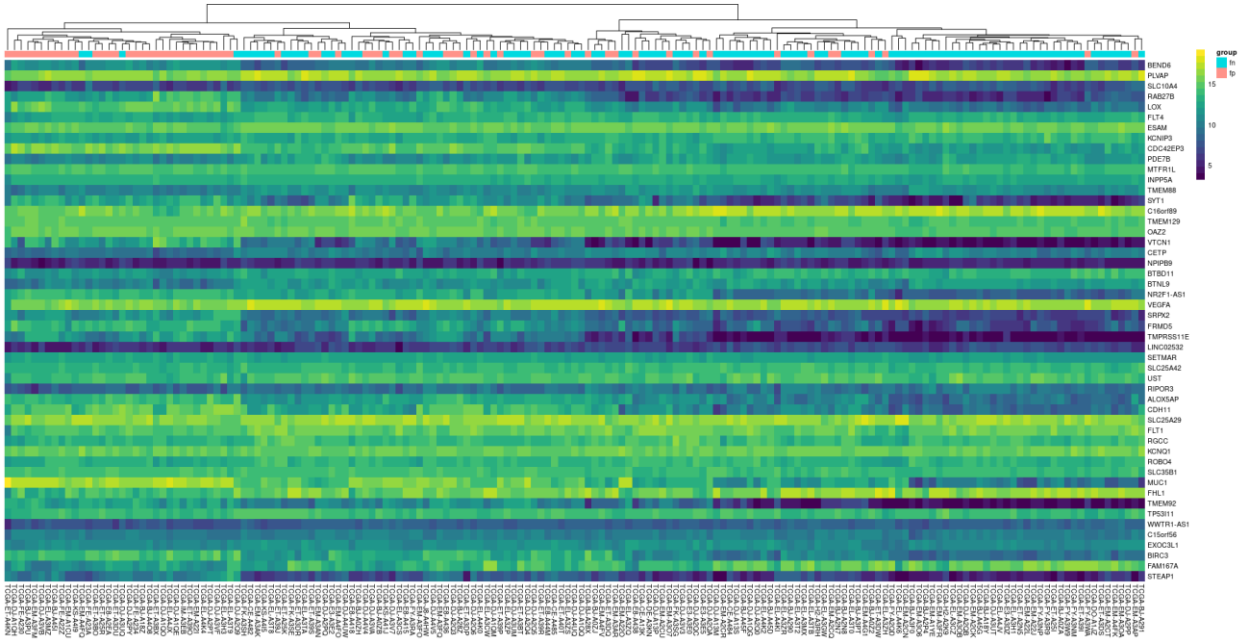

Figure 61 Heat maps of gene expression in the reannotated subset of the TCGA-THCA study. The top 50 differentially expressed genes between the fibrosis positive (fp - pink) group and the fibrosis negative (fn - light blue) group were chosen. The samples are clustered based on those genes' expressions using hierarchical clustering.

The frequent presence of pathways such as the Pathways Regulation of actin cytoskeleton and ECM-receptor interaction in the abovementioned comparative studies as well as the presence of RISC compounds in pseudoinclusions indicates the potential implication of RISC in EMT regulation.

Not surprisingly, VEGFA, a common molecule of EMT, was found to be intensely altered between samples with presence or absence of fibrosis (Figure 61). Additionally, synaptotagmin (Syt1) an integral membrane protein of synaptic vesicles, thought to serve as Ca^{2+} sensors in the process of vesicular trafficking and exocytosis and FHL1 implicated in ion channel and metal ion binding for processes such as cell differentiation, negative regulation of G1/Sb and G2/M transition of mitotic cell cycle and regulation of membrane depolarization, are among the most important deregulated molecules during fibrogenesis and fibrosis progression. The precise molecular mechanism regarding the formation of the grooves and pseudoinclusions and the molecular events that they relate the latter with fibrosis remains to be elucidated.

CHAPTER 2

Focusing on RISC complex fine-tuning regulation of gene expression during EMT cytoskeletal remodeling that we observed in pseudoinclusions, we examined the implication of AGO members in cell division phenomena of normal and cancer cells. Especially, AGO2 was of great significance due to its catalytic activity during translational repression and mRNA degradation.

Subcellular distribution of AGO2 - AGO2 resides in protrusional structures.

The AGO2 protein is located into the cytoplasm as well as into the nucleus of all the examined epithelial and mesenchymal cell lines, normal (thyroid NTHY ori 3-1, primary mammary HMEC-1 and hepatic stellate LX-2) and cancer (breast cancer MDA-MB 231, melanoma A375 and liver cancer HepG2), exhibiting a punctuate pattern (Figure 64a and Figure 62a-f). Despite the big differences in the relative expression of the cell lines regarding each AGO member as well as the panAGO expression, in protein level, excluding LX-2, we observed small differences (Figure 63). More specifically, based on the mRNA expression, NTHY ori 3-1 cells, overall, appear to have decreased AGO2 expression. The expression levels of NTHY ori 3-1 and LX-2 are similar demonstrating that the more normal or close to normal are the cells, the more decreased levels of AGO, they have. They also express more AGO1 than AGO2. MDA MB-231 and HepG2 cells, as aggressive cancer cells, had increased AGO expression levels and AGO2 demonstrated elevated levels compared to the other cell lines tested (Figure 63, top). On the contrary to the normal cell lines, AGO2 has a higher expression than AGO1 in MDA MB-231 and HepG2 cells. Universally, AGO3 and AGO4 have decreased expression levels, as expected, since they have a more subsidiary role. The experiments need to be repeated with other sets of primers, cell lines and primary cultures, to verify the previous findings.

In protein level, AGO2 localizes inside the cytoplasm in a dotty diffuse pattern. In some cases, areas with high AGO2 concentration were observed, corresponding to AGO2 that resides in GW-bodies, P-bodies or stress granules. Besides the sub-cytoplasmic distribution, AGO2 also localizes into the nucleus, following a diffused or granular pattern. Also, it can have an intense signal into the nucleus and less concentrated into the cytoplasm or vice versa, as well as it can have equal distribution inside and outside the nucleus. The reason of this AGO2 protein distribution is under investigation.

Interestingly, AGO2 was also localized in protrusions, demonstrating differences in shape and density. More specifically, AGO2 resided in Actin filopodial-like structures that are many per cell (Figure 64a,b), and in tubular protrusions that are always formed in paired cells (Figure 64a,c,d). The tubular protrusions demonstrate two different AGO2 distribution patterns, a low immunofluorescence AGO2 signal, termed open-ended tubes (Figure 64c), and an intense AGO2 signal, termed close-ended tubes (Figure 64d). The AGO2 open-ended tubes is usually correlated with loosely-shaped tunneling nanotubes while the close-ended appear as a compact and dense structure bearing a “gap” lacking AGO2, usually in the middle-line of the tube. To track the dynamic behavior of AGO2 in the two types of paired protrusions, time-lapse experiments were performed using cells expressing AGO2-GFP chimeric protein. In the open-ended nanotubes, AGO2 components displayed flow and motility across the tube (Figure 64e,f). AGO2 close-ended formations exhibited high flexibility, non-homogeneous structure, with distinctively larger AGO2 complexes, when compared to open-ended nanotubes; the close-ended formation breaks, eventually leading to separation of the involved cells (Figure 64g,h). Next, we investigated the presence and distribution of Drosha, DGCR8 and Dicer proteins, in the AGO2-enriched open- and close-ended paired structures. These crucial components of the RNAi-machinery functions, although they are known to reside mainly into the nucleus and cytoplasm, they were also

detected in the AGO2 tubes (Figure 65a-f). Immunofluorescence assays demonstrated that Drosha and DGCR8 exhibited punctuate expression patterns within both tunneling open- (Figure 65a,b) and close-ended nanotubes similar to those observed with AGO2. Dicer was detected within and along the open-ended nanotubes (Figure 65c), while in close-ended protrusions it was situated primarily in the middle-line ("gap") of the tubes (Figure 65f). Notably, Staufen, a double-stranded RNA (dsRNA) binding protein responsible for dsRNA transport and mRNA localization, was mainly cytoplasmic. It was also found, though at lower signal intensities, inside the open-ended tunneling nanotubes (Figure 65g) but it was almost undetected in close-ended cellular protrusions (Figure 65h). Altogether, it seems that in the open-ended tunneling nanotubes, AGO2 is loaded with dsRNA species, able to travel in between neighboring cells, communicating intercellular messages, most likely miRNAs, through structured channels, as indicated by the presence of Staufen. This does not seem to apply to the AGO2 close-ended protrusions, at least as suggested by the absence of Staufen. Importantly, in these "close-ended" formations, AGO-arm structures exhibit high flexibility, stretching or shrinking, until their separation. These novel and dynamic formations do not seem to serve as communication channels in between cells. Given the strong signal of AGO2 in the close-ended structures and the distinct pattern with the "gap" in the middle of the tube, their composition and functional contribution to cellular physiology needs to be further elucidated.

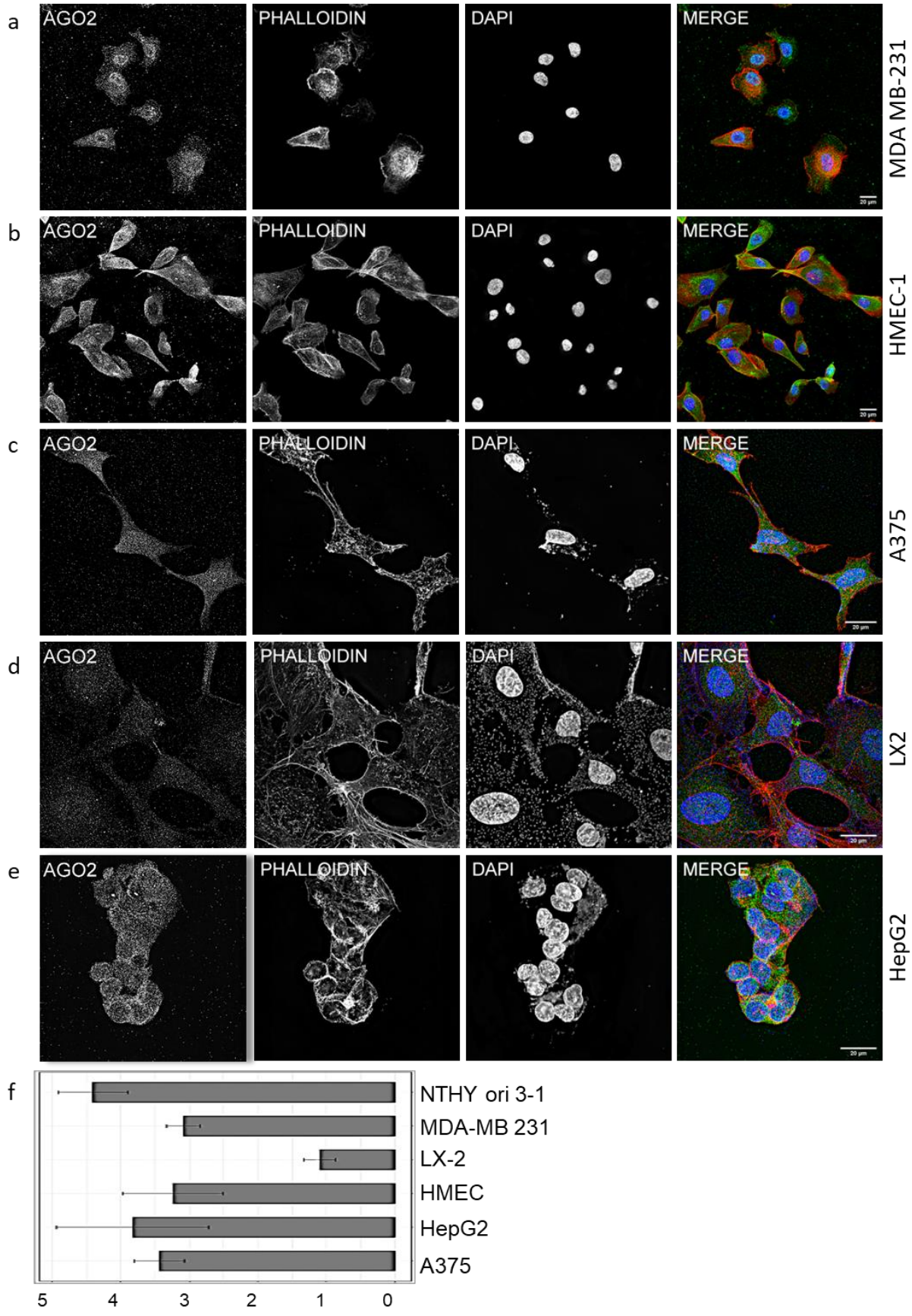
a
AGO2
PHALLOIDIN
DAPI
MERGE
MDA MB-231
b
AGO2
PHALLOIDIN
DAPI
MERGE
HMEC-1
c
AGO2
PHALLOIDIN
DAPI
MERGE
A375
d
AGO2
PHALLOIDIN
DAPI
MERGE
LX2
e
AGO2
PHALLOIDIN
DAPI
MERGE
HepG2
f
NTHY ori 3-1
MDA-MB 231
LX-2
HMEC
HepG2
A375
5
4
3
2
1
0

Figure 62 Subcellular distribution of AGO2 in different cell lines. Representative images of (a) MDA MB-231, (b) HMEC, (c) A375, (d) LX-2 and (e) HepG2 cells. AGO2 in green, F-Actin (phalloidin) in red and nuclei in blue (DAPI) (scale bar: 20μm). (f) Barplot of AGO2 mean signal intensity per cell in the respective cell lines measured by Imaris using 3D surface reconstruction of confocal images.

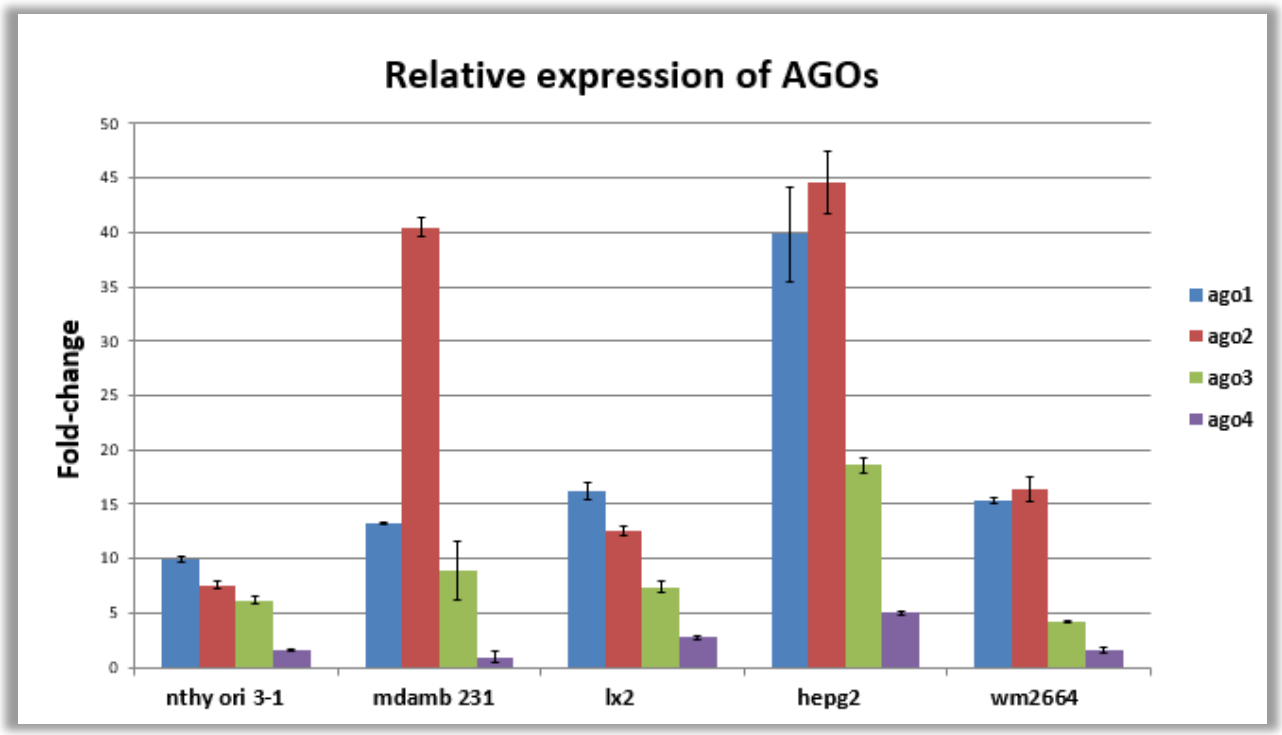

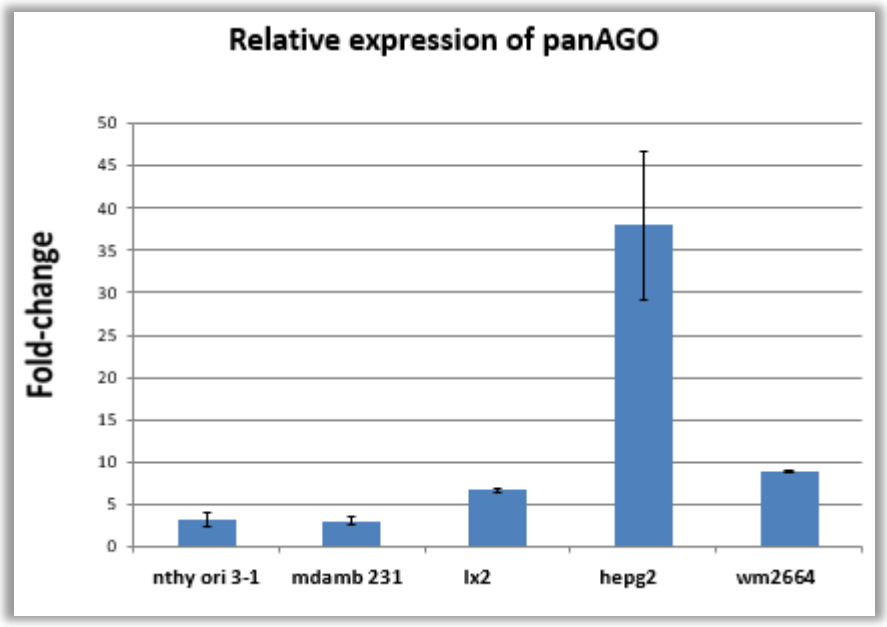

Figure 63 Relative expression of AGO proteins across cell lines. Expression levels of AGO1, 2,3 AND 4 in NTHY ori 3-1, MDA MB-231, LX2, HepG2 and WM2664 (top). Expression levels of panAGOs in Nthy ori 3-1, MDA MB-231, LX2, HepG2 and WM2664 (bottom).

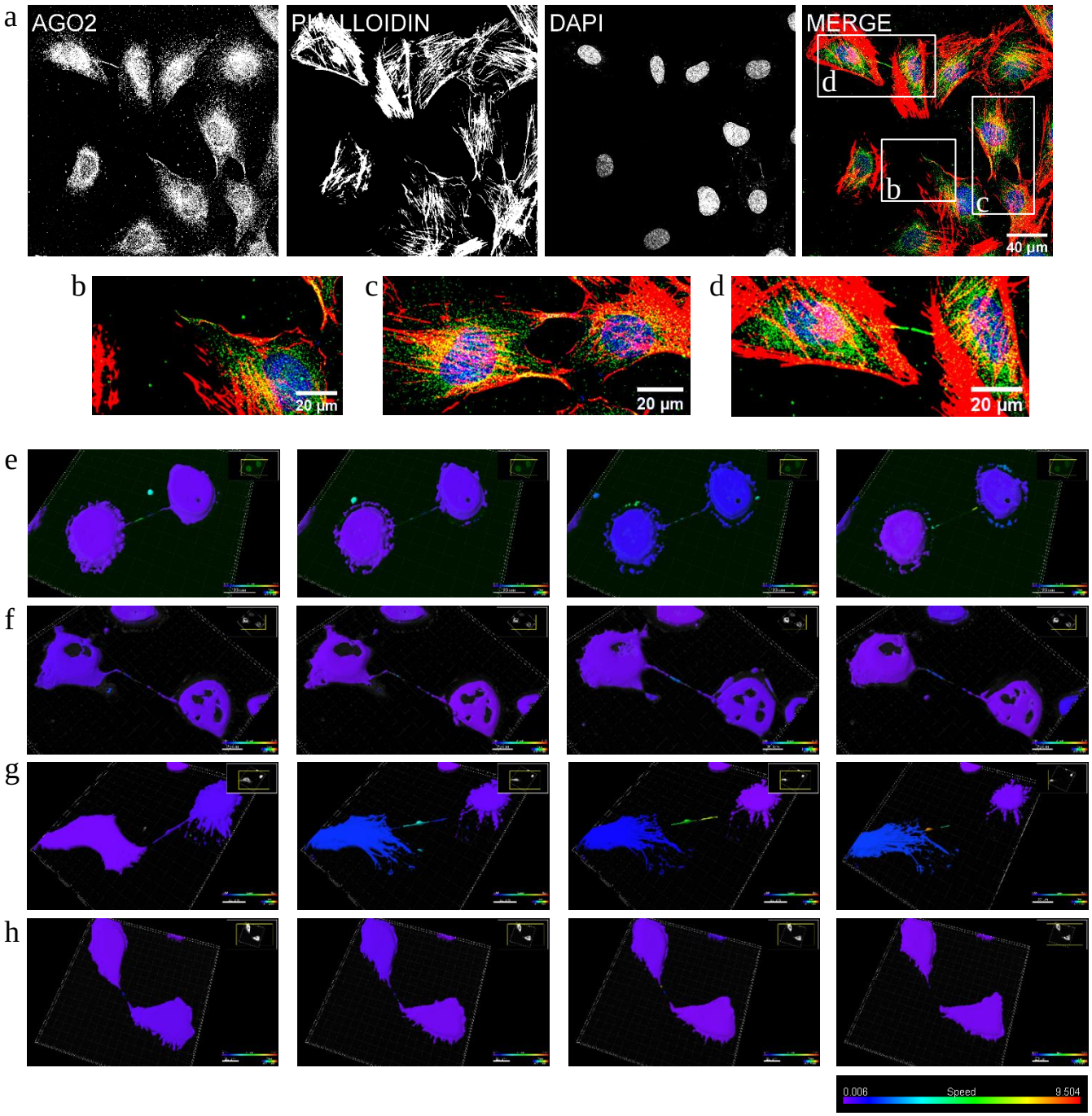

Figure 64 Subcellular distribution of AGO2. (a) Representative immunofluorescence images of the NTHY ori 3-1 cells (scale bar: 40μm). Three types of AGO2 cellular protrusions are presented: (b) the typical Actin-filopodial structure (scale bar: 20μm), (c) the open-ended tunneling nanotube (scale bar: 20μm) and (d) the close-ended tubes (scale bar: 20μm). AGO2 was depicted in green, F-Actin in red (Texas red-phalloidin) and nuclei in blue (DAPI). 3D surface reconstruction of time points from time lapse experiments of AGO2-GFP expressing cells; (e,f) open-ended tubes and (g,h) close-ended tubes, processed by Imaris software. Surfaces are color-coded (blue to red) according to speed (low to high), showcasing the motility of the respective objects. The scale bar is 20μm.

AGO2 close-ended protrusions constitute a different type than typical Actin-filopodial structures.

To obtain more information regarding the structure of AGO2 close-ended protrusions we compared them to the well-established Actin filopodial-like ones. 168 Confocal Laser Scanning Microscopy (CLSM) images of individual cells (Figure 66, 67a,b), from at least 3 independent biological experiments, were collected and processed. The number of protrusions per cell, their lengths and the tip-to-midpoint width of both types of structures were measured. The statistical analysis of the measurements revealed significant differences that clearly distinguish between the two types of protrusions. 38 Actin-filopodial protrusions on average were present per cell, whereas only one AGO2 protrusion could be maximally identified per cell. Intriguingly, although the length of Actin-filopodial protrusions range from 0.48 to 37.76 μm with a mean of 2.85 μm, the AGO2 close-ended protrusions exhibit less divergence (0.88 to 19.00 μm) and their mean length was significantly ($p = 2.2e\text{-}16$) larger (5.37 μm) (Figure 67). In an attempt to obtain a model shape of the structures, the average tip-to-midpoint width ratio of all protrusions was calculated. The average ratio of AGO2-carrying structures (1.03 μm) differed significantly ($p = 7.58e{-}07$, Figure 67d) from the typical triangular shape of Actin-filopodial protrusions (mean ratio 0.85 μm), showing a tendency towards a parallelogram-like formation (Figure 67e). In conclusion, AGO2 close-ended protrusions differ from the typical Actin-filopodial ones as they are infrequent, parallelogram-shaped and always formed in paired cells.

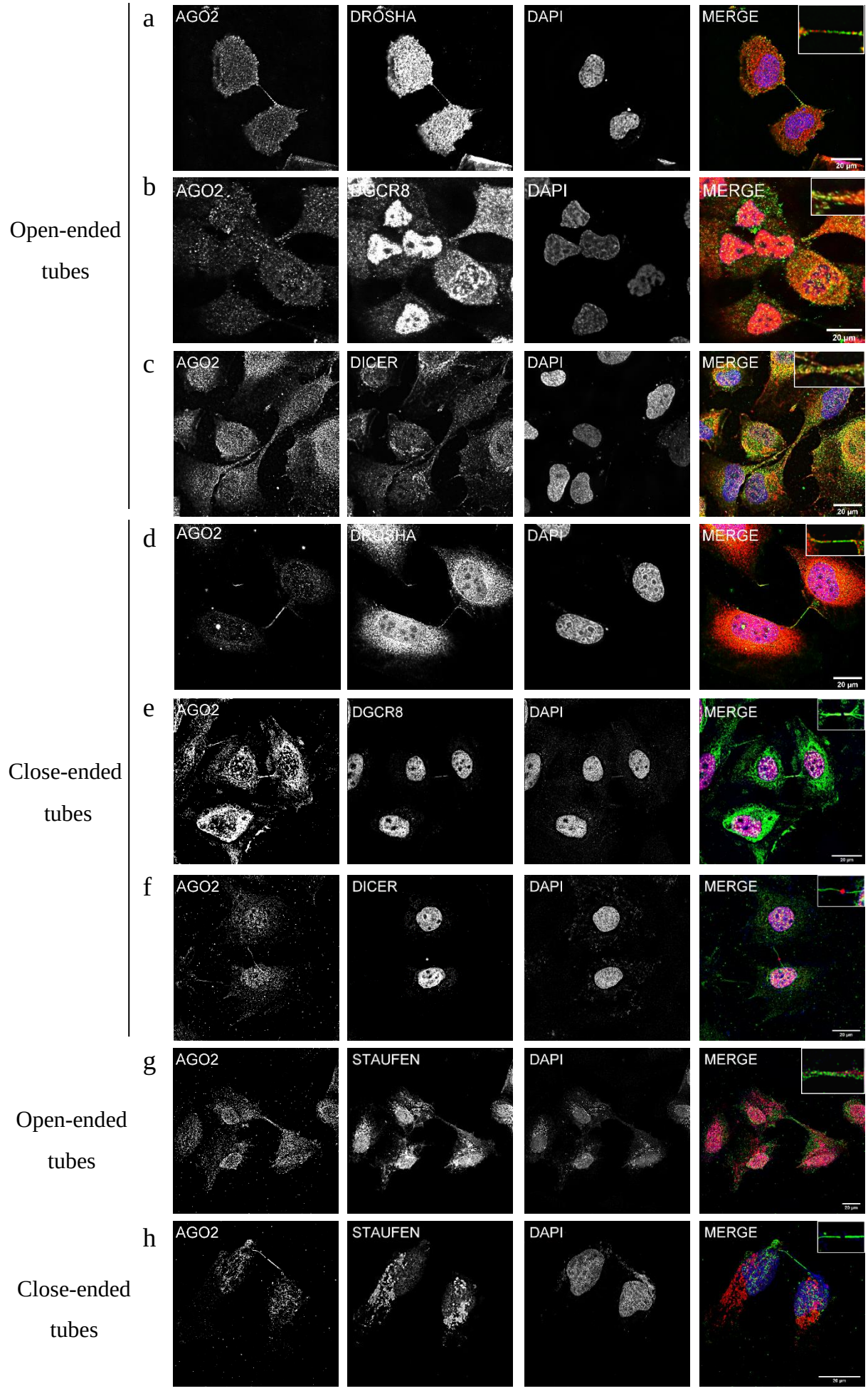
Open-ended tubes
a
AGO2
DROSHA
DAPI
MERGE
b
AGO2
DGCR8
DAPI
MERGE
c
AGO2
DICER
DAPI
MERGE
Close-ended tubes
d
AGO2
DROSHA
DAPI
MERGE
e
AGO2
DGCR8
DAPI
MERGE
f
AGO2
DICER
DAPI
MERGE
Open-ended tubes
g
AGO2
STAUFEN
DAPI
MERGE
Close-ended tubes
h
AGO2
STAUFEN
DAPI
MERGE

Figure 65 AGO2 resides in protrusional structures along with other components of the RNAi-machinery. Representative immunofluorescence images of NTHY ori 3-1 cells of (a,b,c,g) AGO2 open-ended tunneling nanotubes and (d,e,f,h) close-ended cellular protrusions with (a,d) Drosha, (b,e) Dgcr8, (c,f) Dicer and (g,h) Staufen. AGO2 was visualized in green, Drosha, Dgcr8 and Dicer in red and nuclei in blue (DAPI). The scale bar is 20μm.

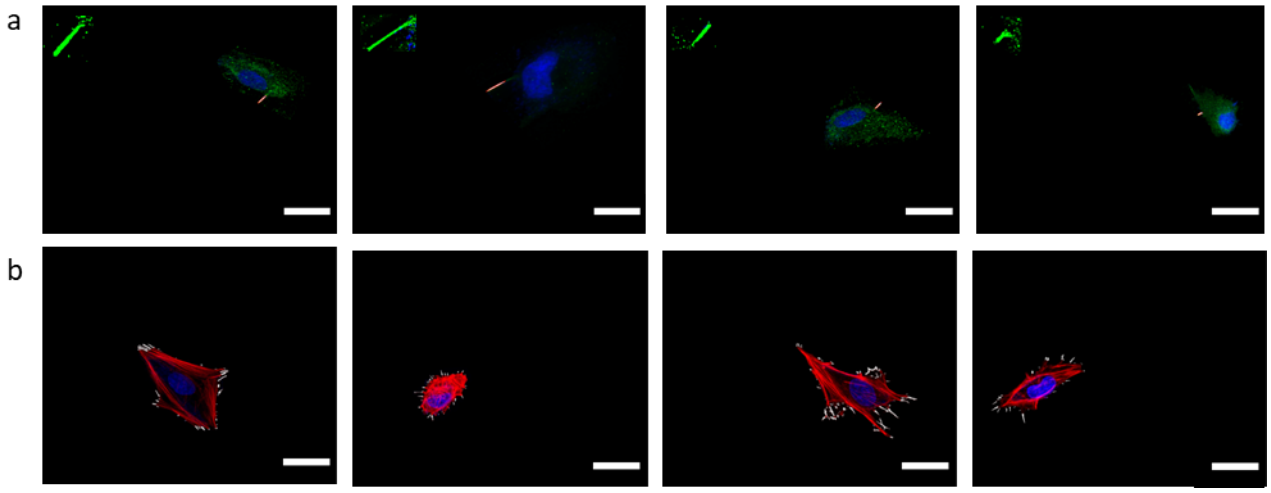

Figure 66 Examples of the output of the Matlab script used to detect, measure and yield statistics from the comparative analysis of (a) AGO2 and (b) Actin-Filopodial protrusions. The identified protrusions are colored white. All measurements were made according to the ellipses created by Matlab's "regionprops" function [shown in red in (a)]. In the top-left corner of (a) the manually cropped protrusions used to extract the AGO2 protrusion among those identified by Matlab's "fibermetric" function are overlaid.

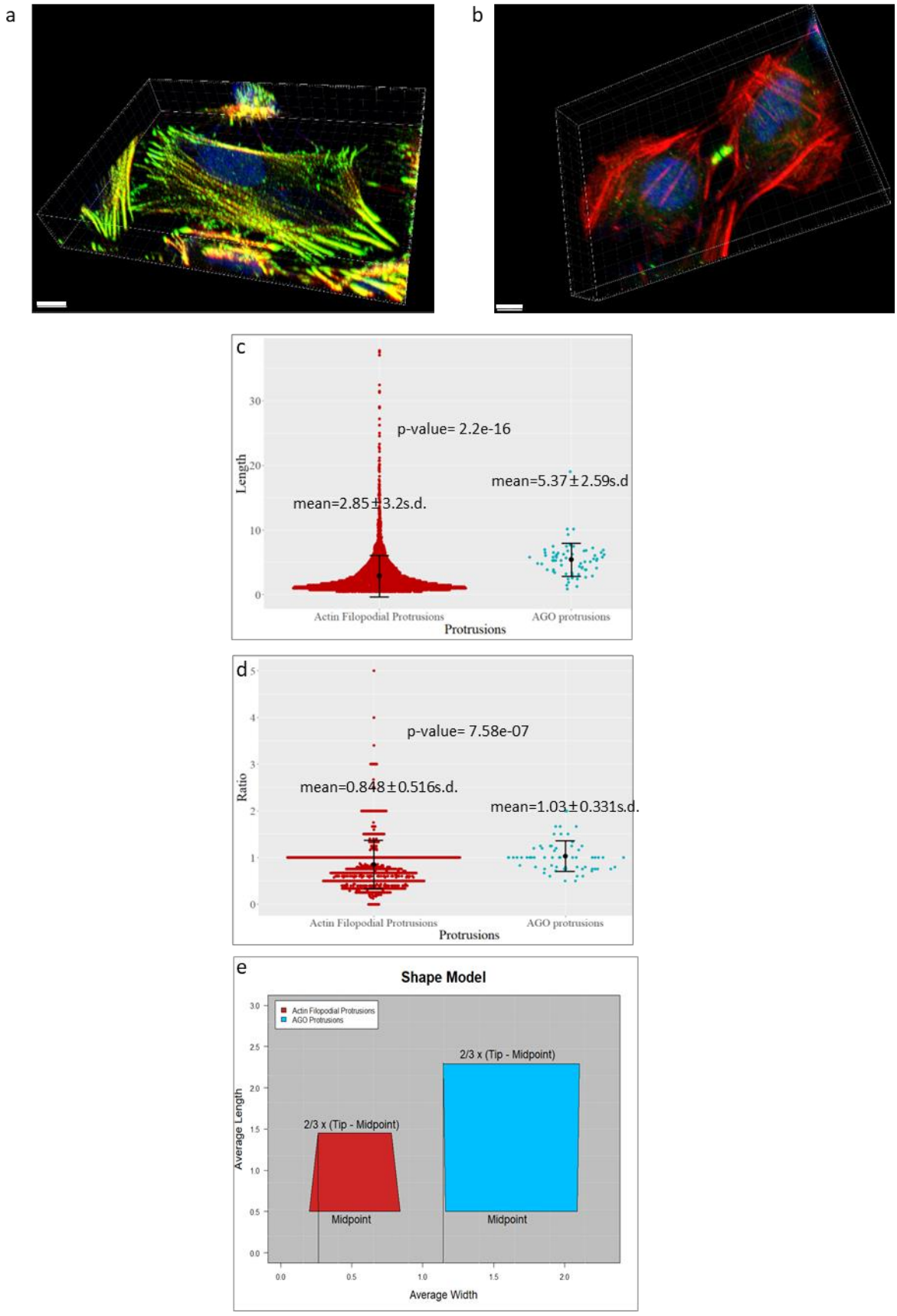

Figure 67 AGO2 close-ended structures differ from the typical Actin-filopodial protrusions. 3D signal reconstruction of representative images of NTHY ori 3-1 cells. (a) F-Actin filopodial (Actinin 4, green; F-Actin [Texas red-phalloidin], red, scale bar: 10 μm) and (b) AGO2

protrusions (AGO2 in green; F-Actin [phalloidin] in red, respectively, scale bar: 8 μm). Sina-plot of Actin-filopodial (at least n=3 biologically independent experiments, statistical test sample size n=3849 filopodial protrusions) and AGO2 protrusion (at least n=5 biologically independent experiments, statistical test sample size n=66 AGO2 protrusions) (c) lengths and (d) tip-to-midpoint width ratios. (e) Shape model based on protrusion mean value of tip-to-midpoint width ratios.

AGO2 close-ended cellular structures are cytokinetic protrusions

Based on the aforementioned findings, we investigated the possibility of the close-ended protrusions to comprise a midbody structure, a narrow intercellular bridge arose during cytokinesis, the final step of cell division. To explore this scenario, we examined the presence of cytokinesis-related proteins in these structures. Citron kinase (CITK), a protein carrying a coiled-coil domain that differentially dictates its subcellular localization and leads to proper midbody stabilization during cytokinesis, was detected in the close-ended AGO2 protrusions. CITK was primarily enveloped at the area called midbody ring (Figure 68a) that in the close-ended protrusions AGO2 signal is absent and thus depicted as “gap”. iPLA experiments of AGO2 and CITK demonstrated the accumulation of fluorescent spots to be restricted into the cytoplasm and almost absent along the intercellular bridge (Figure 68b). In contrast, Aurora B, the other critical cell-division kinase that is essential for the functional midbody architecture through CITK cross-regulation, exhibited a striking overlap with AGO2 (Figure 68c). The AGO2-Aurora strong correlation was also confirmed with the iPLA experiments (Figure 68d). Colocalization analysis (Figure 100e-h) and corresponding statistical tests strongly supported these findings (Table 8). In particular, the CITK-AGO2 pair exhibits low M2 value - proportion of CITK channel occupying pixels of the AGO2 channel - (M2=0.336) since CITK is primarily detected at the midbody ring whereat AGO2 is absent (Figure 100e). On the contrary, strong colocalization emerged between AGO2 and Aurora B (R=0.718, M1=0.889, M2=0.786), as Aurora B resided almost entirely along the intercellular bridge being occupied by AGO2 (Figure 68f). CITK and Aurora B demonstrated differential distribution, in complementary patterns, in the AGO2 close-ended cellular structures (Figure 68g). Finally, Dicer was primarily located at the midbody ring (Figure 69a-c), as indicated by the intensity plots (Figure 68h). The presence of CITK and Aurora B kinases in the AGO2 close-ended cellular structures revealed that these comprise cytokinetic protrusions.

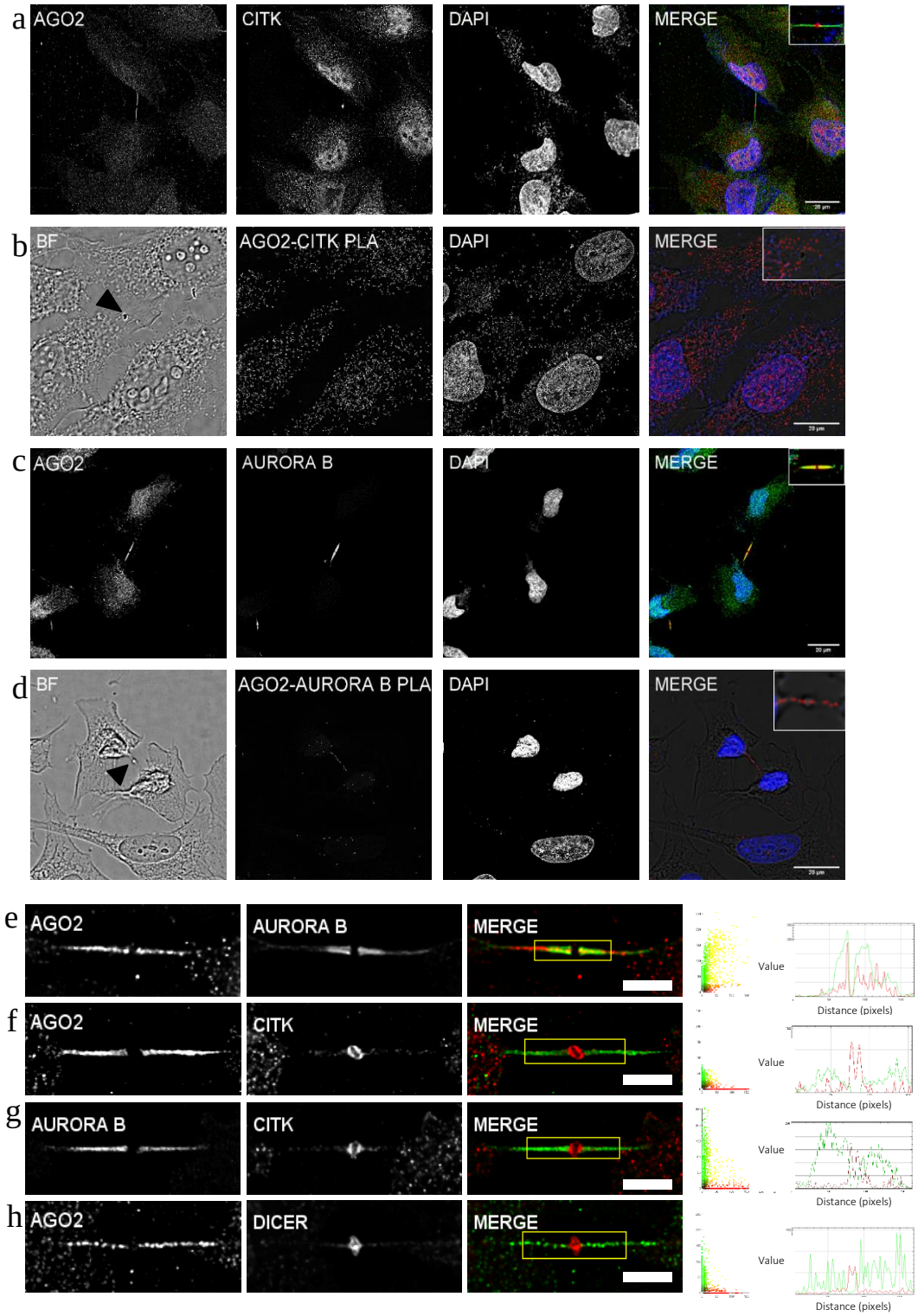
a
AGO2
CITK
DAPI
MERGE
b
BF
AGO2-CITK PLA
DAPI
MERGE
c
AGO2
AURORA B
DAPI
MERGE
d
BF
AGO2-AURORA B PLA
DAPI
MERGE
e
AGO2
AURORA B
MERGE
f
AGO2
CITK
MERGE
g
AURORA B
CITK
MERGE
h
AGO2
DICER
MERGE
Value
Distance (pixels)

Figure 68 AGO2 close-ended cellular structures are cytokinetic protrusions. Representative immunofluorescence images of NTHY ori 3-1 cells depicting the subcellular localization of AGO2 (green) with (a) Citron kinase (CITK) (red) and (c) Aurora B (red). Cell nuclei were stained blue (DAPI). (b,d) iPLA assays depicted the proximity of (b) AGO2-CITK and (d) AGO2-Aurora B as indicated by red foci. The black arrowheads in the Brightfield (BF) images indicate the midbody ring. The scale bar is 20μm. Visual assessment (merged images, scatterplots and intensity lineplots) of colocalization between paired proteins included in the yellow region of interest of the merged images. (f,h) AGO2 (green) with CITK and Dicer (red), respectively. (e,g) Aurora B in green with AGO2 and CITK in red, respectively. Lineplots indicate the signal intensity of the paired proteins along the lines overlaid on the corresponding images that appear in Figure 69d-h. The colocalization metrics (Pearson [R] and Manders' [M1 and M2] coefficients) and respective p-values are presented in Table 8 (n=6 biologically independent samples). Scale bar: 5μm.

Pairs for line plots		Pearson coefficient	Manders' coefficient	
		R	M1	M2
AGO2 - CITK	mean	0.126	0.221	0.336
	p-value	0.0007	0.0002	0.0007
AGO2 - AURORA B	mean	0.718	0.889	0.786
	p-value	8.00e-07	6.68e-07	4.62e-07
AURORA B - CITK	mean	0.172	0.323	0.461
	p-value	8.19e-06	9.43e-06	2.73e-05
AGO2 - DICER	mean	0.221	0.350	0.719
	p-value	0.0017	0.0007	0.0004
AURORA B - DICER	mean	0.233	0.342	0.593
	p-value	0.0181	0.0008	0.0004
AGO2 - αTUB	mean	0.770	0.786	0.958
	p-value	4.1e-08	1.36e-07	1.28e-09
AGO2 - PHALLOIDIN	mean	0.153	0.328	0.203
	p-value	0.0087	0.0099	0.0068
αTUB - PHALLOIDIN	mean	0.266	0.368	0.602
	p-value	0.0138	0.0096	0.0004
αTUB - DICER	mean	0.261	0.387	0.815
	p-value	0.0012	0.0006	3.15e-06

DICER - PHALLOIDIN	mean	0.077	0.291	0.148
	p-value	0.0088	0.0102	0.0306
PHALLOIDIN LAMIN A/C (non colocalized area)	mean	0.024	0.003	0.340
	p-value	0.0916	0.1257	0.0263

Table 8 Colocalization metrics (Pearson [R] and Manders' [M1 and M2] coefficients) and respective p-values of the paired proteins depicted in yellow ROIs in Figure 68e-h, Figure 70c-e, Figure 69a-c.

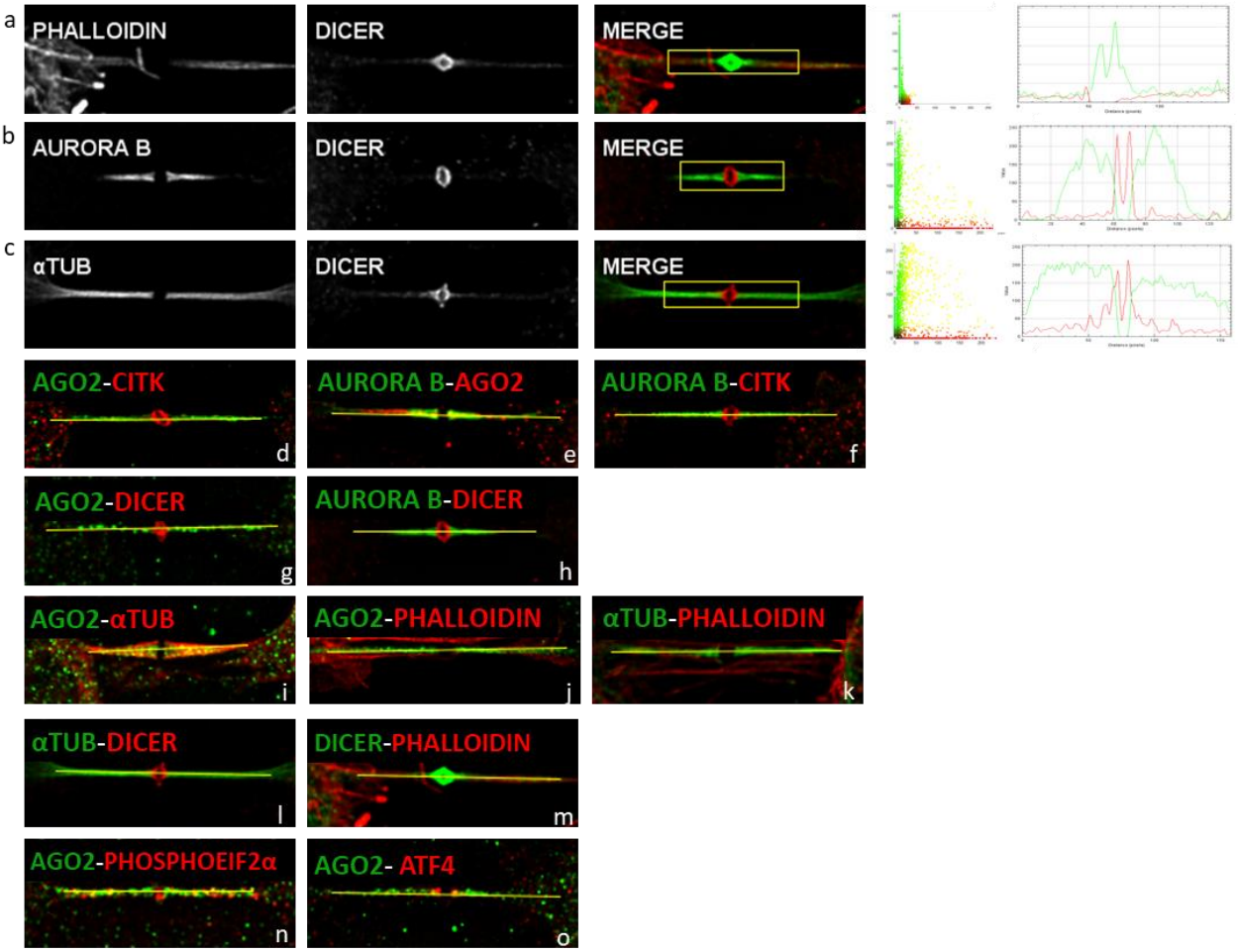

Figure 69 Colocalization analysis of the intercellular bridge content. (a-c) Representative images of NTHY ori 3-1 cells and visual assessment (merged images, scatterplots and intensity line plots) of colocalization. The colocalization metrics (Pearson [R] and Manders' [M1 and M2] coefficients) and respective p-values are presented in Table 8 (n=6 biologically independent samples). (d-o) Line plots indicate the signal intensity of Dicer and the paired protein along the lines. Line overlays on merged channels from all conditions shown in Figure 100e-h, Figure 102c-e, Figure 117e-f and Figure 101a-c used to obtain the corresponding line plots.

α-Tubulin alterations and cytoskeletal changes influence AGO2 localization.

Given that AGO2 appears to reside in cytokinetic protrusions, the possibility of a tight configuration with α-Tubulin polymers (microtubules) was investigated. Polymerized α-Tubulin was strongly colocalized with AGO2 in the emerged blebs of cytokinesis and it was absent from the ring of midbody formation (Figure 70a,c). This was also demonstrated through iPLA assays with multiple foci being observed along the midbody arms, but not at the midbody ring (Figure 70b). However, F-Actin (G-Actin polymer), the other fundamental cytoskeleton component, was presented with significantly lower degree of colocalization with AGO2 (Table 8). Actin filaments were mainly located close to the starting point of the protrusions and were attenuated along the intercellular bridge (Figure 70d,e). A representation of the distribution patterns of all the herein examined proteins (AGO2, Dicer, CITK, Aurora B, α-Tubulin and F-Actin) across the intercellular bridge, is illustrated in Figure 70f.

We further investigated the relationship of AGO2 with the two pivotal components of cytoskeleton, α-Tubulin and F-Actin, in a drug-induced depolymerization manner. To this end, Demecolcine and Cytochalasin D, specific inhibitors targeting the microtubule and Actin-filament depolymerization, respectively, were applied and their effects on cell morphology, AGO2 distribution and formation of cytokinetic and cytoplasmic protrusions were examined. After 5h of Demecolcine treatment α-Tubulin was not totally depolymerized across the intercellular bridges and AGO2 exhibited decreased signal intensity (Figure 71a,b). The midbody formation was not completely disrupted as indicated via the normal distribution of CITK (Figure 71c). Most importantly, after 7h of Demecolcine treatment, a depolymerization of intercellular bridges was induced as indicated by the disruption of α-Tubulin structures, with a similar fragmentation of AGO2 protrusions (Figure 71d,f,g). The AGO2 expression signal was directed towards the cytoplasm at lamellipodia and in membrane ruffles (Figure 71d). However, the localization profile of CITK clearly points towards an intact midbody ring formation (Figure 71e). In conclusion, AGO2 distribution is related to the intact polymerization of α-Tubulin, indicating that α-Tubulin can constitute a capable scaffold for AGO2 transfer and function (Figure 71f,g). Exposure to Cytochalasin D did not cause detectable changes in AGO2 typical distribution (Figure 72a,b,f,g). Nevertheless, Cytochalasin D prevented Dicer accumulation in the midbody and compelled, in some cases, its distribution along the AGO2 midbody arms (Figure 72c,d,h,i). Remarkably, the localization pattern of CITK remained unaffected, hence, indicating the specificity and component-selectivity of the drug-induced molecular phenotype (Figure 72e). Dicer-specific foci, frequently observed inside the cytoplasm and in the milieu, proved to serve as markers of midbody remnants after abscission completion (Figure 72c). It seems that the scattering of AGO2 and Dicer is likely dictated by different regulatory mechanisms.

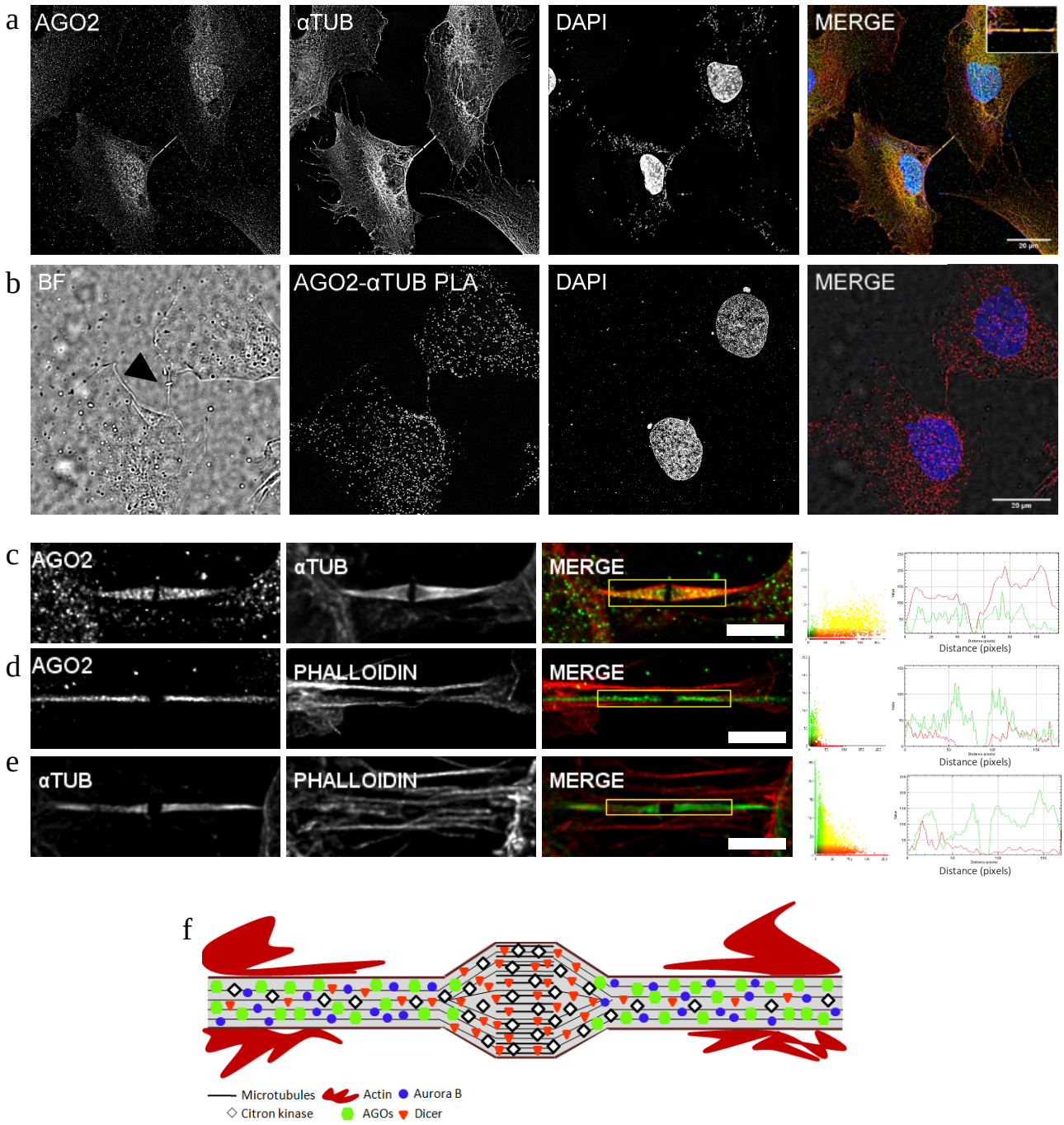

Figure 70 AGO2 colocalizes with α-Tubulin in mitotic protrusions. (a) Representative immunofluorescence images of NTHY ori 3-1 cells depicting the colocalization of AGO2 (green) with α-Tubulin (red). Cell nuclei were stained blue (DAPI). (b) iPLA assays demonstrated the high proximity of AGO2 and α-Tubulin by the presence of red foci. The black arrowhead in the BF images indicates the midbody ring. The scale bar is 20μm. (c-e) Visual assessment (merged images, scatterplots and intensity lineplots) of colocalization. Lineplots indicate the signal intensity of the paired proteins along the lines overlaid on the corresponding images that appear in Figure 69i-k. The colocalization metrics (Pearson [R] and Manders' [M1 and M2] coefficients) and respective p-values are presented in Table 8. (c,d) AGO2 in green, α-Tubulin and F-Actin (Texas red-phalloidin) in red. (e) α-Tubulin in green, F-Actin in red (n=6 biologically independent samples). (f) Diagrammatic representation of the components of the cytokinetic intercellular bridge including AGO2, Dicer, CITK, Aurora B, α-Tubulin and F-Actin. Scale bar: 5μm.

AGO2 follows the α-Tubulin cellular expression patterning during cell division.

As the strong correlation between AGO2 and α-Tubulin was already demonstrated, it is not surprising that AGO2 follows the α-Tubulin cytoskeleton distribution pattern during the different phases of cell cycle (Figure 73). In particular, in metaphase that is typified by chromosomes being aligned during central spindle assembly, AGO2 showed a dense cytoplasmic signal with the exception of the area in-between the chromosomes. However, AGO2 and Dicer immunofluorescent topologies, following the mitotic spindle, become concentrated at the mitotic poles (Figure 73a, Figure 74a). In anaphase, AGO2 was highly accumulated in the centrosomal area (Figure 73b), while Dicer followed the microtubule-segregation (Figure 74b). In this phase, the initial cue for cytoskeleton rearrangement, the creation of microtubule-bundling area called midzone, and the cleavage furrow ingression become readily recognizable. In telophase, AGO2-localization pattern demonstrated a "gap" in the middle of the midzone area, similar to the α-Tubulin configuration (Figure 73c). In parallel, Dicer was mainly located at the midbody ring (Figure 74c). The intercellular bridge starts its formation during late telophase, with a simultaneous compression of midzone and the development of microtubule midbody. AGO2 and Dicer reside in the intercellular bridge; during the process of stabilization of cleavage furrow ingression AGO2 formed a tight arrangement inside and along the α-Tubulin bridge (Figure 73d), while Dicer was mainly distributed around the ring and gradiently decreased inside the arms (Figure 74d). Then, the cleavage furrow begins the narrowing until the intercellular bridge is disintegrated and the two daughter cells are emancipated (Figure 73e, Figure 74e). Following the α-Tubulin constriction and abscission, AGO2 regressed towards the daughter cells following the midbody together with the arm-structure into the cell cytoplasm for autophagy-mediated elimination (Figure 73f). The Dicer-labeled midbody ring was digested from one cell in the case of asymmetric division or removed to the cell milieu in case of symmetric division (Figure 74f). Altogether, the AGO2 expression pattern during mitosis and its resemblance to the -polymerized- α-Tubulin respective one reinforces the notion that AGO2 sustains important roles in cell division.

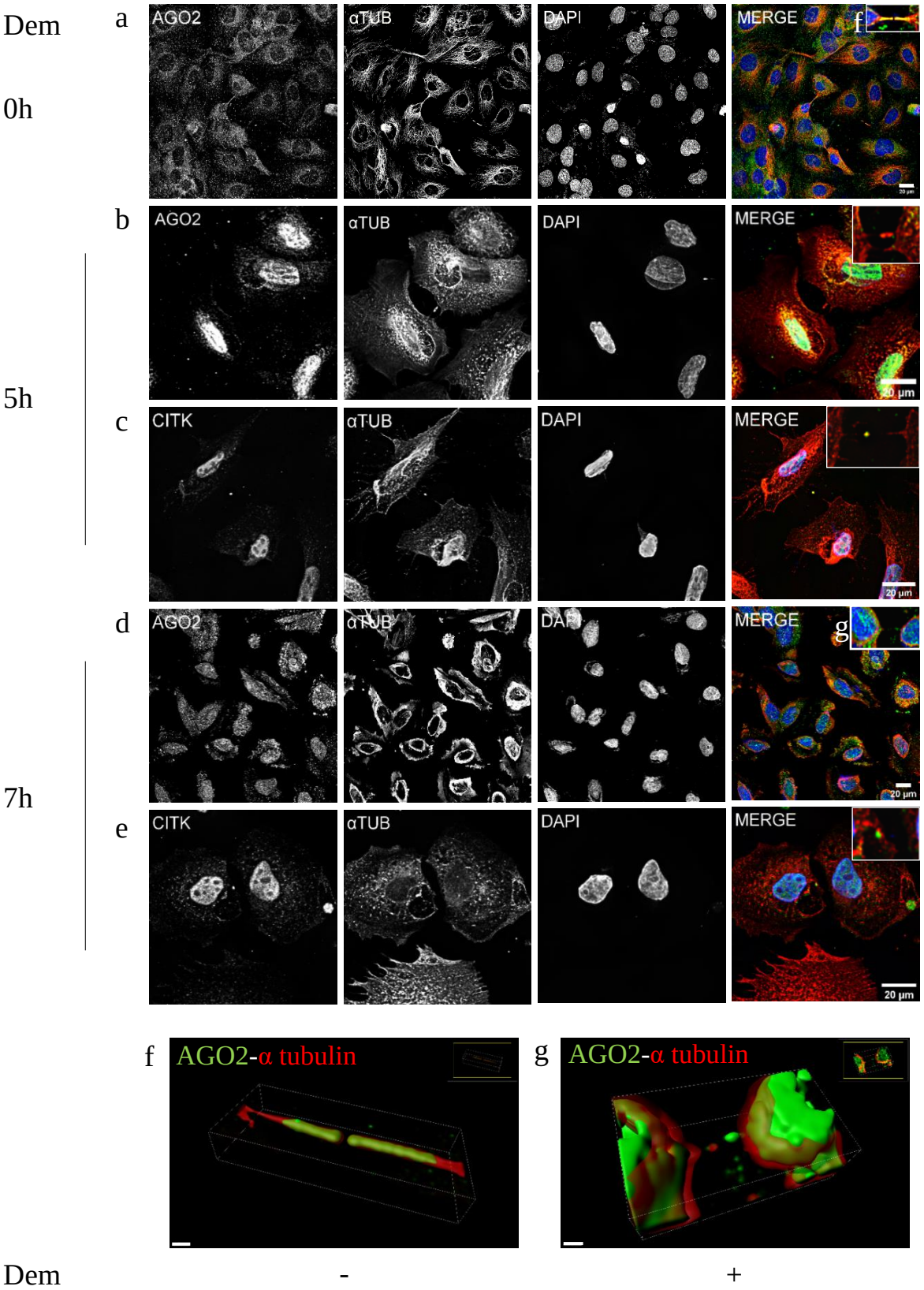

Figure 71 *α*-Tubulin alterations and cytoskeletal changes influence AGO2 localization. Representative images of NTHY ori 3-1 cells (a) before treatment with Demecolcine (Dem) and at (b,c) 5h and (d,e) 7h after treatment. (a,b,d,f,g) AGO2 was stained green, (a-g) *α*-Tubulin red and (c,e) CITK green. Nuclei of cells were visualized in blue (DAPI). The scale bar is 20μm. 3D surface reconstruction by Imaris of the cytokinetic bridges (f) before (scale bar: 15μm) and (g) after Demecolcine treatment (scale bar: 10μm).

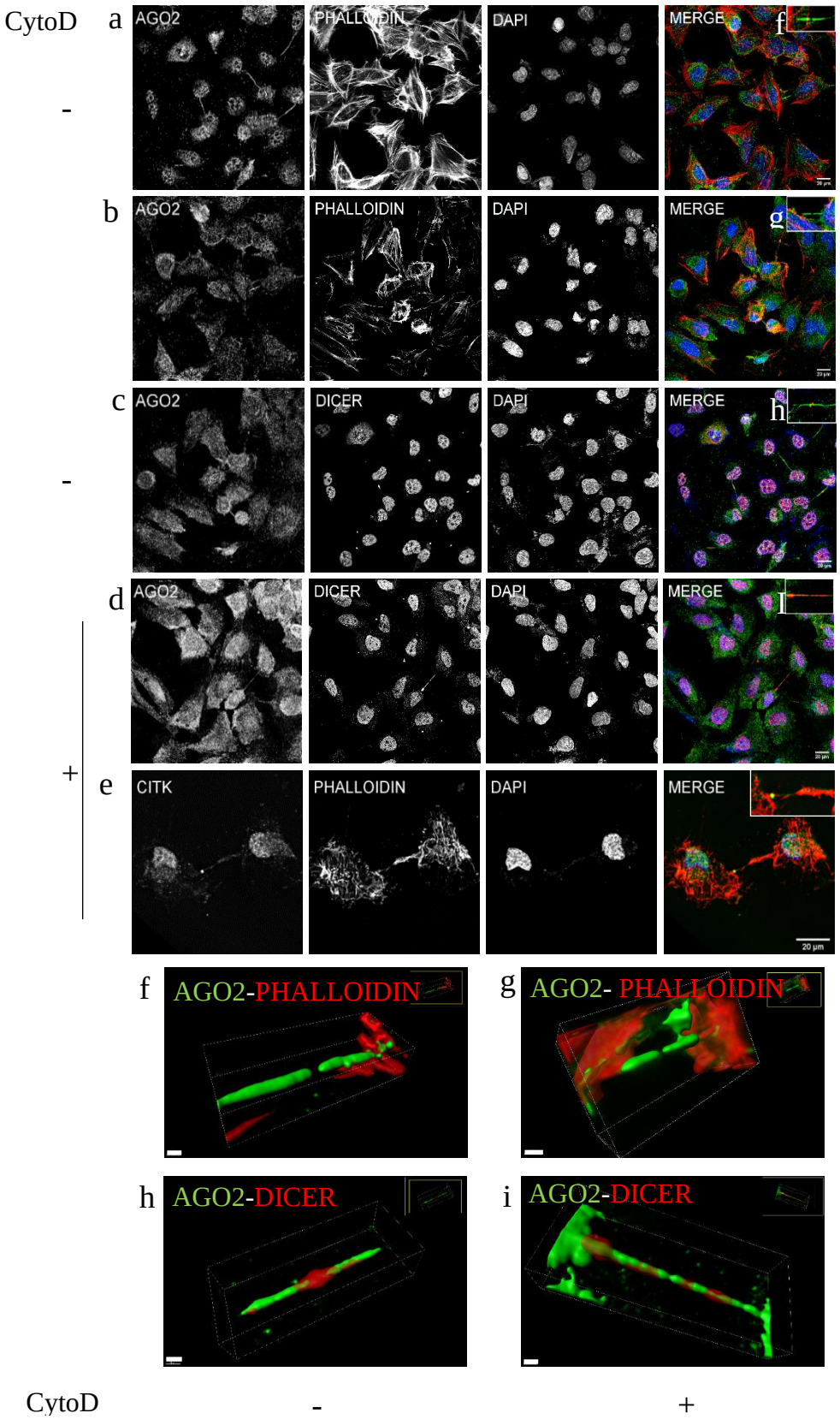

Figure 72 Dicer distribution associated with F-Actin. Representative images of NTHY ori 3-1 cells (a,c) before and (b,d) after Cytochalasin D (Cyto D) treatment. (a-d,f-i) AGO2 in green, (a,b,e-g) F-Actin in red, (c,d,h,i) Dicer in red and (e) CITK in green (scale bar: 20μm). Nuclei of cells were visualized by blue staining (DAPI). 3D-surface reconstruction by Imaris of the cytokinetic bridges (f,h) before (scale bar: 15μm) and (g,i) after Cyto D treatment (scale bar: 3μm and 10μm, respectively).

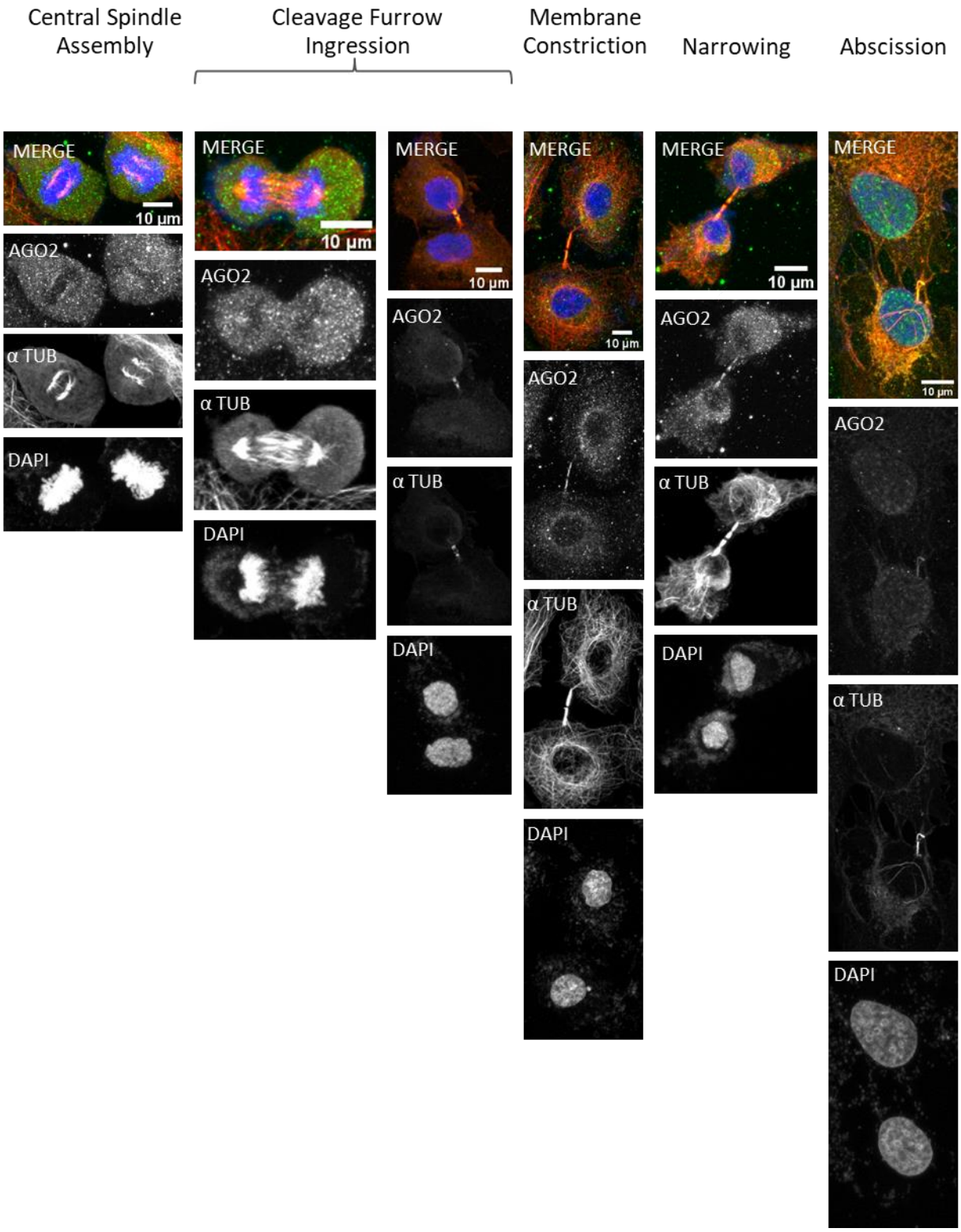

Figure 73 AGO2 distribution during cell division. Representative immunofluorescence images of NTHY ori 3-1 cells. AGO2 colocalization with α-Tubulin was visualized in a time-course manner. AGO2 in green. α-Tubulin in red and nuclei in blue (DAPI). Images depict (a) central spindle, (b,c) assembly cleavage furrow ingression, (d) membrane constriction, (e) narrowing and (f) abscission (scale bar: 10 μm).

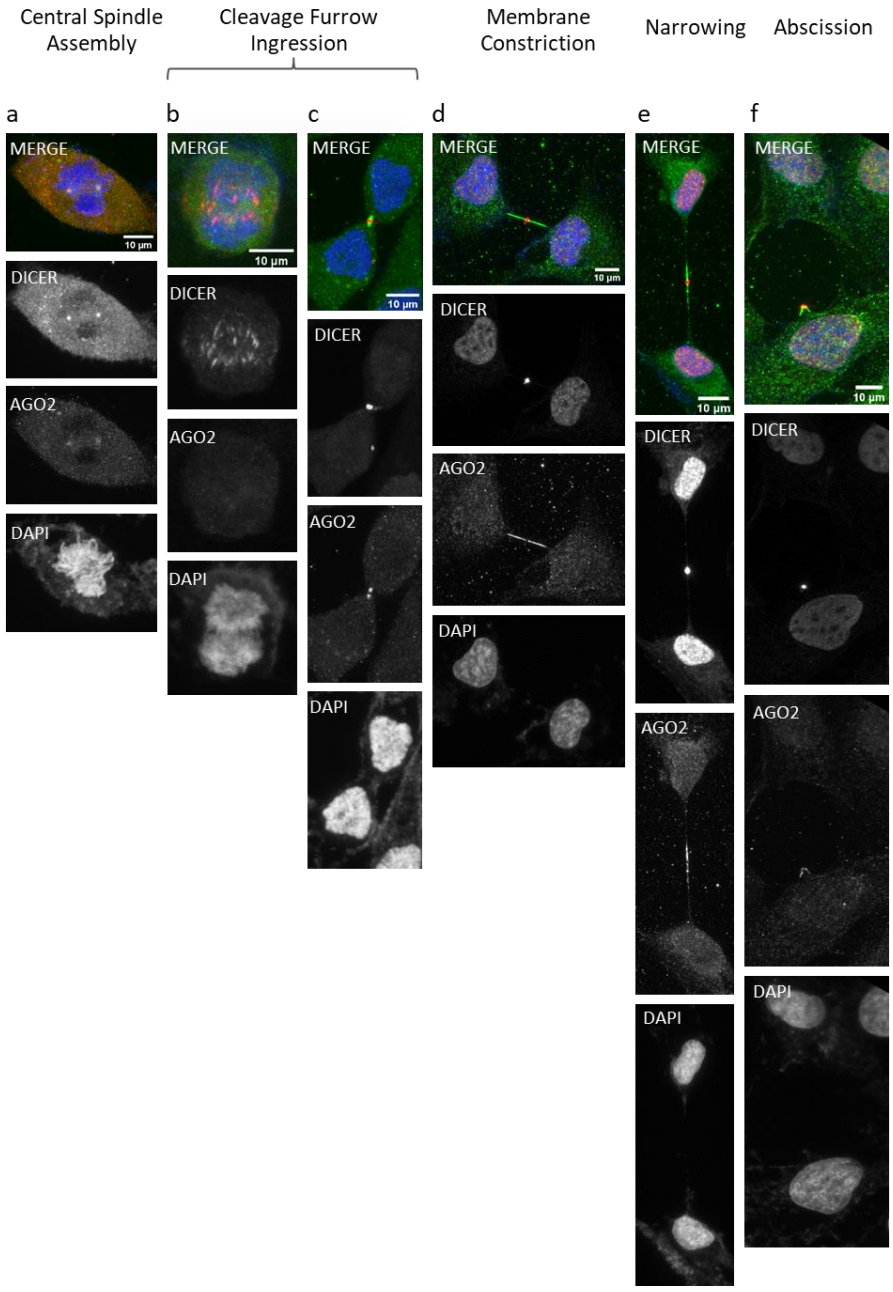

Figure 74 Dicer distribution pattern during cell division. Representative images of AGO2 and Dicer subcellular distribution in NTHY ori 3-1 dividing cells, was visualized in a time-course manner. Dicer in red, AGO2 in green and nuclei of cells in blue (DAPI). Images depict (a) central spindle assembly, (b,c) cleavage furrow ingression, (d) membrane constriction, (e) narrowing and (f) abscission (scale bar: 10 μm).

AGO2 over-expression generates aneuploidy via cytokinesis errors.

To further study the contribution of AGO2 to the fidelity of cell division, we examined the effect of over-expression and down-regulation of AGO2 in chromosome segregation. HCT116 cells were transfected to transiently express AGO2-GFP. The AGO2 over-expression induced statistically significant micronuclei formation (Figure 75a-d,m) and numerical chromosomal deregulation (gain or loss) (Figure 75m, 76a-c). However, although there were detected lagging chromosomes in anaphase and cytokinesis (Figure 75e-l), the percentage was similar to the control, an observation that needs further investigation. These

findings lead to the conclusion of AGO2 implication in aneuploidy, reflecting post-replicative events and cytokinesis errors. By knocking down AGO2 (almost 2-fold-changes) (Figure 76h, 77a) no statistically significant changes in numerical chromosomal deregulation and micronuclei formation were observed, but structural alterations emerged (Figure 76d-g). Cytokinesis-failure events such as binuclear cell formations and midbody abnormalities such as double midbody rings after AGO2 knock down were observed (Figure 76i-k) demonstrating that AGO2 influences the integrity and the succession of cytokinesis.

Interestingly, the knocking down of AGO2, by transfecting the cells with siAGO2, eventually affected the expression levels of the other AGO family members (Figure 77). In general, AGO2 demonstrated the highest expression in comparison with other AGOs, followed by AGO1 and then by AGO3. Moreover, although AGO1 and AGO2 expression appeared to be unaffected 24 hours siAGO2 post-transfection, they demonstrated a downregulation at 48 hours. The same expression pattern was also observed when primers were used to amplify all AGO members. Transfected cells with siAGO2 display 2fold-change AGO2 knocked down as measure by PCR. However, the protein levels appeared to further affect as demonstrated using immunofluorescence confocal imaging (Figure 78). AGO4 is expressed in lower lever when compared to the other AGOs. Probably the most interesting observation though was that there was a subsequent 2fold-change AGO4 increase both at 24- and 48-hours post-transfection. This finding is leading to the suggestion of a compensatory role of AGO4 in AGO2 depletion.

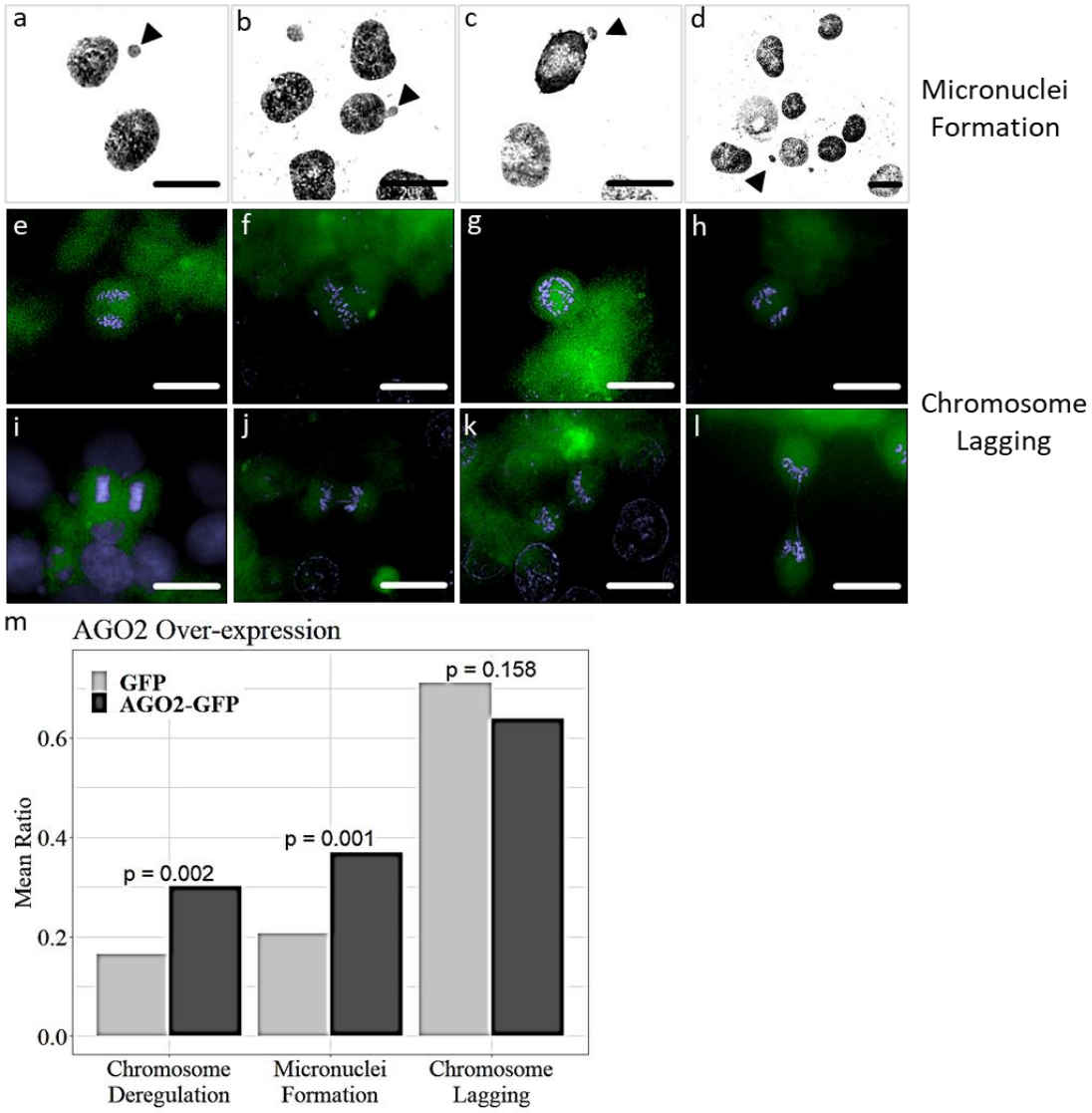

Figure 75 AGO2 over-expression leads to numerical chromosomal instability and micronuclei formation. (a-d) Representative images of HCT116 AGO2-GFP transfected cells depicting (a,c,d) micronuclei formations and (b) bleb nuclei, as indicated by the black arrowheads. (e,i) normal anaphase and cytokinesis. AGO2-GFP transfected cells carry (f) abnormal metaphase congression, (g) anaphase or (j) cytokinetic chromosomal bridges and (h) lagging chromosomes in telophase or (k,l) in cytokinesis. GFP expression in green and nuclei in blue (DAPI) (scale bar: 10μm). (m) Bar plot of the effects of AGO2 over-expression on numerical chromosome deregulation, micronuclei formation and lagging chromosomes. z-test was used to evaluate their significance. Bar height indicates the ratio of deregulated chromosomes (n=3 biologically independent experiments, statistical sample size n1=188 GFP cells, n2=182 AGO2-GFP cells), cells with micronuclei formation (n=3 biologically independent experiments, statistical sample size n1=174 GFP cells, n2=168 AGO2-GFP cells) and with lagging chromosomes (n=3 biologically independent experiments, statistical sample size n1=176 GFP cells, n2=169 AGO2-GFP cells), respectively.

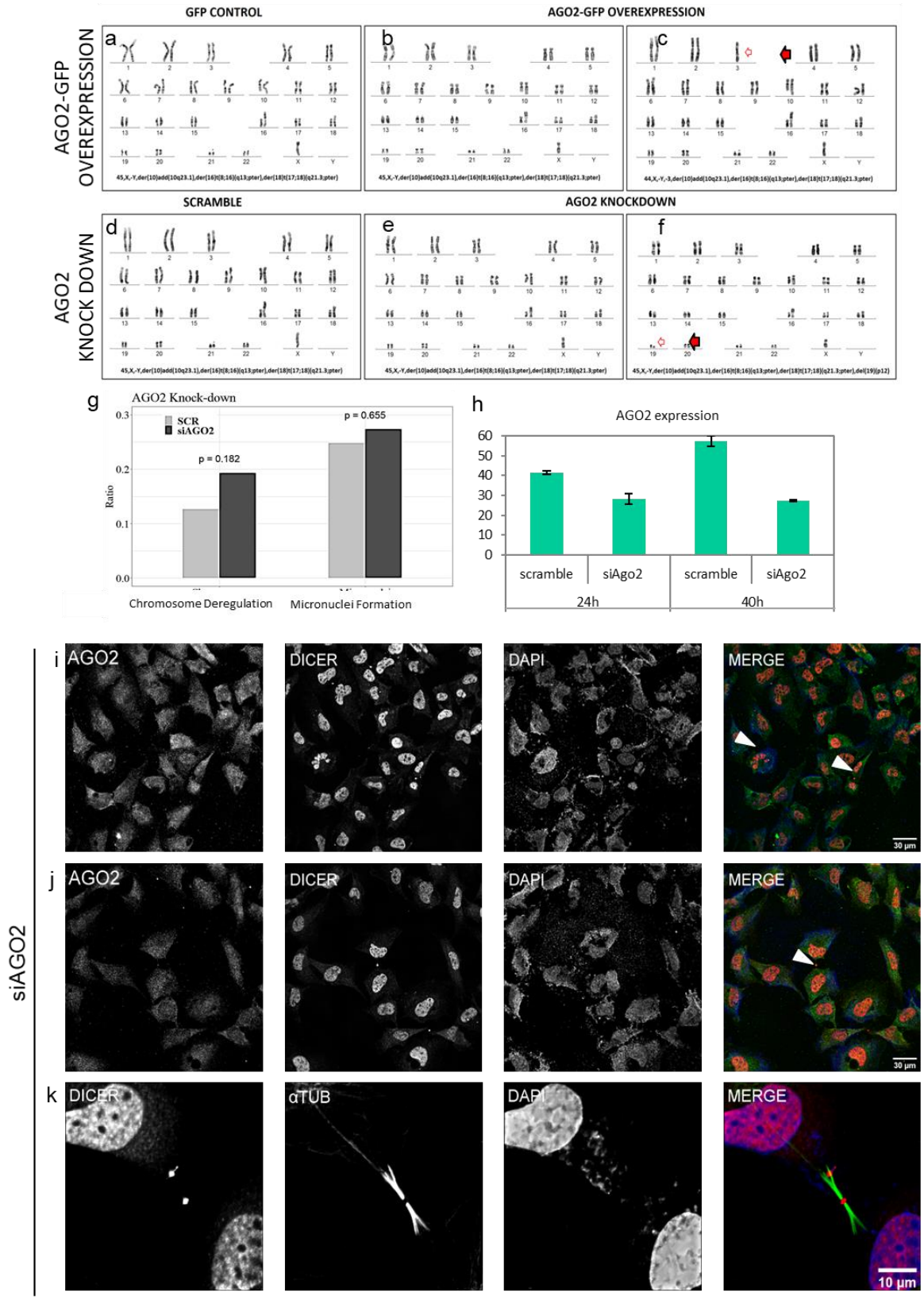

Figure 76 AGO2 over-expression and down-regulation effect on cell division. Karyotypes of HCT116 (a) GFP-control cells and (b,c) AGO2-GFP over-expressing cells. Karyotypes of HCT116 (d) cells transfected with scramble control and (e,f) AGO2-knocked down cells. (g) Bar plot of the effects of AGO2 down-regulation in HCT116 cells on numerical chromosome instability and micronuclei formation. z-test was used to evaluate their significance. Bar height indicates the ratio of deregulated chromosomes (n=2 biologically independent experiments, statistical sample size n1=103 SCR cells, n2=114 siAGO2 cells) and cells with micronuclei formation (n=2 biologically

independent experiments, statistical sample size n1=117 SCR cells, n2=117 siAGO2 cells), respectively (h) Bar plot indicates AGO2 expression levels in 24 and 40h following siAGO2 transfection determined by quantitative PCR analysis. (i-k) Representative images of NTHY ori 3-1 AGO2 knocked-down cells. White arrowheads indicate abnormalities such as (i) abnormal nucleus (scale bar: 30 μm), (i,j) intercellular bridge (scale bar: 30 μm) and (k) double midbody ring (scale bar: 10 μm). (i,j) AGO2 and (k) α-Tubulin in green and (i-k) Dicer in red. Nuclei in blue (DAPI).

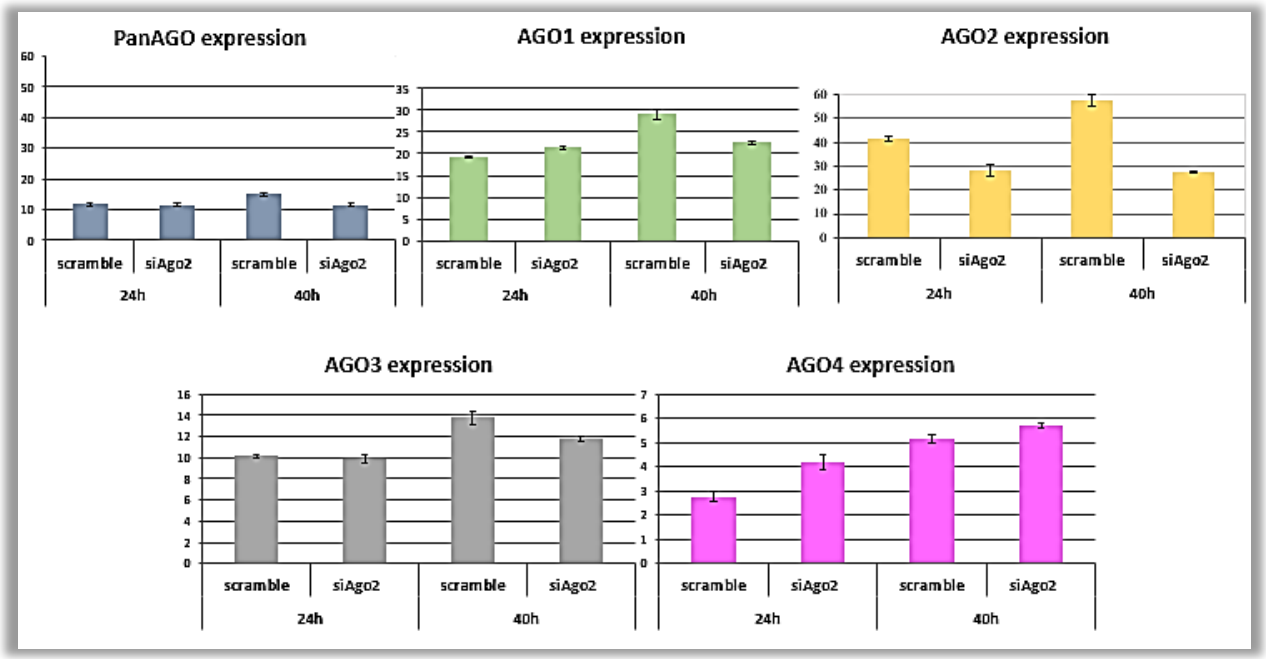

Figure 77 AGO2 mRNA expression levels were knocked down AGO2 almost 2-folds after siAGO2 treatment. The cells were transfected with siAGO2 and the RNA was extracted and the expression was measures 24 and 48 hours after the transfection. Primers, for QPCR screening, were designed to bind either on all members of AGO family (AGO1-4) or recognize a specific AGO (AGO1, 2, 3 or 4). As control a scrambled mixture was used.

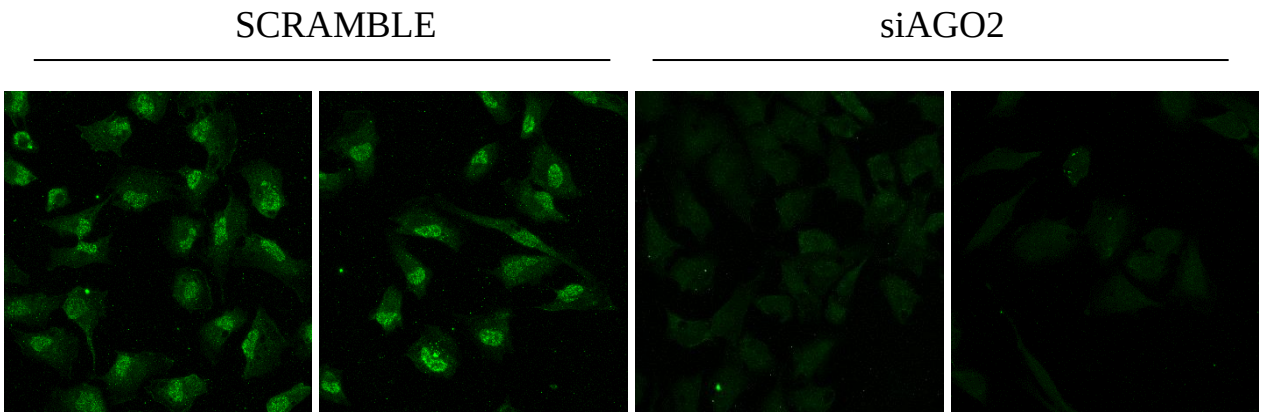

Figure 78 Representative images of NTHY ori 3-1 cells following transfection with scramble or siAGO2. In the siAGO2 cells the signal intensity of AGO2 is dramatically decreased in 24 hours compared to the scrambled ones.

AGO2 colocalizes with Lamin A/C and DNA damage response components.

We were aware from the literature that Lamin is suggested to be a requirement for a reinforcement of the spindle envelope, which supports the formation of central spindle microtubules also essential for cytokinesis succession (Hayashi et al., 2016). Interestingly, our observations advocate in this

direction. The colocalization of Lamin A/C and Lamin A/C remnants together with AGO2, across the open-ended (Figure 79a) and close-ended tubes (Figure 79b,c) respectively, demonstrating that parts of the nuclear membrane probably together with additional chromosomal material from previous or current cytokinesis failures colocalize with AGO2 for local regulation of gene expression. In detail, we showed that Lamin A/C has an intense signal across the nuclear membrane. Inside the open-ended tubes, we showed cyclic structures with Lamin and probably they were moving into the communication channel that is formed from the tube and is filled with AGO2. In case of close-ended tubes, besides the signal of DAPI across the cytokinetic bridge which indicate the presence of dsDNA that exist either from the mitochondrial network or from nuclear DNA that travels, there are Lamin remnants especially in the final step of abscission (Figure 79c). This phenomenon is not universal, however wherever exists there is a continuous signal till the abscission point. Lamin A/C is appeared in structures called micronuclei which include a small number of chromosomes after a cytokinesis failure. We observed that AGO2 distribution faithfully follows Lamin A/C distribution across the intercellular bridge either during normal cytokinesis or in cytokinesis failure.

Notably, it has already been reported that Lamin A/C in cinjunction with TRF2 on chromosome structure during cell division (Wood et al., 2014).

TRF1 and TRF2 fundamental components of the telomere nucleoprotein complex, present at telomeres throughout the cell cycle and with the functional role of a telomerase inhibitor, together with BRAC1, are known to have an implication in telomere length homeostasis for preventing the telomere dysfunction and therefore, the chromosomal instability, were found strongly colocalized with AGO2 (Figure 80a,b,c). In most cases, BRAC1 seems to reside gradiently across the cytokinetic bridge and it has a higher concentration in the tips of midbody arms. The localization of AGO2 is uniform without fluctuations across the bridge. However, both proteins have a strong visual colocalization. Even more intense is the colocalization between AGO2 with TRF1 and TRF2 into the nucleus, in the cytoplasm and across the intercellular bridges indicating that AGO2 may interact with these key molecules. Also, we had the knowledge of a negative interplay between Aurora A/B and BRCA1/2 inversely controls the cell proliferation, cell cycle progression, cell multinuclearity, and tetraploidization to modulate tumorigenesis (Y. Wang et al., 2014). Aurora B, in our settings, has a similar distribution across the bridges with AGO2, TRF1 and TRF2.

The exact mechanisms whereby decreased *BRCA1* expression can lead to uncontrolled anchoring of microtubules to the kinetochore are still unclear. The consequences of these abnormalities on the normal events needed to ensure proper homeostasis during mitotic progression are also incompletely understood. Aurora B might be especially affected by the dysregulation in microtubule anchoring associated with deficiencies in BRCA1, as one of its functions includes correction of abnormal attachments to the kinetochores (Austria et al., 2018). These results illustrate the implication of AGO2 together with crucial molecules in fine-tuning chromosomal regulatory mechanisms, safeguarding the cell division and therefore, the chromosomal segregation success.

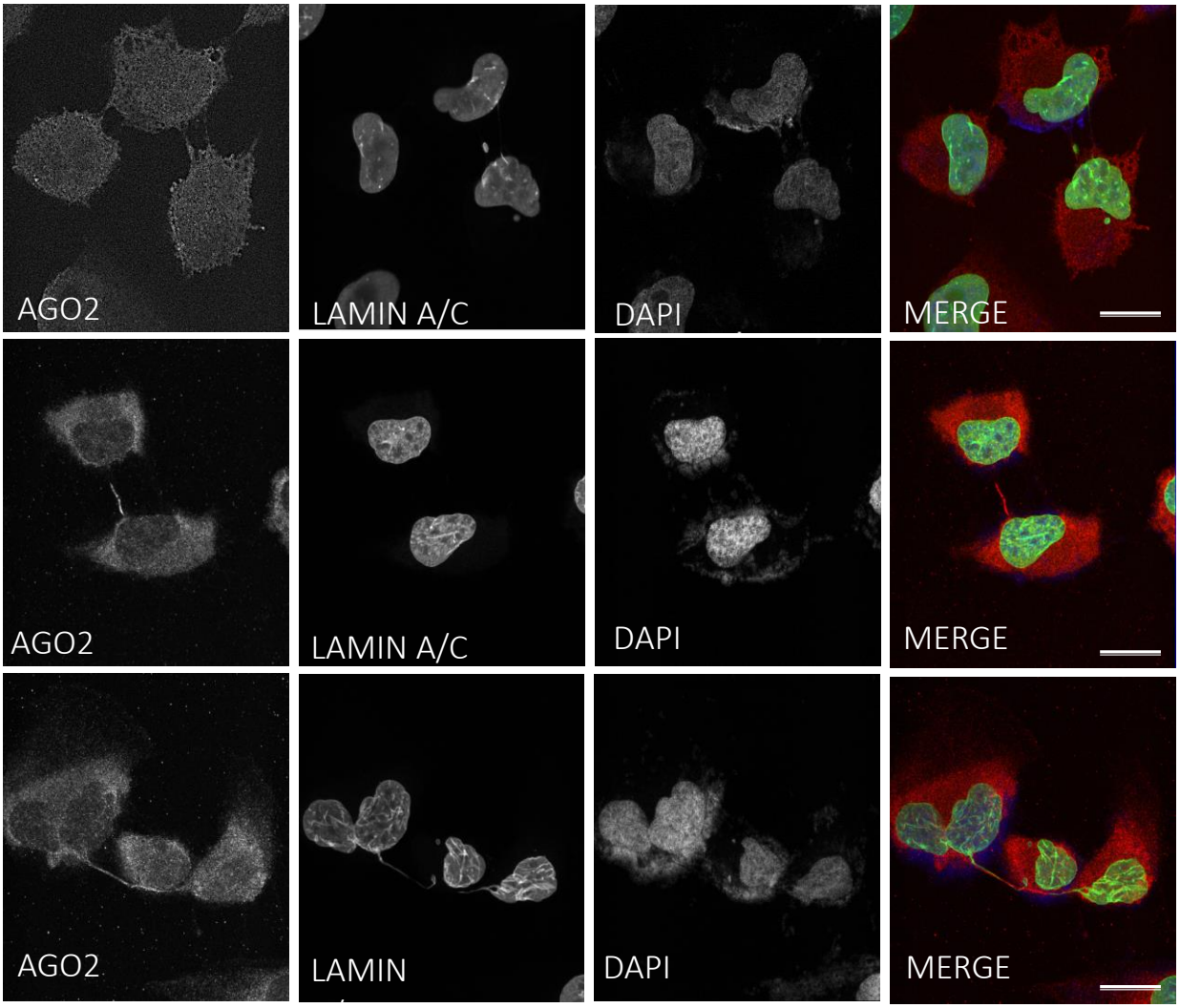

Figure 79 Representative images of NTHY ori 3-1 cell line. Colocalization between Lamin A/C and AGO2. Lamin A/C (a) across an open-ended tube (remnants) and across cytokinetic bridges (b,c) with intact lamin signal into nuclei (b) and lamin remnants across the cytokinetic bridge. AGO2 stained in red, Lamin A/C stained in green and nuclei stained in blue.

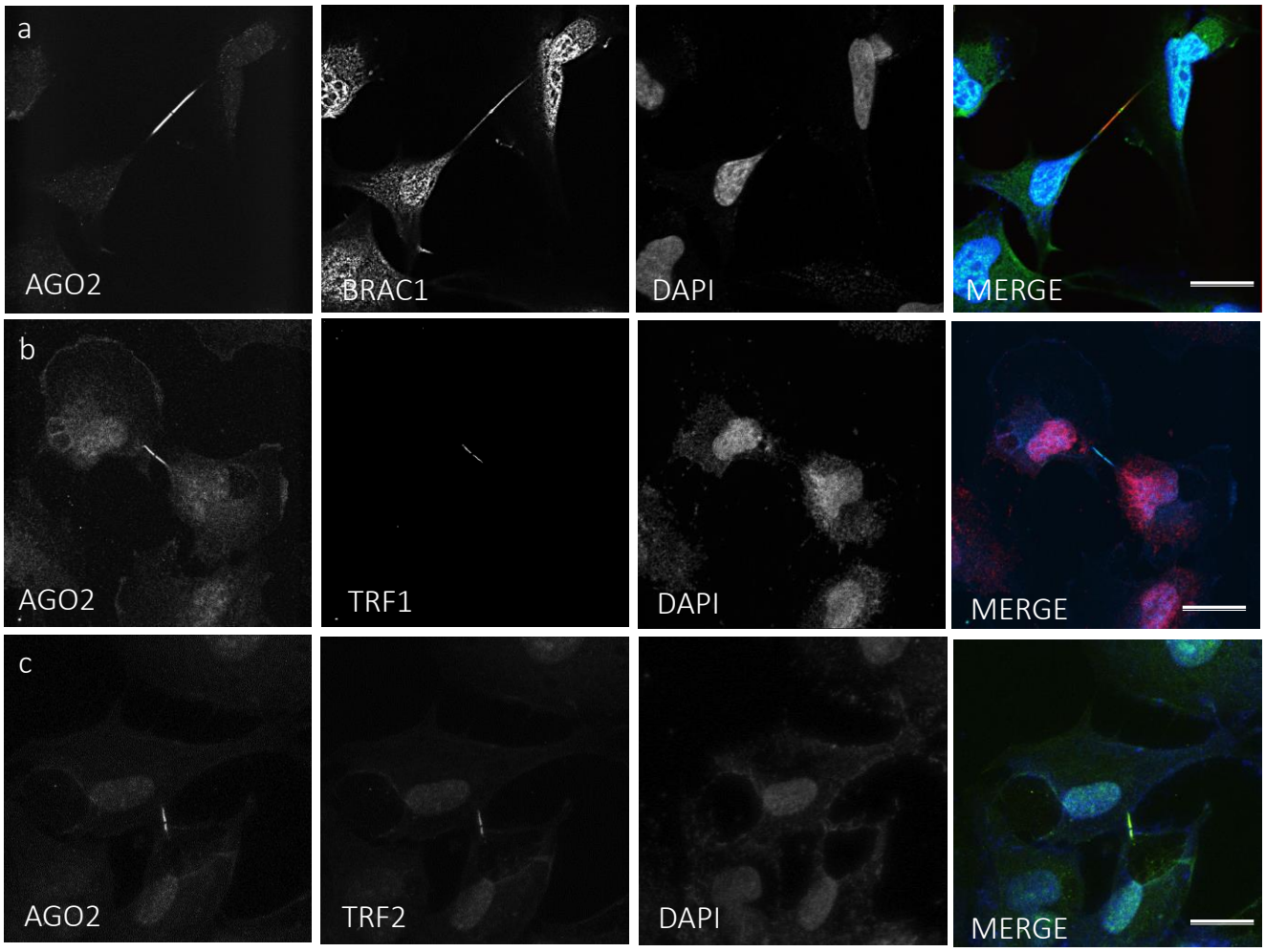

Figure 80 Representative images of NTHY ori 3-1 cell line. Colocalization between AGO2 and (a) BRAC1, (b) TRF1, (c) TRF2. AGO2 stained in red (AGO2-BRAC1) or green (pairs AGO2-TRF1, AGO2-TRF2), TRF1 and TRF2 stained in green, BRAC1 stained in green and nuclei stained in blue.

Kinases follow the AGO2/Dicer distribution in the midbody structure.

The role of AGO2 in the midbody might be an unrecognized contribution to cell division or related to a function of the known -typical- AGO2 pathway. In an attempt to distinguish between the two scenarios and better understand AGO2 involvement, we herein investigated the presence of poly-A^+ tailed transcripts along the cytokinesis bridge (Figure 81a). Surprisingly, the hybridization (oligo dT) probe followed the AGO2 pattern. This finding together with the complementary Dicer distribution pattern indicated a Dicer-independent AGO2 function in the arms of the midbody structures.

However, as the lack of AGO2 detection from the midbody ring was striking, we further investigated the possibility that post-translationally modified AGO2 protein molecules also resided at this site. Phosphorylation is a crucial regulation step of AGO2 activation and therefore, we explored the occurrence of different activated kinases in the cytokinetic bridge during the late steps of cell division.

Then, we performed colocalization analysis in order to examine any correlation/association between AGO2 and the kinases and phosphorylated kinases in subcellular level across the intercellular bridge.

Colocalization analysis of a small kinome including phospho-MEK (Figure 81b), phospho-ERK (Figure 8c), phospho-p38 MAPK (Figure 81d), phospho-JNK (Figure 81e), phospho-Akt (Figure 82a), phospho-AMPK (Figure 82b) showed that there are two distinct, almost complementary to each other, patterns in the cytokinetic structure.

Phospho-MEK, -ERK, -p38 and -JNK, although being present along the midbody arms, were highly concentrated at the ring following Dicer's distribution, while phospho-Akt (Figure 82a) and phospho-AMPK (Figure 82b) occupied the cytokinetic protrusions leaving a small "gap" at the midbody ring resembling the AGO2 pattern. The specificity of these distribution patterns is enhanced by the fact that other cell cycle-specific kinases such as Phospho-CHK2 were absent across the cytokinetic bridge (Figure 78b). Due to the midbody distribution of phospho-MEK/ERK/p38/JNK and the fact that the p38 MAPK pathway enhances the phosphorylation of AGO2 at the catalytic residue Serine ^{387}, we investigated the presence of phospho-AGO2 Ser^{387} in the midbody. Interestingly, the phospho-AGO2 Ser^{387} follows the phospho-MEK/ERK/p38/JNK pattern, exhibiting high concentration in the midbody ring (Figure 81f). To strengthen the p38-dependent AGO2 phosphorylation in the bridge, we treated the cells with SB203580, a selective inhibitor of p38 MAPK. Indeed, the phospho-AGO2 Ser^{387} was relocated in a number of cytokinetic bridges, moving from the ring to the arms of the midbody (Figure 81g,h). In conclusion, the phospho-AGO2 Ser^{387} is located in the ring of the midbody in a p38 MAPK-dependent manner. The presence of Dicer in the same locus suggests an active RISC machinery in a non-expected location, thus implying an alternative function of the complex during cell division.

.

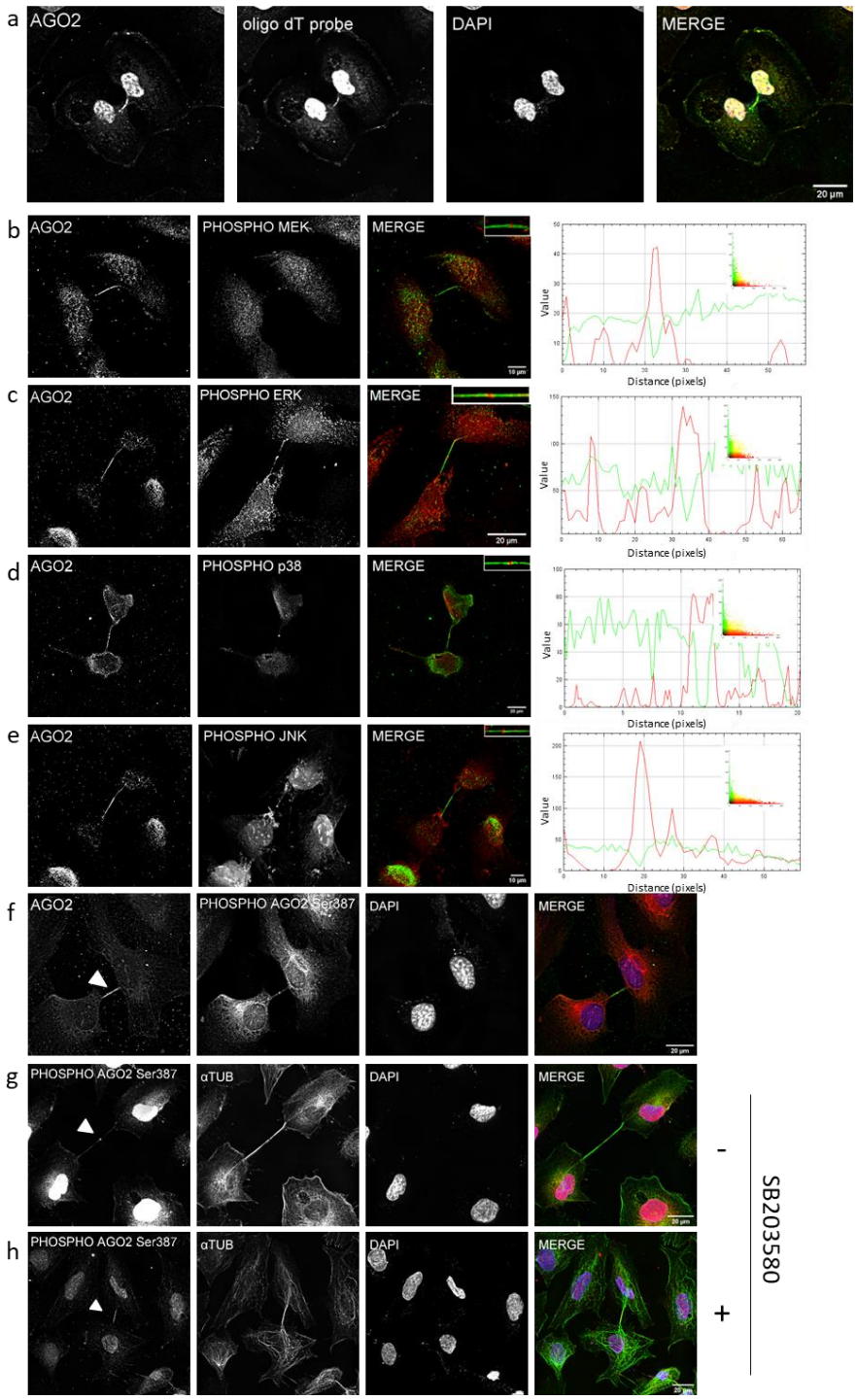

Figure 81 Activated kinases follow the AGO2/Dicer distribution in the midbody structure. Representative images of NTHY ori 3-1 cells. AGO2 colocalization with (a) biotinylated oligo dT probe (scale bar: 20μm). Small kinome analysis of (b) AGO2-phospho-MEK (scale bar: 10μm), (c) AGO2-phospho-ERK (scale bar: 20μm), (d) AGO2-phospho-p38 (scale bar: 20μm), (e) AGO2-phospho-JNK (scale bar: 10μm). (a-e) AGO2 proteins were visualized in green, oligo dT probe, phospho-MEK, phospho-ERK, phospho-p38 and phospho-JNK were visualized in red. (b-e) Visual assessment (merged images, scatterplots and intensity lineplots) of colocalization. (b-e) Lineplots indicate the signal intensity of the two paired proteins. Images of AGO2 colocalization with (f) phospho-AGO2 Ser387 and phospho-AGO2 Ser387 with α-Tubulin in (g) untreated and (h) treated cells with SB205380 p38 inhibitor. (f-h) Phospho-AGO2 Ser387 in red, (f) AGO2 and (g,h) α-Tubulin in green, respectively. Nuclei were visualized in blue (DAPI). Scale bar: 20μm.

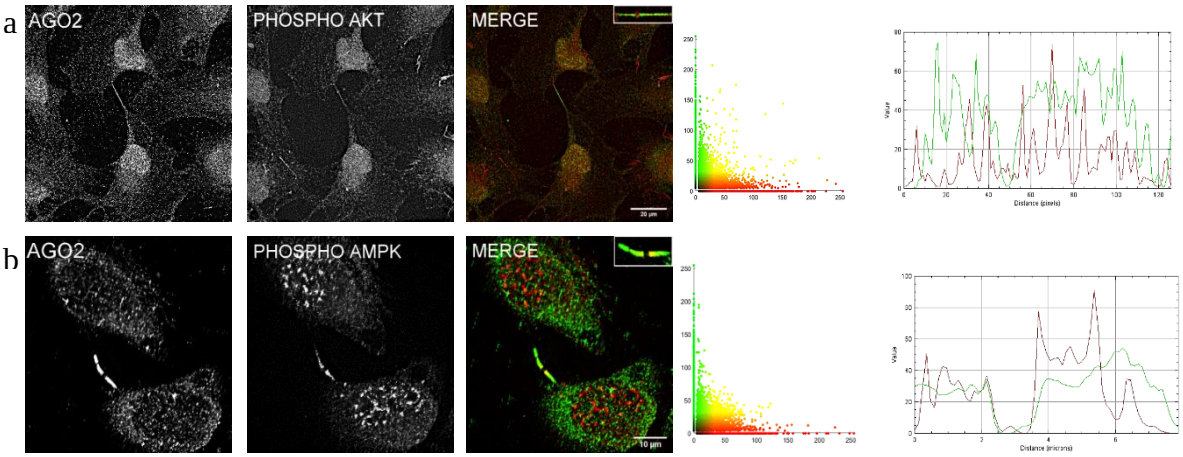

Figure 82 Phospho-Akt and phospho-AMPK kinase profiling follow the AGO2 distribution in the midbody structure. Representative images of NTHY ori 3-1 cells. (a) AGO2 (green) and phospho-Akt (scale bar: 20 μm), (b) AGO2 (green) and phospho-AMPK (red) (scale bar: 10 μm). Nuclei in blue (DAPI). Visual assessment (merged images, scatterplots and intensity lineplots) of colocalization. Lineplots indicate the signal intensity of the two paired proteins.

AGO2 is a stress-sensitive molecule.

The above findings support the strong implication of AGO2 in successful cell division. The dividing cells are known to be under tremendous stress (Mohan et al., 2012) a finding corroborated by the existence of the abovementioned phospho-kinases locally. As the role of kinases in mechanical stress has been previously reported (Mourouzis et al., 2013), the presence of several activated kinases in the midbody/midzone area is likely associated with the development of locally applied stress, during late cell division. To support this, we conducted TEM and SEM high-resolution technologies. A proteinaceous electron-dense material was observed at the midzone of microtubule bundles with the typical distance being highly varied (Figure 83a-g). In SEM images, light-colored, electron-dense material was apparent (Figure 83c,d). This material, likely containing molecular cargoes and proteins, circuited at the protrusions providing views of rough surfaces (Figure 83e). When abscission occurs (Figure 83f,g) the midbody is withdrawn and uptaken/fused with one daughter cell for digestion. Notably, dividing cells did not carry filopodial protrusions anti-diametrically of the intercellular bridge (Figure 83f), indicating that during the exertion of mechanical forces -polymerized- α-Tubulin and F-Actin cytoskeleton, together with membrane depositions, are rearranged for the formation of midzone arms and midbody ring. After abscission mitotic arm protrusions become contracted (Figure 83f) and vesicle inventories (Figure 83h) are conspicuous, probably for membrane deposition and remodeling. Immunogold experiments demonstrate the co-existence of Dicer and AGO2 molecules across the abscised intercellular bridge (Figure 83m). We used two different-sized gold particles, AGO2 10nm and Dicer 15nm and they found to be in proximal position across the intercellular bridge. Since the dividing cells are under tremendous stress and AGO2 appeared to carry a functional role in cell division, we reasoned that AGO2 is a stress sensitive molecule. Indeed, heat shock treatment malformed or abolished AGO2 close-ended protrusions (Figure 83i-l). The finding was strengthened by noteworthy changes in colocalization of AGO2 with the stress-related proteins, Upf1 and TIAR. In particular, under local basal stress, Upf1 and TIAR proteins were detected at the midzone area and their granules were weakly co-

localized with AGO2 protein (Figure 83i,k). After heat shock, the AGO2 foci were co-localized with Upf1 stress granules and the malformed cytokinetic bridges, wherever they developed, demonstrated a strong colocalization pattern with the Upf1 and TIAR respective ones (Figure 83j,l). These findings supported the stress sensitive nature of AGO2 that was accompanied by cytokinesis failure events.

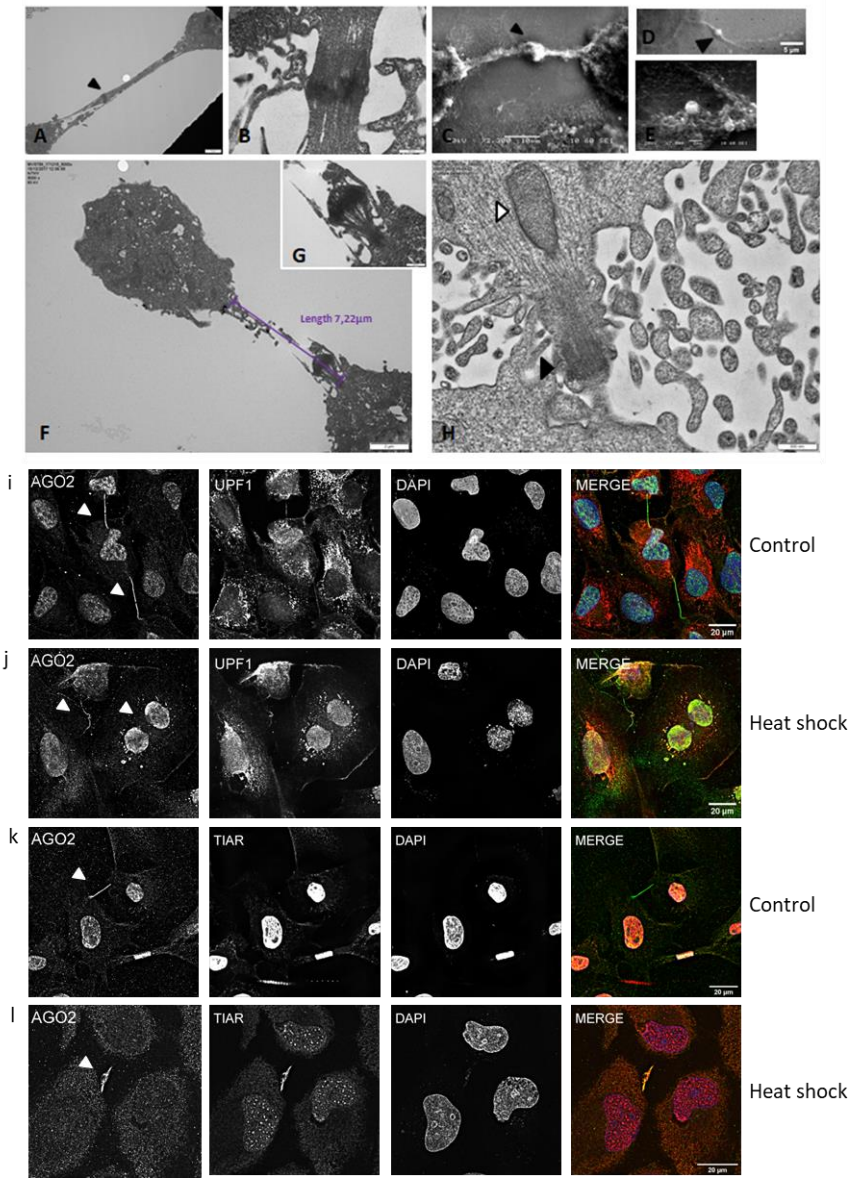
A
B
C
D
E
F
G
H
Length 7,22μm
i
AGO2
UPF1
DAPI
MERGE
Control
j
AGO2
UPF1
DAPI
MERGE
Heat shock
k
AGO2
TIAR
DAPI
MERGE
Control
l
AGO2
TIAR
DAPI
MERGE
Heat shock
m
MV10253_190808_23000x
08/08/2019 16:17:06
Ago 10nm
Diser 15nm
23000 x
60 kV
500 nm

Figure 83 AGO2 is a stress sensitive molecule. Electron microscopy images of the stages of cell division of NTHY ori 3-1 cells depicting the cytokinetic structures up to abscission. (a,b,f-h) Section transmission electron micrographs and (c-e) scanning electron micrographs of dividing cells. (a) Dense bundled microtubules (black arrowhead) in the midzone and (b) a magnified midzone. (c,d) The midbody core and the electron-dense material (flemming body) concentrated at the midzone. (e) Cargoes are transferred through the microtubule protrusions. (f,g) A discontinued intercellular bridge between two daughter cells after abscission. The nucleus of the left-hand cell is visible. (g) A magnified abscission point. (h) The characteristic structural architecture of microtubular axoneme after the completion of abscission (black arrowhead). Membrane deposition is pictured by the black arrowhead. Scale bars: (a) 2 μm, (b) 500 nm, (c) 10 μm, (d) 5 μm, (e) 2 μm, (f) 2 μm, (g) 500 nm and (h) 500 nm. (i-l) Representative images of NTHY ori 3-1 cells before and after heat shock. AGO2, Upf1 and TIAR subcellular distribution in (i,k) control and (j,l) heat-shocked cells. AGO2 is represented in green, Upf1, TIAR in red and nuclei in DAPI (blue). The white arrowheads indicate cytokinetic events (scale bar: 20μm), m: abscission point with immunogold by using two different-sized gold particles, AGO2 10nm and Dicer 15nm, scale bar: 500nm.

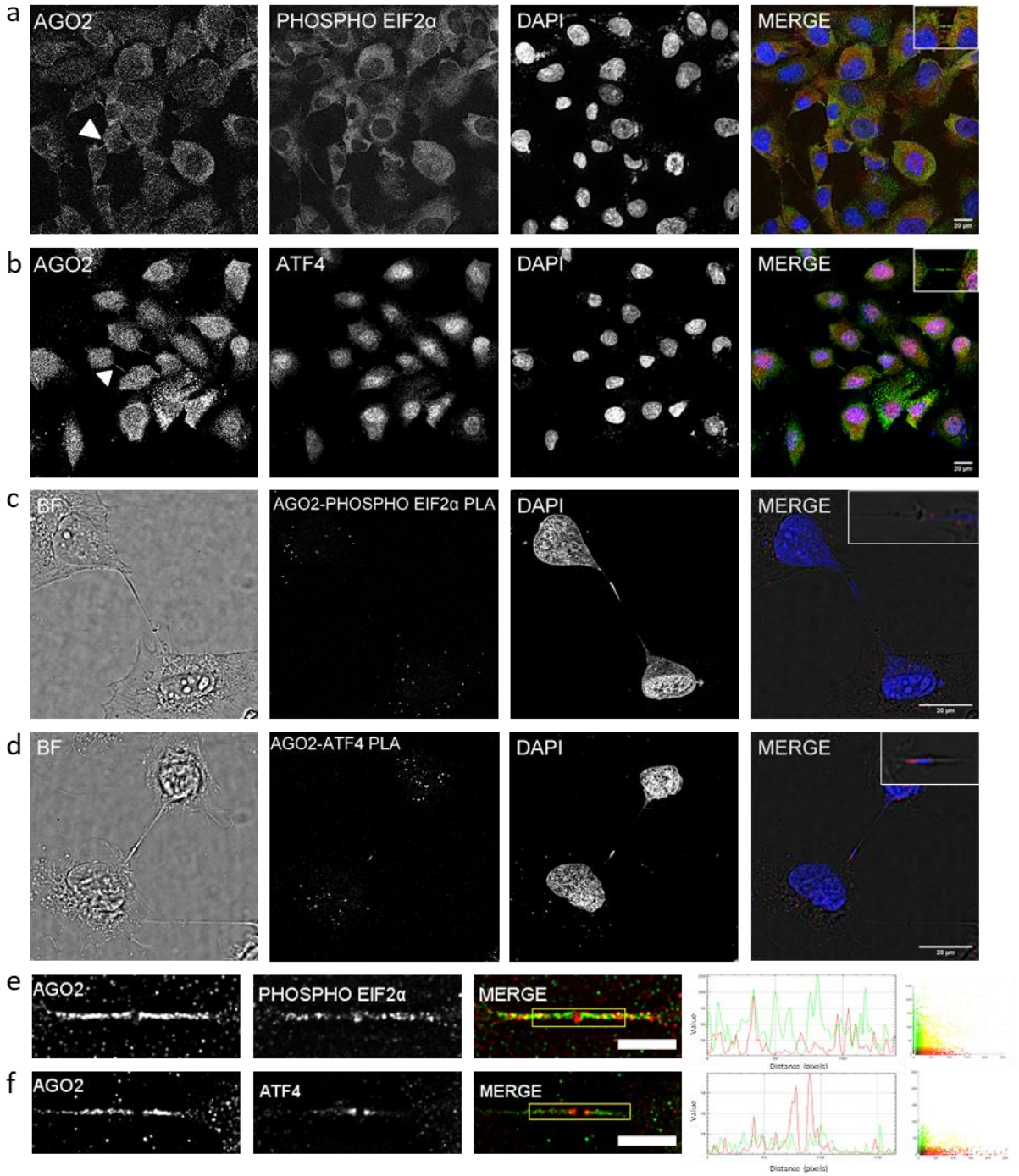

Figure 84 Subcellular localization and interaction between AGO2 and ER-stress regulators. Representative images of NTHY ori-3-1 cells showing AGO2 colocalization with (a) phospho-Elf2α and (b) ATF4. AGO2 proteins in green, phospho-Elf2α and ATF4 in red. Nuclei of cells were visualized in blue (DAPI). iPLA foci between (c) AGO2-phospho-Elf2α and (d) AGO2-ATF4 in red. (e-f) Visual assessment (merged images, scatterplots and intensity lineplots) of colocalization. Lineplots indicate the signal intensity of the paired proteins along the lines overlaid on the corresponding images that appear in Figure 69(e-f). Scale bar: 20μm (full images), 5μm (zoomed images).

We further investigated the implication of AGO2 to a specific type of stress, ER-stress, which is required for a successful cytokinesis. ER-stress modulated effectors such as eIF2α translation factor and its downstream target, ATF4, are found along the intercellular bridge and into the midbody ring (Figure 84a,e and b,f). iPLA foci of AGO2-phospho-eIF2α and AGO2-ATF4, although located into the cell matrix, were also sparsely located within the bridge (Figure 84c,d) indicating that AGO2 may

trigger ER-stress effectors for ATF4 activation. The interaction foci were detected in both sides of the bridge likely implying a cytoprotective regulation of local-type transcript homeostasis of gene expression. The coexistence of the four activated phospho-kinases, MEK, ERK, p38 and JNK, together with the phospho-eIF2α and ATF4 proteins into the AGO2-enriched cytokinetic structures strongly suggests the simultaneous and synergistic activation of the MAPK-signaling network and RNAi-machinery. This is probably due to stress response (mechanical and/or ER) and functions in a topology-specific manner, most likely for the restoration of local -transcript- homeostasis during cytokinesis.

Conclusively, AGO2 resides in the nucleus, into the cytoplasm but surprisingly in protrusional structures along with other components of the RNAi-machinery. These structures are open- or close-ended tubes. Open-ended protrusions form the spatial margin for the existence and motility of AGO2 and other RNAi machinery components probably facilitating intercellular trafficking and transferring dsRNA species. On the other hand, AGO2 close-ended protrusions discrete in two types: the typical Actin-filopodial structures which are many per cell and probably detect cues in the microenvironment and the cytokinetic bridges during mitosis. α-Tubulin alterations across these bridges and cytoskeletal changes influence AGO2 localization, which follows the α-Tubulin cellular expression patterning during cell division. When AGO2 is over-expressed generates aneuploidy via cytokinesis errors. To this direction, AGO2 has been investigated in areas across the intercellular bridges together with Lamin A/C and DNA damage response components and appears to be a stress-sensitive molecule changing its distribution pattern depending on the pattern of other stress-related molecules such as Upf1 and TIAR under local basal stress. In the midbody structure and across midbody arms, a small kinome also was tested and kinases seem to follow the AGO2/Dicer distribution leading to the idea that a local fine-tuning regulation occurs to overcome the local mitotic stress, polarity and mitotic defects as well as chromosome segregation and to compensate the local-transcript homeostasis. EMT as a genetic program characterized by the loss of both tight and apical junctions, loss of apical–basal polarity, leads to the opposite direction. AGO2 seems to safeguard the epithelial homeostasis, both mechanical and biological, through transcript control.

CHAPTER 3

Determining that the regulation of gene expression provides essential information for understanding the condition, morphology and function of the cell, the molecular mechanisms being affected are under investigation. A variety of mechanisms are implicated in EMT with a consequent contribution to cytokinesis failure and mitotic defects. Gene expression can be regulated via different cellular procedures including RISC complex and loaded miRNAs. The miR function is expanded at a post-transcriptional level dictating cellular and subcellular transcript homeostasis. Therefore, we used thyroid cell lines, normal and malignant, as a substrate/model system to study the "active" functional miRNome, ie the set of miRNAs that bind to the RISC complex and in particular to AGO2. The applied methodology was High-Sequencing of RNAs isolated by Cross-Linking Immuno-Precipitation (HITS-CLIP) (Figure 85) that allowed us to map the tripartite complex AGO2::miRNA::mRNA, followed by bioinformatic analysis. Then, we focused on a specific miR, miR26 in order to examine it, as a potential therapeutic approach.

HITS-CLIP protocol

Cell lines in HITS-CLIP protocol

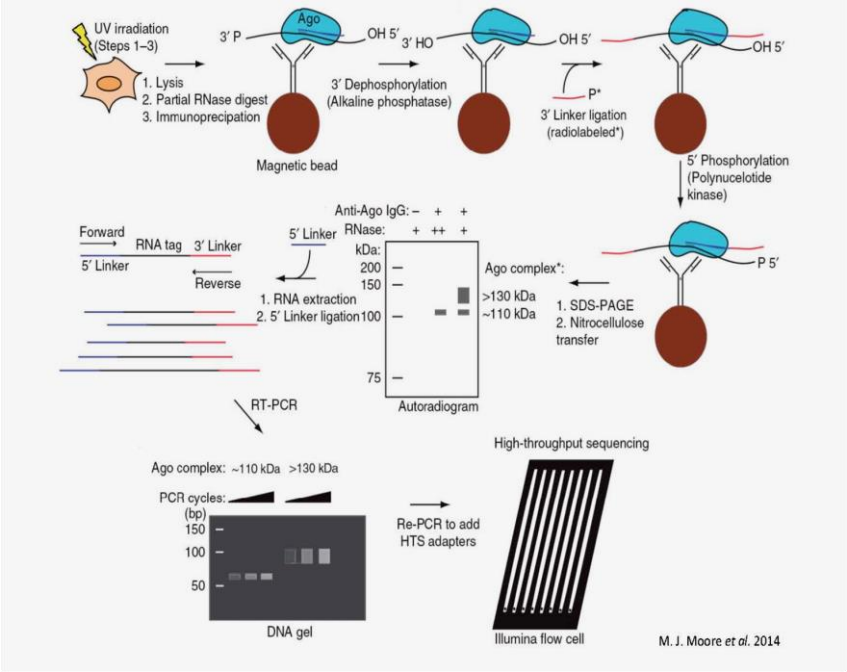

Figure 85 Workflow of HITS-CLIP methodology.

Three cell lines of thyroid origin were used to perform the experimental assays; one was representative of normal thyroid follicular cells and two cell lines were of papillary and follicular thyroid carcinoma origin, respectively. Specifically,

NTHY-ori 3-1: cell line derived from epithelial cells of the follicular thyroid gland. The cells were immortalized via transfection with a plasmid that carries part of the genome of the oncogenic virus

SV40. The cell line retains specific features of thyroid epithelial cells, such as thyroglobulin production and iodine binding.

TPC1: cell line derived from papillary thyroid carcinoma (PTC). It carries the RET/PTC1 rearrangement, a fusion of the 5' end of the CCDC6 gene (coiled-coil domain containing gene 6) to the tyrosine kinase domain of the RET proto-oncogene. The product of this rearrangement encodes a constitutively active tyrosine kinase domain. The TPC1 cell line also carries a silent mutation (His27His) in the HRAS gene.

FTC133: cell line derived from lymph node metastatic thyroid carcinoma (FTC). It is characterized by a point mutation in the tumor suppressor gene PTEN, which produces a premature termination codon (R130STOP). The cells carry and additional mutation in the tumor suppressor gene TP53, which causes an amino acid change from arginine to histidine (R273H).

HITS-CLIP breakthrough in mapping RNA-protein interactions *in vivo* came with the development of crosslinking-immuno-purification (CLIP) strategies. In CLIP, individual cell types are treated with UV-B irradiation. This generates a covalent bond between RNA-protein complexes that are in close contact within the intact cell or tissue. Following formation of this bond, RNABPs can be purified under very stringent conditions. While any purification method can, in theory, be used in practice, proteins are generally purified by virtue of antibodies to the RNABPs themselves or protein epitope tags. In the course of this purification, RNA is intentionally reduced in size -typically to a modal size of ~50 nt- to facilitate identification of binding sites (e.g. crosslinked RNAs from ~20 nt to 100 nt). Once sufficient purity has been obtained, the protein component of the crosslinked complex is removed with proteinase K and the RNA is purified. RNA ligase was used to ligate RNA linkers, followed by cDNA synthesis with an antisense primer and reverse transcriptase (RT), to generate templates for sequencing.

Detection of AGO2: RNA complexes by autoradiography

Electrophoretic separation of the AGO2::miRNA and AGO2::miRNA::mRNA complexes was performed under denaturing conditions. The protein:RNA complexes were then transferred to a nitrocellulose membrane and images were acquired via autoradiographic film exposure. The assay was performed in triplicates for the NTHY-ori 3-1 and TPC1 cell lines, while there was one out three successful replicate, FTC133 and a second round of HITS-CLIP experiment included FTC133 and NTHY ori 3-1 in triplicates (data not shown). The biological replicates - hereinafter referred to as rep1, rep2, rep3 - ensure the reproducibility of the findings. Two controls were also included for each cell line:

(i) a control sample without ultraviolet radiation (Non-UV control) in order to exclude the radioactive labeled RNAs that are not covalently linked to the AGO2 protein. Usually, the signal from these samples is significantly low, although there are exceptions. A typical example is the AGO2 complexes:miRNAs that are resistant to cleavage due to the close proximity between the Ago2 protein-miRNAs and, therefore, maintained even in the absence of covalent bond.

(ii) a control sample in which the anti-AGO2 monoclonal antibody (rat anti-AGO2 hybridoma) was replaced by a non-specific IgG antibody of the same isotype and derived from the same animal, ie rat IgG (IgG control). This control allows to ensure the specificity of the immunoprecipitation. Therefore, miRNAs and mRNAs found in both immunoprecipitation samples, the IgG control and the anti-AGO2 antibody immunoprecipitation, are reckoned in the bioinformatics analysis for non-specific binding and considered for elimination of the following procedure.

The autoradiographic images of the cell lines, the NTHY ori 3-1 (Figure 86), the PTC (Figure 87) and the FTC-133 (Figure 88) are presented below. It is expected that the AGO2::miRNA complexes would appear at ~110-kDa while AGO2::miRNA::mRNA complexes are expected to run at ~130kDa.

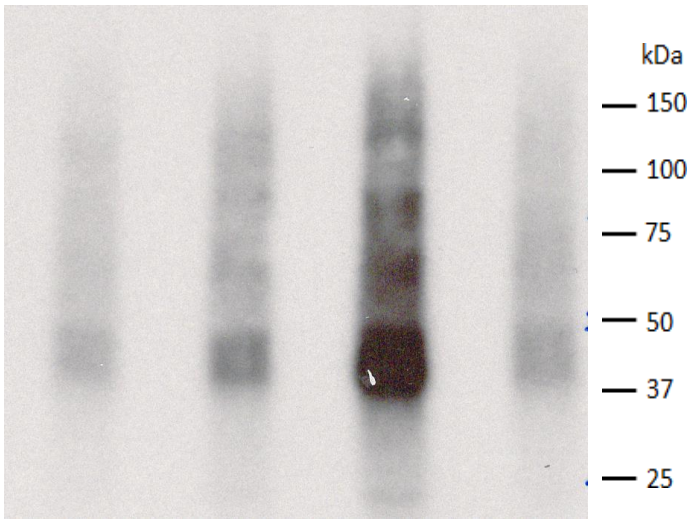

Figure 86 NTHY ori 3-1 cell line autoradiogram after ^{32}P labeling of RNAs covalently linked to the AGO2 protein. In the first three lanes from the left, biological replicates rep1, rep2, rep3 were loaded and run. The IgG control is in the last (right) lane. The immunoprecipitation was performed with anti-AGO2 antibody. The protein-RNA complexes are resolved on an SDS-page gel [NuPAGE 4-12 % Bis-Tris precast gel (Invitrogen)] to select only complexes of the expected size.

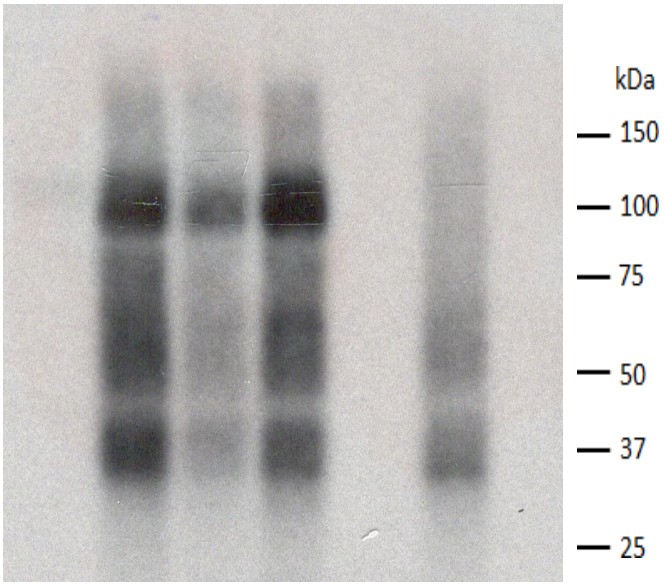

Figure 87 Autoradiogram of the TPC1 cell line. In the first three lanes from the left, biological replicates rep1, rep2, rep3 were loaded and run. The IgG control is in the last (right) lane. The immunoprecipitation was performed with anti-AGO2 antibody. The control IgG has run on the last lane. The protein-RNA complexes are resolved on an SDS-page gel [NuPAGE 4–12 % Bis-Tris precast gel (Invitrogen)] to select only complexes of the expected size.

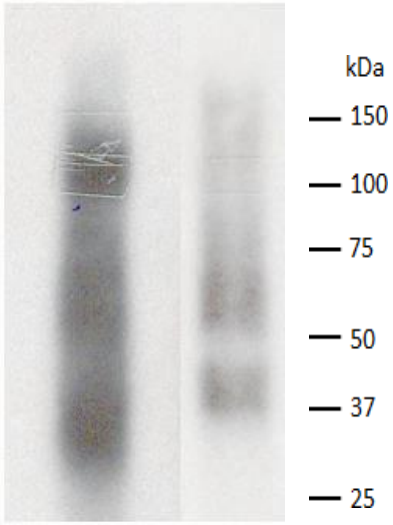

Figure 88 Autoradiogram of the FTC133 cell line. In the first lane from the left lane the sample has been run in which the immunoprecipitation was done with anti-AGO2 antibody. The control IgG has run on the right lane. The protein-RNA complexes are resolved on an SDS-page gel [NuPAGE 4–12 % Bis-Tris precast gel (Invitrogen)] to select only complexes of the expected size.

Qualitative and quantitative analysis of DNA libraries

The autoradiogram bands with sizes of 110kDa and 130kDa which correspond to AGO2::miRNA and AGO2::miRNA::mRNA complexes, were detached and the isolated RNA was used as a template for cDNA Synthesis and Preparation of Deep Sequencing Libraries.

After reverse transcription, DNA libraries were amplified by PCR using primers compatible with the sequencing platform. Quality and quantity control of the libraries was accomplished by a bioanalyzer. The DNA concentration of each library was determined and the samples were merged (each with a separate barcode) in equal amounts for sequencing.

From the visualization of the electrophoresis were expected the following bands:

(i) 110kDa Ago2 complexes: miRNA, a 150 bp band corresponding to miRNAs. PCR-,nhanced miRNAs have 5 'and 3' adapters compatible with the sequencing platform at both ends, thus increasing their length (Figure 89-96).

(ii) from the > 130kDa Ago2 complexes: miRNA: mRNA, a 150 bp band corresponding to miRNAs and a range of 160 - 250 bp corresponding to mRNAs (variety in size)(Figure 89-96). The mRNAs also have 5 'and 3' adapters compatible with the sequencing platform at both ends.

In the control IgG samples, the miRNAs and mRNA tags bands should be absent.

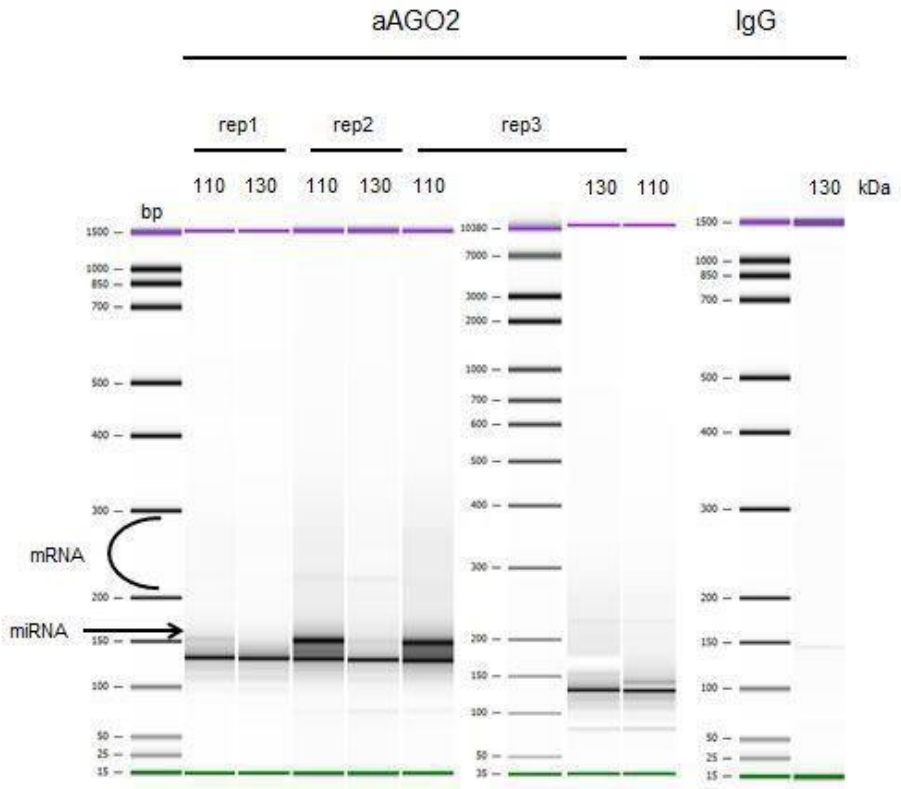

Figure 89 Quality control of DNA libraries of the NTHY-ori 3-1 cell line. In the three samples of the NTHY-ori 3-1 cell line rep1, rep2, rep3, Ago2:RNA complexes were immunoprecipitated with anti-AGO2 antibody, while in the control sample with non-specific IgG

antibody. From the 110kDa complexes emerged 150 bp products derived from miRNAs. From the >130kDa complexes, mainly emerged 160 - 250 bp products derived from mRNAs. Non-specific bands are present in the IgG control. The green and purple bands at the ends of each lane correspond to the high and low molecular weight for calibration of the bioanalyzer.

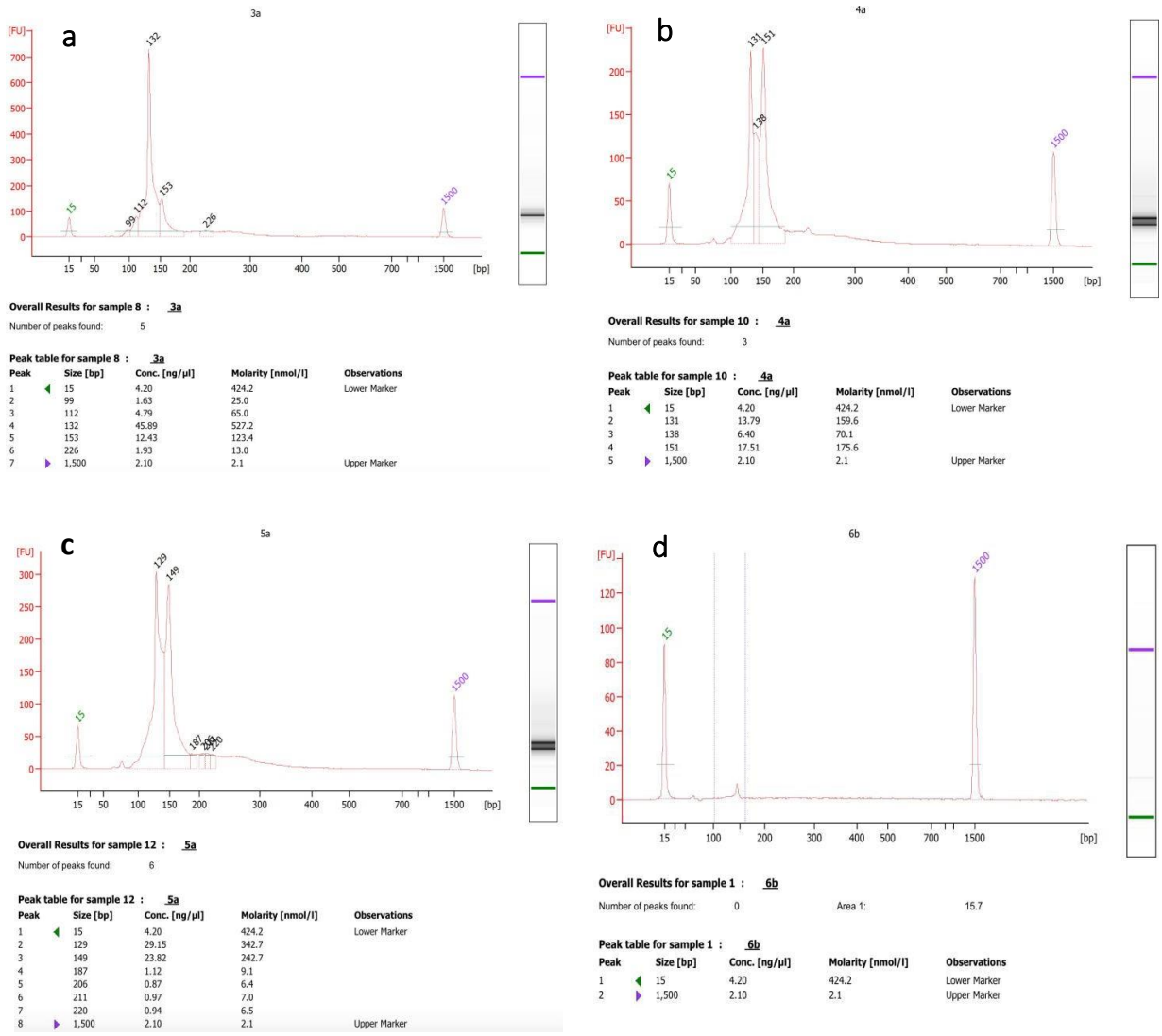

Figure 90 Quantitative analysis of the DNA libraries of the NTHY ori 3-1 cell lines. (a) DNA library of 110kDa complexes from rep1 sample. (b) DNA library of 110kDa complexes from sample rep2. (c) DNA library of 110kDa complexes from sample rep3. (d) DNA library of AGO2::miRNA::mRNA complexes from IgG control. The peak at 130 bp was due to primer dimers. The peak at 150 bp derived from miRNAs, while the mRNAs are captured in the range 160 - 250 bp. In the immunoprecipitation control, a peak absence was observed in both, miRNAs and mRNAs. For a given size of bps present in each electrophoresis, the concentration of DNA is specified.

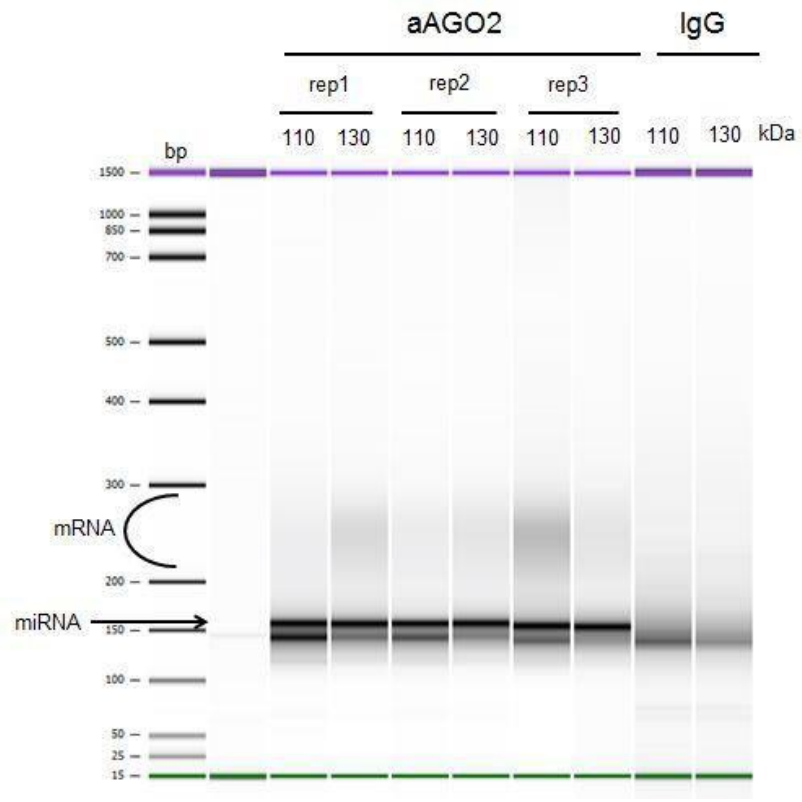

Figure 91 Analysis of the quality of DNA libraries of the PTC1 cell line with electrophoresis. In the three samples of the PTC1 cell line rep1, rep2, rep3, the AGO2::RNA complexes were immunoprecipitated with anti-AGO2 antibody, while in the immunoprecipitation control with non-specific IgG antibody. In the IgG control, only non-specific bands were observed. The green and purple bands at the ends of each lane correspond to the high and low molecular weight for calibration of the bioanalyzer.

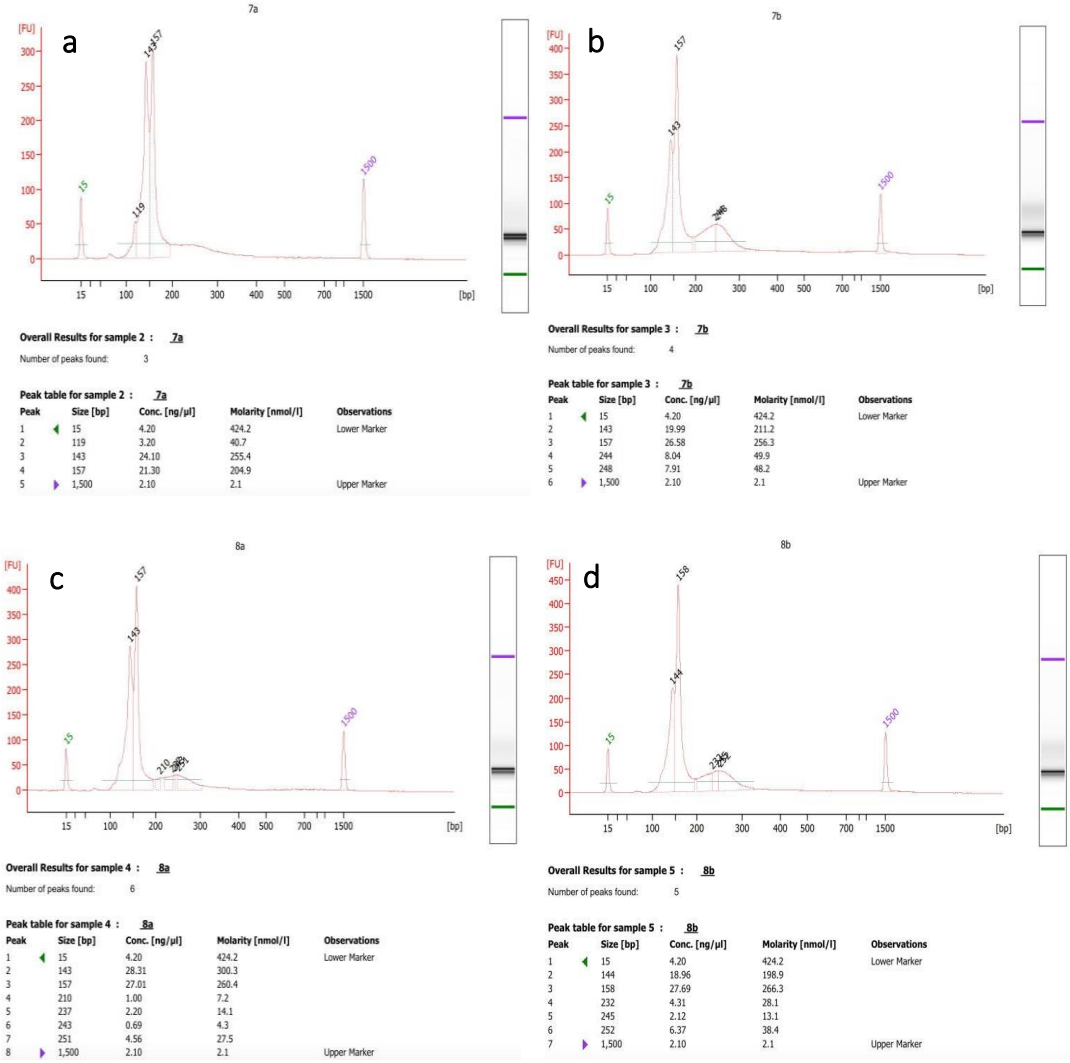

Figure 92 Quantitative analysis of DNA libraries of TPC1 cell lines. (a) DNA library of 110kDa complexes from rep1 sample. (b) DNA library of complexes > 130kDa from sample rep1. (c) DNA library of 110kDa complexes from sample rep2. (d) DNA library of complexes >130kDa from sample rep2. The peak at 143 - 144 bp was due to primer dimers. The peak at 157 - 158 bp derived from miRNAs, while the mRNAs were present in the range 160 - 250 bp. In the immunoprecipitation control, a peak absence was observed in both, miRNAs and mRNAs. For a given size of bps present in each electrophoresis, the concentration of DNA is specified.

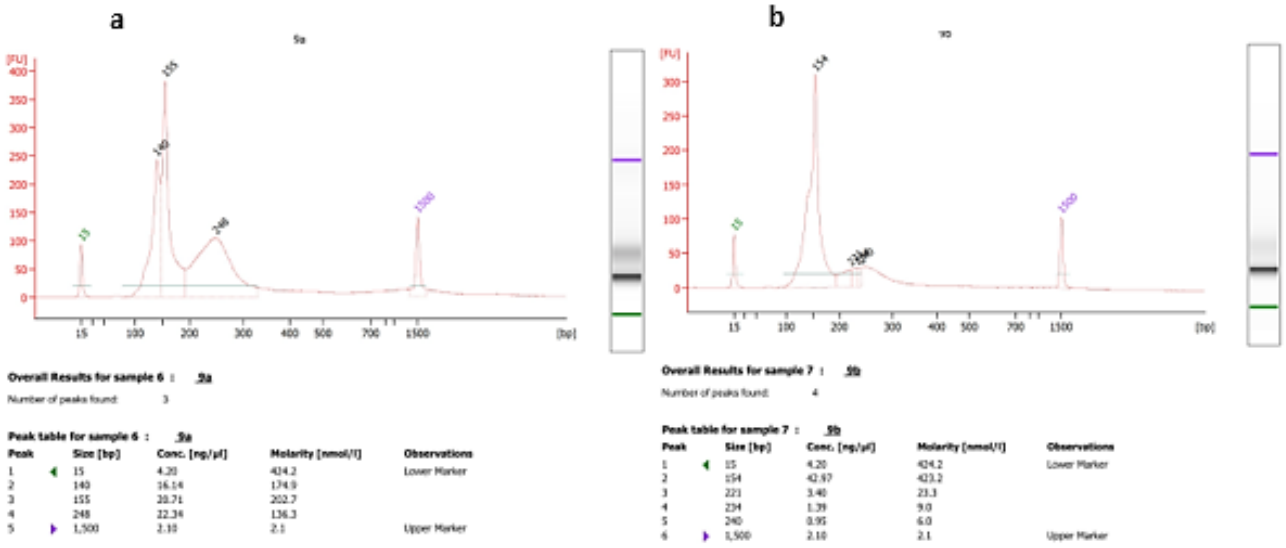

Figure 93 Quantitative analysis of DNA libraries of TPC1 cell line. (a) DNA library of 110kDa complexes from sample rep3. (b) DNA library of complexes > 130kDa from rep3 sample. The peak at 143 - 144 bp was due to primer dimers. The peak at 157 - 158 bp derived from miRNAs, while the mRNAs were present in the range 160 - 250 bp. For a given size of bps present in each electrophoresis, the concentration of DNA is specified.

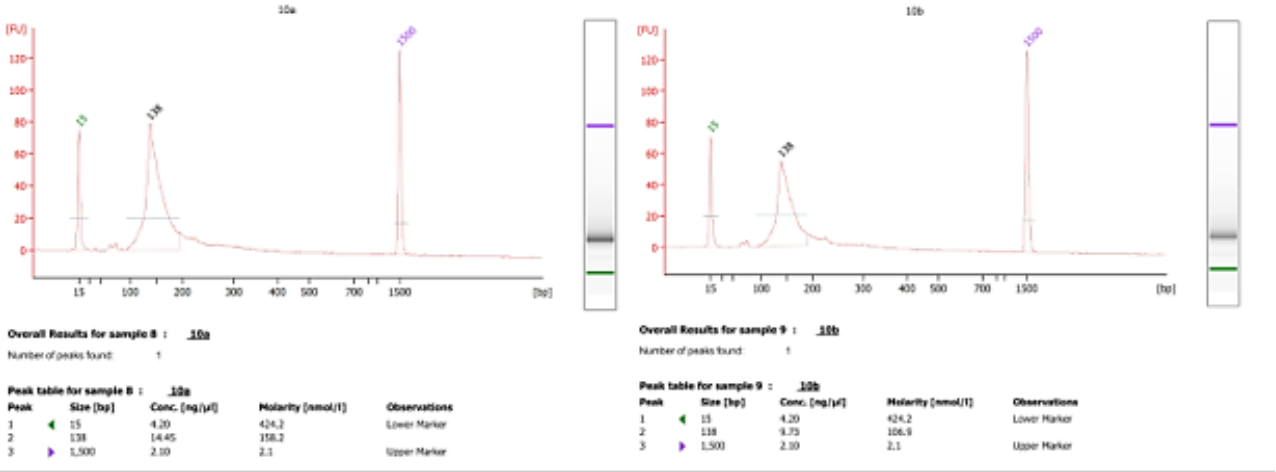

Figure 94 Quantitative analysis of DNA libraries of TPC1 cell line (Left) DNA library of 110kDa complexes from control IgG. (Right) DNA library of >130kDa complexes from IgG control. The peak at 143 - 144 bp was due to primer dimers. The peak at 157 - 158 bp derived from miRNAs, while the mRNAs were present in the range 160 - 250 bp. In the immunoprecipitation control, a peak absence was observed in both, miRNAs and mRNAs. For a given size of bps present in each electrophoresis, the concentration of DNA is specified.

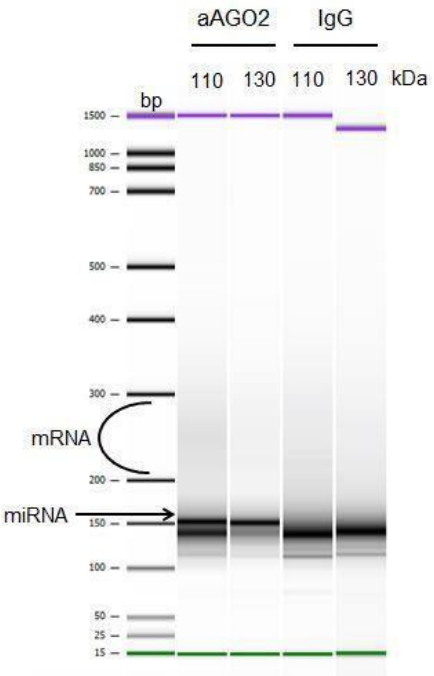

Figure 95 Analysis of the quality of DNA libraries of the FTC133 cell line (electrophoresis). In the FTC133 sample, the AGO2::RNA complexes were immunoprecipitated with anti-AGO2 antibody, while the control was immunoprecipitated with non-specific IgG antibody. Non-specific bands were observed in the IgG control. The green and purple bands at the end of each lane correspond to the high and low molecular weight for the calibration of bioanalyzer.

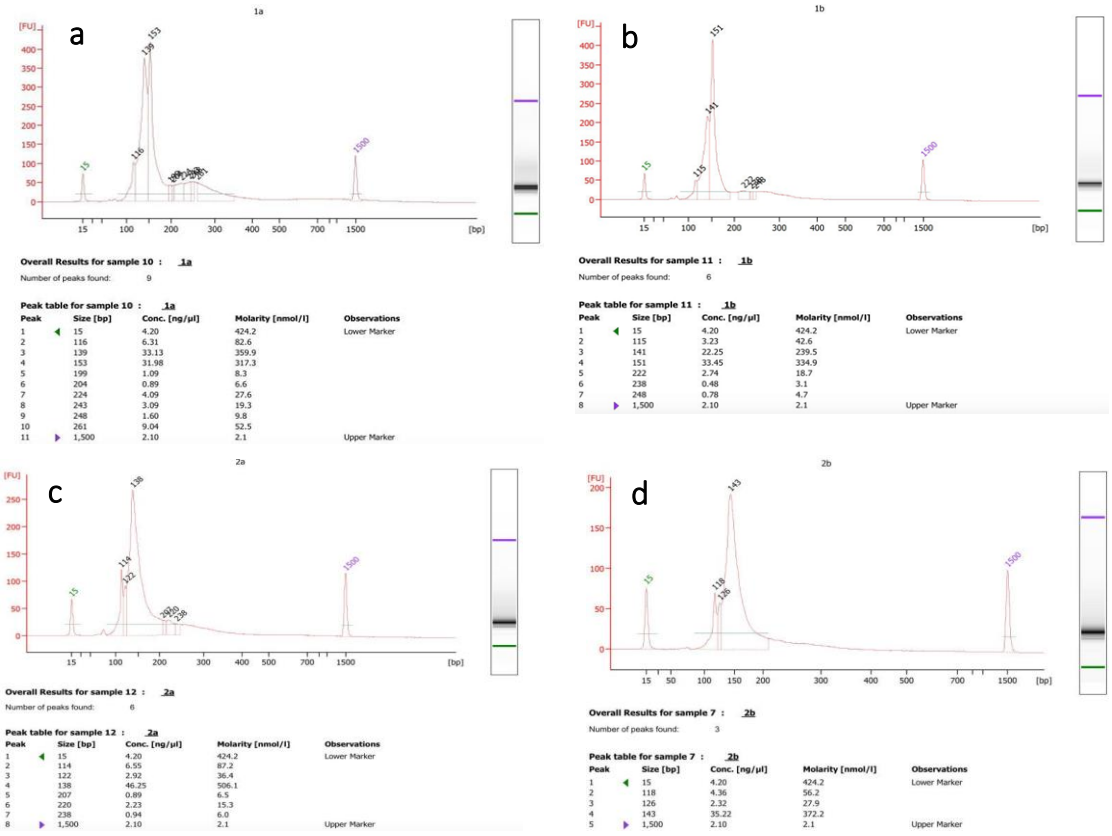

Figure 96 Quantitative analysis of DNA libraries of FTC133 cell line. (a) DNA library of 110kDa complexes isolated by anti-AGO2 immunoprecipitation. (b) DNA library of >130kDa complexes isolated by anti-AGO2 immunoprecipitation. (c) DNA library of 110kDa

complexes from IgG control. (d) DNA library of> 130kDa complexes from IgG control. The peak at 138 - 143 bp was due to primer dimers. The peak at 153 bp derived from miRNAs, while the mRNAs were present in the range 160 - 250 bp. In the immunoprecipitation control, an absence of peaks was observed in both miRNAs and mRNAs. For a given size of bps present in each electrophoresis, the concentration of DNA is specified.

Sequencing platform and library preparation

The DNA libraries were prepared for sequencing by adding a different barcode to each library (Table 8). Therefore, multiplication and simultaneous sequencing of different libraries (multiplexed sequencing) was possible. Libraries with 160-250 bp DNA segments (derived from mRNAs) do not coexist in the same sequencing lane with libraries of 150 bp DNA segments (derived from miRNAs) because there is non-equal sequencing efficiency between molecules that have a large deviation in their length. Given that the total number of libraries is twenty, five of them are classified in each sequencing lane (Table 9).

	mRNA		miRNA	
Samples	**Lane1**	**Lane2**	**Lane3**	**Lane4**
	L5Aa: NTHY Ago2 Rep1	L5Aa: NTHY Ago2 Rep2	L5Aa: NTHY Ago2 Rep1	L5Aa: NTHY Ago2 Rep2
	L5Ab: NTHY Ago2 Rep3	L5Ab: NTHY IgG	L5Ab: NTHY Ago2 Rep3	L5Ab: NTHY IgG
	L5Ac: PTC Ago2 Rep2	L5Ac: PTC Ago2 Rep1	L5Ac: PTC Ago2 Rep2	L5Ac: PTC Ago2 Rep1
	L5Cc: PTC IgG	L5Cc: PTC Ago2 Rep3	L5Cc: PTC IgG	L5Cc: PTC Ago2 Rep3
	L5Cd: FTC Ago2	L5Cd: FTC IgG	5LCd: FTC Ago2	5LCd: FTC IgG

Table 9 Schematic representation of the DNA libraries preparation for sequencing. Each library was tag with a specific barcode. Five different libraries were loaded by sequencing lane.

Analysis of HITS-CLIP data

Main workflow of bioinformatic analysis

The extracted data of a large-scale and high-throughput sequencing of the libraries, was initially subject of quality control. This was followed by their classification based on the barcodes, attached at the 5' end. Next, the sequence of the adapters was removed. The analysis of the data from this point onwards progressed in parallel for the two data sets: i) the miRNAs segments and ii) the mRNAs segments (Figure 97).

The miRNA fragments were identified and a list of all miRNAs loaded on the AGO2 protein was compiled. The miRNAs of IgG control samples present in the libraries were eliminated from the list. The sequencing platform also provided quantitative data on the abundance of these miRNAs, so a comparative analysis of their expression (differential expression) was performed between the cancer cell lines (PTC1 and FTC133) and the normal NTHY ori 3-1 cells (PTC1 vs NTHY ori 3-1 and FTC133 vs NTHY ori 3-1 cell line).

mRNA fragments (trimmed reads) were first mapped/aligned with the reference genome (in this case the whole human genome) to identify the regions of the genome where peaks are formed from specific mRNA fragments. The peaks are then filtered by removing those present in the IgG control sample libraries, leaving only those representing the actual AGO2 protein binding sites in the mRNAs.

The remaining peaks were scanned for the presence of miRNAs (miRNA recognition elements, MREs) in the list compiled by the analysis of the first data set. The HITS-CLIP methodology guided the search for MREs in the peak regions, minimizing the probability of false-positive or negative interaction results between miRNAs and mRNAs.

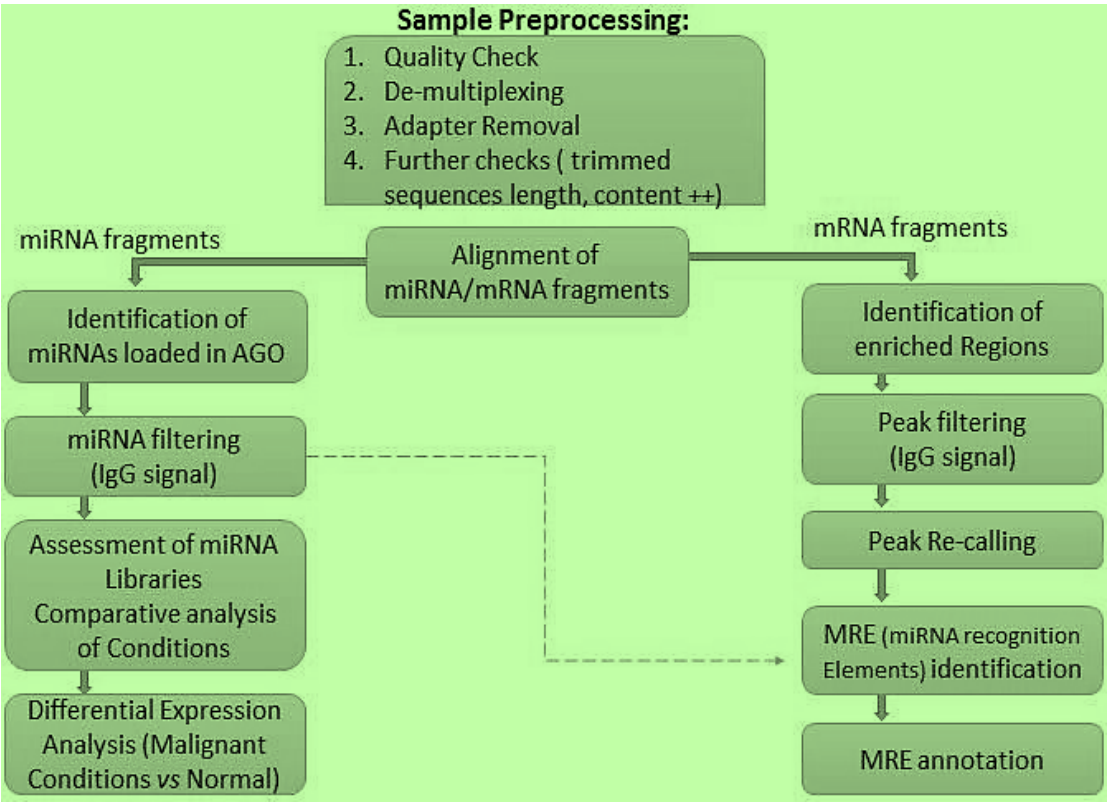

Figure 97 The basic steps of bioinformatics analysis of the data resulting from the sequencing of DNA libraries.

According to the barcode of each library the sequenced and the aligned reads emerged (Table 10). The mapping rate of the miRNAs sequenced libraries varied but was always greater than 75%. Exceptions were the libraries of the IgG control samples, as expected, with a lower mapping rate, ranging between 62% and 44%. The sequenced and the aligned reads of the mRNA libraries has been also presented (Table 11), showing the size of the data emerged from the sequencing analysis. The mapping rate varied and was lower than that of the miRNA libraries.

Library		Sequenced Reads(after de-multiplexing)	Preprocessed Reads	Aligned Reads
Lane 3	L5Aa: NTHY Ago2 Rep1	28,720,410	16,851,374	12,835,958 (76.17%)
	L5Ab: NTHY Ago2 Rep3	39,727,040	31,397,017	25,582,319 (81.48%)
	L5Ac: PTC Ago2 Rep2	31,073,222	24,801,991	21,346,982 (86.07%)
	L5Cc: PTC IgG	33,113,657	20,107,349	12,512,107 (62.23%)
	5LCd: FTC Ago2	49,507,092	31,152,297	23,843,688 (76.54%)
Lane 4	L5Aa: NTHY Ago2 Rep2	32,466,046	26,021,846	21,136,523 (81.23%)
	L5Ab: NTHY IgG	9,332,798	4,694,413	2,074,068 (44.18%)
	L5Ac: PTC Ago2 Rep1	23,940,996	16,923,252	14,362,572 (84.87%)
	L5Cc: PTC Ago2 Rep3	72,929,697	50,322,306	44,466,138 (88.36%)
	5LCd: FTC IgG	42,543,185	17,460,952	10,193,405 (58.38%)

Table 10 The size of miRNAs libraries and the percentage of mapping of their data in the reference genome

Library		Sequenced Reads	Preprocessed Reads	Aligned Reads
Lane 1	L5Aa: NTHY Ago2 Rep1	20,421,508	3,764,024	1,581,221 (40.5%)
	L5Ab: NTHY Ago2 Rep3	38,381,226	31,772,066	16,045,500 (50%)
	L5Ac: PTC Ago2 Rep2	30,076,966	26,726,049	17,891,782 (67%)
	L5Cc: PTC IgG	57,359,716	51,807,742	28,198,006(54.3%)
	L5Cd: FTC Ago2	50,325,999	45,337,970	24,637,256 (54.2%)
Lane 2	L5Aa: NTHY Ago2 Rep2	50,394,279	37,688,271	9,103,051 (24%)
	L5Ab: NTHY IgG	265,044	220,176	71,336 (32,4%)
	L5Ac: PTC Ago2 Rep1	29,906,567	24,653,518	15,753,659 (64%)
	L5Cc: PTC Ago2 Rep3	45,805,364	38,899,966	*pending*
	L5Cd: FTC IgG	57,116,730	43,476,017	24,817,729 (57%)

Table 11 The size of mRNA libraries and the rate of mapping of their data to the reference genome.

Differential expression of miRNAs between cell lines

The analysis of miRNA expression levels among libraries revealed those with the most increased expression (Table 12). Based on the expression pattern of the fifty most abundant miRNAs, libraries of the replicates from the same cell line were grouped together, and the TPC1 and FTC133 cancer cell lines against the normal NTHY ori 3-1 cell line (Figure 98). Comparative analysis revealed the miRNAs with differential expression (Figure 97). Noteworthy is the fact that differential expression uncovered the subset of miRNAs loaded on the AGO2 protein (Tables 13 and 14).

ID	FTC_Ago2	NTHY_Ago2_Rep1	NTHY_Ago2_Rep2	NTHY_Ago2_Rep3	PTC_Ago2_Rep1	PTC_Ago2_Rep2	PTC_Ago2_Rep3
hsa-miR-16-5p	178598218,4	108807082	122635698,7	93985613,26	33814322,45	324601777,5	340481404,5
hsa-miR-26a-5p	21074020,31	32351434,77	40663957,19	29309457,81	2490407,872	20637229,1	24544133,93
hsa-miR-21-5p	11849896,92	24077535,9	29072465,78	36695497,21	2484871,111	18009419,7	14665805,67
hsa-miR-30c-5p	18822954,34	8899818,644	11214464,98	8545865,188	3344215,403	23880300,48	38446349,85
hsa-let-7a-5p	17362049,34	11775560,66	14680916,1	9829070,251	3448320,689	26468526,47	24617214,66
hsa-miR-30a-5p	8580791,849	5105816,728	6522349,604	4292980,045	2431914,386	18207336,78	20411644,75
hsa-miR-31-5p	8253147,077	2861367,492	3717873,713	2943948,033	2813117,715	23561716,36	21408634,52
hsa-miR-30b-5p	4584975,52	9508712,287	12129200,03	7740838,929	566835,4995	3780048,863	5866190,208
hsa-let-7i-5p	7583988,11	4284410,411	5281689,3	3558304,867	927753,1292	6106555,756	7982948,476
hsa-let-7f-5p	4007005,109	4938241,884	5659551,504	3839641,918	1118159,796	8240713,414	6860674,681
hsa-miR-30d-5p	3827168,782	6174381,11	7653142,365	5425711,495	613729,5598	5321915,703	6126080,286
hsa-miR-125b-5p	2666775,757	1401864,92	1468944,092	1299569,299	1233663,601	9778624,956	17257287,68
hsa-miR-181b-5p	3635630,856	2636120,107	3277114,073	2162820,623	1181374,596	9855844,563	9213357,674
hsa-miR-181a-5p	1539832,523	2212874,13	2917805,897	2188434,942	1113420,754	9493813	9206366,161
hsa-miR-15b-5p	2182464,758	4545733,662	5161076,181	3933841,393	525880,0141	4518229,365	6747703,482
hsa-miR-138-5p	9364426,02	280338,0944	308421,9047	233085,2573	837805,878	6858549,379	6429492,533
hsa-let-7b-5p	11010109,06	1395131,223	1666376,138	1125079,109	518706,4519	4218934,929	4364821,037
hsa-let-7d-5p	2343956,147	1941432,889	2493021,345	1777882,649	699717,7611	5238458,894	5476296,829
hsa-miR-155-5p	2369084,282	1888958,901	2296854,889	1980173,542	488292,6757	4242484,171	3452117,846
hsa-miR-15a-5p	2018595,752	2717168,693	3148740,26	2106580,122	361744,8939	2528379,271	3510361,034
hsa-miR-100-5p	337341,7137	1296149,372	1925607,185	1747256,468	336412,8833	1995996,02	4736788,953
hsa-miR-17-5p	982980,9334	1788511,686	1976541,214	1647826,491	333092,0086	2721184,886	2623371,075
hsa-miR-30e-5p	2287452,809	1407900,824	1705036,332	1192621,529	264192,7214	1961645,77	2219591,773
hsa-miR-125a-5p	1698223,688	638375,3718	627852,0549	643973,9161	455615,741	3322177,362	3589656,445
hsa-miR-186-5p	3762064,069	1057504,373	1253722,148	761281,7789	131700,4557	948267,7311	2933289,313
hsa-miR-20a-5p	877223,6535	1396282,581	1831189,392	1430146,826	314579,0183	2375522,176	1983977,783
hsa-miR-26b-5p	879228,3099	1740538,458	2394902,299	1633530,909	207206,0382	1549868,714	1503330,679
hsa-miR-106b-5p	3446097,587	1145879,78	1492273,931	1327672,731	114983,8104	922254,0336	748150,1622
hsa-miR-484	1978059,735	882637,5994	1022620,631	870045,9292	134613,6074	1158811,341	2503893,884

Table 12 The thirty miRNAs with the highest expression among all libraries.

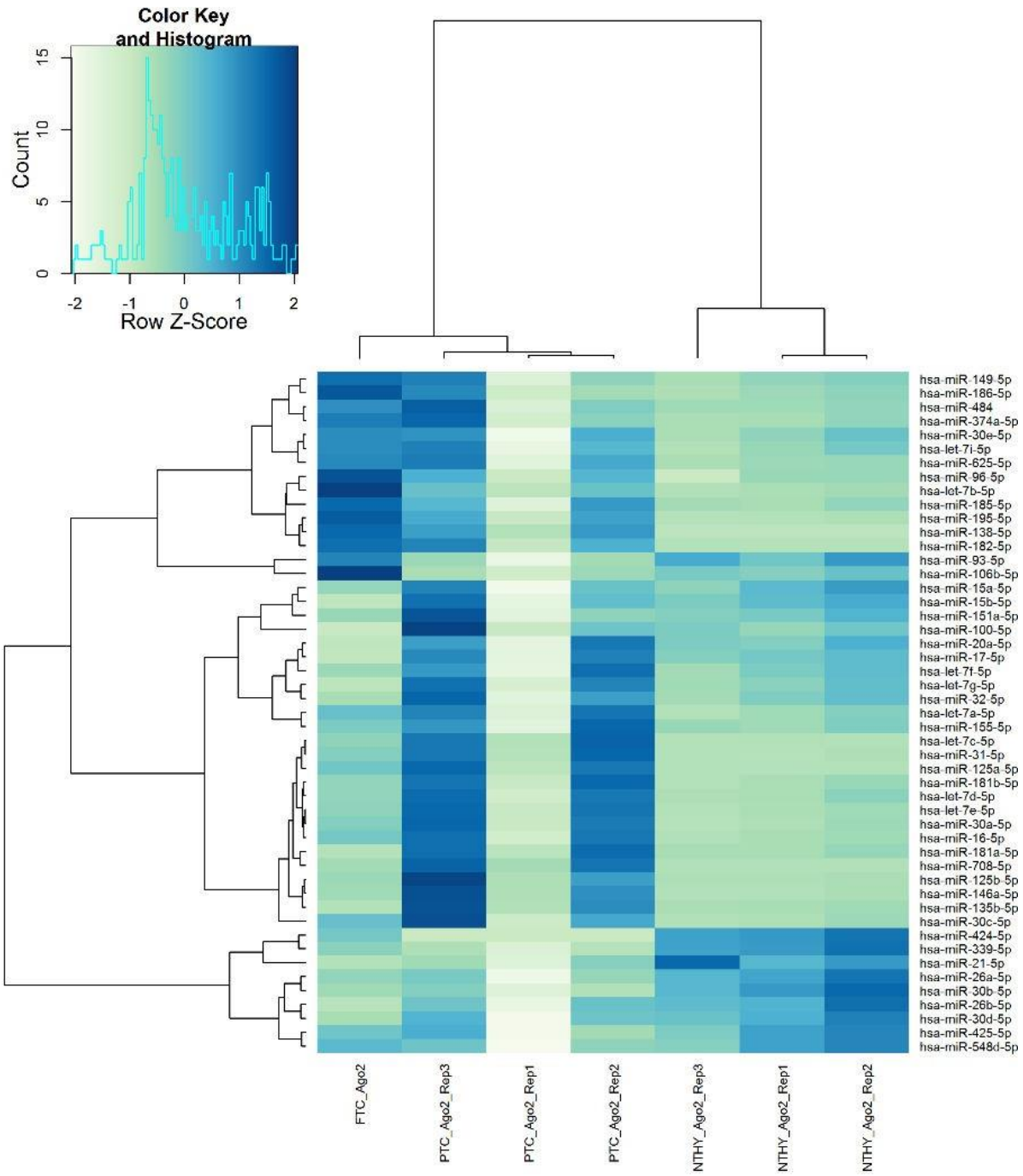

Figure 98 The expression pattern of the fifty most abundant miRNAs among the three cell lines (NTHY-ori 3-1, TPC1, FTC133). Blue: high expression, green: low expression.

mature miRNA	Normalized_NTHY	Normalized_PTC	foldChange
hsa-miR-424-5p	79084,52192	11,29895365	0,000142872
hsa-miR-450a-5p	6992,274866	1	0,000143015
hsa-miR-204-5p	1	3530,043155	3530,043155
hsa-miR-196a-5p	4248,13078	1	0,000235398
hsa-miR-493-5p	3264,836434	1	0,000306294
hsa-miR-503-5p	3942,936216	4,894888944	0,001241432
hsa-miR-335-5p	3640,371586	10,30197805	0,002829925
hsa-miR-134-5p	3243,946017	4,048173956	0,001247917
hsa-miR-708-5p	5268,178288	90571,74917	17,19223311
hsa-miR-411-5p	3638,697564	9,805835873	0,002694875
hsa-miR-138-5p	11644,69755	208185,4854	17,87813591
hsa-miR-432-5p	3202,114835	1	0,000312294
hsa-miR-34c-5p	3048,041081	35,87081192	0,01176848
hsa-miR-136-5p	1401,84091	1	0,000713348

Table 13 Differential expression of miRNAs between TPC1 and NTHY-ori 3-1 cell lines. Red indicates reduced expression in the TPC1 series compared to the NTHY-ori 3-1 series, while green indicates increased expression respectively. Expression values are normalized between the three copies of each cell line.

mature miRNA	Normalized_NTHY	Normalized_FTC	foldChange
hsa-miR-138-5p	12369,72163	295341,5057	23,87616428
hsa-let-7b-5p	62663,68067	347243,9779	5,541391348
hsa-miR-105-5p	1	7517,301368	7517,301368
hsa-miR-26a-5p	1536215,566	664645,2398	0,432651025
hsa-miR-196b-5p	5,34099027	7200,446332	1348,148184
hsa-miR-15b-5p	205372,0314	68832,79425	0,335161481
hsa-miR-204-5p	1	4900,122879	4900,122879
hsa-miR-30d-5p	288824,8476	120704,3897	0,417915532
hsa-miR-195-5p	15298,84968	60956,99843	3,98441711
hsa-miR-335-5p	3859,278576	1	0,000259116
hsa-miR-411-5p	3870,351652	1	0,000258374
hsa-miR-182-5p	13237,92393	54777,95764	4,137956822
hsa-miR-186-5p	45766,15344	118651,0809	2,59255087
hsa-miR-493-5p	3467,660097	1	0,000288379

Table 14 Differential expression of miRNAs between FTC133 and NTHY-ori 3-1 cell lines. Red indicates reduced expression in the FTC133 cell line compared to NTHY-ori 3-1, while green indicates increased expression, respectively. Expression values are normalized between the three replicates of each cell line.

Network of miRNAs - mRNAs interactions and molecular pathway involvement

Statistical analysis was performed to identify genes that target the PTC1 cell line exclusively from miRNAs that show increased expression when compared to the NTHY ori 3-1 sequence. A group of 31 miRNAs (Table 15) with high statistical significance (p-value) was emerged, which then, was correlated with target genes.

Pathway Description	Kegg Id	Number_of _miRNAs_in _Pathway	miRNA	interacting_genes_Names _for_miRNA
Metabolic pathways	hsa01100	21	hsa-miR-181b-5p	STT3B
			hsa-miR-4677-5p	STT3A
			hsa-miR-125a-5p	BTD,GCNT1
			hsa-miR-330-5p	AGPAT4,GALNS,POLD3,UGDH
			hsa-miR-182-5p	GCNT1,PLD1,PPAP2A,PTGIS
			hsa-miR-181a-5p	STT3B
			hsa-miR-16-5p	DLD,GALNT7,MUT,PLD1,POLR1C,S T3A,STT3B
			hsa-miR-30c-5p	ALDH2,H6PD,IDH1
			hsa-let-7b-5p	ACER2,AGPAT9,CS,EHHADH,GALE NME6,PLCE1,POLR1B
			hsa-miR-5579-3p	POLR1D
			hsa-miR-96-5p	GCNT1,PAPSS1,PLD1,PTGIS
			hsa-miR-130b-5p	ALG9
			hsa-miR-19a-5p	NMRK1
			hsa-miR-9-5p	FUT8
			hsa-miR-24-1-5p	UGT8
			hsa-let-7c-5p	ACER2,CS,EHHADH,GALE,NME6,P CE1,POLR1B
			hsa-let-7e-5p	ACER2,CS,EHHADH,GALE,NME6,P CE1,POLR1B
			hsa-miR-30a-5p	ALDH2,H6PD,IDH1
			hsa-let-7d-5p	ACER2,AGPAT4,AGPAT9,GALE,GM PA,NME6,PLCE1
			hsa-miR-195-5p	DLD,GALNT7,MUT,PLD1,POLR1C,S T3A,STT3B
			hsa-miR-125b-5p	BTD,GCNT1
Pathways in cancer	hsa05200	16	hsa-miR-181b-5p	PIK3R3
			hsa-miR-125a-5p	CASP8
			hsa-miR-182-5p	PLD1
			hsa-miR-16-5p	PLD1

			hsa-miR-181a-5p	PIK3R3
			hsa-miR-30c-5p	EDNRA,NFKB1,PIK3CD
			hsa-let-7b-5p	FAS,FZD2,RALB
			hsa-miR-96-5p	PLD1
			hsa-miR-204-5p	BCL2
			hsa-miR-130b-5p	LAMC2
			hsa-let-7c-5p	FAS,FZD2,RALB
			hsa-let-7e-5p	FZD2,PTCH1,RALB
			hsa-let-7d-5p	FAS,RALB
			hsa-miR-30a-5p	EDNRA,NFKB1,PIK3CD
			hsa-miR-195-5p	PLD1
			hsa-miR-125b-5p	CASP8
Protein processing in endoplasmic reticulum	hsa04141	14	hsa-miR-181b-5p	STT3B
			hsa-miR-4677-5p	STT3A
			hsa-miR-96-5p	EIF2AK4,SEC63
			hsa-miR-204-5p	BCL2,EIF2AK4
			hsa-miR-876-5p	MAP3K5
			hsa-miR-182-5p	EIF2AK4
			hsa-miR-181a-5p	STT3B
			hsa-miR-16-5p	PLAA,STT3A,STT3B
			hsa-miR-9-5p	EIF2AK4
			hsa-let-7c-5p	EIF2AK4,UBE4B
			hsa-let-7e-5p	EIF2AK4,UBE4B
			hsa-let-7d-5p	UBE4B
			hsa-miR-195-5p	PLAA,STT3A,STT3B
			hsa-let-7b-5p	EIF2AK4,UBE4B
Sphingolipid signaling pathway	hsa04071	14	hsa-miR-181b-5p	PIK3R3,PPP2R3A
			hsa-miR-96-5p	PLD1
			hsa-miR-204-5p	BCL2
			hsa-miR-182-5p	PLD1
			hsa-miR-876-5p	MAP3K5
			hsa-miR-16-5p	PLD1
			hsa-miR-181a-5p	PIK3R3,PPP2R3A
			hsa-let-7c-5p	ACER2
			hsa-let-7e-5p	ACER2
			hsa-let-7d-5p	ACER2
			hsa-miR-30a-5p	NFKB1,PIK3CD,PPP2R2A
			hsa-miR-30c-5p	NFKB1,PIK3CD,PPP2R2A
			hsa-miR-195-5p	PLD1
			hsa-let-7b-5p	ACER2
			hsa-miR-5579-3p	RASA1
			hsa-miR-181b-5p	PIK3R3
			hsa-miR-4677-5p	RASA1

Ras signaling pathway	hsa04014	14	hsa-miR-96-5p	PLD1,RASA1
			hsa-miR-182-5p	PLD1,RASA1
			hsa-miR-16-5p	PLD1
			hsa-miR-181a-5p	PIK3R3
			hsa-let-7c-5p	PLCE1,RALB
			hsa-let-7e-5p	PLCE1,RALB
			hsa-miR-30a-5p	NFKB1,PIK3CD,RASA1,RGL1,TBK1
			hsa-let-7d-5p	PLCE1,RALB
			hsa-miR-30c-5p	NFKB1,PIK3CD,RASA1,RGL1,TBK1
			hsa-miR-195-5p	PLD1
			hsa-let-7b-5p	PLCE1,RALB

Table 15 Correlation of miRNAs and their target genes with molecular pathways in the TPC1 cell line. Each path has a unique code from the KEGG database. miRNAs and their target genes involved in each pathway were listed.

Based on the target genes of the miRNAs (Table 14), molecular pathways enriched in these target genes and therefore, regulated by the respective miRNAs emerged (Table 15). The nomenclature and coding of the molecular pathways extracted from the KEGG PATHWAY (Kyoto Encyclopedia of Genes and Genomes) database. This database is a collection of molecular pathways that depicts the complex network of molecular interactions and thus, enable the mapping of the data from big data analyses in order to obtain a biological interpretation.

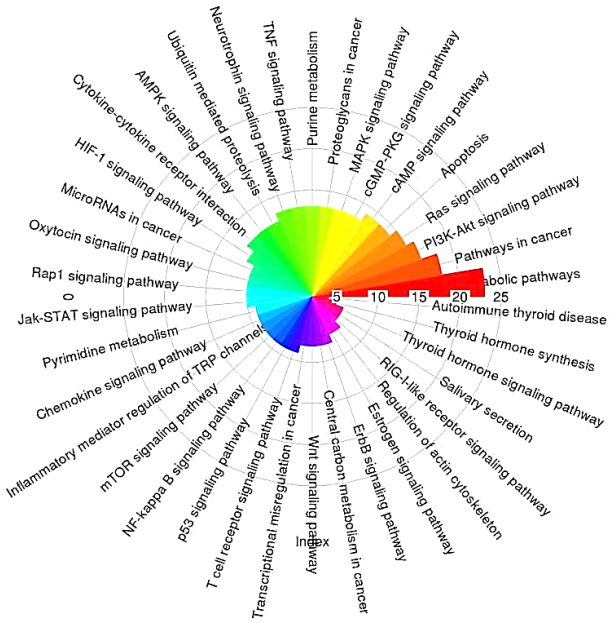

Figure 99 Circular classification of the pathways of based on the number of miRNAs involved.

Evaluation of the data (Table 15) demonstrated that some pathways are regulated by multiple miRNAs (Figure 99). Moreover, multiple genes were involved in these pathways (Figure 100) that are under the control of these miRNAs. The multiplication of miRNAs-gene interactions is responsible for the tight regulation of each pathway as well as their coordinated operation. Further investigation needs to be performed to verify these interactions, dissect their role in the abovementioned pathways and feature their involvement in thyroid pathogenesis.

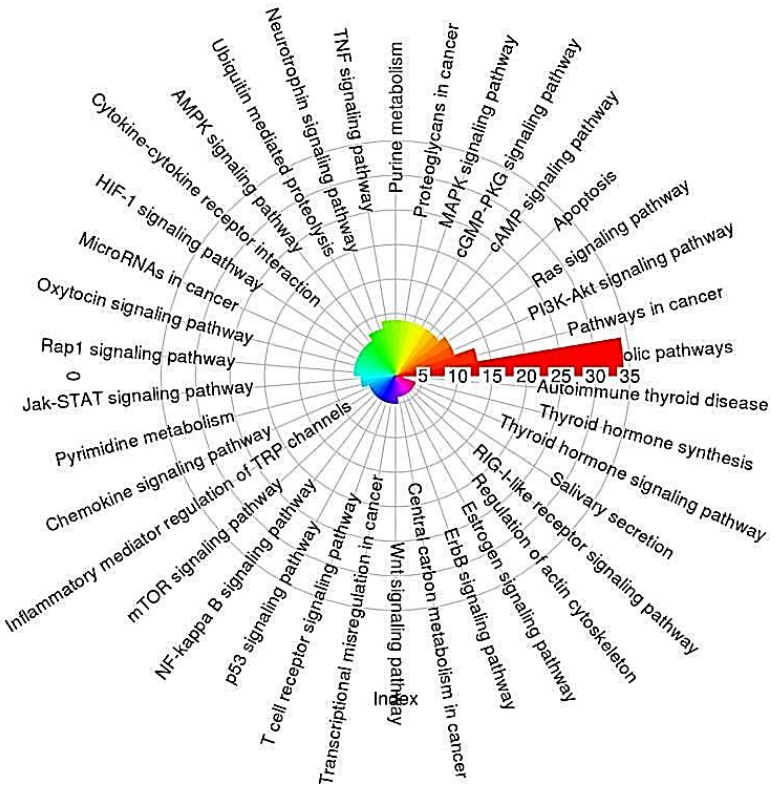

Figure 100 Circular classification of the emerged pathways based on the number of genes targeted by the miRNAs.

miR26 is downregulated in thyroid cancer cell lines and its restoration promote less aggressive phenotypes.

To further investigate the miRNA contribution in thyroid cancer and therefore in EMT, we decided to focus on specific miRNAs. Another important evaluation of the data refers to a summary-categorization of the miRs of interest for thyroid cancer with expression levels' criterion (Table 16). Among them, miR26 was a promising target, since in the literature as well as in HITS-CLIP data has the same transcriptional behavior across cancer cell lines.

The miR-26 family is highly conserved and composed of miR-26a-1, miR-26a-2 and miR-26b. The mature miRNA for miR-26a-1 and miR-26a-2 have the same sequence, which only differs from the mature miR-26b sequence by two nucleotides. Hsa-miR-26a1-5p (UUCAAGUAAUCCAGGAUAGGCU), Hsa-miR26a2-5p (UUCAAGUAAUCCAGGAUAGGCU) and Hsa-miR26b-5p (UUCAAGUAAUCCAGGAUAGGU). The mature sequences of miR-26 family members arise from the 5′ arm. Proportional levels of conservation exist among Hsa-miR-26a1-3p (CCUAUUCUUGGUUACUUGCACG), Hsa-miR26a2-3p (CCUAUUCUUGAUUACUUGUUUC) and Hsa-

miR26b-3p (CCUGUUCUCCAUUACUUGGCUC). Therefore, all the aforementioned miR26members were considered as an entirety.

miRNAs	Literature			CLIP data		
	NTHY	PTC	FTC	NTHY	PTC	FTC
miR-146b	-			-		
miR-222	-			-		-
miR-181b	-			-		-
miR-26	-		-	-		
miR-30d	-		-	-		
miR-21				-		-
let-7f	-		-	-	-	
miR-125a	-	-		-		
miR-221	-			-	-	-
miR-339		-	-	-		

red: downregulated

grey: upregulated

Table 16 Presentation of the most important downregulated and upregulated miRs in thyroid cancer cells lines in the literature and in HITS-CLIP data.

Additional reasons for our research to focus on miR26 were the facts that (i) it is down regulated both in PTC1 and FTC133, when compared to NTHY (ii) it is one of the top deregulated miRs in FTC, (iii) both miR26a and b are down regulated in cancer cell lines and (iv) these results obtained from the HITS-CLIP experiments are in accordance with the literature. Moreover, we examined miR26 expression levels, analyzing 14 PTC specimens of a Greek cohort. The samples were in pairs with adjacent "normal" tissue. 13 out of 14 PTC also demonstrated statistically significant increase of miR26 in cancer tissue (Figure 101). As follicular cancers are very rare and difficult to acquire, we performed an informatics analysis using a dataset from the TCGA database. Particularly, we examined miR26 expression levels in common variants of PTC, follicular variants of PTC and in normal tissue samples from TCGA database. Not surprisingly, miR26a1, -a2, -b were found downregulated in thyroid cancer samples compared to the normal tissues. Moreover, miR26a seemed to be downregulated in follicular variants of PTC compared to common variants of PTC leading to the conclusion that follicular cancer type of cells presents a significant decrease regarding miR26 expression levels (Figure 102).

To investigated the role of miR26 in thyroid cancer we performed *in vitro* and *in vivo* assays using cell-cultures and mice, respectively. However, xenografts can be generated only with FTCs, and not PTCs, as the latter do not generate tumors. Therefore, and in combination with the above results that demonstrate more significant downregulation of miR26 expression in FTC, from now on our investigation was concentrated on FTCs.

Synthetic mimic sequence for miR26 was used to transfected FTC133 cells in an attempt to increase the expression of miR26 and therefore invert the cancer phenotype. As a control, a scramble sequence was applied. miR26 expression increased significantly (> 20 times) as demonstrated by real time PCR experiments (Figure 103). The corresponding amplification curves and Tm peaks showed the differential cqs of mimic miR26 (Figure 104, left) and the two isoforms, miR26a1 and miR26a2 (Figure 104, right).

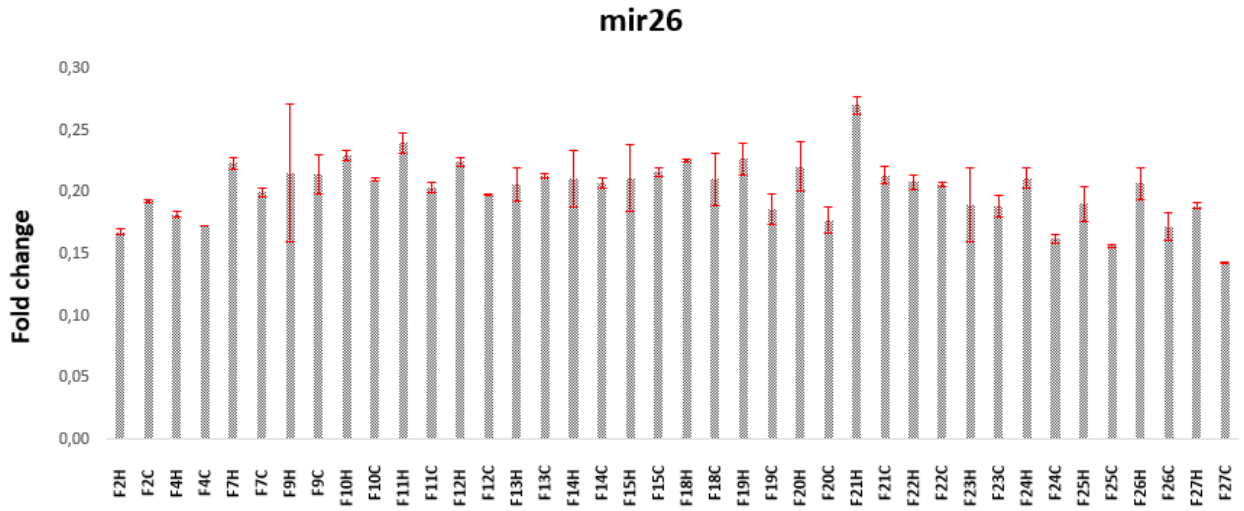

Figure 101 Relative expression levels of miR26 in PTC samples. 20 matched pairs were selected. mir26 was downregulated in Cancer (C) vs Healthy (H) in all samples with an exception in F2 sample. Statistically significant differences presented in F2,4,7,9,10,12,13,14,15,18,22,23,24.

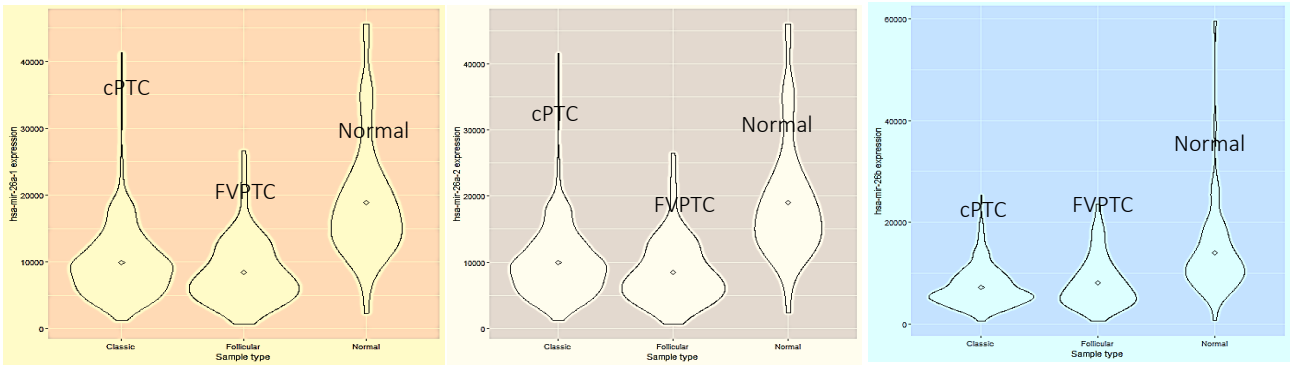

Figure 102 miR26a1, miR26a2 and miR26b expression levels in common variants of PTC, in follicular variants of PTC and in normal thyroid tissues from the Cancer Genome Atlas (TCGA) project database.

Figure 103 Expression levels of miR26 in mimic miR26 and scramble FTC133 transfected cells in real time pcr experiments. The relative *fold change was* calculated using the *2−ΔΔCt method*.

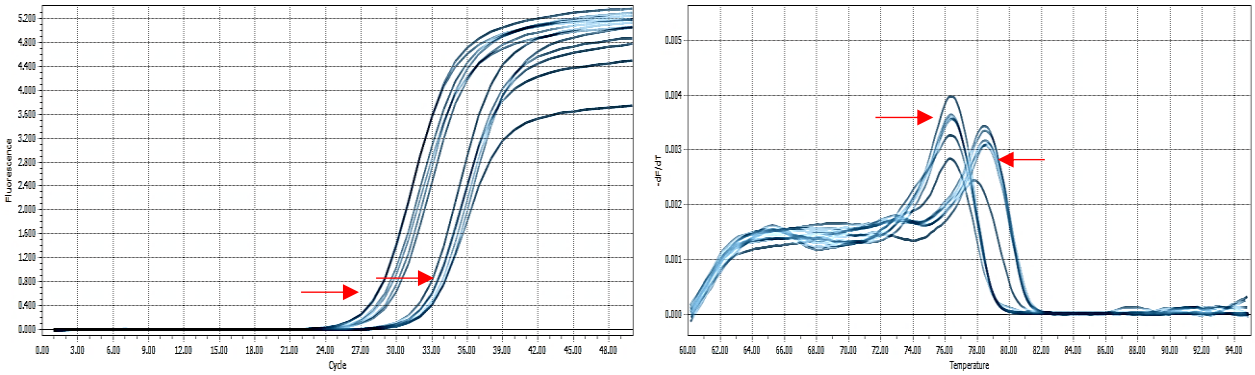

Figure 104 Amplification curves (bottom, left) and Tm peaks (bottom, right) of miR26 reactions between mimic miR26 and scrambled FTC133 transfected cells. The retardation in amplification peaks correspond to scrambled cells. The double peak in Tm peaks uncovers the existence of two members of miR26 family besides that the mimic sequence corresponds only to miR26a-5p.

Mimic miR26 transfected FTC133 cells were used to perform growth curves and wound healing assays. Mimic miR26 transfected cells demonstrated reduced growth rate (Figure 105) reveling a reversed correlation of miR26 expression and the potential proliferation capacity of the cells. However, regarding the involvement of miR26 to wound healing, no statistically significant differences between the mimic and scramble transfected cells were observed (Figure 106, 107). This indicated that miR26 did not demonstrate strong association with wound healing. Therefore, miR26 probably does not alter the wound repair and cancer invasion/migration ability.

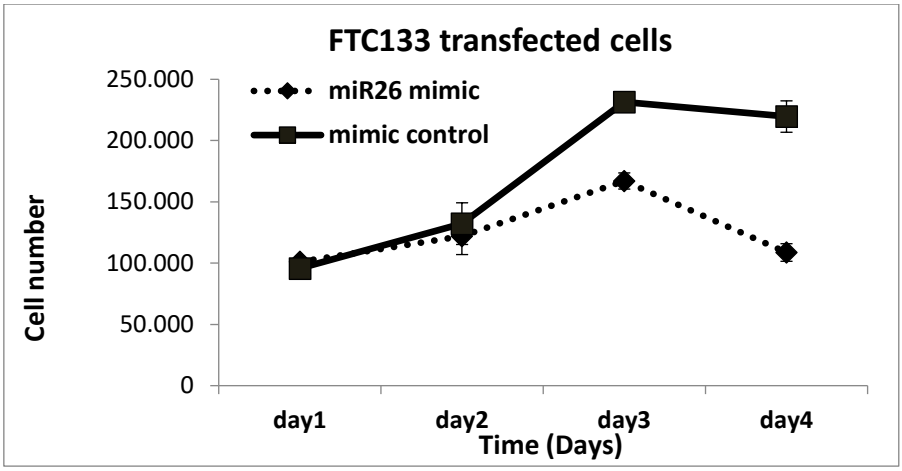

Figure 105 Increased miR26 expression correlated with decreased growth rate. Growth curves of FTC133 cells transfected with mimic-miR26 or scrambled sequences. The cells were counted every 24 hours. The experiment was performed in biological triplicates.

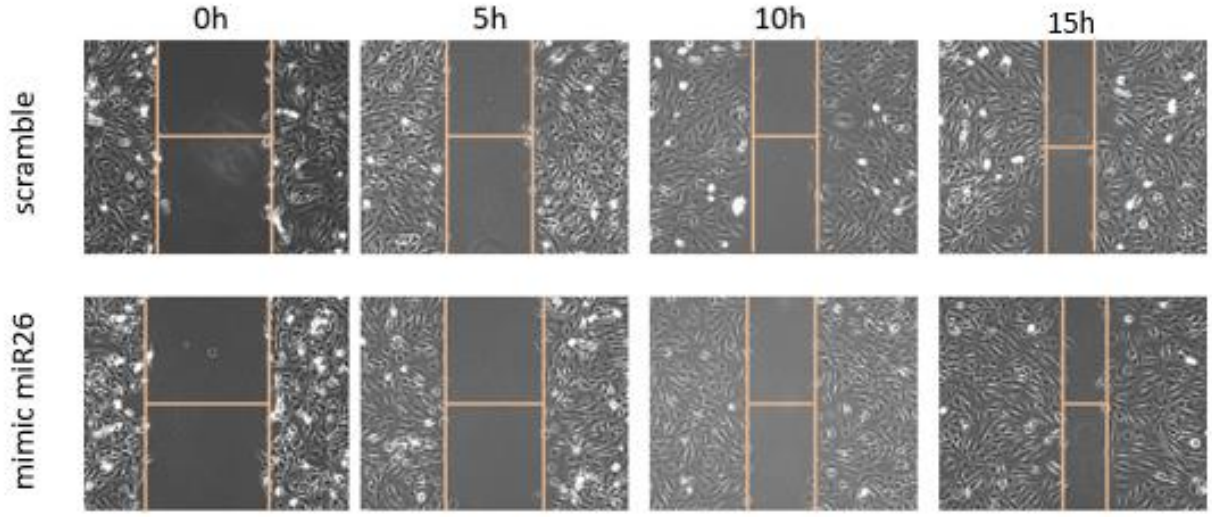

Figure 106 Wound healing assay for the mimic-miR26 and scrambled FTC-133 transfected cells at 0,5, 10 and 15 hours. The horizontal distance between two lines that delimit the cell population was calculated as the wound healing.

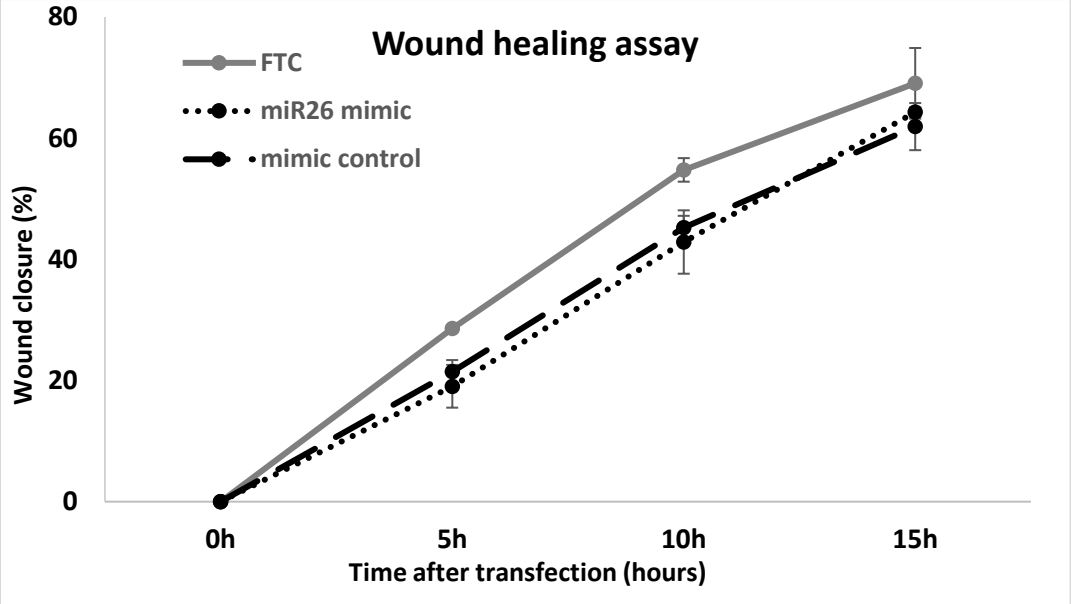

Figure 107 Graph of the wound healing in mimic-miR26 and scrambled FTC-133 transfected cells at 0,5, 10 and 15 hours. FTC133 (grey line), mimic miR26 (dotty line) and mimic scrambled sequence (dashed line).

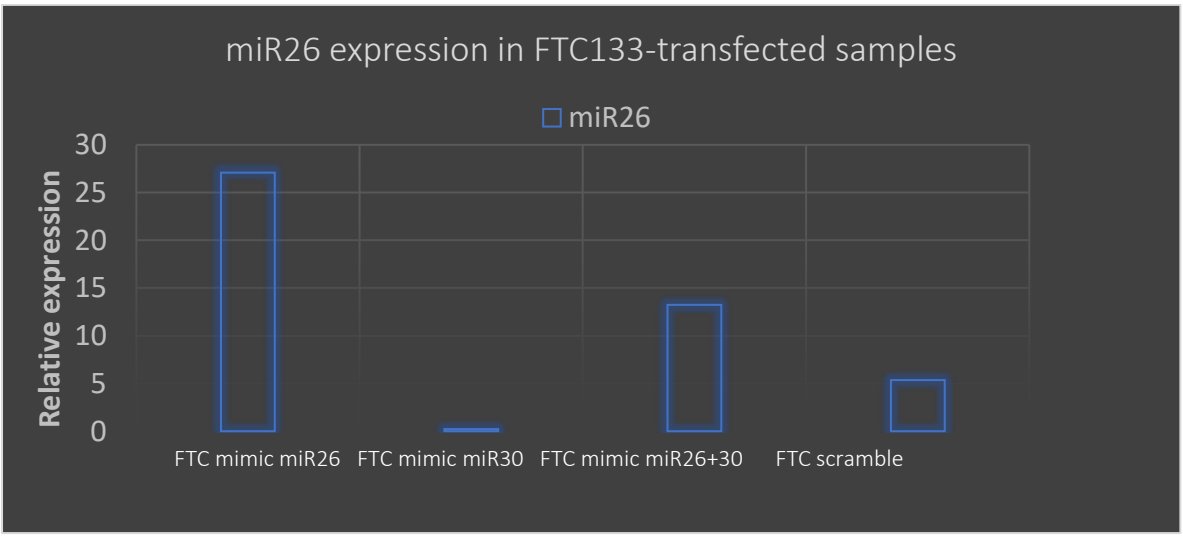

Figure 108 miR26 expression levels in FTC133 miR26, miR30 and combinatorial relative expression levels in FTC133-transfected samples.

Together our results suggest that miR26 leads to a restriction of the oncogenic potential of the thyroid cancer constituting a promising biomarker for early diagnosis and a potential component for future therapeutic approaches.

An additional experimental effort included the transfection of FTC133 cells with miR30 but due to the contradictive impact of the different members of this family and the combinatorial effect in the targets, transfected cells had no clear results (Figure 107). Testing the combinatorial effect of miR26+30, we observed a half relative expression of miR26 confirming the ineffective role of miR30 (Figure 108) probably due to the fact that half of the amount of mimic miR26 amount was used in these assays. The other half was mimic miR30, so the total amount of mimics should be unaltered and the same as in the above experiments.

miR26 affects the FTC tumor formation in mouse xenografts

The effect of miR26 expression was studied *in vivo*, in mouse xenografts generated by FTC133 cells transfected with mimics or scramble. Initially, NTHY ori 3-1, PTC1 and FTC133 cells were injected *subcutaneously* in male NOD/SCID mice and the generation of tumors was investigated. NTHY ori 3-1 and TPC1 cells failed to produce tumors regardless the number of cells injected. On the contrary, FTC cells were oncogenic. Three individual experiments were followed that FTC133 cells transfected with mimics or scramble were *subcutaneous*ly injected and the mice were examined at specific time intervals. The injection of cells carrying mimic miR26 sequences in mice (Figure 109a-e) lead to a reduction of the thyroid tumor mass development when compared to scrambled sequences (Figure 109b,c). Specifically, 200.000 cells were injected per mouse and the generation of tumors was examined. After 2 months, the tumor size in the FTC mimic-miR26 transfected mice were statistically significantly smaller than that of those transfected with scrambled sequences (1,44*0,82 versus 1,83*1,06). Mice were also injected with FTC133 cells transfected with miR30b, let7f or miR26a+30b mimics. Let7f also demonstrated a reduction on the rate of the tumor development, however miR26 promotes the higher one. miR30 did not show any changes while the combination of miR26a+30b reduces the effect of miR26 regarding the tumor size probably because a half of the amount of miR26 was used (the other half was miR30 so the total amount used for each transfection would be the same). Surprisingly, splenomegaly was not always related to the tumor size (Figure 109a).

NTHY ori 3-1 cells treated with miR26 inhibitor (synthetic sequence) failed to generated tumors. It is not clear if this effect was due to technical issues affecting the efficacy or due to a biological protective mechanism.

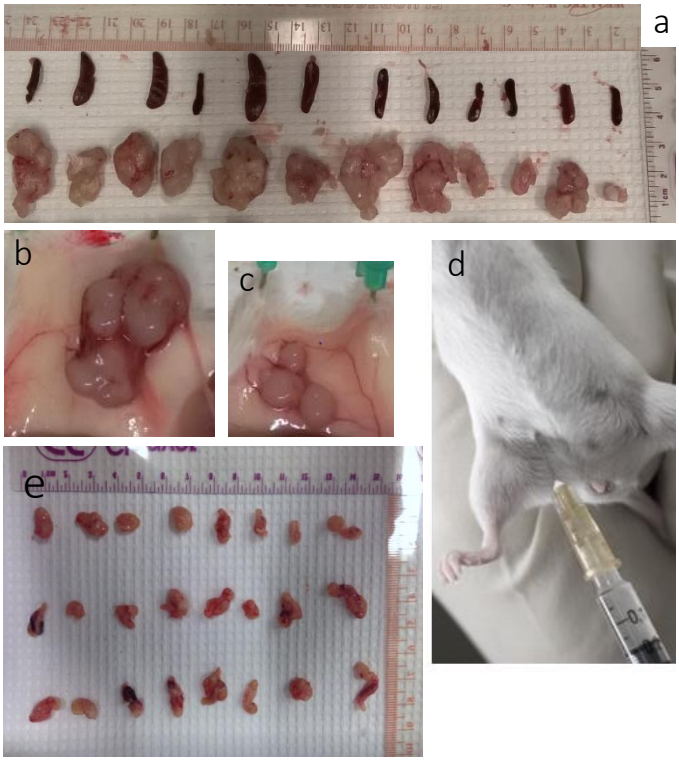

Figure 109 *Subcutaneous* injection of mimic miR26 sequences in mice. *(a)* The dimensions of the xenograft tumors developed and spleens of the tumor mice*, (b) a representative tumor mass from scrambled mice versus (c) small tumor mass from mimic miR26 mice. (d) Subcutaneous* injection. (e) Tumor masses from mimic miR26 mice.

	Tumor Dimensions	Mean Value
FTC scramble		1,83 x 1,06
mouse #1	2,0 x 1,5	
mouse #2	1,2 x 1,3	
mouse #3	1,9 x 0,9	
mouse #4	2,4 x 1,0	
mouse #5	2,4 x 1,6	
mouse #6	1,6 x 1,3	
mouse #7	2,2 x 1,5	
FTC miR26		1,44 x 0,82
mouse #1	1,5 x 1,0	
mouse #2	1,3 x 0,6	
mouse #3	1,6 x 0,9	
mouse #4	0,7 x 0,4	
mouse #5	1,5 x 0,7	
mouse #6	1,3 x 0,8	
mouse #7	1,6 x 1,0	
FTC let7		
mouse #1	1,0 x 0,6	
mouse #2	1,4 x 0,8	
FTC miR26+30		
mouse #1	2,1 x 1,7	
mouse #2	2,3 x 0,7	
mouse #3	2,2 x 1,0	

Table 17 Representative numbers of mice injected with FTC133 scramble, miR26a-5p, let7f and miR26a-5p+30b of the first in vivo experiment in xenografts NOD/SCID.

Table 17 showed some representative numbers of the tumor masses of the injected mice with FTC133 scrambled, mimic miR26a-5p, mimic let7f and mimic miR26a-5p+30b sequences of the first in vivo experiment in NOD/SCID xenografts. Five representative, in vivo experiments, were performed in order to have a rough result for the restoration of miR26 in miR26-depleted tumors.

Histological characteristics of mice tissues

The histological features of miR26-FTC133 and scrambled tumors were examined. The scrambled mice showed tumors of poor differentiation (solid, trabecular or islet-cell) and aggressive background. Numerous atypical mitoses (e.g. tripolar mitosis), extensive cytoplasm, presence of central necrosis with ghost shadows and recognition of scattered atypia (Figure 110a,b,c). The central necrosis does exist probably due to the hypoxic conditions of the tumor mass. Polymorphonuclear neutrophils were observed in the necrotic area (Figure 110a,b).

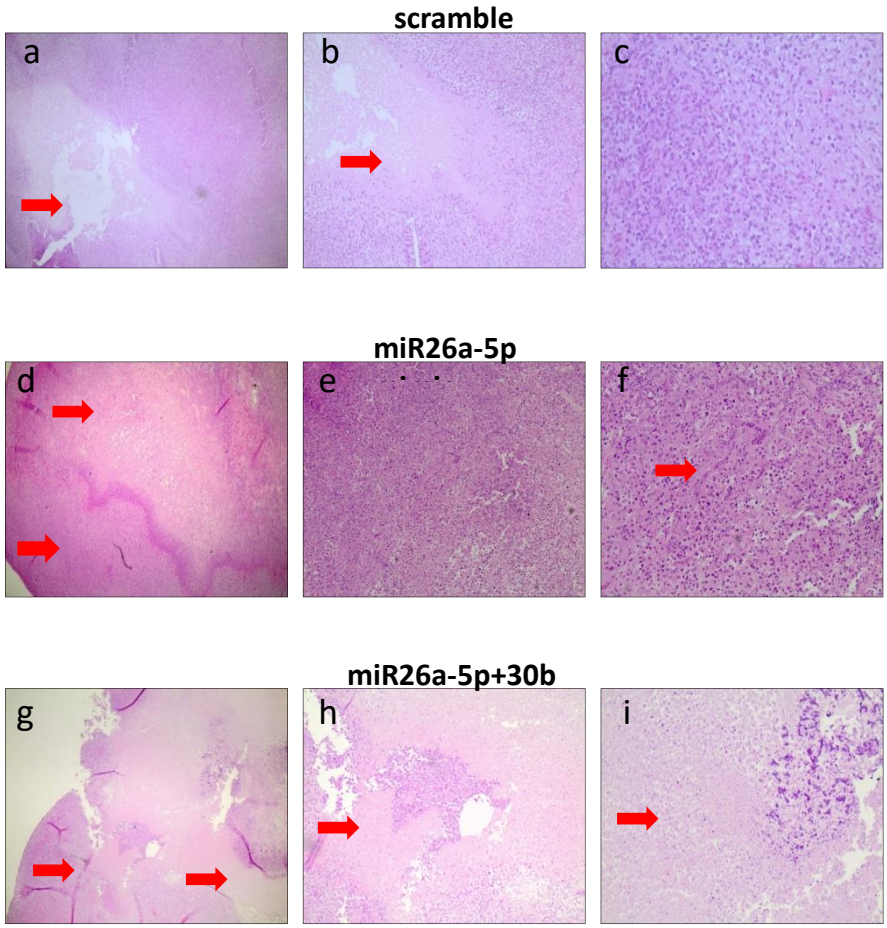

Figure 110 Hematoxylin/eosin staining of paraffin embedded tissue samples. Hematoxylin colors the nucleus of living cells in purple while eosin colors the cytoplasm in pink. Red arrows demonstrate the necrotic areas. Intense purple demonstrated the calcifications, (a-c) transfection of scrambled sequences, (d-f) miR26a-5p mimic sequences, (g-i) miR26a-5p+30b mimic sequences.

Scattered eosinophils (orange) were also observed. However, mir26 mimic-injected mice showed geographical type of necrosis with necrobiotic elements and high cellularity (Figure 110d,e,f). miR30 mimic-injected mice showed extensive necrosis, central but also peripheral, also visible macroscopically like scrambled mice (data not shown). The area of necrosis did not have a solid texture unlike the rest of the tumor. Calcifications could also be visible. In case of miR26a-5p+30b mimic-injected mice homocentric circles with necrosis were present. Necrosis exists but was not so extensive (Figure 110g,h,i).

Differential expression analysis of mRNA targets of miR26 – correlation pathway communities using a disease-related map of integrated information (Pathwalks)

To better understand the crucial targets, interactions and pathways related to miR26, we further pursue the examination of the differential gene expression via RNA sequencing of FTC133 cells overexpressing miR26. The cells were transfected with mimic mir26 or scrambled sequences, followed by RNA extraction, evaluation of RNA (Figure 111,112), DNA library construction and two paired

sequencing. From the differential expression analysis emerged 1,201 statistically significant deregulated genes, of which 605 were upregulated and 596 were downregulated.

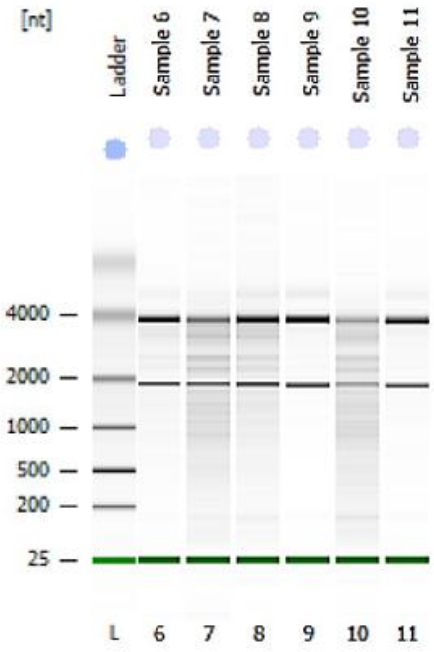

Figure 111 Electrophoresis File Run Summary for identification of RNA integrity by Eukaryote Total RNA Nano assay.

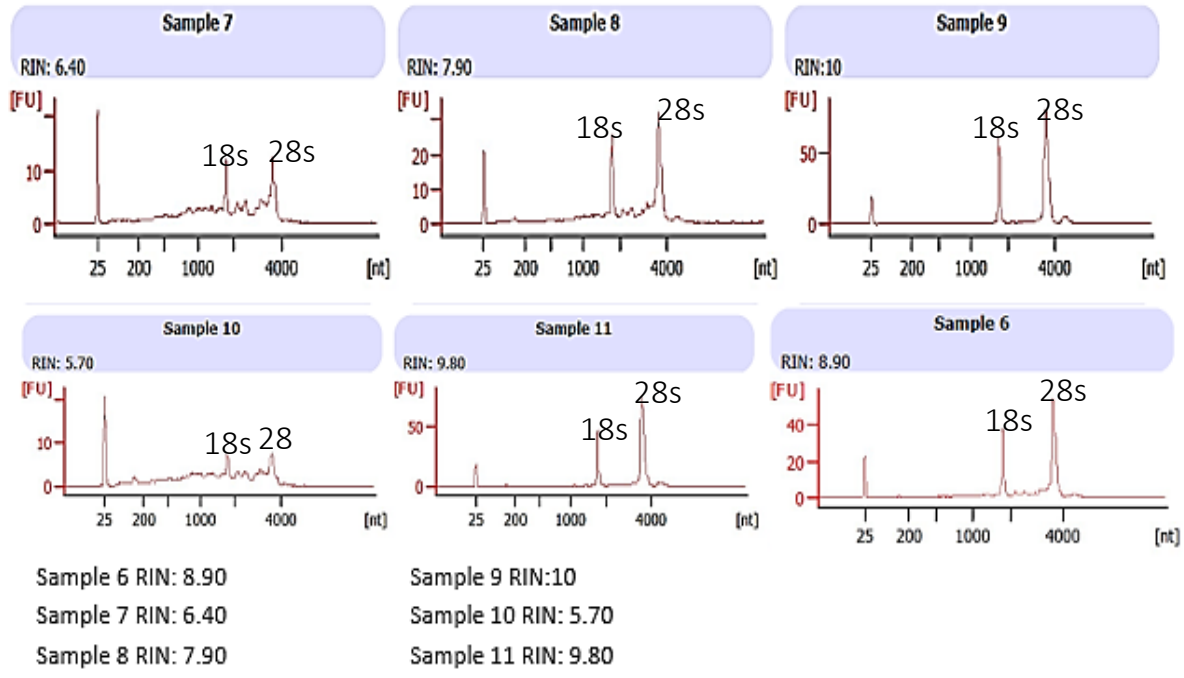

Figure 112 Electropherogram with RNA integrity number (RIN). The four peaks indicated as markers, 5S (almost undetectable) denotes small RNA, 18S and 28S denote ribosomal RNA respectively. Parameterization of the gel and assignment of RIN value by a bioanalyzer (analysis of the intensity profile).

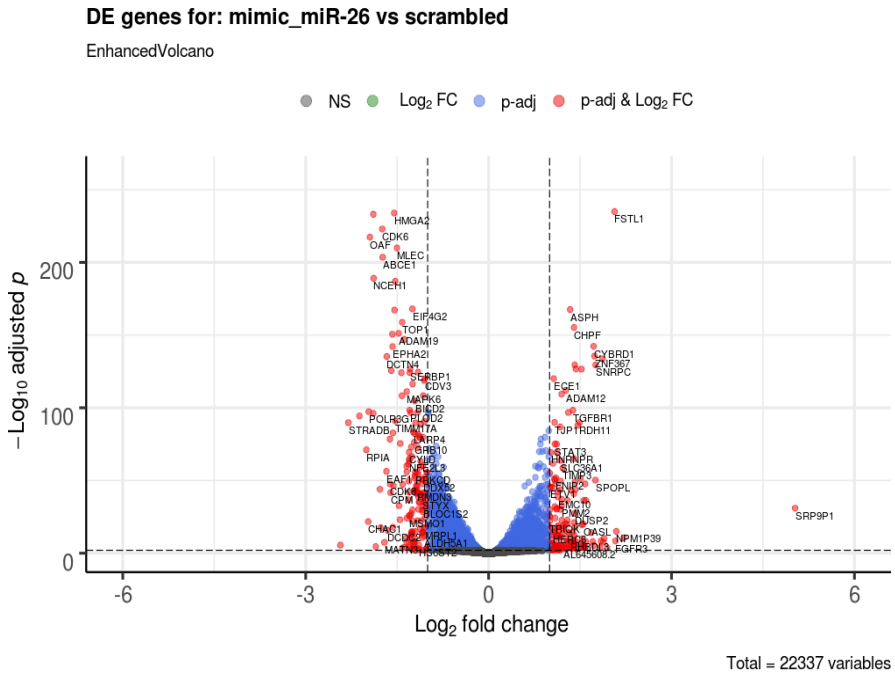

Figure 113 Volcano plot for visualization and identification of genes with large fold changes that are also statistically significant. Scattered points represent genes showing statistical significance (log10 adjusted p-value) versus magnitude of change (2fold-change). The most upregulated genes are towards the right, the most downregulated genes are towards the left, and the most statistically significant genes are towards the top ("EnchancedVolcano" package, R).

Visualization of the genes with large fold changes that are also statistically significant was achieved by using Volcano plot (Figure 113). The top 50 differentially expressed genes emerged from the filtering (p-value, fold-change) of the genes displayed in the volcano plot were used to construct a heatmap (Figure 113).

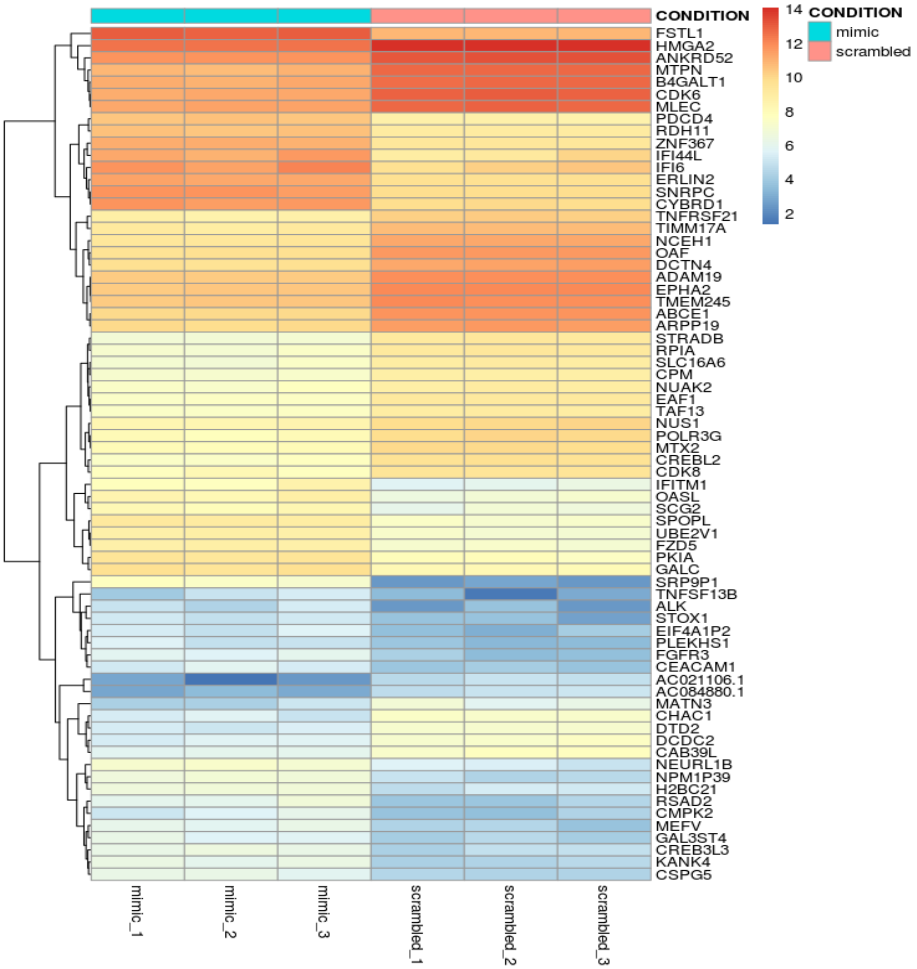

Figure 114 HeatMap for hierarchical clustering of the top 70 differentially expressed genes between miR26 mimic and scramble samples. The color and intensity of the boxes represent changes of gene expression. The red color indicated the up-regulated genes while blue represents down-regulated genes ("pheatmap" package, R).

The deregulated genes are related to cell cycle, apoptosis, cell division, cell adhesion and transcriptional mis-regulation in cancer. Representative examples of important molecules differentially expressed in the presence of miR26 overexpression included Serine/threonine protein kinase STE20 subfamily (STRADB) (log-fold change= -2.3, p-value <0.01), Programmed Cell Death 4 (PDCD4) (log-fold change= 1.87, p-value <0,01), CEA Cell Adhesion Molecule 1 (CEACAM1) (log-fold change= 1.52, p-value <0.01), Cyclin Dependent Kinase 8 (CDK8) (log-fold change= -1.61, p-value <0.01) and Cyclin Dependent Kinase 6 (CDK6) (log-fold change= -1.74, p-value <0.01).

STRADB is a component of a complex involved in the activation of serine/threonine kinase 11, a master kinase that regulates cell polarity and energy-generating metabolism(https://www.ncbi.nlm.nih.gov/gtr/genes/55437). It is engaged in the relocation of this kinase from the nucleus to the cytoplasm, and it is essential for G1 cell cycle arrest mediated by this kinase. The protein encoded by this gene can also interact with the X chromosome-linked inhibitor of apoptosis protein, and this interaction enhances the anti-apoptotic activity of this protein via the JNK1 signal transduction pathway. Its antiapoptotic function might be reduced via its downregulation promoted by mimic miR26 function.

PDCD4 is a protein coding gene associated with Colorectal Cancer and Tongue Squamous Cell Carcinoma. Among its related pathways are mTOR signaling pathway (Pathway Interaction

Database) and Proteoglycans in cancer (Matsuhashi et al., 2019). It has been reported that PI3K/Akt/mTOR pathway constitutively suppresses expression of programmed cell death 4 (PDCD4) tumor suppressor protein in acute myeloid leukemia and breast cancer cells. In our case, PDCD4 was found highly upregulated suggesting that the function of PI3K/Akt/mTOR pathway is suppressed.

CEACAM1 appear to have multiple cellular activities including roles in the differentiation and arrangement of tissue three-dimensional structure, angiogenesis, apoptosis, tumor suppression, metastasis, and the modulation of innate and adaptive immune responses. Specifically, CEACAM1 constitutes a tumor suppressor whose expression is known to be lost in the majority of early adenomas and carcinomas; the loss of CEACAM1 expression is more common in neoplastic tumors (https://doi.org/10.1038/sj.onc.1208259). Its upregulation is probably guided by the protective action of mimic miR26 increasing the apoptotic potential of the tumor.

Other worth-mentioned deregulated genes are the CDKs. They are pivotal kinases in cell cycle regulation and progression. CDK8 kinase and its regulatory subunit, cyclin C, are components of the mediator transcriptional regulatory complex, involved in both transcriptional activation and repression by phosphorylation of the carboxy-terminal domain of the largest subunit of RNA polymerase II. CDK6, along with its partner CDK4, are key players in cell cycle progression. The complex has been implicated in a number of cancer types, and is the focus of therapeutic research and development. Also, there is one targeted therapy for CDK inhibition is palbociclib, which may lag the growth of advanced stage cancers. The fact that they were found downregulated in miR26 overexpressing cells, advocating the retardation of the cell proliferation in thyroid tumors.

We continued the informatics analysis aiming to uncover the miR26 targets involved in cell proliferation, apoptosis or necroptosis pathways.

In order to identify the experimentally verified targets of miR26a-5p, we integrated our results with direct targets of miR26 (3,149 mRNAs) as listed in TarBase V8. From 605 upregulated genes, 133 are experimentally verified direct targets of miR26. From 596 downregulated genes, 328 are experimentally verified direct targets of miR26. The fact that the 51,6% of the downregulated genes are confirmed targets of miR26 by TarBase V8, suggests that the other 48,4% of currently unconfirmed targets probably contains true targets.

The 100 top-expressed genes (upregulated and downregulated) used for pathway analysis and functional annotation utilizing the PathWalks algorithm.

It was used as a stochastic approach that can be used for both efficient discovery of strong connections and identification of communities formed in networks. A random walker can cross a pathway-to-pathway network under the guidance of a disease-related map. The latter is a gene network that we construct by integrating multi-source information regarding a specific condition such as the therapeutic function of mimic miR26 in thyroid cancer. The most frequent trajectories highlight communities of pathways that are expected to be strongly related to this specific disease.

Thus, the network of the 100 most important pathway-to-pathway interactions constructed using Cytoscape (Figure 115). The most important nodes (bigger size) regarding the degree (metric in which the size of a node reflects its interaction with other nodes) appeared to be: metabolic pathways, PI3K/Akt, MAPK, pathways in cancer and cell cycle pathway.

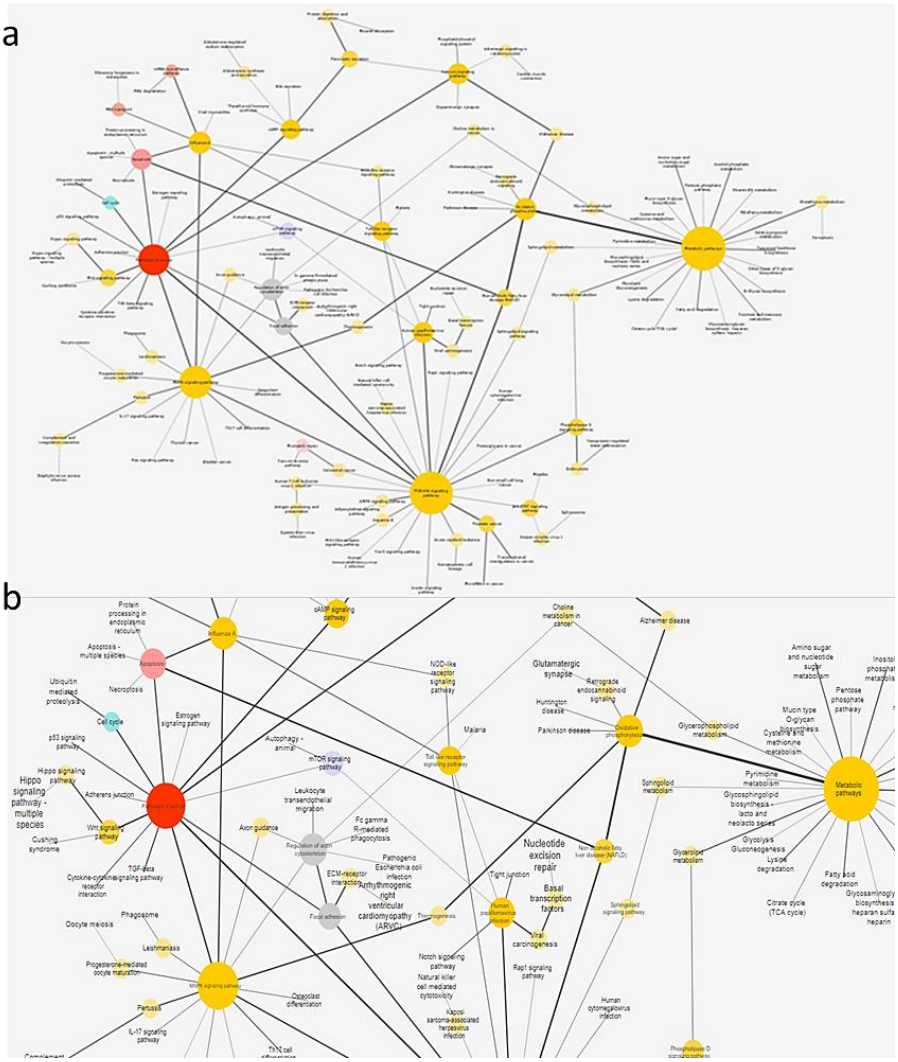

Figure 115 (a) The PathWalks gene map/network consists of 100 gene nodes representing KEGG pathways and 1965 connections. The node size and transparency are based on the node's degree and the edge width and transparency on the edge weights and (b) zoomed network in interactions of cell cycle.

Moreover, taking into account the shared integrated information (genetic interactions, physical interactions, gene co-expression, colocalization, common pathways), 11 clusters of pathways emerged. Cluster 3 containing 78 pathways appeared to be the cluster of interest, since it contains fundamental pathways such as cell cycle, microRNAs in cancer, parathyroid hormone synthesis, secretion and action, thyroid hormone signaling, PI3K-Akt, pathways in cancer, ubiquitin, tight junction, adherens junction, Hippo signaling, cellular senescence and cytosolic DNA sensing. Cluster 3 found to have 52 common pathways with the other Clusters, 9 unique Pathways are downregulated and 15 pathways upregulated (Figure 117). Downregulated ones are in focus on this study because they might direct targets of miR26.

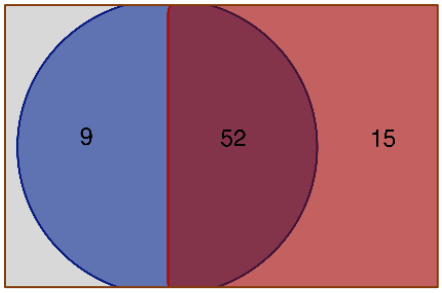

Figure 116 Venn Diagram regarding the activated pathways (upregulated and downregulated) in Cluster 3. 52 common pathways between Cluster 3 and the other Clusters. 9 unique Pathways are downregulated and 15 pathways upregulated in Cluster 3.

Specifically, cell cycle pathway, amongst others, is regulated by 5 downregulated experimentally verified targets of miR26a-5p that have previously reported (Xu et al., 2020) by Sander and colleagues suggesting that came specifically of the function of miR26a-5p. More specifically, the genes, found downregulated in our cluster and also investigated in the aforementioned study, were CCNB1, CCNE2, CDK8, CDC25A, MYC and SKPT2 strengthening our results. Further analysis is needed in order to examine specific predicted targets in wet lab as promising diagnostic and therapeutic strategies.

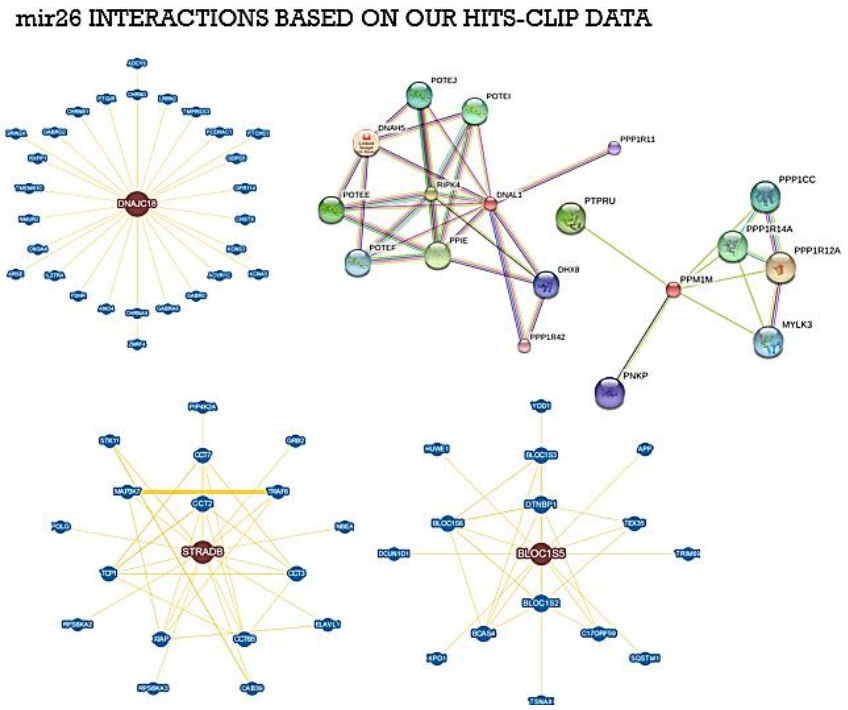

Figure 117 miR26 interactions that emerged from HITS-CLIP analysis data.

Then, we attempted to explore its direct targets. Based on the HITS-CLIP data DNAJC18, PPM2M, BLOC155, CLSN, RAB26, USP9, USP12 RBM5, PAWR and STRADB are among the most important ones, as well as their interactions (Figure 117). Further investigation followed based on RNAseq experiments, aiming to verify the crucial targets, interactions and pathways related to miR26. From the cross-examination, PAWR and STRADB are presented in both experiments. PAWR (Pro-Apoptotic WT1 Regulator) is a pro-apoptotic protein capable of selectively inducing apoptosis in cancer cells, sensitizing the cells to diverse apoptotic stimuli and causing regression of tumors in animal models and STRADB (STE20 Related Adaptor Beta) is a master kinase that regulates cell polarity and energy-

generating metabolism. The latter is essential for G1 cell cycle arrest mediated by this kinase. The clarification of PAWR and STRADB role in thyroid cancer development is still pending. In any case, miR26 emerges as a potential important molecule for early diagnosis, prognosis and therapy.

DISCUSSION

Thyroid pathologies are a common medical condition that affects the function of the thyroid gland. The incidence of thyroid nodules detected with ultrasonography is 19%-67% in the general population and exceeds 50% in patients over the age of 65 years. The prevalence of palpable thyroid nodules varies between populations and ranges from 4% to 7% within the USA, which represents approximately 10-18 million affected individuals (Dean & Gharib, 2008; Keutgen et al., 2013).Besides iodine deficiency, other epidemiologic and genetic risk factors include female sex, increasing age, previous head and neck radiation and familial predisposition (Cooper et al., 2009; Dean & Gharib, 2008). However, histopathological findings have revealed that significant number of nodules (up to 15%) display malignant biological behavior, so adequate evaluation is essential ((Cooper et al., 2009; Yassa et al., 2007).

Thyroid cancer constitutes the most common malignancy of the endocrine system, representing 3.8% of all new cancer cases in the United States (Nguyen et al., 2015). Estimates of the rate of malignancy in thyroid nodules are subjected to several biases, because not all nodules undergo surgical resection and confirmatory pathological examination. Moreover, the recent years, the increase in incidence of thyroid cancer without an accompanying rise in mortality may reflect the growing detection of indolent forms of thyroid cancer (Jegerlehner et al., 2017). This probably triggered early intervention with impressive results but simultaneously fueled unnecessary thyroidectomies. Comparing recent trends in surgical intervention rate for thyroid cancer with the incidence and mortality of thyroid cancer, main aim is to assess overdiagnosis and resulting overtreatment. Tumors such as NIFTP, WDT-UMP, FT-UMP that are borderline and encapsulated, remains to be determined if a surgical intervention could be avoided.

In this population study, we characterized the Greek cohort regarding the pathophysiology, the tumor location, subtyping and eventually micro-staging features. We correlated clinico-pathological features under the prism of the deep understanding of the aggressiveness as a result of EMT transition of specific subtypes of thyroid tumors with poor prognosis. Usually, the retrospective and prospective studies have biases such as the implication of different physicians which follow different ways of evaluation of patient histological sections. A second important bias is that those patients that are guided to a surgical thyroidectomy have a burdened medical history and intercurrent characteristics as a reasonable consequence of the malignancy, that created precarious conclusions for seemingly related variables. To overcome all these issues, we used the histological records of one physician, Dr Sofia Tseleni, with consistency in the histological descriptions and medical conclusions due to her work experience, minimizing the bias.

From the analysis, according to Cancer SEER STAT of American Society (Database of the National Cancer Institute (NIH), we compared them to our Greek cohort data and we found that the incidence differs regarding the age decade of onset. American patients present a rise in age decade 45-64, while Greek patients present a rise quite earlier from the third decade of life and more specifically, in 20-54. The previous observations together with the tumor sizes that in high percent do not exceed the 1,9 cm probably reflecting an early intervention in Greece during the last decades.

The distribution of subtypes of thyroid cancer in the same cohort is similar to that in other European countries in the bibliography with a predominant percentage of PTC (46,45 %). Among the PTC variants, the most predominant ones are the common variant in a striking percentage of 52,78 % which is followed by follicular variants (26,39 %). TCVs are following with a non-negligible percentage of 11,11 %. In any case, given that a patient has a thyroid pathological condition malignancy, benign

nodule or specifically hyperplasia or autoimmune thyroiditis, Hashimoto (HT), he/she could have the same chances to be a male or female. However, the prevalence of women to men is 4:1 for thyroid pathological conditions, such as HT and malignancies. To better understand whether Hashimoto constitutes a prognostic factor, for tumorigenesis, a detailed follow-up study is needed.

The interrelationship of HT and PTC was firstly disclosed by Dailey and colleagues back in 1955 (Dailey et al., 1955). Since then, in numerous population studies, attempts were made to confirm or even contradict this conclusive result through massive patients' screenings. Slightly over 14 million were affected from HT in the United States and especially women. Both diseases are widespread worldwide and the increasing prevalence rate makes the requirement of the clarification of their conjunction more imperative and indispensable. Despite the fact that the correlation between them, remains to be a controversial issue, the coincidence of the thyroid malignancy and HT declare that the latter constitutes a crucial risk factor for the tumor progression (Consorti et al., 2010; Feldt-Rasmussen, 2020; Lee et al., 2013; Liang et al., 2017). Beyond doubt, the presence of the HT in patients with thyroid cancer indicates better prognosis (Liu et al., 2014; Pilli et al., 2018; Selek et al., 2017). Several studies greatly support that practically, the risk factor of thyroid malignancy is the up-regulation of TSH levels which coexists HT and not the HT per se (Fiore et al., 2011; Zhang et al., 2012).

Interestingly, Castagna et al. in 2014 (Castagna et al., 2014) perceived and noted the idea that the strong correlation between HT and PTC may also derives from the patient selection bias. The samples, *on most* occasions, were retrospectively analyzed after total thyroidectomy, thereby exhibiting, inaccurately, HT as an important risk factor for thyroid tumor development. As might be expected, when the sampling method is the Fine-needle aspiration (FNA), another strictly limiting factor is the experience and the good technique of the Cytologist which affect the results or the histological reports of a cohort from different Cytologists. It is also worth noting that a large group of people suffering from PTC are completely unaware of the chronic or recent existence of HT. Therefore, the aforementioned bias could affect the results regarding the relation and correlation of the autoimmune thyroiditis and PTC carcinoma suggesting HT an independent factor for thyroid tumorigenesis.

Additionally, individuals with malignancies seem to have lighter thyroid glands (around normal weight ranges). An almost 75% of the individuals of the Greek cohort is concentrated under and around 40 grammars of the thyroid gland indicating that thyroid cancer occurs even in normal thyroid glands. This is in agreement with the fact that thyroid cancer is a 'few hit' cancer. Nevertheless, the tumor focality does not change the distribution of the patients with malignancies, however in different types of thyroid cancer there were statistically significant differences in thyroid weight range. PDC carcinomas were present in heavier glands when compared to PTC carcinomas and the latter have a more intense tendency to be developed in heavier glands than microPTC making thyroid weight an extra potential prognostic factor. Interestingly, MTC are slightly shifted and they present an increase in ~60 grammar-thyroid glands.

A trend for the right lobe preference in thyroid pathologies was also observed. This preference was responded in the groups of microPTC and TCV carcinomas with statistical significance demonstrating that the existence of a right focal finding needs more attention from the clinical doctor. Differences between left-sided and right-sided malignancies is not a novel observation since in colorectal cancer, it is essential to evaluate right-sided and left-sided tumors as separate entities, and thus, design more effective therapy regime considering the differences (Baran et al., 2018).

Now, other characteristics of thyroid cancer aid to micro-staging of each surgical specimen. Among them, extra-thyroid extension or thyroid capsule invasion, the presence of tall cells, the presence of

intranuclear inclusion structures, pseudoinclusions and the presence of fibrotic regions inside the tumors were tested and related with high tumor aggressiveness.

Importantly, we found that the percentage of extra-thyroid extension increases exponentially in TCVs, enhancing the idea of the high aggressiveness and infiltration.

The TCV was firstly described by Hawk and Hazard in 1976 (Hawk & Hazard, 1976); but the descriptions of PTC with tall cell morphology in the bibliography date back to 1948 (Crile et al., 1948). TCV has specific attributes such as elongated tall cells with oncocytic cytoplasm, distinct cell borders, different intranuclear inclusions (compared with classic PTC), prominent central nucleoli, multiple inclusions within the same nucleus imparting a ‘‘soap bubble appearance’’, and higher frequency of cases with lymphocytic infiltration (Solomon et al., 2002).

Established prognostic features such as gross extra-thyroid extension and extensive vascular invasion is vital when deciding on the extent of surgery or the need for adjuvant therapy. A microTCV may not need more than a simple lobectomy while TCV carcinomas with gross extra-thyroid extension in the trachea will need total thyroidectomy with or without tracheal resection depending on the extent of the tumor. The fundamental surgical principle of ‘‘gross total excision’’, with an R0 resection when feasible must remain the gold standard for planning surgery for thyroid cancer.

Regarding the intranuclear inclusions structures responded in TCVs, besides cPTC carcinoma exist in gastric adenocarcinoma, in primary gastric lymphoma, in malignant melanomas, in benign melanocytic lesions, in 75% of patients suffering from non-alcoholic steatohepatitis (NASH) but only in 10% of patients with alcoholic hepatitis, in meningioma, and in usual ductal hyperplasia of the breast (Pinto et al., 1996; Saito et al., 1986; Zhu et al., 2013). Ultrastructural studies of hepatocytes disclosed that the inclusions contained cytoplasmic structures, often with degenerative changes, supporting the assumption that the pseudoinclusions are independent from the cytoplasm (Frajola et al., 1956).

In our settings, pseudoinclusions are present in a striking percentage of 92,54 % in TCVs while in follicular and cPTC do exist in a smaller proportion. Inclusions were stained intensely with eosin, since they have eosinophilic/oncocytic cytoplasm revealing acidophilic environment which provides basic structure binding such as proteins. The pseudoinclusions observed were morphologically similar to the “plump cells”, which are mostly eosinophilic (Virk et al., 2014). Mediators of eosinophilic environment include peroxidase, lipase, plasminogen, nucleases (RNAases), growth factors, cytokines and ROS.

As intranuclear inclusions as cytoplasmic invaginations into the nucleus that mimic true nuclear inclusions, they have been reported, for the first time, by Paul Ehrlich with the term vacuoles in the cellular protoplasm of diabetic individuals, in 1883 (Ehrlich, 1883; ; Schiller, 1949). Induction of nuclear inclusions can be achieved by externally administered drugs such as long-term colchicine in *in vivo* models (Wessel, 1958). Electron microscopy ultra-structural details of the nuclear inclusions demonstrated that they do not necessarily have a limiting membrane. This structure resembles to nuclear membrane (Leduc & Wilson, 1959). Their autonomous nature has been indicated by the fact that the enclosed substances can vary from autophagic vacuoles with lysosomal bodies suggesting an active macro-autophagy process and ubiquitination in case of neural tissue (Jaskólski et al., 2012; Wenzel et al., 2010) till viral particles surfactants, immunoglobulin, glycogen, biotin, nuclear lamins, or polyglutamine (Ip et al., 2010). The so called nuclear *pseudo*-inclusions (INCI) belong to the first category where cytoplasmic invaginations are formed into the nucleus and they are sharply bordered by nuclear membrane and condensed chromatin (Ip et al., 2010).

In PTC, pseudoinclusions have been found in 50-100% of aspirates. MTC, PDC, ATC and very rarely, benign thyroid nodules (e.g., nodular goiter, follicular adenoma, and lymphocytic thyroiditis) also have pseudoinclusions, ending up that these structures do not present clear specificity (Cibas & Ali, 2017). Consequently, they should always be interpreted under the prism of the other architectural and nuclear features.

A potential precursor condition of an intranuclear inclusion may constitute a nuclear groove present in papillary (85-100% of cases), in non-papillary neoplasms (70-80% of cases) and in non-neoplastic thyroid lesions (50-60% of cases) (Gould et al., 1989; Shurbaji et al., 1988). In 1987, Deligiorgi-Politi mentioned that infoldings of nuclear membrane might be the early stage of deep cytoplasmic invaginations, responsible for the formation of pseudoinclusions (Das, 2005). Simultaneous presence of creases and pseudoinclusions were not observed, but grooves and pseudoinclusions rarely did exist.

Accordingly, in our cohort, only a small percentage of TCVs is characterized by pseudoinclusion absence and the fact that histological sections with grooves have no significant number of pseudoinclusions and vice versa, leads to the assumption of a sequence of the molecular and cellular events. The presence of pseudoinclusions seems to follow the formation of grooves and invaginations and the latter seems to follow the presence of tall cell formation. In a way, the cells appear to be synchronized in each step and probably after every hit, are guided to the next cytoskeletal alteration dependent on specific circumstances. In consonance with this scenario of synchronization, young individuals having solid variant phenotype are characterized by the presence of grooves, whereas elderly individuals are characterized by the presence of pseudoinclusions, but it needs further investigation.

Oyama et al have been reported that pseudoinclusions enclosed enlarged RER, many Golgi vesicles, small vesicles (diameter of 300–500 nm) and fragments of mitochondria or crumpled membranes caused by increased protein synthesis and/or protein accumulation (Oyama, 1989), as well as small vesicles inside them (Söderström & Biörklund, 1973). Also, in an effort to clarify the biological function of these formations, Schwertheim and colleagues reported the presence of autophagy-associated proteins within the inclusions together with degenerated organelles and lysosomal proteases suggesting their involvement in autophagy and proteolysis (Schwertheim et al., 2019). The number of pseudoinclusions with positive immunostaining for autosomal proteins p62, ubiquitin, LC3B, cathepsin B and cathepsin D were statistically higher in PTC cases harboring $BRAF^{V600E}$ mutation compared to those PTC tumors with *BRAF* wild-type. A positive correlation between $BRAF^{V600E}$ mutation and nuclear features of PTC including pseudoinclusions do exist and tumor cells, firstly, defined by Finkelstein and colleagues as “plumb eosinophilic cells” also showing inclusions (Austria et al., 2018).

In line with that, molecular studies reported a correlation between the existence of tall cells and the aforementioned inflammatory and altered background with the existence of $BRAF^{V600E}$. More specifically, targeted expression of $BRAF^{V600E}$ in thyroid cells of transgenic mice resulted in irregularity of nuclear contours and occasional nuclear grooves-invaginations (Fischer et al., 2010; Knauf et al., 2005). Also, Rusinek and colleagues found that in thyroid glands of a significant fraction of *BRAF* (+) mice, changes in nuclei were observed that classified these cases as not healthy but not yet PTC. They were also characterized by the presence of single nuclei with grooves or pseudoinclusions, heterogeneous nuclei, and separation of altered cells in single foci (Rusinek et al., 2015). Runx2 has been reported as a mediator of resistance to $BRAF^{V6OOE}$ targeted therapy. The continued existence of actin inside the nucleus forming rod like structures is related to the induction of osteogenic genes in a Runx2 dependent manner. Runx1 is frequently involved in acute myelogenous leukemias and myelodysplastic syndromes through acquired chromosomal rearrangement and point mutations (Niu

et al., 2012). Runx2 is implicated in osteogenic differentiation in solid tumors such as thyroid, breast and pancreas (Niu et al., 2012). Deletion of Runt domain of Runx2 demonstrated that is essential for proliferation and migration (Deiana et al., 2018). In cBioportal cohort, Runx2 was found elevated in $BRAF^{V600E}$ positive samples in pathways of parathyroid hormone synthesis and transcription regulation in cancer. Also, Runx1 has been upregulated in $BRAF^{V600E}$ positive samples with the coexistence of pseudoinclusions. These two observations explain in a way the intense metastatic potential and the tendency for tumor growth and invasion.

In human melanoma cells, $BRAF^{V600E}$ induces spindle abnormalities, excess centrosomes and mis-aggregation of chromosomes leading to aneuploidy (Cui et al., 2010) and phosphorylation of MPS1 by $BRAF^{V600E}$ (Liu et al., 2013). Fischer and colleagues reviewed the causalities for alterations in the nuclear envelope in human cancers (Fischer, 2014). They reported that *RET/PTC1* micro-injection in normal human thyroid epithelial cells induced nuclear envelope irregularity during the interphase and the formation of inclusions (Fischer et al., 1998; Fischer et al., 2003) they concluded that *BRAF* mutations may directly drive to inclusions by altering nuclear envelope and chromatin organization but without a clear association (Fischer, 2014).

Despite several observational studies, the mechanisms which are involved in the formation and biological function of inclusions are still quite unclear (Bozler et al., 2014; Lammerding et al., 2006; Maniotis et al., 1997). Fundamental molecules of regulation of gene transcription and chromatin remodeling are microprocessor components, DROSHA and DGCR8 and miRISC components, AGO2 and Dicer. We further investigated their subnuclear distribution to find out their intensity and accumulation inside the pseudoinclusions as well as in the rest nuclear area. AGO2 and Dicer were intensely resided inside the pseudoinclusions and in some cases, in the borders of the nuclear membrane. In some cells, AGO2 and DROSHA are concentrated in specific subnuclear areas suggesting that could constitute a capable cue for the pseudoinclusion formation. DGCR8 seems not to have a clear subnuclear localization. RISC complex acting as an EMT effector probably trigger local transcript regulation leading to cytoskeletal remodeling and nuclear envelope alterations. The specific subcellular and subnuclear material may create a niche for the restoration of the local transcript needs. Excessive nuclear membrane material and altered dynamics are required for the groovy and invagination-like shape enclosing cytoplasmic content intranuclearly that probably determines the cell fate.

Therefore, we further pursue the investigation another genetically well-characterized cohort registered in cBioportal (an open platform for exploring multidimensional cancer genomics data) regarding the molecular profile of the tumors having pseudoinclusions. In this cohort, samples with pseudoinclusions were often BRAF mutated, rarely RET mutated and never RAS mutated samples.

An analysis of the pathways that are activated in presence of pseudoinclusions indicates, among others, that Protein processing in Endoplasmic reticulum, NFKβ, adherens junction and regulation of actin cytoskeleton pathways are the most important ones. It is known that correctly folded proteins are packaged into transport vesicles that shuttle them to the Golgi complex. On the contrary, misfolded proteins are maintained within the ER lumen in complex with molecular chaperones. The next step for the terminally misfolded proteins is the binding to BiP and then, their direction toward degradation through the proteasome in a process called ER-associated degradation (ERAD) (Araki & Nagata, 2011). In case of an accumulation of misfolded proteins in the ER, ER stress is promoted and activating the unfolded protein response (UPR). In certain severe situations, such as probably, in our case, the protective mechanisms activated by the UPR are not sufficient for the restoration of normal ER function and cells die by apoptosis. This scenario explains, adequately, the activation of NF-κβ. NF-

κβ target inflammation and it does not only increase the production of inflammatory cytokines, chemokines and adhesion molecules, but also regulates the morphogenesis, cell proliferation, apoptosis, and differentiation (Liu et al., 2017).

Notably, AGO2 has already been linked to ER stress during cell division regulating transcript homeostasis (Pantazopoulou V.I. et al., 2021). On the other hand, Kim YJ and colleagues found that loaded and active hsAgo2 was found to be mostly membrane-associated, while the slicing product was solely associated with rER fractions. These findings led to the conclusion that both hsAgo2 RISC formation and target RNA slicing occur on the rER and that the outer rER membrane thus acts as a central nucleation site for siRNA-mediated RNA silencing (Kim et al., 2014).
Then, we examined the survival rates of these individuals to explore the affection of these formations in patient's overall survival.
The trend of poorer survival rates of those with pseudoinclusions compared to those without pseudoinclusions, lead to the same direction. Next, comparing $BRAF^{V600E}$(+)/ pseudoinclusions(+) samples with $BRAF^{V600E}$ (-)/pseudoinclusions (-)/ RAS(+) samples the activated pathways that emerged were spliceosome, extracellular matrix (ECM), lupus (including inflammatory genes) and Parkinson (including mitochondrial components) Extracellular matrix (ECM) including collagen is known to provide signaling cues that regulate EMT, cell behavior and orchestrate functions of cells in tissue formation and homeostasis. Collagen constitutes a major abundant fibrous protein in the extracellular matrix. Collagens, the primary structural elements of the ECM, provide tensile strength, regulate cell adhesion, support chemotaxis and migration, and direct tissue development (Kusindarta D.L. & Wihadmadyatami, 2018; Rozario & DeSimone, 2010). ECM as a highly dynamic structural network that continuously undergoes remodeling and associate with the cytoskeleton is capable to assist in cytoskeletal rearrangements resulting in cytoplasmic intranuclear formations. The tensile changes, motility and regulation of cell adhesion are present during the development of the invaginations.
The existence of the pseudoinclusions in high proximity in the location of fibrotic areas with a concurrent expression of $BRAF^{V600E}$ suggest a severe clinical condition. When these samples compared to RAS negative samples without presence of fibrosis and pseudoinclusions, pathways such as cell-cell adhesion, Parkinson (including mitochondrial components), PI3K signaling and Focal adhesion were found activated. Interestingly, the concurrent presence of pseudoinclusions and fibrosis significantly deteriorate the survival rates of individuals.
Fibrogenesis constitutes a progressive event derived from disrupted regular wound healing due to repeated tissue injury and can end in organ failure, such as in liver cirrhosis. The key molecules, in this process, interact with each other by soluble factors but also by direct cell-cell contact mediated by cell adhesion molecules. Also, cell adhesion molecules also support binding to the ECM representing excellent biosensors in the surrounding microenvironment.

Mechanistically, organ fibrosis and failure seem to be the result of an integration loss between actin cytoskeletal filaments and mechanosensitive components of the nuclear lamina which alters the transcriptional machinery (Chen et al., 2012; Lammerding et al., 2004). Interestingly, absence of lamins or mutations in these structural nuclear components often lead to an impaired cellular response to mechanical stress and perturbations in cytoskeletal organization resulting in increased tissue fibrosis (Chapman et al., 2014; Zuela et al., 2012). These observations raise the possibility that changes in

tissue mechanical environments may directly impact nuclear architecture and gene transcription during fibrotic tissue remodeling, suggesting an increase in matrix stiffness capable to promote persistent global changes in gene transcription (Tschumperlin et al., 2018).

Then, Focusing on RISC complex fine-tuning regulation of gene expression during EMT cytoskeletal remodeling that we observed in pseudoinclusions, we examined the implication of AGO members in in cell cycle phenomena of normal and cancer cells. Especially, AGO2 was of great significance due to its catalytic activity during translational repression and mRNA degradation. AGO2 is the most well-characterized AGO member due to its abundance in cell lines and tissues.

AGO2, a protein of miRISC machinery, catalyzes the mRNA degradation or translational repression in the cytoplasm, through guidance by miRNAs that are loaded on AGO2 complexes. Nevertheless, AGO2 can also reside into the nucleus, acting in a typical RNAi manner (Meister, 2013)). Alternative splicing process, RNA-mediated epigenetic regulation through RISC-chromatin interactions and double strand-break repair are among the emerging nuclear functions of AGO-family members (Francia et al., 2012; Huang & Li, 2014; Janowski et al., 2006; Li, 2014; Meister, 2013; Michalik et al., 2012). In mammalian cells AGOs are located and operate through canonical and non-canonical pathways both into the cytoplasm and nucleus (Morris et al., 2004) in discrete foci (Gagnon et al., 2014; G. Meister et al., 2004; Robb et al., 2005) in physiological and pathological conditions (Pantazopoulou et al., 2020). RISC can also function in GW-bodies, P-bodies and stress granules (Detzer et al., 2010; Leung & Sharp, 2013; Patel et al., 2016), along apical junctions (Kourtidis et al., 2017) and in *Drosophila* nanotubes transmitting intercellular signals (Karlikow et al., 2016), regulating translation of mRNA targets locally (Antoniou et al., 2014) and therefore dictating the spatio-temporal homeostasis. In addition to the above, we herein provided evidence of an AGO2-niche in membrane protrusions, suggesting its critical role(s) in these structures. Specifically, we demonstrated the accumulation of AGO2 in open-ended tunneling nanotubes and close-ended cytokinetic protrusions, in human cells.

Human cellular protrusions are known to be involved in intercellular trafficking of cytoplasmic or genetic material (Antanavičiūtė et al., 2014; Rustom et al., 2004), pathogen transmission (Gousset et al., 2009; Sowinski et al., 2008), mitochondria, calcium and other cargoes transportation (Antanavičiūtė et al., 2014; Smith et al., 2011), and miRNA and protein communication (Thayanithy et al., 2014). In dendritic spines, AGO2 constitutes an important element for de-repression of dendritic mRNAs and local protein synthesis triggered by synaptic activity, thus introducing the concept of spatio-temporal participation of AGO2 in local protein regulation (Paradis-Isler & Boehm, 2018). Our findings support a similar AGO2-dictated local regulation in other cell types such as epithelial cells. In our experimental setting the AGO2-niche correlated with loosely-shaped tunneling nanotubes termed open-ended tubes. Drosha, DGCR8 and Dicer, crucial components of the miRNA machinery, as well as Staufen, a dsRNA-binding protein, were also shown to reside into these nanotubes. Live imaging demonstrated the AGO2 protein motion inside the nanotube. Combined with the presence of the abovementioned proteins in these loci indicate RNAi machinery motility in these structures. Through this action, cells can conduct intermolecular cross-talking, exchange RNA signals and regulate

transcript instability (half-life time) or translational repression at a very specific local (micro-) environment.

In the case of AGO2 close-ended protrusions, alternative regulatory functions are likely engaged. The Dicer pattern, the detected Staufen protein and the presence of oligo dT probe at the intercellular bridge indicated alternative, non-typical AGO2 functions, probably deployed in a miRISC-independent manner. The AGO2 close-ended tubes were different structures from the Actin-filopodial ones, as they were unique per cell, parallelogram-shaped and always appearing in paired cells. The detection of CITK and Aurora B kinases in these cellular structures confirmed that they comprise *bona fide* cytokinetic protrusions (Aurora B regulates cytokinesis through microtubule interactions and stabilization of microtubule structures (Carmena et al., 2009; Xu et al., 2010)). Stably growing and rapidly shrinking microtubules actively participate in cytoskeletal remodeling, delivering dramatic cell changes (Fletcher & Mullins, 2010). AGO2 is present in a tight configuration along α-Tubulin polymers (microtubules) into the intercellular bridges of cytokinesis. Although it resided in extremely high concentrations in the midbody arms, also reported by M.C. Casey et al. in 2019 (Casey et al., 2019), it leaves an empty space, a "gap", in the area of midbody ring. α-Tubulin distribution in cells exposed to Demecolcine, a specific inhibitor of tubulin polymerization, was disorganized and AGO2 protrusions were forced to fragmentation and AGO2 is concentrated at lamellipodia. This indicates that α-Tubulin may serve as a major scaffold for AGO2 local motility. On the other hand, Dicer, highly accumulated in the midbody ring, was significantly affected by F-Actin. Architectural derangement of F-Actin induced by Cytochalasin D cell exposure prevented Dicer accumulation in the midbody and occasionally compelled it in unexpected areas along AGO2 arms. The above indicate the differential regulation of AGO2 and Dicer and reinforced the notion that AGO2 sustains an important role in cell division.

AGO involvement in chromosome division phenomena has been previously reported in a number of model organisms such as yeast, *Drosophila* and mouse. TbAGO1 is known to be crucial for mitotic spindle assembly and chromosome segregation in the *Trypanosome brucei* parasite (Durand-Dubief & Bastin, 2003). In yeast deletion of *Dicer1* or *AGO1* was found to disrupt chromosome segregation, leading to chromosome lagging and centromere-silencing abrogation Volpe, T. *et al.* RNA interference (Volpe et al., 2003). In *Drosophila melanogaster* epigenetic gene silencing modulation and cytokinesis are regulated via the interaction of AGO1-sticky/Citron kinase (CITK) (Sweeney et al., 2008). In case of meiosis the germ cell-specific rice gene *MEL1*, an AGO family member in plants that controls the division of pre-meiotic germ cells, properly modifies the meiotic chromosomes (Nonomura et al., 2007). In mice AGO4 is implicated in the precise chromosome segregation and is required for the proper entry into meiosis in germ cells (Oliver et al., 2016; Theotoki et al., 2020). Additionally, Dicer can prevent mitotic defects during meiosis in mouse oocytes (Stein et al., 2015). In mammals AGO2 catalytic activity, but not the classical miRNA pathway, is crucial for proper chromosome segregation. Moreover, Dicer generates ASAT (α-satellite) siRNAs, which, synergistically with AGO2, control satellite RNAs (Huang et al., 2015). These reports support the mechanistic association of AGO2 with cell division machinery in a wide evolutionary spectrum of organisms, including humans. Our findings underpin this association, since over-expression of *AGO2* results in a numerical deregulation (gain, or loss) of chromosomes. Moreover, these cells present statistically significant micronuclei formation, providing evidence for aneuploidy events. Down-regulation of *AGO2* induces a number of abnormalities, such

as binuclear formations, blebs, double midbody rings and structural chromosomal instabilities, thus indicating the indispensable contribution of AGO2 to the regulation, progression and success of cytokinesis.

As mitosis requires high cytoskeletal rearrangements and continuous supply of energy and biomolecules for its successful and unimpaired implementation, the presence of kinases such as phospho-MEK, -ERK, -JNK, -p38, -Akt and -AMPK in the cytokinetic bridge was not unexpected. Previous studies have highlighted the crucial regulatory roles of the herein examined kinases in the midbody formation and cytokinesis (Rannou et al., 2012; Shapiro et al., 1998; Vazquez-Martin et al., 2011; Vazquez-Martin et al., 2012), with their contribution to cell division mostly being manifested through activation of critical downstream targets for regulating microtubule dynamics and F-Actin cytoskeletal integrity (Gotoh et al., 1991). In our experiments phospho-Akt and -AMPK, a major energy and nutrient sensor (Hardie et al., 2012), proved to follow the AGO2-distribution pattern at the arms of the midbody structure, whereas phospho-MEK, -ERK, -p38 and -JNK showed a Dicer-like-distribution motif, being mainly concentrated in the ring and at the tips of the midbody arms. Interestingly, phospho-AGO2 Ser^{387} follows the phospho-MEK/ERK/p38/JNK expression pattern, exhibiting a high concentration in the ring area. Phosphorylation of AGO2 at Ser^{387} by the activated p38 MAP Kinase is induced by cellular stress (Zeng et al., 2008). In accordance, a selective inhibitor of the p38 MAP Kinase (SB203580), causes relocalization of phospho-AGO2 Ser^{387} in a number of cytokinetic bridges, shifting its location from the ring to the midbody arms. The detection of both p38-dependent phospho-AGO2 Ser^{387} and Dicer in the midbody ring provides evidence for the existence of an active RISC machinery, suggesting a yet unrecognized role of the complex in cell division.

The dividing cells are under tremendous stress, as corroborated by our findings regarding the existence of stress related proteins such as phospho-Akt, -AMPK, -ERK, -MEK, -JNK and -p38 activated kinases in the midzone. In conjunction with the localization of AGO2 and phospho-AGO2, these findings underline the probable implementation of AGO2 in the regulation of spatio-temporal homeostasis in order to beneficially manage local stress. The stress sensitive nature of AGO2 was further supported by heat-shock treatments that resulted in malformed or abolished AGO2 close-ended protrusions and by the strong colocalization pattern with the stress-related proteins Upf1 and TIAR. Moreover, the presence of phospho-eIF2α and ATF4 (ER-stress) proteins into the AGO2-enriched cytokinetic structures, further suggests the simultaneous and synergistic activation of a MAPK-signaling network and the RNAi machinery in response to stress, in a topology-specific manner, most likely for the restoration of local transcript homeostasis during cytokinesis.

In conclusion, we herein demonstrate the AGO2 involvement in the tubular protrusions' locasome, including open-ended tunneling nanotubes and close-ended cytokinetic bridges. Altogether, our results provide evidence for the discovery of an AGO2-niche in the midzone carrying essential properties for successful cytokinesis and cell-division integrity, although further investigation needs to be performed to thoroughly dissect the exact roles of AGOs, and their protein- and RNA-interactors, in a cell-division setting.

Determining that the regulation of gene expression provides essential information for understanding the condition, morphology and function of the cell, the exact molecular mechanisms being affected are under investigation. A variety of mechanisms are implicated in EMT with a consequent

contribution to cytokinesis failure and mitotic defects. Gene expression can be regulated via different cellular procedures including RISC complex and loaded miRNAs. HITS-CLIP methodology (High-Sequencing of RNAs isolated by Cross-Linking Immuno-Precipitation mapped the tripartite complex AGO2::miRNA::mRNA and bioinformatic analysis identified the RISC-bound miRNAs and their target mRNAs. The AGO2 HITS-CLIP methodology being achieved in the cell lines NTHY ori 3-1, TPC1 and FTC133 provides important results regarding: the differential expression of the subset of miRNAs loaded on the AGO2 protein between the three cell lines which represent three different thyroid conditions with discrete clinical outcomes and prognosis and the miRNAs-target gene interactions that occur exclusively in the TPC1 and FTC133 cell line and involve miRNAs that showed an increase expression in the TPC1 cell line compared to the NTHY ori 3-1 cell line.

The results of the miRNA differential expression exhibit a distinct expression profile for its cell line. Distinguishment of cell lines based on the expression profile of miRNAs loaded on the AGO2 protein suggests that the transformation of normal thyroid follicle epithelial cells into TPC1 or follicular FTC133 cancer cells requires a series of expression level changes. This fact is supported by a research work of Hossain and colleagues which identified differentially expressed genes and differentially expressed miRNAs, molecular pathways and transcription factors reflecting molecular mechanisms that differ between FTC tumors and benign follicular adenoma (FTA) (Hossain et al., 2020).

miRNAs with tumor suppressive activity were found downregulated, while the expression of oncogenic miRNAs was upregulated. Notable examples are miR-146a, miR-222 and miR-181a/b which have oncogenic activity and their expression was increased in the TPC1 cell line compared to the NTHY ori 3-1 cell line. The observation that the TPC1 and FTC133 cell lines differ in the expression of miRNAs can be attributed to the different deregulated molecular pathways in the respective carcinomas.

The TPC1 cell line carries the RET/PTC1 rearrangement triggering the continuous activation of the MAPK pathway. The rearrangement involves the fusion of a region of the RET proto-oncogene, encoding a membrane receptor with tyrosine kinase activity, with a heterologous gene, usually the CCDC6 gene. The region of the RET proto-oncogene involved in this rearrangement carries tyrosine kinase activity, while the CCDC6 gene region is responsible for the dimerization of the RET/PTC protein and its continuous activation (Santoro & Carlomagno, 2013). This ensures the continuous signaling of the MAPK pathway making RET a promising reagent for therapeutic treatments (Santoro & Carlomagno, 2013) . In contrast, in FTC133 cell line, PI3K-Akt pathway is active due to non-sense mutation in the tumor suppressor PTEN gene. Mutation in the PTEN gene results in the suppression of conversion of the (3,4,5) triphosphate phosphatidylinositol to (4,5) diphosphate phosphatidylinositol which normally inhibits the activation signal of Akt serine/threonine kinase.

The increased expression levels of specific miRNAs targeting the cancer suppressors of these pathways is favored and, respectively, the decreased expression levels of miRNAs targeting the activators of these pathways is also favored.

The classification of the three cell lines based on the expression profile of miRNAs can constitute a tool for a valid diagnosis of the thyroid carcinoma subtype. Such a perspective can provide a solution in cases where the fine needle aspiration biopsy (FNAB) of a thyroid sample obtained would fail to reveal the subtype of carcinoma. Another aspect is that every tumor having a precise profile even if it can be classified in a specific subtype, it can have a molecular profile referring to another clinical condition. This differential analysis can constitute a guidance for a precise classification regarding the matching of tumor’s unique profile leading to the precision medicine.

Upon the miRNA analysis, 31 overexpressed miRNAs emerged overexpressed in the TPC1 cell line compared to the NTHY ori 3-1 cell line. These miRNAs appear to primarily regulate metabolic and signal transduction pathways.

Metabolic pathways include the metabolism of carbohydrates, lipids, amino acids, and nucleotides. More specifically in nucleotide metabolism, miRNAs regulate the biosynthesis pathways of purines and pyrimidines. In lipid metabolism, the metabolic pathways of phosphor-glycerol lipids, sphingolipids and fatty acids are included. The signal transduction pathways are summarized in Ras (14 miRNAs), cAMP (13 miRNAs), TNF (12 miRNAs), MAPK (11 miRNAs), Jak-STAT (11 miRNAs), PI3K-Akt (11 miRNAs), HIF-1 (9 miRNAs), Calcium (9 miRNAs), Rap1 (8 miRNAs), Wnt (7 miRNAs), NF-kappa B (7 miRNAs), mTOR (6 miRNAs) and p53 (6 miRNAs) signaling pathway. The Ras signaling pathway is the target of most miRNAs. Among the various targets is the RASA1 gene, which encodes a GAP (GTPase-activating protein) factor to convert the active form of Ras-GTP to the inactive form of Ras-GDP, thus interrupting the signaling of the MAPK pathway.

As mentioned above, the activation of the MAPK pathway in the TPC1 cell line is due to the RET/PTC1 rearrangement. Targeting the RASA1 gene, which encodes a MAPK pathway inhibitor, by 6 miRNAs (miR-5579-3p, miR-4677-5p, miR-96-5p, miR-182-5p, miR-30a-5p, miR- 30c-5p) contributes to oncogenesis through continuous activation of the MAPK pathway.

To fully evaluate and interpret the action of miRNAs, the DIANA-miRPath v3 tool used to detect molecular pathways targeted by specific miRNAs, using a target gene enrichment analysis algorithm in molecular pathways. In line with that, for each pathway from KEGG database, the miRNAs-gene interactions are schematically mapped. Also, in order to extend the analysis beyond the group of 31 miRNAs of the PTC cell line, it is necessary to compare the data of the AGO2 HITS-CLIP methodology with assays that directly detect changes in mRNA or protein levels, thus ensuring that the interactions of miRNA-mRNA target genes affect gene expression.

Assays such as transcript level analysis via RNA sequencing (RNA-seq) and quantitative proteomic analysis platforms, such as the SILAC (Stable Isotope Labeling with Amino Acids in Culture) method aid to this direction.

As a future perspective, the AGO2 HITS-CLIP methodology could be applied to a representative cell line of anaplastic thyroid carcinoma (ATC) to reveal the full range of interactions of miRNAs-genes from normal follicular cell to fully squamous cell carcinoma. Finally, since Greek population patients with PTC carcinomas do not carry the classical RET/PTC rearrangement, it would be important to additionally examine a PTC cell line with the absence of the specific rearrangement.

In an effort to distinguish crucial miRs for therapeutic approaches from HITS-CLIP data, miR26 family was set apart due to a shared tumor suppressive behavior (all the miR26 members were downregulated in cancer conditions in thyroid gland) between the members of this family and was used for further analysis. Additional reasons for our research focus on miR26 are regarding (i) its down regulation both in PTC1 and FTC133, when compared to NTHY ori 3-1 (ii) it is one of the top deregulated in FTC carcinomas, (iii) both miR26a and b are down regulated in cancer cell lines and (iv) these results obtained from the HITS-CLIP experiments are in accordance with the literature. miR30 and let-7 were also used with no significant results probably because of the contradictive function of their family members making the discrete functions of each one, not clearly detectable.

More specifically, miR26a1, miR26a2 and miR26b are the only 3 members of the hsa-miR26 family, located in chromosomes 3, 12 and 2, respectively (Gao & Liu, 2011). The mature isoforms are 21-22

nucleotides in length, with a seed region of approximately 6-7 nucleotides. Bladder and breast cancer, oral squamous cell carcinoma, anaplastic carcinomas, Burkitt lymphoma, HCC and rhabdomyosarcoma were a group of tumors presenting a decrease in the expression levels of miR26. Therefore, it is considered to be a miRNA suppressor in those tumors. In our case, in 2007, Visone and colleagues reported that miR26a was significantly decreased in anaplastic carcinomas (ATC) in comparison to normal thyroid tissue (Visone et al., 2007). On the contrary, GBM tumors were found to have increased miR26 expression levels uncovering an oncogenic function via tumor cell growth and proliferation promotion.

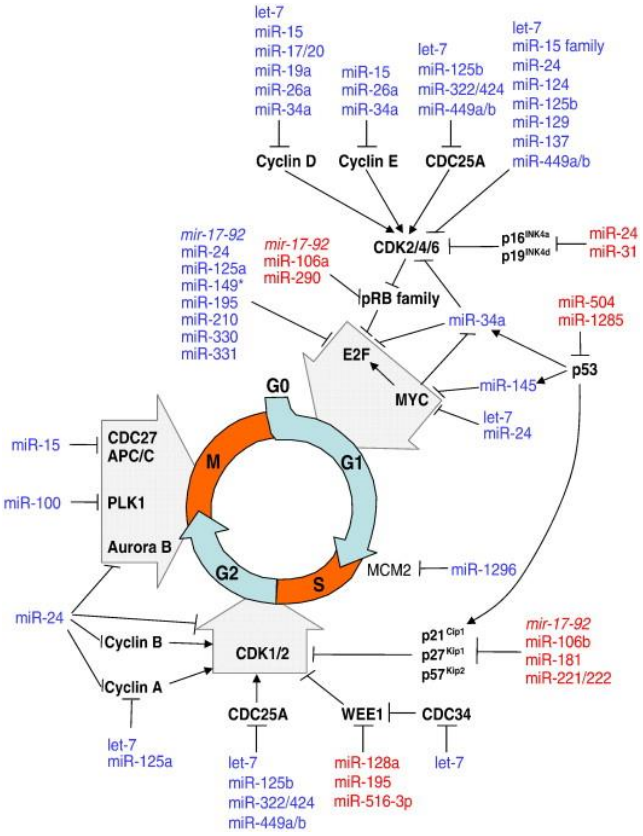

Figure 118 An overview to cell cycle control by microRNAs. Some interactions have been omitted for clarity. Most miRNA names correspond to mature forms whereas miRNAs clusters are shown in italics. miRNAs with proliferative potential are shown in red whereas antiproliferative miRNAs are in blue. S, S-phase; M, Mitosis; G1 and G2 indicate transition phases of the cell cycle whereas G0 indicate quiescent cells (Bueno & Malumbres, 2011).

In general, miR26 is instrumental to normal tissue growth and development by impacting on cell proliferation and differentiation. Various studies also showed that EZH2, PTEN, SMAD1 and MTDH are potential downstream target genes of miR26 (Gao & Liu, 2011; Shi et al., 2019).

In thyroid cancer, inhibitory effects were reported for miR26a-5p and miR26b-5p functions (Gong et al., 2018; Zhou et al., 2019). Our aim was to prove that the miR26 mimic sequences could reverse the phenomenon of rapid cell proliferation in cell lines and mouse models, as well as to deeply understand via RNA seq, the molecular basis underlying these changes. The results from the transfected cell lines demonstrate that cell cycle, microRNAs in cancer, parathyroid hormone synthesis, secretion and action, thyroid hormone signaling, PI3K-Akt, pathways in cancer, ubiquitin, tight junction, adherens junction, Hippo signaling, cellular senescence and cytosolic DNA sensing are among the pathways

affected leading to a protective effect of miR26 in tumorigenesis and tumor progression. We identified in our settings, CCNB1, CCNE2, CDK8, CDC25A, MYC and SKPT2 downregulated in mimic miR26 transfected cells, previously reported by Sander and colleagues suggesting that came specifically of the function of miR26a-5p and strengthening our results regarding the cell cycle affection from miR26 function (Xu et al., 2020).

Gong and colleagues reported *in vitro* and *in vivo* observations suggesting that miR26a could target the 3'UTR of cAMP regulated phosphoprotein 19 ARPP19 directly and inhibit PTC cell proliferation via ARPP19 up-regulation (Gong et al., 2018). In our case, the mechanism covered under follicular cancer conditions, being represented by FTC133, is still unknown. Given that follicular cancer is a cancer with increased mortality, related to the degree of vascular invasion and distant metastasis and poor prognosis are common, this makes the unmet need for disclosure of the mechanistic causality and therapy more imperative. The reduction in tumor size after miR26 treatment is a quite promising result. Mimicking sequences do not have the side effects of a drug treatment. The investigation of all the synergistic results in the variety of targets have to be completed before a mimic therapy would be in a clinical trial.

It has already been reported a phase I clinical trial investigated microRNA-based therapy in patients with malignant pleural mesothelioma. Treatment with TargomiRs, microRNA mimics with novel sequence packaged in EGFR antibody-targeted bacterial minicells, revealed clear signs of clinical activity (Winata et al., 2017). There are also efforts for antagomiR-based therapies. Recently, RG-101 is an N-acetyl-D-galactosamine- conjugated RNA antagomiR that also targets miR-122 in HCV infected hepatocytes (Baek et al., 2014). However, the clinical results for AntagomiRs are more precarious due to limited specificity in targeting miRs that have high similarity in their sequences. The fine-tuning balance is complex since the miR sequence is quite small creating difficulties in specificity. In any case, sice miRNAs are endogenous factors, these applications illustrate the utility and versatility of synthetic mimicking sequences as molecular tools with minimal side-effects in biomedical research.

References

Abdullah, M. I., Junit, S. M., Ng, K. L., Jayapalan, J. J., Karikalan, B., & Hashim, O. H. (2019). Papillary Thyroid Cancer: Genetic Alterations and Molecular Biomarker Investigations. *Int J Med Sci*, *16*(3), 450-460. https://doi.org/10.7150/ijms.29935

Adeniran, A. J., Zhu, Z., Gandhi, M., Steward, D. L., Fidler, J. P., Giordano, T. J., Biddinger, P. W., & Nikiforov, Y. E. (2006). Correlation between genetic alterations and microscopic features, clinical manifestations, and prognostic characteristics of thyroid papillary carcinomas. *Am J Surg Pathol*, *30*(2), 216-222. https://doi.org/10.1097/01.pas.0000176432.73455.1b

Agrawal, N., Akbani, R., Aksoy, B. A., Ally, A., Arachchi, H., Asa, Sylvia L., Auman, J. T., Balasundaram, M., Balu, S., Baylin, Stephen B., Behera, M., Bernard, B., Beroukhim, R., Bishop, Justin A., Black, Aaron D., Bodenheimer, T., Boice, L., Bootwalla, Moiz S., Bowen, J., Bowlby, R., Bristow, Christopher A., Brookens, R., Brooks, D., Bryant, R., Buda, E., Butterfield, Yaron S. N., Carling, T., Carlsen, R., Carter, Scott L., Carty, Sally E., Chan, Timothy A., Chen, Amy Y., Cherniack, Andrew D., Cheung, D., Chin, L., Cho, J., Chu, A., Chuah, E., Cibulskis, K., Ciriello, G., Clarke, A., Clayman, Gary L., Cope, L., Copland, John A., Covington, K., Danilova, L., Davidsen, T., Demchok, John A., DiCara, D., Dhalla, N., Dhir, R., Dookran, Sheliann S., Dresdner, G., Eldridge, J., Eley, G., El-Naggar, Adel K., Eng, S., Fagin, James A., Fennell, T., Ferris, Robert L., Fisher, S., Frazer, S., Frick, J., Gabriel, Stacey B., Ganly, I., Gao, J., Garraway, Levi A., Gastier-Foster, Julie M., Getz, G., Gehlenborg, N., Ghossein, R., Gibbs, Richard A., Giordano, Thomas J., Gomez-Hernandez, K., Grimsby, J., Gross, B., Guin, R., Hadjipanayis, A., Harper, Hollie A., Hayes, D. N., Heiman, David I., Herman, James G., Hoadley, Katherine A., Hofree, M., Holt, Robert A., Hoyle, Alan P., Huang, Franklin W., Huang, M., Hutter, Carolyn M., Ideker, T., Iype, L., Jacobsen, A., Jefferys, Stuart R., Jones, Corbin D., Jones, Steven J. M., Kasaian, K., Kebebew, E., Khuri, Fadlo R., Kim, J., Kramer, R., Kreisberg, R., Kucherlapati, R., Kwiatkowski, David J., Ladanyi, M., Lai, Phillip H., Laird, Peter W., Lander, E., Lawrence, Michael S., Lee, D., Lee, E., Lee, S., Lee, W., Leraas, Kristen M., Lichtenberg, Tara M., Lichtenstein, L., Lin, P., Ling, S., Liu, J., Liu, W., Liu, Y., LiVolsi, Virginia A., Lu, Y., Ma, Y., Mahadeshwar, Harshad S., Marra, Marco A., Mayo, M., McFadden, David G., Meng, S., Meyerson, M., Mieczkowski, Piotr A., Miller, M., Mills, G., Moore, Richard A., Mose, Lisle E., Mungall, Andrew J., Murray, Bradley A., Nikiforov, Yuri E., Noble, Michael S., Ojesina, Akinyemi I., Owonikoko, Taofeek K., Ozenberger, Bradley A., Pantazi, A., Parfenov, M., Park, Peter J., Parker, Joel S., Paull, Evan O., Pedamallu, Chandra S., Perou, Charles M., Prins, Jan F., Protopopov, A., Ramalingam, Suresh S., Ramirez, Nilsa C., Ramirez, R., Raphael, Benjamin J., Rathmell, W. K., Ren, X., Reynolds, Sheila M., Rheinbay, E., Ringel, Matthew D., Rivera, M., Roach, J., Robertson, A. G., Rosenberg, Mara W., Rosenthal, M., Sadeghi, S., Saksena, G., Sander, C., Santoso, N., Schein, Jacqueline E., Schultz, N., Schumacher, Steven E., Seethala, Raja R., Seidman, J., Senbabaoglu, Y., Seth, S., Sharpe, S., Shaw, Kenna R. M., Shen, John P., Shen, R., Sherman, S., Sheth, M., Shi, Y., Shmulevich, I., Sica, Gabriel L., Simons, Janae V., Sinha, R., Sipahimalani, P., Smallridge, Robert C., Sofia, Heidi J., Soloway, Matthew G., Song, X., Sougnez, C., Stewart, C., Stojanov, P., Stuart, Joshua M., Sumer, S. O., Sun, Y., Tabak, B., Tam, A., Tan, D., Tang, J., Tarnuzzer, R., Taylor, Barry S., Thiessen, N., Thorne, L., Thorsson, V., Tuttle, R. M., Umbricht, Christopher B., Van Den Berg, David J., Vandin, F., Veluvolu, U., Verhaak, Roel G. W., Vinco, M., Voet, D., Walter, V., Wang, Z., Waring, S., Weinberger, Paul M., Weinhold, N., Weinstein, John N., Weisenberger, Daniel J., Wheeler, D., Wilkerson, Matthew D., Wilson, J., Williams, M., Winer, Daniel A., Wise, L., Wu, J., Xi, L., Xu, Andrew W., Yang, L., Yang, L., Zack, Travis I., Zeiger, Martha A., Zeng, D., Zenklusen, Jean C., Zhao, N., Zhang, H., Zhang, J., Zhang, J., Zhang, W.,

Zmuda, E., & Zou, L. (2014). Integrated Genomic Characterization of Papillary Thyroid Carcinoma. *Cell*, *159*(3), 676-690. https://doi.org/https://doi.org/10.1016/j.cell.2014.09.050

Agrawal, N., Jiao, Y., Sausen, M., Leary, R., Bettegowda, C., Roberts, N. J., Bhan, S., Ho, A. S., Khan, Z., Bishop, J., Westra, W. H., Wood, L. D., Hruban, R. H., Tufano, R. P., Robinson, B., Dralle, H., Toledo, S. P. A., Toledo, R. A., Morris, L. G. T., Ghossein, R. A., Fagin, J. A., Chan, T. A., Velculescu, V. E., Vogelstein, B., Kinzler, K. W., Papadopoulos, N., Nelkin, B. D., & Ball, D. W. (2013). Exomic Sequencing of Medullary Thyroid Cancer Reveals Dominant and Mutually Exclusive Oncogenic Mutations in RET and RAS. *The Journal of Clinical Endocrinology & Metabolism*, *98*(2), E364-E369. https://doi.org/10.1210/jc.2012-2703 %J The Journal of Clinical Endocrinology & Metabolism

Ahlenstiel, C. L., Lim, H. G., Cooper, D. A., Ishida, T., Kelleher, A. D., & Suzuki, K. (2012). Direct evidence of nuclear Argonaute distribution during transcriptional silencing links the actin cytoskeleton to nuclear RNAi machinery in human cells. *Nucleic Acids Res*, *40*(4), 1579-1595. https://doi.org/10.1093/nar/gkr891

Al-Bedeary, S., Getta, H., & Al-Sharafi, D. (2020). The hallmarks of cancer and their therapeutic targeting in current use and clinical trials [Review Article]. *9*(1), 1-10. https://doi.org/10.4103/ijh.ijh_24_19

Al-Salamah, S. M., Khalid, K., & Bismar, H. A. (2002). Incidence of differentiated cancer in nodular goiter. *Saudi Med J*, *23*(8), 947-952.

Allen, E., & Fingeret, A. (2021). Anatomy, Head and Neck, Thyroid. In *StatPearls*. StatPearls Publishing

Copyright © 2021, StatPearls Publishing LLC.

Ambros, V. (2004). The functions of animal microRNAs. *Nature*, *431*(7006), 350-355. https://doi.org/10.1038/nature02871

Ameyar-Zazoua, M., Rachez, C., Souidi, M., Robin, P., Fritsch, L., Young, R., Morozova, N., Fenouil, R., Descostes, N., Andrau, J. C., Mathieu, J., Hamiche, A., Ait-Si-Ali, S., Muchardt, C., Batsché, E., & Harel-Bellan, A. (2012). Argonaute proteins couple chromatin silencing to alternative splicing. *Nat Struct Mol Biol*, *19*(10), 998-1004. https://doi.org/10.1038/nsmb.2373

Andersson, L. (2010). Embryonic origin and development of thyroid progenitor cells. An experimental study focused on endoderm, EphA4 and Foxa2 [Doctoral thesis].

Antanavičiūtė, I., Rysevaitė, K., Liutkevičius, V., Marandykina, A., Rimkutė, L., Sveikatienė, R., Uloza, V., & Skeberdis, V. A. (2014). Long-Distance Communication between Laryngeal Carcinoma Cells. *PLoS One*, *9*(6), e99196. https://doi.org/10.1371/journal.pone.0099196

Antoniou, A., Baptista, M., Carney, N., & Hanley, J. G. (2014). PICK1 links Argonaute 2 to endosomes in neuronal dendrites and regulates miRNA activity. *EMBO Rep*, *15*(5), 548-556. https://doi.org/10.1002/embr.201337631

Aponte, J. C., Yang, H., Vaisberg, A. J., Castillo, D., Málaga, E., Verástegui, M., Casson, L. K., Stivers, N., Bates, P. J., Rojas, R., Fernandez, I., Lewis, W. H., Sarasara, C., Sauvain, M., Gilman, R. H., & Hammond, G. B. (2010). Cytotoxic and anti-infective sesquiterpenes present in Plagiochila disticha (Plagiochilaceae) and Ambrosia peruviana (Asteraceae). *Planta Med*, *76*(7), 705-707. https://doi.org/10.1055/s-0029-1240681

Araki, K., & Nagata, K. (2011). Protein folding and quality control in the ER. *Cold Spring Harb Perspect Biol*, *3*(11), a007526. https://doi.org/10.1101/cshperspect.a007526

Arighi, E., Borrello, M. G., & Sariola, H. (2005). RET tyrosine kinase signaling in development and cancer. *Cytokine & Growth Factor Reviews*, *16*(4), 441-467. https://doi.org/https://doi.org/10.1016/j.cytogfr.2005.05.010

Asare, A., Levorse, J., & Fuchs, E. (2017). Coupling organelle inheritance with mitosis to balance growth and differentiation. *Science*, *355*(6324). https://doi.org/10.1126/science.aah4701

Atilla-Gokcumen, G. E., Castoreno, A. B., Sasse, S., & Eggert, U. S. (2010). Making the cut: the chemical biology of cytokinesis. *ACS Chem Biol*, *5*(1), 79-90. https://doi.org/10.1021/cb900256m

Austria, T., Marion, C., Yu, V., Widschwendter, M., Hinton, D. R., & Dubeau, L. (2018). Mechanism of cytokinesis failure in ovarian cystadenomas with defective BRCA1 and P53 pathways. *Int J Cancer*, *143*(11), 2932-2942. https://doi.org/10.1002/ijc.31659

Bütepage, M., Eckei, L., Verheugd, P., & Lüscher, B. (2015). Intracellular Mono-ADP-Ribosylation in Signaling and Disease. *Cells*, *4*(4), 569-595. https://doi.org/10.3390/cells4040569

Baek, J., Kang, S., & Min, H. (2014). MicroRNA-targeting therapeutics for hepatitis C. *Arch Pharm Res*, *37*(3), 299-305. https://doi.org/10.1007/s12272-013-0318-9

Baloch, Z. W., & LiVolsi, V. A. (2018). Special types of thyroid carcinoma. *Histopathology*, *72*(1), 40-52. https://doi.org/10.1111/his.13348

Baran, B., Mert Ozupek, N., Yerli Tetik, N., Acar, E., Bekcioglu, O., & Baskin, Y. (2018). Difference Between Left-Sided and Right-Sided Colorectal Cancer: A Focused Review of Literature. *Gastroenterology Res*, *11*(4), 264-273. https://doi.org/10.14740/gr1062w

Berman, H. M., Westbrook, J., Feng, Z., Gilliland, G., Bhat, T. N., Weissig, H., Shindyalov, I. N., & Bourne, P. E. (2000). The Protein Data Bank. *Nucleic Acids Res*, *28*(1), 235-242. https://doi.org/10.1093/nar/28.1.235 %J Nucleic Acids Research

Bermisheva, M. A., Takhirova, Z. R., Gilyazova, I. R., & Khusnutdinova, E. K. (2018). MicroRNA Biogenesis Pathway Gene Polymorphisms Are Associated with Breast Cancer Risk. *Russian Journal of Genetics*, *54*(5), 568-575. https://doi.org/10.1134/S1022795418040051

Bhutta, M. S., McInerny, C. J., & Gould, G. W. (2014). ESCRT function in cytokinesis: location, dynamics and regulation by mitotic kinases. *International journal of molecular sciences*, *15*(12), 21723-21739. https://doi.org/10.3390/ijms151221723

Bian, X.-J., Zhang, G.-M., Gu, C.-Y., Cai, Y., Wang, C.-F., Shen, Y.-J., Zhu, Y., Zhang, H.-L., Dai, B., & Ye, D.-W. (2014). Down-regulation of Dicer and Ago2 is associated with cell proliferation and apoptosis in prostate cancer. *Tumor Biology*, *35*(11), 11571-11578. https://doi.org/10.1007/s13277-014-2462-3

Bohmert, K., Camus, I., Bellini, C., Bouchez, D., Caboche, M., & Benning, C. (1998). AGO1 defines a novel locus of Arabidopsis controlling leaf development. *Embo j*, *17*(1), 170-180. https://doi.org/10.1093/emboj/17.1.170

Bongarzone, I., Vigneri, P., Mariani, L., Collini, P., Pilotti, S., & Pierotti, M. A. (1998). RET/NTRK1 rearrangements in thyroid gland tumors of the papillary carcinoma family: correlation with clinicopathological features. *Clin Cancer Res*, *4*(1), 223-228.

Bounacer, A., Wicker, R., Caillou, B., Cailleux, A. F., Sarasin, A., Schlumberger, M., & Suárez, H. G. (1997). High prevalence of activating ret proto-oncogene rearrangements, in thyroid tumors from patients who had received external radiation. *Oncogene*, *15*(11), 1263-1273. https://doi.org/10.1038/sj.onc.1200206

Bozler, J., Nguyen, H. Q., Rogers, G. C., & Bosco, G. (2014). Condensins exert force on chromatin-nuclear envelope tethers to mediate nucleoplasmic reticulum formation in Drosophila melanogaster. *G3 (Bethesda)*, *5*(3), 341-352. https://doi.org/10.1534/g3.114.015685

Broderick, J. A., Salomon, W. E., Ryder, S. P., Aronin, N., & Zamore, P. D. (2011). Argonaute protein identity and pairing geometry determine cooperativity in mammalian RNA silencing. *Rna*, *17*(10), 1858-1869. https://doi.org/10.1261/rna.2778911

Bueno, M. J., & Malumbres, M. (2011). MicroRNAs and the cell cycle. *Biochimica et Biophysica Acta (BBA) - Molecular Basis of Disease*, *1812*(5), 592-601. https://doi.org/https://doi.org/10.1016/j.bbadis.2011.02.002

Cabanillas, M. E., McFadden, D. G., & Durante, C. (2016). Thyroid cancer. *Lancet*, *388*(10061), 2783-2795. https://doi.org/10.1016/s0140-6736(16)30172-6

Cancer, A. J. C. o. (2002). [Book]. *AJCC Cancer Staging Manual*.

Carim, S. C., Kechad, A., & Hickson, G. R. X. (2020). Animal Cell Cytokinesis: The Rho-Dependent Actomyosin-Anilloseptin Contractile Ring as a Membrane Microdomain Gathering, Compressing, and Sorting Machine. *Front Cell Dev Biol*, *8*, 575226. https://doi.org/10.3389/fcell.2020.575226

Carlton, J. G., Jones, H., & Eggert, U. S. (2020). Membrane and organelle dynamics during cell division. *Nature Reviews Molecular Cell Biology*, *21*(3), 151-166. https://doi.org/10.1038/s41580-019-0208-1

Carlton, J. G., & Martin-Serrano, J. (2007). Parallels between cytokinesis and retroviral budding: a role for the ESCRT machinery. *Science*, *316*(5833), 1908-1912. https://doi.org/10.1126/science.1143422

Carmena, M., Ruchaud, S., & Earnshaw, W. C. (2009). Making the Auroras glow: regulation of Aurora A and B kinase function by interacting proteins. *Curr Opin Cell Biol*, *21*(6), 796-805. https://doi.org/https://doi.org/10.1016/j.ceb.2009.09.008

Casey, M. C., Prakash, A., Holian, E., McGuire, A., Kalinina, O., Shalaby, A., Curran, C., Webber, M., Callagy, G., Bourke, E., Kerin, M. J., & Brown, J. A. (2019). Quantifying Argonaute 2 (Ago2) expression to stratify breast cancer. *19*(1), 712. https://doi.org/10.1186/s12885-019-5884-x

Castagna, M. G., Belardini, V., Memmo, S., Maino, F., Di Santo, A., Toti, P., Carli, A. F., Caruso, G., & Pacini, F. (2014). Nodules in autoimmune thyroiditis are associated with increased risk of thyroid cancer in surgical series but not in cytological series: evidence for selection bias. *J Clin Endocrinol Metab*, *99*(9), 3193-3198. https://doi.org/10.1210/jc.2014-1302

Celton-Morizur, S., Merlen, G., Couton, D., Margall-Ducos, G., & Desdouets, C. (2009). The insulin/Akt pathway controls a specific cell division program that leads to generation of binucleated tetraploid liver cells in rodents. *J Clin Invest*, *119*(7), 1880-1887. https://doi.org/10.1172/jci38677

Cen, P., Walther, C., Finkel, K. W., & Amato, R. J. (2014). Chapter 3 - Biomarkers in Oncology and Nephrology. In K. W. Finkel & S. C. Howard (Eds.), *Renal Disease in Cancer Patients* (pp. 21-38). Academic Press. https://doi.org/https://doi.org/10.1016/B978-0-12-415948-8.00003-9

Chaigne, A., Labouesse, C., White, I. J., Agnew, M., Hannezo, E., Chalut, K. J., & Paluch, E. K. (2020). Abscission Couples Cell Division to Embryonic Stem Cell Fate. *Dev Cell*, *55*(2), 195-208.e195. https://doi.org/10.1016/j.devcel.2020.09.001

Chan, S.-H., & Wang, L.-H. (2015). Regulation of cancer metastasis by microRNAs. *Journal of Biomedical Science*, *22*(1), 9. https://doi.org/10.1186/s12929-015-0113-7

Chapman, M. A., Zhang, J., Banerjee, I., Guo, L. T., Zhang, Z., Shelton, G. D., Ouyang, K., Lieber, R. L., & Chen, J. (2014). Disruption of both nesprin 1 and desmin results in nuclear anchorage defects and fibrosis in skeletal muscle. *Hum Mol Genet*, *23*(22), 5879-5892. https://doi.org/10.1093/hmg/ddu310

Chen, C. Y., Chi, Y. H., Mutalif, R. A., Starost, M. F., Myers, T. G., Anderson, S. A., Stewart, C. L., & Jeang, K. T. (2012). Accumulation of the inner nuclear envelope protein Sun1 is pathogenic in progeric and dystrophic laminopathies. *Cell*, *149*(3), 565-577. https://doi.org/10.1016/j.cell.2012.01.059

Chen, Y., Sadow, P. M., Suh, H., Lee, K. E., Choi, J. Y., Suh, Y. J., Wang, T. S., & Lubitz, C. C. (2016). BRAF(V600E) Is Correlated with Recurrence of Papillary Thyroid Microcarcinoma: A Systematic Review, Multi-Institutional Primary Data Analysis, and Meta-Analysis. *Thyroid*, *26*(2), 248-255. https://doi.org/10.1089/thy.2015.0391

Chen, Z., Lai, T. C., Jan, Y. H., Lin, F. M., Wang, W. C., Xiao, H., Wang, Y. T., Sun, W., Cui, X., Li, Y. S., Fang, T., Zhao, H., Padmanabhan, C., Sun, R., Wang, D. L., Jin, H., Chau, G. Y., Huang, H. D., Hsiao, M., & Shyy, J. Y. (2013). Hypoxia-responsive miRNAs target argonaute 1 to promote angiogenesis. *J Clin Invest*, *123*(3), 1057-1067. https://doi.org/10.1172/jci65344

Cheng, N., Li, Y., & Han, Z. G. (2013). Argonaute2 promotes tumor metastasis by way of up-regulating focal adhesion kinase expression in hepatocellular carcinoma. *Hepatology*, *57*(5), 1906-1918. https://doi.org/10.1002/hep.26202

Chung, K.-W., & Song, D. E. (2019). Borderline Thyroid Tumors: a Surgeon's Perspectives. *ijt*, *12*(1), 15-18. https://doi.org/10.11106/ijt.2019.12.1.15

Cibas, E. S., & Ali, S. Z. (2017). The 2017 Bethesda System for Reporting Thyroid Cytopathology. *Thyroid*, *27*(11), 1341-1346. https://doi.org/10.1089/thy.2017.0500

Cochran, W. G. (1952). The chi square Test of Goodness of Fit. *Ann. Math. Statist.*, *23*(3), 315-345. https://doi.org/10.1214/aoms/1177729380

Cochran, W. G. (1954). Some Methods for Strengthening the Common χ² Tests. *Biometrics*, *10*(4), 417-451. https://doi.org/10.2307/3001616

Cohen, S. M., Brennecke, J., & Stark, A. (2006). Denoising feedback loops by thresholding--a new role for microRNAs. *Genes Dev*, *20*(20), 2769-2772. https://doi.org/10.1101/gad.1484606

Collison, J. (2018). Systemic sclerosis: Promoting apoptosis is key to reversing fibrosis. *Nat Rev Rheumatol*, *14*(2), 61. https://doi.org/10.1038/nrrheum.2017.222

Colombo, M., Raposo, G., & Théry, C. (2014). Biogenesis, secretion, and intercellular interactions of exosomes and other extracellular vesicles. *Annu Rev Cell Dev Biol*, *30*, 255-289. https://doi.org/10.1146/annurev-cellbio-101512-122326

Conger, A. K., Martin, E. C., Yan, T. J., Rhodes, L. V., Hoang, V. T., La, J., Anbalagan, M., Burks, H. E., Rowan, B. G., Nephew, K. P., Collins-Burow, B. M., & Burow, M. E. (2016). Argonaute 2 Expression Correlates with a Luminal B Breast Cancer Subtype and Induces Estrogen Receptor Alpha Isoform Variation. *Noncoding RNA*, *2*(3). https://doi.org/10.3390/ncrna2030008

Consorti, F., Loponte, M., Milazzo, F., Potasso, L., & Antonaci, A. (2010). Risk of malignancy from thyroid nodular disease as an element of clinical management of patients with Hashimoto's thyroiditis. *Eur Surg Res*, *45*(3-4), 333-337. https://doi.org/10.1159/000320954

Cooper, D. S., Doherty, G. M., Haugen, B. R., Kloos, R. T., Lee, S. L., Mandel, S. J., Mazzaferri, E. L., McIver, B., Pacini, F., Schlumberger, M., Sherman, S. I., Steward, D. L., & Tuttle, R. M. (2009). Revised American Thyroid Association management guidelines for patients with thyroid nodules and differentiated thyroid cancer. *Thyroid*, *19*(11), 1167-1214. https://doi.org/10.1089/thy.2009.0110

Crile, G., Jr., Hazard, J. B., & Dinsmore, R. S. (1948). Carcinoma of the thyroid gland, with special reference to a clinicopathologic classification. *J Clin Endocrinol Metab*, *8*(9), 762-765. https://doi.org/10.1210/jcem-8-9-762

Cui, Y., Borysova, M. K., Johnson, J. O., & Guadagno, T. M. (2010). Oncogenic B-Raf(V600E) induces spindle abnormalities, supernumerary centrosomes, and aneuploidy in human melanocytic cells. *Cancer Res*, *70*(2), 675-684. https://doi.org/10.1158/0008-5472.Can-09-1491

Cunningham, F., Achuthan, P., Akanni, W., Allen, J., Amode, M R., Armean, I. M., Bennett, R., Bhai, J., Billis, K., Boddu, S., Cummins, C., Davidson, C., Dodiya, K. J., Gall, A., Girón, C. G., Gil, L., Grego, T., Haggerty, L., Haskell, E., Hourlier, T., Izuogu, O. G., Janacek, S. H., Juettemann, T., Kay, M., Laird, M. R., Lavidas, I., Liu, Z., Loveland, Jane E., Marugán, J. C., Maurel, T., McMahon, A. C., Moore, B., Morales, J., Mudge, J. M., Nuhn, M., Ogeh, D., Parker, A., Parton, A., Patricio, M., Abdul Salam, A. I., Schmitt, B. M., Schuilenburg, H., Sheppard, D., Sparrow, H., Stapleton, E., Szuba, M., Taylor, K., Threadgold, G., Thormann, A., Vullo, A., Walts, B., Winterbottom, A.,

Zadissa, A., Chakiachvili, M., Frankish, A., Hunt, S. E., Kostadima, M., Langridge, N., Martin, F. J., Muffato, M., Perry, E., Ruffier, M., Staines, D. M., Trevanion, S. J., Aken, B. L., Yates, A. D., Zerbino, D. R., & Flicek, P. (2018). Ensembl 2019. *Nucleic Acids Res*, *47*(D1), D745-D751. https://doi.org/10.1093/nar/gky1113 %J Nucleic Acids Research

Cyniak-Magierska, A., Wojciechowska-Durczyńska, K., Krawczyk-Rusiecka, K., Zygmunt, A., & Lewiński, A. (2011). Assessment of RET/PTC1 and RET/PTC3 rearrangements in fine-needle aspiration biopsy specimens collected from patients with Hashimoto's thyroiditis. *Thyroid Res*, *4*(1), 5. https://doi.org/10.1186/1756-6614-4-5

Dailey, M. E., Lindsay, S., & Skahen, R. (1955). Relation of thyroid neoplasms to Hashimoto disease of the thyroid gland. *AMA Arch Surg*, *70*(2), 291-297. https://doi.org/10.1001/archsurg.1955.01270080137023

Das, D. K. (2005). Intranuclear cytoplasmic inclusions in fine-needle aspiration smears of papillary thyroid carcinoma: a study of its morphological forms, association with nuclear grooves, and mode of formation. *Diagn Cytopathol*, *32*(5), 264-268. https://doi.org/10.1002/dc.20233

Davies, L., & Welch, H. G. (2006). Increasing incidence of thyroid cancer in the United States, 1973-2002. *Jama*, *295*(18), 2164-2167. https://doi.org/10.1001/jama.295.18.2164

de Gonzalo-Calvo, D., & Thum, T. (2018). Circulating non-coding RNAs as biomarkers to predict and monitor the response to exercise: chances and hurdles. *Eur Heart J*, *39*(38), 3552. https://doi.org/10.1093/eurheartj/ehy457

De Santa, F., Iosue, I., Del Rio, A., & Fazi, F. (2013). microRNA biogenesis pathway as a therapeutic target for human disease and cancer. *Curr Pharm Des*, *19*(4), 745-764.

Dean, D. S., & Gharib, H. (2008). Epidemiology of thyroid nodules. *Best Pract Res Clin Endocrinol Metab*, *22*(6), 901-911. https://doi.org/10.1016/j.beem.2008.09.019

Deiana, M., Dalle Carbonare, L., Serena, M., Cheri, S., Parolini, F., Gandini, A., Marchetto, G., Innamorati, G., Manfredi, M., Marengo, E., Brandi, J., Cecconi, D., Mori, A., Mina, M. M., Antoniazzi, F., Mottes, M., Tiso, N., Malerba, G., Zipeto, D., & Valenti, M. T. (2018). New Insights into the Runt Domain of RUNX2 in Melanoma Cell Proliferation and Migration. *Cells*, *7*(11). https://doi.org/10.3390/cells7110220

DeLellis, R. A. (2006). Pathology and genetics of thyroid carcinoma. *J Surg Oncol*, *94*(8), 662-669. https://doi.org/10.1002/jso.20700

Delitala, A. P., Capobianco, G., Cherchi, P. L., Dessole, S., & Delitala, G. (2019). Thyroid function and thyroid disorders during pregnancy: a review and care pathway. *Archives of Gynecology and Obstetrics*, *299*(2), 327-338. https://doi.org/10.1007/s00404-018-5018-8

Denli, A. M., Tops, B. B. J., Plasterk, R. H. A., Ketting, R. F., & Hannon, G. J. (2004). Processing of primary microRNAs by the Microprocessor complex. *Nature*, *432*(7014), 231-235. https://doi.org/10.1038/nature03049

Detzer, A., Engel, C., Wünsche, W., & Sczakiel, G. (2010). Cell stress is related to re-localization of Argonaute 2 and to decreased RNA interference in human cells. *Nucleic Acids Res*, *39*(7), 2727-2741. https://doi.org/10.1093/nar/gkq1216

Di Leva, G., & Croce, C. (2013). The Role of microRNAs in the Tumorigenesis of Ovarian Cancer [Review]. *3*(153). https://doi.org/10.3389/fonc.2013.00153

Diana, T., Olivo, P. D., & Kahaly, G. J. (2018). Thyrotropin Receptor Blocking Antibodies. *Horm Metab Res*, *50*(12), 853-862. https://doi.org/10.1055/a-0723-9023

Díaz-Martín, J., Díaz-López, A., Moreno-Bueno, G., Castilla, M., Rosa-Rosa, J. M., Cano, A., & Palacios, J. (2014). A core microRNA signature associated with inducers of the epithelial-to-mesenchymal transition. *J Pathol*, *232*(3), 319-329. https://doi.org/10.1002/path.4289

Diederichs, S., & Haber, D. A. (2007). Dual role for argonautes in microRNA processing and posttranscriptional regulation of microRNA expression. *Cell*, *131*(6), 1097-1108. https://doi.org/10.1016/j.cell.2007.10.032

Dobrijević, Z., Matijašević, S., Savić-Pavićević, D., & Brajušković, G. (2020). Association between genetic variants in genes encoding Argonaute proteins and cancer risk: A meta-analysis. *Pathol Res Pract*, *216*(5), 152906. https://doi.org/10.1016/j.prp.2020.152906

Donné, R., Nader, M. B., & Desdouets, C. (2018). Cellular and Molecular Mechanisms Controlling Ploidy. In *Reference Module in Life Sciences*. Elsevier. https://doi.org/https://doi.org/10.1016/B978-0-12-809633-8.12290-3

Durand-Dubief, M., & Bastin, P. (2003). TbAGO1, an argonaute protein required for RNA interference, is involved in mitosis and chromosome segregation in Trypanosoma brucei. *BMC Biol*, *1*, 2. https://doi.org/10.1186/1741-7007-1-2

Eggert, U. S., Mitchison, T. J., & Field, C. M. (2006). Animal cytokinesis: from parts list to mechanisms. *Annu Rev Biochem*, *75*, 543-566. https://doi.org/10.1146/annurev.biochem.74.082803.133425

Ehrlich, P. (1883;). Ueber das Vorkommen von Glykogen im diabetischen und im normalen Organismus. . *Z Klin Med*, *6: 33–46*.

Elia, N., Sougrat, R., Spurlin, T. A., Hurley, J. H., & Lippincott-Schwartz, J. (2011). Dynamics of endosomal sorting complex required for transport (ESCRT) machinery during cytokinesis and its role in abscission. *Proc Natl Acad Sci U S A*, *108*(12), 4846-4851. https://doi.org/10.1073/pnas.1102714108

Elisei, R., Ugolini, C., Viola, D., Lupi, C., Biagini, A., Giannini, R., Romei, C., Miccoli, P., Pinchera, A., & Basolo, F. (2008). BRAF(V600E) mutation and outcome of patients with papillary thyroid carcinoma: a 15-year median follow-up study. *J Clin Endocrinol Metab*, *93*(10), 3943-3949. https://doi.org/10.1210/jc.2008-0607

Fabbro, M., Zhou, B. B., Takahashi, M., Sarcevic, B., Lal, P., Graham, M. E., Gabrielli, B. G., Robinson, P. J., Nigg, E. A., Ono, Y., & Khanna, K. K. (2005). Cdk1/Erk2- and Plk1-dependent phosphorylation of a centrosome protein, Cep55, is required for its recruitment to midbody and cytokinesis. *Dev Cell*, *9*(4), 477-488. https://doi.org/10.1016/j.devcel.2005.09.003

Faehnle, Christopher R., Elkayam, E., Haase, Astrid D., Hannon, Gregory J., & Joshua-Tor, L. (2013). The Making of a Slicer: Activation of Human Argonaute-1. *Cell Reports*, *3*(6), 1901-1909. https://doi.org/https://doi.org/10.1016/j.celrep.2013.05.033

Fagman, H., Grände, M., Gritli-Linde, A., & Nilsson, M. (2004). Genetic deletion of sonic hedgehog causes hemiagenesis and ectopic development of the thyroid in mouse. *Am J Pathol*, *164*(5), 1865-1872. https://doi.org/10.1016/s0002-9440(10)63745-5

Fagman, H., Liao, J., Westerlund, J., Andersson, L., Morrow, B. E., & Nilsson, M. (2007). The 22q11 deletion syndrome candidate gene Tbx1 determines thyroid size and positioning. *Hum Mol Genet*, *16*(3), 276-285. https://doi.org/10.1093/hmg/ddl455

Fang, X., Yin, Z., Li, X., Xia, L., & Zhou, B. (2016). Polymorphisms in GEMIN4 and AGO1 Genes Are Associated with the Risk of Lung Cancer: A Case-Control Study in Chinese Female Non-Smokers. *International journal of environmental research and public health*, *13*(10), 939. https://doi.org/10.3390/ijerph13100939

Fassina, A., Cappellesso, R., Simonato, F., Siri, M., Ventura, L., Tosato, F., Busund, L. T., Pelizzo, M. R., & Fassan, M. (2014). A 4-MicroRNA signature can discriminate primary lymphomas from anaplastic carcinomas in thyroid cytology smears. *Cancer Cytopathol*, *122*(4), 274-281. https://doi.org/10.1002/cncy.21383

Feldt-Rasmussen, U. (2020). Hashimoto's thyroiditis as a risk factor for thyroid cancer. *Curr Opin Endocrinol Diabetes Obes*, *27*(5), 364-371. https://doi.org/10.1097/med.0000000000000570

Felekkis, K., Touvana, E., Stefanou, C., & Deltas, C. (2010). microRNAs: a newly described class of encoded molecules that play a role in health and disease. *Hippokratia*, *14*(4), 236-240.

Filetti, S., Durante, C., & Torlontano, M. (2006). Nonsurgical approaches to the management of thyroid nodules. *Nat Clin Pract Endocrinol Metab*, *2*(7), 384-394. https://doi.org/10.1038/ncpendmet0215

Fiore, E., Rago, T., Latrofa, F., Provenzale, M. A., Piaggi, P., Delitala, A., Scutari, M., Basolo, F., Di Coscio, G., Grasso, L., Pinchera, A., & Vitti, P. (2011). Hashimoto's thyroiditis is associated with papillary thyroid carcinoma: role of TSH and of treatment with L-thyroxine. *Endocr Relat Cancer*, *18*(4), 429-437. https://doi.org/10.1530/erc-11-0028

Fischer, A. H. (2014). The diagnostic pathology of the nuclear envelope in human cancers. *Adv Exp Med Biol*, *773*, 49-75. https://doi.org/10.1007/978-1-4899-8032-8_3

Fischer, A. H., Bond, J. A., Taysavang, P., Battles, O. E., & Wynford-Thomas, D. (1998). Papillary thyroid carcinoma oncogene (RET/PTC) alters the nuclear envelope and chromatin structure. *Am J Pathol*, *153*(5), 1443-1450. https://doi.org/10.1016/s0002-9440(10)65731-8

Fischer, A. H., Taysavang, P., & Jhiang, S. M. (2003). Nuclear envelope irregularity is induced by RET/PTC during interphase. *Am J Pathol*, *163*(3), 1091-1100. https://doi.org/10.1016/s0002-9440(10)63468-2

Fischer, A. H., Zhao, C., Li, Q. K., Gustafson, K. S., Eltoum, I. E., Tambouret, R., Benstein, B., Savaloja, L. C., & Kulesza, P. (2010). The cytologic criteria of malignancy. *J Cell Biochem*, *110*(4), 795-811. https://doi.org/10.1002/jcb.22585

Flaherty, K. T., Puzanov, I., Kim, K. B., Ribas, A., McArthur, G. A., Sosman, J. A., O'Dwyer, P. J., Lee, R. J., Grippo, J. F., Nolop, K., & Chapman, P. B. (2010). Inhibition of Mutated, Activated BRAF in Metastatic Melanoma. *363*(9), 809-819. https://doi.org/10.1056/NEJMoa1002011

Fletcher, D. A., & Mullins, R. D. (2010). Cell mechanics and the cytoskeleton. *Nature*, *463*(7280), 485-492. https://doi.org/10.1038/nature08908

Frajola, W. J., Greider, M. H., & Kleinfeld, R. G. (1956). Electron microscopy of intranuclear inclusions found in human and rat liver parenchymal cells. *J Biophys Biochem Cytol*, *2*(4 Suppl), 435-438. https://doi.org/10.1083/jcb.2.4.435

Francia, S., Michelini, F., Saxena, A., Tang, D., de Hoon, M., Anelli, V., Mione, M., Carninci, P., & d'Adda di Fagagna, F. (2012). Site-specific DICER and DROSHA RNA products control the DNA-damage response. *Nature*, *488*(7410), 231-235. https://doi.org/10.1038/nature11179

Fujiwara, T., Bandi, M., Nitta, M., Ivanova, E. V., Bronson, R. T., & Pellman, D. (2005). Cytokinesis failure generating tetraploids promotes tumorigenesis in p53-null cells. *Nature*, *437*(7061), 1043-1047. https://doi.org/10.1038/nature04217

Gagnon, K. T., Li, L., Chu, Y., Janowski, B. A., & Corey, D. R. (2014). RNAi factors are present and active in human cell nuclei. *Cell Rep*, *6*(1), 211-221. https://doi.org/10.1016/j.celrep.2013.12.013

Gao, J., & Liu, Q. G. (2011). The role of miR-26 in tumors and normal tissues (Review). *Oncol Lett*, *2*(6), 1019-1023. https://doi.org/10.3892/ol.2011.413

Gao, M., Wei, W., Li, M. M., Wu, Y. S., Ba, Z., Jin, K. X., Li, M. M., Liao, Y. Q., Adhikari, S., Chong, Z., Zhang, T., Guo, C. X., Tang, T. S., Zhu, B. T., Xu, X. Z., Mailand, N., Yang, Y. G., Qi, Y., & Rendtlew Danielsen, J. M. (2014). Ago2 facilitates Rad51 recruitment and DNA double-strand break repair by homologous recombination. *Cell Res*, *24*(5), 532-541. https://doi.org/10.1038/cr.2014.36

Gershony, O., Pe'er, T., Noach-Hirsh, M., Elia, N., & Tzur, A. (2014). Cytokinetic abscission is an acute G1 event. *Cell Cycle*, *13*(21), 3436-3441. https://doi.org/10.4161/15384101.2014.956486

Gibbings, D., Mostowy, S., Jay, F., Schwab, Y., Cossart, P., & Voinnet, O. (2012). Selective autophagy degrades DICER and AGO2 and regulates miRNA activity. *Nat Cell Biol*, *14*(12), 1314-1321. https://doi.org/10.1038/ncb2611

Gong, Y., Wu, W., Zou, X., Liu, F., Wei, T., & Zhu, J. (2018). MiR-26a inhibits thyroid cancer cell proliferation by targeting ARPP19. *Am J Cancer Res*, *8*(6), 1030-1039.

Gotoh, Y., Nishida, E., Matsuda, S., Shiina, N., Kosako, H., Shiokawa, K., Akiyama, T., Ohta, K., & Sakai, H. (1991). In vitro effects on microtubule dynamics of purified Xenopus M phase-activated MAP kinase. *Nature*, *349*(6306), 251-254. https://doi.org/10.1038/349251a0

Gould, E., Watzak, L., Chamizo, W., & Albores-Saavedra, J. (1989). Nuclear grooves in cytologic preparations. A study of the utility of this feature in the diagnosis of papillary carcinoma. *Acta Cytol*, *33*(1), 16-20.

Gousset, K., Schiff, E., Langevin, C., Marijanovic, Z., Caputo, A., Browman, D. T., Chenouard, N., de Chaumont, F., Martino, A., Enninga, J., Olivo-Marin, J. C., Mannel, D., & Zurzolo, C. (2009). Prions hijack tunnelling nanotubes for intercellular spread. *Nat Cell Biol*, *11*(3), 328-336. https://doi.org/10.1038/ncb1841

Greening, D. W., Gopal, S. K., Mathias, R. A., Liu, L., Sheng, J., Zhu, H. J., & Simpson, R. J. (2015). Emerging roles of exosomes during epithelial-mesenchymal transition and cancer progression. *Semin Cell Dev Biol*, *40*, 60-71. https://doi.org/10.1016/j.semcdb.2015.02.008

Grieco, M., Santoro, M., Berlingieri, M. T., Melillo, R. M., Donghi, R., Bongarzone, I., Pierotti, M. A., Della Porta, G., Fusco, A., & Vecchio, G. (1990). PTC is a novel rearranged form of the ret proto-oncogene and is frequently detected in vivo in human thyroid papillary carcinomas. *Cell*, *60*(4), 557-563. https://doi.org/10.1016/0092-8674(90)90659-3

Guizetti, J., & Gerlich, D. W. (2010). Cytokinetic abscission in animal cells. *Semin Cell Dev Biol*, *21*(9), 909-916. https://doi.org/10.1016/j.semcdb.2010.08.001

Guo, Z., Shu, Y., Zhou, H., & Zhang, W. (2016). Identification of diagnostic and prognostic biomarkers for cancer: Focusing on genetic variations in microRNA regulatory pathways (Review). *Mol Med Rep*, *13*(3), 1943-1952. https://doi.org/10.3892/mmr.2016.4782

Guyétant, S., Josselin, N., Savagner, F., Rohmer, V., Michalak, S., & Saint-André, J. P. (2003). C-cell hyperplasia and medullary thyroid carcinoma: clinicopathological and genetic correlations in 66 consecutive patients. *Mod Pathol*, *16*(8), 756-763. https://doi.org/10.1097/01.Mp.0000081727.75778.0c

Győrffy, B., Lanczky, A., Eklund, A. C., Denkert, C., Budczies, J., Li, Q., & Szallasi, Z. (2010). An online survival analysis tool to rapidly assess the effect of 22,277 genes on breast cancer prognosis using microarray data of 1,809 patients. *Breast Cancer Research and Treatment*, *123*(3), 725-731. https://doi.org/10.1007/s10549-009-0674-9

Ha, M., & Kim, V. N. (2014). Regulation of microRNA biogenesis. *Nature Reviews Molecular Cell Biology*, *15*(8), 509-524. https://doi.org/10.1038/nrm3838

Hansen, T. B., Venø, M. T., Jensen, T. I., Schaefer, A., Damgaard, C. K., & Kjems, J. (2016). Argonaute-associated short introns are a novel class of gene regulators. *Nature Communications*, *7*(1), 11538. https://doi.org/10.1038/ncomms11538

Harder, E., Damm, W., Maple, J., Wu, C., Reboul, M., Xiang, J. Y., Wang, L., Lupyan, D., Dahlgren, M. K., Knight, J. L., Kaus, J. W., Cerutti, D. S., Krilov, G., Jorgensen, W. L., Abel, R., & Friesner, R. A. (2016). OPLS3: A Force Field Providing Broad Coverage of Drug-like Small Molecules and Proteins. *J Chem Theory Comput*, *12*(1), 281-296. https://doi.org/10.1021/acs.jctc.5b00864

Hardie, D. G., Ross, F. A., & Hawley, S. A. (2012). AMPK: a nutrient and energy sensor that maintains energy homeostasis. *Nat Rev Mol Cell Biol*, *13*(4), 251-262. https://doi.org/10.1038/nrm3311

Haugen, B. R., Alexander, E. K., Bible, K. C., Doherty, G. M., Mandel, S. J., Nikiforov, Y. E., Pacini, F., Randolph, G. W., Sawka, A. M., Schlumberger, M., Schuff, K. G., Sherman, S. I., Sosa, J. A., Steward, D. L., Tuttle, R. M., & Wartofsky, L. (2016). 2015 American Thyroid Association Management Guidelines for Adult Patients with Thyroid Nodules and Differentiated Thyroid Cancer: The American Thyroid Association Guidelines Task Force on Thyroid Nodules and Differentiated Thyroid Cancer. *Thyroid*, *26*(1), 1-133. https://doi.org/10.1089/thy.2015.0020

Hauptmann, J., Dueck, A., Harlander, S., Pfaff, J., Merkl, R., & Meister, G. (2013). Turning catalytically inactive human Argonaute proteins into active slicer enzymes. *Nat Struct Mol Biol*, *20*(7), 814-817. https://doi.org/10.1038/nsmb.2577

Hawk, W. A., & Hazard, J. B. (1976). The many appearances of papillary carcinoma of the thyroid. *Cleve Clin Q*, *43*(4), 207-215. https://doi.org/10.3949/ccjm.43.4.207

Hayashi, D., Tanabe, K., Katsube, H., & Inoue, Y. H. (2016). B-type nuclear lamin and the nuclear pore complex Nup107-160 influences maintenance of the spindle envelope required for cytokinesis in Drosophila male meiosis. *Biol Open*, *5*(8), 1011-1021. https://doi.org/10.1242/bio.017566

Henke, L. E., Pfeifer, J. D., Baranski, T. J., DeWees, T., & Grigsby, P. W. (2018). Long-term outcomes of follicular variant vs classic papillary thyroid carcinoma. *Endocr Connect*, *7*(12), 1226-1235. https://doi.org/10.1530/ec-18-0264

Höck, J., & Meister, G. (2008). The Argonaute protein family. *Genome Biology*, *9*(2), 210. https://doi.org/10.1186/gb-2008-9-2-210

Horikawa, Y., Wood, C. G., Yang, H., Zhao, H., Ye, Y., Gu, J., Lin, J., Habuchi, T., & Wu, X. (2008). Single nucleotide polymorphisms of microRNA machinery genes modify the risk of renal cell carcinoma. *Clin Cancer Res*, *14*(23), 7956-7962. https://doi.org/10.1158/1078-0432.Ccr-08-1199

Hossain, M. A., Asa, T. A., Rahman, M. M., Uddin, S., Moustafa, A. A., Quinn, J. M. W., & Moni, M. A. (2020). Network-Based Genetic Profiling Reveals Cellular Pathway Differences Between Follicular Thyroid Carcinoma and Follicular Thyroid Adenoma. *International journal of environmental research and public health*, *17*(4). https://doi.org/10.3390/ijerph17041373

Hou, P., Li, L., Chen, F., Chen, Y., Liu, H., Li, J., Bai, J., & Zheng, J. (2018). PTBP3-Mediated Regulation of ZEB1 mRNA Stability Promotes Epithelial-Mesenchymal Transition in Breast Cancer. *Cancer Res*, *78*(2), 387-398. https://doi.org/10.1158/0008-5472.Can-17-0883

Howlader N, N. A., Krapcho M, Miller D, Bishop K, Altekruse SF, Kosary CL, Yu M, Ruhl J, Tatalovich Z, Mariotto A, Lewis DR, Chen HS, Feuer EJ, Cronin KA (eds). . (2015). SEER Cancer Statistics Review, 1975-2013. *National Cancer Institute. Bethesda, MD*. https://seer.cancer.gov/archive/csr/1975_2013/

Hu, Q., Tanasa, B., Trabucchi, M., Li, W., Zhang, J., Ohgi, K. A., Rose, D. W., Glass, C. K., & Rosenfeld, M. G. (2012). DICER- and AGO3-dependent generation of retinoic acid-induced DR2 Alu RNAs regulates human stem cell proliferation. *Nat Struct Mol Biol*, *19*(11), 1168-1175. https://doi.org/10.1038/nsmb.2400

Hu, Q., Tanasa, B., Trabucchi, M., Li, W., Zhang, J., Ohgi, K. A., Rose, D. W., Glass, C. K., & Rosenfeld, M. G. (2012). DICER- and AGO3-dependent generation of retinoic acid–induced DR2 Alu RNAs regulates human stem cell proliferation. *Nature Structural & Molecular Biology*, *19*(11), 1168-1175. https://doi.org/10.1038/nsmb.2400

Huang, C., Wang, X., Liu, X., Cao, S., & Shan, G. (2015). RNAi pathway participates in chromosome segregation in mammalian cells. *Cell Discov*, *1*, 15029. https://doi.org/10.1038/celldisc.2015.29

Huang, V., & Li, L. C. (2014). Demystifying the nuclear function of Argonaute proteins. *RNA Biol*, *11*(1), 18-24. https://doi.org/10.4161/rna.27604

Huang, V., Zheng, J., Qi, Z., Wang, J., Place, R. F., Yu, J., Li, H., & Li, L. C. (2013). Ago1 Interacts with RNA polymerase II and binds to the promoters of actively transcribed genes in human cancer cells. *PLoS Genet*, *9*(9), e1003821. https://doi.org/10.1371/journal.pgen.1003821

Humphrey, W., Dalke, A., & Schulten, K. (1996). VMD: Visual molecular dynamics. *Journal of Molecular Graphics*, *14*(1), 33-38. https://doi.org/https://doi.org/10.1016/0263-7855(96)00018-5

Hunt, J. L., & Barnes, E. L. (2003). Non-tumor-associated psammoma bodies in the thyroid. *Am J Clin Pathol*, *119*(1), 90-94. https://doi.org/10.1309/rwpp-ycby-t2jv-a023

Huntzinger, E., & Izaurralde, E. (2011). Gene silencing by microRNAs: contributions of translational repression and mRNA decay. *Nat Rev Genet*, *12*(2), 99-110. https://doi.org/10.1038/nrg2936

Hurley, J. H., & Hanson, P. I. (2010). Membrane budding and scission by the ESCRT machinery: it's all in the neck. *Nat Rev Mol Cell Biol*, *11*(8), 556-566. https://doi.org/10.1038/nrm2937

Huse, J. T., Brennan, C., Hambardzumyan, D., Wee, B., Pena, J., Rouhanifard, S. H., Sohn-Lee, C., le Sage, C., Agami, R., Tuschl, T., & Holland, E. C. (2009). The PTEN-regulating microRNA miR-26a is amplified in high-grade glioma and facilitates gliomagenesis in vivo. *Genes Dev*, *23*(11), 1327-1337. https://doi.org/10.1101/gad.1777409

Hutvagner, G., & Simard, M. J. (2008). Argonaute proteins: key players in RNA silencing. *Nat Rev Mol Cell Biol*, *9*(1), 22-32. https://doi.org/10.1038/nrm2321

Ingenito, F., Roscigno, G., Affinito, A., Nuzzo, S., Scognamiglio, I., Quintavalle, C., & Condorelli, G. (2019). The Role of Exo-miRNAs in Cancer: A Focus on Therapeutic and Diagnostic Applications. *International journal of molecular sciences*, *20*(19). https://doi.org/10.3390/ijms20194687

Iosue, I., Quaranta, R., Masciarelli, S., Fontemaggi, G., Batassa, E. M., Bertolami, C., Ottone, T., Divona, M., Salvatori, B., Padula, F., Fatica, A., Lo-Coco, F., Nervi, C., & Fazi, F. (2013). Argonaute 2 sustains the gene expression program driving human monocytic differentiation of acute myeloid leukemia cells. *Cell Death Dis*, *4*(11), e926. https://doi.org/10.1038/cddis.2013.452

Ip, Y. T., Dias Filho, M. A., & Chan, J. K. (2010). Nuclear inclusions and pseudoinclusions: friends or foes of the surgical pathologist? *Int J Surg Pathol*, *18*(6), 465-481. https://doi.org/10.1177/1066896910385342

Jan, S. Z., Vormer, T. L., Jongejan, A., Röling, M. D., Silber, S. J., de Rooij, D. G., Hamer, G., Repping, S., & van Pelt, A. M. M. (2017). Unraveling transcriptome dynamics in human spermatogenesis. *Development*, *144*(20), 3659-3673. https://doi.org/10.1242/dev.152413

Janowski, B. A., Huffman, K. E., Schwartz, J. C., Ram, R., Nordsell, R., Shames, D. S., Minna, J. D., & Corey, D. R. (2006). Involvement of AGO1 and AGO2 in mammalian transcriptional silencing. *Nat Struct Mol Biol*, *13*(9), 787-792. https://doi.org/10.1038/nsmb1140

Jaskólski, D., Papierz, T., Liberski, P. P., & Sikorska, B. (2012). Ultrastructure of meningiomas: autophagy is involved in the pathogenesis of "intranuclear vacuoles". *Folia Neuropathol*, *50*(2), 187-193.

Jayanthan, A., Ruan, Y., Truong, T. H., & Narendran, A. (2014). Aurora kinases as druggable targets in pediatric leukemia: heterogeneity in target modulation activities and cytotoxicity by diverse novel therapeutic agents. *PloS one*, *9*(7), e102741. https://doi.org/10.1371/journal.pone.0102741

Jegerlehner, S., Bulliard, J.-L., Aujesky, D., Rodondi, N., Germann, S., Konzelmann, I., Chiolero, A., & Group, N. W. (2017). Overdiagnosis and overtreatment of thyroid cancer: A population-based

temporal trend study. *PloS one*, *12*(6), e0179387-e0179387. https://doi.org/10.1371/journal.pone.0179387

Ji, J., Shi, J., Budhu, A., Yu, Z., Forgues, M., Roessler, S., Ambs, S., Chen, Y., Meltzer, P. S., Croce, C. M., Qin, L. X., Man, K., Lo, C. M., Lee, J., Ng, I. O., Fan, J., Tang, Z. Y., Sun, H. C., & Wang, X. W. (2009). MicroRNA expression, survival, and response to interferon in liver cancer. *N Engl J Med*, *361*(15), 1437-1447. https://doi.org/10.1056/NEJMoa0901282

Jin, H. Y., Gonzalez-Martin, A., Miletic, A. V., Lai, M., Knight, S., Sabouri-Ghomi, M., Head, S. R., Macauley, M. S., Rickert, R. C., & Xiao, C. (2015). Transfection of microRNA Mimics Should Be Used with Caution. *Front Genet*, *6*, 340. https://doi.org/10.3389/fgene.2015.00340

Jolly, M. K., Boareto, M., Huang, B., Jia, D., Lu, M., Ben-Jacob, E., Onuchic, J. N., & Levine, H. (2015). Implications of the Hybrid Epithelial/Mesenchymal Phenotype in Metastasis. *Front Oncol*, *5*, 155. https://doi.org/10.3389/fonc.2015.00155

Jonas, S., & Izaurralde, E. (2015). Towards a molecular understanding of microRNA-mediated gene silencing. *Nature Reviews Genetics*, *16*(7), 421-433. https://doi.org/10.1038/nrg3965

Josa-Prado, F., Henley, J. M., & Wilkinson, K. A. (2015). SUMOylation of Argonaute-2 regulates RNA interference activity. *Biochemical and Biophysical Research Communications*, *464*(4), 1066-1071. https://doi.org/https://doi.org/10.1016/j.bbrc.2015.07.073

Joshua-Tor, L. (2006). The Argonautes. *Cold Spring Harb Symp Quant Biol*, *71*, 67-72. https://doi.org/10.1101/sqb.2006.71.048

Jung, L. (KenHub GmbH). e-book. *Claudia Bednarek*, *www.kenhub.com*

Kaestner, K. H. (2005). The making of the liver: developmental competence in foregut endoderm and induction of the hepatogenic program. *Cell Cycle*, *4*(9), 1146-1148. https://doi.org/10.4161/cc.4.9.2033

Kahaly, G. J., Bartalena, L., Hegedüs, L., Leenhardt, L., Poppe, K., & Pearce, S. H. (2018). 2018 European Thyroid Association Guideline for the Management of Graves' Hyperthyroidism. *Eur Thyroid J*, *7*(4), 167-186. https://doi.org/10.1159/000490384

Kakudo, K., Bai, Y., Liu, Z., Li, Y., Ito, Y., & Ozaki, T. (2012). Classification of thyroid follicular cell tumors: with special reference to borderline lesions [Review]. *Endocrine Journal*, *59*(1), 1-12. https://doi.org/10.1507/endocrj.EJ11-0184

Kalluri, R., & Weinberg, R. A. (2009). The basics of epithelial-mesenchymal transition. *J Clin Invest*, *119*(6), 1420-1428. https://doi.org/10.1172/jci39104

Kameda, Y., Nishimaki, T., Chisaka, O., Iseki, S., & Sucov, H. M. (2007). Expression of the epithelial marker E-cadherin by thyroid C cells and their precursors during murine development. *J Histochem Cytochem*, *55*(10), 1075-1088. https://doi.org/10.1369/jhc.7A7179.2007

Kantarjian, H., Sawyers, C., Hochhaus, A., Guilhot, F., Schiffer, C., Gambacorti-Passerini, C., Niederwieser, D., Resta, D., Capdeville, R., Zoellner, U., Talpaz, M., & Druker, B. (2002). Hematologic and Cytogenetic Responses to Imatinib Mesylate in Chronic Myelogenous Leukemia. *346*(9), 645-652. https://doi.org/10.1056/NEJMoa011573

Karlikow, M., Goic, B., Mongelli, V., Salles, A., Schmitt, C., Bonne, I., Zurzolo, C., & Saleh, M. C. (2016). Drosophila cells use nanotube-like structures to transfer dsRNA and RNAi machinery between cells. *Sci Rep*, *6*, 27085. https://doi.org/10.1038/srep27085

Kaserer, K., Scheuba, C., Neuhold, N., Weinhäusel, A., Haas, O. A., Vierhapper, H., & Niederle, B. (2001). Sporadic versus familial medullary thyroid microcarcinoma: a histopathologic study of 50 consecutive patients. *Am J Surg Pathol*, *25*(10), 1245-1251. https://doi.org/10.1097/00000478-200110000-00004

Kaserer, K., Scheuba, C., Neuhold, N., Weinhäusel, A., Vierhapper, H., Haas, O. A., & Niederle, B. (1998). C-cell hyperplasia and medullary thyroid carcinoma in patients routinely screened for

serum calcitonin. *Am J Surg Pathol*, *22*(6), 722-728. https://doi.org/10.1097/00000478-199806000-00009

Kelly, L. M., Barila, G., Liu, P., Evdokimova, V. N., Trivedi, S., Panebianco, F., Gandhi, M., Carty, S. E., Hodak, S. P., Luo, J., Dacic, S., Yu, Y. P., Nikiforova, M. N., Ferris, R. L., Altschuler, D. L., & Nikiforov, Y. E. (2014). Identification of the transforming STRN-ALK fusion as a potential therapeutic target in the aggressive forms of thyroid cancer. *Proc Natl Acad Sci U S A*, *111*(11), 4233-4238. https://doi.org/10.1073/pnas.1321937111

Keutgen, X. M., Filicori, F., & Fahey, T. J., 3rd. (2013). Molecular diagnosis for indeterminate thyroid nodules on fine needle aspiration: advances and limitations. *Expert Rev Mol Diagn*, *13*(6), 613-623. https://doi.org/10.1586/14737159.2013.811893

Khan YS, F. A. (2020). Histology, Thyroid Gland. . *In: StatPearls [Internet]. Treasure Island (FL): StatPearls Publishing;* . https://www.ncbi.nlm.nih.gov/books/NBK551659/

Khanafshar, E., & Lloyd, R. V. (2011). The spectrum of papillary thyroid carcinoma variants. *Adv Anat Pathol*, *18*(1), 90-97. https://doi.org/10.1097/PAP.0b013e3182026da6

Kim, N. W., Piatyszek, M. A., Prowse, K. R., Harley, C. B., West, M. D., Ho, P. L., Coviello, G. M., Wright, W. E., Weinrich, S. L., & Shay, J. W. (1994). Specific association of human telomerase activity with immortal cells and cancer. *Science*, *266*(5193), 2011-2015. https://doi.org/10.1126/science.7605428

Kim, T. Y., Kim, W. B., Song, J. Y., Rhee, Y. S., Gong, G., Cho, Y. M., Kim, S. Y., Kim, S. C., Hong, S. J., & Shong, Y. K. (2005). The BRAF mutation is not associated with poor prognostic factors in Korean patients with conventional papillary thyroid microcarcinoma. *Clin Endocrinol (Oxf)*, *63*(5), 588-593. https://doi.org/10.1111/j.1365-2265.2005.02389.x

Kim, Y. J., Maizel, A., & Chen, X. (2014). Traffic into silence: endomembranes and post-transcriptional RNA silencing. *Embo j*, *33*(9), 968-980. https://doi.org/10.1002/embj.201387262

Kirshner, H., Aguet, F., Sage, D., & Unser, M. (2013). 3-D PSF fitting for fluorescence microscopy: implementation and localization application. *J Microsc*, *249*(1), 13-25. https://doi.org/10.1111/j.1365-2818.2012.03675.x

Klionsky, D. J., Abdelmohsen, K., Abe, A., Abedin, M. J., Abeliovich, H., Acevedo Arozena, A., Adachi, H., Adams, C. M., Adams, P. D., Adeli, K., Adhihetty, P. J., Adler, S. G., Agam, G., Agarwal, R., Aghi, M. K., Agnello, M., Agostinis, P., Aguilar, P. V., Aguirre-Ghiso, J., Airoldi, E. M., Ait-Si-Ali, S., Akematsu, T., Akporiaye, E. T., Al-Rubeai, M., Albaiceta, G. M., Albanese, C., Albani, D., Albert, M. L., Aldudo, J., Algül, H., Alirezaei, M., Alloza, I., Almasan, A., Almonte-Beceril, M., Alnemri, E. S., Alonso, C., Altan-Bonnet, N., Altieri, D. C., Alvarez, S., Alvarez-Erviti, L., Alves, S., Amadoro, G., Amano, A., Amantini, C., Ambrosio, S., Amelio, I., Amer, A. O., Amessou, M., Amon, A., An, Z., Anania, F. A., Andersen, S. U., Andley, U. P., Andreadi, C. K., Andrieu-Abadie, N., Anel, A., Ann, D. K., Anoopkumar-Dukie, S., Antonioli, M., Aoki, H., Apostolova, N., Aquila, S., Aquilano, K., Araki, K., Arama, E., Aranda, A., Araya, J., Arcaro, A., Arias, E., Arimoto, H., Ariosa, A. R., Armstrong, J. L., Arnould, T., Arsov, I., Asanuma, K., Askanas, V., Asselin, E., Atarashi, R., Atherton, S. S., Atkin, J. D., Attardi, L. D., Auberger, P., Auburger, G., Aurelian, L., Autelli, R., Avagliano, L., Avantaggiati, M. L., Avrahami, L., Awale, S., Azad, N., Bachetti, T., Backer, J. M., Bae, D. H., Bae, J. S., Bae, O. N., Bae, S. H., Baehrecke, E. H., Baek, S. H., Baghdiguian, S., Bagniewska-Zadworna, A., Bai, H., Bai, J., Bai, X. Y., Bailly, Y., Balaji, K. N., Balduini, W., Ballabio, A., Balzan, R., Banerjee, R., Bánhegyi, G., Bao, H., Barbeau, B., Barrachina, M. D., Barreiro, E., Bartel, B., Bartolomé, A., Bassham, D. C., Bassi, M. T., Bast, R. C., Jr., Basu, A., Batista, M. T., Batoko, H., Battino, M., Bauckman, K., Baumgarner, B. L., Bayer, K. U., Beale, R., Beaulieu, J. F., Beck, G. R., Jr., Becker, C., Beckham, J. D., Bédard, P. A., Bednarski, P. J., Begley, T. J., Behl, C., Behrends, C., Behrens, G. M., Behrns, K. E., Bejarano, E.,

Belaid, A., Belleudi, F., Bénard, G., Berchem, G., Bergamaschi, D., Bergami, M., Berkhout, B., Berliocchi, L., Bernard, A., Bernard, M., Bernassola, F., Bertolotti, A., Bess, A. S., Besteiro, S., Bettuzzi, S., Bhalla, S., Bhattacharyya, S., Bhutia, S. K., Biagosch, C., Bianchi, M. W., Biard-Piechaczyk, M., Billes, V., Bincoletto, C., Bingol, B., Bird, S. W., Bitoun, M., Bjedov, I., Blackstone, C., Blanc, L., Blanco, G. A., Blomhoff, H. K., Boada-Romero, E., Böckler, S., Boes, M., Boesze-Battaglia, K., Boise, L. H., Bolino, A., Boman, A., Bonaldo, P., Bordi, M., Bosch, J., Botana, L. M., Botti, J., Bou, G., Bouché, M., Bouchecareilh, M., Boucher, M. J., Boulton, M. E., Bouret, S. G., Boya, P., Boyer-Guittaut, M., Bozhkov, P. V., Brady, N., Braga, V. M., Brancolini, C., Braus, G. H., Bravo-San Pedro, J. M., Brennan, L. A., Bresnick, E. H., Brest, P., Bridges, D., Bringer, M. A., Brini, M., Brito, G. C., Brodin, B., Brookes, P. S., Brown, E. J., Brown, K., Broxmeyer, H. E., Bruhat, A., Brum, P. C., Brumell, J. H., Brunetti-Pierri, N., Bryson-Richardson, R. J., Buch, S., Buchan, A. M., Budak, H., Bulavin, D. V., Bultman, S. J., Bultynck, G., Bumbasirevic, V., Burelle, Y., Burke, R. E., Burmeister, M., Bütikofer, P., Caberlotto, L., Cadwell, K., Cahova, M., Cai, D., Cai, J., Cai, Q., Calatayud, S., Camougrand, N., Campanella, M., Campbell, G. R., Campbell, M., Campello, S., Candau, R., Caniggia, I., Cantoni, L., Cao, L., Caplan, A. B., Caraglia, M., Cardinali, C., Cardoso, S. M., Carew, J. S., Carleton, L. A., Carlin, C. R., Carloni, S., Carlsson, S. R., Carmona-Gutierrez, D., Carneiro, L. A., Carnevali, O., Carra, S., Carrier, A., Carroll, B., Casas, C., Casas, J., Cassinelli, G., Castets, P., Castro-Obregon, S., Cavallini, G., Ceccherini, I., Cecconi, F., Cederbaum, A. I., Ceña, V., Cenci, S., Cerella, C., Cervia, D., Cetrullo, S., Chaachouay, H., Chae, H. J., Chagin, A. S., Chai, C. Y., Chakrabarti, G., Chamilos, G., Chan, E. Y., Chan, M. T., Chandra, D., Chandra, P., Chang, C. P., Chang, R. C., Chang, T. Y., Chatham, J. C., Chatterjee, S., Chauhan, S., Che, Y., Cheetham, M. E., Cheluvappa, R., Chen, C. J., Chen, G., Chen, G. C., Chen, G., Chen, H., Chen, J. W., Chen, J. K., Chen, M., Chen, M., Chen, P., Chen, Q., Chen, Q., Chen, S. D., Chen, S., Chen, S. S., Chen, W., Chen, W. J., Chen, W. Q., Chen, W., Chen, X., Chen, Y. H., Chen, Y. G., Chen, Y., Chen, Y., Chen, Y., Chen, Y. J., Chen, Y. Q., Chen, Y., Chen, Z., Chen, Z., Cheng, A., Cheng, C. H., Cheng, H., Cheong, H., Cherry, S., Chesney, J., Cheung, C. H., Chevet, E., Chi, H. C., Chi, S. G., Chiacchiera, F., Chiang, H. L., Chiarelli, R., Chiariello, M., Chieppa, M., Chin, L. S., Chiong, M., Chiu, G. N., Cho, D. H., Cho, S. G., Cho, W. C., Cho, Y. Y., Cho, Y. S., Choi, A. M., Choi, E. J., Choi, E. K., Choi, J., Choi, M. E., Choi, S. I., Chou, T. F., Chouaib, S., Choubey, D., Choubey, V., Chow, K. C., Chowdhury, K., Chu, C. T., Chuang, T. H., Chun, T., Chung, H., Chung, T., Chung, Y. L., Chwae, Y. J., Cianfanelli, V., Ciarcia, R., Ciechomska, I. A., Ciriolo, M. R., Cirone, M., Claerhout, S., Clague, M. J., Clària, J., Clarke, P. G., Clarke, R., Clementi, E., Cleyrat, C., Cnop, M., Coccia, E. M., Cocco, T., Codogno, P., Coers, J., Cohen, E. E., Colecchia, D., Coletto, L., Coll, N. S., Colucci-Guyon, E., Comincini, S., Condello, M., Cook, K. L., Coombs, G. H., Cooper, C. D., Cooper, J. M., Coppens, I., Corasaniti, M. T., Corazzari, M., Corbalan, R., Corcelle-Termeau, E., Cordero, M. D., Corral-Ramos, C., Corti, O., Cossarizza, A., Costelli, P., Costes, S., Cotman, S. L., Coto-Montes, A., Cottet, S., Couve, E., Covey, L. R., Cowart, L. A., Cox, J. S., Coxon, F. P., Coyne, C. B., Cragg, M. S., Craven, R. J., Crepaldi, T., Crespo, J. L., Criollo, A., Crippa, V., Cruz, M. T., Cuervo, A. M., Cuezva, J. M., Cui, T., Cutillas, P. R., Czaja, M. J., Czyzyk-Krzeska, M. F., Dagda, R. K., Dahmen, U., Dai, C., Dai, W., Dai, Y., Dalby, K. N., Dalla Valle, L., Dalmasso, G., D'Amelio, M., Damme, M., Darfeuille-Michaud, A., Dargemont, C., Darley-Usmar, V. M., Dasarathy, S., Dasgupta, B., Dash, S., Dass, C. R., Davey, H. M., Davids, L. M., Dávila, D., Davis, R. J., Dawson, T. M., Dawson, V. L., Daza, P., de Belleroche, J., de Figueiredo, P., de Figueiredo, R. C., de la Fuente, J., De Martino, L., De Matteis, A., De Meyer, G. R., De Milito, A., De Santi, M., de Souza, W., De Tata, V., De Zio, D., Debnath, J., Dechant, R., Decuypere, J. P., Deegan, S., Dehay, B., Del Bello, B., Del Re, D. P., Delage-Mourroux, R., Delbridge, L. M., Deldicque, L., Delorme-Axford, E., Deng, Y., Dengjel, J.,

Denizot, M., Dent, P., Der, C. J., Deretic, V., Derrien, B., Deutsch, E., Devarenne, T. P., Devenish, R. J., Di Bartolomeo, S., Di Daniele, N., Di Domenico, F., Di Nardo, A., Di Paola, S., Di Pietro, A., Di Renzo, L., DiAntonio, A., Díaz-Araya, G., Díaz-Laviada, I., Diaz-Meco, M. T., Diaz-Nido, J., Dickey, C. A., Dickson, R. C., Diederich, M., Digard, P., Dikic, I., Dinesh-Kumar, S. P., Ding, C., Ding, W. X., Ding, Z., Dini, L., Distler, J. H., Diwan, A., Djavaheri-Mergny, M., Dmytruk, K., Dobson, R. C., Doetsch, V., Dokladny, K., Dokudovskaya, S., Donadelli, M., Dong, X. C., Dong, X., Dong, Z., Donohue, T. M., Jr., Doran, K. S., D'Orazi, G., Dorn, G. W., 2nd, Dosenko, V., Dridi, S., Drucker, L., Du, J., Du, L. L., Du, L., du Toit, A., Dua, P., Duan, L., Duann, P., Dubey, V. K., Duchen, M. R., Duchosal, M. A., Duez, H., Dugail, I., Dumit, V. I., Duncan, M. C., Dunlop, E. A., Dunn, W. A., Jr., Dupont, N., Dupuis, L., Durán, R. V., Durcan, T. M., Duvezin-Caubet, S., Duvvuri, U., Eapen, V., Ebrahimi-Fakhari, D., Echard, A., Eckhart, L., Edelstein, C. L., Edinger, A. L., Eichinger, L., Eisenberg, T., Eisenberg-Lerner, A., Eissa, N. T., El-Deiry, W. S., El-Khoury, V., Elazar, Z., Eldar-Finkelman, H., Elliott, C. J., Emanuele, E., Emmenegger, U., Engedal, N., Engelbrecht, A. M., Engelender, S., Enserink, J. M., Erdmann, R., Erenpreisa, J., Eri, R., Eriksen, J. L., Erman, A., Escalante, R., Eskelinen, E. L., Espert, L., Esteban-Martínez, L., Evans, T. J., Fabri, M., Fabrias, G., Fabrizi, C., Facchiano, A., Færgeman, N. J., Faggioni, A., Fairlie, W. D., Fan, C., Fan, D., Fan, J., Fang, S., Fanto, M., Fanzani, A., Farkas, T., Faure, M., Favier, F. B., Fearnhead, H., Federici, M., Fei, E., Felizardo, T. C., Feng, H., Feng, Y., Feng, Y., Ferguson, T. A., Fernández Á, F., Fernandez-Barrena, M. G., Fernandez-Checa, J. C., Fernández-López, A., Fernandez-Zapico, M. E., Feron, O., Ferraro, E., Ferreira-Halder, C. V., Fesus, L., Feuer, R., Fiesel, F. C., Filippi-Chiela, E. C., Filomeni, G., Fimia, G. M., Fingert, J. H., Finkbeiner, S., Finkel, T., Fiorito, F., Fisher, P. B., Flajolet, M., Flamigni, F., Florey, O., Florio, S., Floto, R. A., Folini, M., Follo, C., Fon, E. A., Fornai, F., Fortunato, F., Fraldi, A., Franco, R., Francois, A., François, A., Frankel, L. B., Fraser, I. D., Frey, N., Freyssenet, D. G., Frezza, C., Friedman, S. L., Frigo, D. E., Fu, D., Fuentes, J. M., Fueyo, J., Fujitani, Y., Fujiwara, Y., Fujiya, M., Fukuda, M., Fulda, S., Fusco, C., Gabryel, B., Gaestel, M., Gailly, P., Gajewska, M., Galadari, S., Galili, G., Galindo, I., Galindo, M. F., Galliciotti, G., Galluzzi, L., Galluzzi, L., Galy, V., Gammoh, N., Gandy, S., Ganesan, A. K., Ganesan, S., Ganley, I. G., Gannagé, M., Gao, F. B., Gao, F., Gao, J. X., García Nannig, L., García Véscovi, E., Garcia-Macía, M., Garcia-Ruiz, C., Garg, A. D., Garg, P. K., Gargini, R., Gassen, N. C., Gatica, D., Gatti, E., Gavard, J., Gavathiotis, E., Ge, L., Ge, P., Ge, S., Gean, P. W., Gelmetti, V., Genazzani, A. A., Geng, J., Genschik, P., Gerner, L., Gestwicki, J. E., Gewirtz, D. A., Ghavami, S., Ghigo, E., Ghosh, D., Giammarioli, A. M., Giampieri, F., Giampietri, C., Giatromanolaki, A., Gibbings, D. J., Gibellini, L., Gibson, S. B., Ginet, V., Giordano, A., Giorgini, F., Giovannetti, E., Girardin, S. E., Gispert, S., Giuliano, S., Gladson, C. L., Glavic, A., Gleave, M., Godefroy, N., Gogal, R. M., Jr., Gokulan, K., Goldman, G. H., Goletti, D., Goligorsky, M. S., Gomes, A. V., Gomes, L. C., Gomez, H., Gomez-Manzano, C., Gómez-Sánchez, R., Gonçalves, D. A., Goncu, E., Gong, Q., Gongora, C., Gonzalez, C. B., Gonzalez-Alegre, P., Gonzalez-Cabo, P., González-Polo, R. A., Goping, I. S., Gorbea, C., Gorbunov, N. V., Goring, D. R., Gorman, A. M., Gorski, S. M., Goruppi, S., Goto-Yamada, S., Gotor, C., Gottlieb, R. A., Gozes, I., Gozuacik, D., Graba, Y., Graef, M., Granato, G. E., Grant, G. D., Grant, S., Gravina, G. L., Green, D. R., Greenhough, A., Greenwood, M. T., Grimaldi, B., Gros, F., Grose, C., Groulx, J. F., Gruber, F., Grumati, P., Grune, T., Guan, J. L., Guan, K. L., Guerra, B., Guillen, C., Gulshan, K., Gunst, J., Guo, C., Guo, L., Guo, M., Guo, W., Guo, X. G., Gust, A. A., Gustafsson Å, B., Gutierrez, E., Gutierrez, M. G., Gwak, H. S., Haas, A., Haber, J. E., Hadano, S., Hagedorn, M., Hahn, D. R., Halayko, A. J., Hamacher-Brady, A., Hamada, K., Hamai, A., Hamann, A., Hamasaki, M., Hamer, I., Hamid, Q., Hammond, E. M., Han, F., Han, W., Handa, J. T., Hanover, J. A., Hansen, M., Harada, M., Harhaji-Trajkovic, L., Harper, J. W., Harrath, A. H., Harris, A. L., Harris, J., Hasler,

U., Hasselblatt, P., Hasui, K., Hawley, R. G., Hawley, T. S., He, C., He, C. Y., He, F., He, G., He, R. R., He, X. H., He, Y. W., He, Y. Y., Heath, J. K., Hébert, M. J., Heinzen, R. A., Helgason, G. V., Hensel, M., Henske, E. P., Her, C., Herman, P. K., Hernández, A., Hernandez, C., Hernández-Tiedra, S., Hetz, C., Hiesinger, P. R., Higaki, K., Hilfiker, S., Hill, B. G., Hill, J. A., Hill, W. D., Hino, K., Hofius, D., Hofman, P., Höglinger, G. U., Höhfeld, J., Holz, M. K., Hong, Y., Hood, D. A., Hoozemans, J. J., Hoppe, T., Hsu, C., Hsu, C. Y., Hsu, L. C., Hu, D., Hu, G., Hu, H. M., Hu, H., Hu, M. C., Hu, Y. C., Hu, Z. W., Hua, F., Hua, Y., Huang, C., Huang, H. L., Huang, K. H., Huang, K. Y., Huang, S., Huang, S., Huang, W. P., Huang, Y. R., Huang, Y., Huang, Y., Huber, T. B., Huebbe, P., Huh, W. K., Hulmi, J. J., Hur, G. M., Hurley, J. H., Husak, Z., Hussain, S. N., Hussain, S., Hwang, J. J., Hwang, S., Hwang, T. I., Ichihara, A., Imai, Y., Imbriano, C., Inomata, M., Into, T., Iovane, V., Iovanna, J. L., Iozzo, R. V., Ip, N. Y., Irazoqui, J. E., Iribarren, P., Isaka, Y., Isakovic, A. J., Ischiropoulos, H., Isenberg, J. S., Ishaq, M., Ishida, H., Ishii, I., Ishmael, J. E., Isidoro, C., Isobe, K., Isono, E., Issazadeh-Navikas, S., Itahana, K., Itakura, E., Ivanov, A. I., Iyer, A. K., Izquierdo, J. M., Izumi, Y., Izzo, V., Jäättelä, M., Jaber, N., Jackson, D. J., Jackson, W. T., Jacob, T. G., Jacques, T. S., Jagannath, C., Jain, A., Jana, N. R., Jang, B. K., Jani, A., Janji, B., Jannig, P. R., Jansson, P. J., Jean, S., Jendrach, M., Jeon, J. H., Jessen, N., Jeung, E. B., Jia, K., Jia, L., Jiang, H., Jiang, H., Jiang, L., Jiang, T., Jiang, X., Jiang, X., Jiang, X., Jiang, Y., Jiang, Y., Jiménez, A., Jin, C., Jin, H., Jin, L., Jin, M., Jin, S., Jinwal, U. K., Jo, E. K., Johansen, T., Johnson, D. E., Johnson, G. V., Johnson, J. D., Jonasch, E., Jones, C., Joosten, L. A., Jordan, J., Joseph, A. M., Joseph, B., Joubert, A. M., Ju, D., Ju, J., Juan, H. F., Juenemann, K., Juhász, G., Jung, H. S., Jung, J. U., Jung, Y. K., Jungbluth, H., Justice, M. J., Jutten, B., Kaakoush, N. O., Kaarniranta, K., Kaasik, A., Kabuta, T., Kaeffer, B., Kågedal, K., Kahana, A., Kajimura, S., Kakhlon, O., Kalia, M., Kalvakolanu, D. V., Kamada, Y., Kambas, K., Kaminskyy, V. O., Kampinga, H. H., Kandouz, M., Kang, C., Kang, R., Kang, T. C., Kanki, T., Kanneganti, T. D., Kanno, H., Kanthasamy, A. G., Kantorow, M., Kaparakis-Liaskos, M., Kapuy, O., Karantza, V., Karim, M. R., Karmakar, P., Kaser, A., Kaushik, S., Kawula, T., Kaynar, A. M., Ke, P. Y., Ke, Z. J., Kehrl, J. H., Keller, K. E., Kemper, J. K., Kenworthy, A. K., Kepp, O., Kern, A., Kesari, S., Kessel, D., Ketteler, R., Kettelhut Ido, C., Khambu, B., Khan, M. M., Khandelwal, V. K., Khare, S., Kiang, J. G., Kiger, A. A., Kihara, A., Kim, A. L., Kim, C. H., Kim, D. R., Kim, D. H., Kim, E. K., Kim, H. Y., Kim, H. R., Kim, J. S., Kim, J. H., Kim, J. C., Kim, J. H., Kim, K. W., Kim, M. D., Kim, M. M., Kim, P. K., Kim, S. W., Kim, S. Y., Kim, Y. S., Kim, Y., Kimchi, A., Kimmelman, A. C., Kimura, T., King, J. S., Kirkegaard, K., Kirkin, V., Kirshenbaum, L. A., Kishi, S., Kitajima, Y., Kitamoto, K., Kitaoka, Y., Kitazato, K., Kley, R. A., Klimecki, W. T., Klinkenberg, M., Klucken, J., Knævelsrud, H., Knecht, E., Knuppertz, L., Ko, J. L., Kobayashi, S., Koch, J. C., Koechlin-Ramonatxo, C., Koenig, U., Koh, Y. H., Köhler, K., Kohlwein, S. D., Koike, M., Komatsu, M., Kominami, E., Kong, D., Kong, H. J., Konstantakou, E. G., Kopp, B. T., Korcsmaros, T., Korhonen, L., Korolchuk, V. I., Koshkina, N. V., Kou, Y., Koukourakis, M. I., Koumenis, C., Kovács, A. L., Kovács, T., Kovacs, W. J., Koya, D., Kraft, C., Krainc, D., Kramer, H., Kravic-Stevovic, T., Krek, W., Kretz-Remy, C., Krick, R., Krishnamurthy, M., Kriston-Vizi, J., Kroemer, G., Kruer, M. C., Kruger, R., Ktistakis, N. T., Kuchitsu, K., Kuhn, C., Kumar, A. P., Kumar, A., Kumar, A., Kumar, D., Kumar, D., Kumar, R., Kumar, S., Kundu, M., Kung, H. J., Kuno, A., Kuo, S. H., Kuret, J., Kurz, T., Kwok, T., Kwon, T. K., Kwon, Y. T., Kyrmizi, I., La Spada, A. R., Lafont, F., Lahm, T., Lakkaraju, A., Lam, T., Lamark, T., Lancel, S., Landowski, T. H., Lane, D. J., Lane, J. D., Lanzi, C., Lapaquette, P., Lapierre, L. R., Laporte, J., Laukkarinen, J., Laurie, G. W., Lavandero, S., Lavie, L., LaVoie, M. J., Law, B. Y., Law, H. K., Law, K. B., Layfield, R., Lazo, P. A., Le Cam, L., Le Roch, K. G., Le Stunff, H., Leardkamolkarn, V., Lecuit, M., Lee, B. H., Lee, C. H., Lee, E. F., Lee, G. M., Lee, H. J., Lee, H., Lee, J. K., Lee, J., Lee, J. H., Lee, J. H., Lee, M., Lee, M. S., Lee, P. J., Lee, S. W., Lee, S. J., Lee, S. J., Lee, S. Y., Lee, S. H., Lee, S. S., Lee, S.

J., Lee, S., Lee, Y. R., Lee, Y. J., Lee, Y. H., Leeuwenburgh, C., Lefort, S., Legouis, R., Lei, J., Lei, Q. Y., Leib, D. A., Leibowitz, G., Lekli, I., Lemaire, S. D., Lemasters, J. J., Lemberg, M. K., Lemoine, A., Leng, S., Lenz, G., Lenzi, P., Lerman, L. O., Lettieri Barbato, D., Leu, J. I., Leung, H. Y., Levine, B., Lewis, P. A., Lezoualc'h, F., Li, C., Li, F., Li, F. J., Li, J., Li, K., Li, L., Li, M., Li, M., Li, Q., Li, R., Li, S., Li, W., Li, W., Li, X., Li, Y., Lian, J., Liang, C., Liang, Q., Liao, Y., Liberal, J., Liberski, P. P., Lie, P., Lieberman, A. P., Lim, H. J., Lim, K. L., Lim, K., Lima, R. T., Lin, C. S., Lin, C. F., Lin, F., Lin, F., Lin, F. C., Lin, K., Lin, K. H., Lin, P. H., Lin, T., Lin, W. W., Lin, Y. S., Lin, Y., Linden, R., Lindholm, D., Lindqvist, L. M., Lingor, P., Linkermann, A., Liotta, L. A., Lipinski, M. M., Lira, V. A., Lisanti, M. P., Liton, P. B., Liu, B., Liu, C., Liu, C. F., Liu, F., Liu, H. J., Liu, J., Liu, J. J., Liu, J. L., Liu, K., Liu, L., Liu, L., Liu, Q., Liu, R. Y., Liu, S., Liu, S., Liu, W., Liu, X. D., Liu, X., Liu, X. H., Liu, X., Liu, X., Liu, X., Liu, Y., Liu, Y., Liu, Z., Liu, Z., Liuzzi, J. P., Lizard, G., Ljujic, M., Lodhi, I. J., Logue, S. E., Lokeshwar, B. L., Long, Y. C., Lonial, S., Loos, B., López-Otín, C., López-Vicario, C., Lorente, M., Lorenzi, P. L., Lõrincz, P., Los, M., Lotze, M. T., Lovat, P. E., Lu, B., Lu, B., Lu, J., Lu, Q., Lu, S. M., Lu, S., Lu, Y., Luciano, F., Luckhart, S., Lucocq, J. M., Ludovico, P., Lugea, A., Lukacs, N. W., Lum, J. J., Lund, A. H., Luo, H., Luo, J., Luo, S., Luparello, C., Lyons, T., Ma, J., Ma, Y., Ma, Y., Ma, Z., Machado, J., Machado-Santelli, G. M., Macian, F., MacIntosh, G. C., MacKeigan, J. P., Macleod, K. F., MacMicking, J. D., MacMillan-Crow, L. A., Madeo, F., Madesh, M., Madrigal-Matute, J., Maeda, A., Maeda, T., Maegawa, G., Maellaro, E., Maes, H., Magariños, M., Maiese, K., Maiti, T. K., Maiuri, L., Maiuri, M. C., Maki, C. G., Malli, R., Malorni, W., Maloyan, A., Mami-Chouaib, F., Man, N., Mancias, J. D., Mandelkow, E. M., Mandell, M. A., Manfredi, A. A., Manié, S. N., Manzoni, C., Mao, K., Mao, Z., Mao, Z. W., Marambaud, P., Marconi, A. M., Marelja, Z., Marfe, G., Margeta, M., Margittai, E., Mari, M., Mariani, F. V., Marin, C., Marinelli, S., Mariño, G., Markovic, I., Marquez, R., Martelli, A. M., Martens, S., Martin, K. R., Martin, S. J., Martin, S., Martin-Acebes, M. A., Martín-Sanz, P., Martinand-Mari, C., Martinet, W., Martinez, J., Martinez-Lopez, N., Martinez-Outschoorn, U., Martínez-Velázquez, M., Martinez-Vicente, M., Martins, W. K., Mashima, H., Mastrianni, J. A., Matarese, G., Matarrese, P., Mateo, R., Matoba, S., Matsumoto, N., Matsushita, T., Matsuura, A., Matsuzawa, T., Mattson, M. P., Matus, S., Maugeri, N., Mauvezin, C., Mayer, A., Maysinger, D., Mazzolini, G. D., McBrayer, M. K., McCall, K., McCormick, C., McInerney, G. M., McIver, S. C., McKenna, S., McMahon, J. J., McNeish, I. A., Mechta-Grigoriou, F., Medema, J. P., Medina, D. L., Megyeri, K., Mehrpour, M., Mehta, J. L., Mei, Y., Meier, U. C., Meijer, A. J., Meléndez, A., Melino, G., Melino, S., de Melo, E. J., Mena, M. A., Meneghini, M. D., Menendez, J. A., Menezes, R., Meng, L., Meng, L. H., Meng, S., Menghini, R., Menko, A. S., Menna-Barreto, R. F., Menon, M. B., Meraz-Ríos, M. A., Merla, G., Merlini, L., Merlot, A. M., Meryk, A., Meschini, S., Meyer, J. N., Mi, M. T., Miao, C. Y., Micale, L., Michaeli, S., Michiels, C., Migliaccio, A. R., Mihailidou, A. S., Mijaljica, D., Mikoshiba, K., Milan, E., Miller-Fleming, L., Mills, G. B., Mills, I. G., Minakaki, G., Minassian, B. A., Ming, X. F., Minibayeva, F., Minina, E. A., Mintern, J. D., Minucci, S., Miranda-Vizuete, A., Mitchell, C. H., Miyamoto, S., Miyazawa, K., Mizushima, N., Mnich, K., Mograbi, B., Mohseni, S., Moita, L. F., Molinari, M., Molinari, M., Møller, A. B., Mollereau, B., Mollinedo, F., Mongillo, M., Monick, M. M., Montagnaro, S., Montell, C., Moore, D. J., Moore, M. N., Mora-Rodriguez, R., Moreira, P. I., Morel, E., Morelli, M. B., Moreno, S., Morgan, M. J., Moris, A., Moriyasu, Y., Morrison, J. L., Morrison, L. A., Morselli, E., Moscat, J., Moseley, P. L., Mostowy, S., Motori, E., Mottet, D., Mottram, J. C., Moussa, C. E., Mpakou, V. E., Mukhtar, H., Mulcahy Levy, J. M., Muller, S., Muñoz-Moreno, R., Muñoz-Pinedo, C., Münz, C., Murphy, M. E., Murray, J. T., Murthy, A., Mysorekar, I. U., Nabi, I. R., Nabissi, M., Nader, G. A., Nagahara, Y., Nagai, Y., Nagata, K., Nagelkerke, A., Nagy, P., Naidu, S. R., Nair, S., Nakano, H., Nakatogawa, H., Nanjundan, M., Napolitano, G., Naqvi, N. I., Nardacci, R., Narendra, D. P.,

Narita, M., Nascimbeni, A. C., Natarajan, R., Navegantes, L. C., Nawrocki, S. T., Nazarko, T. Y., Nazarko, V. Y., Neill, T., Neri, L. M., Netea, M. G., Netea-Maier, R. T., Neves, B. M., Ney, P. A., Nezis, I. P., Nguyen, H. T., Nguyen, H. P., Nicot, A. S., Nilsen, H., Nilsson, P., Nishimura, M., Nishino, I., Niso-Santano, M., Niu, H., Nixon, R. A., Njar, V. C., Noda, T., Noegel, A. A., Nolte, E. M., Norberg, E., Norga, K. K., Noureini, S. K., Notomi, S., Notterpek, L., Nowikovsky, K., Nukina, N., Nürnberger, T., O'Donnell, V. B., O'Donovan, T., O'Dwyer, P. J., Oehme, I., Oeste, C. L., Ogawa, M., Ogretmen, B., Ogura, Y., Oh, Y. J., Ohmuraya, M., Ohshima, T., Ojha, R., Okamoto, K., Okazaki, T., Oliver, F. J., Ollinger, K., Olsson, S., Orban, D. P., Ordonez, P., Orhon, I., Orosz, L., O'Rourke, E. J., Orozco, H., Ortega, A. L., Ortona, E., Osellame, L. D., Oshima, J., Oshima, S., Osiewacz, H. D., Otomo, T., Otsu, K., Ou, J. H., Outeiro, T. F., Ouyang, D. Y., Ouyang, H., Overholtzer, M., Ozbun, M. A., Ozdinler, P. H., Ozpolat, B., Pacelli, C., Paganetti, P., Page, G., Pages, G., Pagnini, U., Pajak, B., Pak, S. C., Pakos-Zebrucka, K., Pakpour, N., Palková, Z., Palladino, F., Pallauf, K., Pallet, N., Palmieri, M., Paludan, S. R., Palumbo, C., Palumbo, S., Pampliega, O., Pan, H., Pan, W., Panaretakis, T., Pandey, A., Pantazopoulou, A., Papackova, Z., Papademetrio, D. L., Papassideri, I., Papini, A., Parajuli, N., Pardo, J., Parekh, V. V., Parenti, G., Park, J. I., Park, J., Park, O. K., Parker, R., Parlato, R., Parys, J. B., Parzych, K. R., Pasquet, J. M., Pasquier, B., Pasumarthi, K. B., Patschan, D., Patterson, C., Pattingre, S., Pattison, S., Pause, A., Pavenstädt, H., Pavone, F., Pedrozo, Z., Peña, F. J., Peñalva, M. A., Pende, M., Peng, J., Penna, F., Penninger, J. M., Pensalfini, A., Pepe, S., Pereira, G. J., Pereira, P. C., Pérez-de la Cruz, V., Pérez-Pérez, M. E., Pérez-Rodríguez, D., Pérez-Sala, D., Perier, C., Perl, A., Perlmutter, D. H., Perrotta, I., Pervaiz, S., Pesonen, M., Pessin, J. E., Peters, G. J., Petersen, M., Petrache, I., Petrof, B. J., Petrovski, G., Phang, J. M., Piacentini, M., Pierdominici, M., Pierre, P., Pierrefite-Carle, V., Pietrocola, F., Pimentel-Muiños, F. X., Pinar, M., Pineda, B., Pinkas-Kramarski, R., Pinti, M., Pinton, P., Piperdi, B., Piret, J. M., Platanias, L. C., Platta, H. W., Plowey, E. D., Pöggeler, S., Poirot, M., Polčic, P., Poletti, A., Poon, A. H., Popelka, H., Popova, B., Poprawa, I., Poulose, S. M., Poulton, J., Powers, S. K., Powers, T., Pozuelo-Rubio, M., Prak, K., Prange, R., Prescott, M., Priault, M., Prince, S., Proia, R. L., Proikas-Cezanne, T., Prokisch, H., Promponas, V. J., Przyklenk, K., Puertollano, R., Pugazhenthi, S., Puglielli, L., Pujol, A., Puyal, J., Pyeon, D., Qi, X., Qian, W. B., Qin, Z. H., Qiu, Y., Qu, Z., Quadrilatero, J., Quinn, F., Raben, N., Rabinowich, H., Radogna, F., Ragusa, M. J., Rahmani, M., Raina, K., Ramanadham, S., Ramesh, R., Rami, A., Randall-Demllo, S., Randow, F., Rao, H., Rao, V. A., Rasmussen, B. B., Rasse, T. M., Ratovitski, E. A., Rautou, P. E., Ray, S. K., Razani, B., Reed, B. H., Reggiori, F., Rehm, M., Reichert, A. S., Rein, T., Reiner, D. J., Reits, E., Ren, J., Ren, X., Renna, M., Reusch, J. E., Revuelta, J. L., Reyes, L., Rezaie, A. R., Richards, R. I., Richardson, D. R., Richetta, C., Riehle, M. A., Rihn, B. H., Rikihisa, Y., Riley, B. E., Rimbach, G., Rippo, M. R., Ritis, K., Rizzi, F., Rizzo, E., Roach, P. J., Robbins, J., Roberge, M., Roca, G., Roccheri, M. C., Rocha, S., Rodrigues, C. M., Rodríguez, C. I., de Cordoba, S. R., Rodriguez-Muela, N., Roelofs, J., Rogov, V. V., Rohn, T. T., Rohrer, B., Romanelli, D., Romani, L., Romano, P. S., Roncero, M. I., Rosa, J. L., Rosello, A., Rosen, K. V., Rosenstiel, P., Rost-Roszkowska, M., Roth, K. A., Roué, G., Rouis, M., Rouschop, K. M., Ruan, D. T., Ruano, D., Rubinsztein, D. C., Rucker, E. B., 3rd, Rudich, A., Rudolf, E., Rudolf, R., Ruegg, M. A., Ruiz-Roldan, C., Ruparelia, A. A., Rusmini, P., Russ, D. W., Russo, G. L., Russo, G., Russo, R., Rusten, T. E., Ryabovol, V., Ryan, K. M., Ryter, S. W., Sabatini, D. M., Sacher, M., Sachse, C., Sack, M. N., Sadoshima, J., Saftig, P., Sagi-Eisenberg, R., Sahni, S., Saikumar, P., Saito, T., Saitoh, T., Sakakura, K., Sakoh-Nakatogawa, M., Sakuraba, Y., Salazar-Roa, M., Salomoni, P., Saluja, A. K., Salvaterra, P. M., Salvioli, R., Samali, A., Sanchez, A. M., Sánchez-Alcázar, J. A., Sanchez-Prieto, R., Sandri, M., Sanjuan, M. A., Santaguida, S., Santambrogio, L., Santoni, G., Dos Santos, C. N., Saran, S., Sardiello, M., Sargent, G., Sarkar, P., Sarkar, S., Sarrias,

M. R., Sarwal, M. M., Sasakawa, C., Sasaki, M., Sass, M., Sato, K., Sato, M., Satriano, J., Savaraj, N., Saveljeva, S., Schaefer, L., Schaible, U. E., Scharl, M., Schatzl, H. M., Schekman, R., Scheper, W., Schiavi, A., Schipper, H. M., Schmeisser, H., Schmidt, J., Schmitz, I., Schneider, B. E., Schneider, E. M., Schneider, J. L., Schon, E. A., Schönenberger, M. J., Schönthal, A. H., Schorderet, D. F., Schröder, B., Schuck, S., Schulze, R. J., Schwarten, M., Schwarz, T. L., Sciarretta, S., Scotto, K., Scovassi, A. I., Screaton, R. A., Screen, M., Seca, H., Sedej, S., Segatori, L., Segev, N., Seglen, P. O., Seguí-Simarro, J. M., Segura-Aguilar, J., Seki, E., Sell, C., Seiliez, I., Semenkovich, C. F., Semenza, G. L., Sen, U., Serra, A. L., Serrano-Puebla, A., Sesaki, H., Setoguchi, T., Settembre, C., Shacka, J. J., Shajahan-Haq, A. N., Shapiro, I. M., Sharma, S., She, H., Shen, C. K., Shen, C. C., Shen, H. M., Shen, S., Shen, W., Sheng, R., Sheng, X., Sheng, Z. H., Shepherd, T. G., Shi, J., Shi, Q., Shi, Q., Shi, Y., Shibutani, S., Shibuya, K., Shidoji, Y., Shieh, J. J., Shih, C. M., Shimada, Y., Shimizu, S., Shin, D. W., Shinohara, M. L., Shintani, M., Shintani, T., Shioi, T., Shirabe, K., Shiri-Sverdlov, R., Shirihai, O., Shore, G. C., Shu, C. W., Shukla, D., Sibirny, A. A., Sica, V., Sigurdson, C. J., Sigurdsson, E. M., Sijwali, P. S., Sikorska, B., Silveira, W. A., Silvente-Poirot, S., Silverman, G. A., Simak, J., Simmet, T., Simon, A. K., Simon, H. U., Simone, C., Simons, M., Simonsen, A., Singh, R., Singh, S. V., Singh, S. K., Sinha, D., Sinha, S., Sinicrope, F. A., Sirko, A., Sirohi, K., Sishi, B. J., Sittler, A., Siu, P. M., Sivridis, E., Skwarska, A., Slack, R., Slaninová, I., Slavov, N., Smaili, S. S., Smalley, K. S., Smith, D. R., Soenen, S. J., Soleimanpour, S. A., Solhaug, A., Somasundaram, K., Son, J. H., Sonawane, A., Song, C., Song, F., Song, H. K., Song, J. X., Song, W., Soo, K. Y., Sood, A. K., Soong, T. W., Soontornniyomkij, V., Sorice, M., Sotgia, F., Soto-Pantoja, D. R., Sotthibundhu, A., Sousa, M. J., Spaink, H. P., Span, P. N., Spang, A., Sparks, J. D., Speck, P. G., Spector, S. A., Spies, C. D., Springer, W., Clair, D. S., Stacchiotti, A., Staels, B., Stang, M. T., Starczynowski, D. T., Starokadomskyy, P., Steegborn, C., Steele, J. W., Stefanis, L., Steffan, J., Stellrecht, C. M., Stenmark, H., Stepkowski, T. M., Stern, S. T., Stevens, C., Stockwell, B. R., Stoka, V., Storchova, Z., Stork, B., Stratoulias, V., Stravopodis, D. J., Strnad, P., Strohecker, A. M., Ström, A. L., Stromhaug, P., Stulik, J., Su, Y. X., Su, Z., Subauste, C. S., Subramaniam, S., Sue, C. M., Suh, S. W., Sui, X., Sukseree, S., Sulzer, D., Sun, F. L., Sun, J., Sun, J., Sun, S. Y., Sun, Y., Sun, Y., Sun, Y., Sundaramoorthy, V., Sung, J., Suzuki, H., Suzuki, K., Suzuki, N., Suzuki, T., Suzuki, Y. J., Swanson, M. S., Swanton, C., Swärd, K., Swarup, G., Sweeney, S. T., Sylvester, P. W., Szatmari, Z., Szegezdi, E., Szlosarek, P. W., Taegtmeyer, H., Tafani, M., Taillebourg, E., Tait, S. W., Takacs-Vellai, K., Takahashi, Y., Takáts, S., Takemura, G., Takigawa, N., Talbot, N. J., Tamagno, E., Tamburini, J., Tan, C. P., Tan, L., Tan, M. L., Tan, M., Tan, Y. J., Tanaka, K., Tanaka, M., Tang, D., Tang, D., Tang, G., Tanida, I., Tanji, K., Tannous, B. A., Tapia, J. A., Tasset-Cuevas, I., Tatar, M., Tavassoly, I., Tavernarakis, N., Taylor, A., Taylor, G. S., Taylor, G. A., Taylor, J. P., Taylor, M. J., Tchetina, E. V., Tee, A. R., Teixeira-Clerc, F., Telang, S., Tencomnao, T., Teng, B. B., Teng, R. J., Terro, F., Tettamanti, G., Theiss, A. L., Theron, A. E., Thomas, K. J., Thomé, M. P., Thomes, P. G., Thorburn, A., Thorner, J., Thum, T., Thumm, M., Thurston, T. L., Tian, L., Till, A., Ting, J. P., Titorenko, V. I., Toker, L., Toldo, S., Tooze, S. A., Topisirovic, I., Torgersen, M. L., Torosantucci, L., Torriglia, A., Torrisi, M. R., Tournier, C., Towns, R., Trajkovic, V., Travassos, L. H., Triola, G., Tripathi, D. N., Trisciuoglio, D., Troncoso, R., Trougakos, I. P., Truttmann, A. C., Tsai, K. J., Tschan, M. P., Tseng, Y. H., Tsukuba, T., Tsung, A., Tsvetkov, A. S., Tu, S., Tuan, H. Y., Tucci, M., Tumbarello, D. A., Turk, B., Turk, V., Turner, R. F., Tveita, A. A., Tyagi, S. C., Ubukata, M., Uchiyama, Y., Udelnow, A., Ueno, T., Umekawa, M., Umemiya-Shirafuji, R., Underwood, B. R., Ungermann, C., Ureshino, R. P., Ushioda, R., Uversky, V. N., Uzcátegui, N. L., Vaccari, T., Vaccaro, M. I., Váchová, L., Vakifahmetoglu-Norberg, H., Valdor, R., Valente, E. M., Vallette, F., Valverde, A. M., Van den Berghe, G., Van Den Bosch, L., van den Brink, G. R., van der Goot, F. G., van der Klei, I. J., van

der Laan, L. J., van Doorn, W. G., van Egmond, M., van Golen, K. L., Van Kaer, L., van Lookeren Campagne, M., Vandenabeele, P., Vandenberghe, W., Vanhorebeek, I., Varela-Nieto, I., Vasconcelos, M. H., Vasko, R., Vavvas, D. G., Vega-Naredo, I., Velasco, G., Velentzas, A. D., Velentzas, P. D., Vellai, T., Vellenga, E., Vendelbo, M. H., Venkatachalam, K., Ventura, N., Ventura, S., Veras, P. S., Verdier, M., Vertessy, B. G., Viale, A., Vidal, M., Vieira, H. L., Vierstra, R. D., Vigneswaran, N., Vij, N., Vila, M., Villar, M., Villar, V. H., Villarroya, J., Vindis, C., Viola, G., Viscomi, M. T., Vitale, G., Vogl, D. T., Voitsekhovskaja, O. V., von Haefen, C., von Schwarzenberg, K., Voth, D. E., Vouret-Craviari, V., Vuori, K., Vyas, J. M., Waeber, C., Walker, C. L., Walker, M. J., Walter, J., Wan, L., Wan, X., Wang, B., Wang, C., Wang, C. Y., Wang, C., Wang, C., Wang, C., Wang, D., Wang, F., Wang, F., Wang, G., Wang, H. J., Wang, H., Wang, H. G., Wang, H., Wang, H. D., Wang, J., Wang, J., Wang, M., Wang, M. Q., Wang, P. Y., Wang, P., Wang, R. C., Wang, S., Wang, T. F., Wang, X., Wang, X. J., Wang, X. W., Wang, X., Wang, X., Wang, Y., Wang, Y., Wang, Y., Wang, Y. J., Wang, Y., Wang, Y., Wang, Y. T., Wang, Y., Wang, Z. N., Wappner, P., Ward, C., Ward, D. M., Warnes, G., Watada, H., Watanabe, Y., Watase, K., Weaver, T. E., Weekes, C. D., Wei, J., Weide, T., Weihl, C. C., Weindl, G., Weis, S. N., Wen, L., Wen, X., Wen, Y., Westermann, B., Weyand, C. M., White, A. R., White, E., Whitton, J. L., Whitworth, A. J., Wiels, J., Wild, F., Wildenberg, M. E., Wileman, T., Wilkinson, D. S., Wilkinson, S., Willbold, D., Williams, C., Williams, K., Williamson, P. R., Winklhofer, K. F., Witkin, S. S., Wohlgemuth, S. E., Wollert, T., Wolvetang, E. J., Wong, E., Wong, G. W., Wong, R. W., Wong, V. K., Woodcock, E. A., Wright, K. L., Wu, C., Wu, D., Wu, G. S., Wu, J., Wu, J., Wu, M., Wu, M., Wu, S., Wu, W. K., Wu, Y., Wu, Z., Xavier, C. P., Xavier, R. J., Xia, G. X., Xia, T., Xia, W., Xia, Y., Xiao, H., Xiao, J., Xiao, S., Xiao, W., Xie, C. M., Xie, Z., Xie, Z., Xilouri, M., Xiong, Y., Xu, C., Xu, C., Xu, F., Xu, H., Xu, H., Xu, J., Xu, J., Xu, J., Xu, L., Xu, X., Xu, Y., Xu, Y., Xu, Z. X., Xu, Z., Xue, Y., Yamada, T., Yamamoto, A., Yamanaka, K., Yamashina, S., Yamashiro, S., Yan, B., Yan, B., Yan, X., Yan, Z., Yanagi, Y., Yang, D. S., Yang, J. M., Yang, L., Yang, M., Yang, P. M., Yang, P., Yang, Q., Yang, W., Yang, W. Y., Yang, X., Yang, Y., Yang, Y., Yang, Z., Yang, Z., Yao, M. C., Yao, P. J., Yao, X., Yao, Z., Yao, Z., Yasui, L. S., Ye, M., Yedvobnick, B., Yeganeh, B., Yeh, E. S., Yeyati, P. L., Yi, F., Yi, L., Yin, X. M., Yip, C. K., Yoo, Y. M., Yoo, Y. H., Yoon, S. Y., Yoshida, K., Yoshimori, T., Young, K. H., Yu, H., Yu, J. J., Yu, J. T., Yu, J., Yu, L., Yu, W. H., Yu, X. F., Yu, Z., Yuan, J., Yuan, Z. M., Yue, B. Y., Yue, J., Yue, Z., Zacks, D. N., Zacksenhaus, E., Zaffaroni, N., Zaglia, T., Zakeri, Z., Zecchini, V., Zeng, J., Zeng, M., Zeng, Q., Zervos, A. S., Zhang, D. D., Zhang, F., Zhang, G., Zhang, G. C., Zhang, H., Zhang, H., Zhang, H., Zhang, H., Zhang, J., Zhang, J., Zhang, J., Zhang, J., Zhang, J. P., Zhang, L., Zhang, L., Zhang, L., Zhang, L., Zhang, M. Y., Zhang, X., Zhang, X. D., Zhang, Y., Zhang, Y., Zhang, Y., Zhang, Y., Zhang, Y., Zhao, M., Zhao, W. L., Zhao, X., Zhao, Y. G., Zhao, Y., Zhao, Y., Zhao, Y. X., Zhao, Z., Zhao, Z. J., Zheng, D., Zheng, X. L., Zheng, X., Zhivotovsky, B., Zhong, Q., Zhou, G. Z., Zhou, G., Zhou, H., Zhou, S. F., Zhou, X. J., Zhu, H., Zhu, H., Zhu, W. G., Zhu, W., Zhu, X. F., Zhu, Y., Zhuang, S. M., Zhuang, X., Ziparo, E., Zois, C. E., Zoladek, T., Zong, W. X., Zorzano, A., & Zughaier, S. M. (2016). Guidelines for the use and interpretation of assays for monitoring autophagy (3rd edition). *Autophagy*, *12*(1), 1-222. https://doi.org/10.1080/15548627.2015.1100356

Knauf, J. A., Ma, X., Smith, E. P., Zhang, L., Mitsutake, N., Liao, X. H., Refetoff, S., Nikiforov, Y. E., & Fagin, J. A. (2005). Targeted expression of BRAFV600E in thyroid cells of transgenic mice results in papillary thyroid cancers that undergo dedifferentiation. *Cancer Res*, *65*(10), 4238-4245. https://doi.org/10.1158/0008-5472.Can-05-0047

Kota, J., Chivukula, R. R., O'Donnell, K. A., Wentzel, E. A., Montgomery, C. L., Hwang, H. W., Chang, T. C., Vivekanandan, P., Torbenson, M., Clark, K. R., Mendell, J. R., & Mendell, J. T. (2009).

Therapeutic microRNA delivery suppresses tumorigenesis in a murine liver cancer model. *Cell*, *137*(6), 1005-1017. https://doi.org/10.1016/j.cell.2009.04.021

Kourtidis, A., Necela, B., Lin, W.-H., Lu, R., Feathers, R. W., Asmann, Y. W., Thompson, E. A., & Anastasiadis, P. Z. (2017). Cadherin complexes recruit mRNAs and RISC to regulate epithelial cell signaling. *J Cell Biol*, *216*(10), 3073-3085. https://doi.org/10.1083/jcb.201612125

Krebs, A. M., Mitschke, J., Lasierra Losada, M., Schmalhofer, O., Boerries, M., Busch, H., Boettcher, M., Mougiakakos, D., Reichardt, W., Bronsert, P., Brunton, V. G., Pilarsky, C., Winkler, T. H., Brabletz, S., Stemmler, M. P., & Brabletz, T. (2017). The EMT-activator Zeb1 is a key factor for cell plasticity and promotes metastasis in pancreatic cancer. *Nat Cell Biol*, *19*(5), 518-529. https://doi.org/10.1038/ncb3513

Krueger, J. E., Maitra, A., & Albores-Saavedra, J. (2000). Inherited medullary microcarcinoma of the thyroid: a study of 11 cases. *Am J Surg Pathol*, *24*(6), 853-858. https://doi.org/10.1097/00000478-200006000-00011

Kuo, T.-C., Chen, C.-T., Baron, D., Onder, T. T., Loewer, S., Almeida, S., Weismann, C. M., Xu, P., Houghton, J.-M., Gao, F.-B., Daley, G. Q., & Doxsey, S. (2011). Midbody accumulation through evasion of autophagy contributes to cellular reprogramming and tumorigenicity. *Nat Cell Biol*, *13*(10), 1214-1223. https://doi.org/10.1038/ncb2332

Kusindarta D.L., & Wihadmadyatami, H. (2018). The Role of Extracellular Matrix in Tissue Regeneration, Tissue Regeneration, . *IntechOpen*. https://doi.org/DOI: 10.5772/intechopen.75728

Lambert, A. W., Pattabiraman, D. R., & Weinberg, R. A. (2017). Emerging Biological Principles of Metastasis. *Cell*, *168*(4), 670-691. https://doi.org/10.1016/j.cell.2016.11.037

Lammerding, J., Fong, L. G., Ji, J. Y., Reue, K., Stewart, C. L., Young, S. G., & Lee, R. T. (2006). Lamins A and C but not lamin B1 regulate nuclear mechanics. *J Biol Chem*, *281*(35), 25768-25780. https://doi.org/10.1074/jbc.M513511200

Lammerding, J., Schulze, P. C., Takahashi, T., Kozlov, S., Sullivan, T., Kamm, R. D., Stewart, C. L., & Lee, R. T. (2004). Lamin A/C deficiency causes defective nuclear mechanics and mechanotransduction. *J Clin Invest*, *113*(3), 370-378. https://doi.org/10.1172/jci19670

Leduc, E. H., & Wilson, J. W. (1959). An electron microscope study of intranuclear inclusions in mouse liver and hepatoma. *J Biophys Biochem Cytol*, *6*(3), 427-430. https://doi.org/10.1083/jcb.6.3.427

Lee, J. H., Kim, Y., Choi, J. W., & Kim, Y. S. (2013). The association between papillary thyroid carcinoma and histologically proven Hashimoto's thyroiditis: a meta-analysis. *Eur J Endocrinol*, *168*(3), 343-349. https://doi.org/10.1530/eje-12-0903

Lee, J. M., Dedhar, S., Kalluri, R., & Thompson, E. W. (2006). The epithelial-mesenchymal transition: new insights in signaling, development, and disease. *J Cell Biol*, *172*(7), 973-981. https://doi.org/10.1083/jcb.200601018

Lee, R. C., Feinbaum, R. L., & Ambros, V. (1993). The C. elegans heterochronic gene lin-4 encodes small RNAs with antisense complementarity to lin-14. *Cell*, *75*(5), 843-854. https://doi.org/10.1016/0092-8674(93)90529-y

Lee, S. S., Min, H., Ha, J. Y., Kim, B. H., Choi, M. S., & Kim, S. (2019). Dysregulation of the miRNA biogenesis components DICER1, DROSHA, DGCR8 and AGO2 in clear cell renal cell carcinoma in both a Korean cohort and the cancer genome atlas kidney clear cell carcinoma cohort. *Oncol Lett*, *18*(4), 4337-4345. https://doi.org/10.3892/ol.2019.10759

Lennox, K. A., & Behlke, M. A. (2011). Chemical modification and design of anti-miRNA oligonucleotides. *Gene Therapy*, *18*(12), 1111-1120. https://doi.org/10.1038/gt.2011.100

Leung, A. K., & Sharp, P. A. (2013). Quantifying Argonaute proteins in and out of GW/P-bodies: implications in microRNA activities. *Adv Exp Med Biol*, *768*, 165-182. https://doi.org/10.1007/978-1-4614-5107-5_10

Leung, A. K., Vyas, S., Rood, J. E., Bhutkar, A., Sharp, P. A., & Chang, P. (2011). Poly(ADP-ribose) regulates stress responses and microRNA activity in the cytoplasm. *Mol Cell*, *42*(4), 489-499. https://doi.org/10.1016/j.molcel.2011.04.015

Leung, A. K. C., & Leung, A. A. C. (2019). Evaluation and management of the child with hypothyroidism. *World J Pediatr*, *15*(2), 124-134. https://doi.org/10.1007/s12519-019-00230-w

Li, C., Li, Y., Lu, Y., Niu, Z., Zhao, H., Peng, Y., & Li, M. (2021). miR-26 family and its target genes in tumorigenesis and development. *Critical Reviews in Oncology/Hematology*, *157*, 103124. https://doi.org/https://doi.org/10.1016/j.critrevonc.2020.103124

Li, L. C. (2014). Chromatin remodeling by the small RNA machinery in mammalian cells. *Epigenetics*, *9*(1), 45-52. https://doi.org/10.4161/epi.26830

Liang, J., Zeng, W., Fang, F., Yu, T., Zhao, Y., Fan, X., Guo, N., & Gao, X. (2017). Clinical analysis of Hashimoto thyroiditis coexistent with papillary thyroid cancer in 1392 patients. *Acta Otorhinolaryngol Ital*, *37*(5), 393-400. https://doi.org/10.14639/0392-100x-1709 (Analisi clinica dell'associazione fra tiroidite di Hashimoto e carcinoma papillare della tiroide in 1392 pazienti.)

Lin, H., & Spradling, A. C. (1997). A novel group of pumilio mutations affects the asymmetric division of germline stem cells in the Drosophila ovary. *Development*, *124*(12), 2463-2476.

Lin, X., Xiang, X., Hao, L., Wang, T., Lai, Y., Abudoureyimu, M., Zhou, H., Feng, B., Chu, X., & Wang, R. (2020). The role of Aurora-A in human cancers and future therapeutics. *Am J Cancer Res*, *10*(9), 2705-2729.

Liu, B., Wu, X., Liu, B., Wang, C., Liu, Y., Zhou, Q., & Xu, K. (2012). MiR-26a enhances metastasis potential of lung cancer cells via AKT pathway by targeting PTEN. *Biochim Biophys Acta*, *1822*(11), 1692-1704. https://doi.org/10.1016/j.bbadis.2012.07.019

Liu, J., Carmell, M. A., Rivas, F. V., Marsden, C. G., Thomson, J. M., Song, J. J., Hammond, S. M., Joshua-Tor, L., & Hannon, G. J. (2004). Argonaute2 is the catalytic engine of mammalian RNAi. *Science*, *305*(5689), 1437-1441. https://doi.org/10.1126/science.1102513

Liu, J., Cheng, X., Zhang, Y., Li, S., Cui, H., Zhang, L., Shi, R., Zhao, Z., He, C., Wang, C., Zhao, H., Zhang, C., Fisk, H. A., Guadagno, T. M., & Cui, Y. (2013). Phosphorylation of Mps1 by BRAFV600E prevents Mps1 degradation and contributes to chromosome instability in melanoma. *Oncogene*, *32*(6), 713-723. https://doi.org/10.1038/onc.2012.94

Liu, R., & Xing, M. (2016). TERT promoter mutations in thyroid cancer. *Endocr Relat Cancer*, *23*(3), R143-155. https://doi.org/10.1530/erc-15-0533

Liu, T., Zhang, H., Fang, J., Yang, Z., Chen, R., Wang, Y., Zhao, X., Ge, S., Yu, J., & Huang, J. (2020). AGO2 phosphorylation by c-Src kinase promotes tumorigenesis. *Neoplasia*, *22*(3), 129-141. https://doi.org/https://doi.org/10.1016/j.neo.2019.12.004

Liu, T., Zhang, L., Joo, D., & Sun, S. C. (2017). NF-κB signaling in inflammation. *Signal Transduct Target Ther*, *2*, 17023-. https://doi.org/10.1038/sigtrans.2017.23

Liu, X., Zhu, L., Cui, D., Wang, Z., Chen, H., Duan, Y., Shen, M., Wu, Y., Rong, R., Zhang, Z., Wang, X., Chen, J., Alexander, E. K., & Yang, T. (2014). Coexistence of Histologically Confirmed Hashimoto's Thyroiditis with Different Stages of Papillary Thyroid Carcinoma in a Consecutive Chinese Cohort. *Int J Endocrinol*, *2014*, 769294. https://doi.org/10.1155/2014/769294

Liu, Z., Jin, Z. Y., Liu, C. H., Xie, F., Lin, X. S., & Huang, Q. (2015). MicroRNA-21 regulates biological behavior by inducing EMT in human cholangiocarcinoma. *Int J Clin Exp Pathol*, *8*(5), 4684-4694.

LiVolsi, V. A. (2011). Papillary thyroid carcinoma: an update. *Mod Pathol*, *24 Suppl 2*, S1-9. https://doi.org/10.1038/modpathol.2010.129

Lloyd, R. V., Buehler, D., & Khanafshar, E. (2011). Papillary Thyroid Carcinoma Variants. *Head and Neck Pathology*, *5*(1), 51-56. https://doi.org/10.1007/s12105-010-0236-9

Lu, J., Getz, G., Miska, E. A., Alvarez-Saavedra, E., Lamb, J., Peck, D., Sweet-Cordero, A., Ebert, B. L., Mak, R. H., Ferrando, A. A., Downing, J. R., Jacks, T., Horvitz, H. R., & Golub, T. R. (2005). MicroRNA expression profiles classify human cancers. *Nature*, *435*(7043), 834-838. https://doi.org/10.1038/nature03702

Lu, J., He, M. L., Wang, L., Chen, Y., Liu, X., Dong, Q., Chen, Y. C., Peng, Y., Yao, K. T., Kung, H. F., & Li, X. P. (2011). MiR-26a inhibits cell growth and tumorigenesis of nasopharyngeal carcinoma through repression of EZH2. *Cancer Res*, *71*(1), 225-233. https://doi.org/10.1158/0008-5472.Can-10-1850

Lu, L. Y., Wood, J. L., Ye, L., Minter-Dykhouse, K., Saunders, T. L., Yu, X., & Chen, J. (2008). Aurora A is essential for early embryonic development and tumor suppression. *J Biol Chem*, *283*(46), 31785-31790. https://doi.org/10.1074/jbc.M805880200

Lv, J., Zhao, H. P., Dai, K., Cheng, Y., Zhang, J., & Guo, L. (2020). Circulating exosomal miRNAs as potential biomarkers for Barrett's esophagus and esophageal adenocarcinoma. *World J Gastroenterol*, *26*(22), 2889-2901. https://doi.org/10.3748/wjg.v26.i22.2889

Lv, M., Zhang, X., Li, M., Chen, Q., Ye, M., Liang, W., Ding, L., Cai, H., Fu, D., & Lv, Z. (2013). miR-26a and its target CKS2 modulate cell growth and tumorigenesis of papillary thyroid carcinoma. *PloS one*, *8*(7), e67591. https://doi.org/10.1371/journal.pone.0067591

Maddox, A. S., Habermann, B., Desai, A., & Oegema, K. (2005). Distinct roles for two C. elegans anillins in the gonad and early embryo. *Development*, *132*(12), 2837-2848. https://doi.org/10.1242/dev.01828

Madeira, F., Park, Y. m., Lee, J., Buso, N., Gur, T., Madhusoodanan, N., Basutkar, P., Tivey, A. R. N., Potter, S. C., Finn, R. D., & Lopez, R. (2019). The EMBL-EBI search and sequence analysis tools APIs in 2019. *Nucleic Acids Res*, *47*(W1), W636-W641. https://doi.org/10.1093/nar/gkz268 %J Nucleic Acids Research

Madhavi Sastry, G., Adzhigirey, M., Day, T., Annabhimoju, R., & Sherman, W. (2013). Protein and ligand preparation: parameters, protocols, and influence on virtual screening enrichments. *Journal of Computer-Aided Molecular Design*, *27*(3), 221-234. https://doi.org/10.1007/s10822-013-9644-8

Maia, F. F., & Zantut-Wittmann, D. E. (2012). Thyroid nodule management: clinical, ultrasound and cytopathological parameters for predicting malignancy. *Clinics (Sao Paulo)*, *67*(8), 945-954. https://doi.org/10.6061/clinics/2012(08)15

Mani, S. A., Guo, W., Liao, M. J., Eaton, E. N., Ayyanan, A., Zhou, A. Y., Brooks, M., Reinhard, F., Zhang, C. C., Shipitsin, M., Campbell, L. L., Polyak, K., Brisken, C., Yang, J., & Weinberg, R. A. (2008). The epithelial-mesenchymal transition generates cells with properties of stem cells. *Cell*, *133*(4), 704-715. https://doi.org/10.1016/j.cell.2008.03.027

Maniotis, A. J., Chen, C. S., & Ingber, D. E. (1997). Demonstration of mechanical connections between integrins, cytoskeletal filaments, and nucleoplasm that stabilize nuclear structure. *Proc Natl Acad Sci U S A*, *94*(3), 849-854. https://doi.org/10.1073/pnas.94.3.849

Maragkakis, M., Vergoulis, T., Alexiou, P., Reczko, M., Plomaritou, K., Gousis, M., Kourtis, K., Koziris, N., Dalamagas, T., & Hatzigeorgiou, A. G. (2011). DIANA-microT Web server upgrade supports

Fly and Worm miRNA target prediction and bibliographic miRNA to disease association. *Nucleic Acids Res*, *39*(Web Server issue), W145-148. https://doi.org/10.1093/nar/gkr294

Marchesi, S., Montani, F., Deflorian, G., D'Antuono, R., Cuomo, A., Bologna, S., Mazzoccoli, C., Bonaldi, T., Di Fiore, P. P., & Nicassio, F. (2014). DEPDC1B coordinates de-adhesion events and cell-cycle progression at mitosis. *Dev Cell*, *31*(4), 420-433. https://doi.org/10.1016/j.devcel.2014.09.009

Margall-Ducos, G., Celton-Morizur, S., Couton, D., Brégerie, O., & Desdouets, C. (2007). Liver tetraploidization is controlled by a new process of incomplete cytokinesis. *J Cell Sci*, *120*(Pt 20), 3633-3639. https://doi.org/10.1242/jcs.016907

Mascanzoni, F., Ayala, I., & Colanzi, A. (2019). Organelle Inheritance Control of Mitotic Entry and Progression: Implications for Tissue Homeostasis and Disease. *Front Cell Dev Biol*, *7*, 133. https://doi.org/10.3389/fcell.2019.00133

Masciarelli, S., Quaranta, R., Iosue, I., Colotti, G., Padula, F., Varchi, G., Fazi, F., & Del Rio, A. (2014). A Small-Molecule Targeting the MicroRNA Binding Domain of Argonaute 2 improves the Retinoic Acid Differentiation Response of the Acute Promyelocytic Leukemia Cell Line NB4. *ACS Chemical Biology*, *9*(8), 1674-1679. https://doi.org/10.1021/cb500286b

Matsuhashi, S., Manirujjaman, M., Hamajima, H., & Ozaki, I. (2019). Control Mechanisms of the Tumor Suppressor PDCD4: Expression and Functions. *International journal of molecular sciences*, *20*(9). https://doi.org/10.3390/ijms20092304

Matsui, M., Li, L., Janowski, B. A., & Corey, D. R. (2015). Reduced Expression of Argonaute 1, Argonaute 2 and TRBP Changes Levels and Intracellular Distribution of RNAi Factors. *Scientific Reports*, *5*(1), 12855. https://doi.org/10.1038/srep12855

McDonald, J. H., & Dunn, K. W. (2013). Statistical tests for measures of colocalization in biological microscopy. *J Microsc*, *252*(3), 295-302. https://doi.org/10.1111/jmi.12093

McKenzie, C., & D'Avino, P. P. (2016). Investigating cytokinesis failure as a strategy in cancer therapy. *Oncotarget*, *7*(52), 87323-87341. https://doi.org/10.18632/oncotarget.13556

Meister, G. (2013). Argonaute proteins: functional insights and emerging roles. *Nat Rev Genet*, *14*(7), 447-459. https://doi.org/10.1038/nrg3462

Meister, G., Landthaler, M., Patkaniowska, A., Dorsett, Y., Teng, G., & Tuschl, T. (2004). Human Argonaute2 Mediates RNA Cleavage Targeted by miRNAs and siRNAs. *Molecular Cell*, *15*(2), 185-197. https://doi.org/https://doi.org/10.1016/j.molcel.2004.07.007

Meister, G., Landthaler, M., Patkaniowska, A., Dorsett, Y., Teng, G., & Tuschl, T. (2004). Human Argonaute2 mediates RNA cleavage targeted by miRNAs and siRNAs. *Mol Cell*, *15*(2), 185-197. https://doi.org/10.1016/j.molcel.2004.07.007

Meyer, W. J., Schreiber, S., Guo, Y., Volkmann, T., Welte, M. A., & Müller, H. A. (2006). Overlapping functions of argonaute proteins in patterning and morphogenesis of Drosophila embryos. *PLoS Genet*, *2*(8), e134. https://doi.org/10.1371/journal.pgen.0020134

Michalik, K. M., Bottcher, R., & Forstemann, K. (2012). A small RNA response at DNA ends in Drosophila. *Nucleic Acids Res*, *40*(19), 9596-9603. https://doi.org/10.1093/nar/gks711

Mihály, Z., Kormos, M., Lánczky, A., Dank, M., Budczies, J., Szász, M. A., & Győrffy, B. (2013). A meta-analysis of gene expression-based biomarkers predicting outcome after tamoxifen treatment in breast cancer. *Breast Cancer Research and Treatment*, *140*(2), 219-232. https://doi.org/10.1007/s10549-013-2622-y

Mincer DL, J. I. (2020). Hashimoto Thyroiditis. . *In: StatPearls [Internet]. Treasure Island (FL): StatPearls Publishing*. https://www.ncbi.nlm.nih.gov/books/NBK459262/

Mishima, M., Kaitna, S., & Glotzer, M. (2002). Central spindle assembly and cytokinesis require a kinesin-like protein/RhoGAP complex with microtubule bundling activity. *Dev Cell*, *2*(1), 41-54. https://doi.org/10.1016/s1534-5807(01)00110-1

Miura, T., Tsujimoto, H., Fukasawa, M., Kodama, T., Shibuya, M., Hasegawa, A., & Hayami, M. (1987). Structural abnormality and over-expression of the myc gene in feline leukemias. *Int J Cancer*, *40*(4), 564-569. https://doi.org/10.1002/ijc.2910400422

Modzelewski, A. J., Holmes, R. J., Hilz, S., Grimson, A., & Cohen, P. E. (2012). AGO4 regulates entry into meiosis and influences silencing of sex chromosomes in the male mouse germline. *Dev Cell*, *23*(2), 251-264. https://doi.org/10.1016/j.devcel.2012.07.003

Mohan, K., Iglesias, P. A., & Robinson, D. N. (2012). Separation anxiety: stress, tension and cytokinesis. *Exp Cell Res*, *318*(12), 1428-1434. https://doi.org/10.1016/j.yexcr.2012.03.028

Morita, E., Sandrin, V., Chung, H. Y., Morham, S. G., Gygi, S. P., Rodesch, C. K., & Sundquist, W. I. (2007). Human ESCRT and ALIX proteins interact with proteins of the midbody and function in cytokinesis. *Embo j*, *26*(19), 4215-4227. https://doi.org/10.1038/sj.emboj.7601850

Morris, K. V., Chan, S. W., Jacobsen, S. E., & Looney, D. J. (2004). Small interfering RNA-induced transcriptional gene silencing in human cells. *Science*, *305*(5688), 1289-1292. https://doi.org/10.1126/science.1101372

Mourouzis, I., Giagourta, I., Galanopoulos, G., Mantzouratou, P., Kostakou, E., Kokkinos, A. D., Tentolouris, N., & Pantos, C. (2013). Thyroid hormone improves the mechanical performance of the post-infarcted diabetic myocardium: a response associated with up-regulation of Akt/mTOR and AMPK activation. *Metabolism*, *62*(10), 1387-1393. https://doi.org/10.1016/j.metabol.2013.05.008

Moussian, B., Schoof, H., Haecker, A., Jürgens, G., & Laux, T. (1998). Role of the ZWILLE gene in the regulation of central shoot meristem cell fate during Arabidopsis embryogenesis. *Embo j*, *17*(6), 1799-1809. https://doi.org/10.1093/emboj/17.6.1799

Moustakas, A., & de Herreros, A. G. (2017). Epithelial-mesenchymal transition in cancer. *Mol Oncol*, *11*(7), 715-717. https://doi.org/10.1002/1878-0261.12094

Mughal, B. B., Fini, J. B., & Demeneix, B. A. (2018). Thyroid-disrupting chemicals and brain development: an update. *Endocr Connect*, *7*(4), R160-r186. https://doi.org/10.1530/ec-18-0029

Neki, N., & Kazal, H. (2006). Solitary Thyroid Nodule@ An Insight.

Nguyen, Q. T., Lee, E. J., Huang, M. G., Park, Y. I., Khullar, A., & Plodkowski, R. A. (2015). Diagnosis and treatment of patients with thyroid cancer. *Am Health Drug Benefits*, *8*(1), 30-40.

Nguyen, T. Q., Sawa, H., Okano, H., & White, J. G. (2000). The C. elegans septin genes, unc-59 and unc-61, are required for normal postembryonic cytokineses and morphogenesis but have no essential function in embryogenesis. *J Cell Sci*, *113 Pt 21*, 3825-3837.

Nieto, M. A. (2009). Epithelial-Mesenchymal Transitions in development and disease: old views and new perspectives. *Int J Dev Biol*, *53*(8-10), 1541-1547. https://doi.org/10.1387/ijdb.072410mn

Nieto, M. A., Huang, R. Y., Jackson, R. A., & Thiery, J. P. (2016). EMT: 2016. *Cell*, *166*(1), 21-45. https://doi.org/10.1016/j.cell.2016.06.028

Nikiforov, Y. E., & Nikiforova, M. N. (2011). Molecular genetics and diagnosis of thyroid cancer. *Nat Rev Endocrinol*, *7*(10), 569-580. https://doi.org/10.1038/nrendo.2011.142

Nikiforov, Y. E., Seethala, R. R., Tallini, G., Baloch, Z. W., Basolo, F., Thompson, L. D., Barletta, J. A., Wenig, B. M., Al Ghuzlan, A., Kakudo, K., Giordano, T. J., Alves, V. A., Khanafshar, E., Asa, S. L., El-Naggar, A. K., Gooding, W. E., Hodak, S. P., Lloyd, R. V., Maytal, G., Mete, O., Nikiforova, M. N., Nosé, V., Papotti, M., Poller, D. N., Sadow, P. M., Tischler, A. S., Tuttle, R. M., Wall, K. B.,

LiVolsi, V. A., Randolph, G. W., & Ghossein, R. A. (2016). Nomenclature Revision for Encapsulated Follicular Variant of Papillary Thyroid Carcinoma: A Paradigm Shift to Reduce Overtreatment of Indolent Tumors. *JAMA Oncol*, *2*(8), 1023-1029. https://doi.org/10.1001/jamaoncol.2016.0386

Nikiforova, M. N., Wald, A. I., Roy, S., Durso, M. B., & Nikiforov, Y. E. (2013). Targeted next-generation sequencing panel (ThyroSeq) for detection of mutations in thyroid cancer. *J Clin Endocrinol Metab*, *98*(11), E1852-1860. https://doi.org/10.1210/jc.2013-2292

Nilsson, M., & Williams, D. (2016). On the Origin of Cells and Derivation of Thyroid Cancer: C Cell Story Revisited. *Eur Thyroid J*, *5*(2), 79-93. https://doi.org/10.1159/000447333

Nishant Agrawal et al., C. G. A. R. N. (2014). Integrated genomic characterization of papillary thyroid carcinoma. *Cell*, *159*(3), 676-690. https://doi.org/10.1016/j.cell.2014.09.050

Niu, D. F., Kondo, T., Nakazawa, T., Oishi, N., Kawasaki, T., Mochizuki, K., Yamane, T., & Katoh, R. (2012). Transcription factor Runx2 is a regulator of epithelial-mesenchymal transition and invasion in thyroid carcinomas. *Lab Invest*, *92*(8), 1181-1190. https://doi.org/10.1038/labinvest.2012.84

Nonomura, K., Morohoshi, A., Nakano, M., Eiguchi, M., Miyao, A., Hirochika, H., & Kurata, N. (2007). A germ cell specific gene of the ARGONAUTE family is essential for the progression of premeiotic mitosis and meiosis during sporogenesis in rice. *Plant Cell*, *19*(8), 2583-2594. https://doi.org/10.1105/tpc.107.053199

Okada, C., Yamashita, E., Lee, S. J., Shibata, S., Katahira, J., Nakagawa, A., Yoneda, Y., & Tsukihara, T. (2009). A high-resolution structure of the pre-microRNA nuclear export machinery. *Science*, *326*(5957), 1275-1279. https://doi.org/10.1126/science.1178705

Oliver, C., Santos, J. L., & Pradillo, M. (2016). Accurate Chromosome Segregation at First Meiotic Division Requires AGO4, a Protein Involved in RNA-Dependent DNA Methylation in Arabidopsis thaliana. *Genetics*, *204*(2), 543-553. https://doi.org/10.1534/genetics.116.189217

Olsson, M. H., Søndergaard, C. R., Rostkowski, M., & Jensen, J. H. (2011). PROPKA3: Consistent Treatment of Internal and Surface Residues in Empirical pKa Predictions. *J Chem Theory Comput*, *7*(2), 525-537. https://doi.org/10.1021/ct100578z

Oszukowska, L., Knapska-Kucharska, M., & Lewiński, A. (2010). Effects of drugs on the efficacy of radioiodine (|) therapy in hyperthyroid patients. *Archives of medical science : AMS*, *6*(1), 4-10. https://doi.org/10.5114/aoms.2010.13499

Oyama, T. (1989). A histopathological, immunohistochemical and ultrastructural study of intranuclear cytoplasmic inclusions in thyroid papillary carcinoma. *Virchows Arch A Pathol Anat Histopathol*, *414*(2), 91-104. https://doi.org/10.1007/bf00718588

Pandit, S. K., Westendorp, B., & de Bruin, A. (2013). Physiological significance of polyploidization in mammalian cells. *Trends Cell Biol*, *23*(11), 556-566. https://doi.org/10.1016/j.tcb.2013.06.002

Pantazopoulou V.I. , A. D. D., Stella Georgiou, Stamatis N. Pagakis, Vicky Filippa, Eleni Dragona, Ismini Kloukina, Elias Chatzitheodoridis, Jonel Trebicka, Athanassios D. Velentzas, Maja Thiele, Sarantis Gagos, Dimitris Thanos,Sofia Ts, , A. D. D., , S. G., , S. N. P., , V. F., , Dragona, E., , I. K., , E. C., Jonel Trebicka, Athanassios D. Velentzas,, Maja Thiele, S. G., , D. T., , S. T.-B., Dimitrios J. Stravopodis &, & Anastasiadou, E. (2021). AGO2 localizes to cytokinetic protrusions in a p38-dependent manner and is needed for accurate cell division. *Communications Biology*.

Pantazopoulou, V. I., Georgiou, S., Kakoulidis, P., Giannakopoulou, S. N., Tseleni, S., Stravopodis, D. J., & Anastasiadou, E. (2020). From the Argonauts Mythological Sailors to the Argonautes

RNA-Silencing Navigators: Their Emerging Roles in Human-Cell Pathologies. *Int J Mol Sci*, *21*(11). https://doi.org/10.3390/ijms21114007

Papageorgis, P. (2015). TGFβ Signaling in Tumor Initiation, Epithelial-to-Mesenchymal Transition, and Metastasis. *J Oncol*, *2015*, 587193. https://doi.org/10.1155/2015/587193

Papini, E., Guglielmi, R., Bianchini, A., Crescenzi, A., Taccogna, S., Nardi, F., Panunzi, C., Rinaldi, R., Toscano, V., & Pacella, C. M. (2002). Risk of Malignancy in Nonpalpable Thyroid Nodules: Predictive Value of Ultrasound and Color-Doppler Features. *The Journal of Clinical Endocrinology & Metabolism*, *87*(5), 1941-1946. https://doi.org/10.1210/jcem.87.5.8504

Paradis-Isler, N., & Boehm, J. (2018). NMDA receptor-dependent dephosphorylation of serine 387 in Argonaute 2 increases its degradation and affects dendritic spine density and maturation. *J Biol Chem*, *293*(24), 9311-9325. https://doi.org/10.1074/jbc.RA117.001007

Paraskevopoulou, M. D., Georgakilas, G., Kostoulas, N., Vlachos, I. S., Vergoulis, T., Reczko, M., Filippidis, C., Dalamagas, T., & Hatzigeorgiou, A. G. (2013). DIANA-microT web server v5.0: service integration into miRNA functional analysis workflows. *Nucleic Acids Res*, *41*(Web Server issue), W169-173. https://doi.org/10.1093/nar/gkt393

Park, M. S., Araya-Secchi, R., Brackbill, J. A., Phan, H. D., Kehling, A. C., Abd El-Wahab, E. W., Dayeh, D. M., Sotomayor, M., & Nakanishi, K. (2019). Multidomain Convergence of Argonaute during RISC Assembly Correlates with the Formation of Internal Water Clusters. *Mol Cell*, *75*(4), 725-740.e726. https://doi.org/10.1016/j.molcel.2019.06.011

Park, M. S., Phan, H.-D., Busch, F., Hinckley, S. H., Brackbill, J. A., Wysocki, V. H., & Nakanishi, K. (2017). Human Argonaute3 has slicer activity. *Nucleic Acids Res*, *45*(20), 11867-11877. https://doi.org/10.1093/nar/gkx916 %J Nucleic Acids Research

Park, S. M., Gaur, A. B., Lengyel, E., & Peter, M. E. (2008). The miR-200 family determines the epithelial phenotype of cancer cells by targeting the E-cadherin repressors ZEB1 and ZEB2. *Genes Dev*, *22*(7), 894-907. https://doi.org/10.1101/gad.1640608

Patel, P. H., Barbee, S. A., & Blankenship, J. T. (2016). GW-Bodies and P-Bodies Constitute Two Separate Pools of Sequestered Non-Translating RNAs. *PLoS One*, *11*(3), e0150291. https://doi.org/10.1371/journal.pone.0150291

Peng, Y., & Croce, C. M. (2016). The role of MicroRNAs in human cancer. *Signal Transduction and Targeted Therapy*, *1*(1), 15004. https://doi.org/10.1038/sigtrans.2015.4

Peterman, E., & Prekeris, R. (2019). The postmitotic midbody: Regulating polarity, stemness, and proliferation. *J Cell Biol*, *218*(12), 3903-3911. https://doi.org/10.1083/jcb.201906148

Pilli, T., Toti, P., Occhini, R., Castagna, M. G., Cantara, S., Caselli, M., Cardinale, S., Barbagli, L., & Pacini, F. (2018). Chronic lymphocytic thyroiditis (CLT) has a positive prognostic value in papillary thyroid cancer (PTC) patients: the potential key role of Foxp3+ T lymphocytes. *J Endocrinol Invest*, *41*(6), 703-709. https://doi.org/10.1007/s40618-017-0794-8

Pinto, H. C., Baptista, A., Camilo, M. E., Valente, A., Saragoça, A., & de Moura, M. C. (1996). Nonalcoholic steatohepatitis. Clinicopathological comparison with alcoholic hepatitis in ambulatory and hospitalized patients. *Dig Dis Sci*, *41*(1), 172-179. https://doi.org/10.1007/bf02208601

Pokhrel B, B. K. (2020). Graves Disease. *In: StatPearls [Internet]. Treasure Island (FL): StatPearls Publishing*. https://www.ncbi.nlm.nih.gov/books/NBK448195/

Press, M. F., Xie, B., Davenport, S., Zhou, Y., Guzman, R., Nolan, G. P., O'Brien, N., Palazzolo, M., Mak, T. W., Brugge, J. S., & Slamon, D. J. (2019). Role for polo-like kinase 4 in mediation of cytokinesis. *Proc Natl Acad Sci U S A*, *116*(23), 11309-11318. https://doi.org/10.1073/pnas.1818820116

Qi, H. H., Ongusaha, P. P., Myllyharju, J., Cheng, D., Pakkanen, O., Shi, Y., Lee, S. W., Peng, J., & Shi, Y. (2008). Prolyl 4-hydroxylation regulates Argonaute 2 stability. *Nature*, *455*(7211), 421-424. https://doi.org/10.1038/nature07186

Quévillon Huberdeau, M., Zeitler, D. M., Hauptmann, J., Bruckmann, A., Fressigné, L., Danner, J., Piquet, S., Strieder, N., Engelmann, J. C., Jannot, G., Deutzmann, R., Simard, M. J., & Meister, G. (2017). Phosphorylation of Argonaute proteins affects mRNA binding and is essential for microRNA-guided gene silencing in vivo. *Embo j*, *36*(14), 2088-2106. https://doi.org/10.15252/embj.201696386

Raftopoulou, C., Roumelioti, F.-M., Dragona, E., Gimelli, S., Sloan-Béna, F., Gorgoulis, V., Antonarakis, S. E., & Gagos, S. (2020). Karyotypic Flexibility of the Complex Cancer Genome and the Role of Polyploidization in Maintenance of Structural Integrity of Cancer Chromosomes. *Cancers*, *12*(3), 591. https://doi.org/10.3390/cancers12030591

Raman, P., & Koenig, R. J. (2014). Pax-8-PPAR-γ fusion protein in thyroid carcinoma. *Nat Rev Endocrinol*, *10*(10), 616-623. https://doi.org/10.1038/nrendo.2014.115

Rand, T. A., Ginalski, K., Grishin, N. V., & Wang, X. (2004). Biochemical identification of Argonaute 2 as the sole protein required for RNA-induced silencing complex activity. *Proc Natl Acad Sci U S A*, *101*(40), 14385-14389. https://doi.org/10.1073/pnas.0405913101

Rannou, Y., Salaun, P., Benaud, C., Khan, J., Dutertre, S., Giet, R., & Prigent, C. (2012). MNK1 kinase activity is required for abscission. *J Cell Sci*, *125*(Pt 12), 2844-2852. https://doi.org/10.1242/jcs.058081

Reczko, M., Maragkakis, M., Alexiou, P., Grosse, I., & Hatzigeorgiou, A. G. (2012). Functional microRNA targets in protein coding sequences. *Bioinformatics*, *28*(6), 771-776. https://doi.org/10.1093/bioinformatics/bts043

Reinhart, B. J., Slack, F. J., Basson, M., Pasquinelli, A. E., Bettinger, J. C., Rougvie, A. E., Horvitz, H. R., & Ruvkun, G. (2000). The 21-nucleotide let-7 RNA regulates developmental timing in Caenorhabditis elegans. *Nature*, *403*(6772), 901-906. https://doi.org/10.1038/35002607

Rhim, Andrew D., Mirek, Emily T., Aiello, Nicole M., Maitra, A., Bailey, Jennifer M., McAllister, F., Reichert, M., Beatty, Gregory L., Rustgi, Anil K., Vonderheide, Robert H., Leach, Steven D., & Stanger, Ben Z. (2012). EMT and Dissemination Precede Pancreatic Tumor Formation. *Cell*, *148*(1), 349-361. https://doi.org/https://doi.org/10.1016/j.cell.2011.11.025

Rivera, M., Ricarte-Filho, J., Knauf, J., Shaha, A., Tuttle, M., Fagin, J. A., & Ghossein, R. A. (2010). Molecular genotyping of papillary thyroid carcinoma follicular variant according to its histological subtypes (encapsulated vs infiltrative) reveals distinct BRAF and RAS mutation patterns. *Mod Pathol*, *23*(9), 1191-1200. https://doi.org/10.1038/modpathol.2010.112

Robb, G. B., Brown, K. M., Khurana, J., & Rana, T. M. (2005). Specific and potent RNAi in the nucleus of human cells. *Nat Struct Mol Biol*, *12*(2), 133-137. https://doi.org/10.1038/nsmb886

Roman, S., Lin, R., & Sosa, J. A. (2006). Prognosis of medullary thyroid carcinoma: demographic, clinical, and pathologic predictors of survival in 1252 cases. *Cancer*, *107*(9), 2134-2142. https://doi.org/10.1002/cncr.22244

Roman, S., & Sosa, J. A. (2013). Aggressive variants of papillary thyroid cancer. *Curr Opin Oncol*, *25*(1), 33-38. https://doi.org/10.1097/CCO.0b013e32835b7c6b

Romei, C., Ciampi, R., & Elisei, R. (2016). A comprehensive overview of the role of the RET proto-oncogene in thyroid carcinoma. *Nature Reviews Endocrinology*, *12*(4), 192-202. https://doi.org/10.1038/nrendo.2016.11

Rosen RD, S. A. (2020). Embryology, Thyroid. *In: StatPearls [Internet]. Treasure Island (FL)*. https://www.ncbi.nlm.nih.gov/books/NBK551611/

Roti, E., degli Uberti, E. C., Bondanelli, M., & Braverman, L. E. (2008). Thyroid papillary microcarcinoma: a descriptive and meta-analysis study. *Eur J Endocrinol*, *159*(6), 659-673. https://doi.org/10.1530/eje-07-0896

Rousset, B., Dupuy, C., Miot, F., & Dumont, J. (2000). Chapter 2 Thyroid Hormone Synthesis And Secretion. In K. R. Feingold, B. Anawalt, A. Boyce, G. Chrousos, W. W. de Herder, K. Dungan, A. Grossman, J. M. Hershman, J. Hofland, G. Kaltsas, C. Koch, P. Kopp, M. Korbonits, R. McLachlan, J. E. Morley, M. New, J. Purnell, F. Singer, C. A. Stratakis, D. L. Trence, & D. P. Wilson (Eds.), *Endotext*. MDText.com, Inc.

Rozario, T., & DeSimone, D. W. (2010). The extracellular matrix in development and morphogenesis: a dynamic view. *Dev Biol*, *341*(1), 126-140. https://doi.org/10.1016/j.ydbio.2009.10.026

Ruby, J. G., Jan, C. H., & Bartel, D. P. (2007). Intronic microRNA precursors that bypass Drosha processing. *Nature*, *448*(7149), 83-86. https://doi.org/10.1038/nature05983

Rusinek, D., Swierniak, M., Chmielik, E., Kowal, M., Kowalska, M., Cyplinska, R., Czarniecka, A., Piglowski, W., Korfanty, J., Chekan, M., Krajewska, J., Szpak-Ulczok, S., Jarzab, M., Widlak, W., & Jarzab, B. (2015). BRAFV600E-Associated Gene Expression Profile: Early Changes in the Transcriptome, Based on a Transgenic Mouse Model of Papillary Thyroid Carcinoma. *PloS one*, *10*(12), e0143688. https://doi.org/10.1371/journal.pone.0143688

Rustom, A., Saffrich, R., Markovic, I., Walther, P., & Gerdes, H. H. (2004). Nanotubular highways for intercellular organelle transport. *Science*, *303*(5660), 1007-1010. https://doi.org/10.1126/science.1093133

Rybak, A., Fuchs, H., Hadian, K., Smirnova, L., Wulczyn, E. A., Michel, G., Nitsch, R., Krappmann, D., & Wulczyn, F. G. (2009). The let-7 target gene mouse lin-41 is a stem cell specific E3 ubiquitin ligase for the miRNA pathway protein Ago2. *Nat Cell Biol*, *11*(12), 1411-1420. https://doi.org/10.1038/ncb1987

Sagona, A. P., & Stenmark, H. (2010). Cytokinesis and cancer. *FEBS Lett*, *584*(12), 2652-2661. https://doi.org/10.1016/j.febslet.2010.03.044

Saito, K., Kuribayashi, K., Nishihara, T., Takano, Y., Ieda, K., Tonoda, S., Kawashima, H., Ishimoto, K., & Nakamine, H. (1986). Primary gastric lymphoma with intranuclear inclusions. An immunohistochemical and ultrastructural study. *Acta Pathol Jpn*, *36*(11), 1769-1779. https://doi.org/10.1111/j.1440-1827.1986.tb02241.x

San Filippo, J., Sung, P., & Klein, H. (2008). Mechanism of eukaryotic homologous recombination. *Annu Rev Biochem*, *77*, 229-257. https://doi.org/10.1146/annurev.biochem.77.061306.125255

San Román Gil, M., Pozas, J., Molina-Cerrillo, J., Gómez, J., Pian, H., Pozas, M., Carrato, A., Grande, E., & Alonso-Gordoa, T. (2020). Current and Future Role of Tyrosine Kinases Inhibition in Thyroid Cancer: From Biology to Therapy. *International journal of molecular sciences*, *21*(14), 4951. https://doi.org/10.3390/ijms21144951

Sander, S., Bullinger, L., Klapproth, K., Fiedler, K., Kestler, H. A., Barth, T. F., Möller, P., Stilgenbauer, S., Pollack, J. R., & Wirth, T. (2008). MYC stimulates EZH2 expression by repression of its negative regulator miR-26a. *Blood*, *112*(10), 4202-4212. https://doi.org/10.1182/blood-2008-03-147645

Santarpia, L., El-Naggar, A. K., Cote, G. J., Myers, J. N., & Sherman, S. I. (2008). Phosphatidylinositol 3-Kinase/Akt and Ras/Raf-Mitogen-Activated Protein Kinase Pathway Mutations in Anaplastic Thyroid Cancer. *The Journal of Clinical Endocrinology & Metabolism*, *93*(1), 278-284. https://doi.org/10.1210/jc.2007-1076 %J The Journal of Clinical Endocrinology & Metabolism

Santoro, M., & Carlomagno, F. (2013). Central role of RET in thyroid cancer. *Cold Spring Harb Perspect Biol*, *5*(12), a009233. https://doi.org/10.1101/cshperspect.a009233

Santoro, M., Dathan, N. A., Berlingieri, M. T., Bongarzone, I., Paulin, C., Grieco, M., Pierotti, M. A., Vecchio, G., & Fusco, A. (1994). Molecular characterization of RET/PTC3; a novel rearranged version of the RETproto-oncogene in a human thyroid papillary carcinoma. *Oncogene*, *9*(2), 509-516.

Santos, F., Moreira, C., Nóbrega-Pereira, S., & Bernardes de Jesus, B. (2019). New Insights into the Role of Epithelial–Mesenchymal Transition during Aging. *20*(4), 891. https://www.mdpi.com/1422-0067/20/4/891

Saunders, W. (2005). Centrosomal amplification and spindle multipolarity in cancer cells. *Semin Cancer Biol*, *15*(1), 25-32. https://doi.org/10.1016/j.semcancer.2004.09.003

Schürmann, N., Trabuco, L. G., Bender, C., Russell, R. B., & Grimm, D. (2013). Molecular dissection of human Argonaute proteins by DNA shuffling. *Nature Structural & Molecular Biology*, *20*(7), 818-826. https://doi.org/10.1038/nsmb.2607

Schiel, J. A., & Prekeris, R. (2013). Membrane dynamics during cytokinesis. *Curr Opin Cell Biol*, *25*(1), 92-98. https://doi.org/10.1016/j.ceb.2012.10.012

Schiller, E. (1949). Kerneinschluesse und Amitose. Z Zellforsch Mikrosk. *Journal of Anatomy*, *34: 356–361*.

Schindelin, J., Arganda-Carreras, I., Frise, E., Kaynig, V., Longair, M., Pietzsch, T., Preibisch, S., Rueden, C., Saalfeld, S., Schmid, B., Tinevez, J.-Y., White, D. J., Hartenstein, V., Eliceiri, K., Tomancak, P., & Cardona, A. (2012). Fiji: an open-source platform for biological-image analysis. *Nature Methods*, *9*(7), 676-682. https://doi.org/10.1038/nmeth.2019

Schirle, N. T., Sheu-Gruttadauria, J., Chandradoss, S. D., Joo, C., & MacRae, I. J. (2015). Water-mediated recognition of t1-adenosine anchors Argonaute2 to microRNA targets. *Elife*, *4*. https://doi.org/10.7554/eLife.07646

Schuster, S., Miesen, P., & van Rij, R. P. (2019). Antiviral RNAi in Insects and Mammals: Parallels and Differences. *11*(5), 448. https://www.mdpi.com/1999-4915/11/5/448

Schwertheim, S., Theurer, S., Jastrow, H., Herold, T., Ting, S., Westerwick, D., Bertram, S., Schaefer, C. M., Kälsch, J., Baba, H. A., & Schmid, K. W. (2019). New insights into intranuclear inclusions in thyroid carcinoma: Association with autophagy and with BRAFV600E mutation. *PloS one*, *14*(12), e0226199. https://doi.org/10.1371/journal.pone.0226199

Selek, A., Cetinarslan, B., Tarkun, I., Canturk, Z., Ustuner, B., & Akyay, Z. (2017). Thyroid autoimmunity: is really associated with papillary thyroid carcinoma? *Eur Arch Otorhinolaryngol*, *274*(3), 1677-1681. https://doi.org/10.1007/s00405-016-4414-6

Shahid MA, A. M., Sharma S. . (2020). Physiology, Thyroid Hormone. . *In: StatPearls. Treasure Island (FL): StatPearls Publishing*. https://www.ncbi.nlm.nih.gov/books/NBK500006/

Shapiro, P. S., Vaisberg, E., Hunt, A. J., Tolwinski, N. S., Whalen, A. M., McIntosh, J. R., & Ahn, N. G. (1998). Activation of the MKK/ERK pathway during somatic cell mitosis: direct interactions of active ERK with kinetochores and regulation of the mitotic 3F3/2 phosphoantigen. *J Cell Biol*, *142*(6), 1533-1545. https://doi.org/10.1083/jcb.142.6.1533

Sharma, N. R., Wang, X., Majerciak, V., Ajiro, M., Kruhlak, M., Meyers, C., & Zheng, Z. M. (2016). Cell Type- and Tissue Context-dependent Nuclear Distribution of Human Ago2. *J Biol Chem*, *291*(5), 2302-2309. https://doi.org/10.1074/jbc.C115.695049

Shay, J. W., & Bacchetti, S. (1997). A survey of telomerase activity in human cancer. *European Journal of Cancer*, *33*(5), 787-791. https://doi.org/https://doi.org/10.1016/S0959-8049(97)00062-2

Shi, D., Wang, H., Ding, M., Yang, M., Li, C., Yang, W., & Chen, L. (2019). MicroRNA-26a-5p inhibits proliferation, invasion and metastasis by repressing the expression of Wnt5a in papillary thyroid carcinoma. *Onco Targets Ther*, *12*, 6605-6616. https://doi.org/10.2147/ott.S205994

Shi, Q., & King, R. W. (2005). Chromosome nondisjunction yields tetraploid rather than aneuploid cells in human cell lines. *Nature*, *437*(7061), 1038-1042. https://doi.org/10.1038/nature03958

Shibue, T., & Weinberg, R. A. (2017). EMT, CSCs, and drug resistance: the mechanistic link and clinical implications. *Nat Rev Clin Oncol*, *14*(10), 611-629. https://doi.org/10.1038/nrclinonc.2017.44

Shmushkovich, T., Monopoli, K. R., Homsy, D., Leyfer, D., Betancur-Boissel, M., Khvorova, A., & Wolfson, A. D. (2018). Functional features defining the efficacy of cholesterol-conjugated, self-deliverable, chemically modified siRNAs. *Nucleic Acids Res*, *46*(20), 10905-10916. https://doi.org/10.1093/nar/gky745 %J Nucleic Acids Research

Shurbaji, M. S., Gupta, P. K., & Frost, J. K. (1988). Nuclear grooves: a useful criterion in the cytopathologic diagnosis of papillary thyroid carcinoma. *Diagn Cytopathol*, *4*(2), 91-94. https://doi.org/10.1002/dc.2840040202

Siemens, H., Jackstadt, R., Hünten, S., Kaller, M., Menssen, A., Götz, U., & Hermeking, H. (2011). miR-34 and SNAIL form a double-negative feedback loop to regulate epithelial-mesenchymal transitions. *Cell Cycle*, *10*(24), 4256-4271. https://doi.org/10.4161/cc.10.24.18552

Silaghi, C. A., Lozovanu, V., Silaghi, H., Georgescu, R. D., Pop, C., Dobrean, A., & Georgescu, C. E. (2020). The Prognostic Value of MicroRNAs in Thyroid Cancers-A Systematic Review and Meta-Analysis. *Cancers (Basel)*, *12*(9). https://doi.org/10.3390/cancers12092608

Singh, A., & Settleman, J. (2010). EMT, cancer stem cells and drug resistance: an emerging axis of evil in the war on cancer. *Oncogene*, *29*(34), 4741-4751. https://doi.org/10.1038/onc.2010.215

Skinner, M. A., Moley, J. A., Dilley, W. G., Owzar, K., Debenedetti, M. K., & Wells, S. A., Jr. (2005). Prophylactic thyroidectomy in multiple endocrine neoplasia type 2A. *N Engl J Med*, *353*(11), 1105-1113. https://doi.org/10.1056/NEJMoa043999

Smida, J., Salassidis, K., Hieber, L., Zitzelsberger, H., Kellerer, A. M., Demidchik, E. P., Negele, T., Spelsberg, F., Lengfelder, E., Werner, M., & Bauchinger, M. (1999). Distinct frequency of ret rearrangements in papillary thyroid carcinomas of children and adults from Belarus. *Int J Cancer*, *80*(1), 32-38. https://doi.org/10.1002/(sici)1097-0215(19990105)80:1<32::aid-ijc7>3.0.co;2-l

Smith-Bindman, R., Lebda, P., Feldstein, V. A., Sellami, D., Goldstein, R. B., Brasic, N., Jin, C., & Kornak, J. (2013). Risk of thyroid cancer based on thyroid ultrasound imaging characteristics: results of a population-based study. *JAMA Intern Med*, *173*(19), 1788-1796. https://doi.org/10.1001/jamainternmed.2013.9245

Smith, I. F., Shuai, J., & Parker, I. (2011). Active generation and propagation of Ca2+ signals within tunneling membrane nanotubes. *Biophys J*, *100*(8), L37-39. https://doi.org/10.1016/j.bpj.2011.03.007

Söderström, N., & Biörklund, A. (1973). Intranuclear cytoplasmic inclusions in some types of thyroid cancer. *Acta Cytol*, *17*(3), 191-197.

Solomon, A., Gupta, P. K., LiVolsi, V. A., & Baloch, Z. W. (2002). Distinguishing tall cell variant of papillary thyroid carcinoma from usual variant of papillary thyroid carcinoma in cytologic specimens. *Diagn Cytopathol*, *27*(3), 143-148. https://doi.org/10.1002/dc.10156

Søndergaard, C. R., Olsson, M. H., Rostkowski, M., & Jensen, J. H. (2011). Improved Treatment of Ligands and Coupling Effects in Empirical Calculation and Rationalization of pKa Values. *J Chem Theory Comput*, *7*(7), 2284-2295. https://doi.org/10.1021/ct200133y

Song, X., Zhong, H., Wu, Q., Wang, M., Zhou, J., Zhou, Y., Lu, X., & Ying, B. (2017). Association between SNPs in microRNA machinery genes and gastric cancer susceptibility, invasion, and metastasis in Chinese Han population. *Oncotarget*, *8*(49), 86435-86446. https://doi.org/10.18632/oncotarget.21199

Sosa, J. A., Hanna, J. W., Robinson, K. A., & Lanman, R. B. (2013). Increases in thyroid nodule fine-needle aspirations, operations, and diagnoses of thyroid cancer in the United States. *Surgery*, *154*(6), 1420-1426; discussion 1426-1427. https://doi.org/10.1016/j.surg.2013.07.006

Sowinski, S., Jolly, C., Berninghausen, O., Purbhoo, M. A., Chauveau, A., Kohler, K., Oddos, S., Eissmann, P., Brodsky, F. M., Hopkins, C., Onfelt, B., Sattentau, Q., & Davis, D. M. (2008). Membrane nanotubes physically connect T cells over long distances presenting a novel route for HIV-1 transmission. *Nat Cell Biol*, *10*(2), 211-219. https://doi.org/10.1038/ncb1682

Stagsted, L. V., Daugaard, I., & Hansen, T. B. (2017). The agotrons: Gene regulators or Argonaute protectors? *Bioessays*, *39*(4). https://doi.org/10.1002/bies.201600239

Stein, P., Rozhkov, N. V., Li, F., Cardenas, F. L., Davydenko, O., Vandivier, L. E., Gregory, B. D., Hannon, G. J., & Schultz, R. M. (2015). Essential Role for endogenous siRNAs during meiosis in mouse oocytes. *PLoS Genet*, *11*(2), e1005013. https://doi.org/10.1371/journal.pgen.1005013

Sternberg. (1983). Biomedical Image Processing. *Computer*, *16*(1), 22-34. https://doi.org/10.1109/MC.1983.1654163

Stivers, N. S., Islam, A., Reyes-Reyes, E. M., Casson, L. K., Aponte, J. C., Vaisberg, A. J., Hammond, G. B., & Bates, P. J. (2018). Plagiochiline A Inhibits Cytokinetic Abscission and Induces Cell Death. *Molecules*, *23*(6). https://doi.org/10.3390/molecules23061418

Stone MB, W. R. (2003). Institute of Medicine (US) Committee on Medicare Coverage of Routine Thyroid Screening; . *Medicare Coverage of Routine Screening for Thyroid Dysfunction. Washington (DC): National Academies Press (US), Pathophysiology and Diagnosis of Thyroid Disease.* . https://www.ncbi.nlm.nih.gov/books/NBK221541/

Straight, A. F., Cheung, A., Limouze, J., Chen, I., Westwood, N. J., Sellers, J. R., & Mitchison, T. J. (2003). Dissecting temporal and spatial control of cytokinesis with a myosin II Inhibitor. *Science*, *299*(5613), 1743-1747. https://doi.org/10.1126/science.1081412

Su, H., Trombly, M. I., Chen, J., & Wang, X. (2009). Essential and overlapping functions for mammalian Argonautes in microRNA silencing. *Genes Dev*, *23*(3), 304-317. https://doi.org/10.1101/gad.1749809

Su, J., Yin, X., Zhou, X., Wei, W., & Wang, Z. (2015). The functions of F-box proteins in regulating the epithelial to mesenchymal transition. *Curr Pharm Des*, *21*(10), 1311-1317. https://doi.org/10.2174/1381612821666141211144203

Sung, H., Jeon, S., Lee, K.-M., Han, S., Song, M., Choi, J.-Y., Park, S. K., Yoo, K.-Y., Noh, D.-Y., Ahn, S.-H., & Kang, D. (2012). Common genetic polymorphisms of microRNA biogenesis pathway genes and breast cancer survival. *BMC Cancer*, *12*(1), 195. https://doi.org/10.1186/1471-2407-12-195

Suzuki, H. I. (2018). MicroRNA Control of TGF-β Signaling. *19*(7), 1901. https://www.mdpi.com/1422-0067/19/7/1901

Sweeney, S. J., Campbell, P., & Bosco, G. (2008). Drosophila sticky/citron kinase is a regulator of cell-cycle progression, genetically interacts with Argonaute 1 and modulates epigenetic gene silencing. *Genetics*, *178*(3), 1311-1325. https://doi.org/10.1534/genetics.107.082511

Tallini, G., & Asa, S. L. (2001). RET oncogene activation in papillary thyroid carcinoma. *Adv Anat Pathol*, *8*(6), 345-354. https://doi.org/10.1097/00125480-200111000-00005

Tallini, G., Santoro, M., Helie, M., Carlomagno, F., Salvatore, G., Chiappetta, G., Carcangiu, M. L., & Fusco, A. (1998). RET/PTC oncogene activation defines a subset of papillary thyroid

carcinomas lacking evidence of progression to poorly differentiated or undifferentiated tumor phenotypes. *Clin Cancer Res*, *4*(2), 287-294.

Tam, W. L., & Weinberg, R. A. (2013). The epigenetics of epithelial-mesenchymal plasticity in cancer. *Nat Med*, *19*(11), 1438-1449. https://doi.org/10.1038/nm.3336

Tandon, D., & Banerjee, M. (2020). Centrosomal protein 55: A new paradigm in tumorigenesis. *European Journal of Cell Biology*, *99*(5), 151086. https://doi.org/https://doi.org/10.1016/j.ejcb.2020.151086

Thanasopoulou, A., Xanthopoulou, A. G., Anagnostopoulos, A. K., Konstantakou, E. G., Margaritis, L. H., Papassideri, I. S., Stravopodis, D. J., Tsangaris, G. T., & Anastasiadou, E. (2012). Silencing of CCDC6 reduces the expression of 14-3-3σ in colorectal carcinoma cells. *Anticancer Res*, *32*(3), 907-913.

Thayanithy, V., Dickson, E. L., Steer, C., Subramanian, S., & Lou, E. (2014). Tumor-stromal cross talk: direct cell-to-cell transfer of oncogenic microRNAs via tunneling nanotubes. *Transl Res*, *164*(5), 359-365. https://doi.org/10.1016/j.trsl.2014.05.011

Theotoki, E. I., Pantazopoulou, V. I., Georgiou, S., Kakoulidis, P., Filippa, V., & Stravopodis, D. J. (2020). Dicing the Disease with Dicer: The Implications of Dicer Ribonuclease in Human Pathologies. *21*(19). https://doi.org/10.3390/ijms21197223

Thiery, J. P., Acloque, H., Huang, R. Y., & Nieto, M. A. (2009). Epithelial-mesenchymal transitions in development and disease. *Cell*, *139*(5), 871-890. https://doi.org/10.1016/j.cell.2009.11.007

Thomson, D. W., Bracken, C. P., Szubert, J. M., & Goodall, G. J. (2013). On measuring miRNAs after transient transfection of mimics or antisense inhibitors. *PloS one*, *8*(1), e55214. https://doi.org/10.1371/journal.pone.0055214

Tschumperlin, D. J., Ligresti, G., Hilscher, M. B., & Shah, V. H. (2018). Mechanosensing and fibrosis. *J Clin Invest*, *128*(1), 74-84. https://doi.org/10.1172/jci93561

Tseleni-Balafouta, S., Gakiopoulou, H., Kavantzas, N., Agrogiannis, G., Givalos, N., & Patsouris, E. (2007). Parathyroid proliferations: a source of diagnostic pitfalls in FNA of thyroid. *Cancer*, *111*(2), 130-136. https://doi.org/10.1002/cncr.22576

Tseleni, S., Kavantzas, N., Yova, D., Alexandratou, E., Karydakis, V., Gogas, J., & Davaris, P. (1997). Findings of computerised nuclear morphometry of papillary thyroid carcinoma in correlation with known prognostic factors. *J Exp Clin Cancer Res*, *16*(4), 401-406.

Tseleni, S., Kavantzas, N., Yova, D., Alexandratou, E., Ioannou-Lambrouli, M., Paraskevakou, H., & Davaris, P. (1997). Findings of computerized nuclear morphometry of papillary thyroid carcinoma in correlation with the age of the patients. *Gen Diagn Pathol*, *143*(1), 23-27.

van den Brink, G. R. (2007). Hedgehog signaling in development and homeostasis of the gastrointestinal tract. *Physiol Rev*, *87*(4), 1343-1375. https://doi.org/10.1152/physrev.00054.2006

Vasilis Constantinides, F. P. (2013). Goitre and thyroid cancer. *Thuroid Disorders*, *Volume 41*(Issue 9), P546-550.

Vazquez-Martin, A., Oliveras-Ferraros, C., Cufi, S., & Menendez, J. A. (2011). Polo-like kinase 1 regulates activation of AMP-activated protein kinase (AMPK) at the mitotic apparatus. *Cell Cycle*, *10*(8), 1295-1302. https://doi.org/10.4161/cc.10.8.15342

Vazquez-Martin, A., Sauri-Nadal, T., Menendez, O. J., Oliveras-Ferraros, C., Cufi, S., Corominas-Faja, B., Lopez-Bonet, E., & Menendez, J. A. (2012). Ser2481-autophosphorylated mTOR colocalizes with chromosomal passenger proteins during mammalian cell cytokinesis. *Cell Cycle*, *11*(22), 4211-4221. https://doi.org/10.4161/cc.22551

Vinciguerra, P., Godinho, S. A., Parmar, K., Pellman, D., & D'Andrea, A. D. (2010). Cytokinesis failure occurs in Fanconi anemia pathway-deficient murine and human bone marrow hematopoietic cells. *J Clin Invest*, *120*(11), 3834-3842. https://doi.org/10.1172/jci43391

Virk, R. K., Theoharis, C. G., Prasad, A., Chhieng, D., & Prasad, M. L. (2014). Morphology predicts BRAF ($V^{600}E$) mutation in papillary thyroid carcinoma: an interobserver reproducibility study. *Virchows Arch*, *464*(4), 435-442. https://doi.org/10.1007/s00428-014-1552-3

Visone, R., Pallante, P., Vecchione, A., Cirombella, R., Ferracin, M., Ferraro, A., Volinia, S., Coluzzi, S., Leone, V., Borbone, E., Liu, C. G., Petrocca, F., Troncone, G., Calin, G. A., Scarpa, A., Colato, C., Tallini, G., Santoro, M., Croce, C. M., & Fusco, A. (2007). Specific microRNAs are downregulated in human thyroid anaplastic carcinomas. *Oncogene*, *26*(54), 7590-7595. https://doi.org/10.1038/sj.onc.1210564

Vlachos, I. S., Kostoulas, N., Vergoulis, T., Georgakilas, G., Reczko, M., Maragkakis, M., Paraskevopoulou, M. D., Prionidis, K., Dalamagas, T., & Hatzigeorgiou, A. G. (2012). DIANA miRPath v.2.0: investigating the combinatorial effect of microRNAs in pathways. *Nucleic Acids Res*, *40*(Web Server issue), W498-504. https://doi.org/10.1093/nar/gks494

Vlachos, I. S., Paraskevopoulou, M. D., Karagkouni, D., Georgakilas, G., Vergoulis, T., Kanellos, I., Anastasopoulos, I. L., Maniou, S., Karathanou, K., Kalfakakou, D., Fevgas, A., Dalamagas, T., & Hatzigeorgiou, A. G. (2015). DIANA-TarBase v7.0: indexing more than half a million experimentally supported miRNA:mRNA interactions. *Nucleic Acids Res*, *43*(Database issue), D153-159. https://doi.org/10.1093/nar/gku1215

Vlachos, I. S., Vergoulis, T., Paraskevopoulou, M. D., Lykokanellos, F., Georgakilas, G., Georgiou, P., Chatzopoulos, S., Karagkouni, D., Christodoulou, F., Dalamagas, T., & Hatzigeorgiou, A. G. (2016). DIANA-mirExTra v2.0: Uncovering microRNAs and transcription factors with crucial roles in NGS expression data. *Nucleic Acids Res*, *44*(W1), W128-134. https://doi.org/10.1093/nar/gkw455

Völler, D., Reinders, J., Meister, G., & Bosserhoff, A. K. (2013). Strong reduction of AGO2 expression in melanoma and cellular consequences. *British Journal of Cancer*, *109*(12), 3116-3124. https://doi.org/10.1038/bjc.2013.646

Volpe, T., Schramke, V., Hamilton, G. L., White, S. A., Teng, G., Martienssen, R. A., & Allshire, R. C. (2003). RNA interference is required for normal centromere function in fission yeast. *Chromosome Res*, *11*(2), 137-146.

Wang, H.-W., Noland, C., Siridechadilok, B., Taylor, D. W., Ma, E., Felderer, K., Doudna, J. A., & Nogales, E. (2009). Structural insights into RNA processing by the human RISC-loading complex. *Nature Structural & Molecular Biology*, *16*(11), 1148-1153. https://doi.org/10.1038/nsmb.1673

Wang, M., Ren, D., Guo, W., Wang, Z., Huang, S., Du, H., Song, L., & Peng, X. (2014). Loss of miR-100 enhances migration, invasion, epithelial-mesenchymal transition and stemness properties in prostate cancer cells through targeting Argonaute 2. *Int J Oncol*, *45*(1), 362-372. https://doi.org/10.3892/ijo.2014.2413

Wang, Y., Wang, Z., Qi, Z., Yin, S., Zhang, N., Liu, Y., Liu, M., Meng, J., Zang, R., Zhang, Z., & Yang, G. (2014). The negative interplay between Aurora A/B and BRCA1/2 controls cancer cell growth and tumorigenesis via distinct regulation of cell cycle progression, cytokinesis, and tetraploidy. *Mol Cancer*, *13*, 94. https://doi.org/10.1186/1476-4598-13-94

Wei, W., Ba, Z., Gao, M., Wu, Y., Ma, Y., Amiard, S., White, C. I., Rendtlew Danielsen, J. M., Yang, Y. G., & Qi, Y. (2012). A role for small RNAs in DNA double-strand break repair. *Cell*, *149*(1), 101-112. https://doi.org/10.1016/j.cell.2012.03.002

Weidner, N., Folkman, J., Pozza, F., Bevilacqua, P., Allred, E. N., Moore, D. H., Meli, S., & Gasparini, G. (1992). Tumor angiogenesis: a new significant and independent prognostic indicator in early-stage breast carcinoma. *J Natl Cancer Inst*, *84*(24), 1875-1887. https://doi.org/10.1093/jnci/84.24.1875

Wenzel, H. J., Hunsaker, M. R., Greco, C. M., Willemsen, R., & Berman, R. F. (2010). Ubiquitin-positive intranuclear inclusions in neuronal and glial cells in a mouse model of the fragile X premutation. *Brain Res*, *1318*, 155-166. https://doi.org/10.1016/j.brainres.2009.12.077

Wessel, W. (1958). [Electron microscopic studies on intranuclear inclusion bodies]. *Virchows Arch Pathol Anat Physiol Klin Med*, *331*(3), 314-328. https://doi.org/10.1007/bf00955258 (Elektronenmikroskopische Untersuchungen von intranucleären Einschlusskörpern.)

Westermarck, J., & Kähäri, V. M. (1999). Regulation of matrix metalloproteinase expression in tumor invasion. *Faseb j*, *13*(8), 781-792.

Winata, P., Williams, M., McGowan, E., Nassif, N., van Zandwijk, N., & Reid, G. (2017). The analysis of novel microRNA mimic sequences in cancer cells reveals lack of specificity in stem-loop RT-qPCR-based microRNA detection. *BMC Res Notes*, *10*(1), 600. https://doi.org/10.1186/s13104-017-2930-0

Winter, J., & Diederichs, S. (2011). Argonaute proteins regulate microRNA stability: Increased microRNA abundance by Argonaute proteins is due to microRNA stabilization. *RNA Biol*, *8*(6), 1149-1157. https://doi.org/10.4161/rna.8.6.17665

Wood, A. M., Rendtlew Danielsen, J. M., Lucas, C. A., Rice, E. L., Scalzo, D., Shimi, T., Goldman, R. D., Smith, E. D., Le Beau, M. M., & Kosak, S. T. (2014). TRF2 and lamin A/C interact to facilitate the functional organization of chromosome ends. *Nat Commun*, *5*, 5467. https://doi.org/10.1038/ncomms6467

Wu, C., So, J., Davis-Dusenbery, B. N., Qi, H. H., Bloch, D. B., Shi, Y., Lagna, G., & Hata, A. (2011). Hypoxia potentiates microRNA-mediated gene silencing through posttranslational modification of Argonaute2. *Mol Cell Biol*, *31*(23), 4760-4774. https://doi.org/10.1128/mcb.05776-11

Xing, M. (2010). Genetic alterations in the phosphatidylinositol-3 kinase/Akt pathway in thyroid cancer. *Thyroid*, *20*(7), 697-706. https://doi.org/10.1089/thy.2010.1646

Xing, M., Alzahrani, A. S., Carson, K. A., Shong, Y. K., Kim, T. Y., Viola, D., Elisei, R., Bendlová, B., Yip, L., Mian, C., Vianello, F., Tuttle, R. M., Robenshtok, E., Fagin, J. A., Puxeddu, E., Fugazzola, L., Czarniecka, A., Jarzab, B., O'Neill, C. J., Sywak, M. S., Lam, A. K., Riesco-Eizaguirre, G., Santisteban, P., Nakayama, H., Clifton-Bligh, R., Tallini, G., Holt, E. H., & Sýkorová, V. (2015). Association between BRAF V600E mutation and recurrence of papillary thyroid cancer. *J Clin Oncol*, *33*(1), 42-50. https://doi.org/10.1200/jco.2014.56.8253

Xing, M., Alzahrani, A. S., Carson, K. A., Viola, D., Elisei, R., Bendlova, B., Yip, L., Mian, C., Vianello, F., Tuttle, R. M., Robenshtok, E., Fagin, J. A., Puxeddu, E., Fugazzola, L., Czarniecka, A., Jarzab, B., O'Neill, C. J., Sywak, M. S., Lam, A. K., Riesco-Eizaguirre, G., Santisteban, P., Nakayama, H., Tufano, R. P., Pai, S. I., Zeiger, M. A., Westra, W. H., Clark, D. P., Clifton-Bligh, R., Sidransky, D., Ladenson, P. W., & Sykorova, V. (2013). Association between BRAF V600E mutation and mortality in patients with papillary thyroid cancer. *Jama*, *309*(14), 1493-1501. https://doi.org/10.1001/jama.2013.3190

Xu, Q., Hou, Y.-x., Langlais, P., Erickson, P., Zhu, J., Shi, C.-X., Luo, M., Zhu, Y., Xu, Y., Mandarino, L. J., Stewart, K., & Chang, X.-b. (2016). Expression of the cereblon binding protein argonaute 2 plays an important role for multiple myeloma cell growth and survival. *BMC Cancer*, *16*(1), 297. https://doi.org/10.1186/s12885-016-2331-0

Xu, Z., Sun, Y., Wei, Z., Jiang, J., Xu, J., & Liu, P. (2020). Suppression of CXCL-1 Could Restore Necroptotic Pathway in Chronic Lymphocytic Leukemia. *Onco Targets Ther*, *13*, 6917-6925. https://doi.org/10.2147/ott.S256993

Xu, Z., Vagnarelli, P., Ogawa, H., Samejima, K., & Earnshaw, W. C. (2010). Gradient of increasing Aurora B kinase activity is required for cells to execute mitosis. *J Biol Chem*, *285*(51), 40163-40170. https://doi.org/10.1074/jbc.M110.181545

Yanaka, Y., Muramatsu, T., Uetake, H., Kozaki, K.-i., & Inazawa, J. (2015). miR-544a induces epithelial–mesenchymal transition through the activation of WNT signaling pathway in gastric cancer. *Carcinogenesis*, *36*(11), 1363-1371. https://doi.org/10.1093/carcin/bgv106 %J Carcinogenesis

Yang, F. Q., Huang, J. H., Liu, M., Yang, F. P., Li, W., Wang, G. C., Che, J. P., & Zheng, J. H. (2014). Argonaute 2 is up-regulated in tissues of urothelial carcinoma of bladder. *Int J Clin Exp Pathol*, *7*(1), 340-347.

Yassa, L., Cibas, E. S., Benson, C. B., Frates, M. C., Doubilet, P. M., Gawande, A. A., Moore, F. D., Jr., Kim, B. W., Nosé, V., Marqusee, E., Larsen, P. R., & Alexander, E. K. (2007). Long-term assessment of a multidisciplinary approach to thyroid nodule diagnostic evaluation. *Cancer*, *111*(6), 508-516. https://doi.org/10.1002/cncr.23116

Yoda, M., Kawamata, T., Paroo, Z., Ye, X., Iwasaki, S., Liu, Q., & Tomari, Y. (2010). ATP-dependent human RISC assembly pathways. *Nat Struct Mol Biol*, *17*(1), 17-23. https://doi.org/10.1038/nsmb.1733

Yoo, S. K., Song, Y. S., Park, Y. J., & Seo, J. S. (2020). Recent Improvements in Genomic and Transcriptomic Understanding of Anaplastic and Poorly Differentiated Thyroid Cancers. *Endocrinol Metab (Seoul)*, *35*(1), 44-54. https://doi.org/10.3803/EnM.2020.35.1.44

Yu, X. M., Schneider, D. F., Leverson, G., Chen, H., & Sippel, R. S. (2013). Follicular variant of papillary thyroid carcinoma is a unique clinical entity: a population-based study of 10,740 cases. *Thyroid*, *23*(10), 1263-1268. https://doi.org/10.1089/thy.2012.0453

Yuan, J., Sun, C., Jiang, S., Lu, Y., Zhang, Y., Gao, X. H., Wu, Y., & Chen, H. D. (2018). The Prevalence of Thyroid Disorders in Patients With Vitiligo: A Systematic Review and Meta-Analysis. *Front Endocrinol (Lausanne)*, *9*, 803. https://doi.org/10.3389/fendo.2018.00803

Zack, G. W., Rogers, W. E., & Latt, S. A. (1977). Automatic measurement of sister chromatid exchange frequency. *J Histochem Cytochem*, *25*(7), 741-753. https://doi.org/10.1177/25.7.70454

Zaret, K. S., & Grompe, M. (2008). Generation and regeneration of cells of the liver and pancreas. *Science*, *322*(5907), 1490-1494. https://doi.org/10.1126/science.1161431

Zeisberg, M., & Neilson, E. G. (2009). Biomarkers for epithelial-mesenchymal transitions. *J Clin Invest*, *119*(6), 1429-1437. https://doi.org/10.1172/jci36183

Zeng, Y., Sankala, H., Zhang, X., & Graves, P. R. (2008). Phosphorylation of Argonaute 2 at serine-387 facilitates its localization to processing bodies. *Biochem J*, *413*(3), 429-436. https://doi.org/10.1042/bj20080599

Zhang, B., Liu, X. X., He, J. R., Zhou, C. X., Guo, M., He, M., Li, M. F., Chen, G. Q., & Zhao, Q. (2011). Pathologically decreased miR-26a antagonizes apoptosis and facilitates carcinogenesis by targeting MTDH and EZH2 in breast cancer. *Carcinogenesis*, *32*(1), 2-9. https://doi.org/10.1093/carcin/bgq209

Zhang, H., Wang, Y., Dou, J., Guo, Y., He, J., Li, L., Liu, X., Chen, R., Deng, R., Huang, J., Xie, R., Zhao, X., & Yu, J. (2019). Acetylation of AGO2 promotes cancer progression by increasing oncogenic miR-19b biogenesis. *Oncogene*, *38*(9), 1410-1431. https://doi.org/10.1038/s41388-018-0530-7

Zhang, L., Li, H., Ji, Q. H., Zhu, Y. X., Wang, Z. Y., Wang, Y., Huang, C. P., Shen, Q., Li, D. S., & Wu, Y. (2012). The clinical features of papillary thyroid cancer in Hashimoto's thyroiditis patients from an area with a high prevalence of Hashimoto's disease. *BMC Cancer*, *12*, 610. https://doi.org/10.1186/1471-2407-12-610

Zhang, X., Graves, P., & Zeng, Y. (2013). Overexpression of human Argonaute2 inhibits cell and tumor growth. *Biochim Biophys Acta*, *1830*(3), 2553-2561. https://doi.org/10.1016/j.bbagen.2012.11.013

Zhao, W. M., Seki, A., & Fang, G. (2006). Cep55, a microtubule-bundling protein, associates with centralspindlin to control the midbody integrity and cell abscission during cytokinesis. *Mol Biol Cell*, *17*(9), 3881-3896. https://doi.org/10.1091/mbc.e06-01-0015

Zhao, X., & Guan, J.-L. (2011). Focal adhesion kinase and its signaling pathways in cell migration and angiogenesis. *Advanced drug delivery reviews*, *63*(8), 610-615. https://doi.org/10.1016/j.addr.2010.11.001

Zhou, A., Chen, G., Cheng, X., Zhang, C., Xu, H., Qi, M., Chen, X., Wang, T., & Li, L. (2019). Inhibitory effects of miR-26b-5p on thyroid cancer. *Mol Med Rep*, *20*(2), 1196-1202. https://doi.org/10.3892/mmr.2019.10315

Zhou, Q., Hu, H., & Li, Z. (2014). Chapter Four - New Insights into the Molecular Mechanisms of Mitosis and Cytokinesis in Trypanosomes. In K. W. Jeon (Ed.), *International Review of Cell and Molecular Biology* (Vol. 308, pp. 127-166). Academic Press. https://doi.org/https://doi.org/10.1016/B978-0-12-800097-7.00004-X

Zhu, X., Yao, J., & Tian, W. (2015). Microarray technology to investigate genes associated with papillary thyroid carcinoma. *Mol Med Rep*, *11*(5), 3729-3733. https://doi.org/10.3892/mmr.2015.3180

Zhu, Y., Lu, Y., Zhang, Q., Liu, J.-J., Li, T.-J., Yang, J.-R., Zeng, C., & Zhuang, S.-M. (2011). MicroRNA-26a/b and their host genes cooperate to inhibit the G1/S transition by activating the pRb protein. *Nucleic Acids Res*, *40*(10), 4615-4625. https://doi.org/10.1093/nar/gkr1278 %J Nucleic Acids Research

Zhu, Y. Z., Li, W. P., Wang, Z. Y., Yang, H. F., He, Q. L., Zhu, H. G., & Zheng, G. J. (2013). Primary pulmonary adenocarcinoma mimicking papillary thyroid carcinoma. *J Cardiothorac Surg*, *8*, 131. https://doi.org/10.1186/1749-8090-8-131

Zoulias, E. A., Asvestas, P. A., Matsopoulos, G. K., & Tseleni-Balafouta, S. (2011). A decision support system for assisting fine needle aspiration diagnosis of thyroid malignancy. *Anal Quant Cytol Histol*, *33*(4), 215-222.

Zuela, N., Bar, D. Z., & Gruenbaum, Y. (2012). Lamins in development, tissue maintenance and stress. *EMBO Rep*, *13*(12), 1070-1078. https://doi.org/10.1038/embor.2012.167

Supplemental Material

Chapter 2

mature miRNA	Normalized_NTHY	Normalized_PTC	foldChange
hsa-miR-424-5p	79084,52192	11,29895365	0,000142872
hsa-miR-450a-5p	6992,274866	1	0,000143015
hsa-miR-204-5p	1	3530,043155	3530,043155
hsa-miR-196a-5p	4248,13078	1	0,000235398
hsa-miR-493-5p	3264,836434	1	0,000306294
hsa-miR-503-5p	3942,936216	4,894888944	0,001241432
hsa-miR-335-5p	3640,371586	10,30197805	0,002829925
hsa-miR-134-5p	3243,946017	4,048173956	0,001247917
hsa-miR-708-5p	5268,178288	90571,74917	17,19223311
hsa-miR-411-5p	3638,697564	9,805835873	0,002694875
hsa-miR-138-5p	11644,69755	208185,4854	17,87813591
hsa-miR-432-5p	3202,114835	1	0,000312294
hsa-miR-34c-5p	3048,041081	35,87081192	0,01176848
hsa-miR-136-5p	1401,84091	1	0,000713348
hsa-miR-379-5p	2774,266618	17,81631225	0,00642199
hsa-miR-34a-5p	2060,765782	18373,46576	8,915843771
hsa-miR-194-5p	4111,370194	32383,62942	7,876602663
hsa-miR-299-5p	993,3513651	1	0,001006693
hsa-miR-146a-5p	8391,786998	52862,54367	6,299319046
hsa-miR-382-5p	1134,58674	2,524086978	0,002224675
hsa-miR-192-5p	1654,977838	15977,50742	9,654212312
hsa-miR-154-5p	1242,352089	4,894888944	0,003940017
hsa-miR-127-5p	833,1657666	1	0,001200241
hsa-miR-450b-5p	761,222495	1	0,001313676
hsa-miR-378d	7412,299481	944,4064956	0,127410731
hsa-miR-330-5p	1272,449941	19414,32304	15,25743561
hsa-miR-125b-5p	59542,86527	370707,1894	6,225887648
hsa-miR-378c	9446,924405	1562,894402	0,165439495
hsa-miR-135b-5p	20661,59598	88331,20514	4,275139502
hsa-miR-589-5p	3770,595133	361,9655421	0,095996926
hsa-miR-744-5p	2852,918014	14412,81608	5,05195593
hsa-miR-99a-5p	205,3369545	19870,97372	96,77251603
hsa-let-7c-5p	11382,23071	66122,84831	5,809304871
hsa-miR-339-5p	42026,297	10364,57288	0,246621131
hsa-miR-671-5p	25675,77386	6714,301952	0,261503392
hsa-miR-31-5p	135466,0082	703721,5312	5,194820018
hsa-miR-125a-5p	27469,99608	109234,9288	3,976517815
hsa-miR-200b-5p	1	469,4691536	469,4691536

mature miRNA	Normalized_NTHY	Normalized_PTC	foldChange
hsa-miR-424-5p	79084,52192	11,29895365	0,000142872
hsa-miR-450a-5p	6992,274866	1	0,000143015
hsa-miR-204-5p	1	3530,043155	3530,043155
hsa-miR-196a-5p	4248,13078	1	0,000235398
hsa-miR-493-5p	3264,836434	1	0,000306294
hsa-miR-503-5p	3942,936216	4,894888944	0,001241432
hsa-miR-335-5p	3640,371586	10,30197805	0,002829925
hsa-miR-134-5p	3243,946017	4,048173956	0,001247917
hsa-miR-708-5p	5268,178288	90571,74917	17,19223311
hsa-miR-411-5p	3638,697564	9,805835873	0,002694875
hsa-miR-138-5p	11644,69755	208185,4854	17,87813591
hsa-miR-432-5p	3202,114835	1	0,000312294
hsa-miR-34c-5p	3048,041081	35,87081192	0,01176848
hsa-miR-136-5p	1401,84091	1	0,000713348
hsa-miR-379-5p	2774,266618	17,81631225	0,00642199
hsa-miR-34a-5p	2060,765782	18373,46576	8,915843771
hsa-miR-194-5p	4111,370194	32383,62942	7,876602663
hsa-miR-299-5p	993,3513651	1	0,001006693
hsa-miR-146a-5p	8391,786998	52862,54367	6,299319046
hsa-miR-382-5p	1134,58674	2,524086978	0,002224675
hsa-miR-192-5p	1654,977838	15977,50742	9,654212312
hsa-miR-154-5p	1242,352089	4,894888944	0,003940017
hsa-miR-127-5p	833,1657666	1	0,001200241
hsa-miR-450b-5p	761,222495	1	0,001313676
hsa-miR-378d	7412,299481	944,4064956	0,127410731
hsa-miR-330-5p	1272,449941	19414,32304	15,25743561
hsa-miR-125b-5p	59542,86527	370707,1894	6,225887648
hsa-miR-378c	9446,924405	1562,894402	0,165439495
hsa-miR-135b-5p	20661,59598	88331,20514	4,275139502
hsa-miR-589-5p	3770,595133	361,9655421	0,095996926
hsa-miR-744-5p	2852,918014	14412,81608	5,05195593
hsa-miR-99a-5p	205,3369545	19870,97372	96,77251603
hsa-let-7c-5p	11382,23071	66122,84831	5,809304871
hsa-miR-339-5p	42026,297	10364,57288	0,246621131
hsa-miR-671-5p	25675,77386	6714,301952	0,261503392
hsa-miR-31-5p	135466,0082	703721,5312	5,194820018
hsa-miR-125a-5p	27469,99608	109234,9288	3,976517815
hsa-miR-200b-5p	1	469,4691536	469,4691536

Table 6 Differential expression of miRNAs between TPC1 and NTHY-ori 3-1 cell lines. Red indicates reduced expression in the TPC1 series compared to the NTHY-ori 3-1 series, while green indicates increased expression respectively. Expression values are normalized between the three copies of each cell line.

mature miRNA	Normalized_NTHY	Normalized_FTC	foldChange
hsa-miR-138-5p	12369,72163	295341,5057	23,87616428
hsa-let-7b-5p	62663,68067	347243,9779	5,541391348
hsa-miR-105-5p	1	7517,301368	7517,301368
hsa-miR-26a-5p	1536215,566	664645,2398	0,432651025
hsa-miR-196b-5p	5,34099027	7200,446332	1348,148184
hsa-miR-15b-5p	205372,0314	68832,79425	0,335161481
hsa-miR-204-5p	1	4900,122879	4900,122879
hsa-miR-30d-5p	288824,8476	120704,3897	0,417915532
hsa-miR-195-5p	15298,84968	60956,99843	3,98441711
hsa-miR-335-5p	3859,278576	1	0,000259116
hsa-miR-411-5p	3870,351652	1	0,000258374
hsa-miR-182-5p	13237,92393	54777,95764	4,137956822
hsa-miR-186-5p	45766,15344	118651,0809	2,59255087
hsa-miR-493-5p	3467,660097	1	0,000288379
hsa-miR-134-5p	3451,264552	1	0,000289749
hsa-miR-30b-5p	438475,6971	144604,5225	0,329789139
hsa-miR-424-5p	83902,70656	31826,18449	0,379322501
hsa-miR-432-5p	3388,265505	1	0,000295136
hsa-miR-1269b	1	3062,216637	3062,216637
hsa-miR-17-5p	81855,77282	31002,80249	0,378749127
hsa-miR-379-5p	2939,679102	1	0,000340173
hsa-miR-26b-5p	86360,75796	27730,59422	0,321101793
hsa-miR-126-5p	6083,087091	92,16014961	0,015150227
hsa-miR-767-5p	17,27179966	4820,725329	279,1096136
hsa-miR-10b-5p	4,108863631	2963,704862	721,2955036
hsa-miR-181a-5p	110096,0951	48565,09938	0,441115549
hsa-miR-146b-5p	3077,503907	18019,8328	5,855340349
hsa-miR-18a-5p	27949,76341	7829,010266	0,280110073
hsa-miR-574-5p	14830,88436	43931,37016	2,962154454
hsa-miR-20a-5p	70206,36004	27667,37024	0,394086379
hsa-miR-769-5p	5984,379262	25191,34295	4,209516451
sa-miR-339-5p	44589,003	16667,1338	0,37379471
hsa-miR-31-5p	143647,99	260293,3688	1,812022243
hsa-miR-15a-5p	119287,80	63664,6019	0,533705883
hsa-let-7f-5p	216164,92	126376,1684	0,584628462
hsa-miR-106a-5p	13276,753	2843,873375	0,21419946
hsa-miR-188-5p	390,35121	6795,371796	17,40835323
hsa-let-7g-5p	36380,338	14813,78915	0,407192175
hsa-miR-136-5p	1491,827	1	0,000670319
hsa-miR-374a-5p	33189,635	66382,49765	2,000097223
hsa-miR-135b-5p	21922,626	7458,488368	0,340218743
hsa-miR-154-5p	1312,3851	1	0,000761971

hsa-miR-423-5p	11524,644	2669,639864	0,231646182
hsa-miR-191-5p	22951,637	8431,108351	0,367342349
hsa-miR-224-5p	14426,613	34823,44199	2,413833435
hsa-miR-589-5p	4007,1151	237,722324	0,059325054
hsa-miR-382-5p	1204,0898	1	0,000830503
hsa-miR-193a-5p	5222,4940	511,9379353	0,098025567
hsa-miR-100-5p	75511,019	10640,27165	0,140910184
hsa-miR-145-5p	7,8045707	1803,618442	231,0977114
hsa-miR-548aq-5p	135,63759	3668,725697	27,04800094
hsa-miR-299-5p	1053,608624	1	0,000949119
hsa-miR-10a-5p	2343,476491	10374,87799	4,427131243
hsa-miR-183-5p	1992,778292	8830,301587	4,431151033
hsa-miR-486-5p	2965,435422	170,0873743	0,057356627
hsa-miR-30c-5p	431470,5021	593649,8623	1,375875893
hsa-miR-127-5p	885,6930475	1	0,001129059
hsa-miR-32-5p	38322,16648	20517,1798	0,53538674
hsa-miR-299-3p	1225,539534	1	0,000815967
hsa-miR-548b-5p	9422,715881	2300,58829	0,244153418
hsa-miR-151a-5p	30858,3611	16388,50722	0,531088063
hsa-miR-125a-5p	29182,36588	53560,52855	1,835373073
hsa-miR-500a-5p	1779,035497	7496,716818	4,213921999
hsa-miR-106b-5p	60187,31922	108685,9532	1,805794885
hsa-miR-98-5p	11479,60562	4217,892082	0,367424825
hsa-miR-185-5p	30669,23789	50864,68767	1,658492065
hsa-miR-96-5p	26573,79092	92434,45105	3,47840665
hsa-miR-425-5p	34759,6953	20306,18816	0,584187749
hsa-miR-34c-5p	3226,80843	542,8147602	0,168220324
hsa-miR-33b-5p	7231,770646	15524,69128	2,146734464
hsa-miR-149-5p	25262,49276	40215,12374	1,59189056
hsa-miR-340-5p	4366,24546	945,6838084	0,216589703
hsa-miR-484	42014,60707	62386,15432	1,484868208
hsa-miR-548d-5p	55080,30842	35677,70081	0,64773967
hsa-miR-337-5p	527,7759865	1	0,001894743
hsa-miR-34a-5p	2189,160927	271,5397988	0,1240383
hsa-miR-409-5p	1340,092496	1	0,000746217
hsa-let-7c-5p	12102,38831	20504,68204	1,694267405
hsa-miR-193b-5p	875,9867631	23,05487491	0,026318748
hsa-miR-9-5p	1155,919957	4550,920693	3,937055213
hsa-miR-125b-5p	63248,55924	84107,26545	1,329789429
hsa-miR-142-5p	1381,992453	4898,652554	3,544630467
hsa-miR-584-5p	783,515425	17,90873743	0,022856905

Table 7 Differential expression of miRNAs between FTC133 and NTHY-ori 3-1 cell lines. Red indicates reduced expression in the FTC133 cell line compared to NTHY-ori 3-1, while green indicates increased expression, respectively. Expression values are normalized between the three replicates of each cell line.

Pathway Description	Kegg Id	Number_of_miRNs_in_Pathway	miRNA	interacting_genes_Names_for_miRNA
Metabolic pathways	hsa01100	21	hsa-miR-181b-5p	STT3B
			hsa-miR-4677-5p	STT3A
			hsa-miR-125a-5p	BTD,GCNT1
			hsa-miR-330-5p	AGPAT4,GALNS,POLD3,UGH
			hsa-miR-182-5p	GCNT1,PLD1,PPAP2A,PTGIS
			hsa-miR-181a-5p	STT3B
			hsa-miR-16-5p	DLD,GALNT7,MUT,PLD1,PCR1C,STT3A,STT3B
			hsa-miR-30c-5p	ALDH2,H6PD,IDH1
			hsa-let-7b-5p	ACER2,AGPAT9,CS,EHHADH,GALE,NME6,PLCE1,POLR1B
			hsa-miR-5579-3p	POLR1D
			hsa-miR-96-5p	GCNT1,PAPSS1,PLD1,PTGIS
			hsa-miR-130b-5p	ALG9
			hsa-miR-19a-5p	NMRK1
			hsa-miR-9-5p	FUT8
			hsa-miR-24-1-5p	UGT8
			hsa-let-7c-5p	ACER2,CS,EHHADH,GALE,NME6,PLCE1,POLR1B
			hsa-let-7e-5p	ACER2,CS,EHHADH,GALE,NME6,PLCE1,POLR1B
			hsa-miR-30a-5p	ALDH2,H6PD,IDH1
			hsa-let-7d-5p	ACER2,AGPAT4,AGPAT9,GALE,GMPPA,NME6,PLCE1
			hsa-miR-195-5p	DLD,GALNT7,MUT,PLD1,PCR1C,STT3A,STT3B
			hsa-miR-125b-5p	BTD,GCNT1
Pathways in cancer	hsa05200	16	hsa-miR-181b-5p	PIK3R3
			hsa-miR-125a-5p	CASP8
			hsa-miR-182-5p	PLD1
			hsa-miR-16-5p	PLD1
			hsa-miR-181a-5p	PIK3R3
			hsa-miR-30c-5p	EDNRA,NFKB1,PIK3CD
			hsa-let-7b-5p	FAS,FZD2,RALB
			hsa-miR-96-5p	PLD1
			hsa-miR-204-5p	BCL2

			hsa-miR-130b-5p	LAMC2
			hsa-let-7c-5p	FAS,FZD2,RALB
			hsa-let-7e-5p	FZD2,PTCH1,RALB
			hsa-let-7d-5p	FAS,RALB
			hsa-miR-30a-5p	EDNRA,NFKB1,PIK3CD
			hsa-miR-195-5p	PLD1
			hsa-miR-125b-5p	CASP8
Protein processing endoplasmic reticulum	hsa04141	14	hsa-miR-181b-5p	STT3B
			hsa-miR-4677-5p	STT3A
			hsa-miR-96-5p	EIF2AK4,SEC63
			hsa-miR-204-5p	BCL2,EIF2AK4
			hsa-miR-876-5p	MAP3K5
			hsa-miR-182-5p	EIF2AK4
			hsa-miR-181a-5p	STT3B
			hsa-miR-16-5p	PLAA,STT3A,STT3B
			hsa-miR-9-5p	EIF2AK4
			hsa-let-7c-5p	EIF2AK4,UBE4B
			hsa-let-7e-5p	EIF2AK4,UBE4B
			hsa-let-7d-5p	UBE4B
			hsa-miR-195-5p	PLAA,STT3A,STT3B
			hsa-let-7b-5p	EIF2AK4,UBE4B
Sphingolipid signali pathway	hsa04071	14	hsa-miR-181b-5p	PIK3R3,PPP2R3A
			hsa-miR-96-5p	PLD1
			hsa-miR-204-5p	BCL2
			hsa-miR-182-5p	PLD1
			hsa-miR-876-5p	MAP3K5
			hsa-miR-16-5p	PLD1
			hsa-miR-181a-5p	PIK3R3,PPP2R3A
			hsa-let-7c-5p	ACER2
			hsa-let-7e-5p	ACER2
			hsa-let-7d-5p	ACER2
			hsa-miR-30a-5p	NFKB1,PIK3CD,PPP2R2A
			hsa-miR-30c-5p	NFKB1,PIK3CD,PPP2R2A
			hsa-miR-195-5p	PLD1
			hsa-let-7b-5p	ACER2
Ras signaling pathway	hsa04014	14	hsa-miR-5579-3p	RASA1
			hsa-miR-181b-5p	PIK3R3
			hsa-miR-4677-5p	RASA1
			hsa-miR-96-5p	PLD1,RASA1
			hsa-miR-182-5p	PLD1,RASA1
			hsa-miR-16-5p	PLD1
			hsa-miR-181a-5p	PIK3R3
			hsa-let-7c-5p	PLCE1,RALB

			hsa-let-7e-5p	PLCE1,RALB
			hsa-miR-30a-5p	NFKB1,PIK3CD,RASA1,RGL1 TBK1
			hsa-let-7d-5p	PLCE1,RALB
			hsa-miR-30c-5p	NFKB1,PIK3CD,RASA1,RGL1 TBK1
			hsa-miR-195-5p	PLD1
			hsa-let-7b-5p	PLCE1,RALB
cAMP signaling pathway	hsa04024	13	hsa-miR-181b-5p	PIK3R3
			hsa-miR-96-5p	PLD1
			hsa-miR-204-5p	CAMK2D
			hsa-miR-182-5p	PLD1
			hsa-miR-16-5p	PLD1
			hsa-miR-181a-5p	PIK3R3
			hsa-let-7c-5p	PLCE1
			hsa-let-7e-5p	PLCE1,PTCH1
			hsa-let-7d-5p	PLCE1
			hsa-miR-30a-5p	EDNRA,NFKB1,PIK3CD
			hsa-miR-30c-5p	EDNRA,NFKB1,PIK3CD
			hsa-miR-195-5p	PLD1
			hsa-let-7b-5p	PLCE1
Endocytosis	hsa04144	12	hsa-miR-181b-5p	RAB11FIP2
			hsa-miR-96-5p	PLD1
			hsa-miR-182-5p	PLD1
			hsa-miR-181a-5p	RAB11FIP2
			hsa-miR-16-5p	PLD1
			hsa-miR-9-5p	VPS4B
			hsa-let-7c-5p	CHMP2B,USP8
			hsa-miR-222-5p	NEDD4
			hsa-let-7e-5p	CHMP2B,USP8
			hsa-let-7d-5p	NEDD4,USP8
			hsa-miR-195-5p	PLD1
			hsa-let-7b-5p	CHMP2B,USP8
TNF signaling pathway	hsa04668	12	hsa-miR-181b-5p	PIK3R3
			hsa-miR-125a-5p	CASP8
			hsa-miR-876-5p	MAP3K5
			hsa-miR-181a-5p	PIK3R3
			hsa-miR-9-5p	CCL2
			hsa-let-7c-5p	FAS
			hsa-let-7e-5p	CFLAR
			hsa-miR-30a-5p	NFKB1,PIK3CD
			hsa-let-7d-5p	CFLAR,FAS
			hsa-miR-30c-5p	NFKB1,PIK3CD
			hsa-miR-125b-5p	CASP8

			hsa-let-7b-5p	FAS
MAPK signaling pathway	hsa04010	11	hsa-miR-5579-3p	RASA1
			hsa-miR-4677-5p	RASA1
			hsa-miR-96-5p	RASA1
			hsa-miR-182-5p	RASA1
			hsa-miR-876-5p	MAP3K5
			hsa-let-7c-5p	DUSP10,DUSP6,FAS,TAOK3
			hsa-let-7e-5p	DUSP10,DUSP6,TAOK3
			hsa-let-7d-5p	DUSP10,FAS
			hsa-miR-30a-5p	NFKB1,PPP3CB,RASA1
			hsa-miR-30c-5p	NFKB1,PPP3CB,RASA1
			hsa-let-7b-5p	DUSP10,DUSP6,FAS,TAOK3
Proteoglycans in cancer	hsa05205	11	hsa-miR-181b-5p	PIK3R3
			hsa-miR-96-5p	ITPR1
			hsa-miR-204-5p	CAMK2D
			hsa-miR-182-5p	ITPR1
			hsa-miR-181a-5p	PIK3R3
			hsa-let-7c-5p	FAS,FZD2,PLCE1
			hsa-let-7e-5p	FZD2,PLCE1,PTCH1
			hsa-miR-30a-5p	PIK3CD
			hsa-let-7d-5p	FAS,PLCE1
			hsa-miR-30c-5p	PIK3CD
			hsa-let-7b-5p	FAS,FZD2,PLCE1
cGMP-PKG signali pathway	hsa04022	11	hsa-miR-181b-5p	PIK3R3
			hsa-miR-5579-3p	MEF2A
			hsa-miR-96-5p	ITPR1,RGS2
			hsa-miR-876-5p	MEF2A
			hsa-miR-182-5p	ITPR1,RGS2
			hsa-miR-181a-5p	PIK3R3
			hsa-let-7c-5p	KCNMA1
			hsa-let-7e-5p	KCNMA1
			hsa-miR-30a-5p	EDNRA,PIK3CD,PPP3CB
			hsa-miR-30c-5p	EDNRA,PIK3CD,PPP3CB
			hsa-let-7b-5p	KCNMA1
Jak-STAT signali pathway	hsa04630	11	hsa-miR-181b-5p	PIK3R3
			hsa-miR-125a-5p	IL6R
			hsa-miR-876-5p	IL6R
			hsa-miR-182-5p	IL6R
			hsa-miR-181a-5p	PIK3R3
			hsa-miR-222-5p	IL4R
			hsa-let-7e-5p	SOCS1
			hsa-let-7d-5p	SOCS1
			hsa-miR-30a-5p	PIK3CD, SOCS1

			hsa-miR-30c-5p	PIK3CD, SOCS1
			hsa-miR-125b-5p	IL6R
Apoptosis	hsa04210	11	hsa-miR-181b-5p	PIK3R3
			hsa-miR-125a-5p	CASP8
			hsa-miR-204-5p	BCL2
			hsa-miR-181a-5p	PIK3R3
			hsa-let-7c-5p	FAS
			hsa-let-7e-5p	CFLAR
			hsa-miR-30a-5p	NFKB1,PIK3CD,PPP3CB
			hsa-let-7d-5p	CFLAR,FAS
			hsa-miR-30c-5p	NFKB1,PIK3CD,PPP3CB
			hsa-miR-125b-5p	CASP8
			hsa-let-7b-5p	FAS
PI3K-Akt signaling pathw	hsa04151	11	hsa-miR-181b-5p	PIK3R3,PPP2R3A
			hsa-miR-125a-5p	IL6R
			hsa-miR-130b-5p	LAMC2
			hsa-miR-204-5p	BCL2
			hsa-miR-876-5p	IL6R
			hsa-miR-182-5p	IL6R
			hsa-miR-181a-5p	PIK3R3,PPP2R3A
			hsa-miR-222-5p	IL4R
			hsa-miR-30a-5p	NFKB1,PIK3CD,PPP2R2A
			hsa-miR-30c-5p	NFKB1,PIK3CD,PPP2R2A
			hsa-miR-125b-5p	IL6R
Ubiquitin mediat proteolysis	hsa04120	10	hsa-miR-19a-5p	UBA6
			hsa-miR-16-5p	CUL4A
			hsa-let-7c-5p	UBE2M,UBE3B,UBE4B
			hsa-miR-222-5p	NEDD4
			hsa-let-7e-5p	SOCS1,UBE2M,UBE3B,UBE-B
			hsa-let-7d-5p	NEDD4,SOCS1,UBE3B,UBE4
			hsa-miR-30a-5p	SOCS1
			hsa-miR-30c-5p	SOCS1
			hsa-miR-195-5p	CUL4A
			hsa-let-7b-5p	UBE2M,UBE3B,UBE4B
Phosphatidylinositol signaling system	hsa04070	10	hsa-miR-181b-5p	PIK3R3
			hsa-miR-96-5p	ITPR1
			hsa-miR-182-5p	ITPR1
			hsa-miR-181a-5p	PIK3R3
			hsa-let-7c-5p	PLCE1
			hsa-let-7e-5p	PLCE1
			hsa-let-7d-5p	PLCE1
			hsa-miR-30a-5p	PIK3CD
			hsa-miR-30c-5p	PIK3CD

			hsa-let-7b-5p	PLCE1
Purine metabolism	hsa00230	10	hsa-miR-5579-3p	POLR1D
			hsa-miR-96-5p	PAPSS1
			hsa-miR-330-5p	POLD3
			hsa-miR-16-5p	ENPP4,POLR1C
			hsa-let-7c-5p	NME6,POLR1B
			hsa-let-7e-5p	NME6,PDE7A,POLR1
			hsa-miR-30a-5p	ENPP4
			hsa-let-7d-5p	NME6
			hsa-miR-195-5p	ENPP4,POLR1C
			hsa-let-7b-5p	NME6,POLR1B
MicroRNAs in cancer	hsa05206	10	hsa-miR-138-5p	ZEB2
			hsa-miR-5579-3p	ZEB2
			hsa-miR-204-5p	BCL2,MARCKS
			hsa-miR-182-5p	MARCKS
			hsa-miR-16-5p	MMP16
			hsa-let-7e-5p	SOCS1
			hsa-miR-30a-5p	MMP16,NFKB1,SOCS1
			hsa-let-7d-5p	SOCS1
			hsa-miR-30c-5p	MMP16,NFKB1,SOCS1
			hsa-miR-195-5p	MMP16
HIF-1 signaling pathway	hsa04066	9	hsa-miR-181b-5p	PIK3R3
			hsa-miR-125a-5p	IL6R
			hsa-miR-204-5p	BCL2,CAMK2D
			hsa-miR-876-5p	IL6R
			hsa-miR-182-5p	IL6R
			hsa-miR-181a-5p	PIK3R3
			hsa-miR-30a-5p	NFKB1,PIK3CD
			hsa-miR-30c-5p	NFKB1,PIK3CD
			hsa-miR-125b-5p	IL6R
Calcium signaling pathway	hsa04020	9	hsa-miR-96-5p	ITPR1
			hsa-miR-204-5p	CAMK2D
			hsa-miR-182-5p	ITPR1
			hsa-let-7c-5p	PLCE1
			hsa-let-7e-5p	PLCE1
			hsa-let-7d-5p	PLCE1
			hsa-miR-30a-5p	EDNRA,PPP3CB
			hsa-miR-30c-5p	EDNRA,PPP3CB
			hsa-let-7b-5p	PLCE1
			hsa-miR-181b-5p	PIK3R3,SIPA1L2
			hsa-miR-181a-5p	PIK3R3,SIPA1L2
			hsa-let-7c-5p	DOCK4,PLCE1,RALB
			hsa-let-7e-5p	DOCK4,PLCE1,RALB

Rap1 signaling pathway	hsa04015	8	hsa-miR-30a-5p	DOCK4,PIK3CD
			hsa-let-7d-5p	DOCK4,PLCE1,RALB
			hsa-miR-30c-5p	DOCK4,PIK3CD
			hsa-let-7b-5p	DOCK4,PLCE1,RALB
Pyrimidine metabolism	hsa00240	8	hsa-miR-5579-3p	POLR1D
			hsa-miR-330-5p	POLD3
			hsa-miR-16-5p	POLR1C
			hsa-let-7c-5p	NME6,POLR1B
			hsa-let-7e-5p	NME6,POLR1B
			hsa-let-7d-5p	NME6
			hsa-miR-195-5p	POLR1C
			hsa-let-7b-5p	NME6,POLR1B
Tight junction	hsa04530	8	hsa-miR-130b-5p	CLDN1
			hsa-let-7c-5p	CLDN1
			hsa-let-7e-5p	CLDN1
			hsa-let-7d-5p	CLDN1
			hsa-miR-30a-5p	PPP2R2A
			hsa-miR-30c-5p	PPP2R2A
			hsa-miR-33a-5p	CASK
			hsa-let-7b-5p	CLDN1
Cell adhesion molecules (CAMs)	hsa04514	8	hsa-miR-130b-5p	CLDN1
			hsa-miR-16-5p	CD274
			hsa-let-7c-5p	CLDN1
			hsa-let-7e-5p	CLDN1
			hsa-let-7d-5p	CLDN1
			hsa-miR-30a-5p	NEGR1
			hsa-miR-30c-5p	NEGR1
			hsa-let-7b-5p	CLDN1
Thyroid hormone signaling pathway	hsa04919	8	hsa-miR-181b-5p	PIK3R3
			hsa-miR-181a-5p	PIK3R3
			hsa-let-7c-5p	PLCE1
			hsa-let-7e-5p	PLCE1
			hsa-miR-30a-5p	PIK3CD
			hsa-let-7d-5p	PLCE1
			hsa-miR-30c-5p	PIK3CD
			hsa-let-7b-5p	PLCE1
Choline metabolism cancer	hsa05231	8	hsa-miR-181b-5p	PIK3R3
			hsa-miR-96-5p	PLD1
			hsa-miR-182-5p	PLD1,PPAP2A
			hsa-miR-16-5p	PLD1
			hsa-miR-181a-5p	PIK3R3
			hsa-miR-30a-5p	PIK3CD
			hsa-miR-30c-5p	PIK3CD

			hsa-miR-195-5p	PLD1
Regulation of act cytoskeleton	hsa04810	8	hsa-miR-181b-5p	PIK3R3
			hsa-miR-181a-5p	PIK3R3
			hsa-let-7c-5p	DIAPH2
			hsa-let-7e-5p	DIAPH2
			hsa-let-7d-5p	DIAPH2
			hsa-miR-30a-5p	PIK3CD
			hsa-miR-30c-5p	PIK3CD
			hsa-let-7b-5p	DIAPH2
Carbon metabolism	hsa01200	8	hsa-miR-876-5p	ESD
			hsa-miR-16-5p	DLD,MUT
			hsa-let-7c-5p	CS,EHHADH
			hsa-let-7e-5p	CS,EHHADH
			hsa-miR-30a-5p	H6PD,IDH1
			hsa-miR-30c-5p	H6PD,IDH1
			hsa-miR-195-5p	DLD,MUT
			hsa-let-7b-5p	CS,EHHADH
Prolactin signali pathway	hsa04917	8	hsa-miR-181b-5p	PIK3R3
			hsa-miR-16-5p	SOCS6
			hsa-miR-181a-5p	PIK3R3
			hsa-let-7e-5p	SOCS1
			hsa-miR-30a-5p	NFKB1,PIK3CD,SOCS
			hsa-let-7d-5p	SOCS1
			hsa-miR-30c-5p	NFKB1,PIK3CD,SOCS
			hsa-miR-195-5p	SOCS6
Transcriptional misregulation in cancer	hsa05202	7	hsa-miR-138-5p	MLLT3
			hsa-let-7c-5p	DUSP6
			hsa-let-7e-5p	DUSP6
			hsa-miR-30a-5p	NFKB1
			hsa-miR-30c-5p	NFKB1
			hsa-miR-9-5p	FUT8
			hsa-let-7b-5p	DUSP6
AMPK signaling pathway	hsa04152	7	hsa-miR-181b-5p	PIK3R3,PPP2R3A
			hsa-miR-30a-5p	PIK3CD,PPP2R2A
			hsa-miR-181a-5p	PIK3R3,PPP2R3A
			hsa-miR-30c-5p	PIK3CD,PPP2R2A
			hsa-miR-16-5p	CAB39
			hsa-miR-33a-5p	RAB8A
			hsa-miR-195-5p	CAB39
Valine, leucine a			hsa-let-7c-5p	EHHADH
			hsa-let-7e-5p	EHHADH
			hsa-miR-30a-5p	ALDH2
			hsa-miR-16-5p	DLD,MUT

isoleucine degradation	hsa00280	7	hsa-miR-30c-5p	ALDH2
			hsa-miR-195-5p	DLD,MUT
			hsa-let-7b-5p	EHHADH
Wnt signaling pathway	hsa04310	7	hsa-let-7c-5p	FZD2
			hsa-let-7e-5p	FZD2
			hsa-miR-204-5p	CAMK2D,PRICKLE2
			hsa-miR-30a-5p	PPP3CB
			hsa-miR-181a-5p	PRICKLE2
			hsa-miR-30c-5p	PPP3CB
			hsa-let-7b-5p	FZD2
NF-kappa B signali pathway	hsa04064	7	hsa-let-7e-5p	CFLAR
			hsa-miR-204-5p	BCL2
			hsa-miR-30a-5p	NFKB1
			hsa-let-7d-5p	CFLAR
			hsa-miR-16-5p	TIRAP
			hsa-miR-30c-5p	NFKB1
			hsa-miR-195-5p	TIRAP
Glycerophospholipid metabolism	hsa00564	7	hsa-miR-96-5p	PLD1
			hsa-miR-330-5p	AGPAT4
			hsa-miR-182-5p	PLD1,PPAP2A
			hsa-let-7d-5p	AGPAT4,AGPAT9
			hsa-miR-16-5p	PLD1
			hsa-miR-195-5p	PLD1
			hsa-let-7b-5p	AGPAT9
Lysine degradation	hsa00310	7	hsa-let-7c-5p	EHHADH
			hsa-miR-130b-5p	SETD2
			hsa-let-7e-5p	EHHADH
			hsa-miR-30a-5p	ALDH2
			hsa-miR-30c-5p	ALDH2
			hsa-miR-9-5p	SETD2
			hsa-let-7b-5p	EHHADH
Citrate cycle (TCA cycle)	hsa00020	7	hsa-let-7c-5p	CS
			hsa-let-7e-5p	CS
			hsa-miR-30a-5p	IDH1
			hsa-miR-30c-5p	IDH1
			hsa-miR-16-5p	DLD
			hsa-miR-195-5p	DLD
			hsa-let-7b-5p	CS
mTOR signaling pathway	hsa04150	6	hsa-miR-181b-5p	PIK3R3
			hsa-miR-30a-5p	PIK3CD
			hsa-miR-181a-5p	PIK3R3
			hsa-miR-30c-5p	PIK3CD
			hsa-miR-16-5p	CAB39,RRAGA

			hsa-miR-195-5p	CAB39,RRAGA
Glycerolipid metabolism	hsa00561	6	hsa-miR-330-5p	AGPAT4
			hsa-miR-182-5p	PPAP2A
			hsa-miR-30a-5p	ALDH2
			hsa-let-7d-5p	AGPAT4,AGPAT9
			hsa-miR-30c-5p	ALDH2
			hsa-let-7b-5p	AGPAT9
Sphingolipid metabolism	hsa00600	6	hsa-let-7c-5p	ACER2
			hsa-let-7e-5p	ACER2
			hsa-miR-182-5p	PPAP2A
			hsa-let-7d-5p	ACER2
			hsa-miR-24-1-5p	UGT8
			hsa-let-7b-5p	ACER2
Focal adhesion	hsa04510	6	hsa-miR-181b-5p	PIK3R3
			hsa-miR-130b-5p	LAMC2
			hsa-miR-204-5p	BCL2
			hsa-miR-30a-5p	PIK3CD
			hsa-miR-181a-5p	PIK3R3
			hsa-miR-30c-5p	PIK3CD
p53 signaling pathway	hsa04115	6	hsa-miR-125a-5p	CASP8
			hsa-let-7c-5p	ATR,FAS,PMAIP1
			hsa-let-7e-5p	ATR,PMAIP1
			hsa-let-7d-5p	ATR,FAS
			hsa-miR-125b-5p	CASP8
			hsa-let-7b-5p	ATR,FAS,PMAIP1
Inositol phospha metabolism	hsa00562	6	hsa-let-7c-5p	PLCE1
			hsa-let-7e-5p	PLCE1
			hsa-let-7d-5p	PLCE1
			hsa-miR-30a-5p	PIK3CD
			hsa-miR-30c-5p	PIK3CD
			hsa-let-7b-5p	PLCE1
NOD-like receptor signali pathway	hsa04621	5	hsa-miR-125a-5p	CASP8
			hsa-miR-30a-5p	NFKB1
			hsa-miR-30c-5p	NFKB1
			hsa-miR-9-5p	CCL2
			hsa-miR-125b-5p	CASP8
2-Oxocarboxylic ac metabolism	hsa01210	5	hsa-let-7c-5p	CS
			hsa-let-7e-5p	CS
			hsa-miR-30a-5p	IDH1
			hsa-miR-30c-5p	IDH1
			hsa-let-7b-5p	CS
			hsa-let-7c-5p	FZD2
			hsa-let-7e-5p	FZD2

Hippo signaling pathway	hsa04390	5	hsa-miR-30a-5p	PPP2R2A
			hsa-miR-30c-5p	PPP2R2A
			hsa-let-7b-5p	FZD2
Fatty acid degradation	hsa00071	5	hsa-let-7c-5p	EHHADH
			hsa-let-7e-5p	EHHADH
			hsa-miR-30a-5p	ALDH2
			hsa-miR-30c-5p	ALDH2
			hsa-let-7b-5p	EHHADH
Amino sugar and nucleoti sugar metabolism	hsa00520	5	hsa-let-7c-5p	GALE
			hsa-miR-330-5p	UGDH
			hsa-let-7e-5p	GALE
			hsa-let-7d-5p	GALE,GMPPA
			hsa-let-7b-5p	GALE
Glyoxylate and	hsa00630	5	hsa-let-7c-5p	CS
dicarboxylate metabolism			hsa-let-7e-5p	CS
			hsa-miR-16-5p	MUT
			hsa-miR-195-5p	MUT
			hsa-let-7b-5p	CS
Biosynthesi s of amino acids	hsa01230	5	hsa-let-7c-5p	CS
			hsa-let-7e-5p	CS
			hsa-miR-30a-5p	IDH1
			hsa-miR-30c-5p	IDH1
			hsa-let-7b-5p	CS
Tryptophan metabolism	hsa00380	5	hsa-let-7c-5p	EHHADH
			hsa-let-7e-5p	EHHADH
			hsa-miR-30a-5p	ALDH2
			hsa-miR-30c-5p	ALDH2
			hsa-let-7b-5p	EHHADH
TGF-beta signaling pathway	hsa04350	5	hsa-let-7c-5p	ACVR2A,E2F5
			hsa-let-7e-5p	ACVR2A,E2F5
			hsa-miR-182-5p	ACVR2A
			hsa-let-7d-5p	ACVR2A,E2F5
			hsa-let-7b-5p	ACVR2A,E2F5
Cytosolic DNA-sensi pathway	hsa04623	5	hsa-miR-5579-3p	POLR1D
			hsa-miR-30a-5p	NFKB1,TBK1
			hsa-miR-16-5p	POLR1C
			hsa-miR-30c-5p	NFKB1,TBK1
			hsa-miR-195-5p	POLR1C
ErbB signaling pathway	hsa04012	5	hsa-miR-181b-5p	PIK3R3
			hsa-miR-204-5p	CAMK2D
			hsa-miR-30a-5p	PIK3CD
			hsa-miR-181a-5p	PIK3R3
			hsa-miR-30c-5p	PIK3CD

Ether lipid metabolism	hsa00565	5	hsa-miR-96-5p	PLD1
			hsa-miR-182-5p	PLD1,PPAP2A
			hsa-miR-16-5p	PLD1
			hsa-miR-195-5p	PLD1
			hsa-miR-24-1-5p	UGT8
Central carbon metabolis in cancer	hsa05230	4	hsa-miR-181b-5p	PIK3R3
			hsa-miR-30a-5p	IDH1,PIK3CD
			hsa-miR-181a-5p	PIK3R3
			hsa-miR-30c-5p	IDH1,PIK3CD
Nucleotide excision repair	hsa03420	4	hsa-miR-5579-3p	GTF2H1
			hsa-miR-330-5p	POLD3
			hsa-miR-16-5p	CUL4A
			hsa-miR-195-5p	CUL4A
VEGF signaling pathway	hsa04370	4	hsa-miR-181b-5p	PIK3R3
			hsa-miR-30a-5p	PIK3CD,PPP3CB
			hsa-miR-181a-5p	PIK3R3
			hsa-miR-30c-5p	PIK3CD,PPP3CB
Cell cycle	hsa04110	4	hsa-let-7c-5p	ATR,E2F5
			hsa-let-7e-5p	ATR,E2F5
			hsa-let-7d-5p	ATR,E2F5
			hsa-let-7b-5p	ATR,E2F5
Glycolysis / Gluconeogenesi	hsa00010	4	hsa-miR-30a-5p	ALDH2
			hsa-miR-16-5p	DLD
			hsa-miR-30c-5p	ALDH2
			hsa-miR-195-5p	DLD
mRNA surveillance pathway	hsa03015	4	hsa-miR-181b-5p	PPP2R3A
			hsa-miR-30a-5p	PPP2R2A
			hsa-miR-181a-5p	PPP2R3A
			hsa-miR-30c-5p	PPP2R2A
Pyruvate metabolism	hsa00620	4	hsa-miR-30a-5p	ALDH2
			hsa-miR-16-5p	DLD
			hsa-miR-30c-5p	ALDH2
			hsa-miR-195-5p	DLD
FoxO signaling pathway	hsa04068	4	hsa-miR-181b-5p	PIK3R3
			hsa-miR-30a-5p	PIK3CD
			hsa-miR-181a-5p	PIK3R3
			hsa-miR-30c-5p	PIK3CD
Carbohydrate digestion and absorption	hsa04973	4	hsa-miR-181b-5p	PIK3R3
			hsa-miR-30a-5p	PIK3CD
			hsa-miR-181a-5p	PIK3R3
			hsa-miR-30c-5p	PIK3CD
			hsa-let-7c-5p	GALE
			hsa-let-7e-5p	GALE

Galactose metabolism	hsa00052	4	hsa-let-7d-5p	GALE
			hsa-let-7b-5p	GALE
Autoimmune thyroid disease	hsa05320	3	hsa-let-7c-5p	FAS
			hsa-let-7d-5p	FAS
			hsa-let-7b-5p	FAS
Fatty acid metabolism	hsa01212	3	hsa-let-7c-5p	EHHADH
			hsa-let-7e-5p	EHHADH
			hsa-let-7b-5p	EHHADH
Ascorbate and aldara metabolism	hsa00053	3	hsa-miR-330-5p	UGDH
			hsa-miR-30a-5p	ALDH2
			hsa-miR-30c-5p	ALDH2
PPAR signaling pathway	hsa03320	3	hsa-let-7c-5p	EHHADH
			hsa-let-7e-5p	EHHADH
			hsa-let-7b-5p	EHHADH
Thyroid hormone synthesis	hsa04918	2	hsa-miR-96-5p	ITPR1
			hsa-miR-182-5p	ITPR1

Table 9 Correlation of miRNAs and their target genes with molecular pathways in the PTC1 cell line. Each path has a unique code from the KEGG database. miRNAs and their target genes involved in each pathway were listed.

Chapter 3

Discrimination of AGO members in mice and in surgical specimens

To better understand the gene expression differences of the four AGO family members, we conducted experiments in mice and more specifically, we isolate different organs of black 6 mice. Liver, testis, spleen and intestines were selected as organs of interest. AGO2 and AGO3 were tested in these organs. An increase in AGO2 and AGO3 was observed, especially, in spleen (Figure S1). AGO3 was also increased in spleen and decreased in other organs suggesting an organ-specific expression of AGO members. Besides, spleen

Then, head, placenta, body and fetal liver from mice (black 6) were also examined regarding AGO2 and AGO3 expression levels (Figure S2). The common event between the two embryos tested is that AGO2 was very increased compared to AGO3, especially in placenta and the embryonic body indicating that the catalytic activity of AGO2 is more essential than that of AGO3.

AGO3 seemed to be decrease and almost stable across the different parts of the embryo.

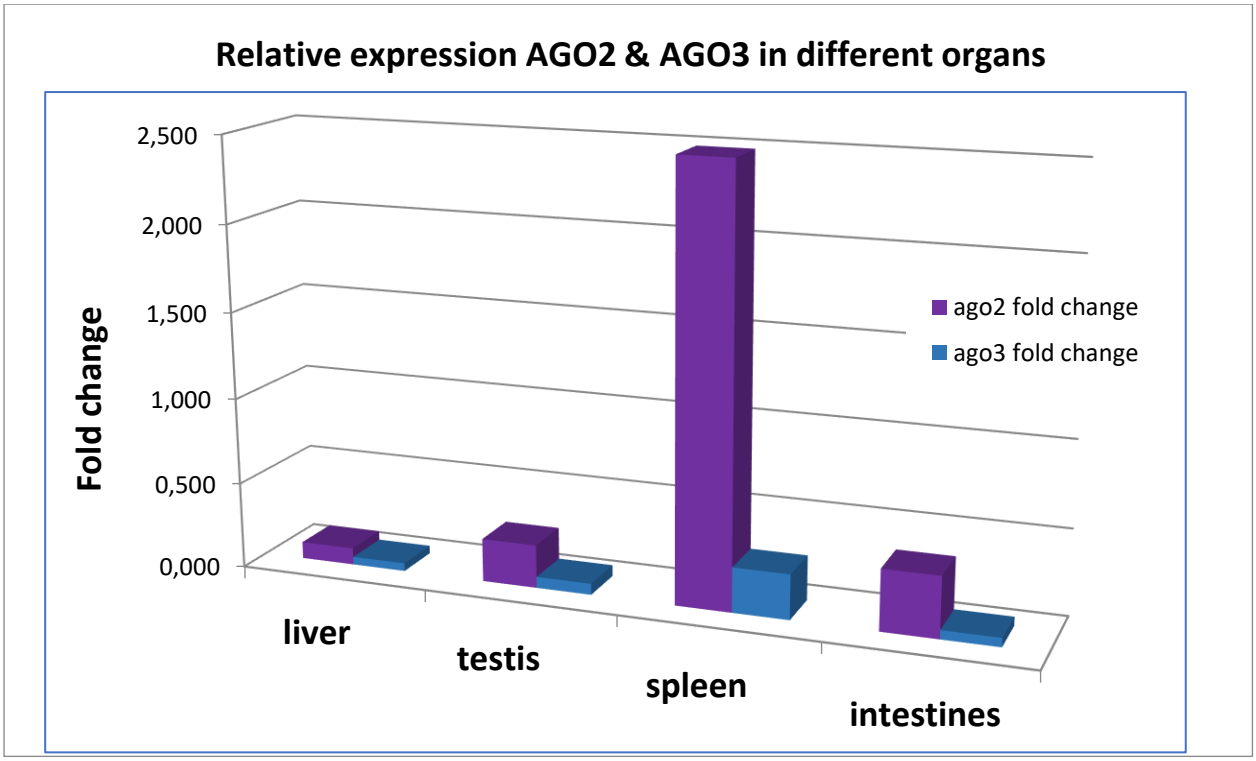

Figure S1 Relative expression levels of AGO2 and AGO3 across different organs: liver, testis, spleen and intestines in mice (black 6).

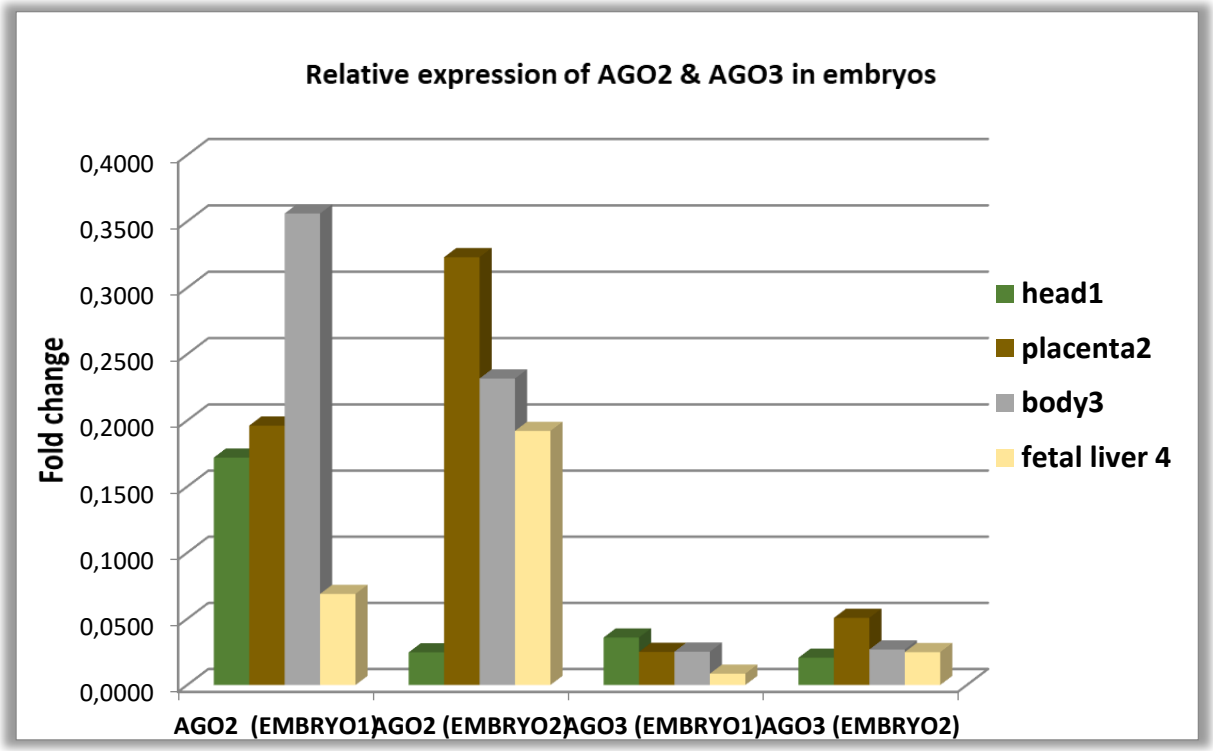

Figure S2 Relative expression levels of AGO2 and AGO3 across different parts: head, placenta, body and fetal liver in mouse embryos (black 6).

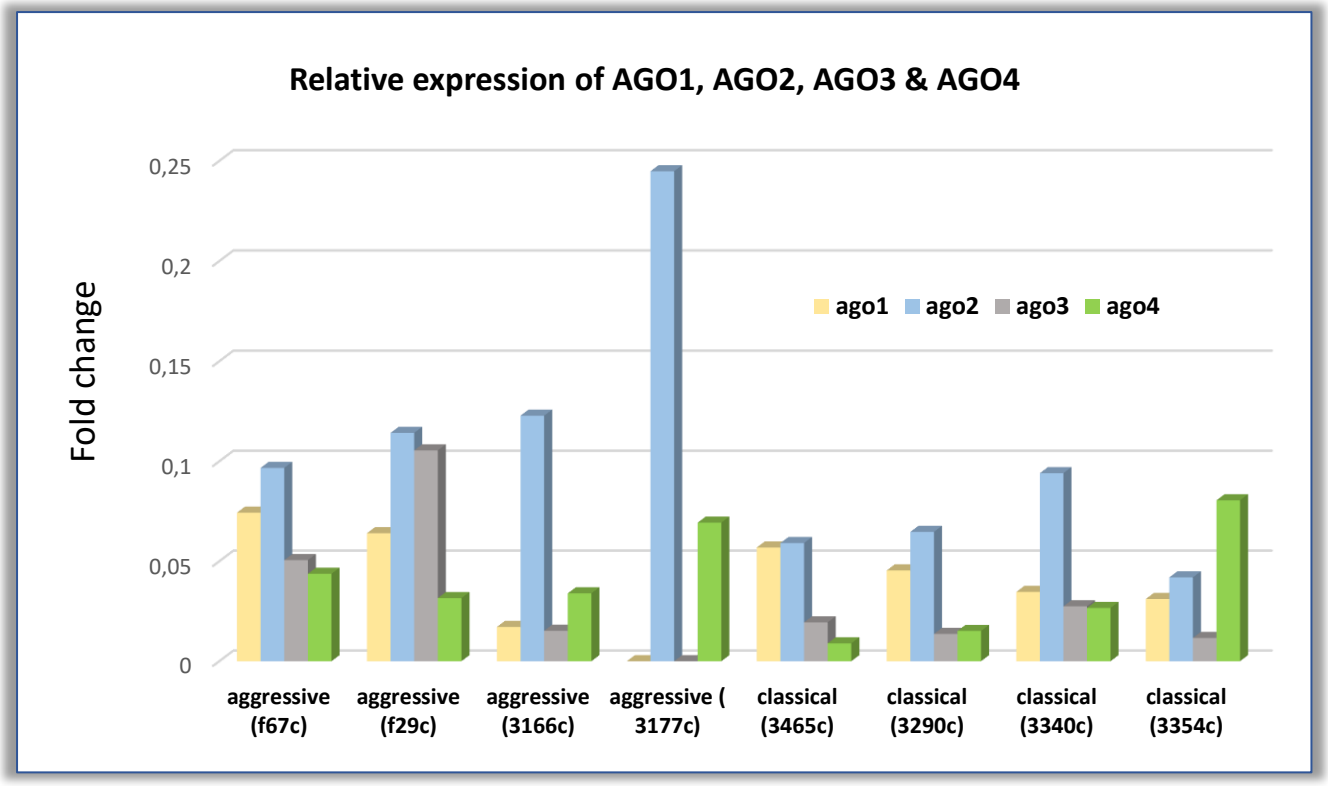

Figure S3 Relative expression levels of AGO1,2,3 and AGO4 across aggressive and classical variants of PTC surgical specimens. c: cancerous tissue. AGO1 in beige, AGO2 in blue, AGO3 in purple and AGO4 in green.

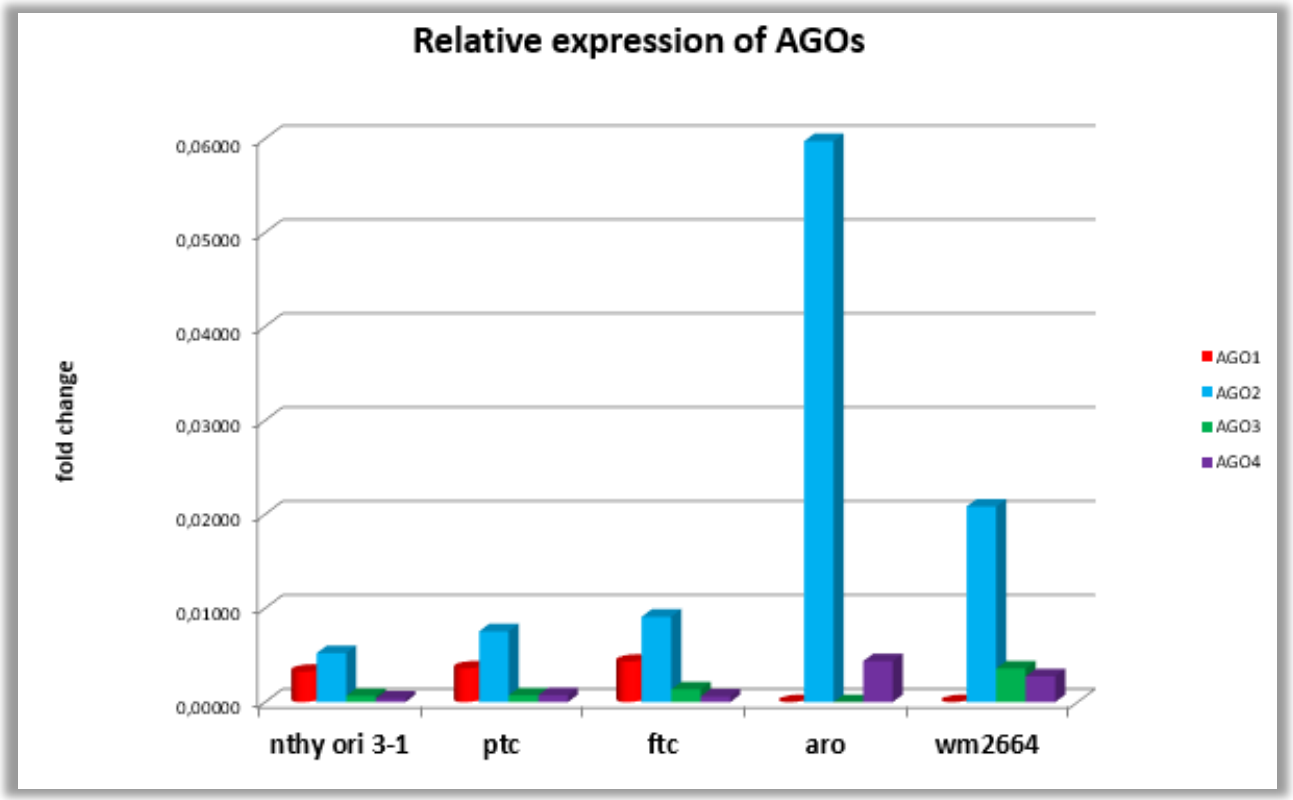

Figure S4 AGO expression levels across thyroid normal and cancer cell lines and of a melanoma cell line. Expression of AGO1, 2, 3 and 4 in NTHY ori 3-1, PTC, FTC133, ARO and WM2664.

Thereafter, we examined the relative expression levels of AGO1,2,3 and AGO4 in human thyroid cancer tissues to corroborate the aforementioned results in mice. We selected 4 aggressive and 4 common-non aggressive cancer tissues. The interesting finding, in this experiment, is that all AGO family members are elevated in aggressive variants, whereas in classic variants, they found noticeably reduced (Figure S3). Also, in classic variants, although all AGO family members are reduced, AGO2 constitutes the highest percentage except one sample. AGO1 and AGO3 do not present a big variance across the non-aggressive samples. An intriguing observation is that in 3177 cancerous tissue, where AGO2 is extremely elevated, AGO1 and AGO3 seem to be dramatically reduced, however AGO4 is expressed in expected levels. The same results were observed in the examination of AGO expression levels in ARO anaplastic cell line when compared to other less aggressive cell lines, such as NTHY ori 3-1, PTC and FTC133 cell line (Figure S4). This suggests an AGO4, almost AGO2-independent, role, however AGO1 and AGO3 are expressed in more decreased levels compared to AGO2 probably acting subsidiarily to the catalytic activity of the latter.

Negative controls during AGO2 colocalization analysis

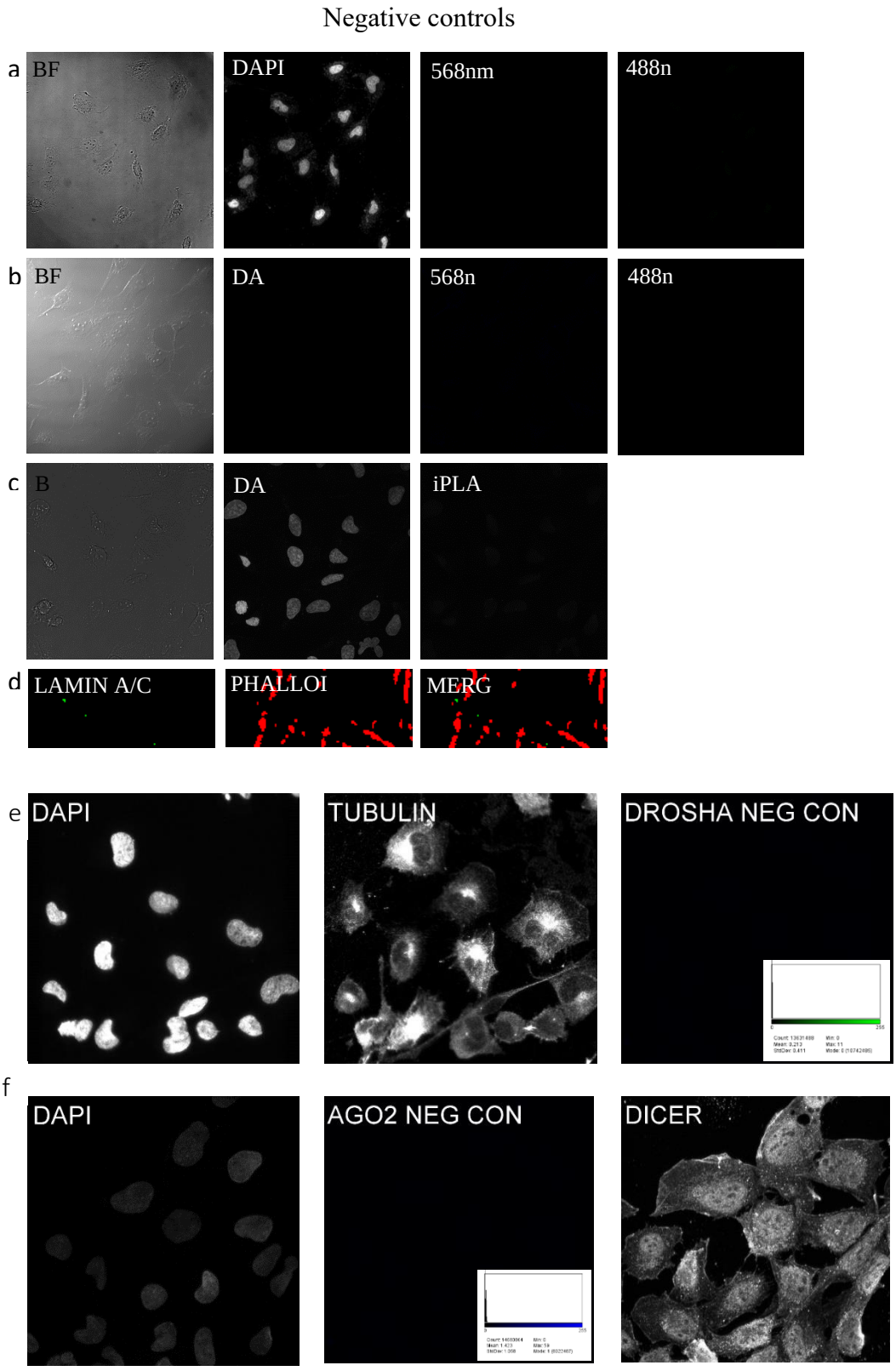

Figure S5 (a) Negative control of NTHY ori 3-1 cells stained with DAPI and secondary antibodies (without primary antibodies), (b) Negative control for autofluorescence (only fixed cells), (c) Negative control for PLAi experiment (IgG control), (d) Colocalization control, cytoplasmic region where Lamin A/C (green) and phalloidin (Texas-red) are known to anti- colocalize. (e) Negative control for red secondary antibody, α-Tubulin (green) and nuclei (blue). In the red channel anti-Drosha primary antibody staining without red secondary antibody. (f) Negative control for green secondary antibody, Dicer stained red and nuclei (blue) by DAPI. In the green channel anti-AGO2 primary antibody staining without green secondary antibody. (e,f) Signal histograms in the negative channels.

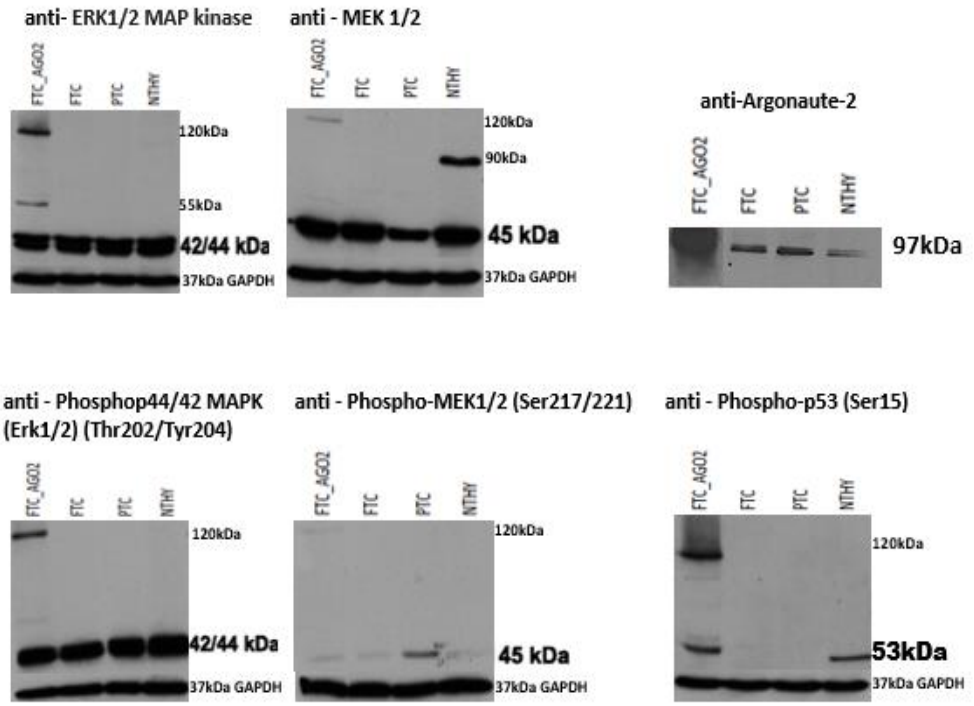

Figure S6 Immunoblotting of kinases. Comparison of protein expression levels between AGO2 and kinases ERK ½, MEK1/2, Phosphop44/42 MAPK (Erk1/2) (Thr202/Tyr204), Phospho-MEK1/2 (Ser217/221), Phospho-p53 (Ser15).

AGOs protein alignment in humans by Clustal Omega

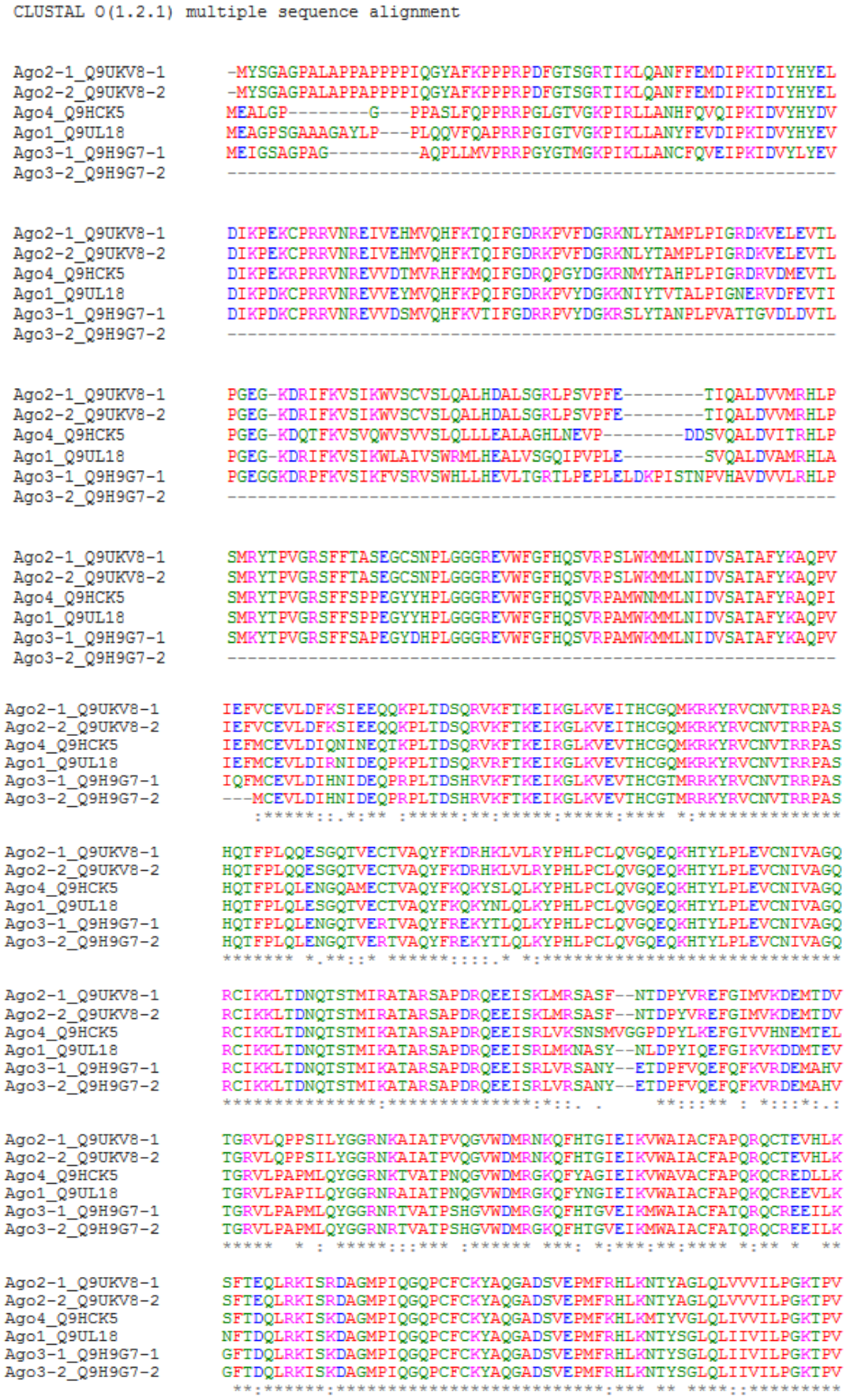

```
Ago2-1_Q9UKV8-1       YAEVKRVGDIVLGMATQCVQMKNVQRTTPQTLSNLCLKINVKLGGVNNILLPQGRPPVFQ
Ago2-2_Q9UKV8-2       YAEVKRVGDIVLGMATQCVQMKNVQRTTPQTLSNLCLKINVKLGGVNNILLPQGRPPVFQ
Ago4_Q9HCK5           YAEVKRVGDILLGMATQCVQVKNVVKTSPQTLSNLCLKINAKLGGINNVLVPHQRPSVFQ
Ago1_Q9UL18           YAEVKRVGDILLGMATQCVQVKNVVKTSPQTLSNLCLKINVKLGGINNILVPHQRSAVFQ
Ago3-1_Q9H9G7-1       YAEVKRVGDILLGMATQCVQVKNVIKTSPQTLSNLCLKINVKLGGINNILVPHQRPSVFQ
Ago3-2_Q9H9G7-2       YAEVKRVGDILLGMATQCVQVKNVIKTSPQTLSNLCLKINVKLGGINNILVPHQRPSVFQ
                      **********:*********:*** :*:************.****:**:*:*: *  ***

Ago2-1_Q9UKV8-1       QPVIFLGADVTHPPAGDGKKPSIAAVVGSMDAHPNRYCATVRVQQHRQE----------I
Ago2-2_Q9UKV8-2       QPVIFLGADVTHPPAGDGKKPSIAAVVGSMDAHPNRYCATVRVQQHRQE----------I
Ago4_Q9HCK5           QPVIFLGADVTHPPAGDGKKPSIAAVVGSMDGHPSRYCATVRVQTSRQEISQELLYSQEV
Ago1_Q9UL18           QPVIFLGADVTHPPAGDGKKPSITAVVGSMDAHPSRYCATVRVQRPRQE----------I
Ago3-1_Q9H9G7-1       QPVIFLGADVTHPPAGDGKKPSIAAVVGSMDAHPSRYCATVRVQRPRQE----------I
Ago3-2_Q9H9G7-2       QPVIFLGADVTHPPAGDGKKPSIAAVVGSMDAHPSRYCATVRVQRPRQE----------I
                      ************************:*******.**.*********  ***          :

Ago2-1_Q9UKV8-1       IQDLAAMVRELLIQFYKSTRFKPTRIIFYRDGVSEGQFQQVLHHELLAIREACIKLEKDY
Ago2-2_Q9UKV8-2       IQDLAAMVRELLIQFYKSTRFKPTRIIFYRDGVSEGQFQQVLHHELLAIREACIKLEKDY
Ago4_Q9HCK5           IQDLTNMVRELLIQFYKSTRFKPTRIIYYRGGVSEGQMKQVAWPELIAIRKACISLEEDY
Ago1_Q9UL18           IEDLSYMVRELLIQFYKSTRFKPTRIIFYRDGVPEGQLPQILHYELLAIRDACIKLEKDY
Ago3-1_Q9H9G7-1       IQDLASMVRELLIQFYKSTRFKPTRIIFYRDGVSEGQFRQVLYYELLAIREACISLEKDY
Ago3-2_Q9H9G7-2       IQDLASMVRELLIQFYKSTRFKPTRIIFYRDGVSEGQFRQVLYYELLAIREACISLEKDY
                      *:**: **********************:** ** ***: *:   **:***.***.**:**

Ago2-1_Q9UKV8-1       QPGITFIVVQKRHHTRLFCTDKNERVGKSGNIPAGTTVDIKITHPTEFDFYLCSHAGIQG
Ago2-2_Q9UKV8-2       QPGITFIVVQKRHHTRLFCTDKNER-------------------------------G
Ago4_Q9HCK5           RPGITYIVVQKRHHTRLFCADKTERVGKSGNVPAGTTVDSTITHPSEFDFYLCSHAGIQG
Ago1_Q9UL18           QPGITYIVVQKRHHTRLFCADKNERIGKSGNIPAGTTVDTNITHPFEFDFYLCSHAGIQG
Ago3-1_Q9H9G7-1       QPGITYIVVQKRHHTRLFCADRTERVGRSGNIPAGTTVDTDITHPYEFDFYLCSHAGIQG
Ago3-2_Q9H9G7-2       QPGITYIVVQKRHHTRLFCADRTERVGRSGNIPAGTTVDTDITHPYEFDFYLCSHAGIQG
                      :****:**************:*:.**                                 *

Ago2-1_Q9UKV8-1       TSRPSHYHVLWDDNRFSSDELQILTYQLCHTYVRCTRSVSIPAPAYYAHLVAFRARYHLV
Ago2-2_Q9UKV8-2       TSRPSHYHVLWDDNRFSSDELQILTYQLCHTYVRCTRSVSIPAPAYYAHLVAFRARYHLV
Ago4_Q9HCK5           TSRPSHYQVLWDDNCFTADELQLLTYQLCHTYVRCTRSVSIPAPAYYARLVAFRARYHLV
Ago1_Q9UL18           TSRPSHYYVLWDDNRFTADELQILTYQLCHTYVRCTRSVSIPAPAYYARLVAFRARYHLV
Ago3-1_Q9H9G7-1       TSRPSHYHVLWDDNCFTADELQLLTYQLCHTYVRCTRSVSIPAPAYYAHLVAFRARYHLV
Ago3-2_Q9H9G7-2       TSRPSHYHVLWDDNCFTADELQLLTYQLCHTYVRCTRSVSIPAPAYYAHLVAFRARYHLV
                      ******* ****** *:;****:**************************:**********

Ago2-1_Q9UKV8-1       DKEHDSAEGSHTSGQSNGRDHQALAKAVQVHQDTLRTMYFA
Ago2-2_Q9UKV8-2       DKEHDSAEGSHTSGQSNGRDHQALAKAVQVHQDTLRTMYFA
Ago4_Q9HCK5           DKDHDSAEGSHVSGQSNGRDPQALAKAVQIHHDTQHTMYFA
Ago1_Q9UL18           DKEHDSGEGSHISGQSNGRDPQALAKAVQVHQDTLRTMYFA
Ago3-1_Q9H9G7-1       DKEHDSAEGSHVSGQSNGRDPQALAKAVQIHQDTLRTMYFA
Ago3-2_Q9H9G7-2       DKEHDSAEGSHVSGQSNGRDPQALAKAVQIHQDTLRTMYFA
                      **:***.**** ******** ********:*:** :*****
```